

## ABSTRACT

MCCORMICK, TRACY LYNN. Three-Dimensional Radar and Total Lightning Characteristics of Mesoscale Convective Systems. (Under the direction of Dr. Lawrence D. Carey).

The radar and electrical characteristics of three linear leading-convective, trailing-stratiform midlatitude mesoscale convective systems (MCSs) that passed through Dallas-Fort Worth, Texas on the following dates are examined: 1) 7-8 April 2002, 2) 12-13 October 2001, and 3) 16 June 2002. Quantitative results from the April and June MCSs are presented, but data problems with the October MCS restricted partitioned analysis to qualitative results. The convective line produced ~69% and ~93% of the total cloud-to-ground (CG) lightning flashes in the April and June MCSs, respectively. The convective line CG flash rate averaged 12.3 flashes  $\text{min}^{-1}$  (53.6 flashes  $\text{min}^{-1}$ ) in the April (June) case study, and only 7.5% (2%) of these flashes were positive in polarity. Lightning Detection and Ranging (LDAR II) source data identified two main electrically-active regions present within the convective line in the following temperature layers: 1) 0 to -25 °C, and 2) -35 to -55 °C. The lower region (1) was most likely a combination of the main negative and the lower positive charge centers of the thunderstorm tripole, and the upper region (2) was most likely the upper positive charge center of this tripole. Convective echo volume aloft ( $\geq 30$  dBZ, 0 to -40 °C) was strongly correlated to convective lightning activity, suggesting that the presence of strong updrafts and differential sedimentation caused convective line electrification via the non-inductive charging (NIC) mechanism.

The stratiform region CG flash rate averaged  $2.2 \text{ flashes min}^{-1}$  ( $4.5 \text{ flashes min}^{-1}$ ) in the April (June) case study, and  $\sim 45\%$  ( $\sim 27\%$ ) of these flashes were positive in polarity. LDAR II source data identified one primary electrically-active layer (at  $-10$  to  $-25 \text{ }^\circ\text{C}$ ) that was sloped from the upper portions of the convective line rearward to just above the bright band in the stratiform region. A small and spatially distinct secondary electrically-active layer (at  $\sim -40 \text{ }^\circ\text{C}$ ) was located towards the rear of the stratiform region. These two layers had smaller average source concentrations than the convective line had, resulting in significantly less lightning production in the stratiform region than in the convective line. Hydrometeor trajectory analyses using storm-relative vertical and horizontal motions determined from synthetic dual-Doppler results indicate that these two stratiform region layers become electrified by a combination of 1) positive charge advection from the upper-positive convective charge center to the stratiform region and 2) stratiform in situ charging via NIC, likely creating an inverted dipole. This inverted dipole may explain why the +CG flash percentage was significantly higher in the stratiform region than in the convective region (where a normal dipole is present). In addition, stratiform echo volume aloft ( $\geq 25 \text{ dBZ}$ ,  $-10$  to  $-40 \text{ }^\circ\text{C}$ ) was strongly correlated to stratiform lightning activity, suggesting that differential sedimentation as a result of the presence of larger ice aggregates (i.e.  $Z > 25 \text{ dBZ}$ ) at these temperatures was required for stratiform region electrification via both charge advection and in-situ charging.

**THREE-DIMENSIONAL RADAR AND TOTAL LIGHTNING CHARACTERISTICS  
OF MESOSCALE CONVECTIVE SYSTEMS**

By  
**TRACY LYNN MCCORMICK**

A thesis submitted to the Graduate Faculty of  
North Carolina State University  
in partial fulfillment of the  
requirements for the Degree of  
Master of Science

**MARINE, EARTH, AND ATMOSPHERIC SCIENCES**

Raleigh

2003

**APPROVED BY:**

---

Dr. Lawrence D. Carey  
(Chair of Advisory Committee)

---

Dr. Gary Lackmann  
(Advisory Committee Member)

---

Dr. Al Riordan  
(Advisory Committee Member)

## **BIOGRAPHY**

Tracy was born in Bellingham, MA in July of 1979. She has always been fascinated with the weather, especially stormy weather of all types, so she decided to attend Lyndon State College (LSC) in Vermont after graduating valedictorian from Bellingham Memorial Jr./Sr. High School in 1997. During the past six years, Tracy has also participated in various internship experiences including two WPRI-TV 12 Meteorological internships in Providence, RI, a Weather Services International (WSI) Meteorological Operations internship in Billerica, MA, the Research Experiences for Undergraduates (REU) program in Norman, OK, and a Science Applications International Corporation (SAIC) internship in Hampton, VA.

After graduating Magna Cum Laude and being named "Outstanding Senior" from LSC with a B.S. in Meteorology and a B.A. in Mathematics in May 2001, Tracy received an American Meteorological Society (AMS) fellowship and began graduate school in atmospheric science at NCSU in August 2001. Tracy presented her preliminary research results on "Three-dimensional radar and total lightning characteristics of mesoscale convective systems" in a poster presentation at the Annual Fall American Geophysical Union (AGU) meeting in San Francisco, CA in December 2002.

## ACKNOWLEDGEMENTS

I would like to thank the members of my advisory committee, Drs. Larry Carey, Gary Lackmann, and Al Riordan, for their insights and helpful suggestions, as well as Dr. Roscoe Braham, who provided a unique perspective on key aspects of this research. I would especially like to thank Dr. Larry Carey for his constant support, ideas, and collaborative efforts. Thank you to Dr. Gary Lackmann for providing me with surface and upper air data for my three MCS cases. Thank you to Martin Murphy and Nick Demetriades for providing LDAR II data for all three case studies and for continuous assistance throughout this research project. I would also like to thank Larry Belcher for his countless computer assistance and the initial IDL code template from which all of the graphical images generated in my research are based. Thank you to NCAR/MMM for use of the CEDRIC software package and to NCDC for providing KFWS radar data for my research. Thank you to the Radar Meteorology group at Colorado State University, especially Robert Cifelli and Paul Hein, for providing me with CEDRIC code and computer help in order to perform synthetic dual-Doppler three-dimensional wind analyses. I would like to thank Richard Yablonsky, my fiancé, for his continuous support, ideas, and helpful suggestions with my MS research, and for carefully proofreading and suggesting revisions to my thesis. Last but not least, I would like to thank all of my family, relatives, and friends for their love, encouragement, and faith in me throughout my educational career. This research is supported by North Carolina State University and a one-year AMS/NOAA Office of Global Programs graduate fellowship.

# TABLE OF CONTENTS

	Page
<b>LIST OF TABLES</b> . . . . .	<b>viii</b>
<b>LIST OF FIGURES</b> . . . . .	<b>ix</b>
<b>1. INTRODUCTION</b> . . . . .	<b>1</b>
1.1 Mesoscale Convective Systems (MCSs) and Their Importance . . . . .	1
1.2 Lightning and Its Importance . . . . .	2
1.3 Conceptual Models . . . . .	2
1.3.1 MCS Structure . . . . .	2
1.3.1.1 Convective Region . . . . .	3
1.3.1.2 Transition Zone . . . . .	5
1.3.1.3 Stratiform Region . . . . .	6
1.3.2 MCS Microphysics . . . . .	8
1.3.3 MCS Formation and Precipitation Structure Classifications . . . . .	10
1.3.3.1 Favorable Synoptic Scale Conditions . . . . .	10
1.3.3.2 Convective Line Formation Characteristics . . . . .	12
1.3.3.3 MCS Evolution . . . . .	13
1.3.3.3.1 Linear and Nonlinear MCSs . . . . .	13
1.3.3.3.2 Trailing, Parallel, and Leading Stratiform Region MCSs . . . . .	14
1.3.3.3.3 Symmetric and Asymmetric MCSs . . . . .	15
1.3.4 Thunderstorm Charge Structure . . . . .	18
1.3.4.1 Electrification . . . . .	18
1.3.4.1.1 Non-inductive Charging . . . . .	18
1.3.4.1.2 Inductive Charging . . . . .	20
1.3.4.1.3 Additional Charging Layers . . . . .	21
1.3.4.1.3.1 Lower Positive Charge Layer . . . . .	21
1.3.4.1.3.2 Screening Layer . . . . .	23
1.3.4.1.4 Field Study Example of Thunderstorm Charge Distribution . . . . .	23
1.3.4.2 Lightning Flash . . . . .	24
1.3.5 MCS Charge Structure . . . . .	26
1.3.5.1 Convective Region . . . . .	27
1.3.5.2 Transition Zone . . . . .	29
1.3.5.3 Stratiform Region . . . . .	30

1.4	Relationship of MCS Structure to Lightning . . . . .	34
1.4.1	Convective Region . . . . .	35
1.4.2	Stratiform Region . . . . .	36
1.4.3	Total Echo Volume Aloft . . . . .	37
1.4.4	Rainfall Rates . . . . .	39
1.5	Motivation and Hypothesis . . . . .	41
<b>2.</b>	<b>DATA AND METHODOLOGY . . . . .</b>	<b>56</b>
2.1	KFWS WSR-88D Level II Radar Data . . . . .	56
2.1.1	Methods of Analysis . . . . .	57
2.1.1.1	Partitioning Techniques . . . . .	59
2.1.1.2	Echo Volume Aloft Calculations . . . . .	62
2.1.1.3	Rainfall Rate Calculations . . . . .	62
2.1.1.4	Dual-Doppler Analysis . . . . .	64
2.1.1.4.1	Overview . . . . .	64
2.1.1.4.2	Synthetic Dual-Doppler Analysis . . . . .	66
2.2	National Lightning Detection Network (NLDN) Data . . . . .	69
2.2.1	Overview . . . . .	69
2.2.2	Subsetting and Analysis Techniques . . . . .	70
2.3	Lightning Detection and Ranging (LDAR II) Network Data . . . . .	71
2.3.1	Detection Technique . . . . .	72
2.3.2	Detection Efficiency and Location Accuracy . . . . .	73
2.3.3	Subsetting and Analysis Techniques . . . . .	74
2.3.4	Flash Algorithms and Plotting Techniques . . . . .	76
<b>3.</b>	<b>CASE STUDY OBSERVATIONS #1: 7-8 APRIL 2002 MCS . . . . .</b>	<b>86</b>
3.1	Synoptic Overview . . . . .	86
3.2	MCS Formation and Precipitation Structure Classifications . . . . .	88
3.2.1	Favorable Synoptic Scale Conditions . . . . .	88
3.2.2	Convective Line Formation Characteristics . . . . .	88
3.2.3	MCS Evolution . . . . .	89
3.2.3.1	Linear and Nonlinear MCSs . . . . .	89
3.2.3.2	Trailing, Parallel, and Leading Stratiform Region MCSs . . . . .	90
3.2.3.3	Symmetric and Asymmetric MCSs . . . . .	90
3.2.4	Important Temperature Levels . . . . .	91
3.2.5	Storm Damage Reports . . . . .	92
3.3	WSR-88D Radar . . . . .	92

3.3.1	Data Gaps . . . . .	92
3.3.2	General MCS Characteristics . . . . .	93
3.3.3	Total Echo Volume Aloft . . . . .	94
	3.3.3.1 Total MCS Characteristics . . . . .	94
	3.3.3.2 Partitioned MCS Characteristics . . . . .	96
3.3.4	Rainfall Rates . . . . .	97
3.3.5	Synthetic Dual-Doppler Analysis . . . . .	98
3.4	NLDN CG Lightning Flash Trends . . . . .	99
	3.4.1 Total Trends . . . . .	99
	3.4.2 Partitioned Trends . . . . .	100
3.5	LDAR II Data . . . . .	102
	3.5.1 Network's Performance . . . . .	102
	3.5.2 VHF Source Trends . . . . .	102
	3.5.2.1 Total Trends . . . . .	102
	3.5.2.2 Partitioned Trends . . . . .	103
	3.5.3 VHF Flash Origin Trends . . . . .	109
	3.5.3.1 Total Trends . . . . .	109
	3.5.3.2 Partitioned Trends . . . . .	109
3.6	Summary . . . . .	111

**4. CASE STUDY OBSERVATIONS #2: 12-13 OCTOBER 2001 MCS 165**

4.1	Background Characteristics . . . . .	165
	4.1.1 Synoptic Overview . . . . .	165
	4.1.2 Storm Damage Reports . . . . .	168
4.2	WSR-88D Radar . . . . .	169
	4.2.1 Data Gaps . . . . .	169
	4.2.2 General MCS Characteristics . . . . .	169
	4.2.3 Total Echo Volume Aloft . . . . .	171
4.3	NLDN CG Lightning Flash Trends . . . . .	172
4.4	LDAR II Data . . . . .	173
	4.4.1 Network's Performance . . . . .	173
	4.4.2 VHF Source Trends . . . . .	173
	4.4.3 VHF Flash Origin Trends . . . . .	175
4.5	Summary . . . . .	176

**5. CASE STUDY OBSERVATIONS #3: 16 JUNE 2002 MCS . . . 204**

5.1	Background Characteristics . . . . .	204
	5.1.1 Synoptic Overview . . . . .	204
	5.1.2 Storm Damage Reports . . . . .	207
5.2	WSR-88D Radar . . . . .	207
	5.2.1 General MCS Characteristics . . . . .	207
	5.2.2 Partitioned Echo Volume Aloft . . . . .	208
	5.2.3 Partitioned Rainfall Rates . . . . .	212

5.2.4	Dual-Doppler Analysis . . . . .	213
5.3	NLDN CG Lightning Flash Trends . . . . .	214
5.3.1	Total Trends . . . . .	214
5.3.2	Partitioned Trends . . . . .	216
5.4	LDAR II Data . . . . .	218
5.4.1	Network's Performance . . . . .	218
5.4.2	VHF Source Trends . . . . .	218
5.4.2.1	Total Trends . . . . .	218
5.4.2.2	Partitioned Trends . . . . .	218
5.4.3	VHF Flash Origin Trends . . . . .	225
5.4.3.1	Total Trends . . . . .	225
5.4.3.2	Partitioned Trends . . . . .	226
5.5	Summary . . . . .	228
<b>6.</b>	<b>DISCUSSION . . . . .</b>	<b>289</b>
<b>7.</b>	<b>CONCLUSIONS AND FUTURE RESEARCH . . . . .</b>	<b>303</b>
<b>8.</b>	<b>REFERENCES . . . . .</b>	<b>308</b>
<b>APPENDICES . . . . .</b>		<b>319</b>
<b>APPENDIX A.</b>	<b>THE RADAR BRIGHT BAND . . . . .</b>	<b>320</b>
<b>APPENDIX B.</b>	<b>THE BULK RICHARDSON NUMBER . . . . .</b>	<b>322</b>
<b>APPENDIX C.</b>	<b>THE DUAL-DOPPLER METHOD . . . . .</b>	<b>323</b>
<b>APPENDIX D.</b>	<b>LDAR II FLASH ALGORITHMS . . . . .</b>	<b>329</b>
<b>APPENDIX E.</b>	<b>THE TORNADIC CELL . . . . .</b>	<b>349</b>

## LIST OF TABLES

	<b>Page</b>
Table 1.1 Weather-related fatalities per year for 30 years(1959-1990), as well as death and injury totals in 1994 (adapted from Curran et al. 2000) . . . . .	43
Table 1.2 Convective weather-related fatalities, injuries, and property damage reports per year from 1992-94 (adapted from Curran et al. 2000).	43
Table D.1 Statistical comparisons between each LDAR II flash algorithm for 04:00-05:00 UTC 13 October 2001 at all height levels . . . . .	334
Table D.2 Same as Table D.1 but for 01:00-02:00 UTC 8 April 2002 . . . . .	336
Table D.3 Correlation coefficients between each algorithm at various 2.0-km height increments for 04:00-05:30 UTC 13 October 2001 . . . . .	338
Table D.4 Same as Table D.3 but for 01:00-02:00 UTC 8 April 2002 . . . . .	339

## LIST OF FIGURES

	<b>Page</b>
FIG. 1.1 Conceptual model of an idealized leading convective, trailing stratiform mature mesoscale convective system (MCS) . . . . .	44
FIG. 1.2 Vertical cross-section conceptual model of the two-dimensional hydrometeor trajectories through a leading convective, trailing stratiform region MCS . . . . .	45
FIG. 1.3 Four idealized types of mesoscale convective line development and their evolution with time . . . . .	46
FIG. 1.4 Three patterns of MCS structure as proposed by Blanchard (1990) . . . . .	46
FIG. 1.5 Conceptual model of the evolution of the three main classifications of MCSs: (a) trailing stratiform (TS), (b) leading stratiform (LS), and (c) parallel stratiform (PS), proposed by Parker and Johnson (2000)	47
FIG. 1.6 Conceptual model of a TS (a) symmetric, and (b) asymmetric MCS . . . . .	47
FIG. 1.7 Conceptual model of (a) a two-dimensional MCS, and (b) an MCS with a mid-level well-defined mesoscale vortex . . . . .	48
FIG. 1.8 Conceptual model of the non-inductive charging method in an ordinary isolated thunderstorm . . . . .	48
FIG. 1.9 Charge (in $10^{-15}$ C) gained by graupel particles resulting from the collision of graupel with ice crystals as a function of cloud liquid water content (LWC) and temperature . . . . .	49
FIG. 1.10 Conceptual model of Wilson's selective ion capture mechanism . . . . .	49

FIG. 1.11	Conceptual model of the mechanism involving rebounding collisions of two polarized hydrometeors . . . . .	50
FIG. 1.12	Schematic of the main convective charge regions in a thunderstorm both within and outside the updraft . . . . .	50
FIG. 1.13	Schematic of the different types of lightning flashes . . . . .	51
FIG. 1.14	Conceptual model of MCS charge structure . . . . .	52
FIG. 1.15	Conceptual model of leading convective line MCS charge structure within updraft and non-updraft regions . . . . .	53
FIG. 1.16	Control run of (a) snow mixing ratio ( $\text{g kg}^{-1}$ ), (b) cloud liquid water content ( $\text{g m}^{-3}$ ), and (c) cloud ice concentration ( $\text{L}^{-1}$ ) at $t = 3$ hr . . . . .	54
FIG. 1.17	Total charge density magnitude ( $\text{nC m}^{-3}$ ) in the stratiform region for the charge advection sensitivity model run at $t = 3$ hr using a the Marshall and Rust (1993) "type A" charge density profile and the Saunders et al. (1991) non-inductive charging data . . . . .	55
FIG. 2.1	VCP11 WSR-88D scanning strategy ("severe weather mode") coverage . . . . .	77
FIG. 2.2	Following the Steiner et al. (1995) partitioning method, the amount of dB a given grid point must exceed the 11 km radius mean background reflectivity value by in order to be classified as convective . . . . .	77
FIG. 2.3	Example of the results obtained using the Steiner et al. (1995) partitioning method using 0.5 km constant altitude KFWS reflectivity data from the 8 April 2002 MCS at 01:29 UTC . . . . .	78

FIG. 2.4	Example of the subjective line partitioning method using a 0.5 km constant altitude KFWS radar reflectivity data from the 8 April 2002 MCS at 01:29 UTC . . . . .	79
FIG. 2.5	Dual-Doppler coverage area (i.e. "dual-Doppler lobes") . . . . .	80
FIG. 2.6	Locations of the 106 NLDN sensors nationwide	81
FIG. 2.7	Locations of the seven sensors associated with the LDAR II network and the KFWS WSR-88D radar . . . . .	82
FIG. 2.8	Photograph of an LDAR II sensor . . . . .	83
FIG. 2.9	Percent (%) of lightning flashes that can be detected by the LDAR II network . . . . .	84
FIG. 2.10	Location accuracy (in km) of VHF source locations detected by the LDAR II network .	85
FIG. 3.1	250-mb analysis for 12 UTC 7 April 2002 . .	114
FIG. 3.2	Same as Fig. 3.1, but for 00 UTC 8 April 2002 . . . . .	115
FIG. 3.3	500-mb analysis for 12 UTC 7 April 2002 . .	116
FIG. 3.4	Same as Fig. 3.3, but for 00 UTC 8 April 2002 . . . . .	117
FIG. 3.5	700-mb analysis for 12 UTC 7 April 2002 . .	118
FIG. 3.6	Same as Fig. 3.5, but for 00 UTC 8 April 2002 . . . . .	119
FIG. 3.7	850-mb analysis for 12 UTC 7 April 2002 . .	120
FIG. 3.8	Same as Fig. 3.7, but for 00 UTC 8 April 2002 . . . . .	121
FIG. 3.9	18 UTC 7 April 2002 manual surface analysis for Texas and surrounding areas . . . . .	122
FIG. 3.10	Dallas-Fort Worth, Texas soundings valid at a) 00 UTC and b) 12 UTC 8 April 2002 . . . .	123

FIG. 3.11	Base NEXRAD reflectivity images of the developing convective line (boxed) located in western TX at (a) 17:30 UTC 7, (b) 17:45 UTC 7, (c) 18:00 UTC 7, and (d) 18:15 UTC 7 April 2002 . . . . .	124
FIG. 3.12	Base NEXRAD reflectivity images of the developing MCS located in central TX at (a) 19:30 UTC 7, (b) 22:00 UTC 7, (c) 00:00 UTC 8, and (d) 00:45 UTC 8 April 2002 . . . . .	125
FIG. 3.13	Base NEXRAD reflectivity images of the MCS located in eastern TX at (a) 02:00 UTC 8, (b) 04:00 UTC 8, (c) 06:00 UTC 8, and (d) 08:00 UTC 8 April 2002 . . . . .	126
FIG. 3.14	Preliminary severe storm damage reports including hail ( $\geq 0.75''$ , green dots), strong winds ( $\geq 58$ mph, blue dots), and tornadoes (red dots) from 12:00 UTC 7 through 12:00 UTC 8 April 2002 . . . . .	127
FIG. 3.15	0.5 km CAPPI image of radar reflectivity (dBZ) in a 200 km $\times$ 200 km grid box at a) 00:24 UTC, b) 00:59 UTC, c) 01:29, and d) 02:23 UTC 8 April 2002 . . . . .	128
FIG. 3.16	(a) A 0.5 km CAPPI image, and b) a line-normal vertical cross-section through (a) at $y = 15$ km at 01:29 UTC 8 April 2002 . . . . .	129
FIG. 3.17	Total echo volume aloft trend $\geq 30$ dBZ from 00 to 04 UTC 8 April 2002, time averaged every 5 min with a 6-point running mean smoother . . . . .	130
FIG. 3.18	Same as Fig. 3.17, but for total echo volume aloft $\geq 35$ dBZ . . . . .	131
FIG. 3.19	Same as Fig. 3.17, but for total echo volume aloft $\geq 40$ dBZ . . . . .	132
FIG. 3.20	Partitioned echo volume aloft trends $\geq 30$ dBZ from 00 to 04 UTC 8 April 2002, time averaged every 5 min with a 6-point running mean smoother . . . . .	133

FIG. 3.21	Same as Fig. 3.20, but echo volume aloft was calculated using the $-10^{\circ}\text{C}$ to $-40^{\circ}\text{C}$ layer . . . . .	134
FIG. 3.22	Partitioned rainfall rate trends calculated from 00 to 04 UTC 8 April 2002, time averaged every 5 min with a 6-point running mean smoother . . . . .	135
FIG. 3.23	Total CG lightning flash trends within a portion of the 7-8 April 2002 MCS that is within the KFWS radar's viewing range from 00 to 04 UTC, time averaged every 5 min with a 6-point running mean smoother . . . . .	136
FIG. 3.24	CG lightning peak positive (red line) and negative (blue line) current (kA) trends from 00 to 04 UTC 8 April 2002, time averaged every 5 min with a 6 point running mean smoother . . . . .	137
FIG. 3.25	0.5 km radar reflectivity (dBZ) CAPPI image of the 7-8 April 2002 MCS at 01:24 UTC 8 overlaid with 5 min of NLDN CG lightning flash data (centered on time of radar image) . . . . .	138
FIG. 3.26	Convective (blue line), stratiform (red line), and total (violet line) CG lightning flash trends from 00 to 04 UTC 8 April 2002, time averaged every 5 min with a 6-point running mean smoother . . . . .	139
FIG. 3.27	Convective region CG lightning flashes (blue line) and the percent of +CG flashes (red line) trends from 00 to 04 UTC 8 April 2002, time averaged every 5 min with a 6-point running mean smoother . . . . .	140
FIG. 3.28	Same as Fig. 3.27, but for the stratiform region . . . . .	141
FIG. 3.29	Temporal evolution of the convective (blue lines) and stratiform (red lines) CG lightning peak positive and negative currents (kA) from 00 to 04 UTC 8 April 2002, time averaged every 5 min with a 6-point running mean smoother . . . . .	142

FIG. 3.30	Detection efficiency of the LDAR II network during the 7-8 April 2002 MCS . . . . .	143
FIG. 3.31	LDAR II source trend within the KFWS radar viewing range from 00 to 04 UTC 8 April 2002, time averaged every 5 min with a 6-point running mean smoother . . . . .	144
FIG. 3.32	0.5 km CAPPI image of radar reflectivity (dBZ) with LDAR II sources overlaid (black dots) at 01:19 UTC 8 April 2002 . . . . .	145
FIG. 3.33	Vertical cross-section of the convective line at 01:19 UTC 8 April 2002 taken line parallel through Fig. 3.32 at a) $x = 34$ km (the leading edge of the convective line), and b) $x = 15$ km (the back edge of the convective line) . . . . .	146
FIG. 3.34	Same as Fig. 3.33, but these vertical cross-sections were taken line-parallel through a) the front edge of the stratiform region at $x = -30$ km, and b) the back edge of the stratiform region at $x = -66$ km, as depicted in Fig. 3.32 . . . . .	147
FIG. 3.35	Vertical cross-sections of the 01:19 UTC 8 April 2002 MCS in Fig. 3.32 taken line-perpendicular through a) the stratiform, transition, and convective regions at $y = 50$ km, and b) the stratiform region, transition zone enhanced reflectivity "bridge", and convective line at $y = -18$ km . . . . .	148
FIG. 3.36	Convective region (blue line) and stratiform region (red line) LDAR II source trends from 00 to 04 UTC 8 April 2002, time averaged every 5 min with a 6-point running mean smoother . . . . .	149
FIG. 3.37	Average (blue line), minimum (pink line), maximum (orange line), median (green line), 25 <sup>th</sup> percentile (violet line), and 75 <sup>th</sup> percentile (brown line) number of sources within the convective region for each 1-km height level from 0 km to 20 km from 00 to 04 UTC 8 April 2002 . . . . .	150

FIG. 3.38	Same as Fig. 3.37, but for the stratiform region . . . . .	151
FIG. 3.39	Line-normal composite radar reflectivity and LDAR II source images at 00:39 UTC 8 April 2002, where a) the number of sources versus line-normal horizontal distance is plotted, b) a vertical cross-section (height versus the x component of distance (km) from the KFWS radar) of average radar reflectivity (dBZ) is line-contoured (0-dBZ, every 5-dBZ), and the total number of LDAR II sources is color-shaded as indicated by the scale, and c) the number of sources versus height (km) is plotted . . . . .	152
FIG. 3.40	Same as Fig. 3.39, except at 00:59 UTC 8 . . . . .	153
FIG. 3.41	Same as Fig. 3.39, except at 01:04 UTC 8 . . . . .	154
FIG. 3.42	Same as Fig. 3.39, except at 01:09 UTC 8 . . . . .	155
FIG. 3.43	Same as Fig. 3.39, except at 01:14 UTC 8 . . . . .	156
FIG. 3.44	Same as Fig. 3.39, except at 01:19 UTC 8 . . . . .	157
FIG. 3.45	Same as Fig. 3.39, except at 02:03 UTC 8 . . . . .	158
FIG. 3.46	Same as Fig. 3.39, except at 02:23 UTC 8 . . . . .	159
FIG. 3.47	LDAR II flash origin trend within the KFWS radar viewing range from 00 to 04 UTC 8 April 2002, time averaged every 5 min with a 6-point running mean smoother . . . . .	160
FIG. 3.48	Temporal trend in the IC:CG ratio from 00 to 04 UTC 8 April 2002, time averaged every 5 min with a 6-point running mean smoother . . . . .	161
FIG. 3.49	Convective region (blue line) and stratiform region (red line) LDAR II flash origin (as determined by the modified NASA algorithm) trends from 00 to 04 UTC 8 April 2002, time averaged every 5 min with a 6-point running mean smoother . . . . .	162

FIG. 3.50	Average (blue line), minimum (pink line), maximum (orange line), median (green line), 25 <sup>th</sup> percentile (violet line), and 75 <sup>th</sup> percentile (brown line) number of LDAR II flash origins within the convective region for each 1-km height level from 0 km to 20 km from 00 to 04 UTC 8 April 2002 . . . . .	163
FIG. 3.51	Same as Fig. 3.50, but for the stratiform region . . . . .	164
FIG. 4.1	250-mb analysis for 12 UTC 12 October 2001 . . . . .	178
FIG. 4.2	Same as Fig. 4.1, but for 00 UTC 13 October 2001 . . . . .	179
FIG. 4.3	500-mb analysis for 12 UTC 12 October 2001 . . . . .	180
FIG. 4.4	Same as Fig. 4.3, but for 00 UTC 13 October 2001 . . . . .	181
FIG. 4.5	700-mb analysis for 12 UTC 12 October 2001 . . . . .	182
FIG. 4.6	Same as Fig. 4.5, but for 00 UTC 13 October 2001 . . . . .	183
FIG. 4.7	850-mb analysis for 12 UTC 12 October 2001 . . . . .	184
FIG. 4.8	Same as Fig. 4.7, but for 00 UTC 13 October 2001 . . . . .	185
FIG. 4.9	21 UTC 12 October 2001 surface analysis for Texas and surrounding areas . . . . .	186
FIG. 4.10	2-km resolution NEXRAD mosaic reflectivity images from a squall line that evolves into a TS MCS at (a) 21 UTC 12, (b) 00 UTC 13, (c) 4 UTC 13, and (d) 08 UTC 13 October 2001 . . . . .	187
FIG. 4.11	Dallas-Fort Worth, Texas soundings valid for (a) 00 UTC 13, and (b) 12 UTC 13 October 2001 . . . . .	188

FIG. 4.12	Preliminary severe storm damage reports, including hail ( $\geq 0.75''$ ) (green dots), strong winds ( $\geq 58$ mph) (blue dots), and tornadoes (red dots) from 12 UTC 12 through 12 UTC 13 October 2001 . . . . .	189
FIG. 4.13	0.5 km constant altitude radar reflectivity images of the development of the 12-13 October 2001 MCS at (a) 01 UTC, (b) 2:29 UTC, (c) 4:32 UTC, and (d) 5:32 UTC . . . . .	190
FIG. 4.14	a) A 0.5 km CAPPI image, and b) a vertical cross-section through (a) at $x = 50$ km at 02:29 UTC 13 October 2001 . . . . .	191
FIG. 4.15	Total echo volume aloft trends $\geq 30$ dBZ (blue line), $\geq 35$ dBZ (maroon line), and $\geq 40$ dBZ (teal line) from 00:45 to 05:32 UTC 13 October 2001, time averaged every 5 min with a 6-point running mean smoother. Total echo volume aloft ( $\text{km}^3$ ) was calculated between the $0^\circ\text{C}$ to $-40^\circ\text{C}$ temperature layer . . . . .	192
FIG. 4.16	0.5 km radar reflectivity (dBZ) CAPPI image of the 12-13 October 2001 MCS at 04:47 UTC 13 overlaid with 5 min of NLDN CG lightning flash data (centered on the time of the radar image) . . . . .	193
FIG. 4.17	CG lightning flash (blue line) and percent of +CG lightning flash (red line) trends from 00:45 to 05:32 UTC 13 October 2001, time averaged every 5 min with a 6-point running mean smoother . . . . .	194
FIG. 4.18	Temporal evolution of the peak positive (red line) and negative (blue line) currents (kA) from 00:45 to 05:32 UTC 13 October 2001, time averaged every 5 min with a 6-point running mean smoother . . . . .	195
FIG. 4.19	Detection efficiency of the LDAR II network during the 12-13 October 2001 MCS . . . . .	196
FIG. 4.20	LDAR II source trend from 00:45 to 05:32 UTC 13 October 2001, time averaged every 5 min with a 6-point running mean smoother . . . . .	197

FIG. 4.21	0.5 km CAPPI image of radar reflectivity (dBZ) with LDAR II sources overlaid (black dots) at 02:29 UTC 13 October 2002 . . . . .	198
FIG. 4.22	Vertical cross-section of the leading convective line at 02:29 UTC 13 October 2001, taken line parallel through Fig. 4.23 at x = 50 km . . . . .	199
FIG. 4.23	Average (blue line), minimum (pink line), maximum (orange line), median (green line), 25 <sup>th</sup> percentile (violet line), and 75 <sup>th</sup> percentile (brown line) of LDAR II sources occurring within each 1-km height level from 0 to 20 km from 00:45 to 05:32 UTC 13 October 2001 . . . . .	200
FIG. 4.24	LDAR II flash origin trend (as determined by the modified NASA algorithm) from 00:45 to 05:32 UTC 13 October 2001, time averaged every 5 min with a 6-point running mean smoother . . . . .	201
FIG. 4.25	Average (blue line), minimum (pink line), maximum (orange line), median (green line), 25 <sup>th</sup> percentile (violet line), and 75 <sup>th</sup> percentile (brown line) of LDAR II flash origins occurring within each 1-km height level from 0 to 20 km from 00:45 to 05:32 UTC 13 October 2001 . . . . .	202
FIG. 4.26	IC:CG ratio trend from 00:45 05:32 UTC 13 October 2001, time averaged every 5 min with a 6-point running mean smoother . . . . .	203
FIG. 5.1	2-km resolution NEXRAD mosaic reflectivity images from a squall line that evolves into a TS MCS at (a) 19 UTC 15, (b) 22 UTC 15, (c) 02 UTC 16, and (d) 06 UTC 16 June 2002 . . . . .	233
FIG. 5.2	250-mb analysis for 12 UTC 15 June 2002 . . . . .	234
FIG. 5.3	Same as Fig. 5.2, but for 00 UTC 16 June 2002 . . . . .	235
FIG. 5.4	500-mb analysis for 12 UTC 15 June 2002 . . . . .	236

FIG. 5.5	Same as Fig. 5.4, but for 00 UTC 16 June 2002 . . . . .	237
FIG. 5.6	700-mb analysis for 12 UTC 15 June 2002 . . . . .	238
FIG. 5.7	Same as Fig. 5.6, but for 00 UTC 16 June 2002 . . . . .	239
FIG. 5.8	850-mb analysis for 12 UTC 15 June 2002 . . . . .	240
FIG. 5.9	Same as Fig. 5.8, but for 00 UTC 16 June 2002 . . . . .	241
FIG. 5.10	12 UTC 15 June 2002 U.S. surface analysis . . . . .	242
FIG. 5.11	Dallas-Fort Worth, Texas soundings valid at a) 00 UTC and b) 12 UTC 16 June 2002 . . . . .	243
FIG. 5.12	Preliminary severe storm damage reports including hail ( $\geq 0.75''$ ) (green dots), strong winds ( $\geq 58$ mph) (blue dots), and tornadoes (red dots) from 12 UTC 15 through 12 UTC 16 June 2002 . . . . .	244
FIG. 5.13	0.5-km constant altitude radar reflectivity images of the development of the 16 June 2002 MCS at (a) 05:25 UTC, (b) 05:54 UTC, (c) 06:24 UTC, and (d) 06:54 UTC . . . . .	245
FIG. 5.14	a) A 0.5-km CAPPI image, and b) a line- normal vertical cross-section through (a) at $y = 26$ km at 06:24 UTC 16 June 2002 . . . . .	246
FIG. 5.15	Convective region total echo volume aloft trend ( $\text{km}^3$ ) $\geq 25$ dBZ (red line), $\geq 30$ dBZ (blue line), $\geq 35$ dBZ (orange line), and $\geq 40$ dBZ (violet line) within the $0^\circ\text{C}$ to $-40^\circ\text{C}$ temperature layer, time averaged every 15 min . . . . .	247
FIG. 5.16	Convective region total echo volume aloft ( $\text{km}^3$ ) $\geq 35$ dBZ for the $0$ to $-40$ C layer (blue line, values on primary y-axis) and the $-10$ to $-40$ C layer (red line, values on secondary y-axis), time averaged every fifteen minutes (x-axis) . . . . .	248

FIG. 5.17	0.5 km constant altitude radar reflectivity images of the evolution of the 16 June 2002 MCS at (a) 05:40 UTC, (b) 05:44 UTC, (c) 05:54 UTC, and (d) 06:09 UTC . . . . .	249
FIG. 5.18	Stratiform region total echo volume aloft trend ( $\text{km}^3$ ) $\geq 25$ dBZ (red line), $\geq 30$ dBZ (blue line), $\geq 35$ dBZ (orange line), and $\geq 40$ dBZ (violet line) and within the $0^\circ\text{C}$ to $-40^\circ\text{C}$ temperature layer, time averaged every 5 min with a 3-point running mean smoother . . . . .	250
FIG. 5.19	Same as Fig. 5.18, but for echo volume aloft within the $-10^\circ\text{C}$ to $-40^\circ\text{C}$ temperature layer . . . . .	251
FIG. 5.20	Convective rainfall rate trend determined using a low-level reflectivity threshold of 5 dBZ (blue line), 10 dBZ (orange line), and 20 dBZ (violet line), time averaged every 5 min with a 3-point running mean smoother . . . . .	252
FIG. 5.21	Stratiform rainfall rate trend determined using a low-level reflectivity threshold of 5 dBZ (blue line), 10 dBZ (orange line), and 20 dBZ (violet line), time averaged every 5 min with a 3-point running mean smoother . . . . .	253
FIG. 5.22	Convective (blue line) and stratiform (red line) region rainfall rate trends from 05:00 to 07:00 UTC 16 June 2002, time averaged every 5 min with a 3-point running mean smoother . . . . .	254
FIG. 5.23	Mean convective region (line with solid diamonds) and stratiform region (line with open squares) vertical velocity ( $\text{ms}^{-1}$ ) from an 80-km long portion of the 16 June 2002 MCS . . . . .	255
FIG. 5.24	Total NLDN-detected CG flash trend (blue line) and the percent +CG lightning flash trend (red line) from 05:00 to 07:00 UTC 16 June 2002, time average every 5 min with a 3-point running mean smoother . . . . .	256

FIG. 5.25	Peak positive (red line) and negative (blue line) CG lightning flash current trends, time averaged every 5 min with a 3-point running mean smoother . . . . .	257
FIG. 5.26	0.5-km radar reflectivity (dBZ) CAPPI image of the 16 June 2002 MCS at 05:54 UTC overlaid with 5 min of NLDN CG lightning flash data (centered on time of radar image)	258
FIG. 5.27	Convective line, stratiform region, and total CG lightning flash trends from 5:00 to 7:00 UTC 16 June 2002, time averaged every 5 min with a 3-point running mean smoother .	259
FIG. 5.28	Convective line (blue line) and stratiform region (red line) percent +CG flash trend from 05:00 to 07:00 UTC 16 June 2002, time averaged every 5 min with a 3-point running mean smoother . . . . .	260
FIG. 5.29	Convective (blue lines) and stratiform (red lines) CG lightning peak positive and negative current trends (kA) from 05:00 to 07:00 UTC 16 June 2002, time averaged every 5 min with a 3-point running mean smoother .	261
FIG. 5.30	Detection efficiency of the LDAR II network during the 16 June 2002 MCS . . . . .	262
FIG. 5.31	Total LDAR II source trend while the 16 June 2002 MCS was within the KFWS radar viewing range (~05:00-07:00 UTC), time averaged every 5 min with a 3-point running mean smoother . . . . .	263
FIG. 5.32	0.5-km CAPPI image of radar reflectivity (dBZ) with LDAR II sources overlaid (black dots) at 06:19 UTC 16 June 2002 . . . . .	264
FIG. 5.33	Vertical cross-sections of the convective line at 06:19 UTC 16 June 2002 taken line-parallel through Fig. 5.32 at a) $x = 38$ km (the leading convective line), and b) $x = 25$ km (the back edge of the convective line) . . .	265

FIG. 5.34	Same as Fig. 5.33, but taken line-parallel through Fig. 5.32 at a) the front edge of the stratiform region at $x = -15$ km and b) the back edge of the stratiform region at $x = -41$ km . . . . .	266
FIG. 5.35	Vertical cross-sections of the 06:19 UTC UTC 16 June 2002 MCS in Fig. 5.32 taken line-perpendicular through a) the stratiform, transition, and convective regions at $y = 41$ km, and b) the stratiform region, transition zone enhanced reflectivity "bridge", and convective line at $y = 23$ km . . . . .	267
FIG. 5.36	Convective (blue line) and stratiform (red line) region LDAR II source trend from 05:00 to 07:00 UTC 16 June 2002, time averaged every 5 min with a 3-point running mean smoother . . . . .	268
FIG. 5.37	Average (blue line), minimum (pink line), maximum (orange line), median (green line), 25 <sup>th</sup> percentile (violet line), and 75 <sup>th</sup> percentile (brown line) of sources within the convective region for each 1-km height level from 0 km to 20 km from 05:00 to 07:00 UTC 16 June 2002 . . . . .	269
FIG. 5.38	Same as Fig. 5.37, but for the stratiform region . . . . .	270
FIG. 5.39	Line-normal composite radar reflectivity and LDAR II source images of the 16 June 2002 MCS at 05:20 UTC, where a) the number of sources versus line-normal horizontal distance is plotted, b) a vertical cross-section (height versus the x-component of distance (km) from the KFWS radar) of average radar reflectivity (dBZ) is line-contoured, and the total number of LDAR II sources is color-shaded according to the scale, and c) the number of sources versus height (km) is plotted . . . . .	271
FIG. 5.40	Same as Fig. 5.39, except at 06:09 UTC . . .	272
FIG. 5.41	Same as Fig. 5.39, except at 06:14 UTC . . .	273

FIG. 5.42	Same as Fig. 5.39, except at 06:19 UTC . . .	274
FIG. 5.43	Same as Fig. 5.39, except at 06:29 UTC . . .	275
FIG. 5.44	Same as Fig. 5.39, except at 06:34 UTC . . .	276
FIG. 5.45	Same as Fig. 5.39, except at 06:44 UTC . . .	277
FIG. 5.46	Same as Fig. 5.40(b) but with the $\sim -10 \text{ ms}^{-1}$ storm-relative front-to-rear flow (horizontal dotted white arrow), the typical hydrometeor fall velocity of $\sim 1.0 \text{ ms}^{-1}$ (vertical dotted white arrow), and the resulting storm-relative hydrometeor trajectory (slanted solid white arrow) overlaid on the downward and rearward sloping LDAR II source region . . . . .	278
FIG. 5.47	LDAR II flash origin trend for the portion of the 16 June 2002 MCS that was within the KFWS radar viewing range from 05:00 to 07:00 UTC, time averaged every 5 min with a 3- point running mean smoother . . . . .	279
FIG. 5.48	IC:CG ratio trend from 5:00 to 7:00 UTC 16 June 2002, time averaged every 5 min with a 3-point running mean smoother . . . . .	280
FIG. 5.49	0.5 km CAPPI image of radar reflectivity (dBZ) with LDAR II flash origins (as determined by the modified NASA algorithm) overlaid (black dots) at 06:19 UTC 16 June 2002 . . . . .	281
FIG. 5.50	Vertical cross-section of the convective line at 06:19 UTC 16 June 2002 taken line- parallel through Fig. 5.49 at a) $x = 38 \text{ km}$ (the leading convective line) and b) $x = 25$ (the back edge of the convective line) . . .	282
FIG. 5.51	Same as Fig. 5.50, but this vertical cross- section was taken line-parallel through Fig. 5.49 at a) the front edge of the stratiform region at $x = -15 \text{ km}$ , and b) the back edge of the stratiform region at $x = -41 \text{ km}$ . . .	283

FIG. 5.52	Vertical cross-sections of the 06:19 UTC 16 June 2002 MCS in Fig. 5.49 taken line-perpendicular through a) the stratiform, transition, and convective regions at $y = 41$ km and b) the stratiform region, transition zone enhanced reflectivity "bridge", and convective line at $y = 23$ km .	284
FIG. 5.53	Convective (blue line) and stratiform (red line) LDAR II flash origin trends (as determined by the modified NASA algorithm) from 05:00 to 07:00 UTC 16 June 2002, time averaged every 5 min with a 3-point running mean smoother . . . . .	285
FIG. 5.54	Average (blue line), minimum (pink line), maximum (orange line), median (green line), 25 <sup>th</sup> percentile (violet line), and 75 <sup>th</sup> percentile (brown line) of LDAR II flash origins within the convective region for each 1-km height level from 0 km to 20 km from 05:00 to 7:00 UTC 16 June 2002 . . . . .	286
FIG. 5.55	Same as Fig. 5.54, but for the stratiform Region . . . . .	287
FIG. 5.56	Convective and stratiform IC:CG ratio trends from 05:00 to 07:00 UTC 16 June 2002, time averaged every 5 min with a 3-point running mean smoother . . . . .	288
FIG. C.1	Diagram of two Doppler radars at different locations sampling a hydrometeor within a precipitation volume . . . . .	328
FIG. D.1	Comparison of seven different algorithms used to group LDAR II sources into flashes for the 8 April 2002 MCS . . . . .	340
FIG. D.2	Comparison of five various LDAR II flash algorithms including the 3.0-km, 0.15-sec; 3.0-km, 0.30-sec; 5.0-km, 0.15-sec; 5.0-km, 0.30-sec; and modified NASA algorithms for the 13 October 2001 MCS . . . . .	341

FIG. D.3	LDAR II flash origins at all heights created by the 3.0-km, 0.15-sec, 2.0-sec algorithm overlaid on the 0.5-km radar reflectivity height level of the Dallas/Fort Worth, TX area (KFWS) (200 × 200 km area) for 1:19 UTC 8 April 2002 MCS . . . . .	342
FIG. D.4	Same as Fig. D.3 but for the 3.0-km, 0.30-sec, 2.0-sec algorithm . . . . .	343
FIG. D.5	Same as Fig. D.3 but for the 5.0-km, 0.15-sec, 2.0-sec algorithm . . . . .	343
FIG. D.6	Same as Fig. D.3 but for the modified NASA algorithm . . . . .	344
FIG. D.7	LDAR II flash origins at all heights created by the 3.0-km, 0.15-sec, 2.0-sec algorithm overlaid on the 0.5-km radar reflectivity height level of the Dallas/Fort Worth, TX area (KFWS) (200 × 200 km area) for 4:47 UTC 13 October 2001 MCS . . . . .	345
FIG. D.8	Same as Fig. D.7 but for the 3.0-km, 0.30-sec, 2.0-sec algorithm . . . . .	346
FIG. D.9	Same as Fig. D.7 but for the 5.0-km, 15-sec, 2.0-sec algorithm . . . . .	346
FIG. D.10	Same as Fig. D.7 but for the modified NASA algorithm . . . . .	347
FIG. D.11	Comparison of the temporal variation of various LDAR II flash algorithms (including the 3.0-km, 0.15-sec; 3.0-km, 0.30-sec; 5.0-km, 0.15-sec; 5.0-km, 0.30-sec; and the modified NASA algorithms) at all heights (0 - 20 km) when the 12 - 13 October 2001 MCS was centered within the LDAR II network	348
FIG. D.12	Same as Fig. D.11 but for 8 April 2002 . . .	348
FIG. E.1	CG lightning flash trend (violet line) and the percent of +CGs (orange line) for the Decatur, Texas tornadic cell from 23:40 UTC 12 to 1:15 UTC 13 October 2001 . . . . .	353

FIG. E.2 Same as Fig. E.1, except the secondary y-axis represents the number of LDAR II flash origins (blue line) produced during a given 5-min time interval, and the number of CG flashes is plotted in red . . . . . 354

# 1. INTRODUCTION

## 1.1 Mesoscale Convective Systems (MCSs) and Their Importance

A mesoscale convective system (MCS)<sup>1</sup> is formally defined as a cloud complex associated with a group of thunderstorms that produces a continuous region of precipitation  $\geq 100$  km in at least one horizontal direction (Houze 1993; Glickman 2000). These large convective systems are also long-lived, with an average lifetime of 10 hrs (Houze et al. 1989). During its mature stage, an MCS is characterized by two main precipitation areas, the convective and stratiform regions, separated by a transition zone of light precipitation. The stratiform region is usually positioned behind the leading convective line, although in some instances, the stratiform region can be located either in front of, or parallel to, the convective line (Parker and Johnson 2000).

MCSs can produce flash floods and severe weather, including tornadoes, large hail, and/or strong winds (Houze 1990). MCSs are responsible for 30-70% of the central US warm-season (April – September) rainfall (Fritsch et al. 1986). In addition, MCSs can produce abundant lightning, with average cloud-to-ground (CG) flash rates of  $42 \text{ min}^{-1}$ , and peak CG flash rates approaching  $60 \text{ min}^{-1}$ . Typical MCS CG lightning flash rates average  $\sim 40 \text{ min}^{-1}$ . MCS CG lightning flashes account for a significant fraction of warm season CG lightning in the central U.S. (Goodman and MacGorman 1986).

---

<sup>1</sup> Note that this study refers to midlatitude squall line type MCSs and excludes other convective systems (e.g. tropical cyclones).

## **1.2 Lightning and Its Importance**

Lightning is an electrical discharge that occurs in the earth's atmosphere, resulting from a buildup of positive and negative electrical space charge generally within convective clouds. CG lightning flashes caused an average of 0.42 reported fatalities per million people per year in the US alone from 1959-1994 (Curran et al. 2000). Lightning is second only to flooding as the greatest cause of reported weather-related fatalities (Table 1), and it is the single greatest cause of reported convective weather-related fatalities (Table 2) (Curran et al. 2000). Actual lightning fatalities may be significantly larger because lightning-related deaths go underreported more often than any other weather event (Curran et al. 2000). Therefore, given the relatively large number of lightning casualties as well as the abundant lightning produced by MCSs, a solid understanding of MCS lightning characteristics may help save lives.

## **1.3 Conceptual Models**

### ***1.3.1 MCS Structure***

A conceptual model of an idealized leading convective, trailing stratiform mature MCS is depicted in Fig. 1.1. This image represents a vertical cross-section of an MCS oriented perpendicular to the leading convective line. The thick, dark line in the figure represents the MCS boundary as seen by weather radar, and the lighter scalloped line details the storm's boundaries as determined by satellite and aircraft observations. Regions of enhanced radar reflectivity are depicted as shaded areas within the MCS. Vertically oriented dark shaded areas of high reflectivity indicate regions of heavy rain and/or hail. Mesoscale low and high pressure areas are indicated by "L<sub>x</sub>" and "H<sub>y</sub>," respectively, where x = 1-4 and

y = 1-3. The dominant storm-relative flow patterns are depicted by arrows, and the freezing level is indicated in the figure.

### **1.3.1.1 Convective Region**

The initial stages of MCS formation begin with the development of the convective region. This region is most intense during its developing stages, when the stratiform precipitation area has not yet formed. At its mature stage, the convective line is generally characterized by: 1) convex arc shape appearance from the downstream vantage point, 2) NE-SW orientation, 3) rapid eastward or southeastward movement  $> 10 \text{ ms}^{-1}$  perpendicular to the line orientation, 4) continuous appearance (more intense cells are connected by less intense cells) with a jagged leading edge, 5) strong reflectivity gradient at the leading edge, 6) elongated intense cells oriented  $45\text{-}90^\circ$  with respect to the convective line, 6) reflectivity echoes  $> 40\text{-dBZ}$ , 7) strong vertical motions ( $\sim 1\text{-}32 \text{ ms}^{-1}$ ), and 8) ascending front-to-rear flow (Weisman and Klemp 1982; Houze et al. 1990; Houze 1993; Parker and Johnson 2000).

The formation of the convective region often begins when warm, moist air is forced to rise over cooler, denser air via a lifting mechanism (e.g. a cold front). The resulting updrafts create new convective cells, as indicated on weather radar by regions of enhanced reflectivity aloft. As water vapor continues to condense and particles accrete liquid water, the hydrometeors grow and are advected rearward and increasingly upward by the storm-relative slantwise-dominant ascending front-to-rear flow that initiates ahead of the convective line (Smull and Houze 1985; Houze et al. 1989; Houze 1993). Observational analysis by Rutledge et al. (1988) found typical storm-relative front-to-rear flow magnitudes of  $15 \text{ ms}^{-1}$ , with peak speeds up to  $25 \text{ ms}^{-1}$ . Similarly, Gallus and Johnson (1995a) determined peak front-to-rear flow magnitudes generally  $> 20 \text{ ms}^{-1}$ , sometimes reaching  $30 \text{ ms}^{-1}$ .

The convective cells develop intense, narrow updrafts (generally  $\leq 1$  km in width) that can penetrate through the tropopause. During the first few hours of development, these updrafts are nearly vertical. Updraft development is followed by the formation of 1) mid- to upper-level convective-scale downdrafts ( $\sim 1-10$   $\text{ms}^{-1}$ ) associated with the downward pressure perturbation force caused by buoyant updrafts and 2) low-level downdrafts ( $\sim 1-10$   $\text{ms}^{-1}$ ), associated with evaporation and precipitation drag of heavy surface rainfall and/or hail (i.e. water loading) (as indicated on radar by enhanced surface reflectivity cores) (Houze et al. 1989; Houze 1993). Later, when the convection begins to weaken, the updrafts become more slantwise due to the forward expansion of the low-level downdraft-generated cold pool near the surface (Rotunno et al. 1988; Houze et al. 1989). A small hydrostatic low ( $L_3$ , Fig. 1.1) develops under the most intense buoyant updraft as a result of latent release in the updraft column (LeMone 1983; Houze et al. 1989).

In addition to the enhancement of the surface cold pool, the low-level downdrafts create a surface mesohigh ( $H_1$ , Fig. 1.1). Both features build and strengthen below the convective cells, leading to the intensification of a gust front along or just ahead of the leading convective line (Smull and Houze 1985; Johnson and Hamilton 1988; Houze et al. 1989; Houze 1993). The MCS will be maintained as long as 1) the surface cold pool behind the gust front is constantly being reinforced by low-level downdrafts, 2) there is warm, moist air out in front of the gust front, 3) there is enough low-level shear to counter the cold outflow circulation produced, and 4) the gust front does not accelerate too far out ahead of the convective line. A weak surface mesolow ( $L_2$ , Fig. 1.1) develops ahead of the leading gust front as new cells continue to form out ahead of or along this front and mature, becoming part of the convective line (Fritsch and Chappell 1980; Houze et al. 1989). Details

concerning the formation of this mesolow are beyond the scope of this paper. Please see Fritsch and Chappell (1980) for more information.

A forward anvil, as pictured in Fig. 1.1, is not always present in an MCS. This anvil develops when environmental upper-level winds normal to the convective line flow from behind the convective region towards the leading edge of the convective line. Smaller ice crystals from the convective line are advected by these winds into the upper levels ahead of the line, producing a forward anvil (Houze 1993; Nachamkin et al. 2000).

Once older convective cells begin to weaken, they are advected by the storm-relative front-to-rear flow over a dense subsiding layer of storm-relative rear inflow and towards the back edge of the convective line (Fig. 1.2). This convective cell evolution persists for a few hours, and remnants from old convective cells will eventually form a stratiform region located behind the 10-50 km wide main convective line (Smull and Houze 1985; Houze et al. 1989; Houze 1993). The formation of a stratiform precipitation region, separated from the convective region by a transition zone, marks the beginning of an MCS's mature stage of development, as pictured in Fig. 1.1 (Houze 1993).

### **1.3.1.2 Transition Zone**

As ice particles are advected out of the convective region by the ascending front-to-rear flow (Fig. 1.2), the larger hydrometeors slowly fall into a transition precipitation zone since their fall speeds ( $\sim 1-3 \text{ ms}^{-1}$ ) are typically greater than the ascending flow ( $\sim 0.5 \text{ ms}^{-1}$ ) (Smull and Houze 1985; Rutledge et al. 1988; Houze 1993). As these hydrometeors fall, unable to effectively grow, their mass is reduced through sublimation and evaporation, and the remaining particles eventually reach the Earth's surface in the form of light precipitation. This transition zone downdraft region is characterized by deep subsidence, mid- to low-level

minimum in reflectivity values, and weak rain rates (Smull and Houze 1985; Biggerstaff and Houze 1991; Houze 1993; Gallus and Johnson 1995a).

### **1.3.1.3 Stratiform region**

Small ice particles with fall speeds less than that of the vertical component of the MCS ascending front-to-rear flow ( $\sim 0.5 \text{ ms}^{-1}$ ) are advected from the convective line past the transition zone into an area that will eventually develop into what is known as the stratiform precipitation region, as seen in Fig. 1.2 (Smull and Houze 1985). When fully developed, this stratiform region is characterized by its: 1) large size (50-150 km wide and  $>10^4 \text{ km}^2$  in horizontal area), 2) rear “notch-like” concavity, 3) reflectivity echoes 20-40-dBZ, 4) small vertical motions ( $<0.5 \text{ ms}^{-1}$ ), and 5) descending rear inflow (Smull and Houze 1985; Houze et al. 1990; Parker and Johnson 2000).

Ice particles slowly fall as they travel past the transition zone, first growing by vapor deposition in the ascending front-to-rear flow and then by aggregation to form large snow aggregates as they approach the freezing level within the stratiform region. The aggregates fall through this freezing level, melt, and produce a resulting radar bright band just below the melting level. As pictured in Fig. 1.2, the region of heaviest stratiform precipitation is located beneath the radar bright band, an area where the largest vertical motions within the stratiform region exist (Smull and Houze, 1985; Houze et al. 1989). For more information about the radar bright band, please see Appendix A.

As pictured in Fig. 1.2, the stratiform region is characterized by weak ( $< 0.5 \text{ ms}^{-1}$ ) mesoscale updraft and downdraft vertical motions separated by dry, descending rear inflow (Johnson and Hamilton 1988; Rutledge et al. 1988; Houze et al. 1989). The mesoscale updraft is found at altitudes above the descending rear inflow, whereas the mesoscale

downdraft extends from the top of the rear inflow down towards the Earth's surface. Observational results from Rutledge et al. (1988) determined storm-relative peak mesoscale updraft magnitudes approaching  $0.5 \text{ ms}^{-1}$ . Similarly, observational results from Gallus and Johnson (1995a) indicate peak updraft magnitudes between  $0.5\text{-}0.6 \text{ ms}^{-1}$  at 8-12 km altitude. Average storm-relative mesoscale updraft values tend to vary from  $0.2 \text{ ms}^{-1}$  in the center of the stratiform region to  $\sim 0\text{-}0.02 \text{ ms}^{-1}$  at the back edge of the stratiform region (Houze 1993). Average storm-relative mesoscale downdraft magnitudes are  $\sim 0.25 \text{ ms}^{-1}$  (Houze 1993), with peak descending motions of  $0.6\text{-}0.75 \text{ ms}^{-1}$  located near melting level (Gallus and Johnson 1995a). Finally, the magnitude of the storm-relative descending rear inflow varies from approximately  $0$  to  $15 \text{ ms}^{-1}$  (Houze 1993). Observational results from both Rutledge et al. (1988) and Nachamkin et al. (2000) found rear inflow magnitudes  $\leq 10 \text{ ms}^{-1}$ , whereas Gallus and Johnson (1995a) found peak magnitudes as large as  $15 \text{ ms}^{-1}$ .

The storm-relative mesoscale updraft is produced and sustained by the storm-relative ascending front-to-rear flow, and it extends the width of the trailing stratiform cloud. The storm-relative mesoscale downdraft is produced by negatively buoyant air as a result of precipitation evaporation, melting, and sublimation and only extends the width of the trailing stratiform precipitation (Smull and Houze 1985; Rutledge et al. 1988; Houze et al. 1989; Biggerstaff and Houze 1991). Ascending front-to-rear flow buoyancy and evaporative cooling and melting processes produce a mesohigh ( $\mathbf{H}_2$ , Fig. 1.1) over the entire MCS cloud system. Melting within the stratiform mesoscale downdraft region leads to significant cooling (Biggerstaff and Houze 1991). This cooling, along with heating aloft due to depositional growth of frozen hydrometeors, results in the development of a mid-level mesolow ( $\mathbf{L}_4$ , Fig. 1.1) at freezing level in the stratiform region (Houze et al. 1989; Gallus

and Johnson 1995a). This mesolow contributes to the internal formation and intensification of the descending rear inflow (Smull and Houze 1987; Braun and Houze 1997).

The descending storm-relative rear inflow marks the base of the stratiform cloud region (Smull and Houze 1985), and it erodes precipitation and cloud material along the back edge of the stratiform region, forming a low reflectivity notch in low-level radar reflectivity images and a surface wake low ( $L_1$ , Fig. 1.1) associated with subsidence warming (Smull and Houze 1985; Johnson and Hamilton 1988). The intensity of the storm-relative rear inflow depends upon the strength of the stratiform region mesoscale downdraft (Gallus and Johnson 1995b) as well as the strength and orientation of the ambient air's upper level flow (Braun and Houze 1997). The storm-relative rear inflow enters the stratiform region at mid- to upper-levels along the back edge of the MCS, just beneath the trailing stratiform clouds (Smull and Houze 1985), then descends through the bright band region, and finally enters the back edge of the convective region at low levels (Houze et al. 1989). The rear inflow's rapid descent through the mesoscale downdraft region is partially due to cooling associated with melting, sublimation, and, especially evaporation (Gallus and Johnson 1995b). Strong rear inflow can reinforce the leading gust front in the convective line, but the exact rear inflow strength required for this reinforcement is not currently known (Houze et al. 1989).

### ***1.3.2 MCS Microphysics***

In order to understand the nature of lightning in MCSs, it is instructive to know the typical microphysical properties of the various hydrometeors present within an MCS. Typical cloud droplets are  $\sim 10 \mu\text{m}$  in radius, have a terminal fall speed of  $0.01 \text{ ms}^{-1}$ , and have a concentration of  $10^6 \text{ L}^{-1}$ . Large cloud droplets are  $\sim 50 \mu\text{m}$  in radius, have a terminal fall speed of  $0.27 \text{ ms}^{-1}$ , and have a concentration of  $10^3 \text{ L}^{-1}$ . Typical raindrops are  $1000 \mu\text{m}$  in

radius, have a terminal fall speed of  $6.5 \text{ ms}^{-1}$ , and have a concentration of  $1 \text{ L}^{-1}$  (Wallace and Hobbs 1977). Unrimed to moderately rimed ice crystals are 0.5 to 8.0 mm in diameter and have terminal fall speeds of 0.3 to  $1.5 \text{ ms}^{-1}$ . Typical ice crystal habits vary with temperature. Thin hexagonal plates, needles, hollow columns, sector plates, and dendrites exist at 0 to  $-4 \text{ }^\circ\text{C}$ ,  $-4$  to  $-6 \text{ }^\circ\text{C}$ ,  $-5$  to  $-10 \text{ }^\circ\text{C}$  and  $-22$  to  $-50 \text{ }^\circ\text{C}$ ,  $-10$  to  $-12 \text{ }^\circ\text{C}$  and  $-16$  to  $-22 \text{ }^\circ\text{C}$ , and  $-12$  to  $-16 \text{ }^\circ\text{C}$ , respectively. Graupel are 2.0 to 5.0 mm in diameter and have a terminal fall speed of 1.5 to  $3.0 \text{ ms}^{-1}$ . Hailstones are commonly 1 cm in diameter, but can grow via riming to be as large as 10-15 cm in diameter. The fall speed of hail ranges from 10 to  $50 \text{ ms}^{-1}$ . Supercooled drops can exist in clouds from 0 to  $-40 \text{ }^\circ\text{C}$ , but at temperatures below  $\sim -40 \text{ }^\circ\text{C}$ , any liquid water drops that exist will spontaneously freeze by homogeneous nucleation (Houze 1993).

The MCS convective region is characterized by both small and large hydrometeors as a result of the strong vertical motions present. These hydrometeors include cloud water, cloud ice, rain, snow, graupel, and hail. Typical cloud liquid water concentrations in convective clouds are  $1.0\text{-}3.0 \text{ g m}^{-3}$  (Rosenfeld and Lensky 1998). Gallus and Johnson (1995b) initialized an MCS simulation using a convective line hydrometeor field based on hydrometeor profiles from Rickenbach (1990) and Rutledge and Houze (1987). In this hydrometeor field, cloud water exists between  $\sim 4.3$  and  $\sim 8.9 \text{ km}$  with a maximum mixing ratio of  $\sim 0.8 \text{ g kg}^{-1}$  at  $\sim 5.5 \text{ km}$ . Cloud ice exists between  $\sim 8.3$  and  $\sim 15.0 \text{ km}$  with a maximum mixing ratio of  $\sim 1.3 \text{ g kg}^{-1}$  at  $\sim 12.0 \text{ km}$ . Snow exists between  $\sim 5.8$  and  $\sim 14.8 \text{ km}$  with a maximum mixing ratio of  $\sim 0.55 \text{ g kg}^{-1}$  at  $\sim 6.8 \text{ km}$ . Finally, graupel exists between  $\sim 4.3$  and  $\sim 13.6 \text{ km}$  with a maximum mixing ratio of  $\sim 0.69 \text{ g kg}^{-1}$  at  $\sim 5.9 \text{ km}$  (Gallus and Johnson 1995a).

The MCS transition zone is characterized by lightly rimed ice columns, needles, and graupel as large as 2.0 mm, as well as cloud ice with a concentration of  $\sim 300 \text{ L}^{-1}$  (Schuur and Rutledge 2000a). The precipitation-sized hydrometeor concentration is less than  $40 \text{ L}^{-1}$ , and the cloud-sized hydrometeor concentration is  $\sim 300 \text{ L}^{-1}$  immediately behind the convective line at  $-10 \text{ }^\circ\text{C}$  (Schuur and Rutledge 2000a).

The stratiform region of a symmetric MCS is characterized by cloud ice, cloud water, and dendrite aggregates (Schuur and Rutledge 2000a; Schuur and Rutledge 2000b). Cloud liquid water content varies from  $\sim 0.1$  to  $0.5 \text{ gm}^{-1}$ , with an average of  $0.2\text{-}0.25 \text{ gm}^{-1}$ . The cloud ice concentration in the mixed-phase region is  $100\text{-}200 \text{ L}^{-1}$ . Dendritic growth forms crystals with sizes ranging from  $< 1 \text{ mm}$  to  $> 3 \text{ mm}$  (Schuur et al. 2000a).

The stratiform region of an asymmetric MCS is characterized by small, irregularly-shaped ice particles and needles. Schuur et al. (2000a) found that no dendritic crystals are present in the stratiform region around  $-8 \text{ }^\circ\text{C}$  because of the slightly subsaturated cloud liquid water content ( $\leq 0.1 \text{ g m}^{-1}$ ).

### ***1.3.3 MCS Formation and Precipitation Structure Classifications***

#### **1.3.3.1 Favorable Synoptic Scale Conditions**

In a study of 88 linear midlatitude MCSs occurring in the central US, Parker and Johnson (2000) identified various surface and upper-air synoptic scale features favorable for MCS development. Both surface and upper air observations were used to determine various surface boundaries, troughs, and jets present at 3-hr intervals prior to and during the life span of the MCSs. Results from this study indicate that 63 out of 64 warm-sector MCSs initiated near a linear synoptic boundary, including warm, stationary, and cold fronts or troughs. This finding agrees with results from Bluestein and Jain (1985) and Bluestein et al. (1987). Linear

synoptic boundaries provide the lower-tropospheric convergence necessary for organized convection. Parker and Johnson (2000) also found that strong southerly low-level jet streams (~10 to 15 kts), responsible for bringing warm, moist, buoyant air into the central US from the Gulf of Mexico, are present in approximately 61% of MCS environments. MCSs generally occur in the right entrance region of an upper tropospheric jet, associated with upper-level divergence and upward motion, and in regions of strong upper-tropospheric cyclonic vorticity advection, also associated with rising motion. Hilgendorf and Johnson (1998) note that MCSs tend to develop east of an upper-level trough in an area of positive vorticity advection, with southwesterly flow aloft and warm advection in the lower levels.

According to the QG-omega equation,

$$\left( \nabla^2 + \frac{f_0^2}{\sigma} \frac{\partial^2}{\partial p^2} \right) \omega = \frac{f_0}{\sigma} \frac{\partial}{\partial p} \left[ V_g \cdot \nabla \left( \frac{1}{f_0} \nabla^2 \Phi + f \right) \right] + \frac{1}{\sigma} \nabla^2 \left[ V_g \cdot \nabla \left( -\frac{\partial \Phi}{\partial p} \right) \right]. \quad [1.1]$$

Eq. [1.1] can be approximated by the following two relations,

$$w \propto \frac{\partial}{\partial z} \left[ -V_g \cdot \nabla (\zeta_g + f) \right] \quad [1.2]$$

and

$$w \propto -V_g \cdot \nabla T. \quad [1.3]$$

Therefore, rising motion is associated with both positive differential vorticity advection (relation 1.2), which can be approximated by positive vorticity advection at upper levels assuming vorticity advection at lower levels is relatively small, and warm advection (relation 1.3). Since both positive vorticity advection and warm advection are present, rising motion, most often associated with a linear synoptic boundary, preconditions the environment by eroding any capping inversions that may be present especially in a potentially unstable environment.

### 1.3.3.2 Convective Line Formation Characteristics

In an 11-yr springtime study in Oklahoma, Bluestein and Jain (1985) used 40 case studies of squall lines (a subset of MCSs) to identify 4 main types of convective squall line development associated with severe weather: 1) broken-line, 2) back-building, 3) broken areal, and 4) embedded areal development (Fig. 1.3). Broken-line and back-building development are more common, while embedded areal development is the least common line formation.

Broken-line development occurs when individual cells instantaneously form along a line, develop, grow, and then merge together to form one continuous squall line. New cells form along this line causing the line to grow with time. Broken-line development typically forms within 70 km of cold fronts. The development process occurs on a time scale of 30-90 min. Environmental conditions favorable for broken-line development include: 1) a large Bulk Richardson ( $R_i$ ) number ( $\sim 111$ ), and 2) a relatively small 0-6 km vertical-shear magnitude (Bluestein and Jain 1985). For more information about Bulk Richardson number ( $R_i$ ), please see Appendix B.

Back-building development occurs when a new cell initiates upstream of an older cell, relative to cell motion. This new cell grows and then merges with the older cell, forming a convective line over time. Back-building formation typically occurs along a preexisting boundary on a timescale of 20-30 min, and unlike the other three convective line formation types, this process can be repeated for as long as 6 hrs. Characteristics of back-building development include: 1) a relatively small  $R_i$  (32), and 2) a relatively large 0-6 km vertical wind shear magnitude (Bluestein and Jain 1985).

The last two types of development, broken-areal and embedded-areal, are less common. Broken-areal development occurs when an amorphous area of moderate to intense individual convective cells develop, merge, and form a solid line of convection in response to an interaction between two outflow boundaries. This type of formation typically occurs along and within 90 km of a quasi-stationary front and 80-200 km east of a surface dryline. Embedded-areal development occurs when individual convective cells form in an area of weaker, stratiform precipitation, merge, and form a convective line. CAPE values are typically lower in cases of broken-areal formation than during the other three types of convective line development, which all exhibit similar CAPE values (Bluestein and Jain 1985).

### **1.3.3.3 MCS Evolution**

#### ***1.3.3.3.1 Linear and Nonlinear MCSs***

Three evolution patterns identified by Blanchard (1990) include linear, occluding, and chaotic midlatitude MCSs (Fig. 1.4). Linear MCSs are the most common, comprising 68% of the MCS case studies in the Oklahoma-Kansas Preliminary Regional Experiment for STORM-central (PRE-STORM) field program (Blanchard 1990). These MCSs have a linear structure with a convective line and a stratiform region separated by a transition zone (Blanchard 1990) that propagate together and share a common leading edge (Parker and Johnson 2000). Linear MCSs generally occur ahead of a cold front and south of the low-pressure center (Blanchard 2000).

Nonlinear midlatitude MCSs are subdivided into occluding and chaotic MCSs, and both generally occur in or near cool air. Occluding MCSs visually represent boundaries separating different air masses. Two lines develop with one line oriented N-S along an

advancing pressure trough and the other line oriented E-W near a quasi-stationary frontal boundary. New cells that develop in the N-S oriented line move northward towards the intersecting point of the two lines, dissipate, and become part of the stratiform precipitation region of the MCS. If there is a circulation present near the intersection point of the two lines, the stratiform precipitation will wrap cyclonically around the center of circulation. An occluding MCS has also been classified as a “weakly classifiable/asymmetric squall line” by Houze et al. (1990) and as a “squall line with a well-developed mesovortex” by Houze et al. (1989). A chaotic MCS forms when many individual cells initiate in an apparently “random” manner over a relatively short time. Unlike occluding MCSs, chaotic MCSs never evolve into linear MCSs. Chaotic MCSs account for 24%, and occluding MCSs account for 8% of the MCSs in the PRE-STORM field experiment (Blanchard 1990).

#### ***1.3.3.3.2 Trailing, Parallel, and Leading Stratiform Region MCSs***

MCSs can generally be grouped into one of three classifications based on the mean location of the stratiform region relative to the convective line (Fig. 1.5). Most midlatitude convective systems for all three stratiform location classifications have a general NE-SW line orientation. A given MCS can evolve from one classification into another during its life span. The difference between these three classes is due to the relative direction of advection of hydrometeors into the stratiform region by the mean middle and upper tropospheric winds (Parker and Johnson 2000; Houze et al. 1989).

Of the three classes, the most common structure is the trailing stratiform (TS) classification (Fig. 1.5(a)). In the central U.S., TS MCSs occur approximately 60% of the time and are characterized by a leading convective line followed by a transition zone and a stratiform region. They are generally associated with cold fronts, occur in air masses that

have the most conditional instability, and propagate faster than (and last twice as long as) the other two MCS types. The other two MCS types frequently evolve into a TS MCS, but a TS MCS rarely evolves into one of the other MCS types. There are typically rearward storm-relative winds (from ~2.5 kts to ~23.5 kts) through all altitudes above 2 km associated with TS MCSs (Parker and Johnson 2000).

Characteristics of the leading stratiform (LS) MCS include a leading stratiform region followed by, in some cases, a transition zone, and then a trailing convective region (Fig. 1.5(b)). In the central U.S., The LS MCS occurs approximately 20% of the time and is associated with mean rear to front storm-relative winds (~1.7 kts to ~6.4 kts) aloft (Parker and Johnson 2000).

Finally, a parallel stratiform (PS) MCS, which occurs approximately 20% of the time in the central U.S., is characterized by movement of the stratiform region parallel to the convective region and to the left of the MCS motion vector throughout its evolution (Fig. 1.5(c)). These MCSs are associated with deep storm line-parallel flow (from ~2.3 kts to ~16.9 kts) above 2 km and occur in air masses of relatively low conditional instability. PS MCSs also move less rapidly than TS and LS MCSs (Parker and Johnson 2000).

#### ***1.3.3.3 Symmetric and Asymmetric MCSs***

TS MCSs are also classified based on their line-normal symmetry, either symmetric or asymmetric, throughout their lifespan (Fig. 1.6). In a study by Houze et al. (1990), 28 out of 42 MCSs (two-thirds) were classifiable as either symmetric or asymmetric based on their precipitation structure. The other 14 MCSs were not classifiable due to their chaotic organization. During its evolution, it is common for a symmetric MCS to evolve into an asymmetric MCS later in its lifetime (Hilgendorf and Johnson 1998). Symmetric MCSs (Fig.

1.6(a)) have a main convective line composed of individual cells of varying intensity distributed uniformly within the line. The stratiform precipitation region in a symmetric MCS aligns itself symmetrically behind this main convective line (Houze et al. 1990; Hilgendorf and Johnson 1998). Asymmetric MCSs (Fig. 1.6(b)) are characterized by 1) a convective line composed of individual cells where the most intense cells line up along the southern end of the line with respect to MCS orientation and 2) a stratiform precipitation region located only along the northern end behind the convective line (Houze et al. 1990; Loehrer and Johnson 1995; Hilgendorf and Johnson 1998).

Differences in precipitation structure between symmetric and asymmetric MCSs are believed to be attributed to low- to mid-level vertical wind shear. Both modeling studies and observational analyses have found that asymmetric systems have a stronger low-level jet, smaller, almost supercellular, values of  $R_i$ , and stronger 0-6 km vertical wind shear than symmetric systems. These characteristics favor strong supercellular-type convective cells to form (and severe weather to be produced) along the southern extent of the convective line and stratiform precipitation to form only along the northern half of the MCS (e.g. Rotunno et al. 1988; Weisman et al. 1988; Houze et al. 1990; Hilgendorf and Johnson 1998). In this environment, cells located along the southern tip of the convective line are exposed to the full amount of shear, whereas cells within the convective line further downwind are exposed to weaker modified shear, mostly from a line-normal shear component. A stronger shear environment along the southern extent of the convective line favors the development of supercellular-type convective cells, whereas the weaker shear environment downwind favors the development of multicellular-type convective cells. As the convective line matures, a

stratiform region begins to form only behind the multicellular-type convective cells and an asymmetric MCS has evolved (Rotunno et al. 1988; Weisman et al. 1988; Houze et al. 1990).

Another plausible explanation for the asymmetric-looking stratiform precipitation structure is due to the strength of the rear inflow jet. As this descending rear inflow interacts with the ascending front-to-rear flow at mid-levels, a cyclonic vorticity maximum is produced in the stratiform region (Fig. 1.7). The dotted line in Fig. 1.7(a) represents the shear line interaction between the two opposing flows (Houze et al. 1989). The strength of the rear inflow has been found to be directly proportional to the strength of the low- to mid-level vertical wind shear (Weisman et al. 1988). In some cases, when the rear inflow jet is particularly strong and a greater amount of dry air is advected into the stratiform region, a stronger mesoscale downdraft, stronger vertical velocity gradients along the back edge of the region, and stronger westerly shear below the melting level result. These strong vertical velocity gradients can tilt the resulting horizontal vorticity into the vertical producing a mesoscale convective vortex (MCV) at mid- to upper-levels, as pictured in Fig. 1.7(b). For more information about MCV formation, please see Scott and Rutledge 1995. The MCV advects dry mid-level air into the southern extent of the stratiform region, as well as convective cell remnants into the northern half of the stratiform region, creating an absence of stratiform precipitation along the southern extent of the MCS (Houze et al. 1989; Scott and Rutledge 1995).

Flooding is commonly produced from symmetric MCSs, whereas severe weather is observed more often in the southern extent of asymmetric MCSs. Flooding is typically associated with large stratiform regions, which generally exist more often in symmetric MCSs than in asymmetric MCSs. Asymmetric MCSs, which have greater along-line mid-

level shear, often produce tornadoes and hail, especially within the southern extent of the convective line where the most intense cells reside (Houze et al. 1990). Houze et al. (1990), in a study based on six years of springtime major rain events in Oklahoma, found that 0.9 tornadoes were reported per symmetric MCS versus 3.1 tornadoes reported per asymmetric MCS. Conversely, 2.4 flooding events per symmetric MCS versus 1.9 flooding events per asymmetric MCS were reported.

### ***1.3.4 Thunderstorm Charge Structure***

#### **1.3.4.1 Electrification**

Electrification in thunderstorms occurs when various mixed phase hydrometeors of differing physical properties undergo rebounding collisions with one another and, in this process, charge is transferred. The mechanisms explaining the charge transfer can be classified into non-inductive and inductive charging. Currently, the most supported mechanism of charge transfer is non-inductive charging (NIC).

##### ***1.3.4.1.1 Non-inductive Charging***

Although thunderstorm electrification is not completely understood, one dominant theory, the non-inductive charging mechanism, has been supported by various laboratory studies to explain the separation of electric charge within a typical thunderstorm (e.g. Takahashi 1978; Gaskell and Illingworth 1980; Jayaratne et al. 1983). According to NIC (Fig. 1.8), charge is transferred independently of the local electric field strength. Graupel (rimed ice crystals ~0.002-0.005 m in diameter), hail (extremely rimed graupel ~0.005-0.08 m or larger in diameter), and ice crystals within a cumulonimbus cloud collide in the presence of significant liquid water content causing charge separation. As a result of their collisions, graupel and hail acquire a net negative charge and the ice crystals acquire a net

positive charge at typical mixed-phase temperatures (e.g.  $-10\text{ }^{\circ}\text{C}$  to  $-30\text{ }^{\circ}\text{C}$ ) and liquid water contents (e.g.  $1\text{ gm}^{-3}$ ). The ice crystals, due to their small terminal fall velocity ( $\sim 0.3\text{ ms}^{-1}$  to  $\sim 1.5\text{ ms}^{-1}$ ), are carried up to the top of the cloud by the storm's updraft where a region of net upper positive charge is established at temperatures  $< -30\text{ }^{\circ}\text{C}$  (Krehbiel 1986; Saunders 1993). The terminal fall speed magnitudes of negatively-charged graupel ( $\sim 1.5\text{ ms}^{-1}$  to  $\sim 3.0\text{ ms}^{-1}$ ) and hail ( $\sim 10\text{ ms}^{-1}$  to  $\sim 50\text{ ms}^{-1}$  for hailstones 0.01-0.08 m in diameter) are generally equal to or greater than the magnitude of the storm's updraft, and these frozen hydrometeors establish a lower region of net negative charge at temperatures between  $0\text{ }^{\circ}\text{C}$  and  $-25\text{ }^{\circ}\text{C}$ , called the main negative charge region (Krehbiel 1986). These two charge layers compose what is known as the electric dipole.

The reason why charge transfers when two hydrometeors collide has been theorized to be a result of the interactions between hydrometeor quasi-liquid layers (QLL). According to both theoretical and experimental studies, there exists a quasi-liquid layer (QLL) between ice-air interfaces, whose thickness is dependent upon temperature and curvature. According to Baker and Dash (1989), hydrometeors with locally warmer and/or higher curvature surfaces have thicker QLLs than cooler and/or less curved hydrometeor surfaces. When two hydrometeors with differing QLL thicknesses collide, negative charge and mass flow from the thicker layer to the thinner layer in an attempt to establish QLL mass equilibrium. As these hydrometeors move away from one another, the original more curved and/or warmer hydrometeor becomes positively-charged, and the original less curved and/or cooler hydrometeor becomes negatively charged, resulting in two electrified particles (Baker and Dash 1989).

Various laboratory studies have found that both temperature and cloud liquid water content (LWC) play a significant role in the thunderstorm electrification process involving collisions between small ice crystals and rimed ice particles in the presence of supercooled water (e.g. Takahashi 1978; Gaskell and Illingworth 1980; Jayaratne et al. 1983; Saunders et al. 1991; Avila and Caranti 1994; Saunders 1994; Avila et al. 1998; Pereyra et al. 2000; Saunders et al. 2001). These studies are in general agreement that significant charge transfer can occur between graupel and ice crystals where graupel charges negatively at temperatures below (cooler than) a “charge reversal temperature” and positively at temperatures above (warmer than) this reversal temperature in the presence of cloud liquid water (Fig. 1.9). This charge reversal temperature is  $\approx -10^{\circ}\text{C}$  for an intermediate LWC value ( $O(1 \text{ g m}^{-3})$ ), but the reversal temperature decreases as cloud LWC either increases or decreases from this intermediate value (Takahashi 1978).

#### ***1.3.4.1.2 Inductive Charging***

Various inductive charging mechanisms have also been proposed in an attempt to explain thunderstorm electrification. Inductive charging differs from non-inductive charging in that a preexisting electric field is required to polarize hydrometeors for inductive charging to occur, whereas no preexisting electric field is needed in a non-inductive charging method. Two dominant methods of inductive charging are 1) Wilson’s selective ion capture mechanism and 2) rebounding collisions of two polarized hydrometeors. According to Wilson’s mechanism (Fig. 1.10), polarized falling hydrometeors selectively capture negative charge from ions as long as the hydrometeor’s velocity is greater than the ion’s velocity. The second inductive charging mechanism involves two polarized hydrometeors colliding as they fall (Fig. 1.11). Negative charge is transferred from the smaller hydrometeor to the larger

hydrometeor. The smaller, now positively-charged, hydrometeor is advected into the upper levels of the cloud forming the main upper positive charge layer, while the larger, now negatively-charged, hydrometeor resides in the main negatively-charged layer due to its larger terminal fall velocity.

Inductive methods are not widely accepted theories for electrification in a thunderstorm because the net charge produced is significantly smaller than typical charging observed in a thunderstorm (MacGorman and Rust 1998). Also, four limitations to these methods include: 1) a strong preexisting electric field is needed for strong charging to occur, 2) the contact time must be long enough for charge to transfer, 3) colliding particles must separate, and 4) after collision, the particles must travel to the correct regions in order to increase the net charge in each region (Beard and Ochs 1986; MacGorman and Rust 1998). Although inductive methods are not widely accepted theories for electrification, they may be important in conjunction with the NIC mechanism.

#### ***1.3.4.1.3 Additional Charging Layers***

##### **1.3.4.1.3.1 Lower Positive Charge Layer**

Various field observations have observed a tripole electric structure in thunderstorms (Fig. 1.8). This structure consists of the upper positive and main negative regions of a normal dipole as well as a weaker layer of lower positive charge beneath this electric dipole (Williams 1989). The exact reason for this lower positive charge region is currently unknown, but a wide range of theories have been proposed. These theories include drop breaking, positive charge associated with melting, positive corona discharge, lightning charge deposition, and the function of temperature on the NIC mechanism. According to the drop breaking theory, large precipitation drops selectively acquire positive charge as they

break up into smaller precipitation drops. The main problems with this theory are: 1) this process does not produce nearly as much charge as what has been observed in thunderstorms, and 2) most precipitation drops in this layer have been observed to be composed of ice, not liquid water (Williams 1989). According to the positive charge associated with melting mechanism, precipitation drops acquire large positive charge during melting. Although this conceptual model explains how drops can become positively charged, it does not account for the positively-charged hydrometeors above the melting level. Also, this mechanism is not likely because most precipitation drops are still frozen at this level. The positive corona discharge theory states that the lower positive charge is created from positive ion generation by point discharge beneath electrified clouds. This process also does not produce nearly as much charge as what has been observed in thunderstorms (Williams 1989). Finally, the lightning charge deposition theory, which states that the lower positive charge region is produced from lightning discharging positive charge on precipitation, cannot be completely rejected, but it is not widely accepted for two reasons: 1) cloud particles are more likely to intercept field-driven ions than precipitation particles, and 2) the lower positive charge region has been observed in electrified clouds before the first lightning flash has occurred (Williams 1989).

Currently, the most widely accepted explanation for the lower positive charge layer is the temperature dependence of the NIC mechanism (Krehbiel 1986; Williams 1989). As mentioned previously, graupel charges positively at temperatures above (warmer than) a “charge reversal temperature” ( $\sim -10$  °C) in the presence of cloud liquid water ( $\sim 1$  gm<sup>-3</sup>). Thus, when ice crystals and graupel collide at temperatures greater than (warmer than) this charge reversal temperature, the resulting positively-charged graupel particles form a smaller

layer of positive charge at lower levels in the thunderstorm cloud, creating the tripole electric structure in the convective cells. The negatively-charged ice crystals formed during this process are lofted by the updraft and reinforce the mid-level negative charge region (Krehbiel 1986; Williams 1989).

#### **1.3.4.1.3.2 Screening Layer**

A screening layer is a relatively small layer of charge that collects along the cloud's boundary (Fig. 1.8). The most common screening layer observed is the upper negative screening layer. It is produced when the upper positive charge layer attracts ions, produced by cosmic radiation, from the environment to the edges of the cloud. These ions attach to small cloud particles at the edge of the cloud, producing a negative screening layer (Krehbiel 1986).

#### ***1.3.4.1.4 Field Study Example of Thunderstorm Charge Distribution***

Stolzenburg et al. (1998b) examined 13 electric field soundings through large, isolated supercell storms over the southern Great Plains and 20 small, isolated storms over the central New Mexico mountains. Results from 7 soundings taken through strong updrafts ( $>10\text{ms}^{-1}$ ) of supercell storms over the Great Plains and 13 soundings in or near the convective cores of the New Mexico thunderstorms show similar charge structure (Fig. 1.12). The Great Plains supercells are characterized by a deep (1-4 km) low-density positive charge peak between  $\sim 4$  km and  $\sim 8$  km (between  $\sim 0$  °C and  $-10$  °C), a shallow mid-level dense negative peak between  $\sim 8$  km and  $\sim 10$  km (between  $\sim -10$  °C and  $-25$  °C), and an upper positive peak between  $\sim 10$  km and  $\sim 12$  km (approximately  $< -30$  °C). The New Mexico thunderstorms are characterized by a lower positive peak charge between  $\sim 3.75$  and  $\sim 6$  km (between  $\sim 5$  °C and  $-5$  °C), a mid-level negative peak between  $\sim 5$  and  $\sim 8$  km (between  $\sim 0$

°C and -15 °C), and an upper positive peak between ~9 and ~11 km (generally < -30 °C). A possible fourth layer of negative charge exists in all of these storms above the upper positive layer but since no sounding made it to cloud top, due to the instrument being destroyed by lightning or the balloon bursting, the upper negative charge layer cannot be confirmed in this study. Those soundings taken within the non-updraft portions of southern Great Plains and New Mexico storms indicate a more complex charge structure with at least 5 distinct charge regions present (Stolzenburg et al. 1998b). Electric charge structure present within the updraft and convective core regions of central Great Plains and New Mexico thunderstorms are consistent with the tripole structure conceptual model of a single cell thunderstorm.

#### **1.3.4.2 Lightning Flash**

The purpose of lightning is to reduce a storm's electrical energy, and its net effect is to transport negative electric current from the upper atmosphere to the Earth's surface (Krehbiel 1986). There are two main types of lightning: cloud-to-ground (CG) and in-cloud (IC) lightning. Most (~90%) CG lightning flashes produced from ordinary thunderstorms lower negative charge to the ground (Orville and Huffines 2001). This percentage can vary for different types of storms. For example, Seimon (1993) noted predominantly (91-100%) positive CG (+CG) flashes (until tornadogenesis) in the Plainfield, Illinois severe cell on 28 August 1990. Within MCSs, negative cloud-to-ground (-CG) flashes account for ~94% of the total CG lightning, although the -CG percentage varies between the stratiform and convective regions (Holle et al. 1994; Knupp et al. 1998; MacGorman and Morgenstern 1998).

A lightning flash is initiated when the electric stresses between two regions of opposing charge (either in cloud or cloud-to-ground) become so large that dielectric

breakdown occurs. Initial lightning flashes in convection are typically IC flashes (Fig. 1.13(a)), where negative charge from the main negative charge layer is transported upward into the main upper positive charge layer, reducing the overall charge in both layers (Krehbiel 1986). -CG lightning flashes (Fig. 1.13(b)) begin when a highly branched “stepped leader” of negative charge from the main negative charge layer of the cloud advances in a step-like fashion horizontally and downward towards the ground. These steps have lengths of 30-80 m and occur at 20-100  $\mu$ s intervals. When the stepped leader is close to the ground (within  $\sim$ 50 m), a positively-charged streamer from the ground rises and connects to this stepped leader to complete a pathway of net negative electric charge to the ground. This contact is called the first “return stroke,” and peak currents from these return strokes vary from several to hundreds of kiloamperes (kA), with typical values around 40 kA. The negative charge transferred in this lightning process neutralizes the leader channel as well as some of the cloud charge. Sometimes there is only one lightning stroke per stepped leader, but more often, a “dart leader” quickly propagates down the same ionized channel producing more return strokes. Lightning generation continues until the electric field is no longer able to support this process (Kridler 1986).

Other types of lightning flashes can also breakdown the electric charge present in thunderstorms. Positive cloud-to-ground (+CG) lightning flashes (not pictured), which lower positive charge to the ground, can occur between the upper positive anvil region of a storm and the negative ground below, or between the lower positive charge layer and the ground. +CG flashes are generally not as common as -CG lightning (Carey et al. 2003b; Carey and Rutledge 2003). In fact, only 15% of warm season (April-September) U.S. severe storms from 1989-98 produced predominantly (>50%) +CG lightning (Carey et al. 2003b). Various

forms of IC lightning also occur, including discharges between two different cells in a multicell thunderstorm (Fig. 1.13(c)), or discharges from the main negative region through the positive region up into the anvil of the storm (Fig. 1.13(e)). Combinations of IC and CG lightning can be produced when (1) a current first travels horizontally through two or more different cells in a multicell thunderstorm, and then discharges downward towards the ground (Fig. 1.13(d)), or (2) the main negatively-charged region of an active cell interacts with the positively-charged region of a dissipating cell, resulting in a horizontally-produced intracloud flash followed by a positive CG flash as the current then discharges to the ground from the positively-charged layer (Fig. 1.13(f)). Overall, IC flashes generally outnumber CG lightning by approximately 5 or 10 to 1 in ordinary convection (Krehbiel 1986), and the IC:CG ratio is thought to increase as a function of storm intensity (Chèze and Sauvageot 1997; Williams 2001).

### ***1.3.5 MCS Charge Structure***

An idealized conceptual model of the charge structure of an MCS is presented in Fig. 1.14. The cloud boundary is outlined in a solid black line; radar reflectivity (10-50-dBZ at 10-dBZ intervals) is contoured in dashed lines with areas of heaviest echo in the convective region shaded. Areas of positive and negative charge are shaded in dark gray and black, respectively, and significant temperature levels (0°C and -20°C) are shown. Thick solid arrows in the convective and transition regions represent updrafts and downdrafts, whereas large open arrows in the stratiform region depict the mesoscale updraft and downdraft motions. Thin solid arrows depict divergent outflows and thin open arrows show storm-relative motions.

### 1.3.5.1 Convective Region

Stolzenburg et al. (1998a) analyzed 16 electric field soundings through midlatitude MCS convective regions to determine their vertical charge structure. Ten soundings were taken through updrafts and six soundings through non-updraft areas within the convective regions. Results from this study (Fig. 1.15) are similar to the charge structure of an ordinary single cell thunderstorm (Fig. 1.12). Four dominant charge layers exist within the updraft region, and six dominant charge layers exist within the non-updraft region of the MCS's leading convective line.

The updraft region's electric field structure alternates in polarity beginning with positive charge at the lowest levels (Fig. 1.15). The lowest positive charge region is found between ~4 to ~6 km (~5 °C to ~ -7 °C) and sometimes extends down to 2 km (~15 °C). The average charge density in this region is  $0.5 \text{ nC m}^{-3}$ , and the average depth is 1.5 km. Above the lower positive charge layer is the main negative charge region that extends from above 6 km to about 8 or 9 km (~ -10 °C to ~ -25 °C). Its center height varies depending on the updraft ascent rate and is typically found between 6.5 and 8 km (~ -10 °C to ~ -20 °C). When the updraft is stronger, the main negative charge region is located at higher altitudes. This region is characterized by a mean depth of 1.3 km and a mean charge density of  $-1.0 \text{ nC m}^{-3}$ . The main upper positive charge region is located between approximately 9.5 and 11.0 km (~ -30 °C to ~ -44 °C). It has a mean charge density of  $0.7 \text{ nC m}^{-3}$  and an average depth of 1.5 km. The largest lightning-related electric field changes occur between this upper positive charge layer and the main negative charge layer below, suggesting that these two charge layers are involved in these lightning flashes (Stolzenburg et al. 1998a). The fourth layer is the uppermost negative charge layer located somewhere between 11.5 and 13.0 km (-47 °C to

~ -53 °C). This uppermost layer has a mean charge density of  $-0.3 \text{ nC m}^{-3}$  and an average depth of 1.0 km (Stolzenburg et al. 1998a).

Stolzenburg et al. (1998a) found that the electric field structure for areas outside of the updraft but within the convective region also alternates in polarity beginning with positive charge located at the lowest levels (Fig. 1.15). The lowest positive charge layer exists at 3.0-3.5 km altitude ( $\sim 6 \text{ }^\circ\text{C}$  to  $\sim 4 \text{ }^\circ\text{C}$ ). It is characterized by a mean depth of 0.5 km and an average charge density of  $0.8 \text{ nC m}^{-3}$ . Above the positive peak is a negative peak at 3.5-4.0 km ( $\sim 4 \text{ }^\circ\text{C}$  to  $\sim 2 \text{ }^\circ\text{C}$ ). This layer has a mean charge density of  $-2.4 \text{ nC m}^{-3}$  and an average depth of 0.5 km. The third layer is another positive layer at approximately 4.0-4.4 km, with a mean charge density of  $5.6 \text{ nC m}^{-3}$  and a mean depth of 0.4 km. Above this layer is the main negative charge layer at 5.0-7.5 km ( $\sim -5 \text{ }^\circ\text{C}$  to  $\sim -20 \text{ }^\circ\text{C}$ ). It has an average depth of 0.5 km and an average charge density of  $-4.0 \text{ nC m}^{-3}$ . Above the main negative charge is the upper positive charge layer with an average height of 11 km ( $\sim -45 \text{ }^\circ\text{C}$ ) in soundings launched ahead of the convective updraft and an average height of 8 km ( $\sim -22 \text{ }^\circ\text{C}$ ) in soundings launched behind the updraft. This layer has an average charge density of  $0.4 \text{ nC m}^{-3}$  and a mean depth of 2 km. Finally, the upper negative charge region, possibly a screening layer, exists around the upper cloud boundary, at about 11.5-12.0 km ( $\sim -50 \text{ }^\circ\text{C}$  to  $\sim -55 \text{ }^\circ\text{C}$ ). This layer has a mean depth of 0.5 km and an average charge density of approximately  $-0.6 \text{ nC m}^{-3}$  (Stolzenburg et al. 1998a).

There are differences between updraft and non-updraft charge layers within MCS convective regions (Fig. 1.15). Maximum electric field magnitudes of non-updraft soundings are larger and are located at lower altitudes than the electric field magnitudes of updraft soundings. In fact, three non-updraft region charge layers are located below 6.5 km ( $> -10$

°C), whereas only one charge layer within the updraft region is located below this height. With the exception of the upper positive region, charge layers in the non-updraft soundings are also shallower and have larger charge densities than the charge layers within updrafts. The upper positive charge region has a smaller charge density in the non-updraft region due to the increased depth it occupies in comparison to the updraft region. Three possible explanations for the large upper positive charge depth include: 1) the charged particles are of varying sizes with different fall speeds, so they become dispersed through a larger region, 2) some of the smaller charged particles disperse due to electrical repulsion, and 3) this region is characterized by downdraft motions and turbulent mixing. Overall, the largest visible difference between non-updraft and updraft MCS charge structures is the increased charge complexity outside of updraft regions (Stolzenburg et al. 1998a).

#### **1.3.5.2 Transition Zone**

Schuur et al. (1991) identified five main charge regions in the transition zone of an Oklahoma MCS on 18 June 1987. These regions alternate in polarity with the lowest region having negative charge. Except for the lowest charge layer, all of the charge layers are located in the front-to-rear flow downwind of the convective charge regions. Thus, at least most of this charge structure could be a result of charge advection from the convective region (Schuur et al. 1991). The lowest and highest altitude charge layers near cloud boundaries, however, are more likely associated with screening layers (Schuur et al. 1991). Some of the internal charge layers in the transition could also be a result of in situ charge mechanism (Rutledge et al. 1990; Schuur et al. 1991).

### 1.3.5.3 Stratiform Region

The charge regions present in the stratiform region of a midlatitude MCS are not well understood but are believed to be similar to the non-updraft convective region charge structure (Fig. 1.14). Stolzenburg et al. (1994) used five electric field soundings to identify five main charge layers throughout most of the stratiform region, except for the parts of the stratiform cloud furthest from the convective region in which only four main charge layers are present because the upper negative charge layer does not exist. This upper negative charge layer may result from negatively charged ice crystals that have been advected into the stratiform region from a screening layer in the convective region. By the time these hydrometeors reach the back of the stratiform region, their charge densities are too small to be detected. A lower negative charge region exists at the base of the stratiform region, except in areas of heavier precipitation under the radar bright band. This lower negative charge region could be a screening layer, or it may result from the in situ drop-breakup charging mechanism whereby negative charge is deposited on the larger of the two or more fragments that exist after the breakup of a drop in a positive electric field (Stolzenburg et al. 1994; Batman et al. 1995). Near the radar bright band close to the 0°C level, a positive charge layer exists that often has the largest charge density magnitude of any of the charge layers in the stratiform region. This positive charge layer could be caused by in situ melting charging, drop-breakup charging, or noninductive collisional charging (Stolzenburg et al. 1994; Bateman et al. 1995; Shepherd et al. 1996). Above the positively-charged 0°C region, a layer of negative charge exists at approximately 5 to 6 km altitude (~0 °C to ~ -10 °C) as a result of either charge advection from the convective region or in situ NIC. During NIC, snow aggregates undergo rebounding collisions with ice crystals in the presence of liquid

water at warm temperatures. Ice aggregates would acquire positive charge as it continues to fall, and the ice crystals left behind would be negatively charged. Above this negatively charged region is a deep positive layer at 6 to 10 km altitude ( $\sim -10$  °C to  $\sim -50$  °C) that may be a result of charge advection from the convective region. In addition to these charge layers, a low-density positive charge region is present between the cloud and the ground. This region is probably composed of positively charged precipitation or positively charged ions, produced by point discharge at the ground (Stolzenburg et al. 1994).

Other studies of the charge layer distributions within trailing stratiform MCSs have identified two different gross charge structures present. Marshall and Rust (1993) identified two types of vertical electrical structures in the stratiform region depending upon certain stratiform region characteristics. These characteristics can be classified into two types: 1) squall-line (type A), which is generally symmetric and 2) bow-echo or well-defined trailing mesovortex (type B), which is generally asymmetric. Type A MCSs are more complex than type B MCSs, with five or six in-cloud charge layers, beginning with negative charge at the lowest cloud levels. Type B MCSs have four distinct charge layers, also beginning with negative charge at the lowest cloud levels. Schuur and Rutledge (2000a) found similar electrical structure patterns in their comparison between a symmetric type A midlatitude MCS and an asymmetric type B midlatitude MCS.

Near the 0°C level, type A MCS soundings indicate significant negative charge, whereas type B soundings indicate significant positive charge (Marshall and Rust 1993). Marshall et al. (2001), for example, studied a type A MCS and found that net negative charge was present at the 0°C altitude (4.2 km) and that the only two distinct in-cloud positive charge regions were located at 5.1-5.6 km ( $\sim -5$  °C to  $\sim -7$  °C) and 6.4-6.8 km ( $\sim -11$  °C to

~ -16 °C), well above the freezing level. Hunter et al. (1992) also identified the 0°C level as negatively charged in the stratiform region of a PS Oklahoma MCS during the spring of 1989.

According to Schuur and Rutledge (2000a), MCS structure may be able to determine the amount of electrification produced within the stratiform region. Hydrometeors in this study's symmetric type A MCS case were advected quickly through the transition zone and into a stratiform region characterized by strong mesoscale ascent ( $>0.5 \text{ ms}^{-1}$ ) and supercooled cloud water ( $\geq 0.2 \text{ g m}^{-3}$ ). These strong upward motions and the presence of supercooled cloud water result in an environment favorable for significant electrification by in situ charging via the NIC mechanism (Schuur and Rutledge 2000a). Hydrometeors in the asymmetric type B MCS, however, traveled at a more line parallel path through a wide transition zone characterized by mesoscale descent where downward motions selectively captured more particles than the transition zone had captured within the symmetric type A MCS. The remaining hydrometeors were exposed to a deep layer of mesoscale descent in the stratiform region. These conditions are unfavorable for non-inductive charging and therefore, may explain why less electrification (peak electric field  $>80\text{kV}^{-1}$ ) occurred in the asymmetric type B MCS than in the symmetric type A MCS (peak electric field  $>100\text{kV}^{-1}$ ) (Schuur and Rutledge 2000a).

Schuur and Rutledge (2000a) note that the above explanation for the electrification differences may not be completely accurate because the electric field soundings in their two MCS cases were taken during different stages of MCS development. The electric field sounding for the symmetric type A MCS was collected during its mature stage of development whereas the asymmetric type B MCS sounding was collected during its

dissipating stage. Therefore, the electrification differences may be attributed to the different stages of development since symmetric MCSs sometimes evolve into asymmetric MCSs.

Various modeling studies also investigate the possible stratiform region electrification mechanism(s). Using observational results, as well as one-dimensional simple charge generation model simulations of a midlatitude MCS, Rutledge et al. (1990) showed that 1) positive charge advection from the convective region may explain most of the +CG flashes produced in the stratiform region, and 2) enough charge may be generated in the stratiform region to account for all of the CG lightning flashes produced within this region. The model showed that an inverted dipole charge structure (i.e. the formation of the main positive charge region below the main negative charge region) was present within the stratiform region. The study also found that the presence of a high concentration of small ice particles, either advected into the stratiform region or formed from the breakup of large particles, is important for significant charge generation (Rutledge et al. 1990).

Schuur and Rutledge's (2000b) results from two-dimensional, time-dependent, bulk microphysical numerical model simulations of the MCS stratiform region show that both in situ charging and charge advection are important in the electrification process of the region. This model was initialized with snow mixing ratios, cloud ice concentrations, and liquid water contents that were modified, using observations discussed in Schuur and Rutledge (2000a), from Gallus and Johnson's (1995a) two-dimensional modeled values at the back edge of symmetric MCS convective regions. A control run was performed (Fig. 1.16) to depict the stratiform region locations and concentrations of snow mixing ratio, cloud liquid water content, and cloud ice at  $t = 3$  hr. It is evident that the peak snow mixing ratio (Fig. 1.16a) descends from  $\sim 8.4$  km ( $\sim -30$  °C) at the back edge of the convective line to  $\sim 4.8$  km

( $\sim -5$  °C) (directly above the radar reflectivity bright band, not shown) at a distance of  $\sim 55$  km from the back edge of the convective line. A model simulation was then initialized with 1) these microphysical concentrations and 2) the convective region total charge density “type A” profile determined by Marshall and Rust (1993) (i.e. with five charge layers at  $T \leq 0$  °C). This model was allowed to run with 1) Saunders et al. (1991) non-inductive charging (i.e. the charge separation per collision is dependent upon both cloud ice size and collision impact velocity) and 2) charge advection of snow, cloud ice, and cloud water from the convective region to the stratiform region by storm-relative horizontal winds (i.e. the front-to-rear flow). Figure 1.17 depicts the resulting total charge density magnitude distribution throughout the stratiform region at  $t = 3$  hr. The positive charge density maximum, similar to the peak snow mixing ratio, descends from  $\sim 8.0$  km ( $\sim -26$  °C) at the back edge of the convective line to  $\sim 5.3$  km ( $\sim -9$  °C) at a distance of  $\sim 50$  km from the back edge of the convective line. Peak positive charge density appears to reside at altitudes  $\sim 1.0$  km above the radar reflectivity bright band in the stratiform region (not shown). For more details about the numerical model, please see Schuur and Rutledge (2000b).

#### **1.4 Relationship of MCS Structure to Lightning**

A midlatitude MCS is characterized by an abundance of lightning activity (up to 60 CG flashes per minute or more), particularly in the convective region (Goodman and MacGorman 1986). The in-cloud (IC) to CG ratio (IC:CG) has been determined to be as large as 40:1 in midlatitude MCSs (Mazur and Rust 1983). Median negative CG lightning peak currents in MCSs are approximately 25-30 kA, and median positive CG peak currents are approximately 10 kA for “small amplitude MCSs” (mode of 9-13 kA with few flashes

>40 kA) and 60 kA for “middle amplitude MCSs” (mode of 13-17 kA with many flashes >40 kA) and “large amplitude MCSs” (mode of 51-56 kA) (MacGorman and Morgenstern 1998). Large amplitude peak flashes tend to produce the lowest maximum total ground flash rates (MacGorman and Morgenstern 1998).

The evolution of lightning in an MCS is directly related to the evolution of the MCS itself. In a study of a midlatitude MCS in Oklahoma, Shafer et al. (2000) noted a dissipating MCS that reintensified over a period of 1 hr. Of particular interest was the corresponding decrease and subsequent increase in CG lightning activity in both the stratiform and convective regions over this period. Rutledge et al. (1990) and Knupp et al. (1998) noted an increase in CG activity coincided with the convective line broadening and the subsequent development of the stratiform region. Goodman and MacGorman (1986) found that hourly flash rates tend to increase exponentially up to 1-2 hrs before maximum MCS cloud shield development, and then decrease exponentially.

#### ***1.4.1 Convective Region***

The convective region of a midlatitude MCS is characterized by an abundant amount of lightning activity (e.g. Mazur and Rust 1983). Approximately 87% of CG flashes produced by an MCS are associated with the convective region (Holle et al. 1994). Various studies have found that convective CG lightning activity is dominated by negative polarity flashes (e.g. Rutledge and MacGorman 1988; Rutledge et al. 1990; Holle et al. 1994; Toracinta et al. 1996; Shafer et al. 2000). In fact, Holle et al. (1994) determined that +CG lightning flashes account for only ~3% of the total CG flashes within the region. In a study using one midlatitude MCS, Petersen and Rutledge (1992) found a mean positive convective CG peak current of ~54 kA. Within the convective line, the majority of both –CG lightning

and IC lightning occurs near regions with highest reflectivities (Krehbiel et al. 1979; Rutledge and MacGorman 1988; Reap and MacGorman 1989; Toracinta et al. 1996) and downwind of the reflectivity core but within the convective band, apparently associated with the storm's wind structure relative to updraft and reflectivity cores (Ray et al. 1987; Keighton et al. 1991).

#### ***1.4.2 Stratiform Region***

Results from various studies indicate that the stratiform region of a midlatitude MCS is characterized by relatively few CG lightning flashes. A greater percentage of +CGs, however, occurs in this region than in the convective region (e.g. Rutledge and MacGorman 1988; Rutledge et al. 1990; Hunter et al. 1992; Holle et al. 1994; Toracinta et al. 1996; Shafer et al. 2000). This relatively high +CG percentage has often been attributed to an “inverted dipole” in the stratiform region, where the main positive charge region develops at a lower altitude than the main negative charge region (e.g. Rutledge and MacGorman, 1988; Orville et al. 1988; Engholm et al. 1990; Rutledge et al. 1990). Holle et al. (1994) determined that overall the stratiform region is associated with ~24% +CG lightning flashes. The percentage of +CGs generally increases within this region at the beginning of the MCS dissipating stage (Holle et al. 1994; Nielsen et al. 1994). This increased +CG percentage is often associated with increased development of the stratiform region (Rutledge et al. 1990; Shafer et al. 2000). Knupp et al. (1998) noted that the beginning of +CG lightning activity corresponds to the development of the radar bright band. Median peak currents are also larger in the stratiform region than in the convective region, and larger regions of stratiform rain were found to have larger median peak currents (Petersen and Rutledge 1992; Rutledge and Petersen 1994; MacGorman and Morgenstern 1998). For example, Petersen and Rutledge

(1992) reported that the mean stratiform +CG peak current from one midlatitude MCS studied was ~81 kA, which is 27 kA larger than the mean convective +CG peak current.

### ***1.4.3 Total Echo Volume Aloft***

Following the theory of non-inductive charging, the evolution of lightning activity can be correlated to the evolution of total echo volume aloft within a storm system. The existence of significant reflectivity echoes ( $\geq 35$  dBZ) in convection at  $T \leq 0$  °C implies the presence of suspended graupel and hail particles within strong updrafts. These updrafts also advect liquid water above the freezing level, resulting in an abundance of supercooled liquid water. Assuming that ice crystals are also present aloft, the graupel, hail, supercooled water, and ice crystals can undergo rebounding collisions, which can lead to charge separation and significant electrification via NIC. Once enough charge separation has occurred, lightning is produced. Therefore an increase (decrease) in echo volume aloft (i.e. sub-freezing echo volume) corresponds to an increase (decrease) in lightning flash rates.

Previous studies have correlated the evolution of echo volume aloft and/or updraft velocity to lightning activity in ordinary multicell convection (e.g. Lhermitte and Williams 1985; Goodman et al. 1988; Williams et al. 1989; Carey and Rutledge 1996; Williams et al. 1999; Carey and Rutledge 2000; Lang et al. 2000; Lang and Rutledge 2002; Wiens et al. 2002) and in MCSs (e.g. Keighton et al. 1991; Zipser and Lutz 1994). This correlation supports electrification via NIC. Lhermitte and Williams (1985) observed dominant negative charge centers present just above the altitude in which precipitation-sized particles were suspended in the convective updraft at 6-7 km. Williams et al. (1989) found a correlation between in-cloud (IC) lightning activity and the accumulation of charged graupel and hail suspended by convective updrafts. Goodman et al. (1988) noted that a peak in total

flash rate corresponded with a peak in echo volume (>30-dBZ). Williams et al. (1999) also noted total lightning jumps that coincided with rapid vertical development. Keighton et al. (1991) determined that lightning flash rate in a severe MCS best correlated to the 50- and 55-dBZ area at 6 km AGL. Zipser and Lutz (1994) suggest that mean updraft velocities must be 6-7  $\text{ms}^{-1}$ , and peak updraft velocities should approach 10-12  $\text{ms}^{-1}$ , for significant electrification to occur.

In a study of a multicell thunderstorm along the Colorado Front Range, Carey and Rutledge (1996) consistently observed an enhanced reflectivity (> 55 dBZ) region between  $\sim -15$  °C and  $\sim -35$  °C (i.e. the main negative charge region) within the convection. This enhanced reflectivity region was composed of graupel and small hail (<2 cm) and was associated with a strong updraft (from 11 to 16  $\text{ms}^{-1}$ ) located from 5.5 km to 9.5 km. IC electrical activity increased when accumulations of graupel and hail increased. The peak in graupel volume occurred  $\sim 12$  min before the peak in IC flash rates. IC electrical activity decreased as the graupel and hail descended in the thunderstorm. CG lightning, however, increased as graupel and hail descended below the  $-10$  °C level (i.e. below the height of the main negative charge region). These results support electrification via the NIC mechanism in multicell convection.

Several studies have also tried to use this echo volume aloft/lightning production relationship to determine the reflectivity threshold at a given temperature level in a convective storm necessary to accurately mark the corresponding onset of lightning activity within a given time period (e.g. Dye et al. 1989; Buechler and Goodman 1990; Michimoto 1991; Hondl and Eilts 1994; Gremillion and Orville 1999; Vincent et al. 2003). Hondl and Eilts (1994) determined that the appearance of a 10-dBZ echo at the 0°C temperature height

is the first definitive sign of a future thunderstorm in Florida. Median lead times in this study were 15 min, and all lightning-producing storms were detected by this method, but some 10-dBZ echoes never produced lightning. Gremillion and Orville (1999), however, determined that the appearance of the 40-dBZ echo at  $-10^{\circ}\text{C}$  temperature height gave the best results in Florida, with a median lag time of 7.5 min. Using 50 case studies of central North Carolina thunderstorms, Vincent et al. (2003) determined that both 1) a one volume scan appearance of a 40-dBZ echo at  $-10^{\circ}\text{C}$ , and 2) a one volume scan appearance of a 40-dBZ echo at  $-15^{\circ}\text{C}$  best forecasted the onset of CG lightning with a median lag time of 14.7 min and 11.0 min, respectively. Examining a different region, Michimoto (1991) determined that the appearance of a 30-dBZ echo at  $-20^{\circ}\text{C}$  temperature height gave the best results in the Hokuriku district. Reflectivity and altitude thresholds vary depending upon the environment in which they are used.

Both laboratory studies (discussed in section 1.3.3.1.1) and field studies (discussed above) have provided supporting evidence in favor of the NIC mechanism for electrification in ordinary convection. The NIC mechanism can be used to explain electrification within the convective region of an MCS. As for the stratiform region, the dominant electrification mechanism(s) is (are) still not completely understood. It is possible that in situ charging via NIC occurs in the stratiform region, but no overwhelming evidence for or against this theory exists to date.

#### ***1.4.4. Rainfall Rates***

The evolution of lightning activity can be correlated to the evolution of rainfall rates in an MCS. Low-level radar reflectivity corresponds to the amount and size of precipitation targets hitting the ground (i.e. higher values of reflectivity correspond to stronger rainfall

rates). Rainfall rate depends upon the amount of hydrometeor mass present at mid- to upper-levels. Electrification and lightning activity are more efficient and rainfall rates are stronger when larger concentrations of mixed-phase hydrometeor mass are lofted into mid- to upper-levels by strong updrafts. Therefore, rainfall rates and lightning activity in a midlatitude MCS are directly related since the same processes drive their development and intensification (Rutledge and MacGorman 1988; Toracinta et al. 1996).

Many studies have found that the areas within MCSs that generate the largest lightning flash rates also produce the highest rainfall rates (e.g. Krehbiel et al. 1979; Rutledge and MacGorman 1988; Reap and MacGorman 1988; Keighton et al. 1991; Chèze and Sauvageot 1997; Molinie et al. 1999). Rutledge and MacGorman (1988), for example, found that a peak in convective –CG and stratiform +CG activity corresponded to the estimated peak in convective and stratiform rainfall activity, respectively. This study also found that a time lag ( $\leq 2$  hr) exists between the peak convective –CG activity and the peak stratiform +CG activity, suggesting that the source of +CGs is related to the advection of positively-charged hydrometeors from the convective region into the stratiform region (Rutledge and MacGorman 1988). Molinie et al. (1999) showed that large lightning flash rates were correlated to areas of intense rainfall and strong reflectivity values at mid-levels (4.5 km, and sometimes 7.5 km). This study also concluded that the maximum flash rates corresponded to the descent of the large precipitation hydrometeors. A time lag was observed between the lightning flash rate and the rainfall rate (Molinie et al. 1999).

## 1.5 Motivation and Hypothesis

Midlatitude MCSs are large, long-lived convective systems that produce an abundance of lightning, both IC and CG. The evolution in lightning activity has been correlated to microphysical processes within an MCS, including echo volume aloft and rainfall rates. The convective region produces most of the observed lightning activity, and CG lightning flashes within this region are predominantly of negative polarity. The stratiform region, however, is characterized by low lightning flash rates. A larger percentage of +CG flashes is produced in the stratiform region than in the convective region.

Stratiform region electrification is still not well understood. Two dominant hypotheses are 1) the advection of positive charge from the upper levels of the convective region into the stratiform region (e.g. Orville et al. 1988; Rutledge and MacGorman 1988; Engholm et al. 1990; Hunter et al 1992; Stolzenburg 1990; Schuur and Rutledge 2000b) and 2) an in situ charging process in the stratiform region (e.g. Rutledge and MacGorman 1988; Engholm et al. 1990; Rutledge et al. 1990; Hunter et al. 1992; Rutledge et al. 1993; Rutledge and Petersen 1994; Schuur and Rutledge 2000b). Most research results favor a combination of in situ and advection mechanisms to explain how the stratiform region becomes electrified. Rutledge and MacGorman (1988) and Rutledge et al. (1990) used simple models to show that both in situ and advection of charge into the stratiform region can produce enough positive charge for observed +CG flash rates in the region. Using two-dimensional, time-dependent, bulk microphysical numerical model simulations of the MCS stratiform region, Schuur and Rutledge (2000b) show that both in situ charging and charge advection are important in the electrification process of the region.

Currently, one of the main interests in MCS research resides in MCS electrification processes, particularly within the stratiform region. This research attempts to determine whether or not particle-scale differential sedimentation and storm-scale vertical and horizontal advection of mixed-phase hydrometeors (large and small precipitating ice in the presence of supercooled water) drive MCS electrification because hydrometeor collisions cause a net charge separation. More specifically, the prominence of –CG lightning in the convective region of an MCS exists because the precipitation processes of mixed-phase hydrometeors vertically separate charge such that negative charge collects at mid-levels and positive charge collects aloft (“normal dipole”). The prominence of +CG lightning in the stratiform region of an MCS, however, exists because the charge and/or the conditions for charging from the upper positive charge area in the convective region are advected into the stratiform region.

Table 1.1. Weather-related fatalities per year for 30 years (1959-1990), as well as death and injury totals in 1994 (adapted from Curran et al. 2000). Data were obtained from the National Oceanic and Atmospheric Administration (NOAA) *Storm Data* publication.

Weather type	30-yr deaths per year	1994 deaths	1994 injuries
Flash flood		59	33
	139		
River flood		32	14
Lightning	87	69	484
Tornado	82	69	1,067
Hurricane	27	9	45
Extreme temperature		81	298
Winter weather		31	2,690
Thunderstorm wind		17	315
Other high wind		12	61
Fog		3	99
Other		6	59
Total		388	5,165

Table 1.2. Convective weather-related fatalities, injuries, and property damage reports per year from 1992-94 (adapted from Curran et al. 2000). Data were obtained from the National Oceanic and Atmospheric Administration (NOAA) *Storm Data* publication.

Convective weather type	Fatalities	Injuries	Damage (\$ million)
Lightning	51	345	32
Tornadoes	47	1,114	551
Thunderstorm wind	18	352	295
Hail	0	43	345

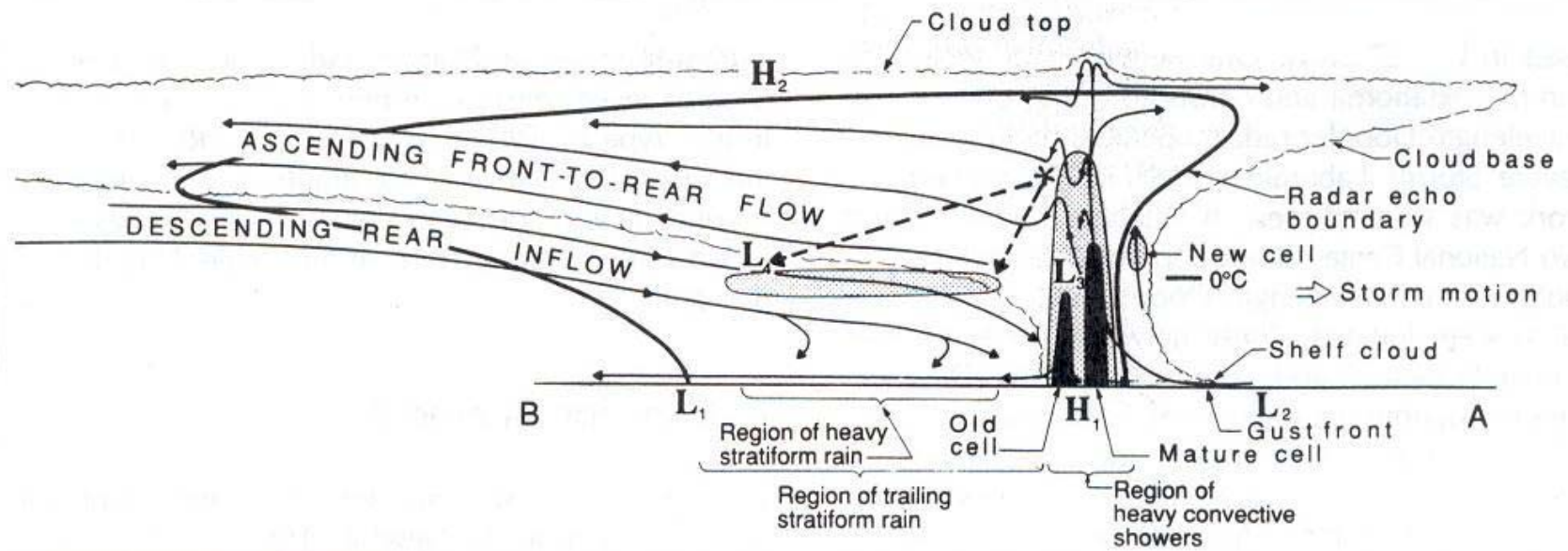


FIG. 1.1. Conceptual model of an idealized leading convective, trailing stratiform mature mesoscale convective system (MCS). See text for further details. Image adapted from Houze et al. (1989).

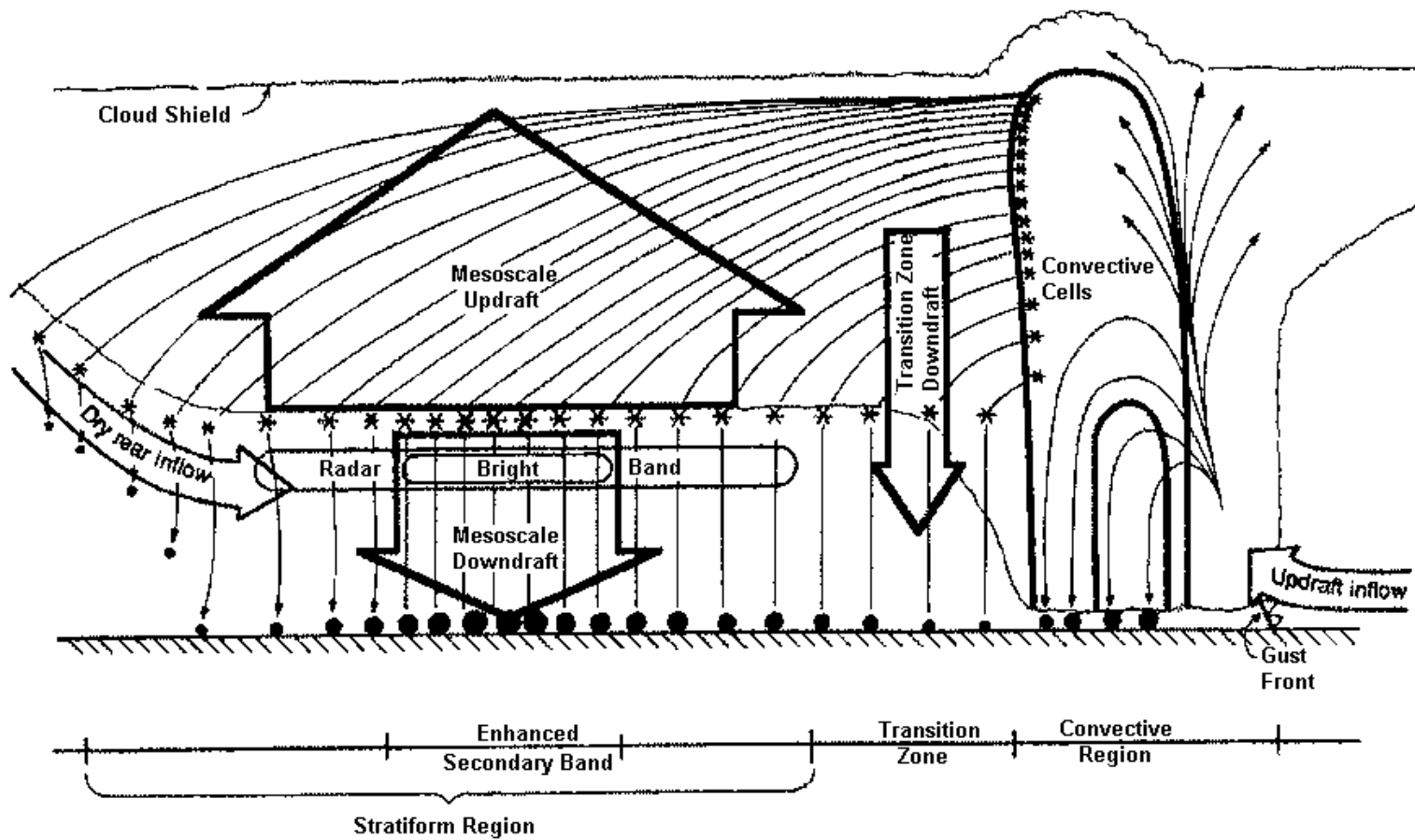


FIG. 1.2. Vertical cross-section conceptual model of the two-dimensional hydrometeor trajectories through a leading convective, trailing stratiform region MCS. Image adapted from Biggerstaff and Houze (1991).

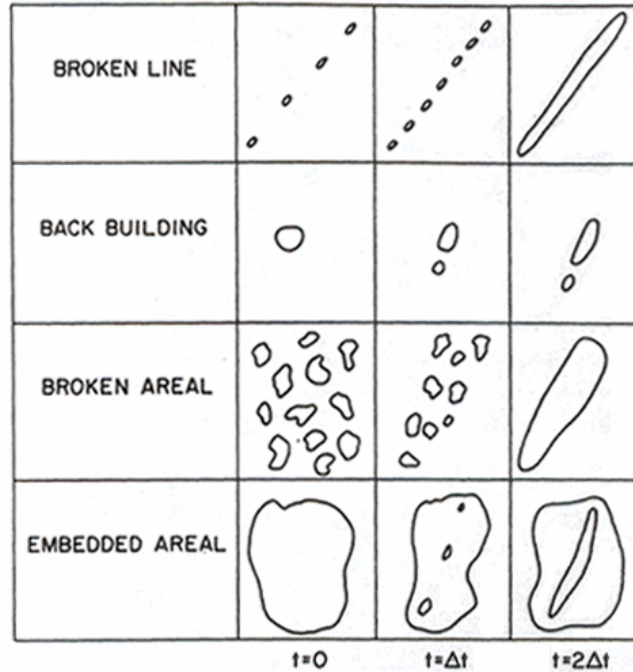


FIG. 1.3. Four idealized types of mesoscale convective line development and their evolution with time. Image adapted from Bluestein and Jain (1985).

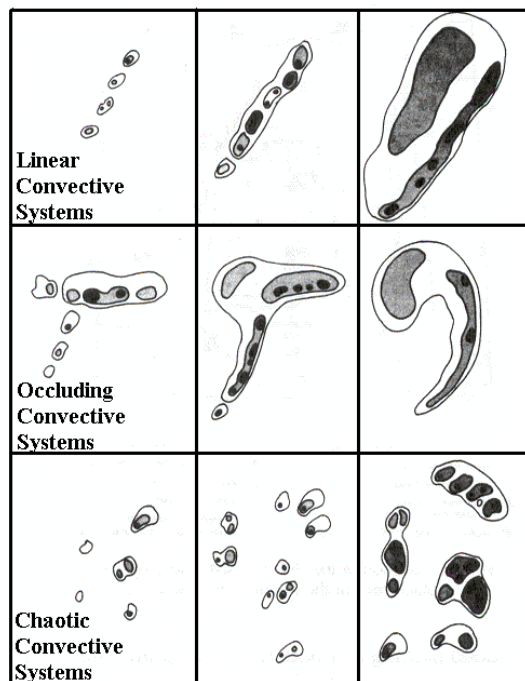


FIG. 1.4. Three patterns of MCS structure as proposed by Blanchard (1990). The three columns, from left to right, represent the evolution of each pattern with time. The various shades of gray represent the reflectivity contours, with the darkest colors representing the highest reflectivity values and, thus, the most intense convective cores. Image adapted from Blanchard (1990).

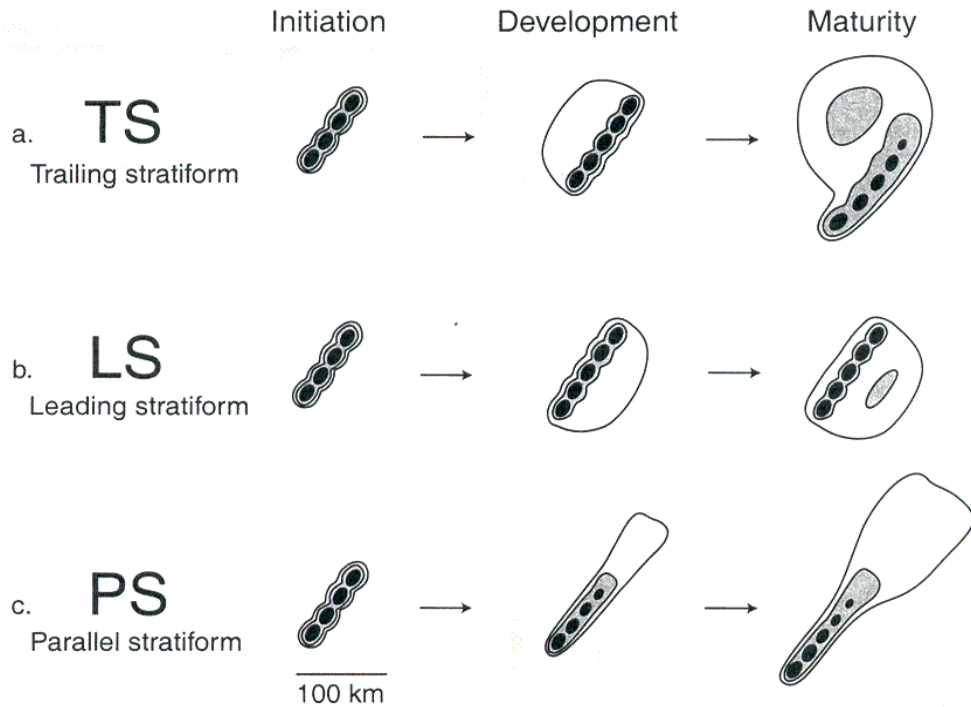


FIG. 1.5. Conceptual model of the evolution of the three main classifications of MCSs: (a) trailing stratiform (TS), (b) leading stratiform (LS), and (c) parallel stratiform (PS), proposed by Parker and Johnson (2000). The various shades of gray represent the reflectivity contours, with the darkest colors representing the highest reflectivity values and, thus, the most intense convective cores. Image adapted from Parker and Johnson (2000).

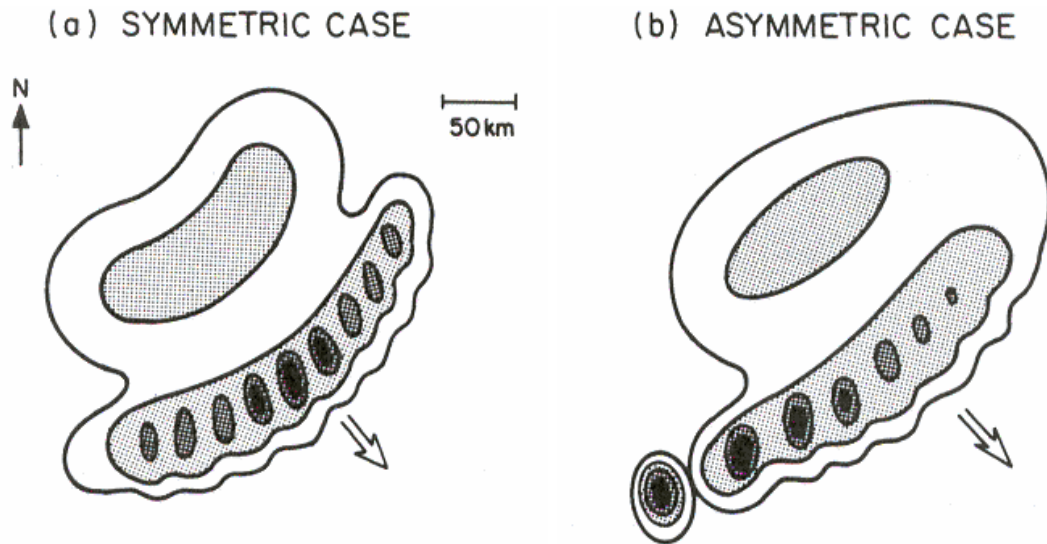


FIG. 1.6. Conceptual model of a TS (a) symmetric, and (b) asymmetric MCS. Arrows indicate the direction of storm motion. The various shades of gray represent the reflectivity contours, with the darkest colors representing the highest reflectivity values and, thus, the most intense convective cores. Image adapted from Houze et al. (1990).

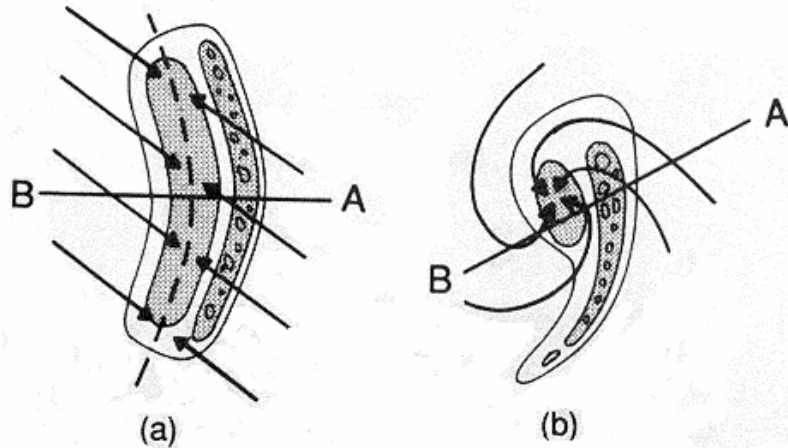


FIG. 1.7. Conceptual model of (a) a two-dimensional MCS, and (b) an MCS with a mid-level well-defined mesoscale vortex. Mid-level storm-relative flow is overlaid on low-level reflectivity contours. The B-A line represents the location of the vertical cross section pictured in Fig. 1. Image adapted from Houze et al. (1989).

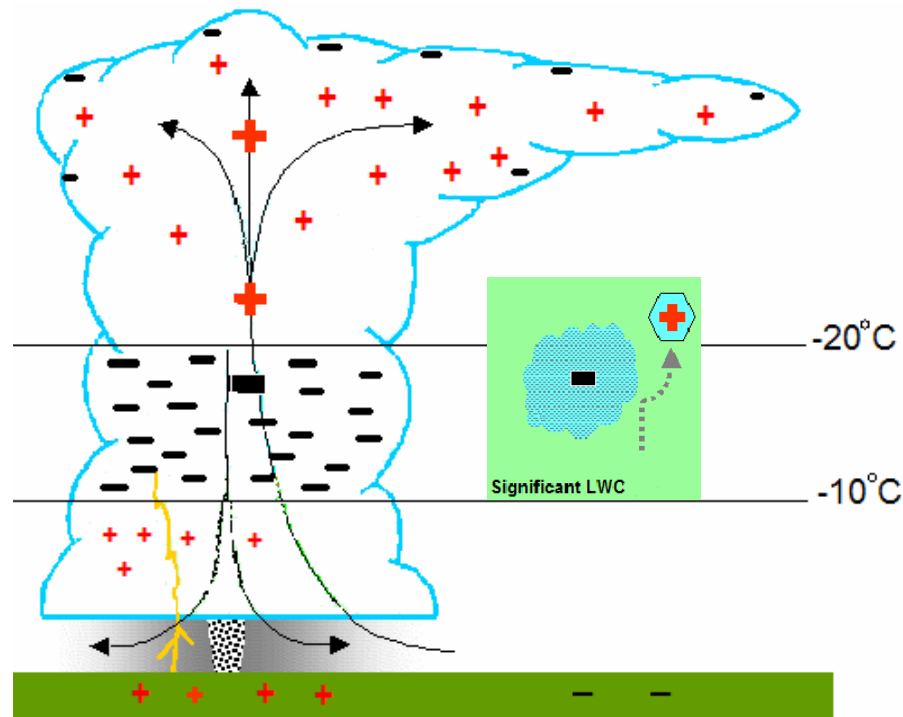


FIG. 1.8. Conceptual model of the non-inductive charging method in an ordinary isolated thunderstorm. The cloud becomes electrified as a result of many collisions between graupel and ice crystals in the presence of significant cloud liquid water content (LWC), where graupel charges negatively and ice crystals positively. Due to the differences in terminal fall velocities, graupel particles establish a main negative charge region at mid-levels, and ice crystals form an upper positive charge region. A smaller area of lower positive charge forms as a result of charge reversal microphysics. At the cloud boundaries, a negative screening layer also exists inside the storm. Image adapted from CSU website: <http://www.cira.colostate.edu/ramm/visit/lgtmet1.html>.

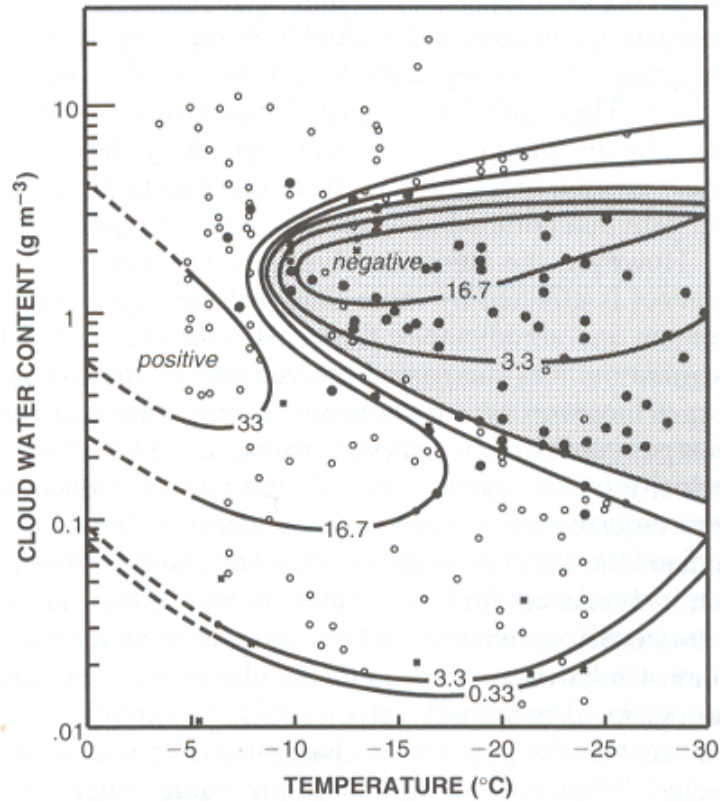


FIG. 1.9. Charge (in  $10^{-15}$  C) gained by graupel particles resulting from the collision of graupel with ice crystals as a function of cloud liquid water content (LWC) and temperature. Solid circles indicate that graupel gained negative charge, open circles indicate that graupel gained positive charge, and “x” indicates that no charge was transferred. Image adapted from Takahashi (1978) and MacGorman and Rust (1998).

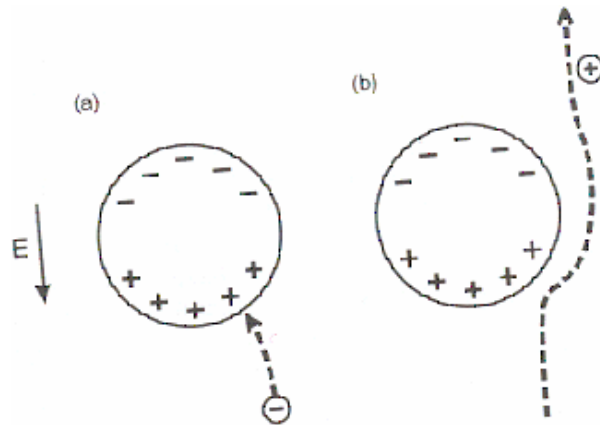


FIG. 1.10. Conceptual model of Wilson's selective ion capture mechanism. According to this mechanism, (a) larger polarized graupel particles selectively capture negative charge from ions as they fall, resulting in (b) positively-charged ice crystals and negatively-charged graupel. The smaller particle is lofted into the upper levels of the storm by the storm's updraft. Image adapted from MacGorman and Rust (1998).

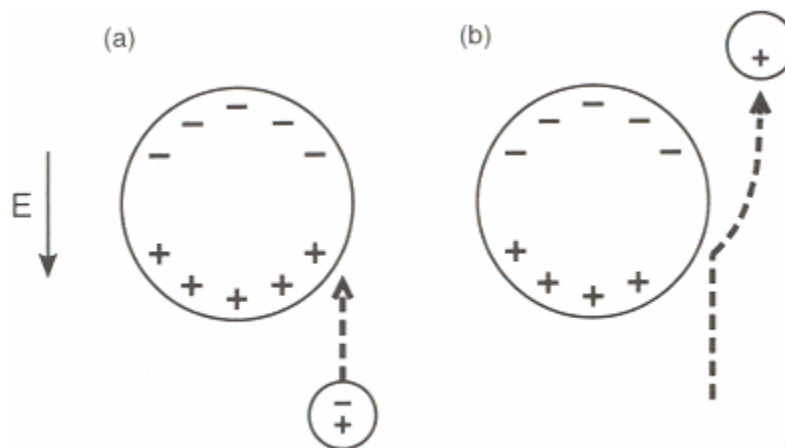


FIG. 1.11. Conceptual model of the mechanism involving rebounding collisions of two polarized hydrometeors. According to this mechanism the difference in terminal fall velocities between large and small hydrometeors causes (a) polarized hydrometeors to collide with one another resulting in (b) a net transfer of negative charge to the larger hydrometeor. The smaller hydrometeor is lofted into the upper levels of the storm by the storm's updraft. Image adapted from MacGorman and Rust (1998).

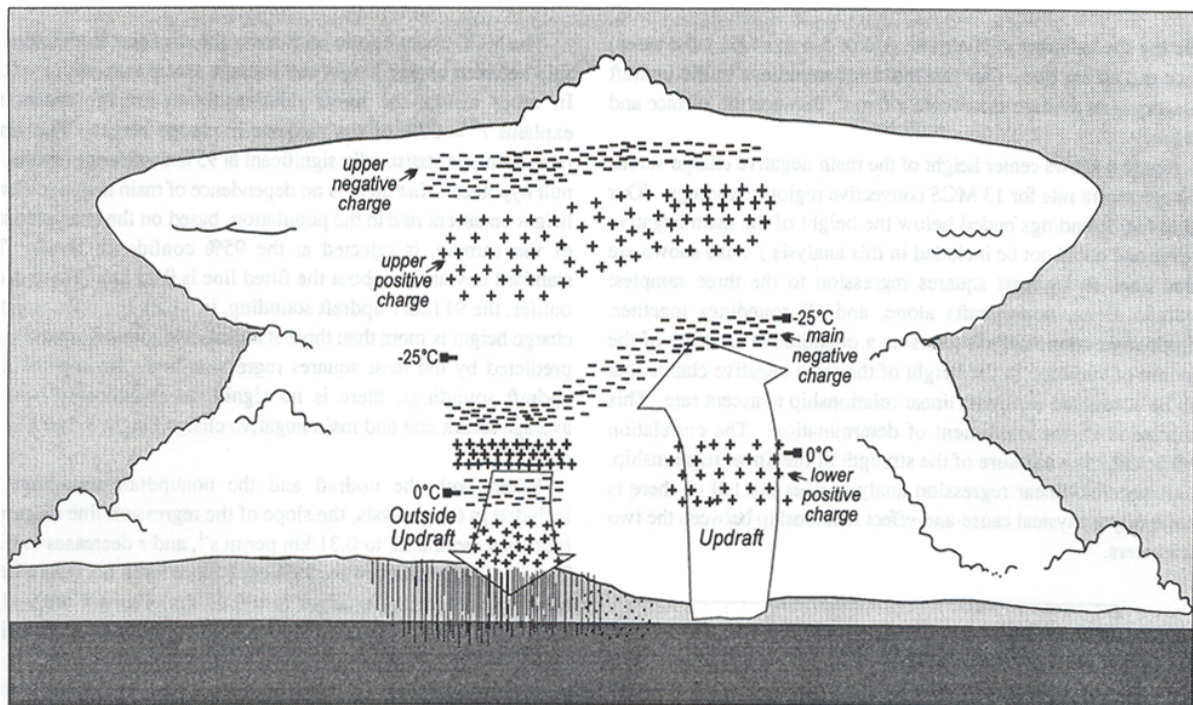


FIG. 1.12. Schematic of the main convective charge regions in a thunderstorm both within and outside the updraft. Four main regions of charge exist within the updraft, but outside the updraft region, up to two additional charge regions may exist at low levels, as shown. Actual heights and temperatures of each charge region may vary from storm to storm. Image adapted from Stolzenburg et al. (1998c).

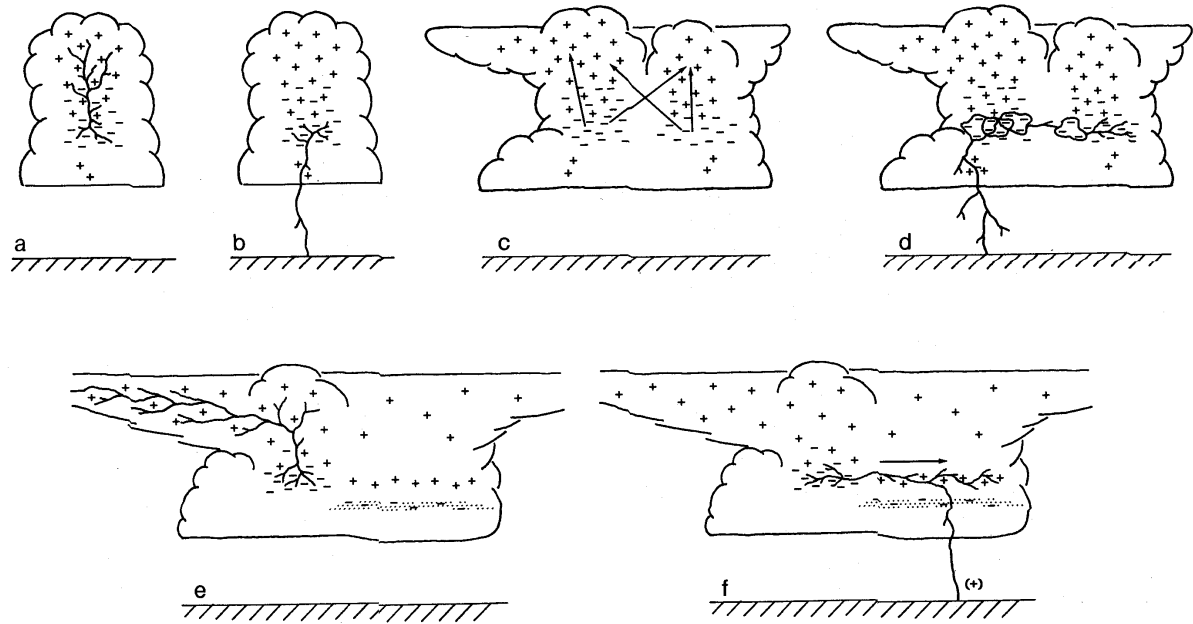


FIG. 1.13. Schematic of the different types of lightning flashes. These flashes include (a) an intracloud flash in an isolated thunderstorm, (b) a negative cloud-to-ground (-CG) flash in an isolated thunderstorm, (c) possible intracloud and cloud-to-cloud flashes within a multicell thunderstorm, (d) discharge that propagates through negatively-charged precipitation particles within the negative charge layer of different cells and then produces a -CG flash, (e) intracloud discharge propagating from the main negative charge region into the positively-charged anvil region of a mature multicell thunderstorm, and (f) horizontally-produced intracloud flashes between a negatively-charge region of an active cell and a positively-charge region of a dissipating cell that subsequently produces a positive CG flash. Image adapted from Krehbiel (1986).

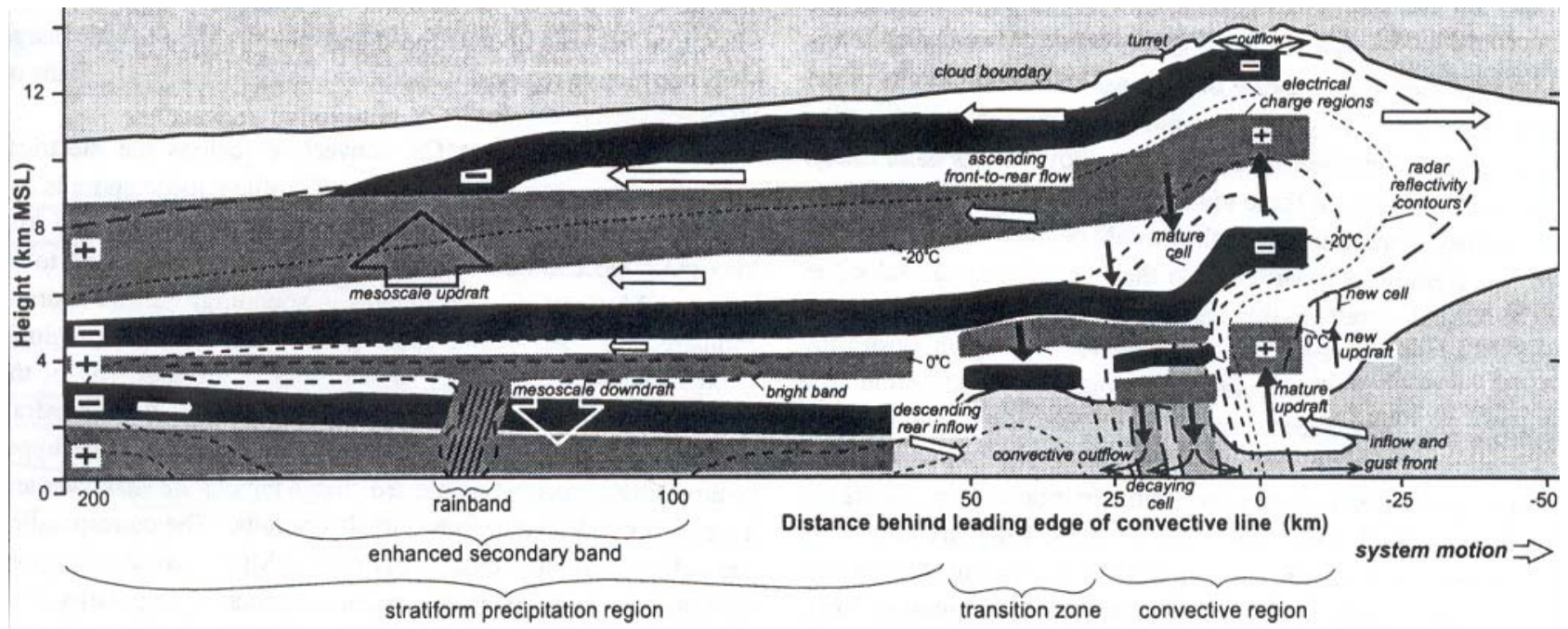


FIG. 1.14. Conceptual model of MCS charge structure. See text for further details. Image adapted from Stolzenburg et al. (1998a).

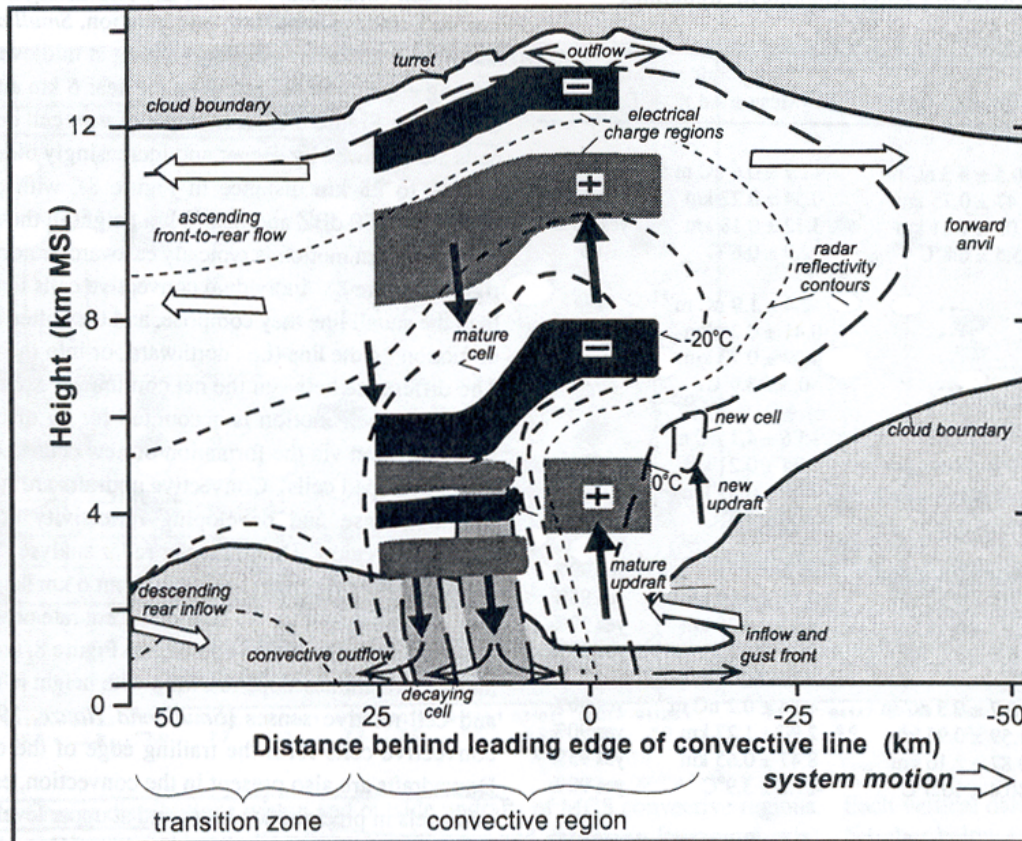


FIG. 1.15. Conceptual model of leading convective line MCS charge structure within updraft and non-updraft regions. The MCS cloud boundary is outlined in a solid black line and reflectivity values (from 10-50 dBZ in 10 dBZ increments) are contoured in dashed black lines, with the largest reflectivity associated with the shaded precipitation cores. Updraft and downdraft motions are depicted in thick solid black arrows, storm-relative motions are shown in open arrows, and divergent outflows are in thin solid black arrows. The negative charge layers are shaded in black, and the positive charge layers are shaded in dark gray. Important temperature levels are indicated on the figure. Note the charge layer similarities between MCS convective regions and typical thunderstorms (Fig. 13). Image adapted from Stolzenburg et al. (1998a).

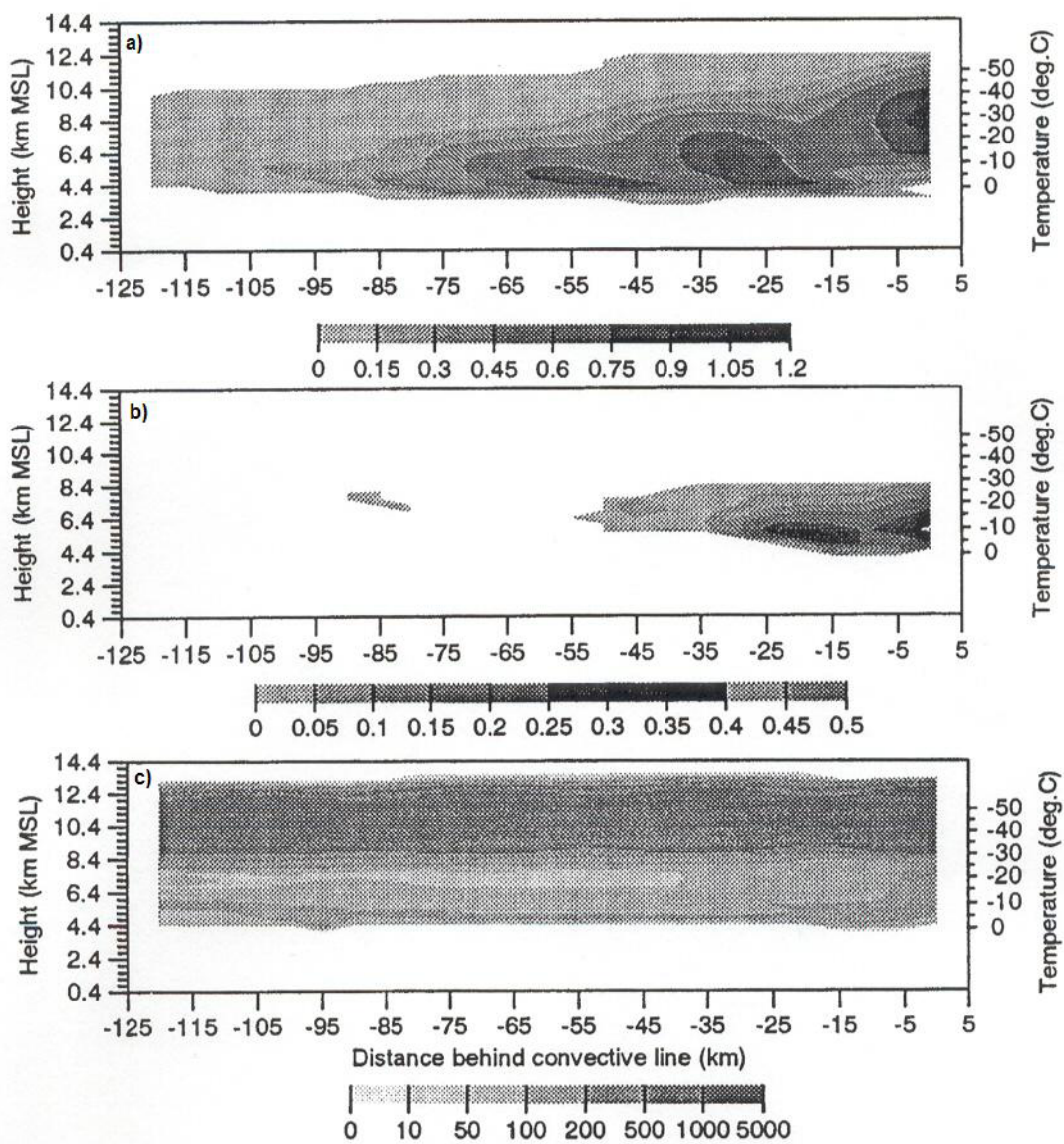


FIG. 1.16. Control run of (a) snow mixing ratio ( $\text{g kg}^{-1}$ ), (b) cloud liquid water content ( $\text{g m}^{-3}$ ), and (c) cloud ice concentration ( $\text{L}^{-1}$ ) at  $t = 3$  hr. Image courtesy of Schuur and Rutledge (2000b).

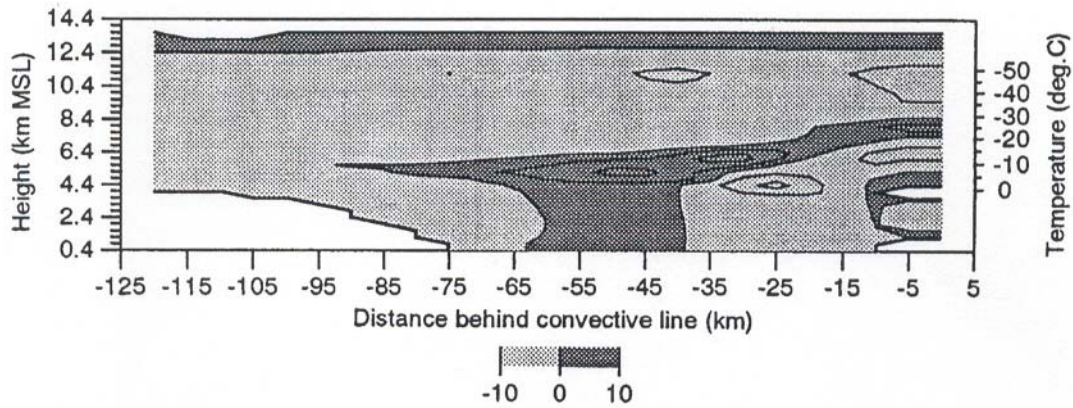


FIG. 1.17. Total charge density magnitude ( $\text{nC m}^{-3}$ ) in the stratiform region for the charge advection sensitivity model run at  $t = 3$  hr using a the Marshall and Rust (1993) “type A” charge density profile and the Saunders et al. (1991) non-inductive charging data. Positive and negative charge region are indicated by dark and light shading, respectively. Charge density contours are drawn every  $1.0 \text{ nC m}^{-3}$ . Image courtesy of Schuur and Rutledge (2000b).

## **2. DATA AND METHODOLOGY**

Three MCS cases are investigated in this study: 1) 0:00-4:30 UTC 8 April 2002, 2) 23:30 UTC 12 – 5:35 UTC 13 October 2001, and 3) 5:00-7:00 UTC 16 June 2002. The following data sets were used for the analysis of these cases:

- 1) Dallas-Fort Worth (DFW) Level II WSR-88D (KFWS) radar data,
- 2) National Lightning Detection Network (NLDN) CG lightning flashes,
- 3) Lightning Detection and Ranging (LDAR II) VHF sources associated with total lightning,
- 4) severe storm reports,
- 5) surface observations, and
- 6) upper-air soundings.

Radar data were obtained from the National Climatic Data Center (NCDC), NLDN CG lightning flash and LDAR II source data came from Vaisala Inc., severe storm reports were obtained from the Storm Prediction Center (SPC) website, and surface observations and upper-air data came from the archive maintained by North Carolina State University (NCSU). These three cases were chosen because they were the only TS MCSs that evolved within the KFWS radar since the LDAR II network has been operational in the DFW region (since 2001).

### **2.1 KFWS WSR-88D Level II Radar Data**

This study uses Level-II Weather Surveillance Radar 1988 Doppler (WSR-88D) archive data (digital base data in polar format) from KFWS (Dallas-Fort Worth, TX) for all

three case studies. The WSR-88D is an S-band radar (10 cm wavelength) that can detect hydrometeors larger than cloud droplets. With a gate spacing of 250 m and a beam width of  $0.95^\circ$ , this radar provides a radial velocity spatial resolution of  $0.95^\circ \times 0.25$  km and a radar reflectivity spatial resolution of  $0.95^\circ \times 1.0$  km (since reflectivity data are averaged every 4 gates) (Crum et al. 1993).

The WSR-88D was operating in “severe weather” mode or Volume Coverage Pattern 11 (VCP11) during all three case studies. In severe weather mode, the radar makes 16 unique  $360^\circ$  azimuthal sweeps (comprising one volume scan) at 14 unique  $360^\circ$  azimuthal sweep angles varying in elevation from  $0.5$ - $19.5^\circ$  in 5 min (Fig. 2.1). The radar completes two sweeps in each of the lowest two elevation angles. The first sweep in each of the two lowest angles is run using a low pulse repetition frequency (PRF) of  $4.7 \mu\text{s}$  to map the reflectivity field out to 460 km range. The next sweep in each of these two angles is run using a higher PRF of  $1.57 \mu\text{s}$  to map the velocity field out to 230 km range. At higher elevation angles, this repetition is not necessary because these functions are performed simultaneously (Crum et al. 1993). Severe weather mode scanning strategy provides the most complete coverage of a storm because each volume scan is faster and has more sweeps than during any other scanning strategy. Even in severe weather mode (Fig. 2.1), however, gaps in data coverage exist (especially at upper levels), and these gaps become more pronounced with increasing distance from the radar.

### ***2.1.1 Methods of Analysis***

WSR-88D data were used in this study to analyze both horizontal and vertical cross-sections of radar reflectivity and radial velocity data during the time period when each of the three MCS case studies were within range of the KFWS radar. The reflectivity data were

also used in a more quantitative sense to calculate total echo volume aloft and rainfall rates within the convective and stratiform regions of each MCS. Finally, the reflectivity and radial velocity data were used to determine mesoscale horizontal and vertical motions within two of the MCS case studies by processing the data through a synthetic dual-Doppler analysis technique.

Before any analyses were performed, level-II WSR-88D data were converted from polar to Cartesian coordinates using SOLO and REORDER (Oye and Case 1995) software programs. SOLO, a software program used for editing and displaying radar data, was used to convert the radar data to universal format (uf). Once the radar files were in uf format, REORDER was employed to grid these data into Cartesian coordinates on constant altitude plan-position indicator (CAPPI) surfaces. The data processed using REORDER were set to have a horizontal grid spacing of 1.0 km and a vertical grid spacing of 0.5 km. The x-, y-, and z- radii of influence were set to 1.0 km, and a three-dimensional Cressman weighting scheme (Cressman, 1959) was used to derive Cartesian grid points from radar data.

The Cressman weighting scheme is a function of the grid spacing and the radii of influence. The radius of influence (R) is defined as:

$$R^2 = dX^2 + dY^2 + dZ^2 \quad [2.1]$$

The weighting function, W, for a particular gate value is defined as:

$$W = \frac{R^2 - r^2}{R^2 + r^2} \quad [2.2]$$

where  $r^2$  is the square of the distance between the gate and the grid point (Oye and Case, 1995). It is evident that grid points closer to the particular gate value have more weight than grid points further away.

The data files processed using REORDER were outputted to a netCDF file and then displayed using Interactive Data Language (IDL) programs. These programs are able to display both horizontal CAPPI and vertical cross-sectional images of radar data in Cartesian coordinates. The horizontal images are  $200 \text{ km} \times 200 \text{ km}$  in area and centered on the KFWS radar. The vertical images of radar data are  $200 \text{ km} \times 20 \text{ km}$ , and the IDL program can either create a North-South or East-West vertical cross-section anywhere within range of a given radar volume scan.

The horizontal images of radar reflectivity were rotated in order to examine vertical cross-sections taken line parallel and line perpendicular to a given MCS and to perform composite analyses. After determining the degree to which a given MCS deviated from due North-South orientation, that MCS was rotated counterclockwise by the appropriate number of degrees to force a North-South orientation. This rotation was performed during the REORDER processing using the “GBASELINE” command, which specifies the azimuth of the x-axis of the grid in degrees. As before, a netCDF file is outputted from the REORDER processing. This file can then be displayed as both horizontal CAPPI and vertical cross-sectional images of radar data in Cartesian coordinates. Composite images were created by averaging all possible line perpendicular vertical cross-sections of radar reflectivity within the  $200 \text{ km} \times 200 \text{ km} \times 20 \text{ km}$  grid volume to produce one vertical cross-section of the “average” MCS convective, transition, and stratiform regions.

#### **2.1.1.1 Partitioning Techniques**

One major focus of this research is to analyze the individual contributions that the convective and stratiform regions provide to the structure and evolution of the MCS as a whole. To accomplish this task, the radar data had to be partitioned according to their

respective location, convective or stratiform, within the MCS. Two different partitioning methods, Steiner et al. (1995) partitioning and subjective line partitioning, are compared and contrasted to determine which technique is more accurate.

According to the Steiner et al. (1995) partitioning method, on a given low-level horizontal plane (0.5 km altitude for this study), radar reflectivity echoes that either exceed a certain intensity or are located within a strong gradient region are classified as convective, and all remaining nonzero reflectivity echoes are then labeled as stratiform. Low-level (0.5 km) reflectivity images are used so that large areas within the stratiform region are not falsely identified as convective due to the appearance of the enhanced reflectivity bright band within the stratiform region at mid-levels (i.e. this partitioning method is accomplished well below melting level). To be classified as part of the convective region, low-level reflectivity echoes must either: 1) be  $\geq 40$  dBZ, 2) exceed an average background intensity (determined by the average of the nonzero radar echoes within an 11 km radius around the grid point) by at least the reflectivity difference defined by Fig. 2.2, or 3) fall within a given echo intensity-dependent radius of another echo that has previously been classified as convective. In this study, echoes that pass the third criteria must be within either a 4 km radius of a 40-dBZ echo, a 3 km radius of a 35-dBZ echo, or a 2 km radius of a 30-dBZ echo.

The second partitioning method used in this study is a subjective line partitioning technique. For a given low-level (0.5 km) radar reflectivity image, a straight line is drawn along the back edge of the subjectively defined convective region. Anything located behind the line is classified as part of the stratiform region, and anything located along or in front of the line is classified as part of the convective region for a given MCS. This partitioning technique works well with TS MCSs, in which the convective and stratiform precipitation

regions are clearly separated, but it would not work well with cases where convective precipitation is embedded within stratiform precipitation, for example. In this study, the transition zone is grouped with the stratiform region because its characteristics are more closely related to the stratiform region than to the convective region.

Radar reflectivity data from two of the three case studies were partitioned using the two methods discussed above, and then the results were compared. Each method was run for the MCSs' duration within radar range, and the algorithm that handled both case studies best was used in this study. Figures 2.3 and 2.4 show a comparison between Steiner et al. (1995) and subjective line partitioning methods for the 8 April 2002 MCS at 1:29 UTC, respectively. Notice that the Steiner et al. (1995) partitioning method incorrectly labels parts of the stratiform region as convective, especially within the enhanced reflectivity echoes in the stratiform region, and parts of the convective region as stratiform, especially along the leading edge of the convective line (Fig. 2.3). Therefore, the errors associated with the Steiner et al. (1995) partitioning method could strongly bias total lightning amounts. The subjective line partitioning method, however, only generates errors along the transition between the convective and stratiform regions, where a nonlinear boundary between the convective and stratiform precipitation is being partitioned based on a straight line (Fig. 2.4). As a result, the subjective line partitioning method was chosen for this study instead of the Steiner et al. (1995) partitioning method.

Subjective line partitioning allowed for various convective and stratiform region analyses, including echo volume aloft and rainfall rate calculations as well as total lightning rates and trends. Once these analyses were performed individually, trends in radar

reflectivity characteristics could then be compared to trends in lightning rates to determine if similarities exist.

#### **2.1.1.2 Echo Volume Aloft Calculations**

This study used echo volume aloft calculations to determine the relative strengths of each MCS, as well as the strengths of their regions, as the systems evolved with time. This research also compared trends in lightning rates to trends in echo volume aloft for each MCS and their respective regions to determine if these two characteristics correlate. The presence of graupel and hail in these layers is important in a storm's electrification process and, therefore, correlate to peaks in lightning rates.

The amount of echo volume aloft within the  $200 \text{ km} \times 200 \text{ km}$  analysis domain of each given MCS was determined by applying an IDL program that first limits the volume vertically based on temperature thresholds that include the region of significant theorized lightning electrification within a cloud and then further limits the volume by counting the number of grid boxes (in three dimensions) satisfying predetermined reflectivity thresholds. Sensitivity tests were performed using the  $0^{\circ}\text{C}$  to  $-40^{\circ}\text{C}$  and  $-10^{\circ}\text{C}$  to  $-40^{\circ}\text{C}$  temperature layers and the following reflectivity thresholds: 25-, 30-, 35-, 40-, 45-, 50-, and 55-dBZ.

After echo volume aloft was calculated using the various temperature and reflectivity thresholds, Microsoft Excel was used to graph the echo volume aloft trends. These results were then compared to lightning flash rates to determine if a correlation exists as previous studies have shown.

#### **2.1.1.3 Rainfall Rate Calculations**

Another quantity that relates MCS microphysical processes to its evolution is the trend in rainfall rate within the convective and stratiform regions. Partitioned convective and

stratiform region rainfall rates can be calculated using a z-R relationship ( $z = aR^b$ ) by making several modifications to the partitioned echo volume aloft program. First, in order to calculate rainfall rates, only the lowest 2 km of a given radar reflectivity image was used. These reflectivity values most accurately represent precipitation that is hitting the ground and also solve the problem of introducing large errors associated with the enhanced reflectivity bright band area in the stratiform region.

Next, since average rainfall rates are measured from a given image, areas not associated with any precipitation were removed. To do this, the radar data were subsetted to only include reflectivity values greater than or equal to a predetermined value. This predetermined value varied from 5- to 25-dBZ in order to test the sensitivity of rainfall rates to smaller reflectivity echoes.

Hail also introduces errors when calculating rainfall rates. Since hail returns large reflectivity values, unreasonably large rainfall rates could result if hail is present. To alleviate this potential problem, all grid points that have reflectivity values greater than 53-dBZ were set equal to 53-dBZ. This approach is similar to that utilized by the Precipitation Processing System (PPS) of the WSR-88D radar (Fulton et al. 1998).

Before using the z-R equation, Z (dBZ) was converted to z ( $\text{mm}^6\text{m}^{-3}$ ), according to the conversion:  $Z = 10\log(z/1\text{mm}^6\text{m}^{-3})$ . Thus,  $z = 10^{(Z/10)}$ , where the units of z are  $\text{mm}^6\text{m}^{-3}$ . Next, from the z-R relationship:  $z = aR^b$ ,  $R = (z/a)^{(1/b)}$ , where R has units of mm/hr. The coefficients “a” and “b” were varied depending on the MCS region. Following Uijlenhoet et al. (2003), the coefficients were defined such that  $a = 300$  and  $b = 1.4$  in the convective region, while  $a = 450$  and  $b = 1.4$  in the stratiform region. Average convective and stratiform region rainfall rates were calculated for each reflectivity image at times during which the

MCS was within the radar's range. These average rainfall rate trends were then compared to other quantities (i.e. echo volume aloft and lightning activity) that are affected by the same microphysical processes within an MCS.

#### **2.1.1.4 Dual-Doppler Analysis**

##### ***2.1.1.4.1 Overview***

Dual-Doppler analysis is a method of determining the three-dimensional wind field present in a storm by using the radial velocity measurements from two Doppler radars at separate vantage points. The horizontal wind fields on a series of horizontal planes are calculated by combining the radial velocity components at each given level and initially assuming the vertical wind field is defined by the hydrometeor's fall speed. The continuity equation is then used to estimate the vertical velocity by calculating horizontal divergence at each given height level and then integrating the divergence with respect to altitude either by top-down or bottom-up integration. A top-down approach is preferred because vertical velocity is dependent upon density and, since density decreases with height, the errors associated with assuming vertical velocity is zero in a top-down approach are less than those errors associated with vertical velocity in a bottom-up approach (Miller and Fredrick 1993).

Once an initial estimate of vertical velocity is determined using the continuity equation, this estimate is then used to recalculate the horizontal wind at each layer. If the original horizontal wind differs from this newly calculated horizontal wind by more than a certain threshold, the same process is repeated using a new vertical velocity value calculated from the continuity equation integration of the newly calculated horizontal wind values. This iteration process ends when the horizontal wind difference is smaller than a predefined threshold value at every level (Miller and Fredrick 1993). For a more mathematical

description of the method used to determine the three-dimensional wind field using two Doppler radars, please see Appendix C.

Dual-Doppler coverage area (i.e. dual-Doppler lobes) is depicted in Fig. 2.5. This area is a function of the radars' spatial resolution, the accuracy of the horizontal wind measurements, and the distance between the two radars. The area can be defined as:

$$A_1(\beta) = 2(d \csc \beta)^2(\pi - 2\beta + 2 \sin 2\beta), \quad [2.3]$$

where  $\beta$  is the “between beam angle” (i.e. the angle between intersecting beams from the two radars ( $0 \leq \beta \leq 90^\circ$ )), and  $d$  is half the distance between the two radars located at  $(\pm d, 0)$ . The coverage area is defined by two circles with centers  $(0, \pm d \cot \beta)$ , and radii  $d \csc \beta$ .  $\beta$  is related to the sum of the error variances for the x ( $\sigma_u^2$ ) and y ( $\sigma_v^2$ ) components divided by the sum of the mean velocity variances of the two radars, as in the following equation:

$$\frac{\sigma_u^2 + \sigma_v^2}{\sigma_1^2 + \sigma_2^2} = \csc^2 \beta \equiv b \quad [2.4]$$

A  $90^\circ$  between beam angle results in a minimum wind field error (Davies-Jones 1979). This error increases as the angle between the two radar beams decreases, and the error associated with an angle  $< 30^\circ$  ( $b = 4$ ) is considered unacceptable (Bluestein et al. 1994).

The spatial resolution (S) of a given point within these dual-Doppler lobes is defined as:

$$S = \frac{R\pi\Delta}{180} \quad [2.5]$$

where  $R$  is the range from a given point to the furthest radar, and  $\Delta$  is the radar's half power beamwidth (Davies-Jones 1979). From equations [2.3] and [2.5], it is evident that increasing the distance between the two radars increases the dual-Doppler coverage area but decreases the spatial resolution.

#### ***2.1.1.4.2 Synthetic Dual-Doppler Analysis***

This study uses the Custom Editing and Display of Reduced Information in Cartesian space (CEDRIC) software program (Miller et al. 1993) to perform a synthetic dual-Doppler analysis on KFWS radar data for two of the MCS case studies. The synthetic dual-Doppler technique is based on the original dual-Doppler technique. Rather than using two different radars, however, the synthetic dual-Doppler technique uses radar images from two different times to estimate the three-dimensional wind field of a storm system, assuming the storm system is quasi-steady and moves at a constant velocity for a sufficiently long time period (Bluestein et al. 1994).

To perform a synthetic dual-Doppler analysis, two radar volume scans approximately one hour apart were chosen for each MCS in this study. First, an average storm system advection vector was determined by analyzing the propagation of the MCS within this one-hour time period. Next, erroneous radar reflectivity data (e.g. second-trip radar reflectivity echoes) were manually deleted, and aliased radial velocity data were unfolded using the National Center for Atmospheric Research's (NCAR) SOLO software package. The resulting data were then converted into Cartesian coordinates using the Cressman weighting function with the aid of the REORDER software package. Horizontal and vertical grid spacings were set to 2 km and 1 km, respectively; horizontal and vertical radii of influence were ultimately set to 6 km and 3 km, respectively. Other radii of influence were tested, but due to lack of radar coverage, especially at upper levels, large radii of influence were needed to smooth data coverage gaps. Klimowski and Marwitz (1992) found in their study that by increasing the horizontal radii of influence from 1.5 km to 6.0 km, and by increasing the vertical radius of influence from 1.5 km to 3.0 km, a substantial increase in similarity was

noted between dual-Doppler and synthetic dual-Doppler analyses for the same squall line case.

Using REORDER, CEDRIC had to be tricked into thinking that there were two Doppler radars (and not two different times) in order for the correct processing within CEDRIC to occur. By renaming, relocating, and re-dating the two radar volume scans to two different x, y locations that share a common time, CEDRIC was forced to assume that the data came from two separate radars. Using REORDER, the renamed radar associated with the later volume scan was advected upstream by half the distance that the storm system moved over the time difference between the two volume scans. Similarly, the renamed radar associated with the earlier volume scan was advected downstream by half the distance the storm system traveled over the time difference between the two volume scans. These moves artificially created one analysis time (the median time between the two original volume scans) and two “radars” for CEDRIC.

Once all of the data had been converted into Cartesian coordinates, renamed, and relocated accordingly, CEDRIC was used to calculate the three-dimensional wind field using the same technique employed in dual-Doppler analysis. In CEDRIC, the dual-Doppler lobe domain was calculated based on  $b = 4$  (as defined earlier), and suspicious data were discarded based on their deviation from the local mean surrounding that particular grid point. Horizontal winds at each height level were then calculated by assuming that the scatterers’ terminal fall velocities could be determined by the  $V_t$ - $Z$  relationship in Appendix C (eq. [C.1]), where  $A = 0.817$ ,  $B = 0.063$ , and  $C = 0.4$  when  $T \leq 0$  °C, and  $A = 2.6$ ,  $B = 0.107$ , and  $C = 0.4$  when  $T > 0$  °C. Horizontal divergence was then calculated and top-down integration was performed using the continuity equation to determine  $w$ . If these new values for the

horizontal wind field differed from the initial horizontal wind values by more than  $0.005 \text{ ms}^{-1}$ , this iteration process was repeated until the horizontal wind difference between the new and older values differed by less than  $0.005 \text{ ms}^{-1}$  or after 25 iterations had been completed. Both the three-dimensional wind and the horizontal convergence were calculated in this manner for each height level and then outputted to a netCDF file. In this study, an IDL program was implemented to plot the resulting three-dimensional wind data, as well as radar reflectivity data, in both the horizontal and vertical planes in Cartesian coordinates.

Synthetic dual-Doppler analysis is useful for determining the gross mesoscale features within a storm system, but it cannot resolve the small-scale features due to the errors present in this technique (Klimowski and Marwitz 1992; Bluestein et al. 1994). Klimowski and Marwitz (1992) determined that synthetic dual-Doppler analysis is sensitive to the amount of time between the two volume scans and the radii of influence used in the Cressman weighting function. Errors can also be introduced if the wind field is not in steady state and the system advection vector has been incorrectly calculated. The synthetic dual-Doppler technique works best when the equivalent dual-Doppler baseline is  $\geq 54 \text{ km}$  so that a sufficiently large Doppler lobe area can be analyzed (Bluestein et al. 1994). This 54-km threshold requires the product of the storm advection speed (in  $\text{km hr}^{-1}$ ) and the duration over which this speed is approximately constant (in hrs) to be  $\geq 54 \text{ km}$ .

In this study, attempts to minimize errors were made by choosing one hour time periods when each MCS appeared to be nearly steady state as well as close to the KFWS radar. Storm advection speeds were greater than  $15 \text{ ms}^{-1}$  ( $54 \text{ km hr}^{-1}$ ) for both case studies, and careful determination of the advection vector was performed. Composite cross-sections were used in lieu of single cross-sections to determine the mesoscale features of the MCS

primarily because the rapidly changing and spatially heterogeneous MCS convective region can deviate significantly from steady state on the convective scale. In addition, previous studies tend to use composite cross-sections instead of single cross-sections, so the use of composite cross-sections in this study makes it possible to directly compare results from this study to previous research.

## **2.2 National Lightning Detection Network (NLDN) Data**

### ***2.2.1 Overview***

The National Lightning Detection Network (NLDN), owned and operated by Vaisala (Tucson, Arizona), detects CG lightning radiation associated with return strokes. The NLDN is comprised of a total of 106 sensors nationwide, with typical baselines (i.e. distances between sensors) of 275-325 km (Fig. 2.6). These sensors are composed of 59 Time of Arrival (TOA) sensors and 47 Improved Accuracy from Combined Technology (IMPACT) sensors that are used to compute an optimum lightning location using a least squares method. IMPACT sensors combine magnetic detection finder (MDF) and TOA information technology.

This network reports the location, time, polarity, peak amplitude, and multiplicity of CG lightning activity throughout the U.S. As the ground-based sensors detect radiation from CG lightning return strokes, the information is transmitted by satellite to the Network Control Center (NCC) in Tucson, Arizona, where the data are processed. The processed data are then transmitted back to the satellite, where they are distributed by Vaisala, Inc. to real-time users nationwide within 40 sec of the initial lightning discharge. These same CG lightning data are

reprocessed within a few days and archived in a permanent database (Cummins et al. 1998), which is also available to users through Vaisala, Inc.

The distance from the sensor location to the location of the CG flash is determined by the TOA sensors, and the direction in which the CG flash occurred is determined by the MDFs. Combining these data and using a least squares method, the optimal lightning flash location can be determined (Cummins et al. 1998; MacGorman and Rust 1998). Typically, a 5 kA CG lightning flash can be detected by 2-4 sensors, a 25 kA flash can be detected by 6-8 sensors, and an 100 kA flash can be detected by 20+ sensors. The NLDN network has a median location accuracy of 0.5 km, a flash detection efficiency of 80-90%, and a time resolution of 0.1 sec (Cummins et al. 1998).

### ***2.2.2 Subsetting and Analysis Techniques***

NLDN data were used to examine the CG lightning flash characteristics within the convective and stratiform regions of three MCS case studies. These characteristics include the percent of +CG lightning flashes and average peak positive and negative current within each MCS region, as well as the areas of dominant CG lightning activity within each case study. These findings were then compared with the assumed microphysical processes occurring within the MCSs as derived from Doppler radar analyses and echo volume aloft and rainfall rate calculations.

Using FORTRAN, NLDN CG lightning data were first subsetted into 5 min increments, approximately centered on the time of the associated radar image. During this process, CG flashes associated with peak currents < 10 kA were discarded, since they are usually associated with cloud discharges and not CG lightning (Cummins et al. 1998; Wacker and Orville 1999). Next, the resulting CG data were overlaid on 200 × 200 km images of

low-level (0.5 km height) radar reflectivity to qualitatively determine the relative locations of CG lightning with respect to MCS structure. An IDL program was created to group each 5 min increment of lightning flash data into convective or stratiform CG flashes based on the subjective line partitioning method. This IDL program also counted the number of positive and negative flashes, as well as the average peak positive and negative current associated with each MCS region. Using Excel, the resulting data were then statistically analyzed and the flash trends were graphed. These flash trends were then compared to trends in rainfall rate and echo volume aloft.

### **2.3 Lightning Detection and Ranging (LDAR II) Network Data**

The Lightning Detection and Ranging II (LDAR II) network detects Very High Frequency (VHF) radiation emissions produced from the electrical discharge processes (i.e. initial breakdown and ionization) associated with total (IC and CG) lightning (hereafter referred to as “LDAR II sources” or “sources”). The network is developed, owned, and operated by Vaisala. LDAR II is comprised of 7 VHF sensors that, together, determine the latitude, longitude, altitude, and emitted time of these sources using a Time of Arrival (TOA) technique (Demetriades et al. 2000). The network can detect up to 10 000 source locations per second (M. Murphy 2002, personal communication). The LDAR II network consists of a central sensor, located at the Dallas-Fort Worth International Airport, surrounded by six sensors with baselines of 20-30 km (Fig. 2.7) (Cummins et al. 2000; Demetriades et al. 2000). The center of the LDAR II network (latitude = 32.896°N, longitude = 97.037°W) is located approximately 44 km northeast of the Dallas-Fort Worth WSR-88D weather radar (Fig. 2.7) (latitude = 32.573°N, longitude = 97.303°W).

Locations of LDAR II sources can provide insight into convective and stratiform charge centers. Since 1) the LDAR II network detects VHF radiation emissions produced from the electrical discharge processes (i.e. initial breakdown and ionization) associated with total (IC and CG) lightning, 2) lightning flashes preferentially travel through net charge centers (Williams et al. 1985; Coleman et al. 2003), and 3) a presence of net charge can be inferred from lightning channels (Coleman et al. 2003), LDAR II source data can be used to study charge centers associated with lightning.

### ***2.3.1 Detection Technique***

The LDAR II network's detection technique is based on both the LDAR-I network, currently operational in Melbourne, FL (Lennon and Maier 1991; Murphy et al. 2000), and the New Mexico Institute of Mining and Technology Lightning Mapping Array (LMA), currently operational in the Magdalena Mountains, NM (Rison et al. 1999; Cummins et al. 2000). LDAR II detects radio frequency (RF) radiation emitted by electrical discharges within the 50-150 MHz frequency range in a bandwidth of 5 MHz (Demetriades et al. 2000; M. Murphy 2002, personal communication). It can detect the initial breakdown and ionization processes associated with CG lightning, including stepped leaders, upward connecting discharges, and dart-leaders (Laroche et al. 1994; Cummins et al. 2000; Demetriades et al. 2000). The network can also detect the initial IC flash breakdown processes, which include 1) the vertical channel that forms between the two main charge regions and 2) the two horizontal channels that extend outwards from the vertical channel in the upper and lower charge regions (Laroche et al. 1994; Cummins et al. 2000). These upper and lower charge regions correspond to the upper positive and main negative charge centers of the storm, respectively. The horizontal extent of the IC flashes is much larger than the

vertical extent (Krehbiel et al. 1999; Shao and Krehbiel 1996). The horizontal extent of IC flashes varies depending upon the storm system's size and morphology. For example, Krehbiel et al. (1999) noted a horizontally-extensive IC flash extended ~75 km in the east-west direction but only 2-3 km in the vertical within a central Oklahoma thunderstorm. Negative polarity breakdown in the positive charge region is inherently noisier in the RF range than positive polarity breakdown in the negative charge region, resulting in a greater concentration of electrical discharges detected in the positive charge region than in the negative charge region (Laroche et al. 1994; Shao and Krehbiel 1996; Rison et al. 1999; Wiens et al. 2000).

Each LDAR II sensor is composed of a hollow aluminum tube that supports a fiberglass linear dipole array and Global Positioning System (GPS) antenna (Fig. 2.8). When a source is detected, each sensor individually records a time and signal strength for each detected VHF signal. The data are then sent to a central computer that uses a TOA technique to map these VHF sources in 3 dimensions. The TOA technique employed involves a least squares regression of more than 4 arrival times (i.e. time data from more than 4 sensors) to determine the position and time of the emitted source (Cummins et al. 2000; M. Murphy 2003, personal communication). The line-of-sight propagation of VHF signals, as well as the large number of short-duration sources produced per flash in this frequency, allows VHF sources to be mapped in detail in 3 dimensions (Cummins et al. 2000).

### ***2.3.2 Detection Efficiency and Location Accuracy***

Although the LDAR II network has a detection rate of up to 10,000 VHF sources  $s^{-1}$ , the line-of-sight propagation of VHF signals limits the network's range of detection (Cummins et al. 2000). The LDAR II's detection efficiency is such that over 90% of

lightning flashes can be detected from the center of the network out to a range of approximately 100 km (Fig. 2.9). At distances greater than 100 km, the detection efficiency rapidly decreases. At 200 km, the detection efficiency is less than 50% (M. Murphy 2002, personal communication).

Within the ring formed by the network's six peripheral sensors, the location of a VHF source can be determined  $\pm 0.1$  km, and out to 40 km from the network's center, the VHF source location can be determined  $\pm 0.25$  km (Fig. 2.10) (Demetriades et al. 2002; M. Murphy 2002, personal communication). This location accuracy decreases with distance, and at a 200-km radius, the accuracy is  $< 16$  km. The time resolution for each source location is 50 ns (M. Murphy 2002, personal communication).

The above description of LDAR II detection efficiency and source location accuracy assumes that the seven network sensors are working properly. Deviations from optimal network performance can decrease the detection efficiency and location accuracy. Specific details of the LDAR II network's performance for each of the three case studies will be discussed later in individual case study chapters.

### ***2.3.3 Subsetting and Analysis Techniques***

This study used data from LDAR II sources for three case studies to determine the overall total lightning trends of an MCS within the KFWS radar's viewing range. LDAR II data were obtained for times when each MCS was within the KFWS radar's viewing range.

Using FORTRAN 77, the LDAR II source data were first subsetted into 5-min increments (similar to the NLDN CG lightning data), approximately centered on the time of the associated radar image. The subsetted LDAR II source data were then rotated so that they could be overlaid on corresponding rotated radar reflectivity images in both the

horizontal and vertical planes using IDL. This LDAR II source rotation was performed within the IDL programs that plotted the data by using simple geometry. First, a given source's distance from the KFWS radar and the source's location angle from true north were determined from the source's known x and y positions. The source was then "rotated" by subtracting the rotation angle (i.e. the angle used to rotate the MCS radar reflectivity data) from the source location angle. This new angle, along with the source's original distance from the KFWS radar, was used to calculate the source's new x and y positions. This procedure was performed on all sources, and the same IDL program then overlaid these "rotated" sources on rotated images of radar reflectivity in both the horizontal and vertical planes. These rotated images allow the dominant LDAR II source activity regions to be analyzed in relation to MCS storm structure.

Next, LDAR II source data were further subsetted based on their 3-dimensional location within the MCS. Using the same subjective line partitioning method employed to subset the WSR-88D radar data, sources were also grouped into "convective" and "stratiform" according to their x-y location in relation to the drawn line. After the data were subsetted, the same IDL code computed the number of sources in each 1 km height layer (i.e. 0-1 km, 1-2 km, ..., 19-20 km), and outputted these values to the screen. Excel was then used to analyze the temporal and spatial trends of these sources. The convective, stratiform, and total source trends were then compared to trends in echo volume aloft and rainfall rate.

Vertical cross-sections of composite reflectivity images line perpendicular through a given MCS overlaid with composite LDAR II source data were also analyzed in this study. For a given composite reflectivity image, the total LDAR II source density at a given x-z position (where x is line perpendicular) was calculated. This process was performed for all

x-z locations, and the resulting source density throughout the vertical cross-section were then overlaid as shaded contours on these images. Dominant source heights and their locations with respect to MCS structure were then analyzed using these composite images. Since MCS conceptual models are constructed from composite results of a storm system's characteristics, it is natural to compare composite results from the case studies presented in this research to these conceptual models.

#### ***2.3.4 Flash Algorithms and Plotting Techniques***

In order to compare results from this study to previous studies and to discuss lightning activity in a more physically meaningful way, LDAR II sources were subsetted into “lightning flashes” according to various temporal and spatial constraints. The first source in time in a given flash is designated the “flash origin.” Various flash algorithms were created using FORTRAN to study algorithm-derived lightning flashes. After detailed analyses, the modified NASA algorithm was determined to be the algorithm that best represented flash characteristics in all three MCS regions, and it was therefore used in this study. For more information about these various algorithms and their results, please see Appendix D.

The same data processing that was performed on LDAR II sources was performed on LDAR II flash origins to determine the relationship of flash origins to MCS structure in the vertical and horizontal planes. Also, flash origin data were grouped into “convective” and “stratiform” regions, and the resulting temporal and spatial trends were analyzed. These trends were also compared to both total echo volume aloft and rainfall rates in each MCS region and to the MCS overall.

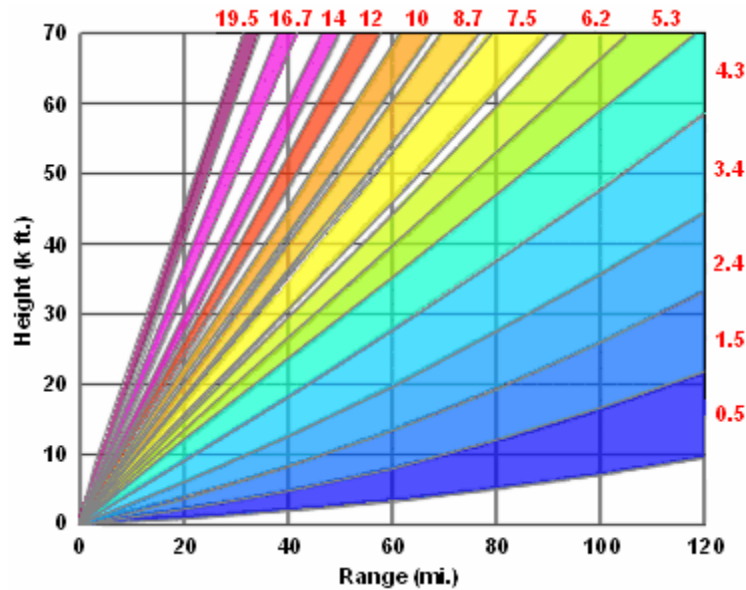


FIG. 2.1. VCP11 WSR-88D scanning strategy (“severe weather mode”) coverage. Image courtesy of the National Weather Service (NWS) Southern Region Headquarters webpage, <http://www.srh.noaa.gov/radar/radinfo/>.

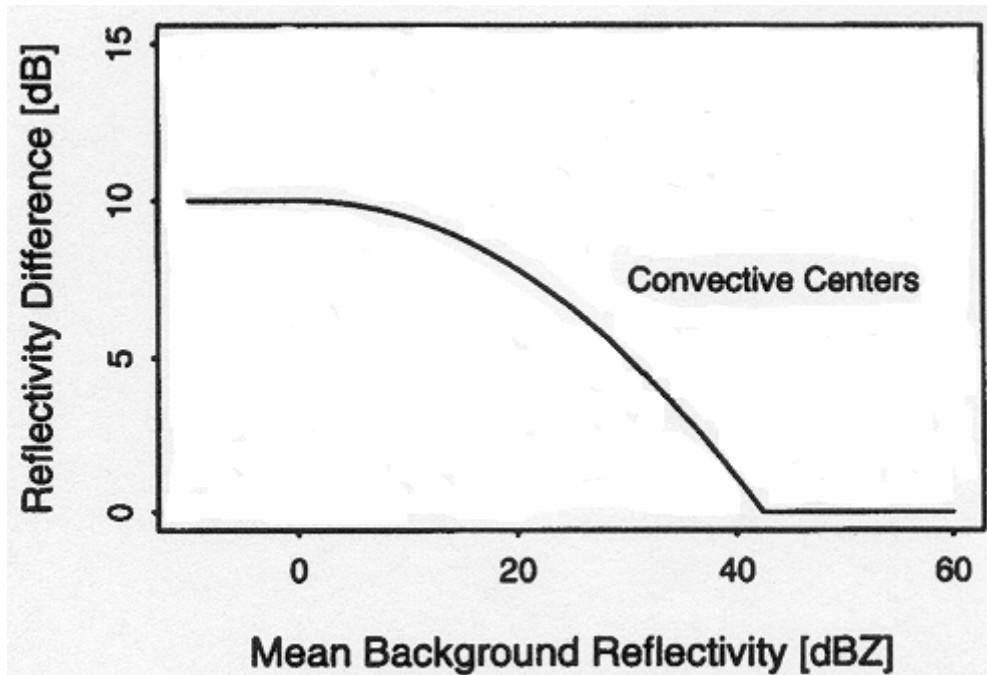


FIG. 2.2. Following the Steiner et al. (1995) partitioning method, the amount of dB a given grid point must exceed the 11 km radius mean background reflectivity value by in order to be classified as convective. Image adapted from Steiner et al. (1995).

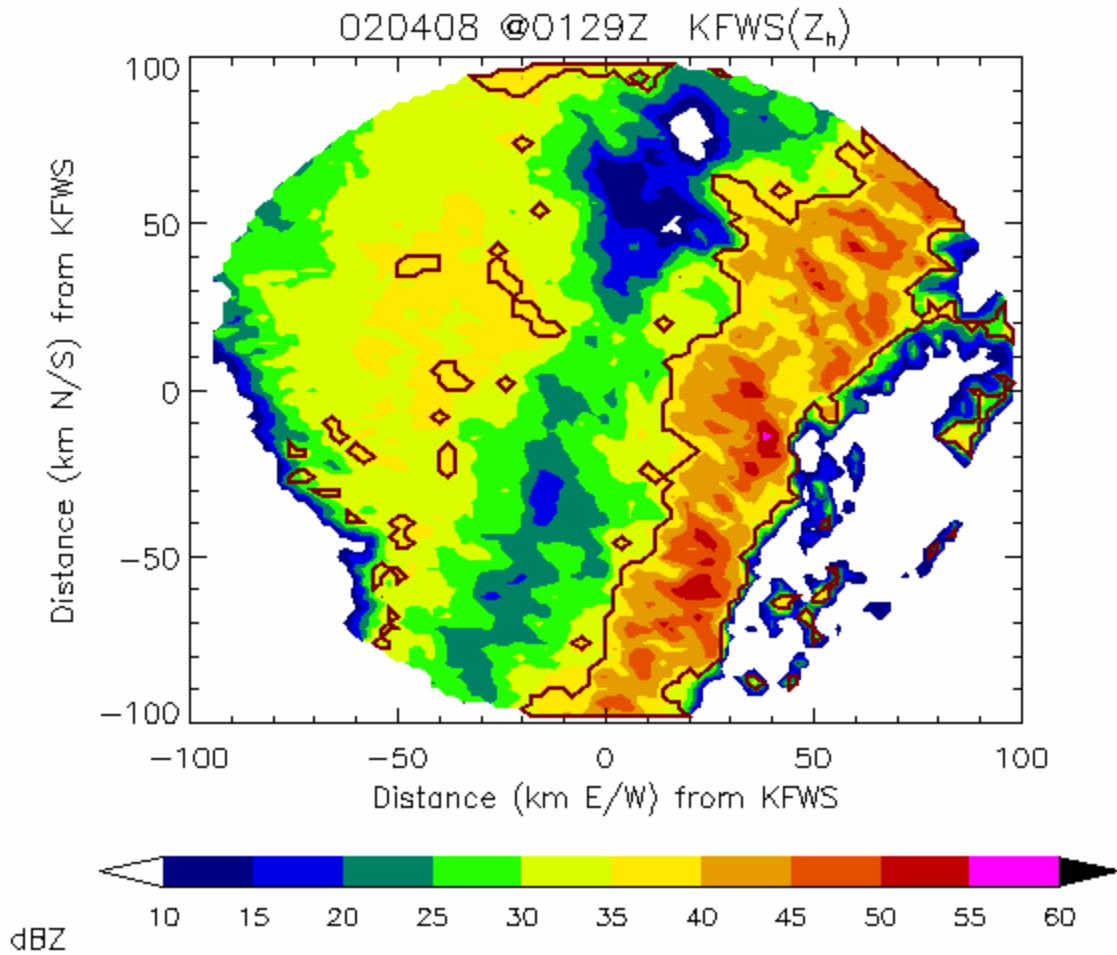


FIG. 2.3. Example of the results obtained using the Steiner et al. (1995) partitioning method using 0.5 km constant altitude KFWS reflectivity data from the 8 April 2002 MCS at 01:29 UTC. Maroon contours represent areas classified as “convective” according to this technique. Reflectivity values (dBZ) are contoured according to the scale, and the center of the image represents the radar location.

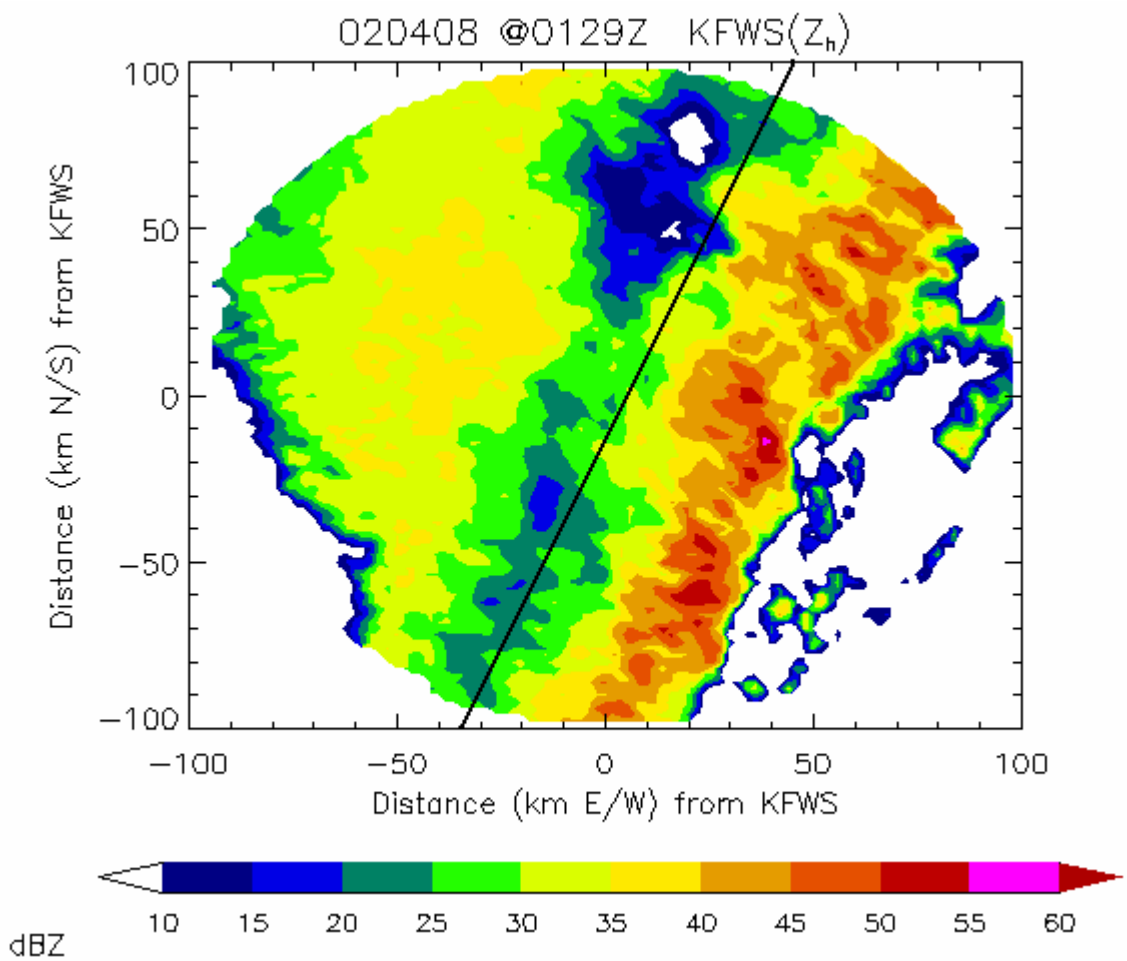


FIG. 2.4. Example of the subjective line partitioning method using a 0.5 km constant altitude KFWS radar reflectivity data from the 8 April 2002 MCS at 01:29 UTC. The black line located along the back edge of the convective line represents the partitioning line used to classify radar and total lightning data as either “convective” or “stratiform.” The two endpoint coordinates of this line are (-35.0, -100.0) and (45.0, 100.0). All grid points located along or to the left of this line are classified as “stratiform,” and all grid points located to the right of this line are classified as “convective.” Reflectivity values (dBZ) are contoured according to the scale, and the center of the image represents the radar location.

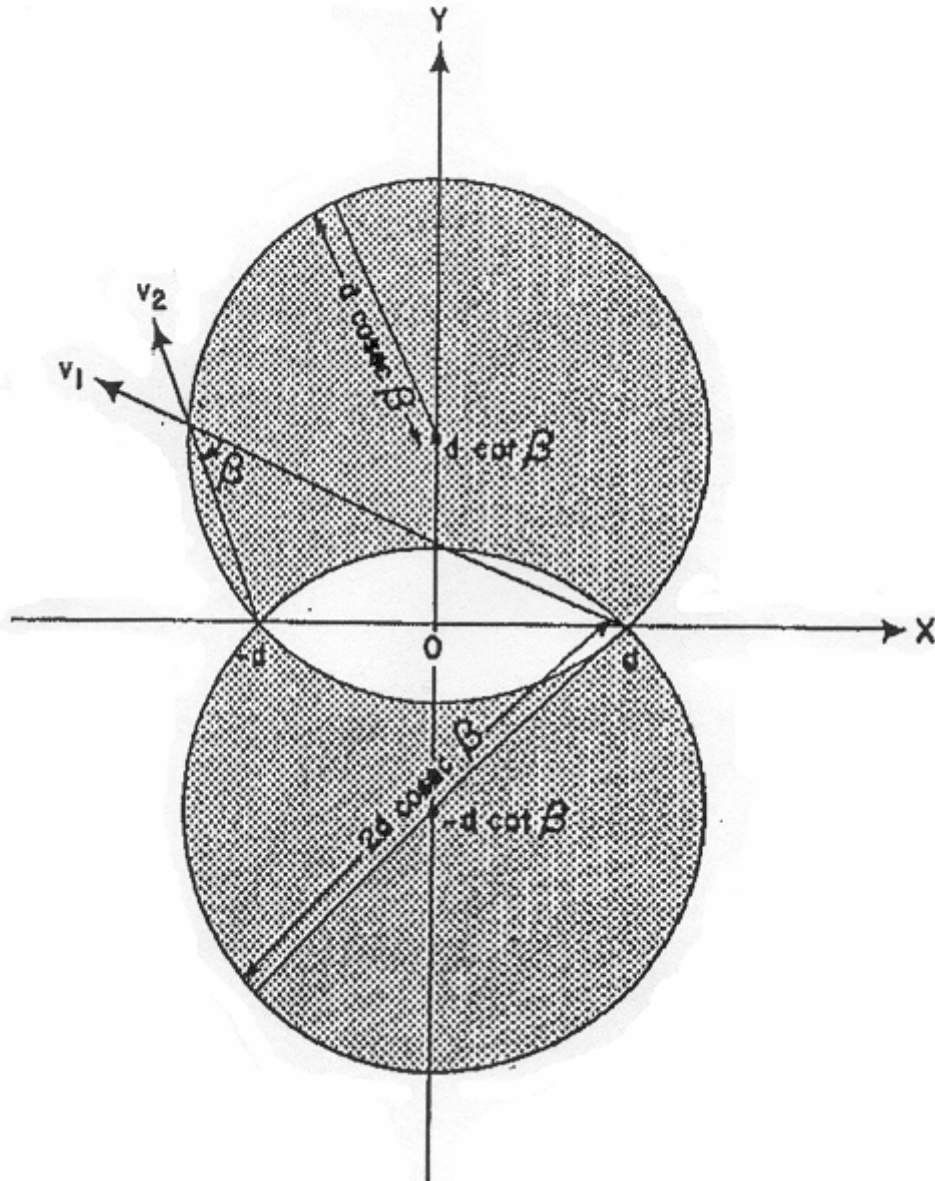


FIG. 2.5. Dual-Doppler coverage area (i.e. “dual-Doppler lobes”). The two radars are located at  $(\pm d, 0)$ . The coverage area is defined by two circles with centers  $(0, \pm d \cot \beta)$ , and radii  $d \csc \beta$ , where  $\beta$ , defined as  $0 \leq \beta \leq 90^\circ$ , is the angle between intersecting beams from the two radars. When  $\beta < 30^\circ$ , the errors in the three-dimensional wind field calculations become intolerably large, so these wind field values are discarded.  $V_1$  and  $V_2$  represent the two radar beams. Image adapted from Davies-Jones (1979).

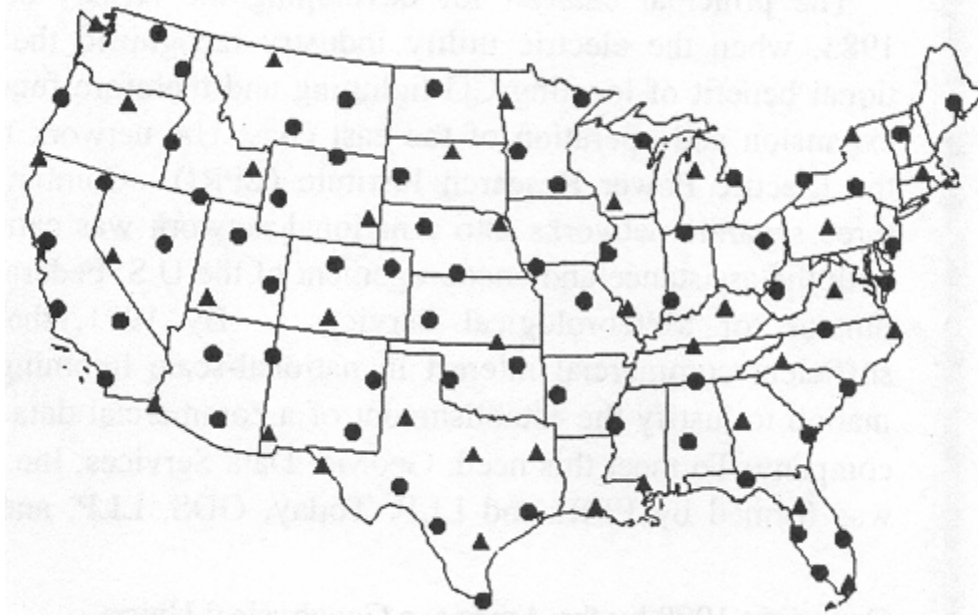


FIG. 2.6. Locations of the 106 NLDN sensors nationwide. Circles represent TOA sensors, and triangles represent IMPACT sensors. Image courtesy of Cummins et al. (1998).



FIG. 2.7. Locations of the seven sensors associated with the LDAR II network and the KFWS WSR-88D radar. The distance between the center of the LDAR II network and the KFWS radar is approximately 44.0 km. Map courtesy of the U.S. Census Bureau U.S. Gazetteer webpage, <http://www.census.gov/cgi-bin/gazetteer>.

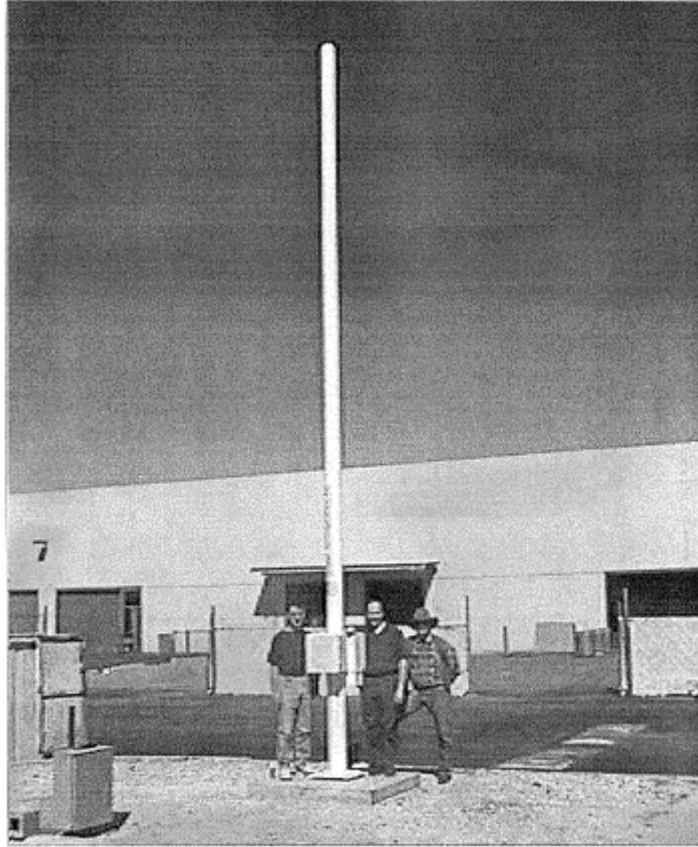


FIG. 2.8. Photograph of an LDAR II sensor. Image courtesy of M. Murphy 2002.

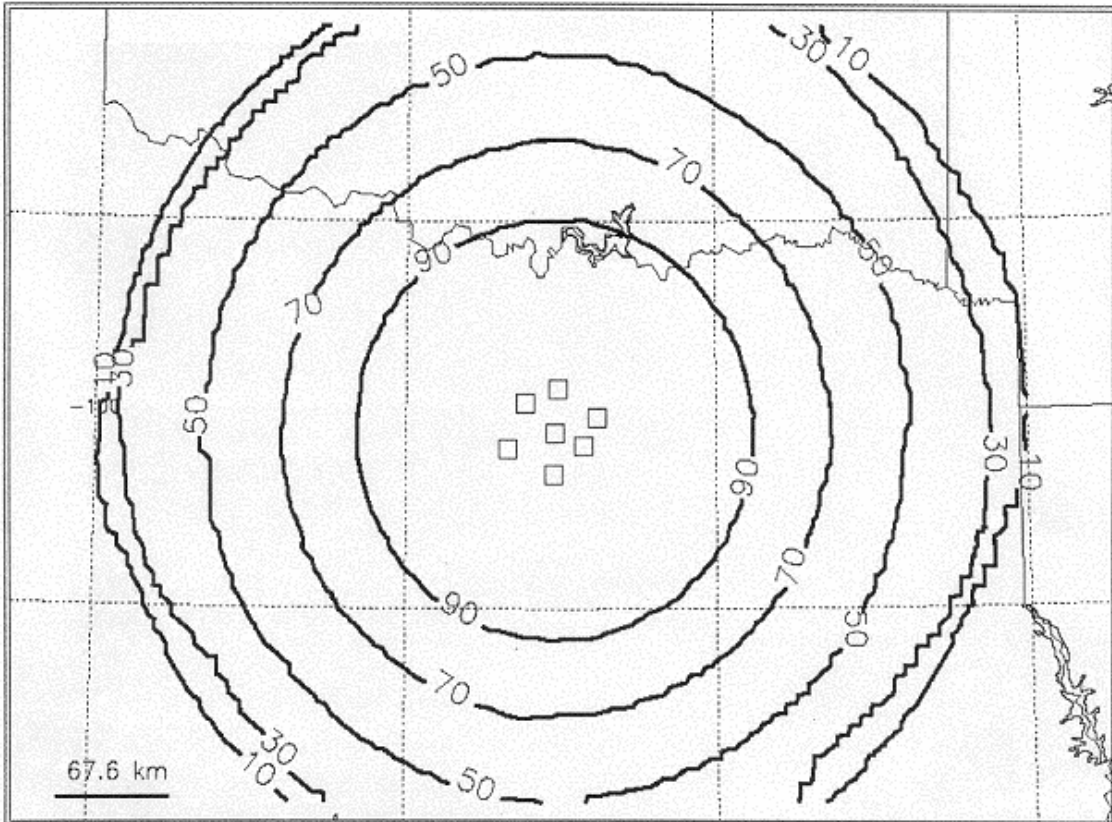


FIG. 2.9. Percent (%) of lightning flashes that can be detected by the LDAR II network. The seven boxes in the center of this image represent the locations of the seven LDAR II sensors. The LDAR II network is able to detect over 90% of lightning flashes out to approximately 100 km from the center of the network. Image courtesy of M. Murphy 2002.

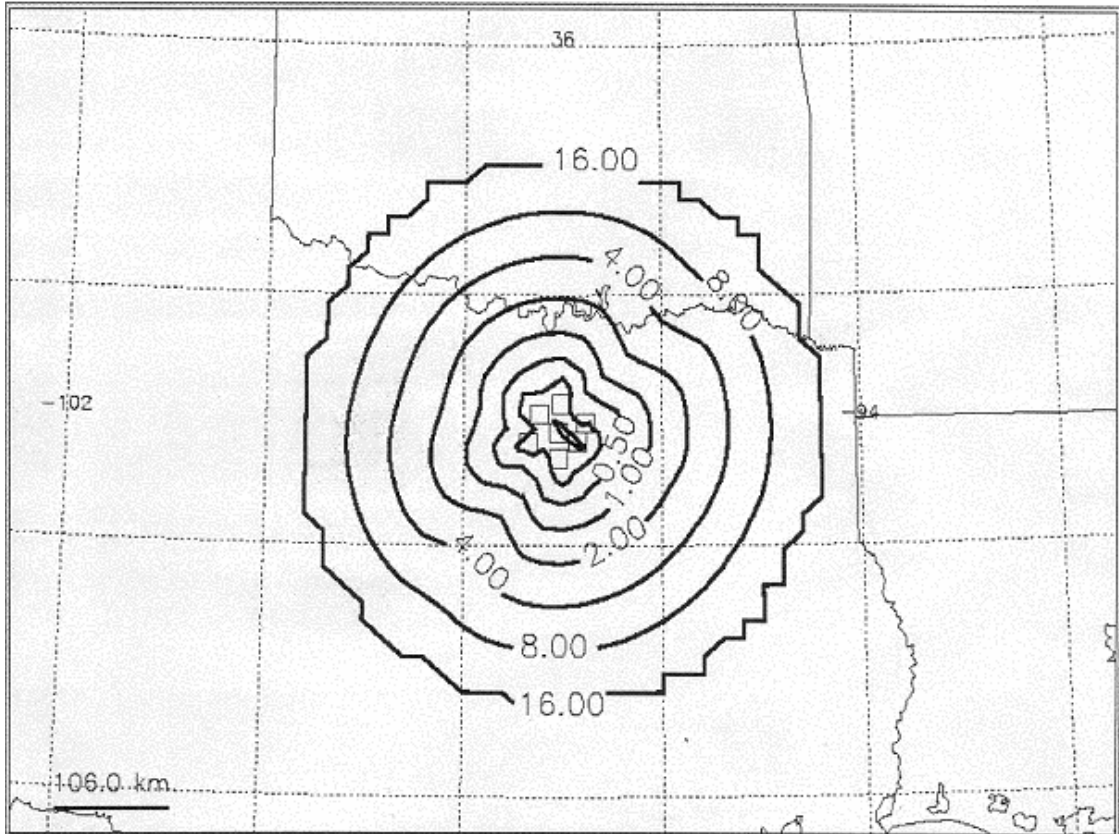


FIG. 2.10. Location accuracy (in km) of VHF source locations detected by the LDAR II network. The seven boxes in the center of this image represent the locations of the seven LDAR II sensors. The LDAR II network can detect the 3-dimensional location of a source with 0.25 km accuracy within 40 km of the network's center. Image courtesy of M. Murphy 2002.

### **3. CASE STUDY OBSERVATIONS #1: 7-8 APRIL 2002 MCS**

#### **3.1 Synoptic Overview**

The 7-8 April 2002 MCS formed in western Texas at approximately 17:45 UTC 7 April. It traversed Texas and eventually merged with a squall line in Mississippi around 14 UTC 8 April. Radar, surface, and upper air data are examined.

The mandatory level (250-, 500-, 700-, and 850-mb) isobaric analyses of the U.S. at 12 UTC 7 April and 00 UTC 8 April are shown in Figs. 3.1-3.8. It is evident from the 250-mb charts (Figs. 3.1-3.2) that the Dallas-Fort Worth (DFW) region is in the left exit region of a jet streak at 12 UTC 7. This jet streak region is favorable for upward motion via a thermally indirect transverse circulation that restores the thermal wind balance and hence, convection if the atmosphere is unstable. By 00 UTC 8, the DFW region is just east of a jet streak axis. The 250-mb isotachs and streamlines also reveal an upper-level trough west of the region that is digging at 12 UTC 7 but not by 00 UTC 8.

The 500-mb analyses (Figs. 3.3-3.4) show the presence of an upper-level closed low pressure system over eastern Arizona/western New Mexico at 12 UTC 7 and over eastern New Mexico at 00 UTC 8. At both 12 UTC 7 and 00 UTC 8, there is positive vorticity advection (PVA) over most of Texas. Note that even though differential PVA is the true indicator of rising motion (along with warm advection), the magnitude of vorticity advection at the surface is assumed to be small in relation to the vorticity advection at 500 mb; thus, PVA at 500 mb is an adequate indicator of synoptic-scale forcing for ascent.

The 700-mb analyses (Figs. 3.5-3.6) depict a trough of low heights present over eastern Arizona/New Mexico at 12 UTC 7 and a closed low height center present over

eastern New Mexico/western Texas at 00 UTC 8. As a result of this low height center west of the DFW region, 700-mb winds are southwesterly at approximately 30 kts at 12 UTC 7, and south-southwesterly at approximately 30 kts at 00 UTC 8. There is warm advection across east Texas. The 12 UTC 7 and 00 UTC 8 700-mb winds also cross dewpoint contours from larger values to smaller values, resulting in moist advection across the DFW region. These conditions lead to rising motion and cloud and precipitation formation within the region.

The 850-mb analyses (Figs. 3.7-3.8) show a low height center present over eastern Colorado/western Kansas at 12 UTC 7 and over southeastern Colorado at 00 UTC 8. As a result, 850-mb winds at 12 UTC 7 are relatively strong (SSW at approximately 40 kts) in the DFW area in relation to surrounding areas. At 00 UTC 8, 850-mb winds are southerly at approximately 20 kts. During the analysis period, there is warm advection and moisture advection in DFW. These conditions lead to rising motion and cloud and precipitation formation within the region.

The 18 UTC 7 manual surface analysis of Texas and surrounding areas (Fig. 3.9) shows a frontal system in place over western Texas at the approximate time and location of convective initiation. This cold front acts as a lifting mechanism for convection.

At 00 UTC 8, CAPE values for DFW were  $\sim 1514 \text{ J kg}^{-1}$ , and the Bulk Richardson Number ( $R_i$ ) was  $\sim 28$  (Fig. 3.10(a)). Advecting winds, determined by first calculating a running average of 0-6 km sounding winds every 500 m (Fig. 3.10(a)) and then averaging the resulting values, were  $\sim 40$  kts from  $200^\circ$ . The total system motion, determined by visually inspecting 500 m radar reflectivity images and averaging the movement of the front edge of the convective line over the time in which the convective line was in range of the radar was

~30 kts from 290°. Thus, the storm propagation (i.e. total system motion minus advecting winds) was ~50 kts from 340°. Storm relative winds at 8 km (-35 °C) (i.e. 8 km sounding winds (Fig. 3.10(a)) minus total system motion) were ~70 kts from 180°. The 0-6 km vertical shear vector, determined from the sounding data, was ~60 kts from 210°, suggesting the development of a long-lined system and severe weather.

### **3.2 MCS Formation and Precipitation Structure Classifications**

#### ***3.2.1 Favorable Synoptic Scale Conditions***

In agreement with Hilgendorf and Johnson's (1998) study, the MCS in this study developed east of an upper-level trough with southwesterly flow aloft and warm advection in the lower levels. Also, this MCS developed in a similar synoptic environment to those described by Parker and Johnson (2000), with the exception that in this case study, the DFW area was associated with the left exit region instead of the right entrance region of the jet streak. Note that both the left exit region and the right entrance region are favorable for upward motion.

#### ***3.2.2 Convective Line Formation Characteristics***

Initial broken-line formation of the 7-8 April 2002 MCS occurs along a surface cold front in western Texas, as evidenced by comparing the surface analysis (Fig. 3.9) to corresponding radar images (Fig. 3.11(a)-(d)) at ~17:45 UTC 7 April 2002. As this convective line developed, it propagated eastward at approximately 60 km hr<sup>-1</sup>, as shown in Fig. 3.11(a)-(d). The mesoscale convective line formation characteristics in this case study agree with Bluestein and Jain (1985) who concluded that broken-line formation occurs in association with a surface cold front.

At 12 UTC 7 April (7), the  $R_i$  in Del Rio is only  $\sim 11$ , and at 00 UTC 8 April (8), it is only  $\sim 19$  (not shown). These  $R_i$  values disagree with the results of broken-line formation from Bluestein and Jain (1985). Similarly, the  $R_i$  (28.39) at 00 UTC 8 for DFW is still significantly low (Fig. 3.10a). At 12 UTC 7 in Del Rio, CAPE values are  $1460 \text{ Jkg}^{-1}$ , and the 0-6 km vertical wind shear vector is  $\sim 50$  kts from  $230^\circ$  (not shown). Therefore, 12 UTC sounding data suggest that the convective line should be formed by back-building according to Bluestein and Jain's (1985) study, but examining radar (Fig. 3.11(a)-(d)) and surface data (Fig. 3.9), it is evident that this case study is representative of the broken-line formation type. Therefore, it is possible that environmental conditions were modified during the 6 hr period between the 12 UTC sounding observations and the 18 UTC convective initiation so that the environment favored broken-line formation at 18 UTC. The surface boundary in this case study provided the mechanism for development of cells within a line, but the strong shear lead to a long-lined system and severe weather.

### ***3.2.3 MCS Evolution***

#### **3.2.3.1 Linear and Nonlinear MCSs**

Fig. 3.12(a)-(d) show the development of the 7-8 April 2002 MCS. At approximately 19:30 UTC 7, MCS development most closely resembles that of a nonlinear occluded MCS. From the detailed surface analysis (Fig. 3.9), it is evident that convection is aligned with two surface boundaries (i.e. the warm and cold fronts) present in Texas. The MCS then evolves into a linear MCS as shown in Fig. 3.12(b)-(d). Therefore, this MCS case study can be classified as a linear MCS since only its early development has nonlinear characteristics.

### **3.2.3.2 Trailing, Parallel, and Leading Stratiform Region MCSs**

The 7-8 April 2002 MCS exhibits a general SSW to NNE orientation, with trailing stratiform (TS) precipitation characteristics throughout its lifespan (Fig. 3.12(a)-(d)). Since the 8 km storm relative winds are ~70 kts from 180°, which is ~20° from parallel to the line, it is evident that old convective cells are being transported north-northwestward behind the convective line, forming a region of trailing stratiform precipitation.

### **3.2.3.3 Symmetric and Asymmetric MCSs**

Similar to previous studies on MCS evolution (e.g. Hilgendorf and Johnson 1998), the 7-8 April 2002 MCS within the DFW region appears characteristically symmetric throughout most of its lifecycle. The April MCS is actually composed of two separate systems at 22 UTC 7 (Fig. 3.12(b)), where the northern  $\frac{3}{4}$  of the system has already evolved from broken line development into a symmetric MCS, and the newer southern  $\frac{1}{4}$  of the system is just beginning to develop via back-building development. The newer cells along the southern end of the line begin to merge with the older convection after 00 UTC 8 (Fig. 3.12(c)). Thus, a stratiform region is constrained to the northern  $\frac{3}{4}$  of the MCS behind the mature part of the convective line from its inception at ~00 UTC 8 (Fig. 3.12(c)). Along the southern  $\frac{1}{4}$  of the convective line, however, intense convective cells are still in the developing MCS phase at this time and have not yet developed a stratiform region. The northern  $\frac{3}{4}$  reaches maturity from ~00:45 to ~02 UTC 8 (Fig. 3.12(d) and Fig. 3.13(a)). 2-3 hrs later (~04 UTC 8), the trailing stratiform region expands southward (Fig. 3.13(b)), and by ~06:00 UTC, the MCS becomes more symmetric along the southern extent of the line (Fig. 3.13(c)). At 08 UTC 8, the stratiform precipitation region behind most of the MCS still looks

symmetric, but intense convective cells continue to back-build behind the extreme southern extent of the convective line (Fig. 3.13(d)).

### ***3.2.4 Important Temperature Levels***

00 UTC 8 April 2002 DFW sounding data were used to determine the approximate heights of the significant temperature levels discussed in this case study, assuming that the temperature in the convective line is approximately equal to the ambient sounding temperature, even though in-cloud temperatures can vary by 0-3 °C from environmental temperatures because of latent heat release and adiabatic expansion/compression. From the 00 UTC 8 April DFW sounding (Fig. 3.10(a)), the 0 °C, -10 °C, -20 °C, and -40 °C isotherms are located at ~3.7 km, ~4.9 km, ~6.3 km, and ~9.1 km, respectively. The wet bulb zero height, representing the actual height that liquid (frozen) hydrometeors would freeze (melt), was ~4.1 km at 00 UTC 8 April (Fig. 3.10(a)). This wet bulb zero height was ~0.4 km higher than the 0 °C isotherm. By 12 UTC 8 April 2002 (Fig. 3.10(b)), at which time the MCS had already propagated through the region, the 0 °C and wet bulb zero heights were ~3.2 km and ~2.9 km, respectively. Since this study's vertical resolution is 0.5 km, and the difference between the 0 °C height and the wet bulb zero height is always less than 0.5 km, using these heights interchangeably should not cause significant calculation errors in this research.

Since microphysical processes present within this large storm system can modify environmental temperatures as the MCS passes over the region, the 0 °C, -10 °C, -20 °C, and -40 °C temperature levels used in this study will be most accurate for the leading convective line, but they may differ by a few degrees within the stratiform region. Using the Eta model (interpolated to 80 km grid spacing) 00 UTC 8 April 2002 500-mb temperature analysis for the Dallas-Fort Worth region, a 2 °C temperature decrease was observed from the leading

convective line to the back edge of the stratiform region. This 2 °C horizontal temperature gradient remained relatively constant throughout the 0 °C to -40 °C layer. Also, the environmental lapse rate in this layer remained relatively constant. Therefore, the ~0.3 km altitude difference observed between each 2° C level implies that a given isotherm in this layer only varies in altitude by ~0.3 km between the front of the convective line and the back of the stratiform region. This height difference is insignificant for the purpose of this study, and therefore, it is assumed that the 00 UTC 8 April 2002 sounding temperature information is representative of the correct temperature levels within the entire MCS.

### ***3.2.5 Storm Damage Reports***

Figure 3.14 depicts the locations and types of severe weather reports, including hail  $\geq$  0.75", winds  $\geq$  58 mph, and all tornadoes that occurred in the U.S. from 12 UTC 7 through 12 UTC 8 April 2002. Comparing this image to Figs. 3.11-3.13, it is evident that severe weather spanned the length of the 7-8 April MCS convective line. Although hail was produced in all parts of the convective line, the larger hailstones were generally located near the southern end of the line. Tornadoes were also more common in the southern part than in the northern part of the convective line. Large hail and tornadoes were more common along the southern extent of the MCS because newer, more intense cells continued to back-build for a longer period in this region than within the main convective line.

## **3.3 WSR-88D Radar**

### ***3.3.1 Data Gaps***

Generally, the WSR-88D radar completes a volume scan approximately every 5 min. The resulting scan data are then archived and stored at NCDC. During the 7-8 April 2002

MCS, however, some radar data are missing from this archive so that 10 min have elapsed between some volume scans. The following times represent data gaps in this study: 0:00, 0:19, 0:34, 0:54, 1:34, 1:44, 1:54, 2:08, 2:28, and 2:54 UTC 8.

### **3.3.2 General MCS Characteristics**

Low-level (0.5 km) CAPPI images of radar reflectivity (Fig. 3.15(a)-(d)) depict the evolution of the portion of the 7-8 April MCS that passed over the DFW region. As the leading convective line propagated into the region (Fig. 3.15(a)) it merged with convective cells ahead of the line. SSE upper-level storm relative winds aided in the formation of a stratiform precipitation region as the storm system evolved (Fig. 3.15(b)). This stratiform region within the DFW analysis area is symmetric during the beginning of the period, but the MCS starts becoming asymmetric around 01:29 UTC 8 (Fig. 3.15(c)), by which time the southern extent of the stratiform region has been depleted within the KFWS radar viewing range. The MCS continued to evolve, and by 02:23 UTC (Fig. 3.15(d)), the convective region had propagated almost completely out of the viewing range.

A rotated image of the 7-8 April MCS at 01:29 UTC is shown in Fig. 3.16(a). Figure 3.16(b) represents a vertical cross section through the MCS in Fig. 3.16(a) at  $y = 15.0$  km. This west-to-east vertical cross section depicts, from left to right, the stratiform, transition, and convective precipitation region, and KFWS is located at (0,0). The radar bright band region associated with the heaviest surface stratiform precipitation is evident just below the freezing level in the stratiform region. The transition zone is marked by a region of low reflectivity echoes ( $\sim 20$ - $25$  dBZ) in the figure. The convective region, however, is characterized by moderate to high reflectivity echoes ( $\sim 35$ - $50$  dBZ) and hence, also by heavy surface precipitation associated with developing and mature convective cells. These

convective cells tilt rearward (i.e. towards the stratiform region) with height at  $\sim 40^\circ$  from the horizontal (note the scaling difference between the x- and y-axes in the figure). Individual convective cells ahead of the convective line (Fig. 3.16(a) and (b)) began to merge with the MCS at this time.

The 7-8 April MCS spans a width of  $\sim 155$  km and has a height of  $\sim 13$  km, where the width and height are defined by radar reflectivity echoes  $\geq 5$  dBZ (Fig. 3.16). The missing data within the center of Fig. 3.16(b) is called a “cone of silence” and is caused by the scanning strategy of the WSR-88D radar, where the highest elevation angle is  $19.5^\circ$ . Regions near the radar that are located at altitudes above the highest elevation angle are not sampled by the radar.

### ***3.3.3 Total Echo Volume Aloft***

#### **3.3.3.1 Total MCS Characteristics**

Figures 3.17-3.19 depict the temporal evolution of total echo volume aloft (within the portion of the 7-8 April MCS that passed through the analysis region) using reflectivity thresholds of 30-dBZ, 35-dBZ, and 40-dBZ, respectively. Each graph shows the evolution of total echo volume aloft calculated between both the  $0^\circ\text{C}$  to  $-40^\circ\text{C}$  and the  $-10^\circ\text{C}$  to  $-40^\circ\text{C}$  layers. All three graphs have the same general trends, with total echo volume aloft decreasing from an initial maximum value to a minimum value at the end of the period. At the time when total echo volume aloft is largest (00:15 UTC 8), 1) the convective region is maturing, 2) additional convective cells ahead of the MCS are beginning to merge with the convective line, and 3) no stratiform region is present. As the convective line matures (00:45 UTC 8), it weakens while a stratiform region begins to form. The weakening of the convective line leads to an overall decrease in large mixed-phase hydrometeors aloft. As the

convective region continues to weaken and propagate out of the radar's range (02:15 UTC 8), and the stratiform region becomes more prominent within the radar's range, total echo volume aloft decreases. Evidently, total echo volume aloft for reflectivity echoes  $\geq 30$  dBZ is dominated by convective region microphysics.

Between 02:15 UTC and 02:45 UTC 8, total echo volume aloft appears to be in steady state, neither decreasing nor increasing in any of the three graphs. During this period, the convective region continues to propagate almost completely out of radar range, and the stratiform region grows in area within the radar's range (not shown), thus balancing the overall total echo volume aloft for a short time period and perhaps explaining this relatively constant echo volume aloft. After 02:45 UTC, the stratiform region has also propagated almost completely out of the radar's viewing range (not shown), resulting in a decrease in total echo volume aloft, as shown in Figs. 3.17-3.19.

The temporal trends in total echo volume aloft between the  $0^{\circ}\text{C}$  to  $-40^{\circ}\text{C}$  and  $-10^{\circ}\text{C}$  to  $-40^{\circ}\text{C}$  layers are strikingly similar in all three figures (Figs. 3.17-3.19). In fact, the correlation coefficients<sup>1</sup> between these two layers using reflectivity echoes  $\geq 30$  dBZ,  $\geq 35$  dBZ, and  $\geq 40$  dBZ to calculate total echo volume aloft are 0.9957, 0.9950, and 0.9857, respectively. These results indicate that the two layers correlate well in all three cases. Various additional reflectivity thresholds were tested, but the three presented here show the

---

<sup>1</sup> A correlation coefficient determines the relationship between two properties. The equation for correlation coefficient is  $\rho_{x,y} = \frac{\text{cov}(X,Y)}{\sigma_x \cdot \sigma_y}$ , where  $-1 \leq \rho_{x,y} \leq 1$ ,  $\text{cov}(X,Y) = \frac{1}{n} \sum_{i=1}^n (x_i - \mu_x)(y_i - \mu_y)$ , where  $\mu_x$  and  $\mu_y$  represent the mean of each population,  $x_i$  and  $y_i$  are individual data values, and the standard deviations for each population are  $\sigma_x = \sqrt{\frac{1}{n} \sum_{i=1}^n (x_i - \mu_x)^2}$ , and  $\sigma_y = \sqrt{\frac{1}{n} \sum_{i=1}^n (y_i - \mu_y)^2}$ . The closer  $\rho_{x,y}$  is to 1, the higher the direct correlation, and closer  $\rho_{x,y}$  is to -1, the higher the inverse correlation that exists between two properties.

best correlation between the two temperature layers. Since these two layers are not independent of one another, it is not surprising that such a high correlation exists between them.

### **3.3.3.2 Partitioned MCS Characteristics**

The temporal trends (from 00 to 04 UTC) in partitioned total echo volume aloft  $\geq 30$  dBZ calculated between the  $0^{\circ}\text{C}$  to  $-40^{\circ}\text{C}$  and  $-10^{\circ}\text{C}$  to  $-40^{\circ}\text{C}$  layers are shown in Figs. 3.20 and 3.21, respectively. Both figures depict the dependency of the amount of convective echo volume aloft on 1) the amount of convective echo within the radar's range, and 2) the evolution of the convective line. Convective echo volume aloft decreases continuously throughout this time period as explained above.

Figures 3.20 and 3.21 indicate that there is little difference in the convective echo volume aloft trend between the two temperature layers, but the stratiform echo volume aloft trend difference is much more significant. This difference exists because different microphysical processes are present in the stratiform region than in the convective region, including enhanced aggregation tendency at warm temperatures ( $T > -10^{\circ}\text{C}$ ). Large aggregates are found in and around the stratiform bright band region, as explained in Appendix A. Thus, echo volume aloft calculated between the  $0^{\circ}\text{C}$  to  $-40^{\circ}\text{C}$  layer will capture some of the larger hydrometeors associated with the bright band, whereas echo volume aloft between the  $-10^{\circ}\text{C}$  to  $-40^{\circ}\text{C}$  layer will not include aggregates present in or near this bright band region. Since the bright band region evolves as the stratiform region evolves, total stratiform echo volume aloft calculated using the  $0^{\circ}\text{C}$  to  $-40^{\circ}\text{C}$  temperature layer captures the evolution of the stratiform region (Fig. 3.20). Therefore, Fig. 3.20 depicts the evolution of the stratiform region from practically nonexistent at 00:15 UTC (total echo volume aloft =

85.8 km<sup>3</sup>), to mature as the convective line weakens around 03:15 UTC (total echo volume aloft = 1674.8 km<sup>3</sup>), and finally to propagating along the outskirts of the range of the KFWS radar at the end of the period (total echo volume aloft = 911.4 km<sup>3</sup>).

The stratiform echo volume aloft  $\geq 30$  dBZ within the  $-10^{\circ}\text{C}$  and  $-40^{\circ}\text{C}$  temperature layer (Fig. 3.21) depicts the evolution of hydrometeors present within the stratiform region as a result of hydrometeor advection from the upper levels of the convective region. An initial stratiform echo volume aloft maximum at 00 UTC reflects subjective line partitioning misidentification of convective echo as stratiform echo volume aloft. A local maximum in echo volume aloft (at  $\sim 7.5$  km<sup>3</sup>) occurs at  $\sim 02:15$  UTC, followed by a local minimum (at  $\sim 1.6$  km<sup>3</sup>) at  $\sim 02:45$  UTC. Afterwards, the stratiform echo volume aloft continues to increase until the end of the analysis period. This trend results from the evolution of the convective line as it begins to weaken and advect more hydrometeors into the stratiform region.

#### **3.3.4 Rainfall Rates**

The temporal evolution of average convective and stratiform region rainfall rates within a portion of the MCS that passed through the DFW region on 8 April 2002 is shown in Fig. 3.22. As a result of the stronger vertical motions present within the convective region than in the stratiform region, average rainfall rates in the convective region ( $\sim 11.0$  mm hr<sup>-1</sup>) are approximately 3.4 times larger than in the stratiform region ( $\sim 3.2$  mm hr<sup>-1</sup>) for the 4-hr period of interest. The convective region has an initial (00:15 UTC) average rainfall rate of 14.8 mm hr<sup>-1</sup>. This rainfall rate first decreases slightly to  $\sim 13.2$  to 13.5 mm hr<sup>-1</sup> between 00:30 and 02:00 UTC and then decreases more rapidly after 02:00 UTC to  $\sim 4$  mm hr<sup>-1</sup> by the end of the period. The observed convective rainfall rate evolution reflects the weakening of

the convective line with time, as observed in the convective echo volume aloft evolution (Figs. 3.20-3.21). The nearly constant rainfall rate between 00:30 UTC and 02:00 UTC could result from the fallout of large mixed-phase hydrometeors as the convective line becomes more downdraft-dominated while it matures and weakens.

The stratiform region, on the other hand, has an initial average rainfall rate of approximately  $2.6 \text{ mm hr}^{-1}$  that increases to a local maximum of  $3.6 \text{ mm hr}^{-1}$  at 01:45 UTC, decreases to a local minimum of  $3.0 \text{ mm hr}^{-1}$  around 02:15 UTC, increases to a maximum of  $3.8 \text{ mm hr}^{-1}$  at 02:45 UTC, and then finally decreases to approximately  $3.1 \text{ mm hr}^{-1}$  at the end of the period (Fig. 3.22). The initial increase of average stratiform rainfall rate is associated with the development of the stratiform region as the convective line matures. At  $\sim 02:15$  UTC, the average stratiform rainfall rate decreases as a result of incorrectly partitioning some of the larger stratiform reflectivity echo as convective. The final decrease in stratiform rainfall rate is due to the propagation of the MCS beyond the KFWS radar's range.

### ***3.3.5 Synthetic Dual-Doppler Analysis***

Synthetic dual-Doppler analysis was attempted using radar data from the 7-8 April 2002 MCS, but this MCS was evolving too rapidly for an accurate derivation of the three-dimensional winds to be performed. During the time in which both the stratiform and convective regions of the MCS were within the KFWS radar's viewing range (00:59-01:59 UTC), the stratiform region evolved from symmetric to asymmetric. Also during this time, the southern two-thirds of the convective line within viewing range propagated at  $16.7 \text{ ms}^{-1}$  from  $290^\circ$ , whereas the northern third of the convective line within viewing range appeared to propagate faster ( $\sim 19.0 \text{ ms}^{-1}$ ) and with a more southerly component (from  $\sim 300^\circ$ ). Since synthetic dual-Doppler analyses are particularly sensitive to the storm's advection vector and

to the assumption that the storm system is quasi-steady (and this MCS failed to meet these conditions), synthetic dual-Doppler analysis was not feasible for this case study.

### **3.4 NLDN CG Lightning Flash Trends**

#### ***3.4.1 Total Trends***

Figure 3.23 shows the temporal evolution of the total number of CG lightning flashes and the percent of +CGs in the portion of the 7-8 April 2002 MCS that occurred within the KFWS radar's range from 00 to 04 UTC 8. A peak total CG flash rate of 26.2 flashes  $\text{min}^{-1}$  occurred at ~01:15 UTC. This time corresponds to both the convective local maximum rainfall rates (Fig. 3.22) and the mature stage of the April MCS. Throughout the 4-hr time period, the storm system had an average CG flash rate of 14.5 flashes  $\text{min}^{-1}$ , with 20.1% of flashes having positive polarity. As the convective line propagated out of the radar's viewing range, the percent of +CG lightning flashes increased from ~15.0% (at 02:00 UTC) to 46.6% (at 03:45 UTC).

Figure 3.24 shows the temporal evolution of CG lightning peak positive and peak negative current for the portion of the April MCS that passed through the KFWS network from 00 to 04 UTC 8. The average peak positive and peak negative lightning currents were 35.0 kA and -20.7 kA, respectively. Peak positive current increased with the development of the stratiform region within the radar's range around 01:00 UTC. After the convective region propagated beyond the radar's range, another increase in positive peak current is evident at the end of the period when only the stratiform region is within view.

### ***3.4.2 Partitioned Trends***

A 0.5-km CAPPI image of radar reflectivity overlaid with NLDN-detected CG flash data for the April 2002 MCS at 01:24 UTC is shown in Fig. 3.25. Most of the CG lightning flashes occur within the convective region, which is dominated by –CG flashes. Also apparent is the higher percentage of +CG flashes in the stratiform region as compared to the convective region. CG lightning flashes are generally associated with relatively high reflectivity cores within a given region. Large reflectivity echoes indicate the presence of large hydrometeors suspended by strong updrafts (important ingredients in the NIC mechanism). Under normal conditions, large hydrometeors (at  $T < -10$  °C and in the presence of significant LWC) charge negatively in the convective region, and large aggregates (at  $T < -10$  °C and in the presence of low LWC) charge positively in the stratiform region (e.g. Saunders et al. 1991), resulting in a predominance of –CGs in the convective line and +CGs in the stratiform region. Since the transition zone lacks upward motions, the NIC mechanism is inefficient, and little or no CG lightning flashes are produced in this region. These trends are consistent throughout the period (00 to 04 UTC) during which the 7-8 April 2002 MCS was within range of the KFWS radar.

The temporal trend of partitioned NLDN-detected CG lightning flashes occurring within the radar’s viewing range is shown in Fig. 3.26. The number of convective CG flashes closely correlates to the total number of CG flashes within the MCS (i.e. the MCS is dominated by CG flashes occurring within the convective region). Within the stratiform region, however, relatively few CG flashes exist. Since the convective region produces over 68.9% of the total CG lightning flashes in the MCS, the observed significant decrease in total

CG flashes towards the latter half of the time period is a result of the propagation of the convective region beyond the KFWS radar range.

Figure 3.27 depicts the temporal evolution of convective region CG lightning flashes within the radar's viewing range. CG lightning flash rates associated with the convective region averaged 12.3 CG flashes  $\text{min}^{-1}$ , 7.5% of which had positive polarity, but at its peak (~01:15 UTC), the CG lightning flash rate was ~23.9 flashes  $\text{min}^{-1}$ . The evolution of the convective CG lightning flash rate resembles the evolution of average convective rainfall rates throughout the period (Fig. 3.22).

Figure 3.28 depicts the temporal evolution of stratiform region CG lightning flashes within the radar's viewing range. CG lightning flash rates associated with the stratiform region averaged 2.2 CG flashes  $\text{min}^{-1}$ , 44.9% of which had positive polarity, but at its peak (~03:15 UTC), the CG lightning flash rate was ~2.8 flashes  $\text{min}^{-1}$ . The evolution of the stratiform CG lightning flash rate lags the evolution of average stratiform rainfall rates (Fig. 3.22) by approximately 30 min, but interestingly, it coincides with stratiform echo volume aloft  $\geq 30$  dBZ between the  $-10^{\circ}\text{C}$  to  $-40^{\circ}\text{C}$  layer (Fig. 3.21) during the latter half of the time period.

The temporal trends in convective and stratiform region peak positive and negative currents associated with NLDN-detected CG lightning flashes are shown in Fig. 3.29. The average peak positive current in the stratiform region (43.0 kA) is over two times larger than the average peak positive current in the convective region (20.2 kA). The average peak negative current in the stratiform region (-22.3 kA) is slightly larger than the average negative current in the convective region (-20.2 kA).

## **3.5 LDAR II Data**

### ***3.5.1 Network's Performance***

The LDAR II network was not performing optimally during the 7-8 April 2002 MCS case study (Fig. 3.30) because only five sensors were operational. The loss of the other two sensors resulted in decreased lightning flash detection efficiency from >90% (typical value) to 60% within the ring formed by the network's six peripheral sensors and from ~90% (typical value) to about 20% at a 120-km range from the network's central sensor (M. Murphy 2003, personal communication). Nevertheless, both total and partitioned LDAR II source and flash origin data are analyzed for this case study.

### ***3.5.2 VHF Source Trends***

#### **3.5.2.1 Total Trends**

Figure 3.31 shows the temporal evolution (00 to 04 UTC) of total LDAR II sources produced from the portion of the 7-8 April 2002 MCS that propagated through the KFWS radar's viewing range. The average LDAR II-detected source rate during this time period was ~2338 sources min<sup>-1</sup>. The evolution of LDAR II sources closely resembles the evolution of NLDN-detected convective region CG lightning flashes (Fig. 3.27). Although the LDAR II-detected peak source rate (~6562 sources min<sup>-1</sup>) occurs ~30 min earlier (at 00:45 UTC) than the NLDN-detected CG flash rate, the two curves show the same general trends. Most of the lightning activity occurs during the first half of the period, while the convective region is present in the viewing range. As the convective region propagates beyond the viewing area, the LDAR II-detected source rate rapidly decreases.

### 3.5.2.2 Partitioned Trends

An example of LDAR II source locations relative to the horizontal radar reflectivity structure of the 7-8 April 2002 MCS at 01:19 UTC is depicted in Fig. 3.32. It is evident that increased numbers of sources are located along: 1) the back half of the leading convective line where the mature-to-dissipating convective cells lay, 2) the leading edge of the stratiform region, and, 3) the enhanced reflectivity “bridge” in the transition zone that connects the convective and stratiform regions. Relatively few sources exist, however, within other portions of the transition and stratiform regions. Since a sufficient amount of time is needed to build up enough electric charge within a convective cell to produce lightning (Krehbiel 1986), it is not unusual that most of the LDAR II source activity is associated with mature-to-dissipating convective cells. The leading edge of the stratiform region is associated with increased LDAR II source activity as a result of either charge advection from the convective region (e.g. Rutledge and MacGorman 1988) or an *situ* charge generation mechanism (e.g. Engholm et al. 1990; Rutledge et al. 1990). Enhanced sources are also found within the enhanced reflectivity bridge in the transition zone, possibly because these large hydrometeors (which produce these enhanced reflectivity echoes observed in the transition zone) carry, or produce through an *in situ* charging mechanism, a net charge through which lightning preferentially travels (Williams et al. 1985), resulting in increased lightning activity in this region.

Examples of vertical cross-sections through the rotated reflectivity image in Fig. 3.32 are shown in Figs. 3.33-3.35. Vertical cross-sections through the front edge (Fig. 3.33(a)) and back edge (Fig. 3.33(b)) of the leading convective line show that most LDAR II sources are associated with moderate reflectivity echoes (35-45 dBZ). Sources also tend to be

located at mid-to-high altitudes (height > 5 km,  $T < -10$  °C) above enhanced convective cores, suggesting the presence of strong updrafts aloft. There is an indication that two dominant source levels exist within the convective line, including 1) a lower region between -10 °C and -25 °C, and 2) an upper region just above -40 °C. These regions could possibly be associated with the main negative and upper positive charge layers theorized in the non-inductive charging mechanism of thunderstorm electrification.

Figure 3.34 (a) and (b) are examples of vertical cross-sections taken through the leading and trailing edge of the stratiform region, respectively. Comparing these two graphs, it is evident that few LDAR II sources are detected within the stratiform region, especially along the region's back edge. Sources occurring within the stratiform region are located at various altitudes, but there appears to be an increased percentage of sources between -10 °C and -25 °C, especially along the leading edge of the stratiform region (Fig. 3.34(a)). Also, at large ranges (>60 km) from the convective line, source locations are near echo top (Fig. 3.34(b)).

Examples of two line perpendicular vertical cross-sections of the 7-8 April 2002 MCS are shown in Fig. 3.35 (a) and (b). The first cross-section is through the stratiform, transition, and convective regions (Fig. 3.35(a)), while the second cross-section is through the stratiform region, the enhanced reflectivity "bridge" through the transition zone, and the leading convective line (Fig. 3.35(b)). In general, there are few sources occurring within the transition zone, except within a portion of the transition zone where the enhanced reflectivity "bridge" has formed. The two dominant source layers within the convective line in Fig. 3.35(a) appear to slope downwards from a peak height associated with the mature convective cells to the back edge of the convective line. In Fig. 3.35(b), however, it appears that the

upper dominant source region continues to descend through the transition zone and into the stratiform region (possibly associated with charge advection from the convective region and into the stratiform region). Unfortunately, problems with detection efficiency, especially in Fig. 3.35(b), limit interpretation of source regions and pathways for this case study.

The decreased detection efficiency of LDAR II sources with range for this case study is especially noticeable in Figs. 3.32-3.33 and 3.35(a). At locations south of the KFWS radar, there are noticeably fewer sources plotted in the convective line than at locations north of the radar. Since the LDAR II network is located approximately 44 km to the north-northeast of the KFWS radar (which is in the center of the image), and the source detection efficiency rapidly decreases with range from the LDAR II network's center (especially in this MCS case study), one would expect a lower number of sources plotted at further distances from the network than at locations close to the network. The low number of LDAR II sources within the stratiform region could be a result of 1) decreased detection efficiency, and/or 2) different microphysical processes occurring within the stratiform region than within the convective line. Since a portion of the convective line was near the network's center at 01:19 UTC 8 when the vertical cross-sectional images were taken, the two dominant source regions observed in this convective line are more likely a result of true microphysical processes than a detection efficiency problem. Therefore, some characteristics observed in Figs. 3.32-3.35 are real atmospheric processes and some are related to detection efficiency. Another case study (see Chapter 5) with better LDAR II network detection efficiency will be needed to discern detection efficiency problems from real atmospheric processes occurring within this MCS, but first, additional qualitative and statistical analyses of LDAR II data from the April 2002 MCS will be discussed.

Figure 3.36 depicts the temporal evolution of convective and stratiform region LDAR II sources from 00 to 04 UTC. The average source rate within the convective region ( $\sim 1993$  sources  $\text{min}^{-1}$ ) is almost six times greater than the average source rate within the stratiform region ( $\sim 345$  sources  $\text{min}^{-1}$ ). The peak source rate in the convective region ( $\sim 6213$  sources  $\text{min}^{-1}$ ) is almost ten times larger than the stratiform peak source rate ( $624$  sources  $\text{min}^{-1}$ ), although the stratiform region's peak in source activity lasts longer than the convective region.

Source rates reflect the evolution of each region. LDAR II source activity in the convective region peaks early (00:45 UTC) and then rapidly decreases as the convective line begins to weaken and propagate out of the radar's viewing range. Source activity in the stratiform region, on the other hand, peaks later (01:45 UTC) and lasts longer than the source activity in the convective region, indicating its growth and prominence within the viewing area later in the time period. The convective LDAR II source trend (Fig. 3.36) closely resembles the trends of 1) total LDAR II sources (Fig. 3.31), 2) convective rainfall rates (Fig. 3.22), and 3) NLDN-detected convective CG lightning flashes (Fig. 3.27), but not the trends of total or convective echo volume aloft during the beginning of the period (Figs. 3.17-3.21). The stratiform region LDAR II source trend resembles the NLDN-detected stratiform CG lightning flash trend, except during the local CG flash minimum that occurred at  $\sim 02:45$  UTC (Fig. 3.28). Decreased LDAR II detection efficiency for this case study could be the reason why echo volume aloft does not correlate well with either LDAR II sources or flashes.

LDAR II sources in the convective and stratiform regions tend to occur within distinct height layers, as indicated in Figs. 3.37 and 3.38, respectively. Within the convective region, two main electrically-active source layers exist. The most pronounced layer is

observed between 8 km and 11 km altitude (the approximate heights of the  $-35\text{ }^{\circ}\text{C}$  and  $-55\text{ }^{\circ}\text{C}$  isotherms), and a small secondary local LDAR II source maximum layer is observed between 4 km and 6 km altitude (the approximate heights of the  $-10\text{ }^{\circ}\text{C}$  and  $-25\text{ }^{\circ}\text{C}$  isotherms) (Fig. 3.37). These two dominant source regions could be associated with the upper positive and main negative charge regions typically found at these temperature layers in a thunderstorm (Shao and Krehbiel 1996). Within the stratiform region, one main electrically-active source layer exists between 5 km and 8 km (the approximate heights of the  $-10\text{ }^{\circ}\text{C}$  and  $-32\text{ }^{\circ}\text{C}$  isotherms). This electrically-active layer corresponds to the source layer that slopes downwards from the convective line and into the stratiform region in Fig. 3.35(a)-(b).

Composite images of average radar reflectivity and the total number of LDAR II sources that occurred within the  $200\text{ km} \times 200\text{ km} \times 20\text{ km}$  KFWS radar volume for various times during the 8 April 2002 MCS are shown in Figs. 3.39-3.46. During the beginning of the time period ( $\sim 00:39\text{ UTC}$ ), many LDAR II sources are detected from two dominant source regions within the convective line. As seen in Fig. 3.35 (a) and (b), these source regions descend from a peak altitude within the mature convective cells downward towards the back edge of the convective line and into the transition zone (Fig. 3.39). A large source concentration also exists within the convective cells ahead of the convective line. Overall, the two dominant electrically-active source layers within this image are at  $\sim 9\text{ km}$  ( $-40\text{ }^{\circ}\text{C}$  temperature level) and  $\sim 3.5\text{ km}$  to  $\sim 5\text{ km}$  altitude ( $0\text{ }^{\circ}\text{C}$  to  $-10\text{ }^{\circ}\text{C}$ ).

By  $00:59\text{ UTC}$  (Fig. 3.40), the individual electrically-active cells ahead of the convective line begin to merge with the convective line of the MCS. At this time, a noticeable increase in and aerial expansion of source concentration within the convective line occurs (from  $\sim 900$  to  $\sim 2250$  sources present at one horizontal location), as well as an overall

height increase within the upper dominant source layer. This surge of sources from the individual cells into the MCS causes a wavelike pattern as the surge passes through the convective line (Figs. 3.41-3.42).

By 01:14 UTC (Fig. 3.43), the convective sources have evolved back to their initial state (Fig. 3.39), with one exception: the two dominant electrically active-regions within the convective line have now shifted 1 km higher in elevation than their original locations. At this time, the lower dominant source region is concentrated from 5 km to 6 km (approximately -10 °C to -20 °C), and the upper dominant source region is now concentrated from 9 km to 11 km (just above -40 °C). This upper dominant source region descends from the convective line into the trailing stratiform region, suggesting that the charge advection mechanism may electrify the stratiform region. By 01:19 UTC (Fig. 3.44) the upper dominant source region extends further into the stratiform region at approximately 5 km to 7 km in altitude (-10 °C to -25 °C) just above a portion of the radar bright band. Another smaller source region is also evident ~60 to 80 km behind the convective region between 8.5 to 11 km altitude at this time.

By 02:03 UTC and 02:23 UTC (Figs. 3.45 and 3.46, respectively), convective LDAR II sources have decreased. This decrease could either be a result of the weakening of the convective line, or, more likely, the decreased LDAR II detection efficiency with range. A continuous layer of sources extending from the convective region and into the stratiform region is still evident. In fact, the dominant source region now extends across the stratiform region directly above the radar bright band. Also at 02:03 UTC, at no x location does the total number of vertically integrated sources detected exceed 160. Towards the back edge of the stratiform region (at ~70 to 90 km behind the convective line), another relative maximum

source layer exists between ~6.5 to 9 km altitude (Fig. 3.46). This additional charge region is at a higher altitude than, and it does not seem to be “connected” to, the main source region that descends from the convective region and into the stratiform region. Therefore, this isolated electrically-active stratiform region could be evidence of an in situ charging process also occurring within the stratiform region.

### **3.5.3 VHF Flash Origin Trends**

#### **3.5.3.1 Total Trends**

Figure 3.47 depicts the temporal trend in total LDAR II flash origins (as determined by the modified NASA algorithm) from 00 to 04 UTC 8 April 2002. A peak in LDAR II flashes of 196.8 flashes  $\text{min}^{-1}$  occurs at 00:45 UTC, and the average flash rate for the period is 103.1 flashes  $\text{min}^{-1}$ . The LDAR II flash origin trend (Fig. 3.47) is similar to the trend in LDAR II sources (Fig. 3.31) from 0:04 to 1:15 UTC. Afterwards, the number of LDAR II sources decreases much more rapidly than the number of LDAR II flash origins, suggesting that either the average number of sources per flash decreases with time, especially after 01:15 UTC, or these trends are a result of decreased LDAR II detection efficiency with range from the network’s center.

The temporal trend in total intra-cloud to CG ratio (IC:CG) for the 7-8 April MCS is depicted in Fig. 3.48. The IC:CG ratio generally increases throughout the time period, with an average ratio of ~7:1 over the period and a maximum ratio of ~9:1 at 03:15 UTC.

#### **3.5.3.2 Partitioned Trends**

Similar to the location trends in LDAR II sources, an increased number of LDAR II flash origins (as determined by the modified NASA algorithm) tend to occur 1) along the back half of the convective line, 2) within the transition zone enhanced reflectivity “bridge,”

and 3) along the front edge of the stratiform region within an MCS (not shown). LDAR II flashes tend to originate in regions of moderate reflectivity (35 – 45 dBZ) at altitudes > 5 km (< -10 °C), suggesting the presence of strong vertical updrafts (not shown).

The convective region dominates lightning flash activity throughout the analysis period with an average of 74.6 flashes min<sup>-1</sup> (Fig. 3.49). A peak in convective LDAR II flash activity of 169.9 flashes min<sup>-1</sup> occurs at ~00:45 UTC 8. The stratiform region, on the other hand, averages 28.6 LDAR II flash origins min<sup>-1</sup> (Fig. 3.49). A peak flash rate of 38.6 flashes min<sup>-1</sup> is observed at approximately 02:15 UTC. The partitioned LDAR II flash origin trend (Fig. 3.49) closely resembles the partitioned NLDN-detected CG lightning flash trend (Fig. 3.26). In addition, the LDAR II flash origin trend within the convective region resembles convective rainfall rates (Fig. 3.22) and both total and convective LDAR II source rates (Figs. 3.31 and 3.36, respectively). The LDAR II flash origin trend within the stratiform region is similar to the stratiform region NLDN-detected CG flash trend. The stratiform region flash origin trend appears to lag the stratiform region rainfall rate trend by ~30 min (Fig. 3.22), but it is similar to the ≥ 30-dBZ echo volume aloft trend in the -10 °C to -40 °C temperature layer (Fig. 3.21).

Dominant LDAR II flash origin height levels for the convective and stratiform regions of the 7-8 April 2002 MCS (Figs. 3.50 and 3.51) are similar to LDAR II source dominant height levels within each region (Figs. 3.37 and 3.38). Within the convective region, two main electrically-active flash origin regions exist, one between 8 km and 11 km altitude (-35 °C to -55 °C), and the other between 4 km and 6 km altitude (-10 °C to -25 °C) (Fig. 3.50). The lower electrically-active charge region in the convective line is more prominent in LDAR II flashes than in the convective LDAR II sources (Fig. 3.37). Within

the stratiform region, one main layer of dominant LDAR II flash origins exists between 5 km and 8 km (Fig. 3.51). Both regions experience a larger number of IC flashes than CG flashes, and the stratiform region has a greater percentage of IC flashes than the convective region. The average IC:CG ratio within the stratiform region is 12.9:1, whereas the average IC:CG ratio within the leading convective line is 5.2:1, less than half that of the stratiform region.

### **3.6 Summary**

The 7-8 April 2002 MCS is a classic leading-line, trailing-stratiform MCS that passed over the DFW region. This MCS provided an opportunity to study the radar and electrical evolution of the convective and stratiform regions, as well as the interactions between these processes in each region and between the regions themselves. Unfortunately, the LDAR II network had decreased source detection efficiency because it was not operating at full capacity during this case study.

The total LDAR II source maxima and minima preceded the total CG flash rate maxima and minima by ~30 min in the April MCS case. Since initial lightning flashes within convection are IC lightning (Krehbiel 1986), it is not surprising that these trends were evident. Trends in echo volume aloft, rainfall rates, NLDN-detected CG flashes, and LDAR II-detected source and flash origin rates within the convective line of the April MCS were also analyzed. A strong correlation between all parameters, except for echo volume aloft during the beginning of the period, exists within the convective region. These strong correlations suggest that the presence of larger hydrometeors suspended by strong updrafts supports the NIC mechanism in the convective line.

Within the stratiform region, both NLDN and LDAR II lightning flash rates corresponded well with each other and with echo volume aloft  $\geq 30$  dBZ between  $-10$  °C and  $-40$  °C throughout the period. This correlation suggests that the presence of larger ice aggregates (i.e.  $Z > 30$  dBZ) due to differential sedimentation at these temperatures is critical for electrification within the stratiform region via either charge advection or in-situ charging. Stratiform LDAR II source rates correlated well with the other quantities at the beginning of the period, but near the end of the period, the correlations were weaker, possibly because of decreased LDAR II detection efficiency during this case. The rainfall rate maxima and minima within the stratiform region tended to precede stratiform echo volume aloft, NLDN CG flash rate, and LDAR II source and flash rates by  $\sim 30$  min.

Echo volume aloft was larger and the rainfall rate was higher in the convective region than in the stratiform region. Since these conditions indicate an abundance of suspended mixed-phase hydrometeors aloft and strong updrafts (ingredients necessary for non-inductive charging), large lightning source and flash rates were also present in the convective region. Thus, the convective region is the dominant charging region present in this MCS, consistent with expectations and earlier studies.

Within the convective region of the 7-8 April 2002 MCS, two dominant electrically-active charge regions were detected by the LDAR II network (e.g. Figs. 3.33, 3.37). These two regions correspond to the two dominant charge regions in the non-inductive theory of electrification: the upper positive charge region (between  $-35$  °C and  $-55$  °C) and the main negative charge region (between  $-10$  °C and  $-25$  °C). Negative polarity breakdown in the positive charge region is inherently noisier in the RF range than positive polarity breakdown in the negative charge region. In this study, the upper electrically-active charge region

exhibits a greater concentration of LDAR II sources than the lower electrically-active region (e.g. Fig. 3.44). Therefore, the upper electrically-active region within the convective line is an area of upper positive charge, and the lower electrically-active region is an area of main negative charge. This charge arrangement agrees with both the theory of non-inductive charging and the charge breakdown processes within the RF range. As observed, predominantly –CG lightning flashes are generally produced from this normal dipole charge arrangement.

Within the stratiform region of the 7-8 April 2002 MCS, one main sloping active charge layer is detected by the LDAR II network. This charge layer appears to have been advected from the upper (positive) charge layer of the convective region into the stratiform region (e.g. Figs. 3.44 and 3.45). The charge region slopes downwards from upper levels (~10 km) within the convective line to low altitudes (~5 km; ~ -10 °C to -25 °C) within the stratiform region. A combination of an in situ process and charge advection may explain the formation of a small upper (possibly negative) charge area within the stratiform region as observed in Figs 3.44-3.46. An inverted dipole becomes established in the stratiform region, producing a large percentage of +CGs. With the absence of strong vertical motions, the stratiform region is an ineffective charge producer. Therefore, the relatively low observed lightning flash rates are consistent with theory.

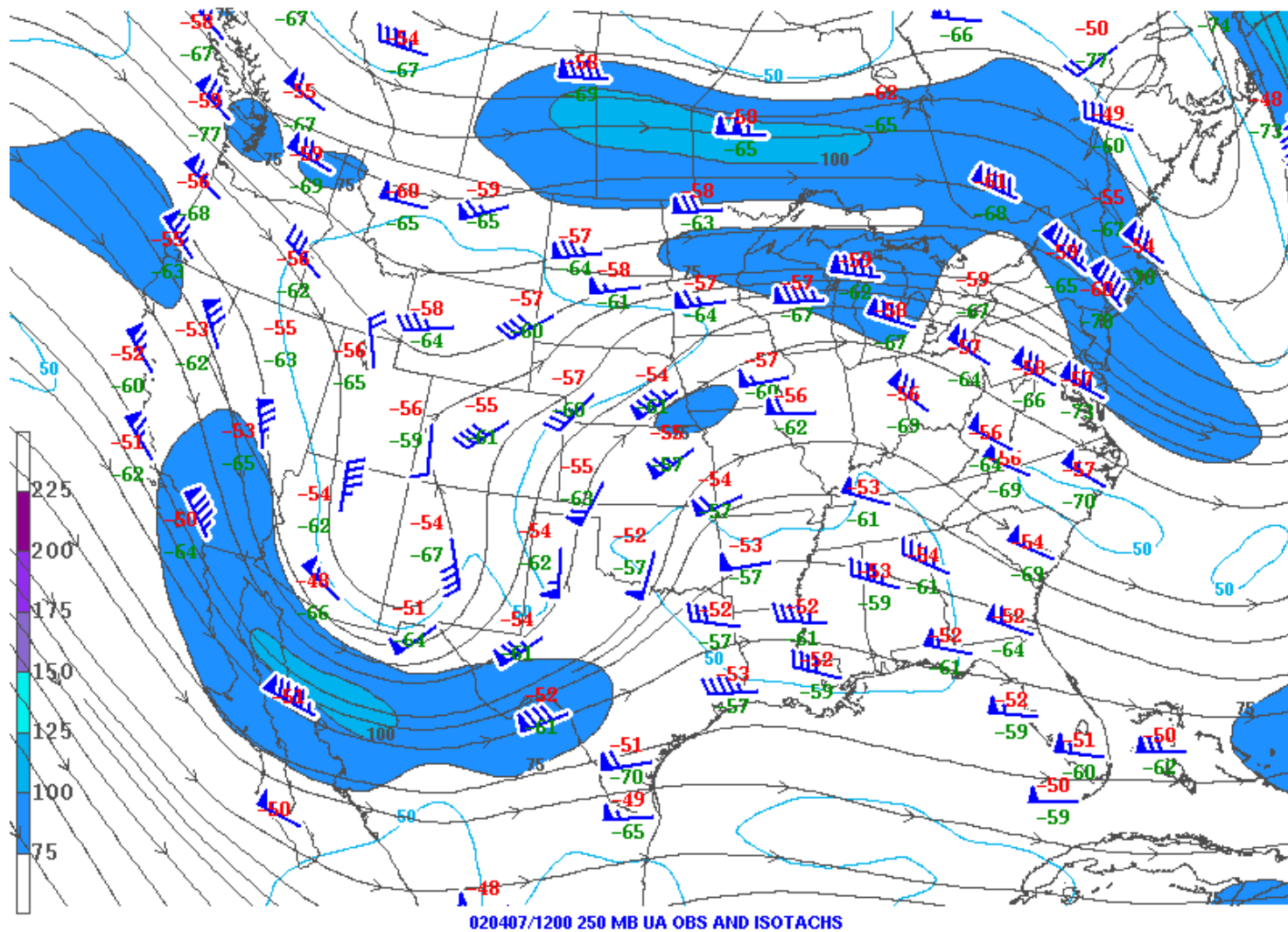


FIG. 3.1. 250-mb analysis for 12 UTC 7 April 2002. Wind speeds  $\geq 75$  kts are shaded according to the contour bar on the left (image courtesy of [www.spc.noaa.gov](http://www.spc.noaa.gov)).

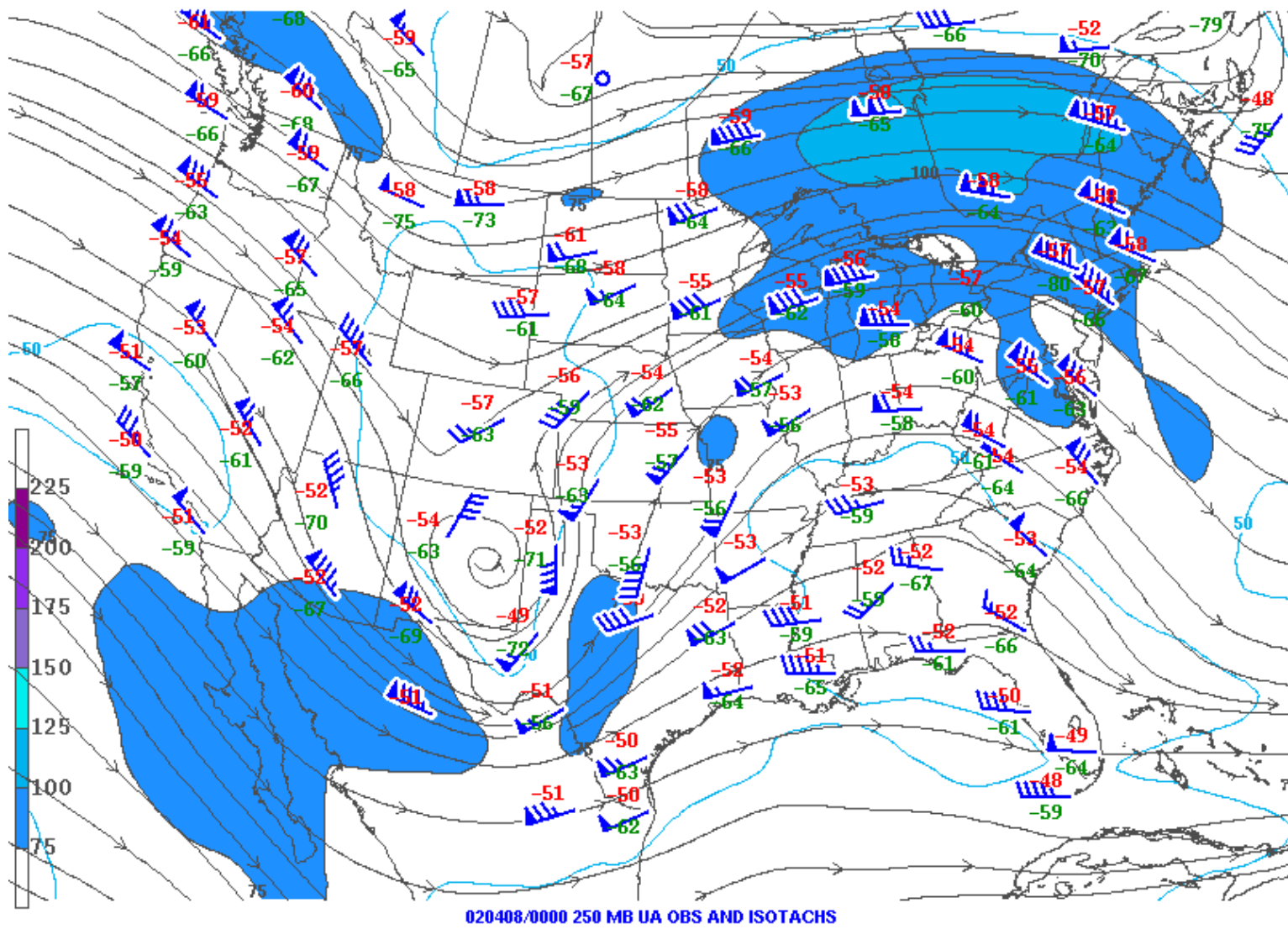


FIG. 3.2. Same as Fig. 3.1, but for 00 UTC 8 April 2002 (image courtesy of [www.spc.noaa.gov](http://www.spc.noaa.gov)).

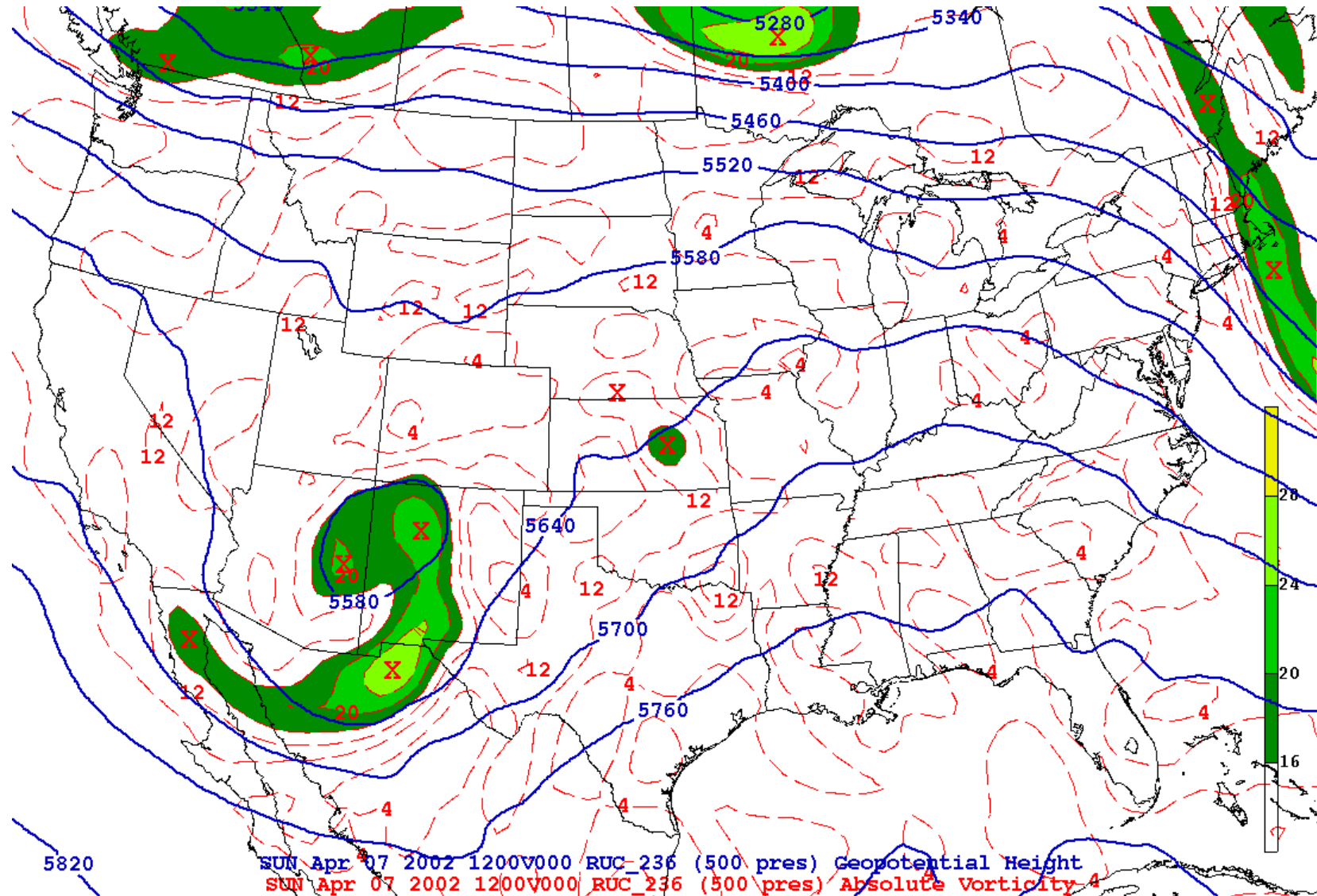


FIG. 3.3. 500-mb analysis for 12 UTC 7 April 2002. Height contours (m) are in solid blue lines, and absolute vorticity contours ( $s^{-1}$ ) are in dashed red lines.

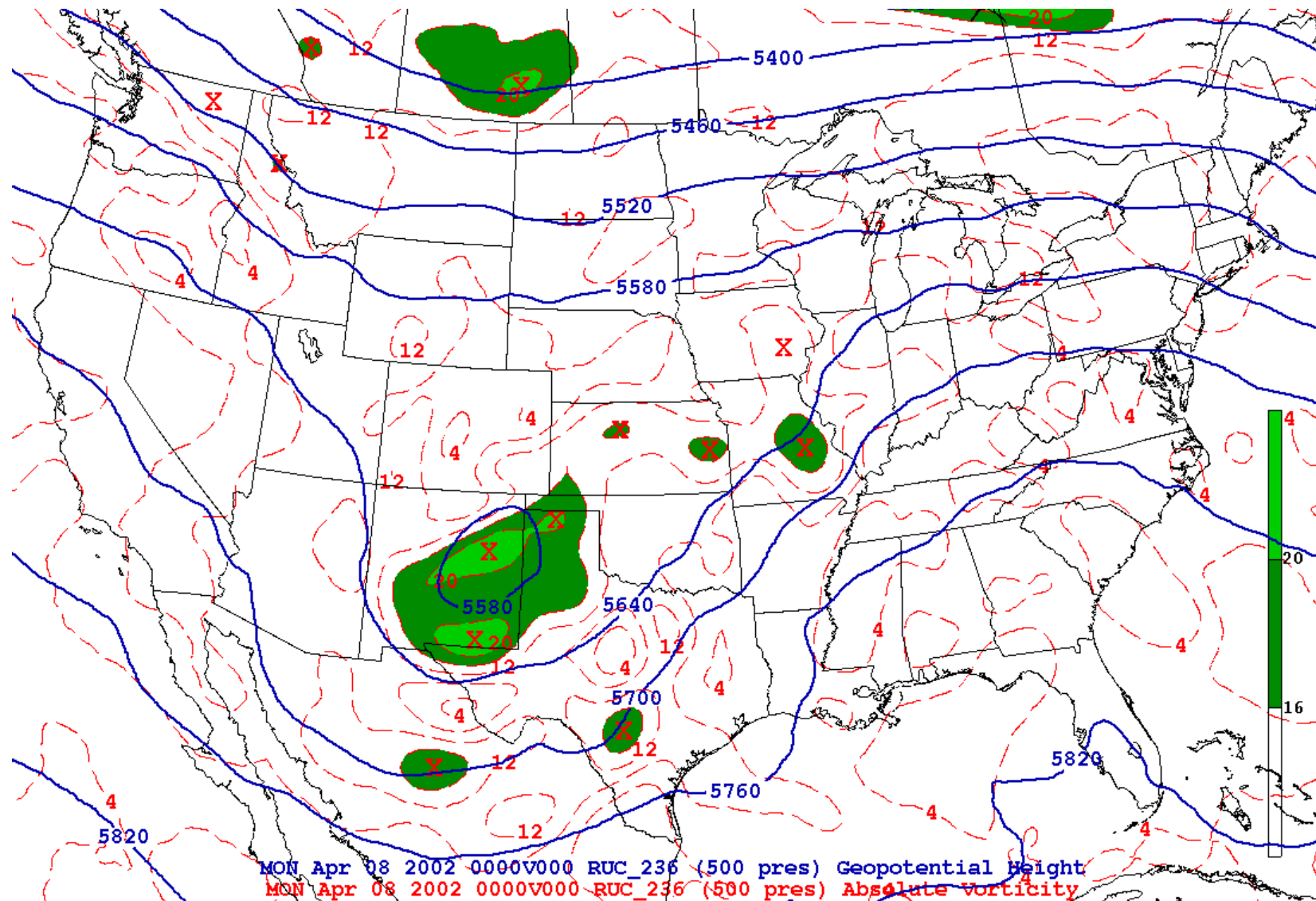


FIG. 3.4. Same as Fig. 3.3, but for 00 UTC 8 April 2002.

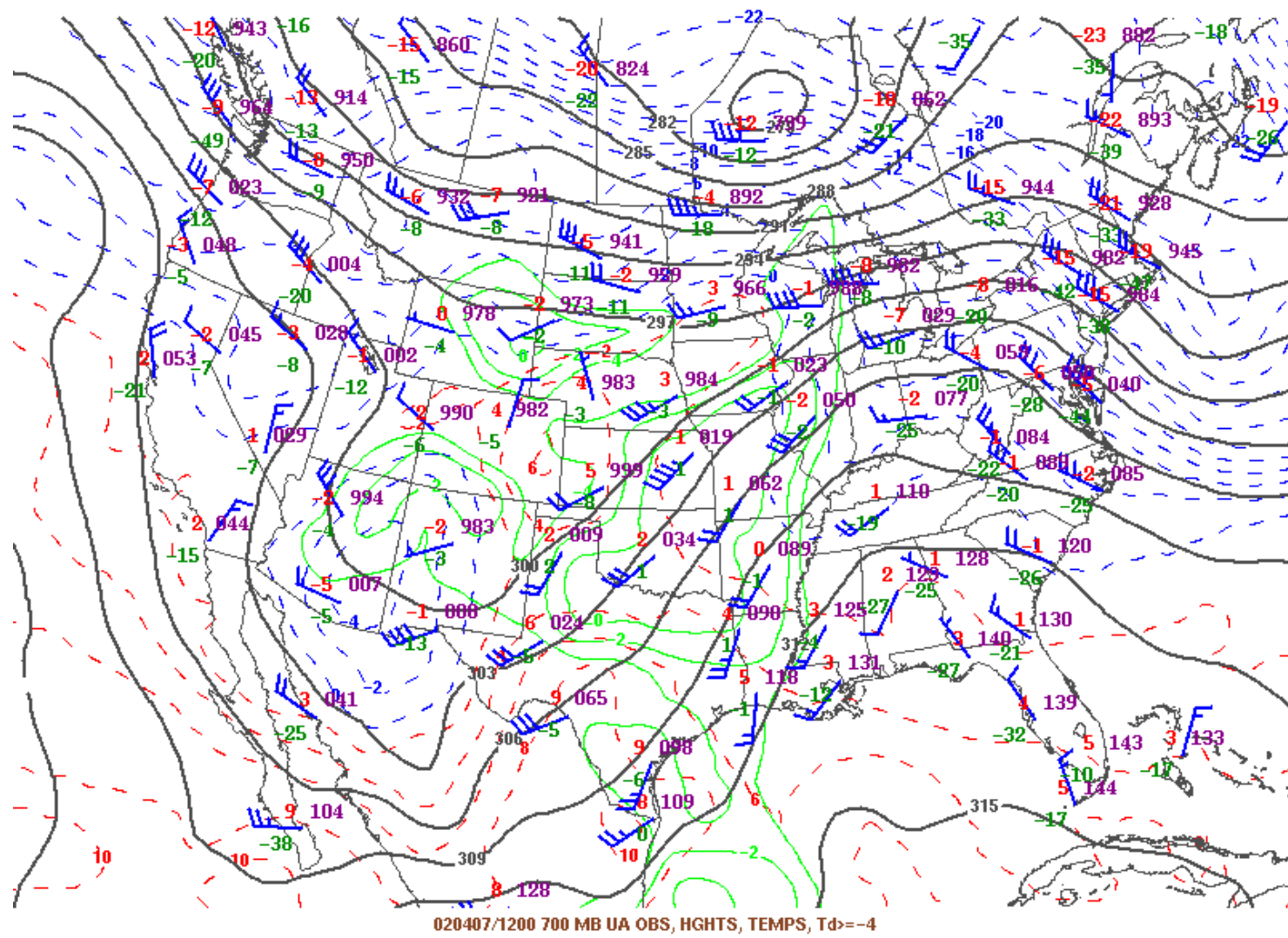


FIG. 3.5. 700-mb analysis for 12 UTC 7 April 2002. Height contours are in solid black lines, isotherms are in dashed red and blue lines, and dew point contours  $\geq -4$  are in solid green lines (image courtesy of [www.spc.noaa.gov](http://www.spc.noaa.gov)).

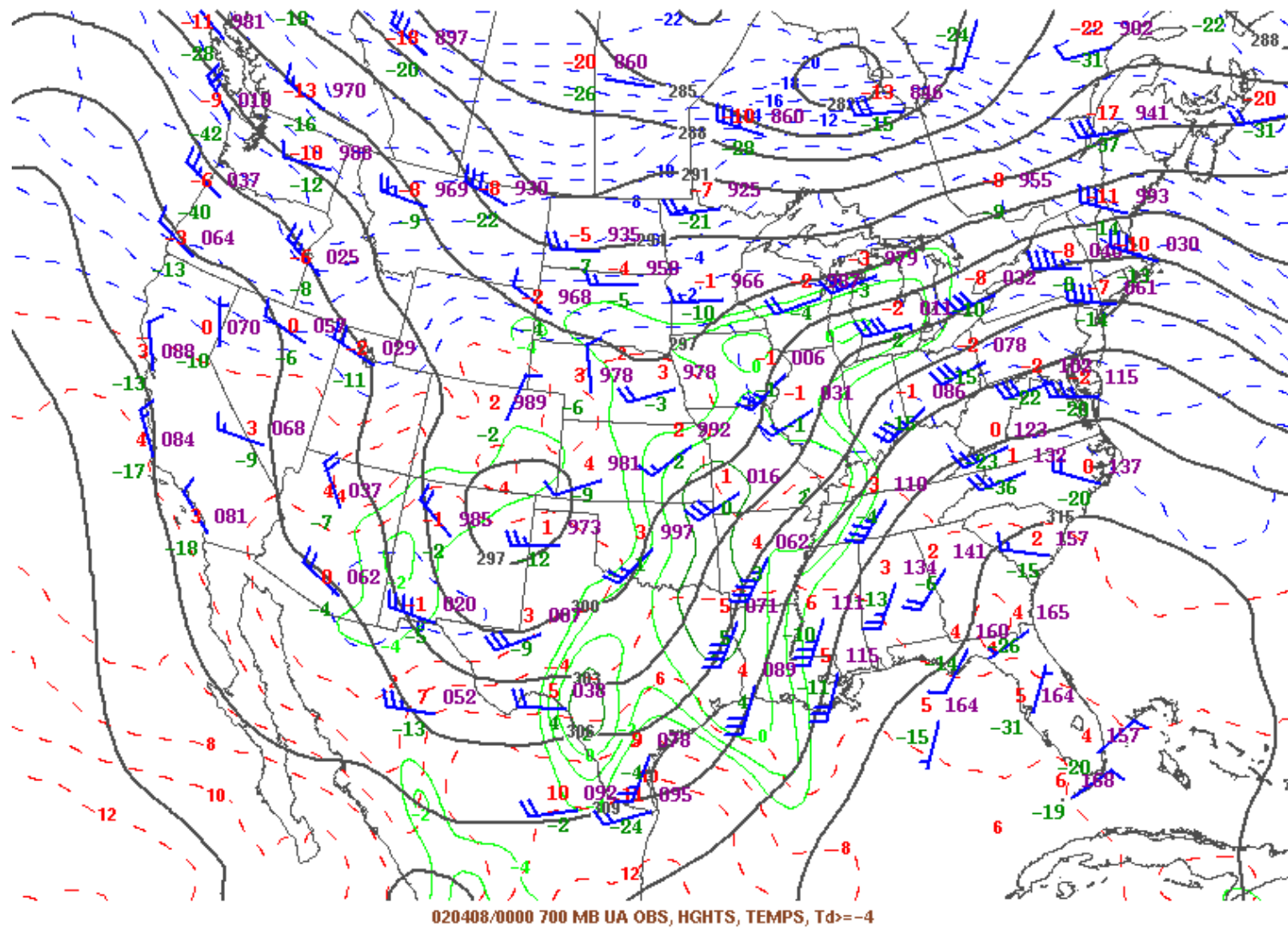


FIG. 3.6. Same as Fig. 3.5, but for 00 UTC 8 April 2002 (image courtesy of www.spc.noaa.gov).

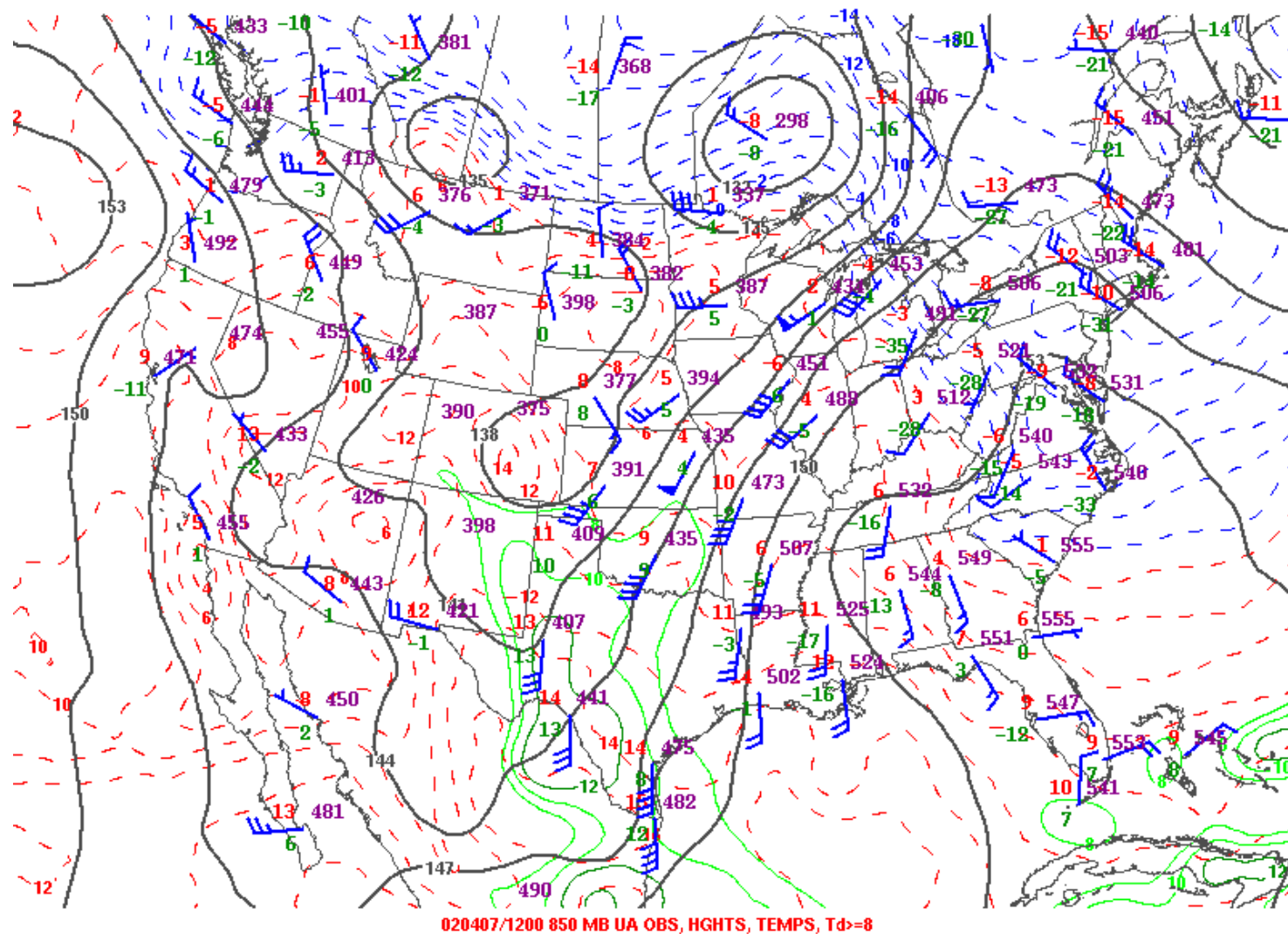


FIG. 3.7. 850-mb analysis for 12 UTC 7 April 2002. Height contours are in solid black lines, isotherms are in dashed red and blue lines, and dew point contours  $\geq 8$  are in solid green lines (image courtesy of [www.spc.noaa.gov](http://www.spc.noaa.gov)).

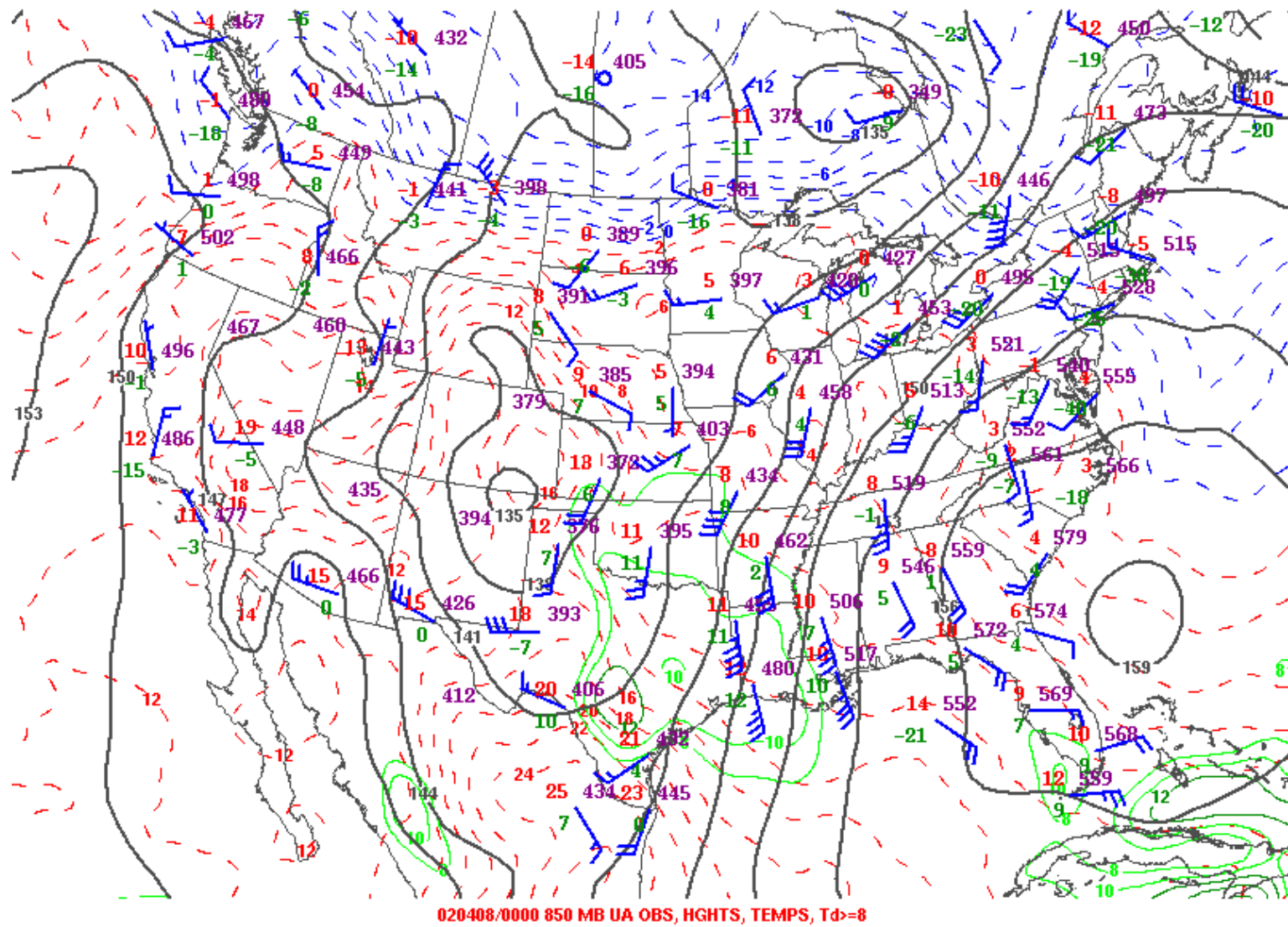


FIG. 3.8. Same as Fig. 3.7, but for 00 UTC 8 April 2002 (image courtesy of www.spc.noaa.gov).

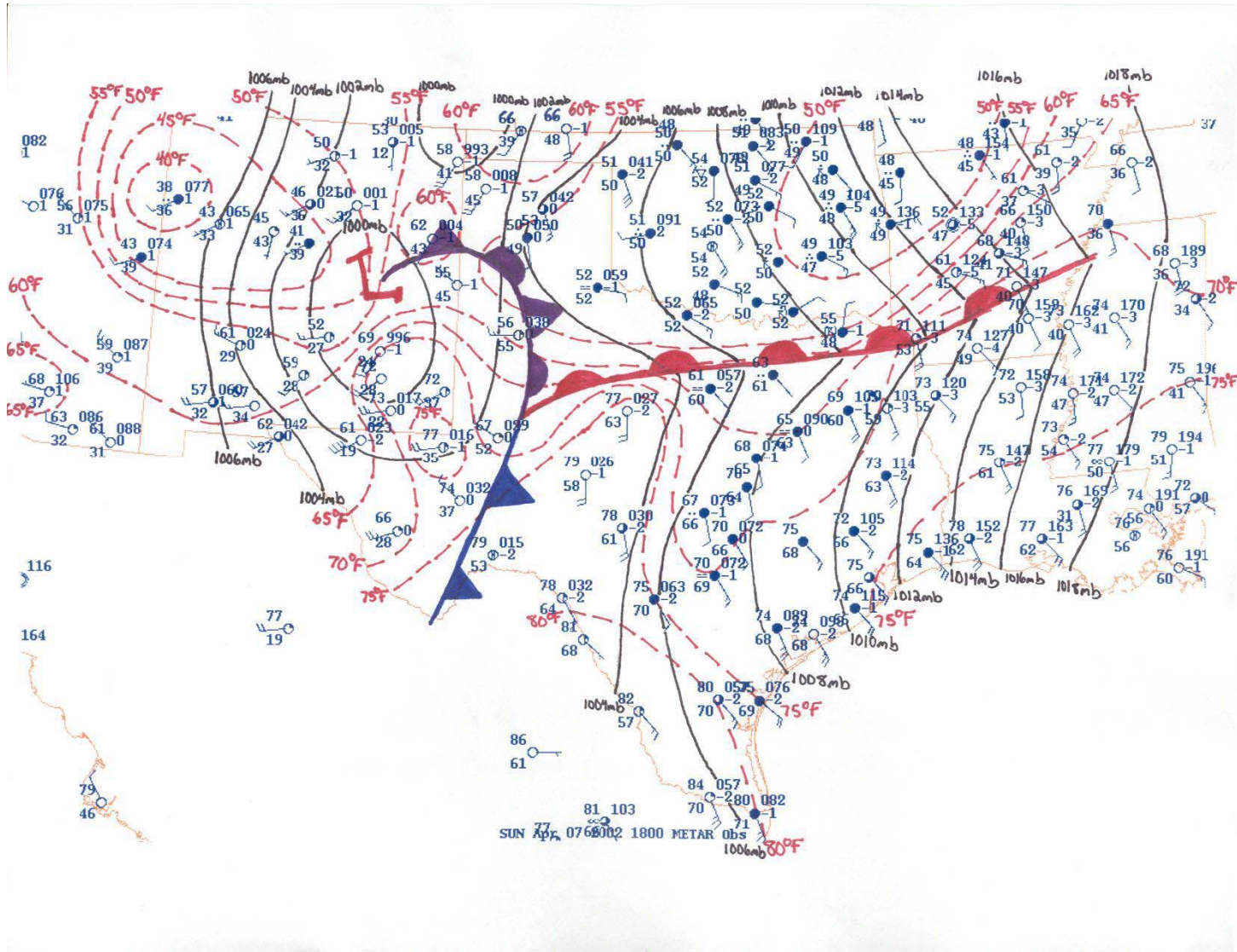


FIG. 3.9. 18 UTC 7 April 2002 manual surface analysis for Texas and surrounding areas. Isobars are in solid back lines, and isotherms are in dashed red lines.

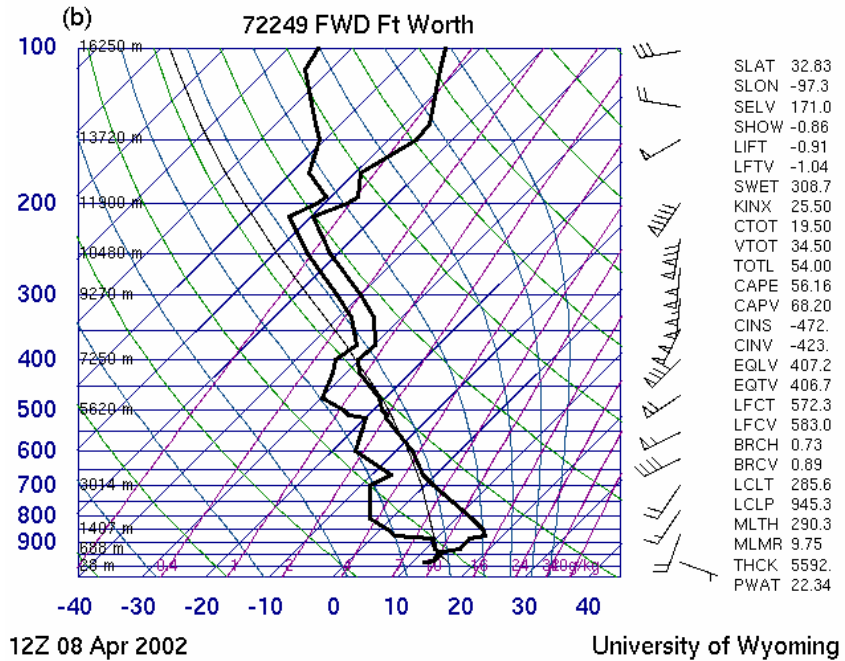
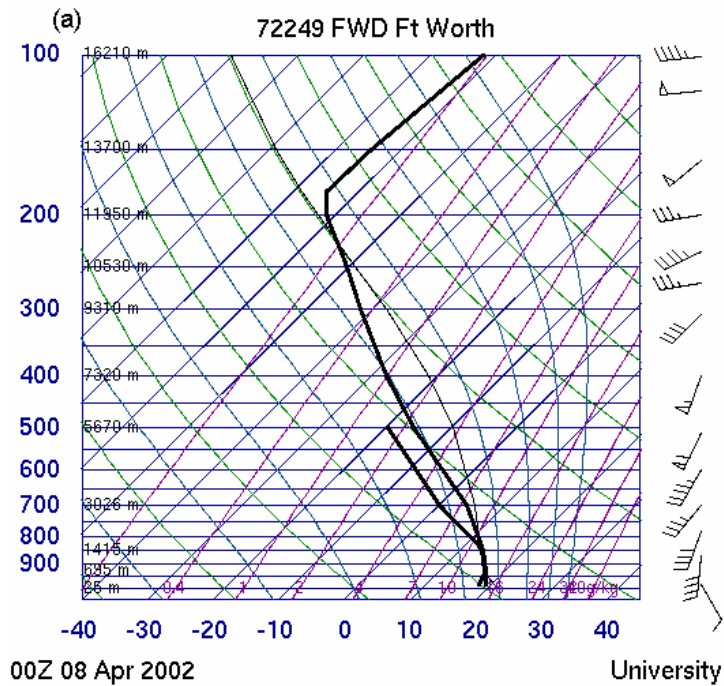


FIG. 3.10. Dallas-Fort Worth, Texas soundings valid at a) 00 UTC and b) 12 UTC 8 April 2002. Image courtesy of the University of Wyoming.

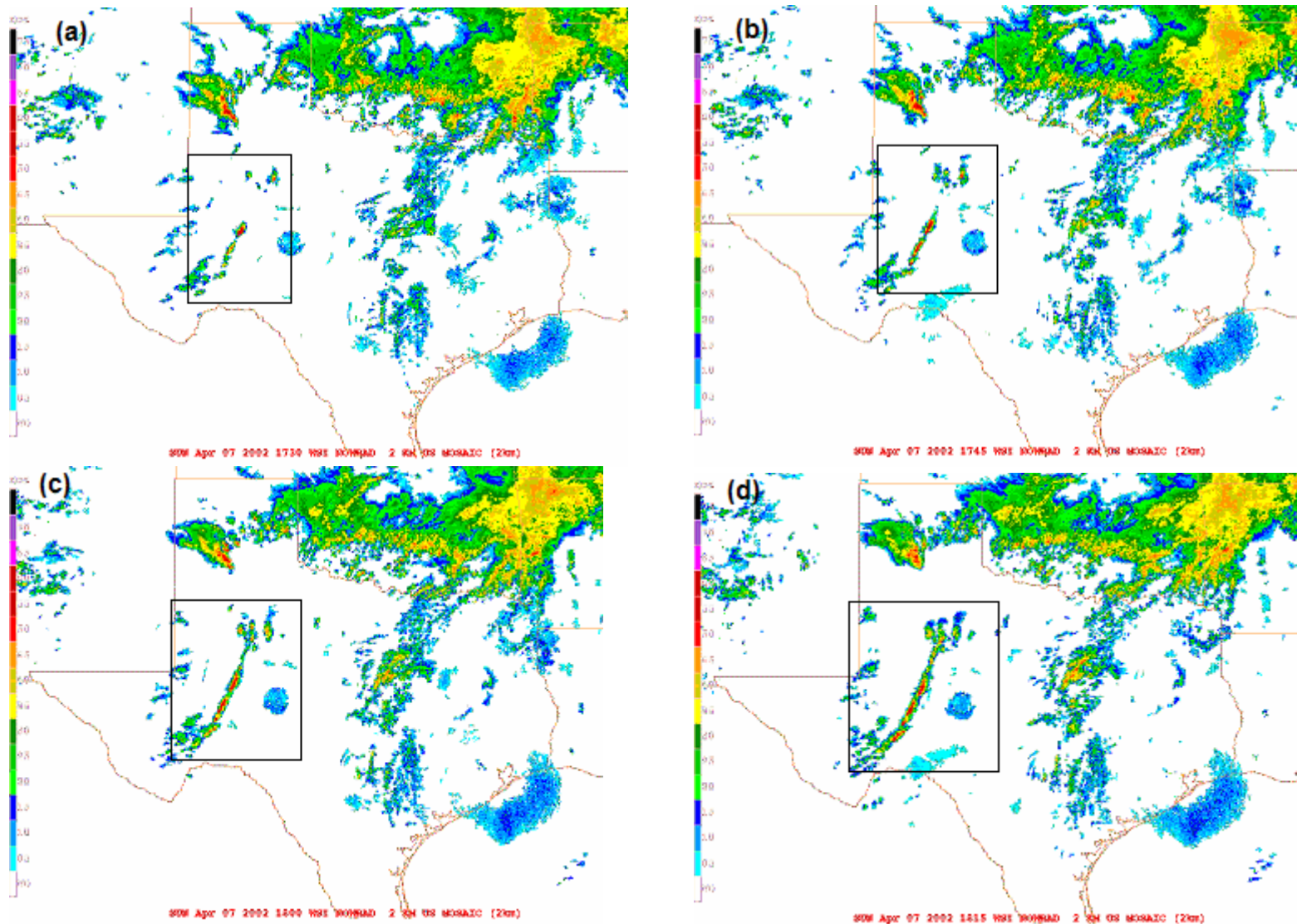


FIG. 3.11. Base NEXRAD reflectivity images of the developing convective line (boxed) located in western TX at (a) 17:30 UTC 7, (b) 17:45 UTC 7, (c) 18:00 UTC 7, and (d) 18:15 UTC 7 April 2002.

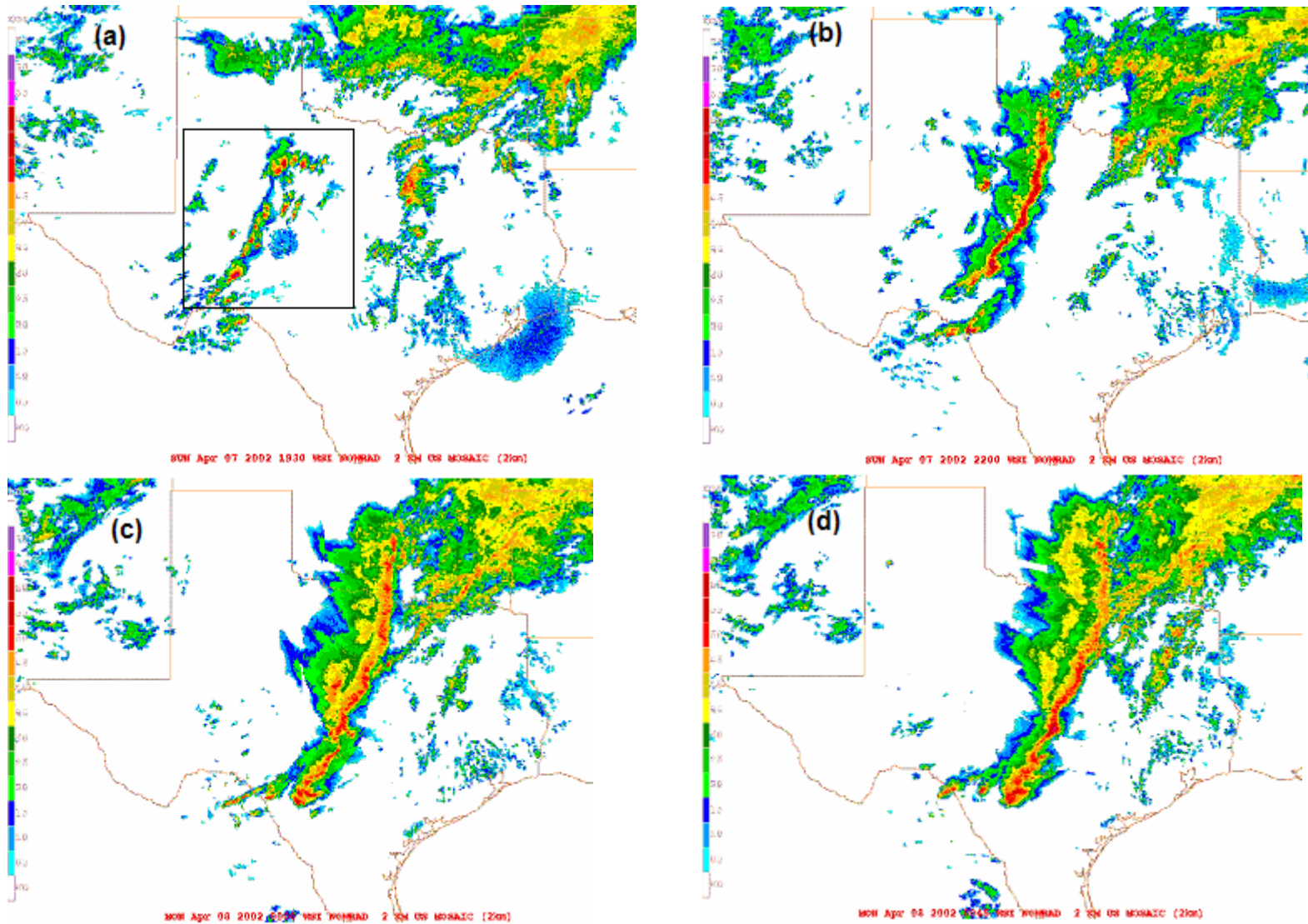


FIG. 3.12. Base NEXRAD reflectivity images of the developing MCS located in central TX at (a) 19:30 UTC 7, (b) 22:00 UTC 7, (c) 00:00 UTC 8, and (d) 00:45 UTC 8 April 2002.

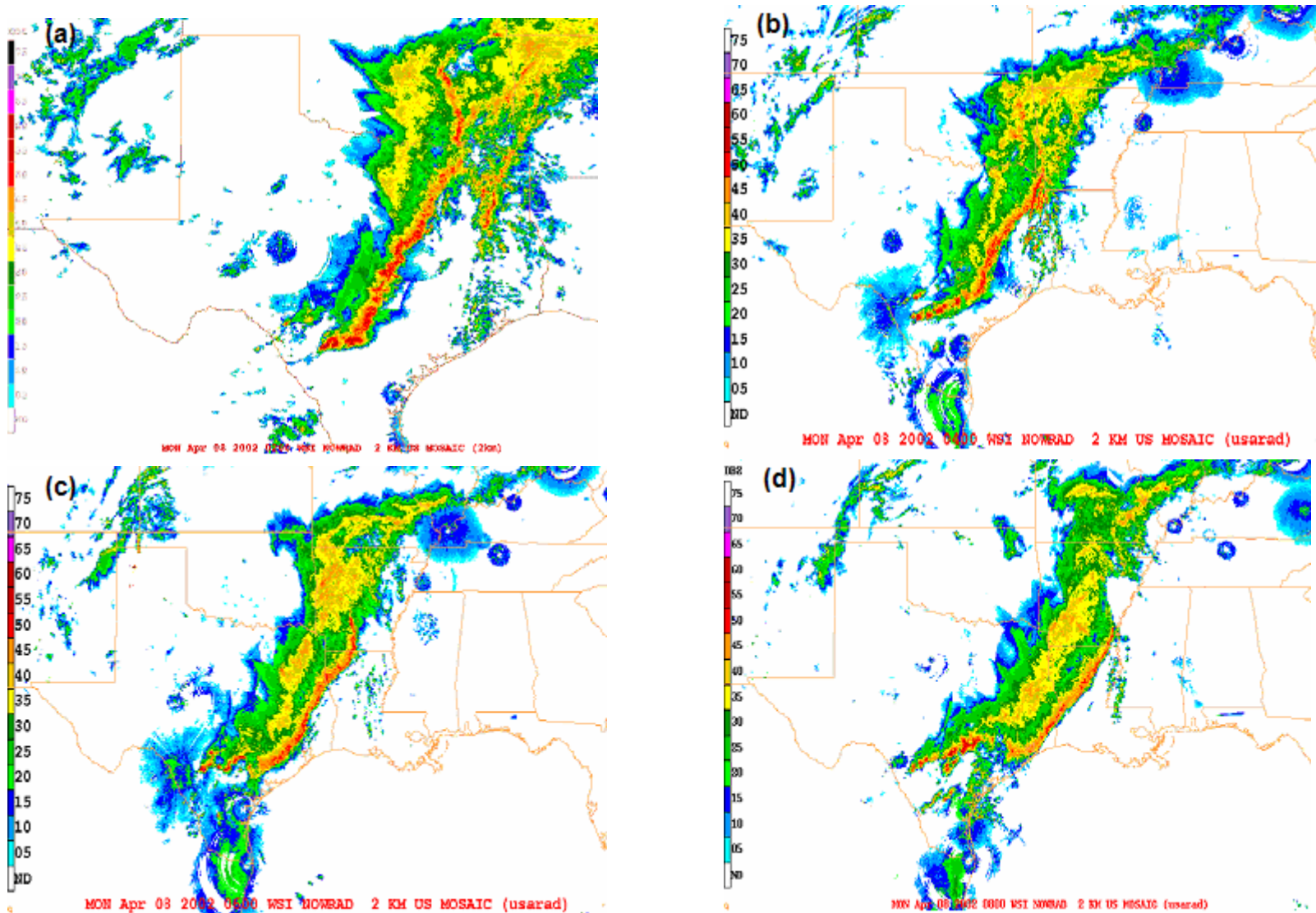


FIG. 3.13. Base NEXRAD reflectivity images of the MCS located in eastern TX at (a) 02:00 UTC 8, (b) 04:00 UTC 8, (c) 06:00 UTC 8, and (d) 08:00 UTC 8 April 2002.

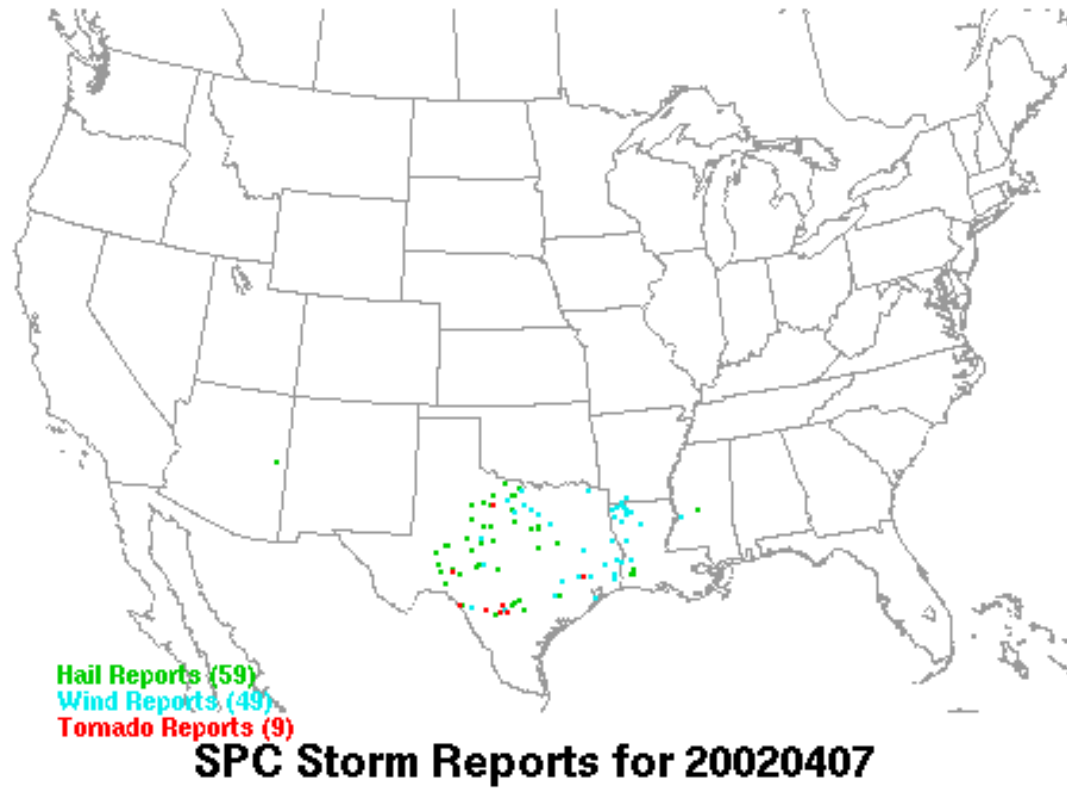


FIG. 3.14. Preliminary severe storm damage reports including hail ( $\geq 0.75''$ , green dots), strong winds ( $\geq 58$  mph, blue dots), and tornadoes (red dots) from 12:00 UTC 7 through 12:00 UTC 8 April 2002 (image courtesy of [www.spc.noaa.gov](http://www.spc.noaa.gov)).

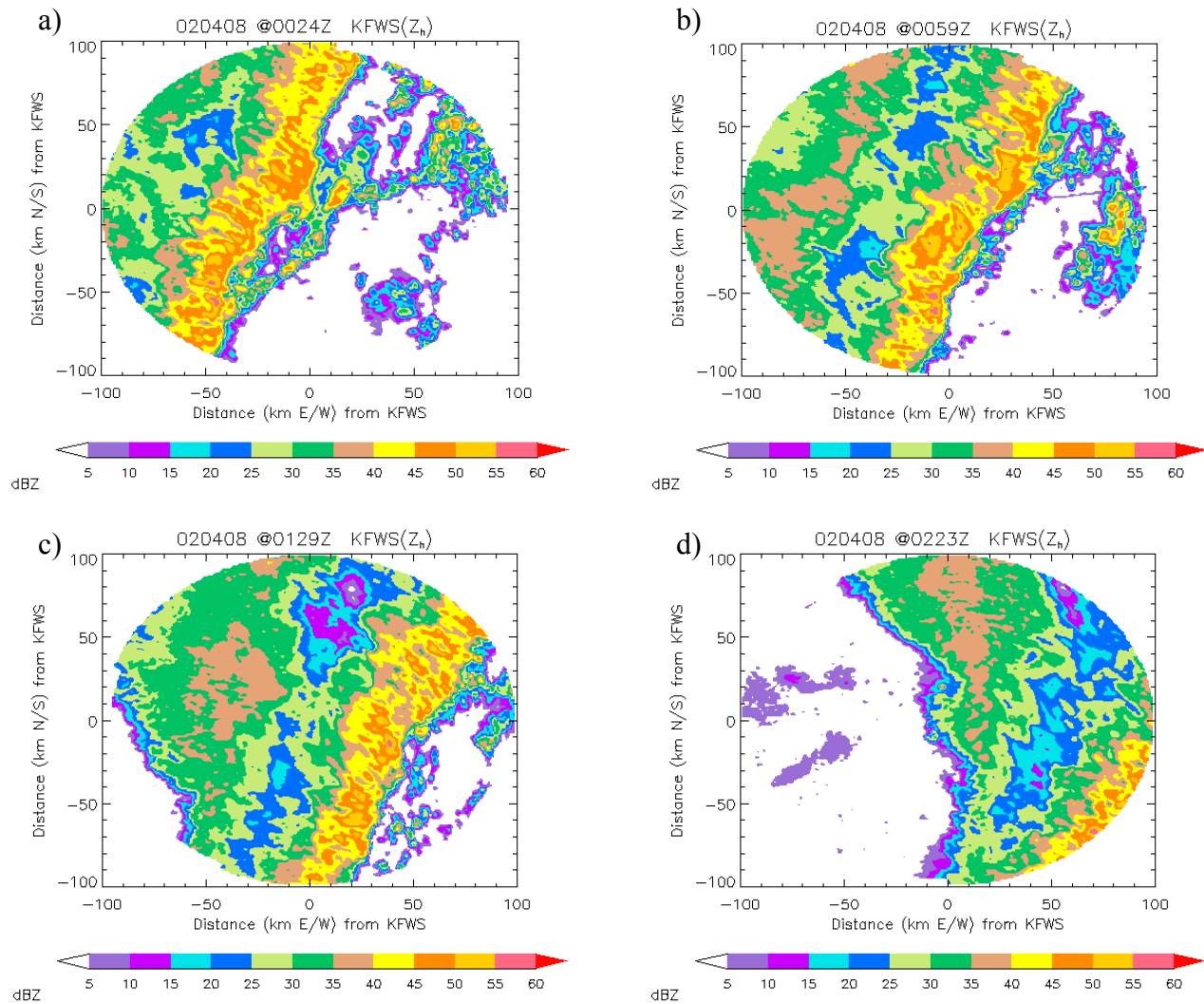


FIG. 3.15. 0.5 km CAPPI image of radar reflectivity (dBZ) in a 200 km  $\times$  200 km grid box at a) 00:24 UTC, b) 00:59 UTC, c) 01:29, and d) 02:23 UTC 8 April 2002. Radar reflectivity is color-shaded according to the scale, and the KFWS radar is located in the center of the image. The x- and y-axes represent the distance (km) north/south and east/west of the KFWS radar, respectively.

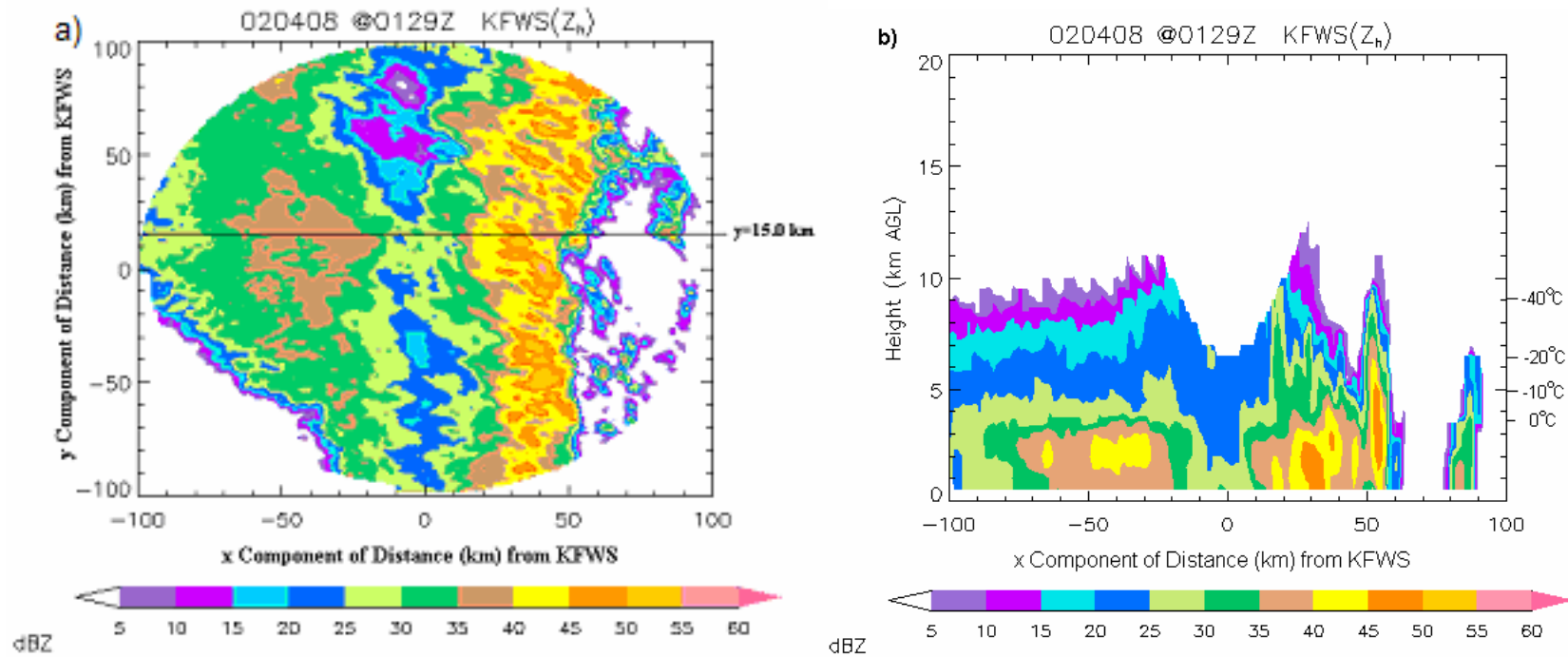


FIG. 3.16. (a) A 0.5 km CAPPI image, and b) a line-normal vertical cross-section through (a) at  $y = 15$  km at 01:29 UTC 8 April 2002. Radar reflectivity (dBZ) is color-shaded according to the scale. The horizontal image has been rotated counterclockwise  $20^\circ$  from its actual orientation (see Fig. 3.15(c)).

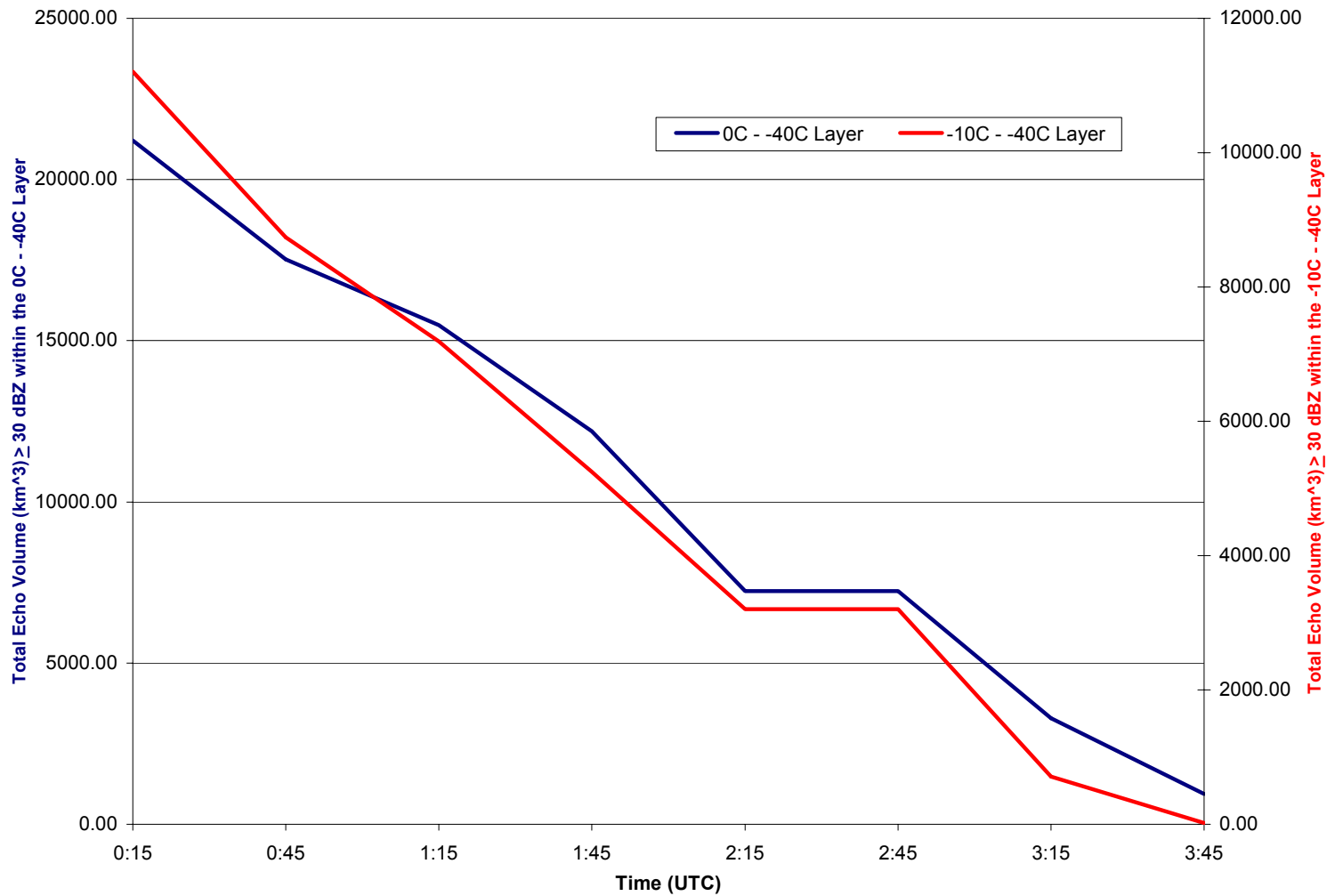


FIG. 3.17. Total echo volume aloft trend  $\geq 30$  dBZ from 00 to 04 UTC 8 April 2002, time averaged every 5 min with a 6-point running mean smoother. Total echo volume aloft ( $\text{km}^3$ ) was calculated between the  $0^\circ\text{C}$  to  $-40^\circ\text{C}$  layer (blue line) and the  $-10^\circ\text{C}$  to  $-40^\circ\text{C}$  layer (red line), and these values are listed along the primary and secondary y-axes, respectively. Time is listed along the x-axis.

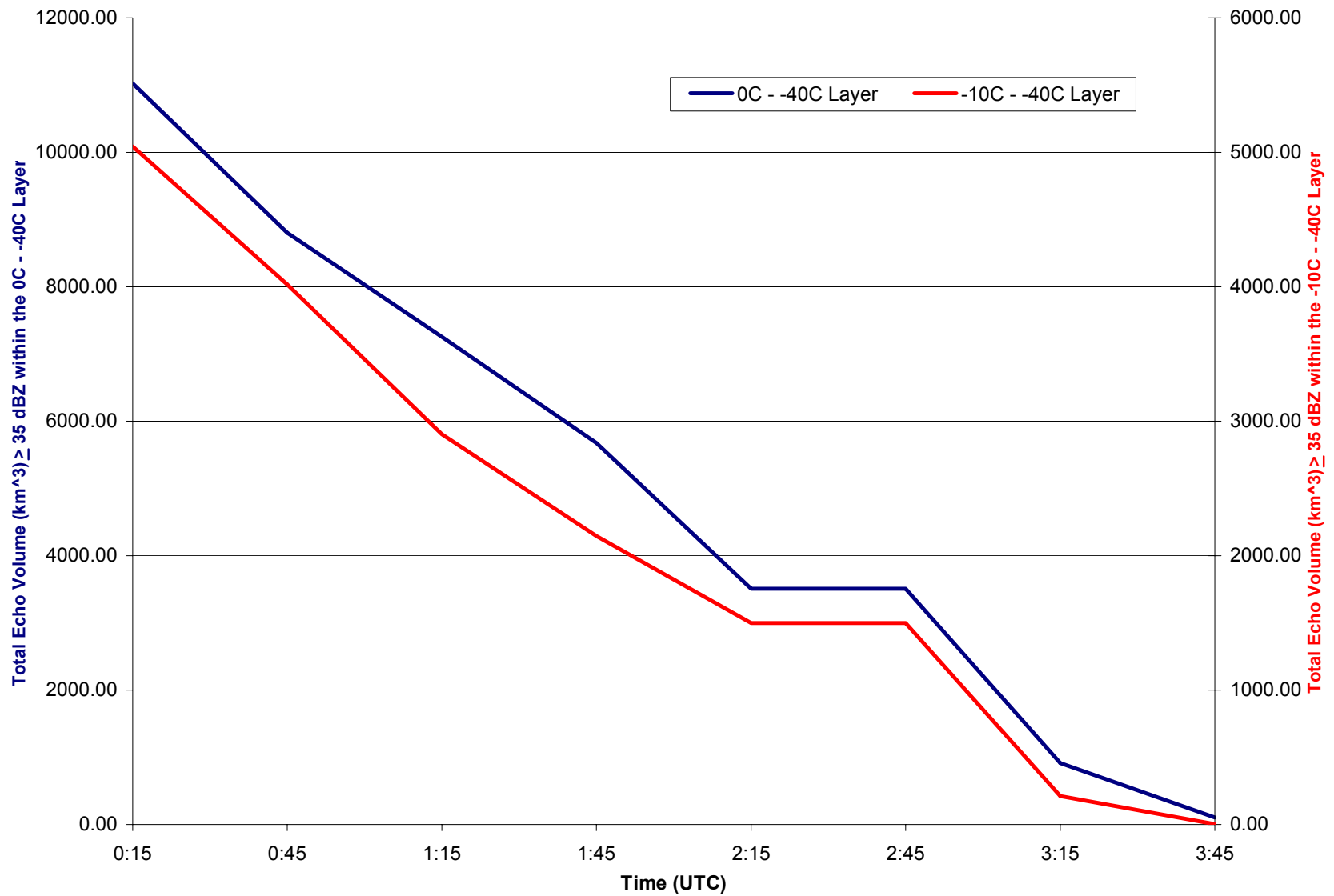


FIG. 3.18. Same as Fig. 3.17, but for total echo volume aloft  $\geq 35$  dBZ.

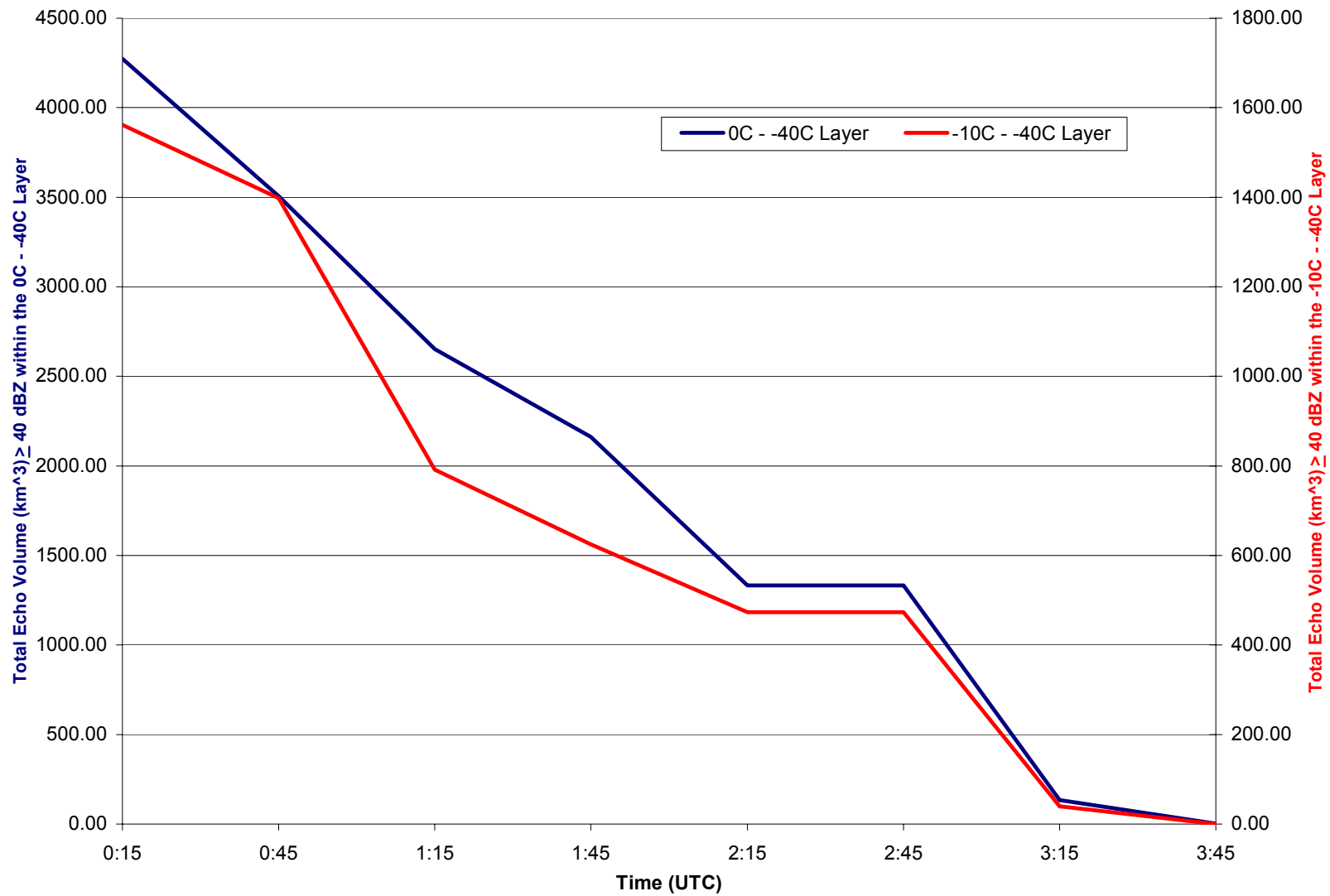


FIG. 3.19. Same as Fig. 3.17, but for total echo volume aloft  $\geq 40$  dBZ.

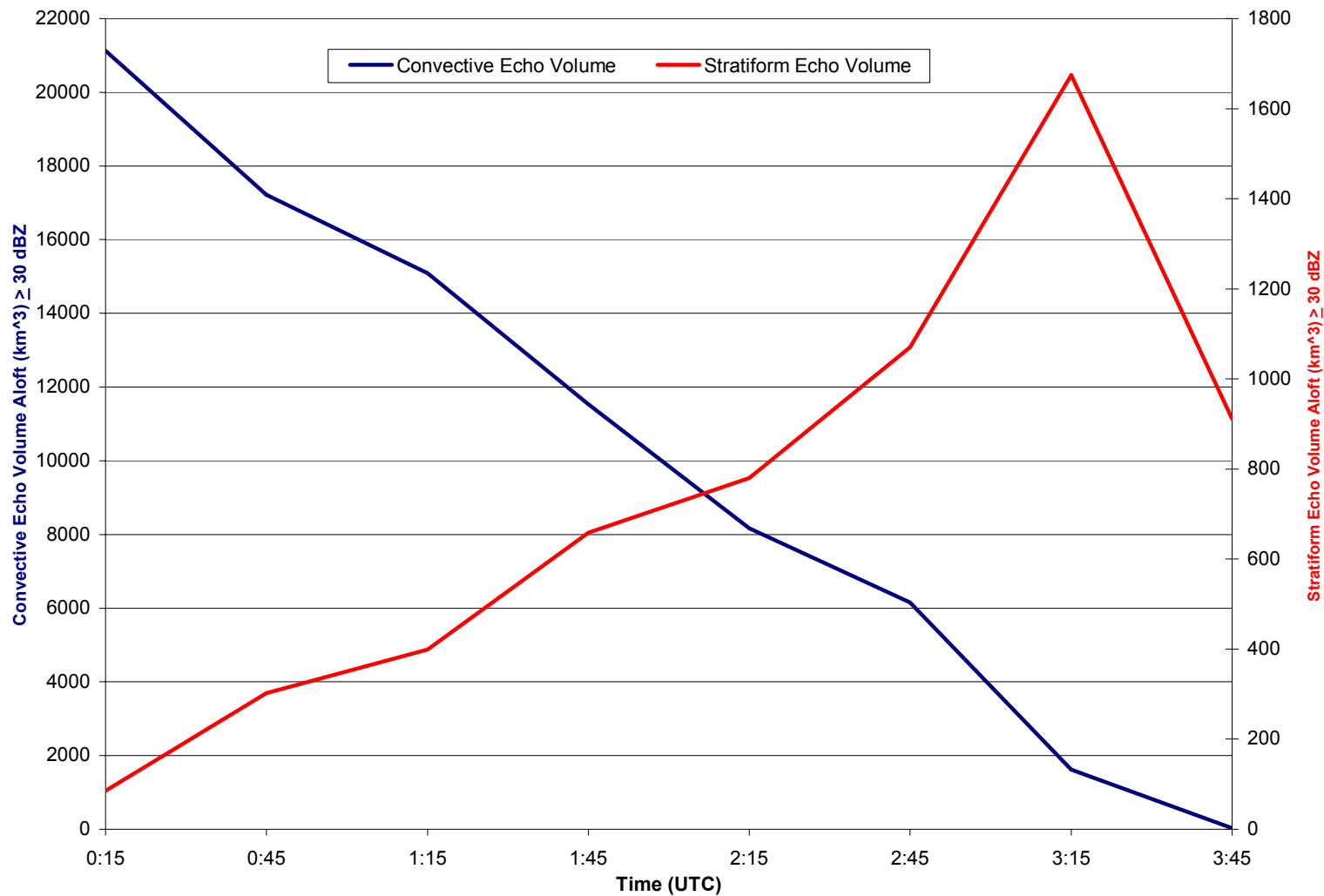


FIG. 3.20. Partitioned echo volume aloft trends  $\geq 30$  dBZ from 00 to 04 UTC 8 April 2002, time averaged every 5 min with a 6-point running mean smoother. Total echo volume aloft ( $\text{km}^3$ ) was calculated using the  $0^\circ\text{C}$  to  $-40^\circ\text{C}$  layer in the convective region (blue line) and stratiform region (red line). Convective and stratiform region echo volume aloft are listed along the primary and secondary y-axes, respectively. Time is listed along the x-axis.

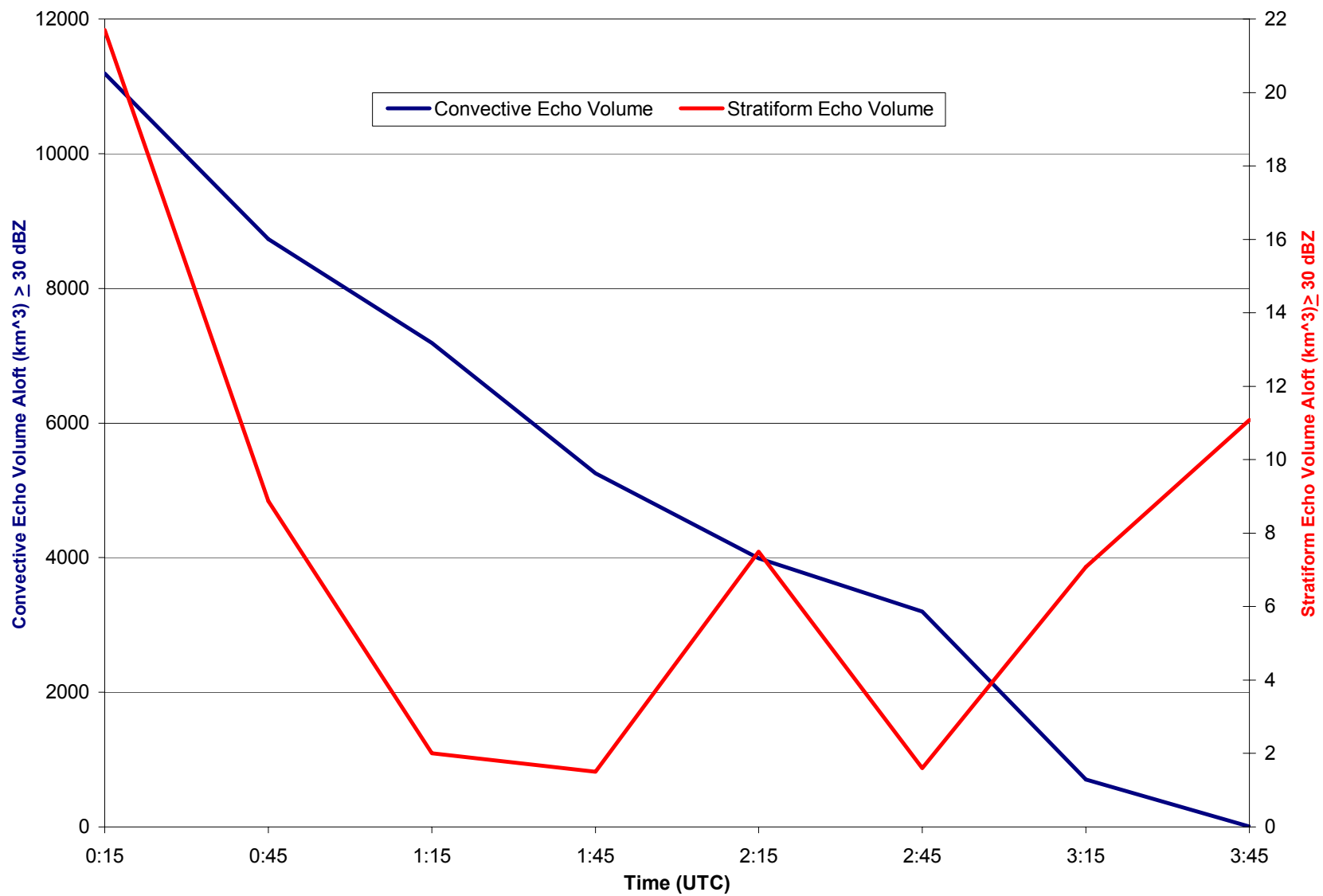


FIG. 3.21. Same as Fig. 3.20, but echo volume aloft was calculated using the -10°C to -40°C layer.

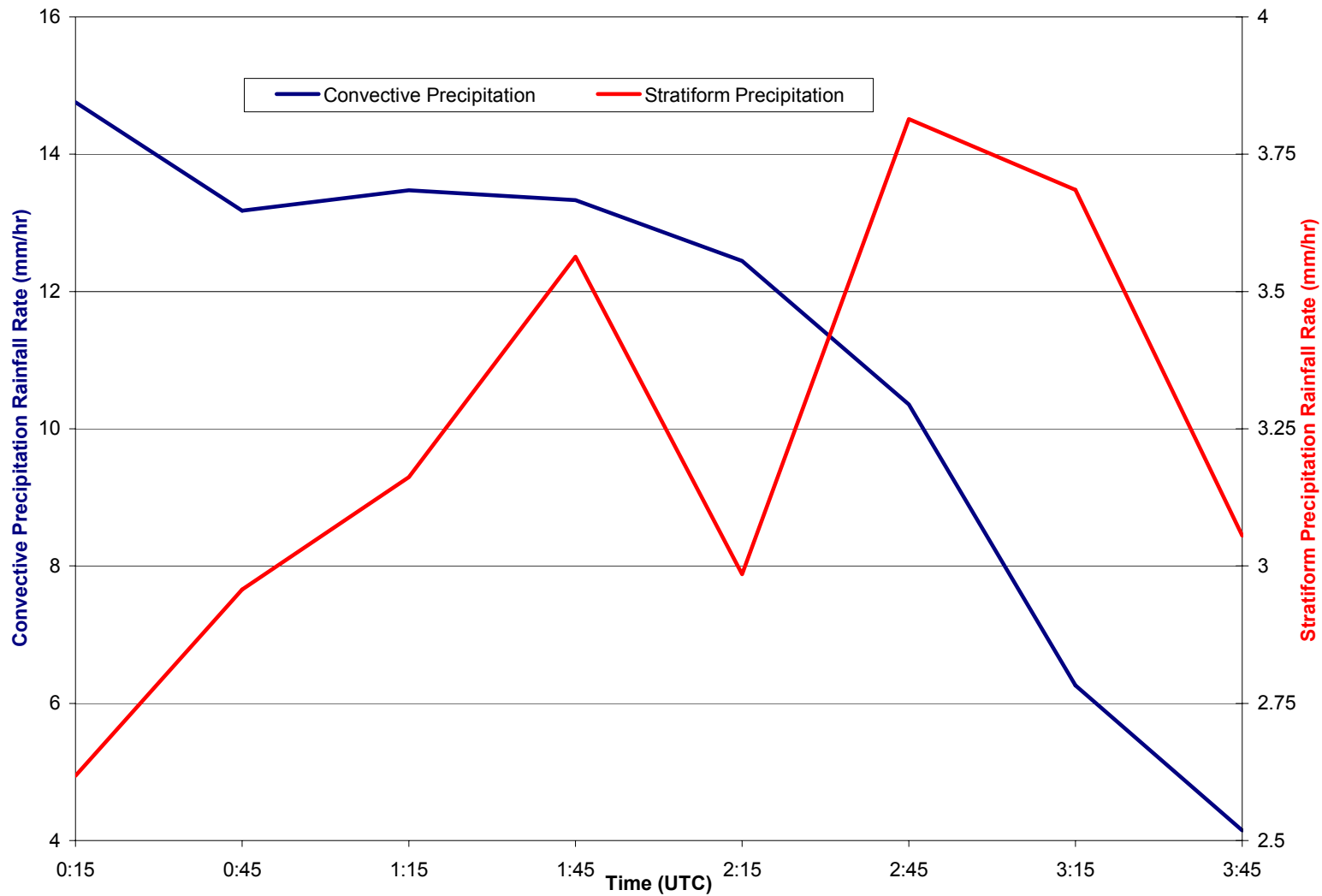


FIG. 3.22. Partitioned rainfall rate trends calculated from 00 to 04 UTC 8 April 2002, time averaged every 5 min with a 6-point running mean smoother. Rainfall rates for the convective region (blue line) and stratiform region (red line) were separately calculated and are listed along the primary and secondary y-axes, respectively. Time is listed along the x-axis.

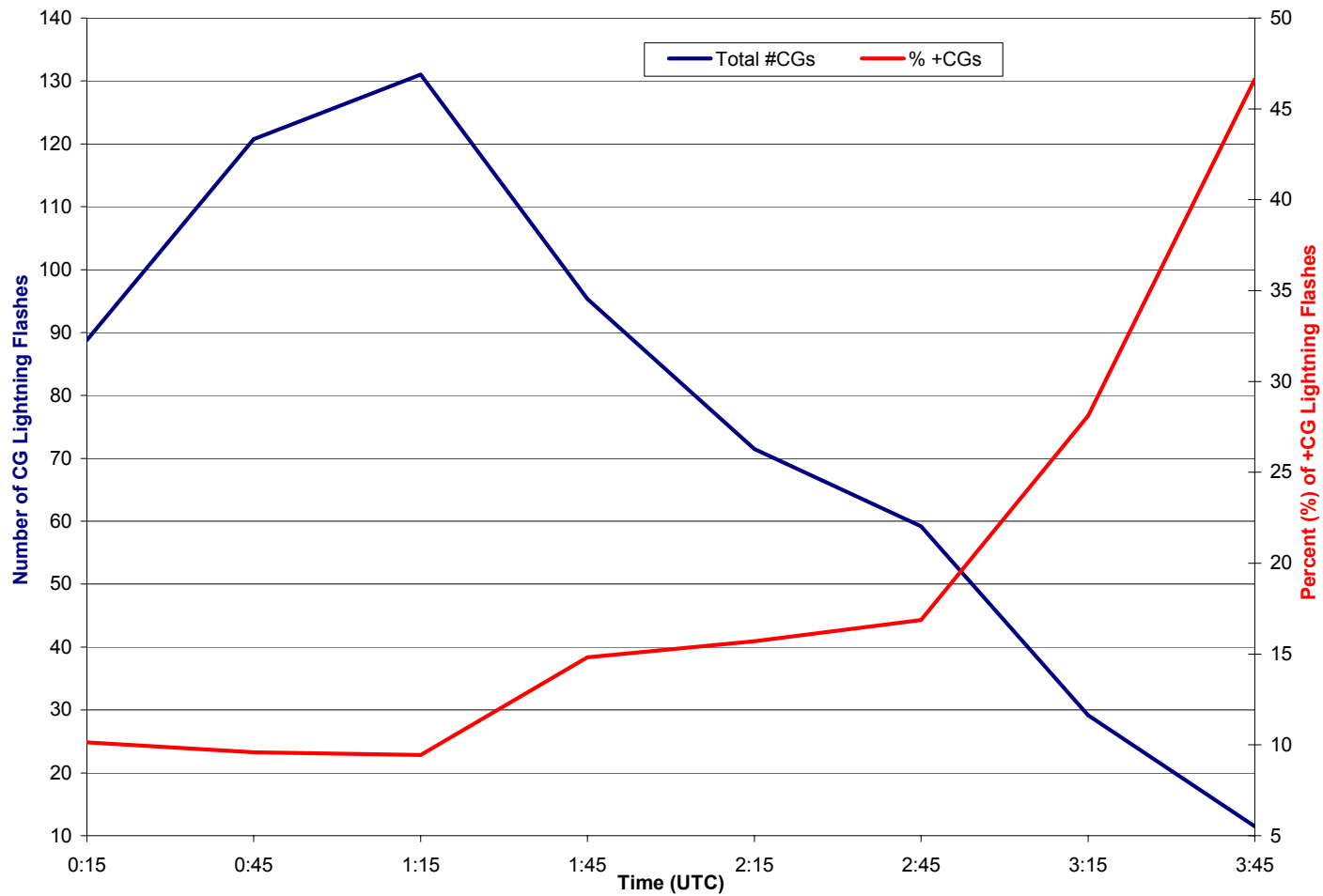


FIG. 3.23. Total CG lightning flash trends within a portion of the 7-8 April 2002 MCS that is within the KFWS radar's viewing range from 00 to 04 UTC, time averaged every 5 min with a 6-point running mean smoother. The total CG lightning flash trend (both positive and negative, in blue) is compared to the percent of +CG lightning flashes (in red). These values are listed along the primary (secondary) y-axis. Time is listed along the x-axis.

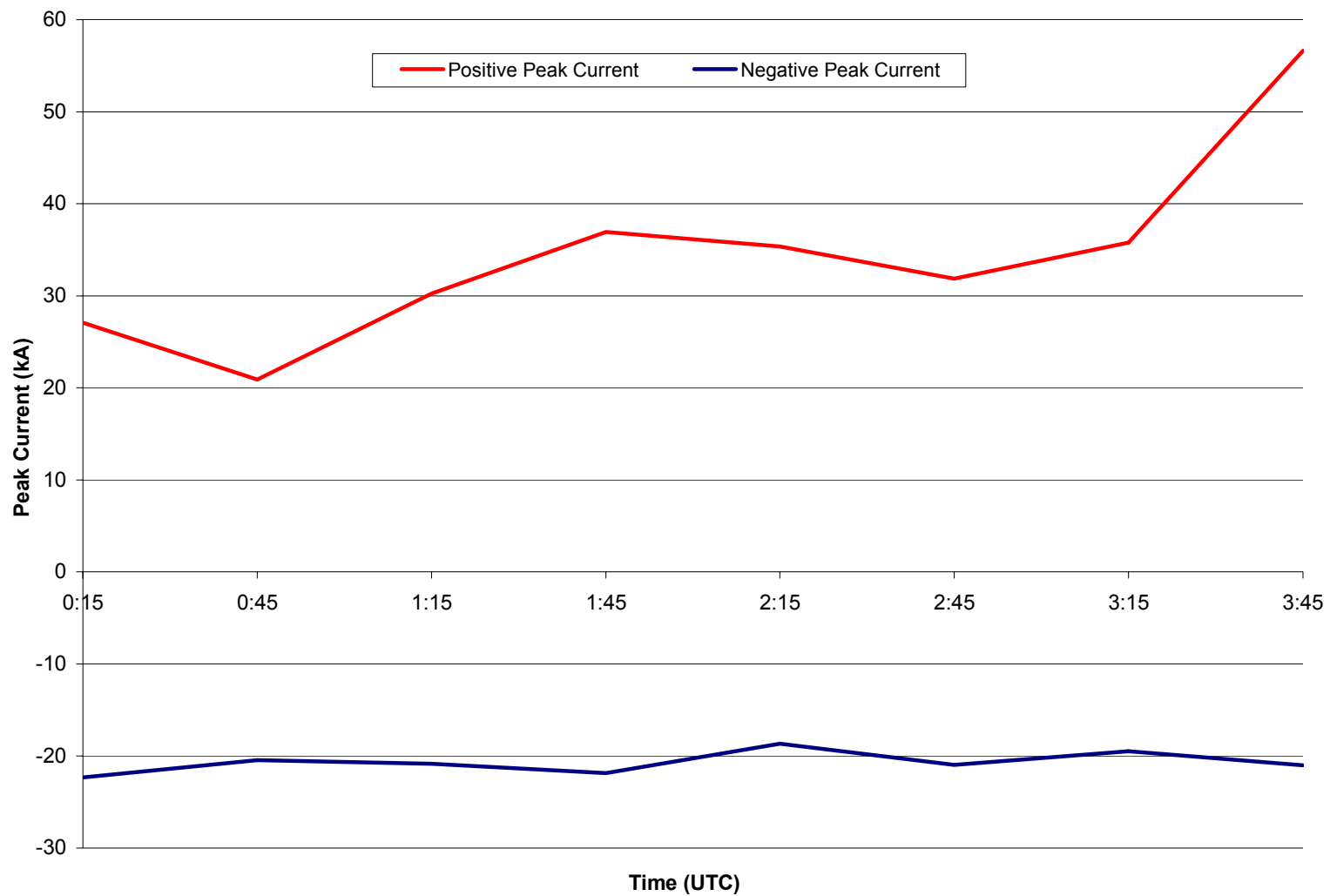


FIG. 3.24. CG lightning peak positive (red line) and negative (blue line) current (kA) trends from 00 to 04 UTC 8 April 2002, time averaged every 5 min with a 6 point running mean smoother. Peak current is listed along the y-axis, and time is listed along the x-axis.



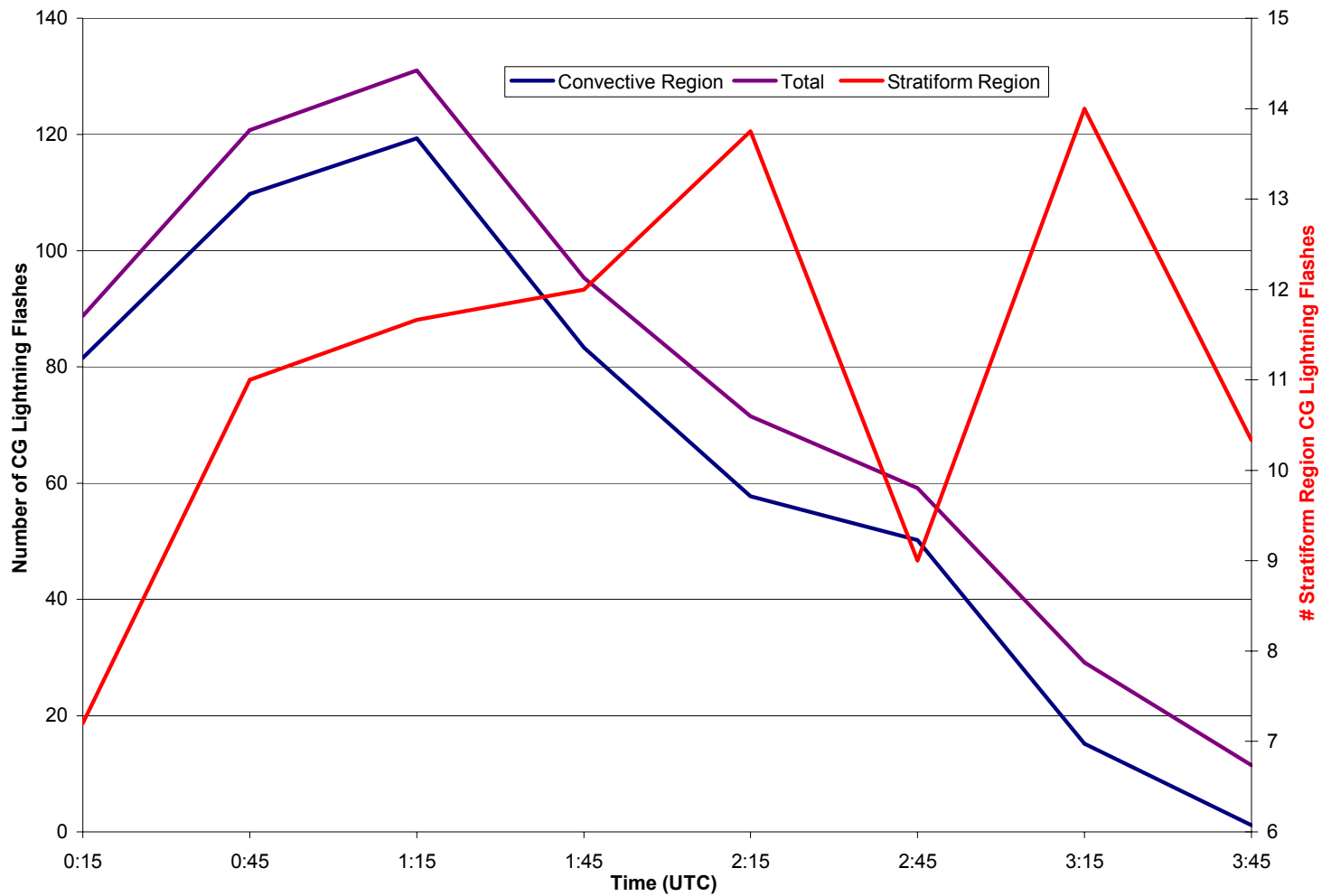


FIG. 3.26. Convective (blue line), stratiform (red line), and total (violet line) CG lightning flash trends from 00 to 04 UTC 8 April 2002, time averaged every 5 min with a 6-point running mean smoother. Note that both the convective and total CG flashes are listed along the primary y-axis and the stratiform CG lightning flashes are listed along the secondary y-axis. Time is listed along the x-axis.

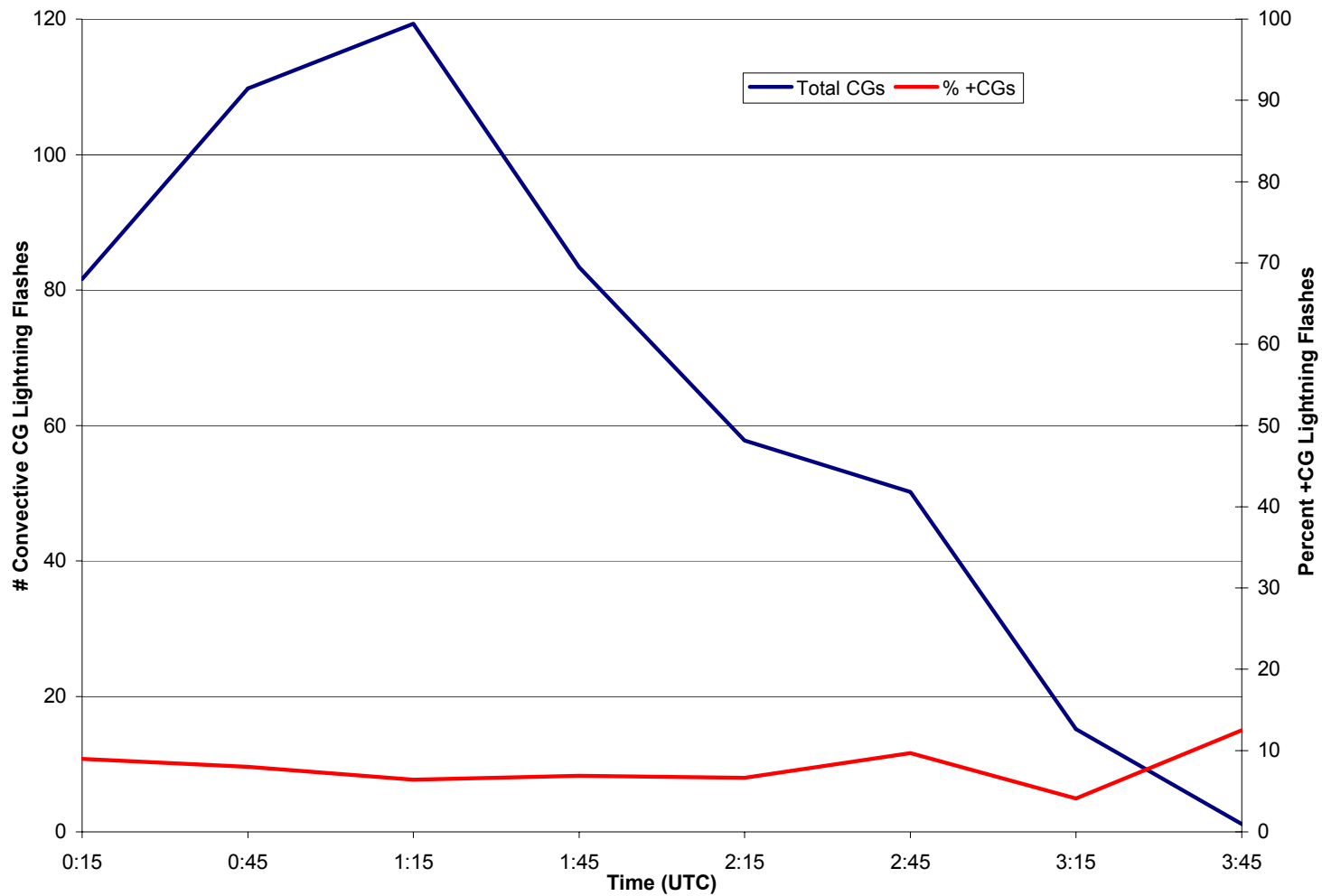


FIG. 3.27. Convective region CG lightning flashes (blue line) and the percent of +CG flashes (red line) trends from 00 to 04 UTC 8 April 2002, time averaged every 5 min with a 6-point running mean smoother. Note that the total number of CGs corresponds to the primary y-axis, and the percent of +CGs corresponds to the secondary y-axis. Time is listed along the x-axis.

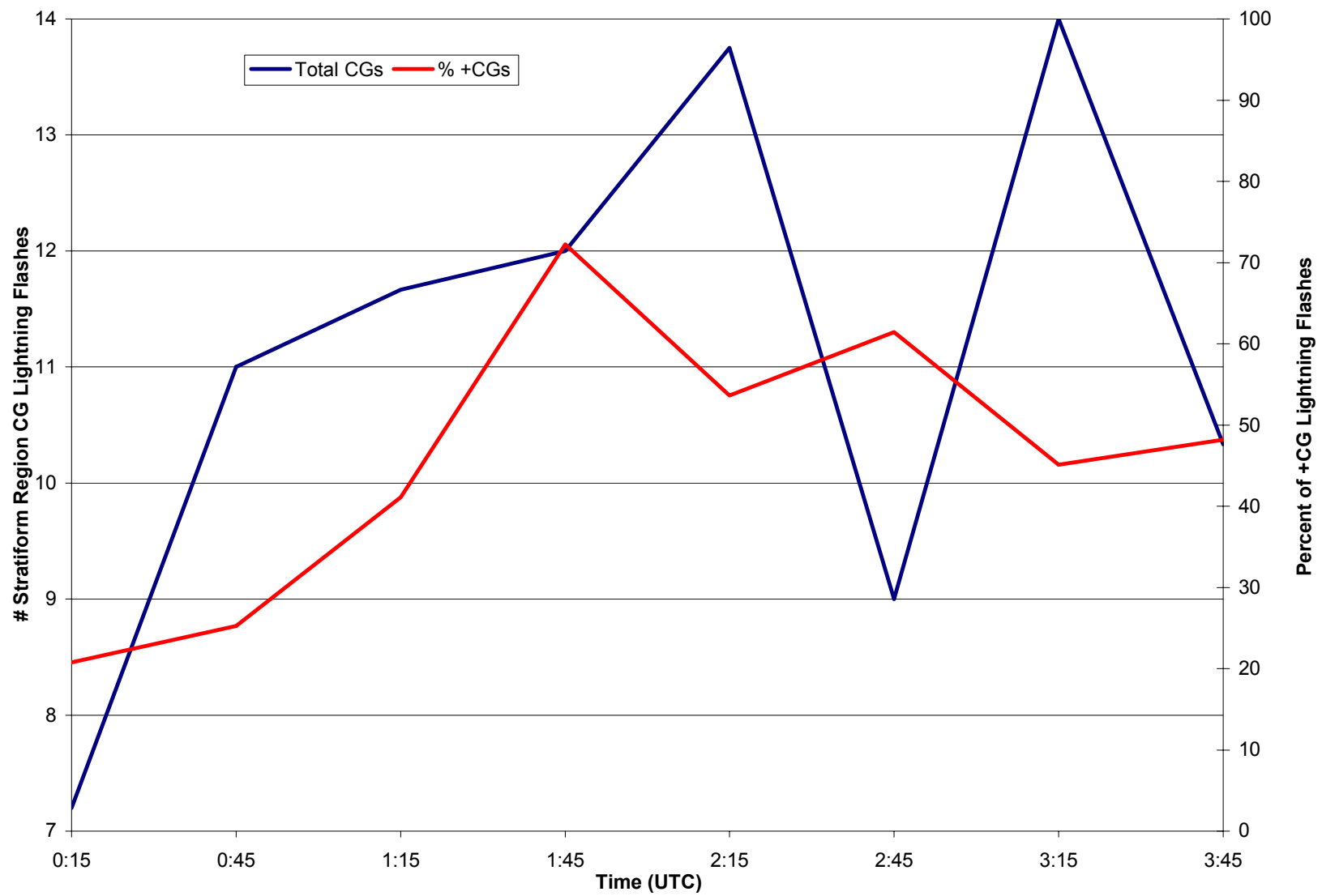


FIG. 3.28. Same as Fig. 3.27, but for the stratiform region.

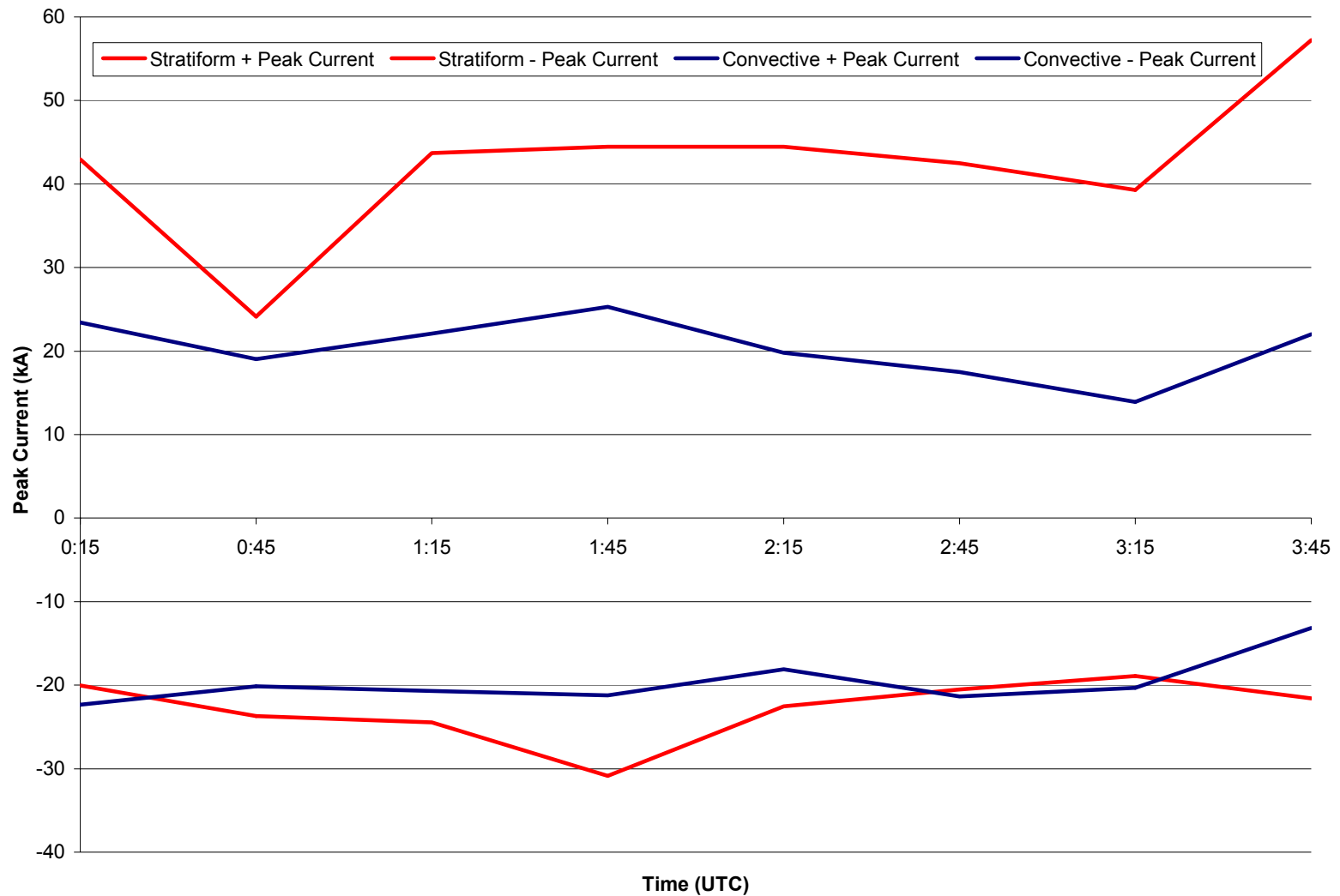


FIG. 3.29. Temporal evolution of the convective (blue lines) and stratiform (red lines) CG lightning peak positive and negative currents (kA) from 00 to 04 UTC 8 April 2002, time averaged every 5 min with a 6-point running mean smoother. Positive and negative currents are listed along the y-axis, and time is listed along the x-axis.

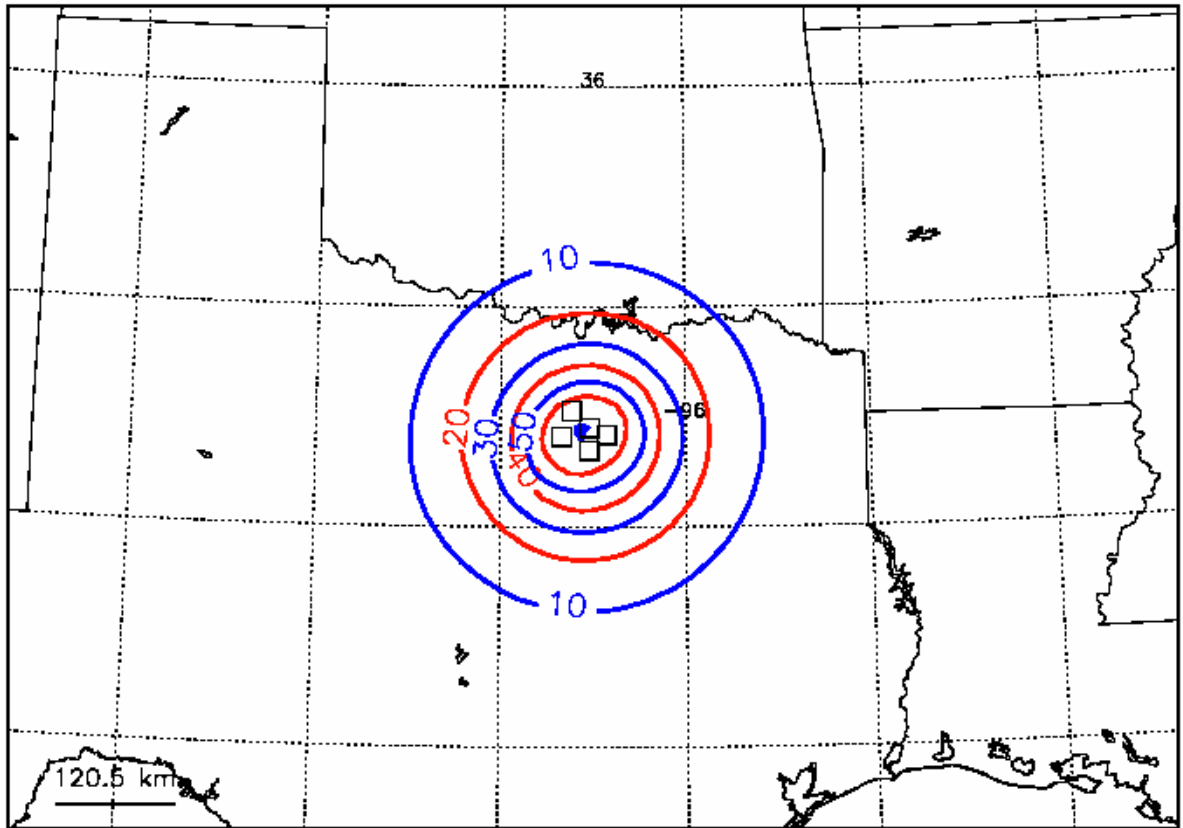


FIG. 3.30. Detection efficiency of the LDAR II network during the 7-8 April 2002 MCS. The five squares represent the five LDAR II sensors that were operational during this case study (the northern and northeastern sensors were not operational and, hence, are not pictured). The circles around the network represent the percent of LDAR II flashes that can be detected out to a given range. Within the network's center, 70% of LDAR II flashes can be detected. (Image adapted from M. Murphy 2003).

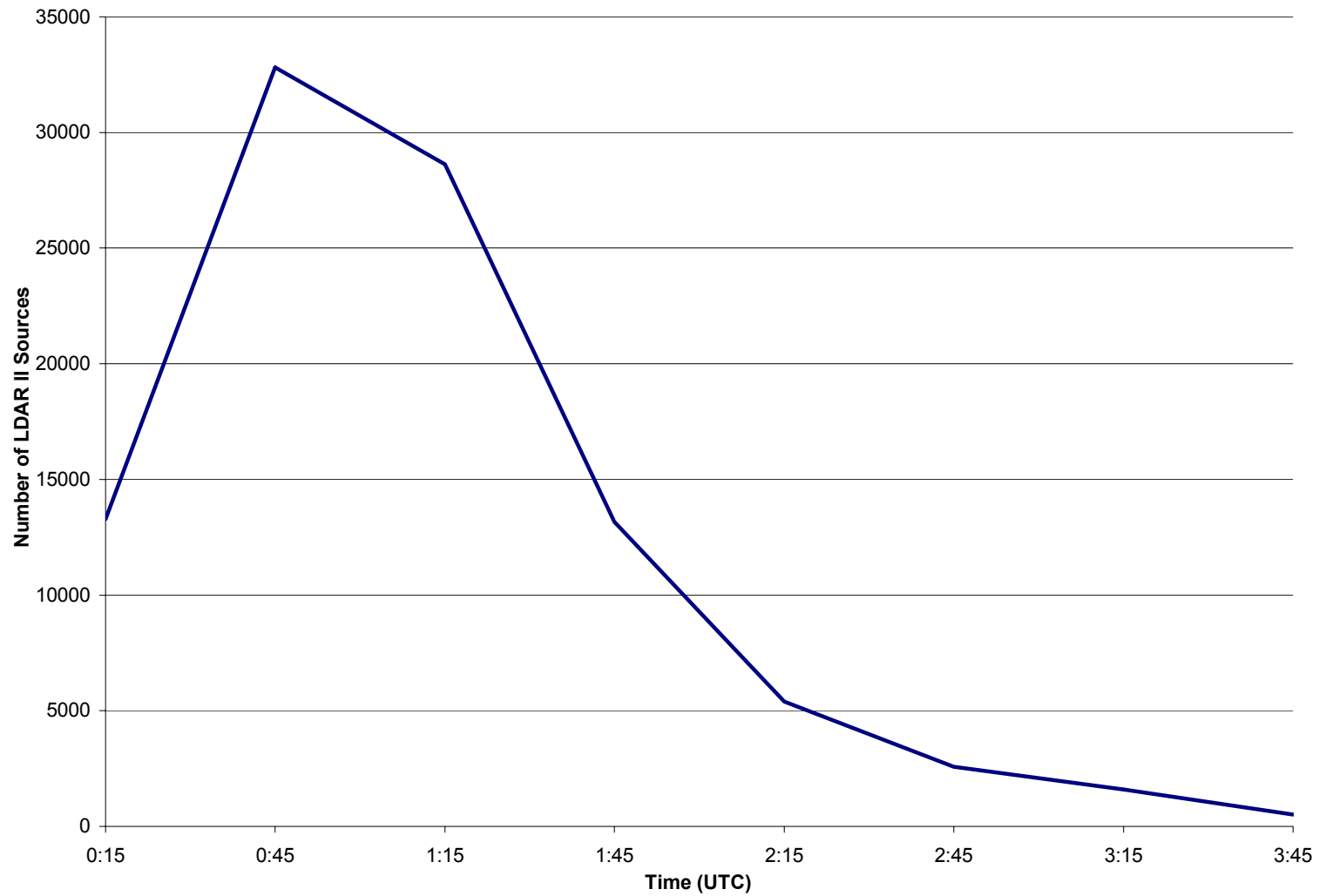


FIG. 3.31. LDAR II source trend within the KFWS radar viewing range from 00 to 04 UTC 8 April 2002, time averaged every 5 min with a 6-point running mean smoother. The number of LDAR II sources is listed on the y-axis, and time is listed along the x-axis.

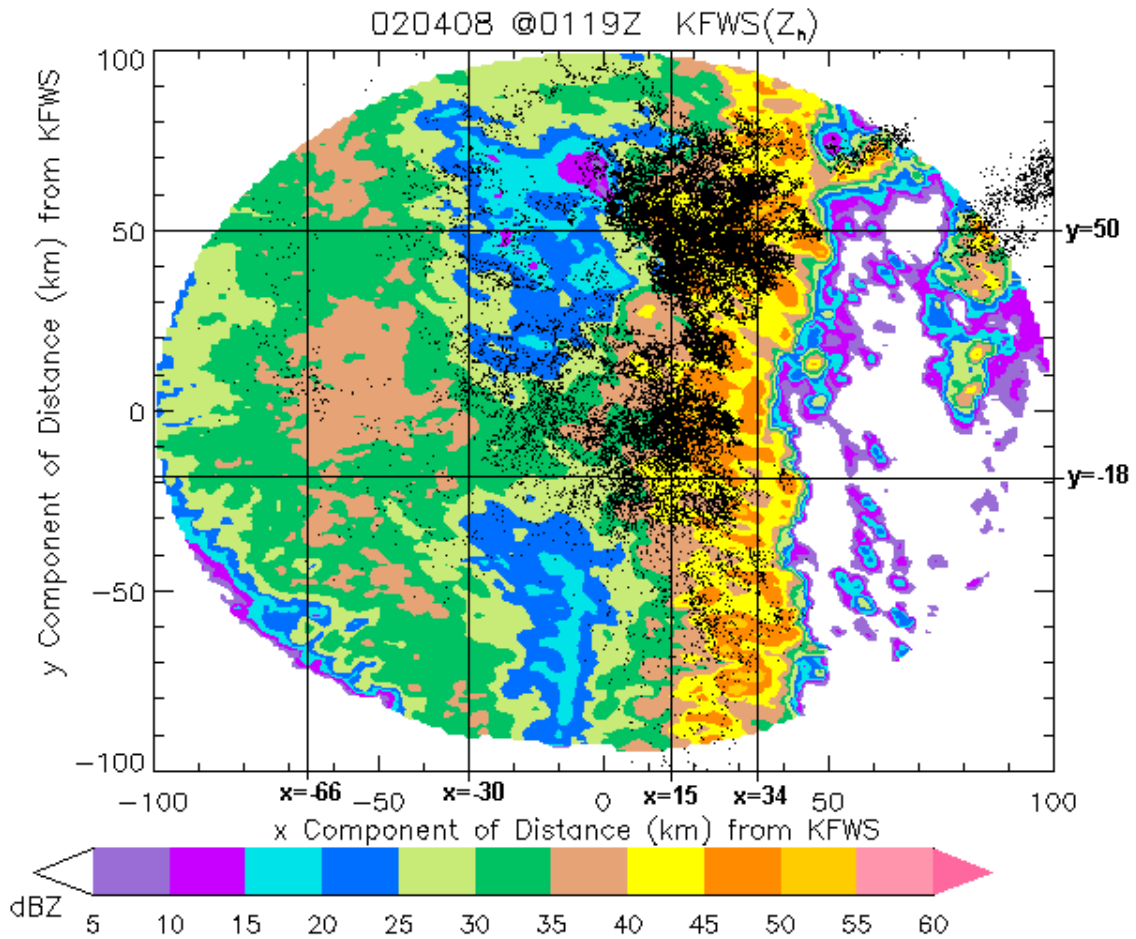


FIG. 3.32. 0.5 km CAPPI image of radar reflectivity (dBZ) with LDAR II sources overlaid (black dots) at 01:19 UTC 8 April 2002. Radar reflectivity is color-shaded according to the scale, and the KFWS radar is located in the center of the image. 5 min of LDAR II sources occurring at all altitudes centered on the time of the radar image are plotted. The reflectivity and LDAR II data have been rotated  $20^\circ$  counterclockwise, so that the x- and y-axes represent the x and y components of distance (km) from the KFWS radar, respectively. The four vertical and two horizontal lines represent the vertical cross-section locations in Figs. 3.33-3.35.

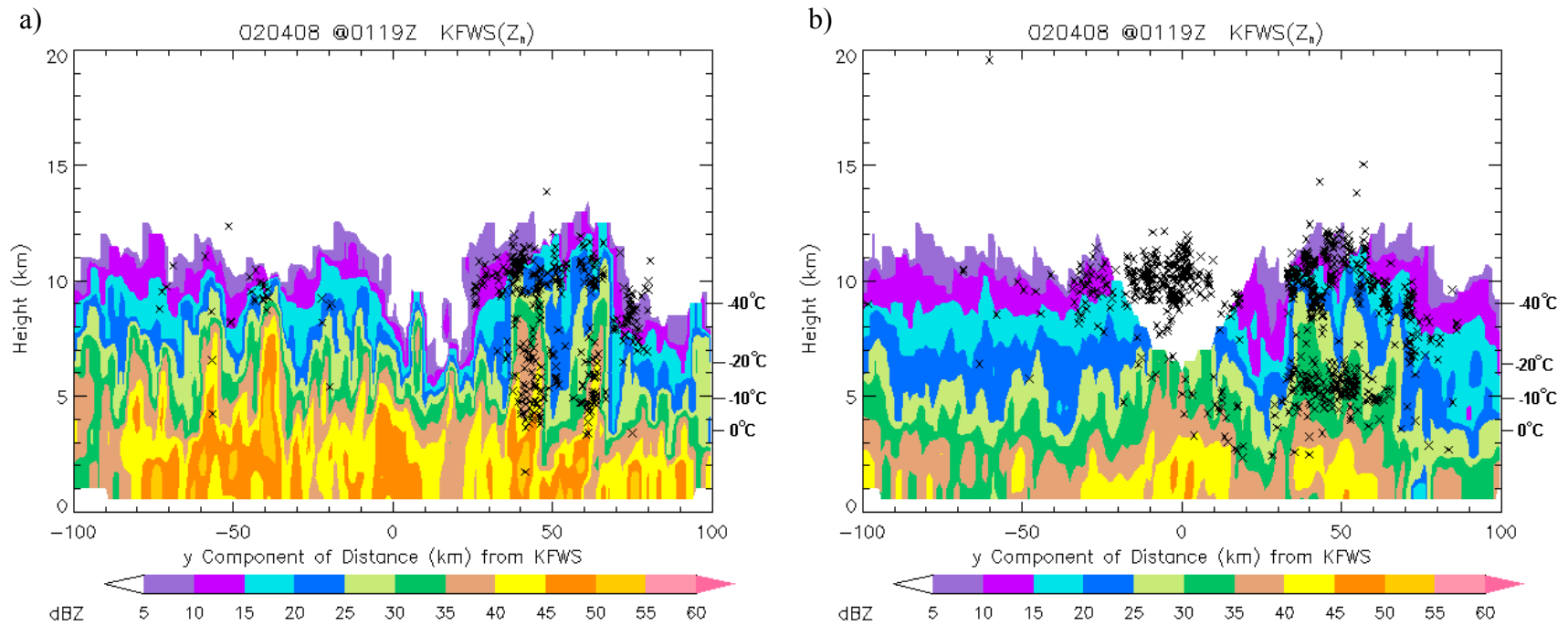


FIG. 3.33. Vertical cross-section of the convective line at 01:19 UTC 8 April 2002 taken line parallel through Fig. 3.32 at a)  $x = 34$  km (the leading edge of the convective line), and b)  $x = 15$  km (the back edge of the convective line). Radar reflectivity (dBZ) is color-shaded according to the scale, and LDAR II sources (at  $x \pm 0.5$  km) are overlaid in black "x"s. The y-axis represents height above ground level (km), and the x-axis represents the x component of distance from the KFWS radar. Significant temperature levels (0 °C, -10 °C, -20 °C, and -40 °C) are listed along the y-axis on the right-hand side of the image.

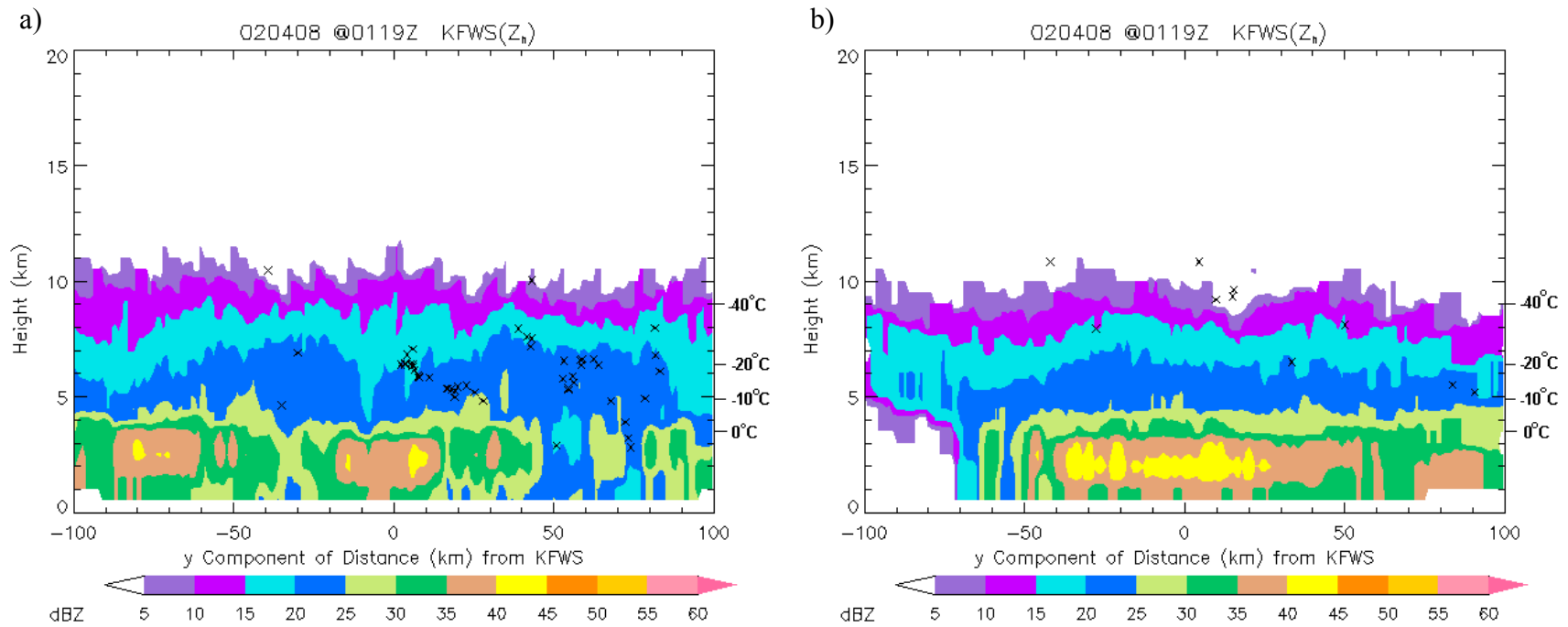


FIG. 3.34. Same as Fig. 3.33, but these vertical cross-sections were taken line-parallel through a) the front edge of the stratiform region at  $x = -30$  km, and b) the back edge of the stratiform region at  $x = -66$  km, as depicted in Fig. 3.32.

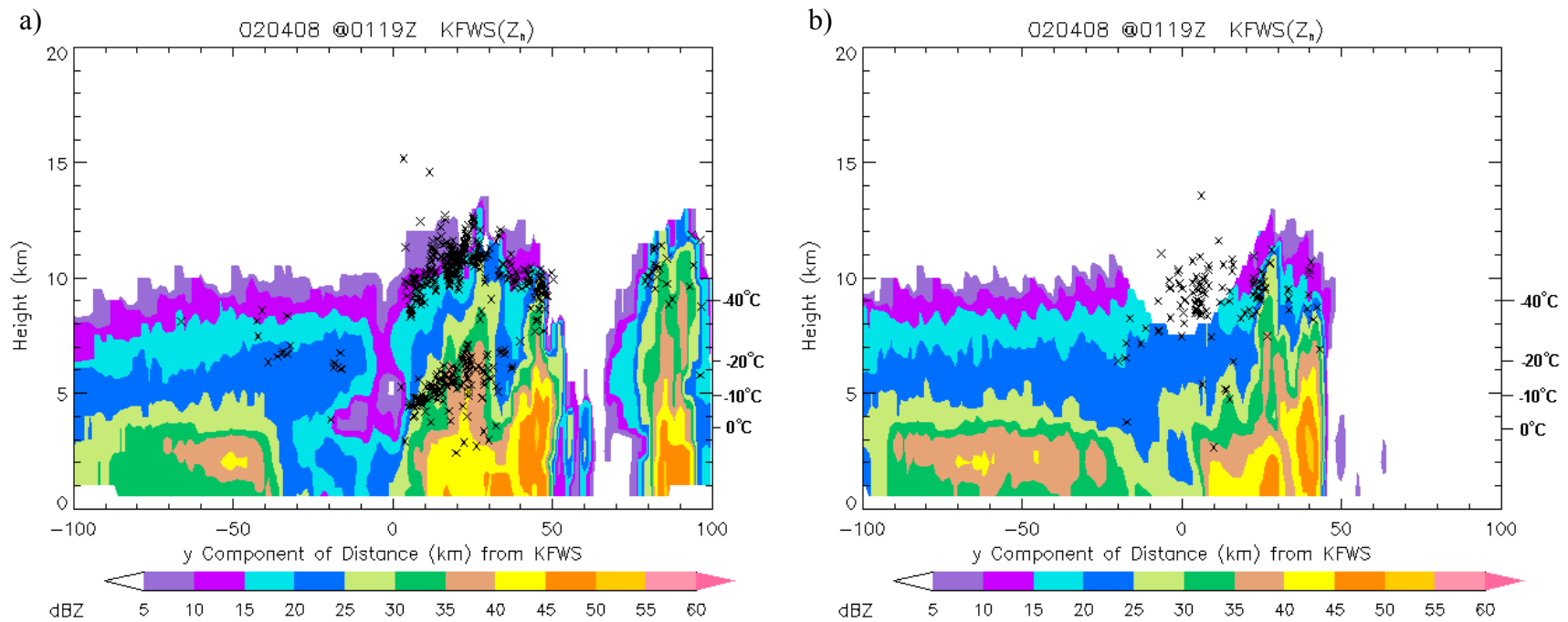


FIG. 3.35. Vertical cross-sections of the 01:19 UTC 8 April 2002 MCS in Fig. 3.32 taken line-perpendicular through a) the stratiform, transition, and convective regions at  $y = 50$  km, and b) the stratiform region, transition zone enhanced reflectivity "bridge", and convective line at  $y = -18$  km. Radar reflectivity (dBZ) is color-shaded according to the scale, and LDAR II sources (at  $x \pm 0.5$  km) are overlaid in black "x"s. The y-axis represents height above ground level (km) and the x-axis represents the y component of distance from the KFWS radar. Significant temperature levels (0 °C, -10 °C, -20 °C, and -40 °C) are listed along the y-axis on the right-hand side of the image.

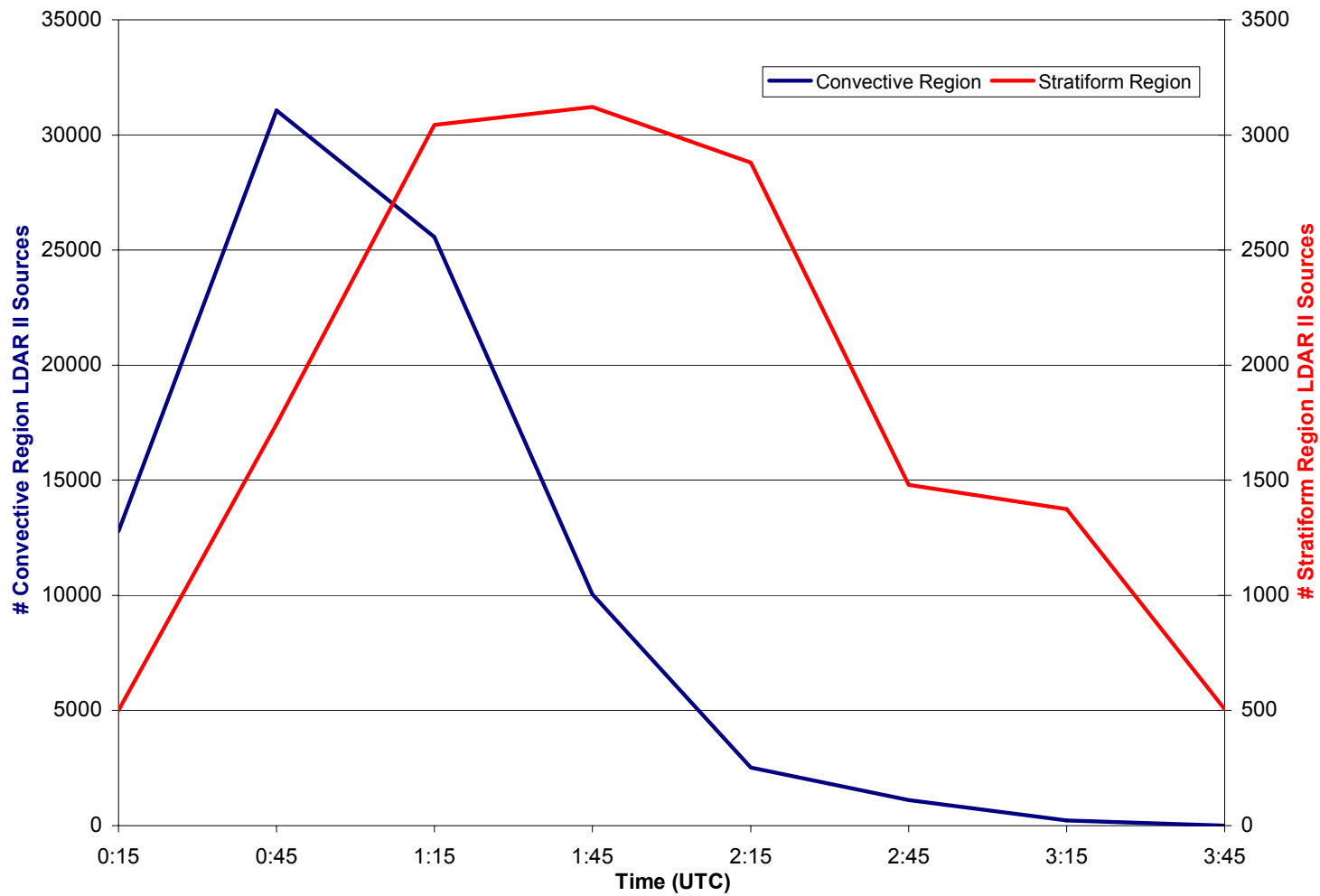


FIG. 3.36. Convective region (blue line) and stratiform region (red line) LDAR II source trends from 00 to 04 UTC 8 April 2002, time averaged every 5 min with a 6-point running mean smoother. Time is listed along the x-axis Note that the number of convective sources corresponds to the primary y-axis, and the number of stratiform sources corresponds to the secondary y-axis.

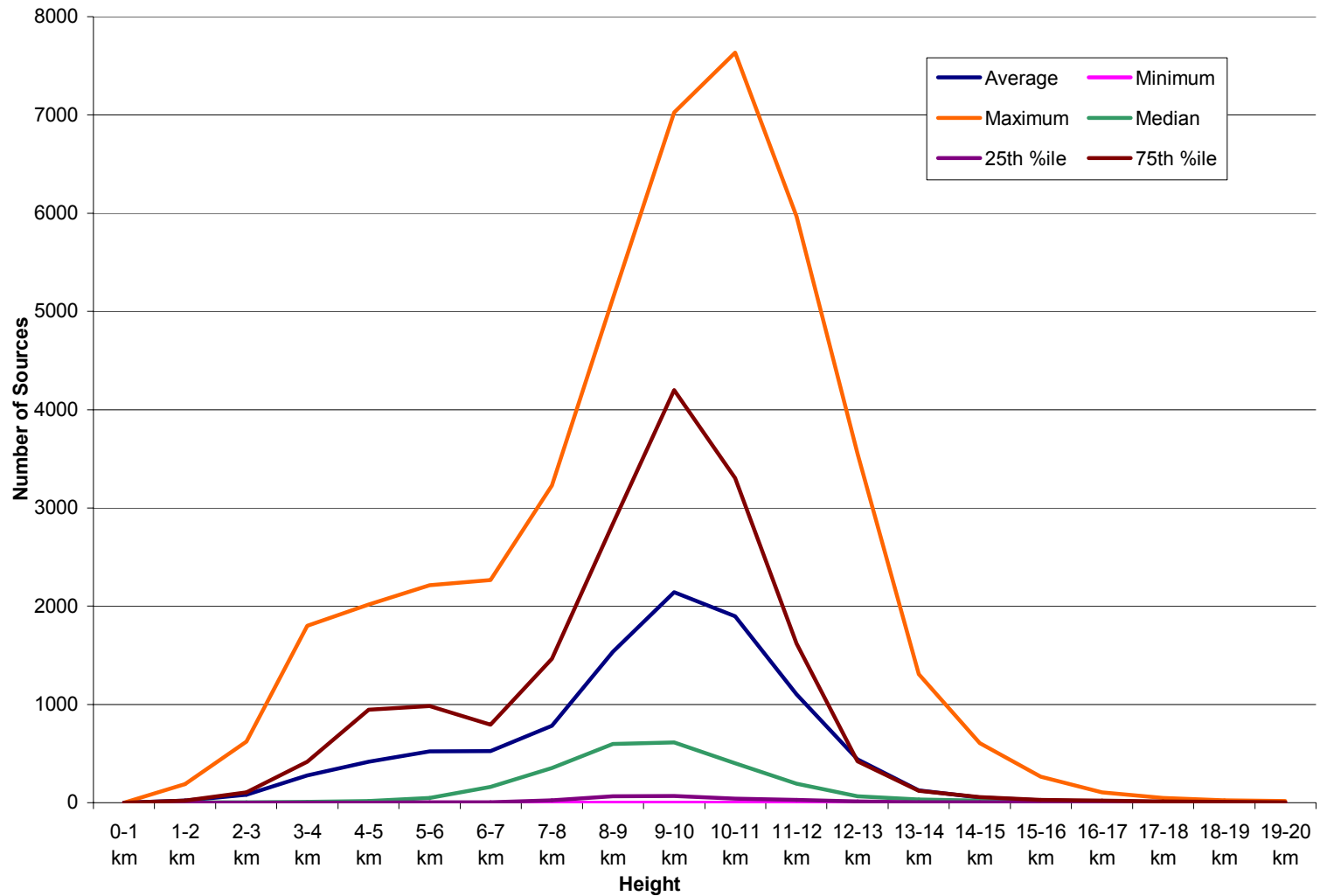


FIG. 3.37. Average (blue line), minimum (pink line), maximum (orange line), median (green line), 25<sup>th</sup> percentile (violet line), and 75<sup>th</sup> percentile (brown line) number of sources within the convective region for each 1-km height level from 0 km to 20 km from 00 to 04 UTC 8 April 2002. Height levels are indicated along the x-axis, and the number of sources per height level is shown along the y-axis.

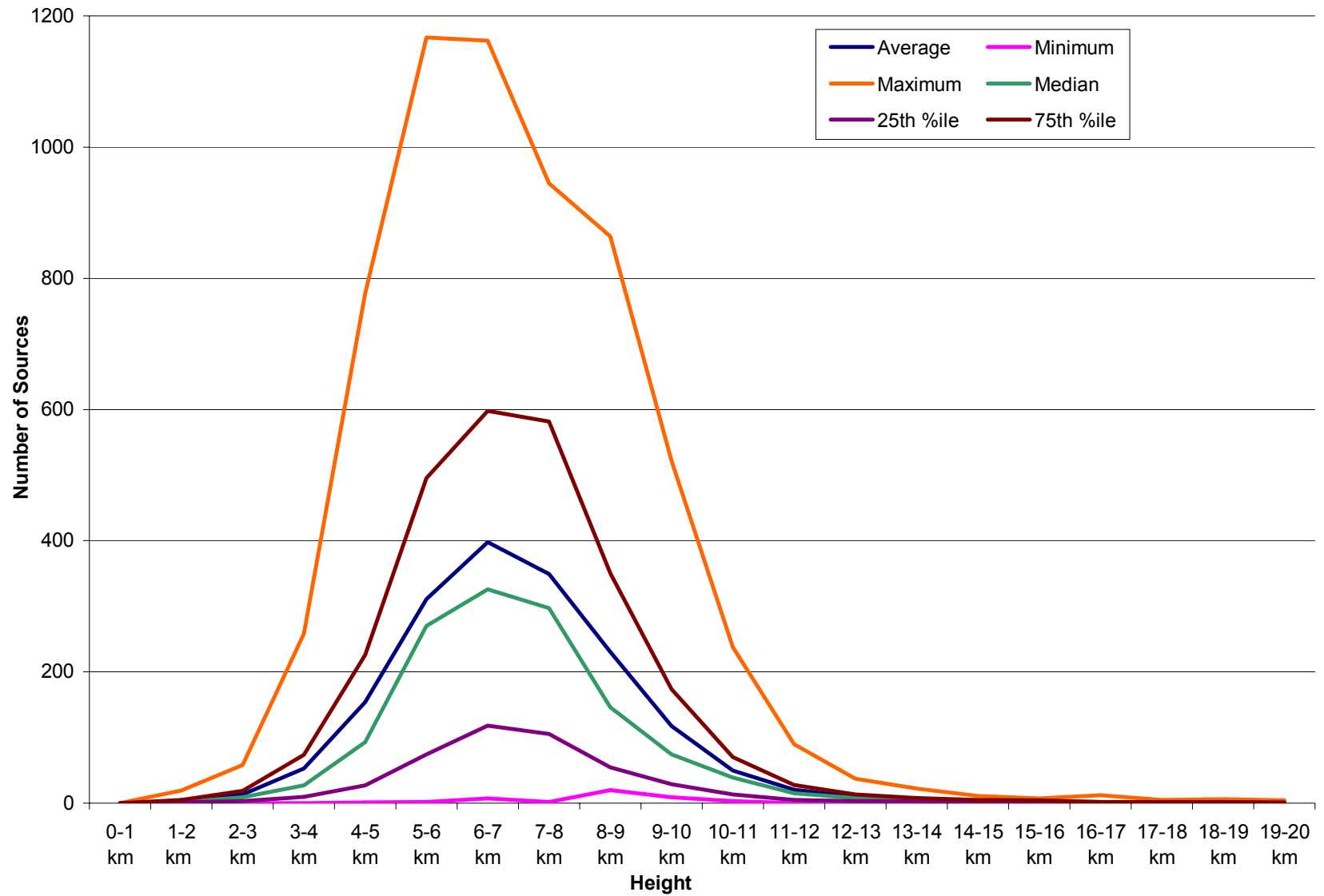


FIG. 3.38. Same as Fig. 3.37, but for the stratiform region.

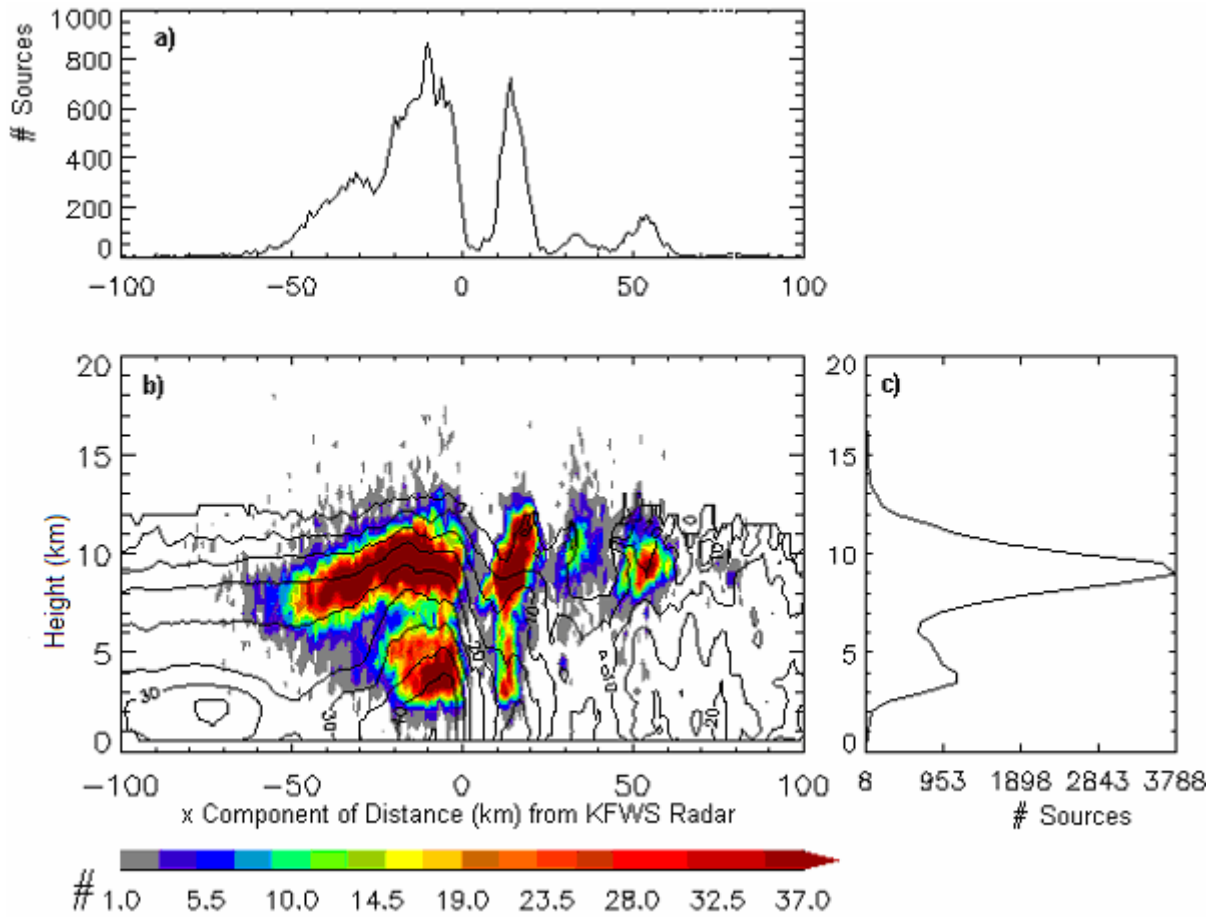


FIG. 3.39. Line-normal composite radar reflectivity and LDAR II source images at 00:39 UTC 8 April 2002, where a) the number of sources versus line-normal horizontal distance is plotted, b) a vertical cross-section (height versus the x component of distance (km) from the KFWS radar) of average radar reflectivity (dBZ) is line-contoured (0-dBZ, every 5-dBZ), and the total number of LDAR II sources is color-shaded as indicated by the scale, and c) the number of sources versus height (km) is plotted. The MCS was rotated 20° counterclockwise before the image was produced.

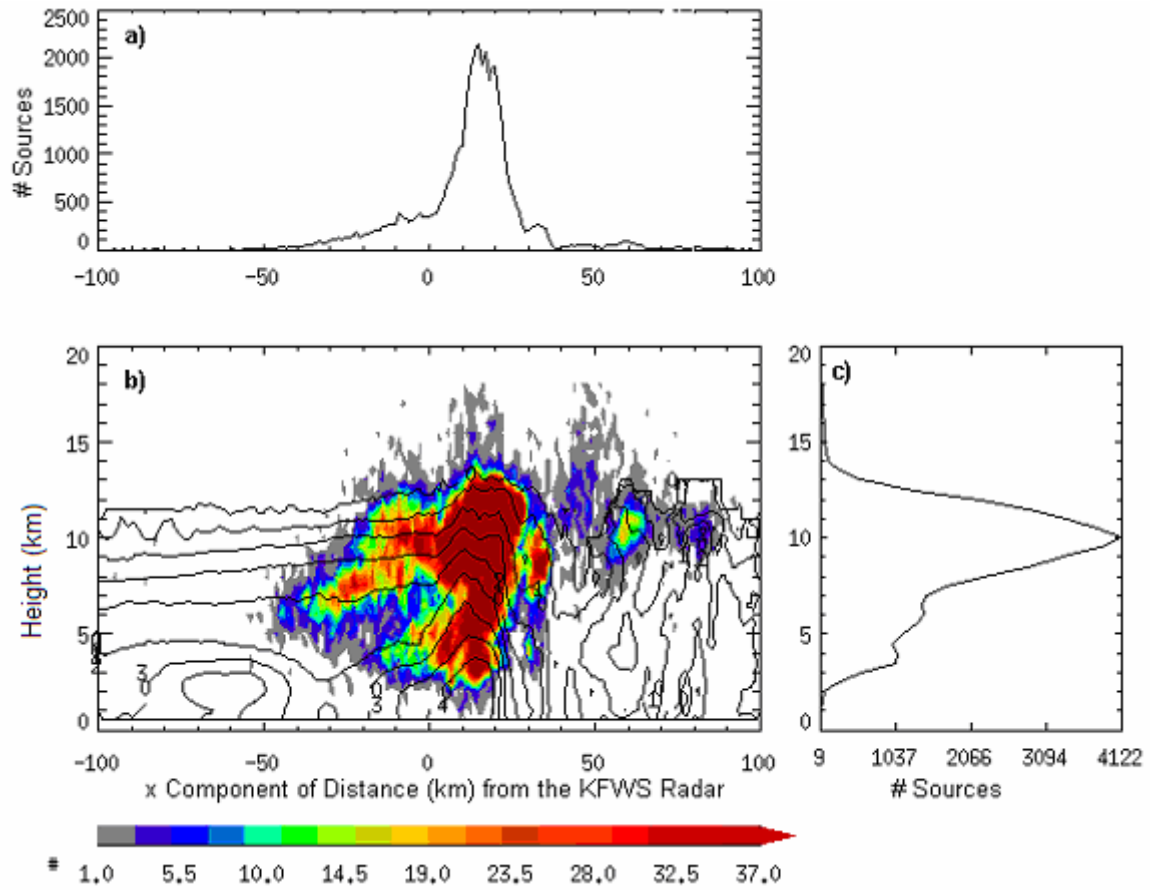


FIG. 3.40. Same as Fig. 3.39, except at 00:59 UTC 8.

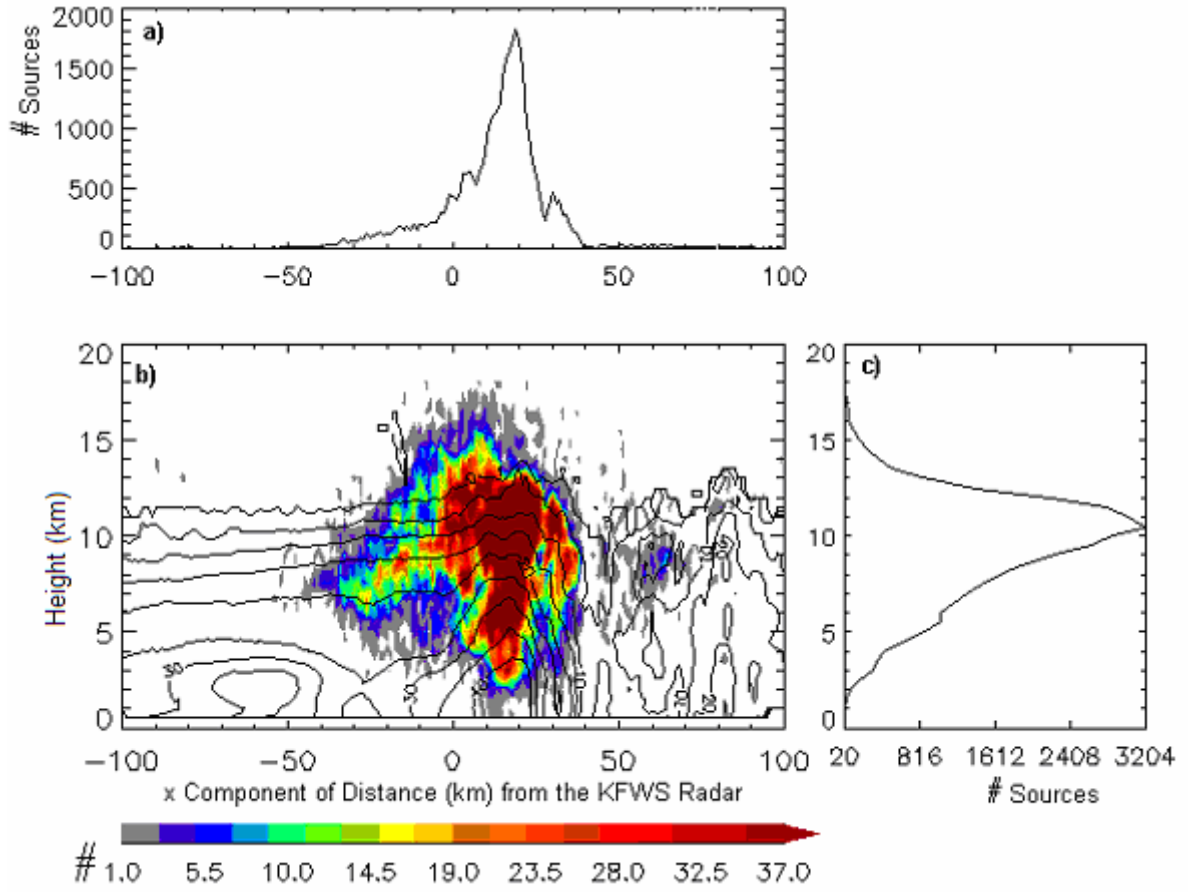


FIG. 3.41. Same as Fig. 3.39, except at 01:04 UTC 8.

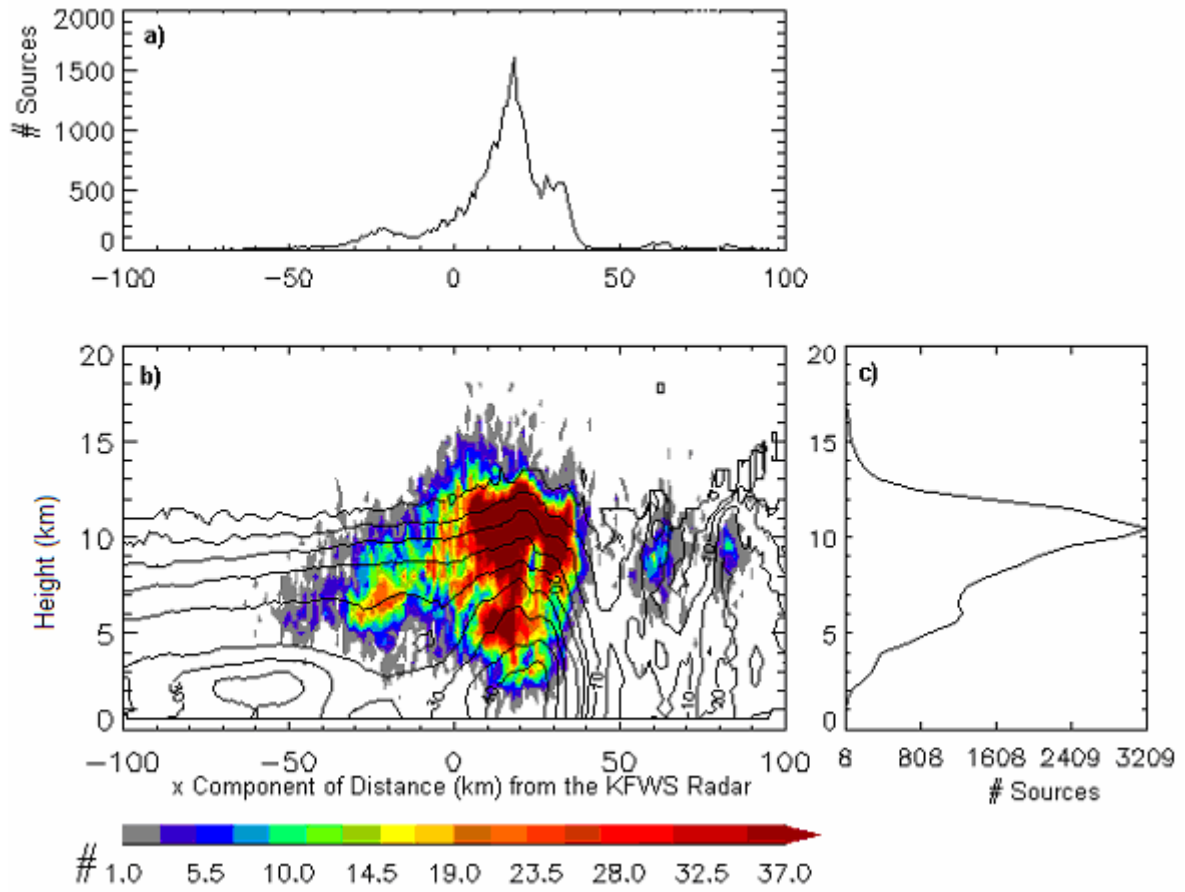


FIG. 3.42. Same as Fig. 3.39, except at 01:09 UTC 8.

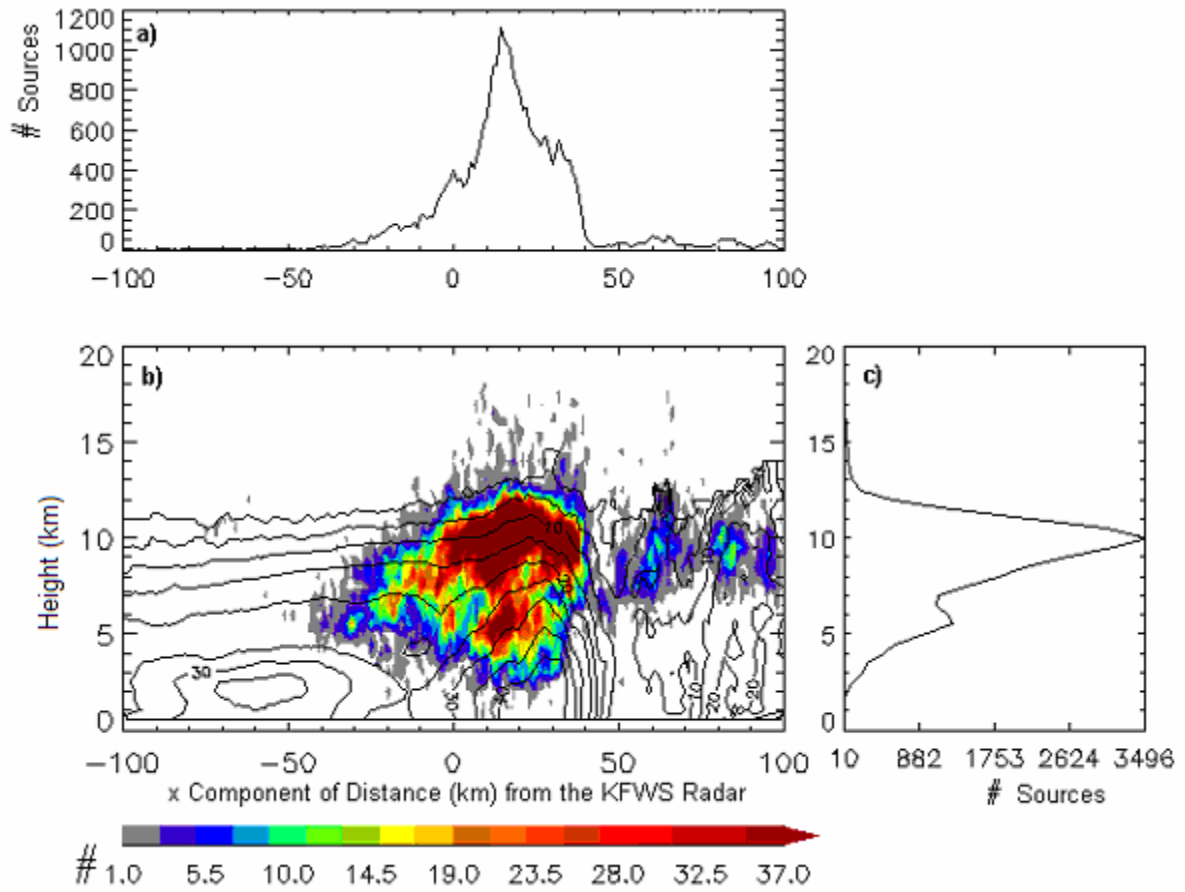


FIG. 3.43. Same as Fig. 3.39, except at 01:14 UTC 8.

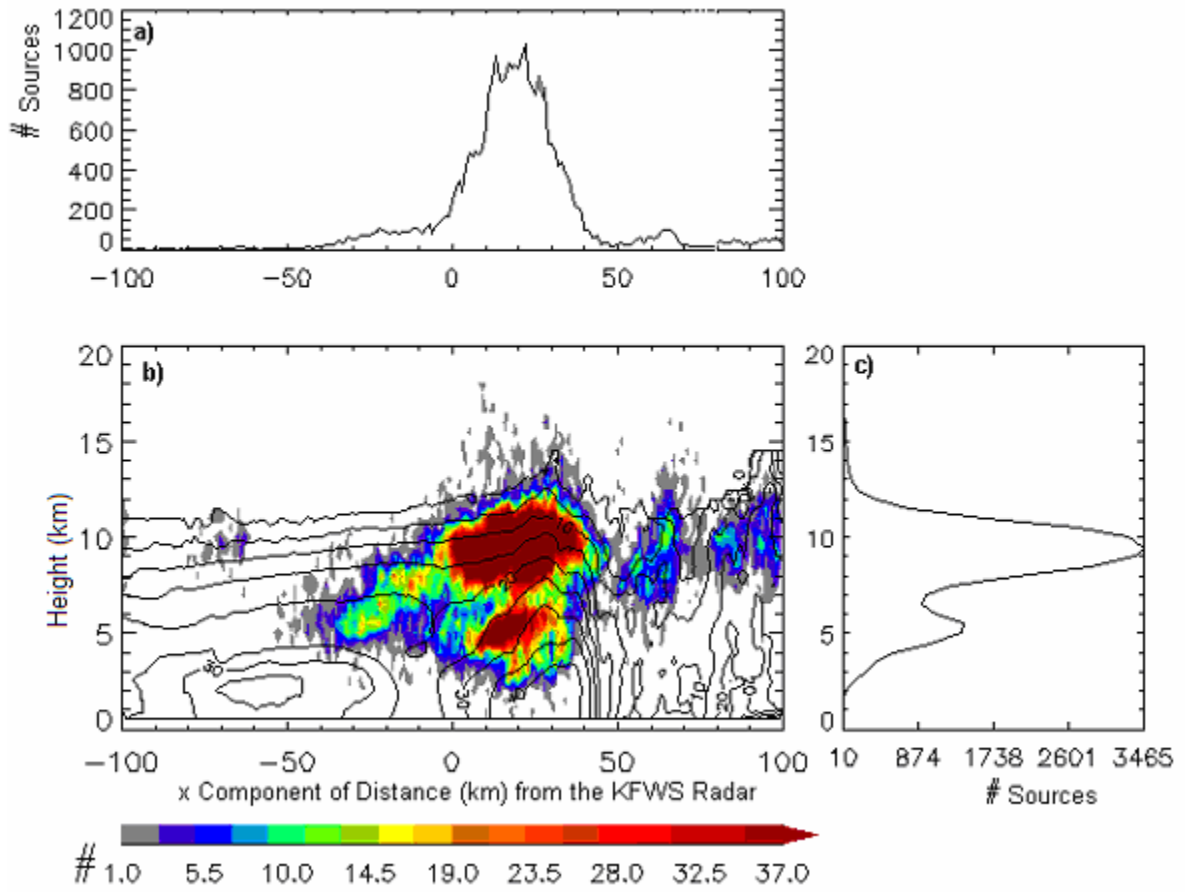


FIG. 3.44. Same as Fig. 3.39, except at 01:19 UTC 8.

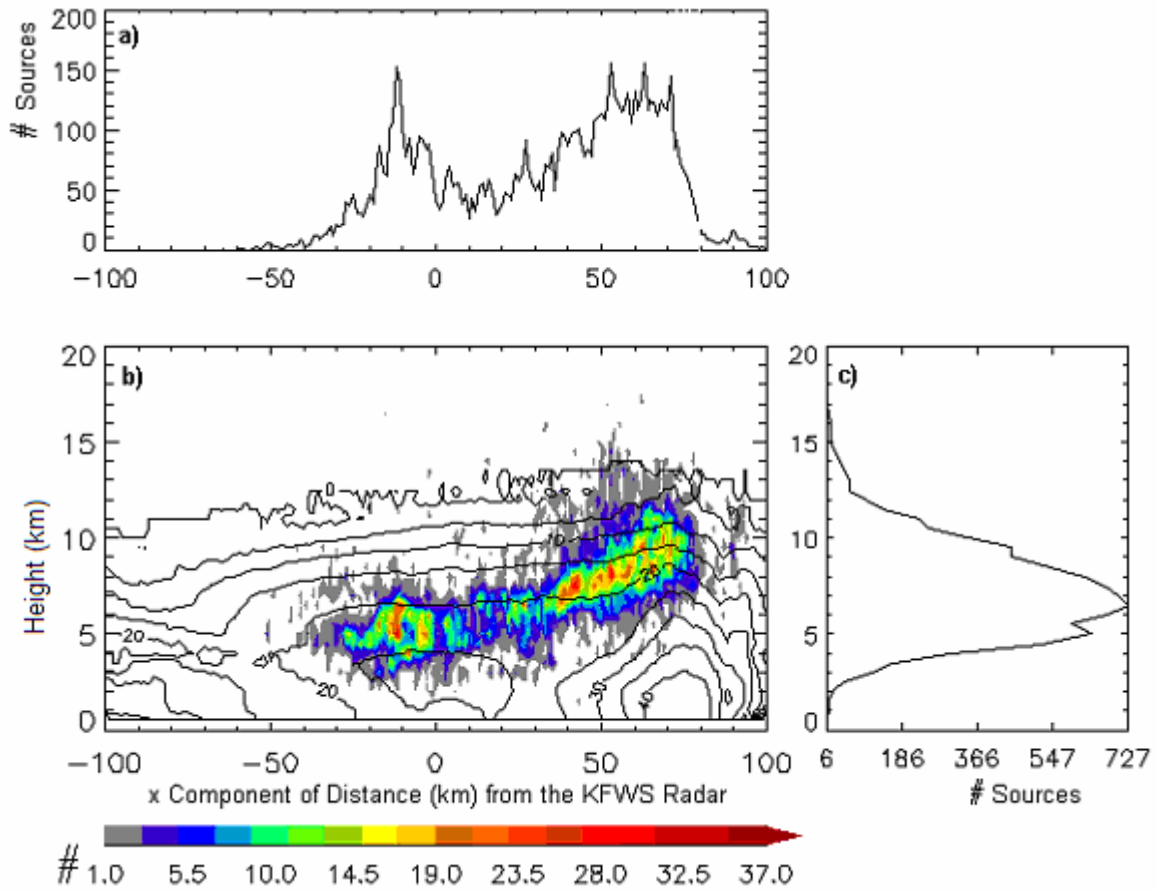


FIG. 3.45. Same as Fig. 3.39, except at 02:03 UTC 8.

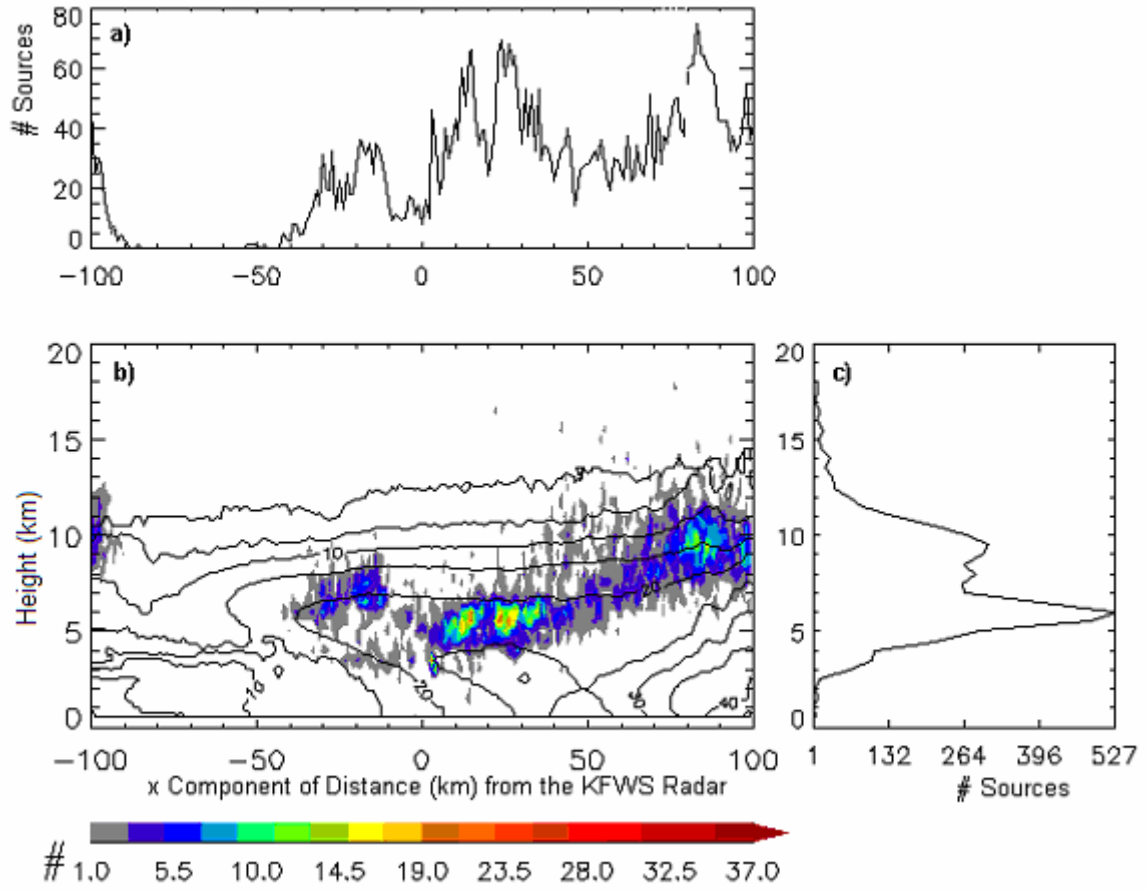


FIG. 3.46. Same as Fig. 3.39, except at 02:23 UTC 8.

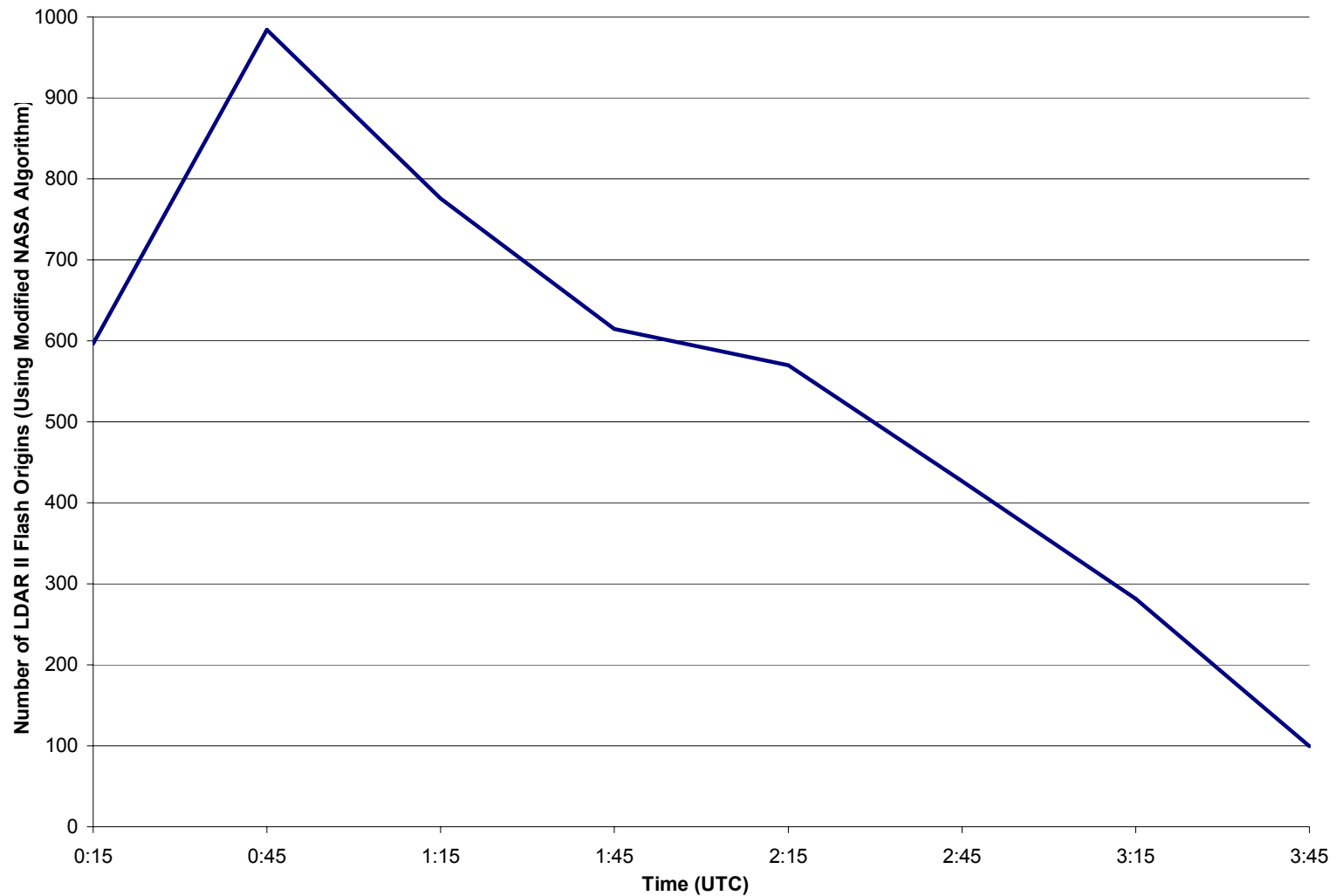


FIG. 3.47. LDAR II flash origin trend within the KFWS radar viewing range from 00 to 04 UTC 8 April 2002, time averaged every 5 min with a 6-point running mean smoother. Time is listed along the x-axis, and the number of LDAR II flash origins are listed along the y-axis. Flash origins were determined using the modified NASA algorithm.

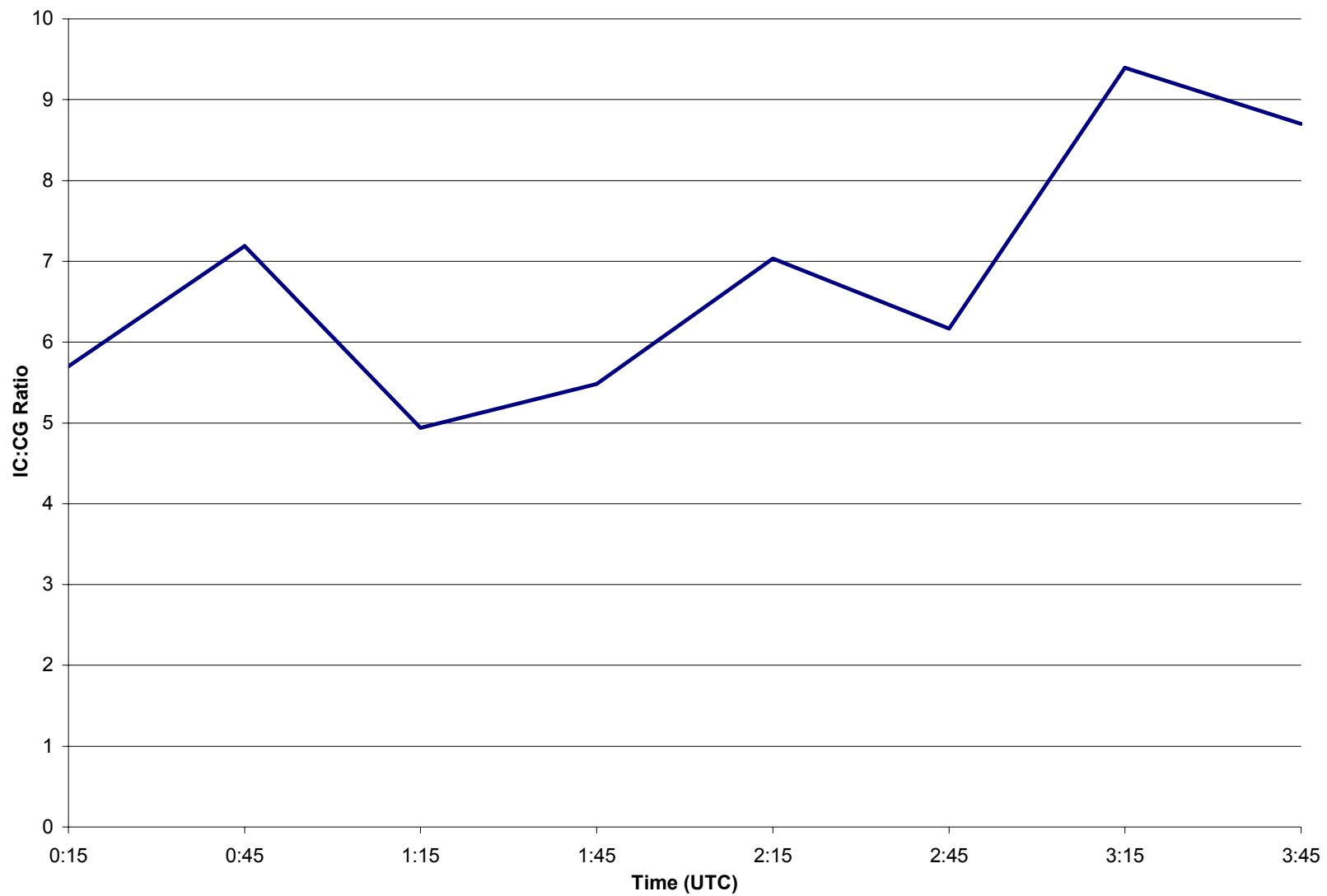


FIG. 3.48. Temporal trend in the IC:CG ratio from 00 to 04 UTC 8 April 2002, time averaged every 5 min with a 6-point running mean smoother. Time is listed along the x-axis, and the IC:CG ratio is listed along the y-axis.

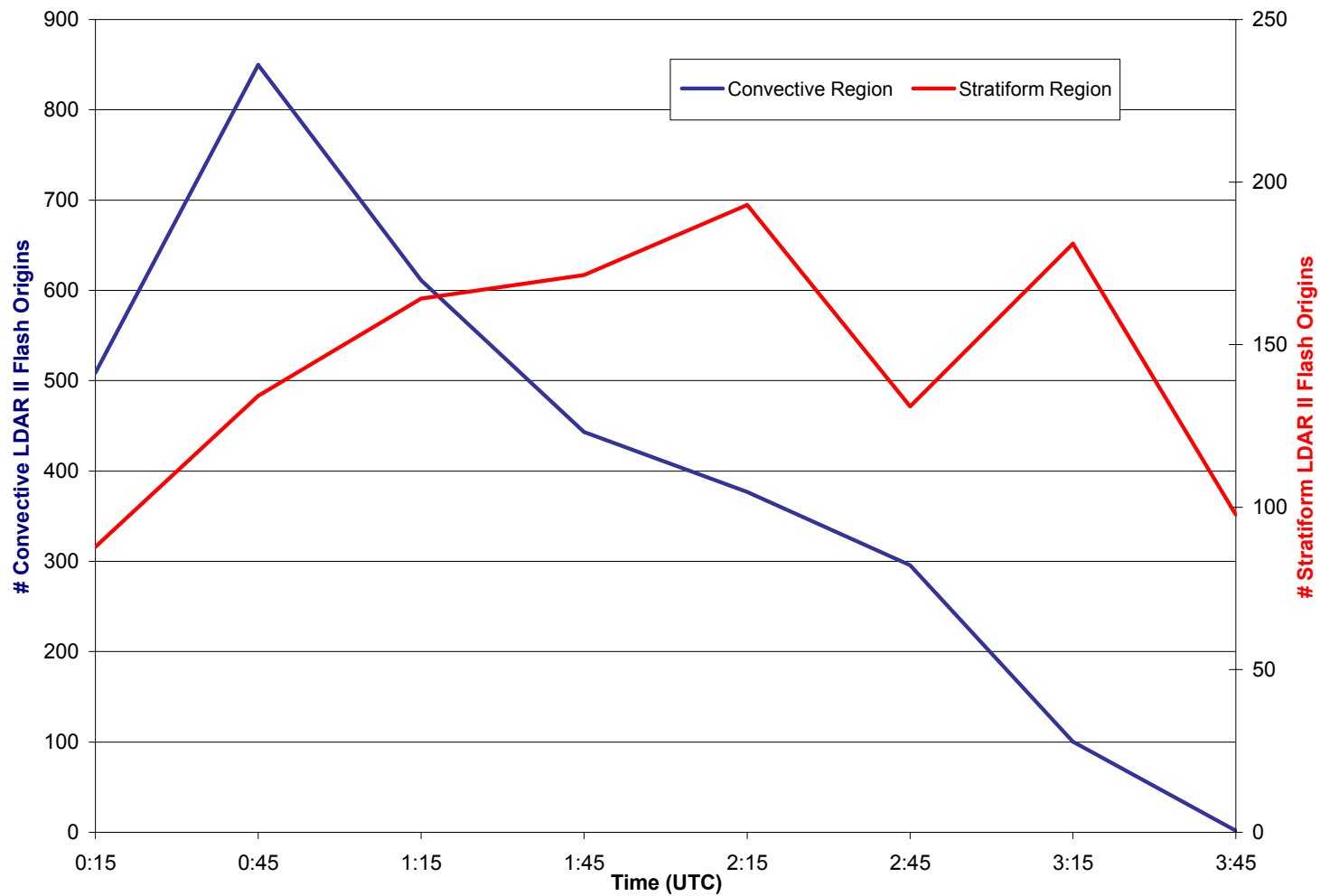


FIG. 3.49. Convective region (blue line) and stratiform region (red line) LDAR II flash origin (as determined by the modified NASA algorithm) trends from 00 to 04 UTC 8 April 2002, time averaged every 5 min with a 6-point running mean smoother. Time is listed along the x-axis. The convective and stratiform region LDAR II flash origins are listed along the primary and secondary y-axes, respectively.

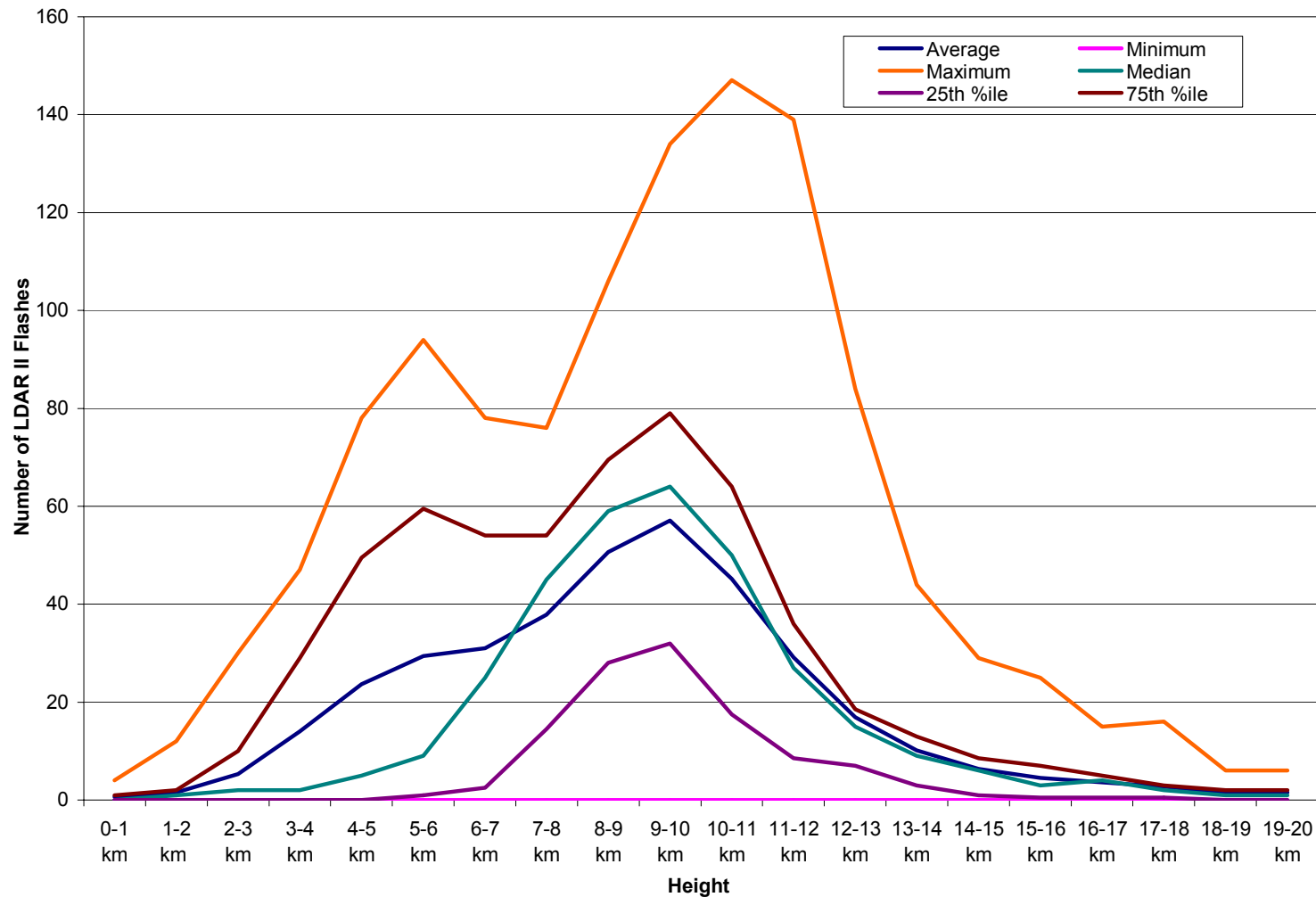


FIG. 3.50. Average (blue line), minimum (pink line), maximum (orange line), median (green line), 25<sup>th</sup> percentile (violet line), and 75<sup>th</sup> percentile (brown line) number of LDAR II flash origins within the convective region for each 1-km height level from 0 km to 20 km from 00 to 04 UTC 8 April 2002. Height levels (km) are listed along the x-axis, and the number of LDAR II flash origins is listed along the y-axis.

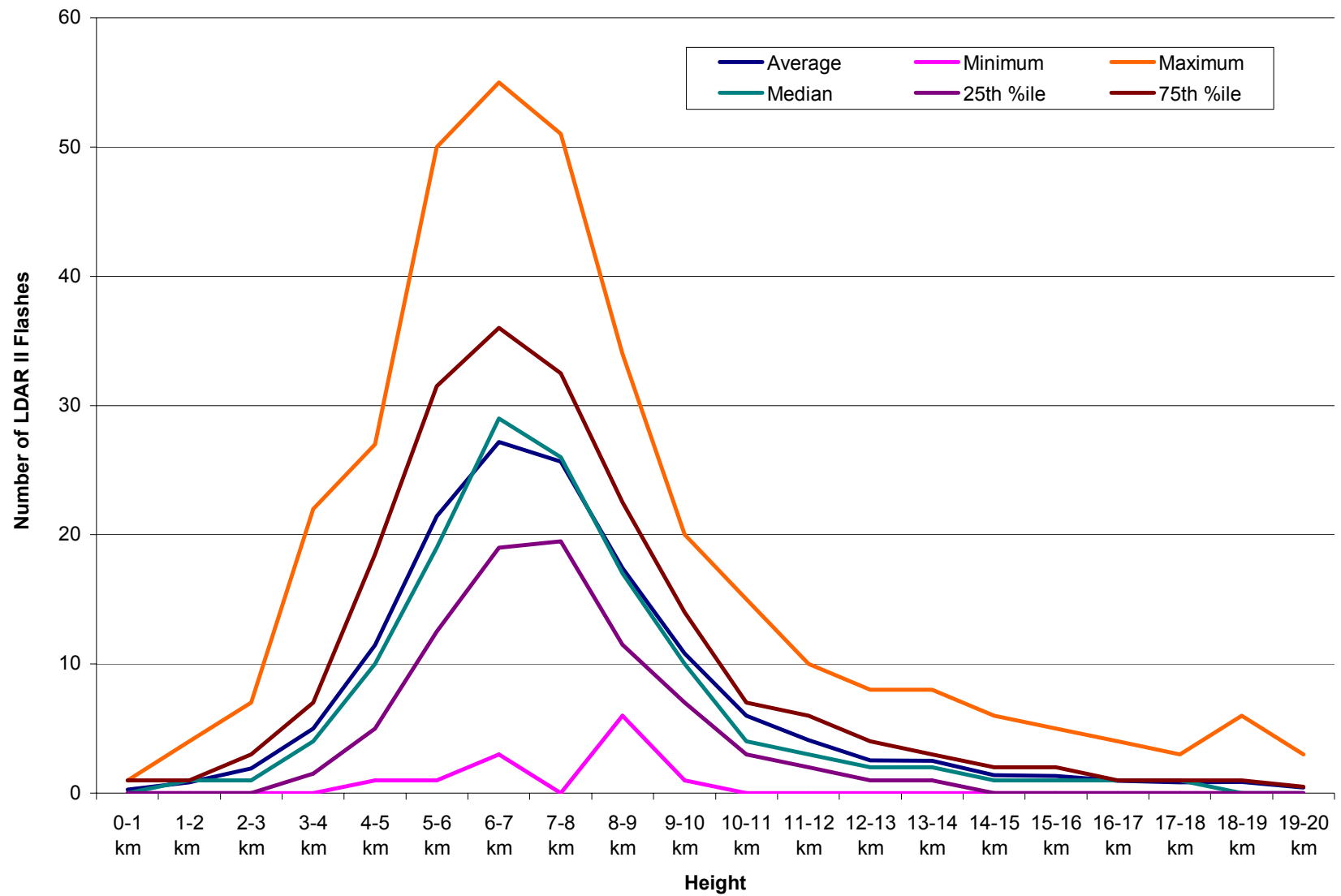


FIG. 3.51. Same as Fig. 3.50, but for the stratiform region.

## **4. CASE STUDY OBSERVATIONS #2: 12-13 OCTOBER 2001 MCS**

### **4.1 Background Characteristics**

#### ***4.1.1 Synoptic Overview***

The 12-13 October 2001 MCS formed from the growth of merging convective cells that initiated ahead of a synoptic cold front in north-central Texas at approximately 21 UTC 12 October. The MCS was in its growing stage as its leading convective line passed over the KFWS radar, and it did not reach maturity (i.e. did not form a stratiform region) until it was almost out of the KFWS radar's viewing range. Therefore, the KFWS radar captured the initial growth of the stratiform region as the developing MCS passed over the area. After it matured, the MCS continued to propagate across eastern Texas and finally into Arkansas where it eventually became a squall line at ~16 UTC 13 October. Radar, surface, and upper air data are examined.

The mandatory level (250-, 500-, 700-, and 850-mb) isobaric analyses of the U.S. at 12 UTC 12 October and 00 UTC 13 October are shown in Figs. 4.1-4.8. The 12 UTC 12 250-mb analysis (Fig. 4.1) indicates that the DFW region is located within the jet stream, just north of a jet streak and just east of an upper-level trough. Resulting 250-mb wind flow at this time over DFW is west-southwesterly at ~50 kts. 12 hrs later, at 00 UTC 13 October (Fig. 4.2), the DFW region is within the weak left exit region of a subtropical jet streak and still just to the east of an upper-level trough (located in western Texas). The DFW region is also in a region of strong speed and directional shear at this time. Resulting 250-mb flow is strong (~60 kts) and southwesterly in this region. Comparing the two 250-mb analyses, it is evident that this trough located just to the west of the region is digging (i.e. the trough is

becoming more amplified). The presence of a strong jet streak within the entrance region of the trough (i.e. upstream of the trough axis) has caused this amplification, as pictured in Figs. 4.1 and 4.2.

The 500-mb analyses show the presence of an upper-level trough to the west of DFW at 12 UTC 12 (Fig. 4.3) and 00 UTC 13 October (Fig. 4.4). The presence of this trough results in 500-mb 30-kt southwesterly winds at 12 UTC 12 and 55 kt south-southwesterly winds at 00 UTC 13 within the DFW region. The propagation of the upper-level trough towards the region creates PVA over north-central Texas.

A 700-mb closed low exists over eastern Colorado/western Kansas at 12 UTC 12 October (Fig. 4.5). This closed low evolves into a trough that propagates into western Texas by 00 UTC 13 (Fig. 4.6). The presence of this trough results in 20 kt southwesterly winds at 12 UTC 12 and 20 kt south-southwesterly winds at 00 UTC 13 in DFW. Warm advection is present across all of Texas at 12 UTC 12. By 00 UTC 13, warm advection and moisture advection are prevalent over the DFW region.

12 UTC 12 and 00 UTC 13 October 2001 850-mb analyses are depicted in Figs. 4.7 and 4.8, respectively. The 12 UTC 12 850-mb analysis indicates the presence of a closed low over southeastern Colorado/northern Texas. By 00 UTC 13, this closed low has evolved into a large trough situated over central Texas. As a result, winds are south-southwesterly at 20 kts at 12 UTC 12 and southerly at 25 kts at 00 UTC 13. Warm advection and moisture advection are present during the analysis period across DFW. At 00 UTC 13, northwestern Texas is experiencing strong cold advection that marks the cold-frontal boundary at the 850-mb level. These conditions lead to rising motion and cloud and precipitation formation within the DFW region.

The 21 UTC 12 October 2001 surface analysis of Texas and surrounding regions (Fig. 4.9) depicts surface conditions at the time of convective initiation. In this figure, a cold front extends through central Texas just to the west of the approximate place where convective initiation occurs, as indicated on radar (Fig. 4.10(a)). Thus, it can be inferred that this cold front acts as the lifting mechanism for convection (although other lifting mechanisms are evident, including a trough, thermal advection patterns, a jet, etc.).

At 00 UTC 13 October, the DFW CAPE was  $\sim 2541 \text{ J kg}^{-1}$ , and the  $R_i$  was  $\sim 33$  (Fig. 4.11(b)). Advecting winds were  $\sim 30$  kts from  $210^\circ$  (Fig. 4.11(a)), and the total system motion was  $\sim 20$  kts from  $310^\circ$ . Thus, the storm system was propagating (i.e. total system motion minus advecting winds) at  $\sim 40$  kts from  $0^\circ$ . Storm relative winds at 9 km ( $-35^\circ\text{C}$ ) (i.e. 9 km sounding winds (Fig. 4.11(a)) minus total system motion) were  $\sim 70$  kts from  $220^\circ$  in DFW. Thus, it appears that this case study should evolve into a PS MCS, but closer inspection of its evolution (Fig. 4.10(c) and (d)) indicates that this storm system developed into a TS MCS. Therefore, the environmental conditions to the north and east of DFW were likely different than the conditions at DFW, favoring the development of a TS MCS later in the period. The 0-6 km vertical shear vector from the 00 UTC 13 DFW sounding was  $\sim 60$  kts from  $210^\circ$  (Fig. 4.11(a)). According to Bluestein and Jain (1985), an environment with small  $R_i$  and large shear favors back-building development of convective cells into a squall line. Back-building appears to be the correct type of development according to the radar images (Figs. 4.10(a) and (b)). For details on how each of these values was calculated, please see Sec. 3.1.

00 UTC 13 October 2001 DFW sounding data were used to determine the approximate height levels that correspond to the significant temperature levels in this case study. From the sounding (Fig. 4.11(b)), the  $0^\circ\text{C}$  isotherm is located at  $\sim 3.6$  km, the  $-10^\circ\text{C}$

isotherm corresponds to ~5.3 km, the -20 °C isotherm corresponds to ~6.6 km, and the -40 °C isotherm is located at ~9.6 km. The wet bulb zero height, representing the actual height that liquid (frozen) hydrometeors would freeze (melt), was ~3.4 km at 00 UTC 13 October (Fig. 4.11(a)). This wet bulb zero height was ~0.2 km higher than the 0 °C isotherm. By 12 UTC 13 October 2002 (Fig. 4.11(b)), at which time the MCS had already propagated through the region, the 0 °C and wet bulb zero heights were ~3.6 km and ~2.5 km, respectively. Since this study's vertical resolution is 0.5 km, and the difference between the 0 °C height and the wet bulb zero height is less than 0.5 km at the time the convective line propagated through DFW, using these heights interchangeably in the convective line should not cause significant calculation errors in this research. Since 1) the wet bulb zero height at 12 UTC 13 is better representative of the stratiform region freezing level than the 00 UTC 13 wet bulb zero height, 2) the difference between the 00 UTC and 12 UTC wet bulb zero heights is ~1.1 km, and 3) this study's vertical resolution is 0.5 km, it is important to use the 12 UTC wet bulb zero height as the correct stratiform region freezing level in this study.

#### ***4.1.2 Storm Damage Reports***

Figure 4.12 shows the locations and types of severe weather reports that occurred within the U.S. from 12 UTC 12 through 12 UTC 13 October 2001. Most tornadoes produced by this MCS occurred along the southern extent of the storm system, except for one tornado, which formed just northwest of Dallas in Decatur, TX (33.23°N, 97.60°W) at ~01 UTC 13 October. This tornado will be examined further because 1) it occurred within the KFWS radar's viewing range, and 2) the convective cell associated with this tornado produced interesting lightning flash rate characteristics. In addition, the MCS produced hail early in its lifetime and damaging winds later in its lifetime, as indicated in Fig. 4.12.

## **4.2 WSR-88D Radar**

### ***4.2.1 Data Gaps***

During the October 2001 MCS, the KFWS radar was not functioning properly. Although it was scanning in severe weather mode (i.e. 14 unique azimuthal sweep angles), the radar recorded as few as six unique azimuthal sweep angles for each volume scan after 04:28 UTC 13 October. The missing elevation angles varied from one volume scan to the next, and they did not follow any particular pattern. These missing data limited echo volume aloft interpretations during the last hour of the analysis period.

### ***4.2.2 General MCS Characteristics***

Low-level (0.5 km) constant altitude radar reflectivity images depict the evolution of the 12-13 October MCS from 01:00 UTC to 05:32 UTC 13 (Fig. 4.13(a)-(d)). At 01 UTC 13 (Fig. 4.13(a)), back-building convective cells, some severe, merge to strengthen a developing squall line. One of the severe convective cells (upper left hand corner of the image) produces a tornado at this time, as indicated by the radar reflectivity hook echo and later confirmed by the local National Weather Service Forecast Office. By 02:29 UTC, a squall line has fully developed within the radar's viewing range (Fig. 4.13(b)). At 04:32 UTC, initial stratiform region development can be seen while the convective line has propagated almost completely beyond the viewing area (Fig. 4.13(c)). By 05:32 UTC, the stratiform region has expanded so that it now occupies much of the KFWS viewing range (Fig. 4.13(d)). A small portion of the back edge of the convective line can barely be seen (lower right-hand corner of the image) just before it exits the region entirely (Fig. 4.13(d)).

Figure 4.14(a) depicts a rotated horizontal image of Fig. 4.13(b), and Fig. 4.14(b) represents a vertical cross-section taken through the leading convective line of Fig. 4.14(a) at  $x = 50$ . The convective cells are characterized by high reflectivity echoes ( $\sim 40$ - $55$  dBZ) and hence, heavy surface precipitation. The cells appear to tilt north-northeastward with height (in accordance with the 9 km storm relative flow) by as much as  $\sim 55^\circ$  from the horizontal (note the scaling difference between the x- and y-axes). Mid-level enhanced reflectivity echoes within the convective cores (as large as 55-60 dBZ) indicate the presence of hail, graupel, and, hence, strong updrafts aloft. At 02:29 UTC, the periphery of these convective cells (defined as areas with radar reflectivity echoes  $\geq 5$  dBZ) extend to almost 15 km altitude, and have cloud bases (according to the DFW 00 UTC 13 sounding) at  $\sim 0.68$  km ( $\sim 20^\circ\text{C}$ ).

Reflectivity and lightning data were not partitioned according to their association with the convective and stratiform regions for this case study because 1) the convective cells did not form a squall line typical of an MCS until late in the period, 2) the convective squall line was not linear, 3) the stratiform region did not form until the convective line had propagated almost completely out of the viewing range (making it difficult to compare the two regions during the same time period of MCS evolution), and 4) there are problems with the radar data by the time the stratiform region develops. Thus, radar and lightning data for this case study are analyzed in terms of total MCS trends. Rainfall rates were not calculated since different Z-R relationships exist for different types of precipitation (i.e. convective versus stratiform). Also, since the convective and stratiform regions did not coexist long enough within this study's area of interest, no synthetic dual-Doppler analyses were attempted for this case study.

### ***4.2.3 Total Echo Volume Aloft***

Total echo volume aloft was calculated for this case study from 00:45 UTC to 05:32 UTC using various minimum reflectivity echo constraints (i.e. 30-, 35-, 40-, 45-, 50-, and 55-dBZ). These echo volumes were calculated between the 0 °C and -40 °C temperature levels. Temporal trends in total echo volume aloft for the six various reflectivity echo constraints in this case study show similar characteristics. Figure 4.15 provides an example of total echo volume aloft trends using the 30-, 35-, and 40-dBZ thresholds. Correlation coefficients between the 30- and 35-dBZ, the 30- and 40-dBZ, and the 35- and 40-dBZ trends are 0.99, 0.96, and 0.99, respectively. Since all correlations are high, the choice of reflectivity threshold is somewhat arbitrary. This study will use the 35-dBZ threshold to compare echo volume aloft trends to other MCS characteristics (i.e. lightning rates).

At the beginning of the time period (00:45 UTC), convective cells are intense and some are even severe, resulting in a relatively large echo volume aloft ( $\sim 14\,327.5\text{ km}^3$ ) (Fig. 4.15). As these cells weaken ( $\sim 01:45\text{ UTC}$ ), echo volume decreases (to  $\sim 11\,801.0\text{ km}^3$ ) and the convective cells begin to merge with one another. It is evident that a peak in echo volume aloft ( $\sim 18\,651.2\text{ km}^3$ ) occurs around 02:45 UTC, at the time a squall line forms from the merging of various convective cells. Afterwards, as the squall line begins to propagate out of the KFWS radar viewing area, total echo volume aloft begins to decrease. The stratiform region begins to form later in the time period, but since the radar information is incomplete from 04:32 UTC until the end of the period, radar echo volume aloft during this time is also incomplete.

### 4.3 NLDN CG Lightning Flash Trends

Figure 4.16 is an example of a 0.5-km constant altitude horizontal radar reflectivity image overlaid with 5 min of NLDN-detected CG lightning flashes (centered on the time of the radar image). At this time (04:47 UTC), the main convective line (lower right-hand corner of the image) is propagating out of the viewing area, but it is evident from the portion still within the image that the convective line is characterized by an abundance of CG lightning flashes, most of which (> 50%) are negative in polarity. The stratiform region dominates the image at this time and has only sporadic CG lightning, but a larger percent of +CGs occur within this region than in the convective line.

Figure 4.17 shows the temporal evolution of the total number of CG lightning flashes and the percent of +CGs in the portion of the 12-13 October 2001 MCS that occurred within the KFWS radar's range from 00:45 to 05:30 UTC. The average CG lightning flash rate was 53.8 flashes  $\text{min}^{-1}$ , and the average percent of +CG flashes was 19.7% during this time period. The peak CG lightning flash rate for the period (78.9 flashes  $\text{min}^{-1}$ ) occurred when a large number of convective cells were within the viewing area (at ~01:45 UTC), and this rate falls off rapidly as the leading convective line propagates beyond the region. As the convective line exits the region (from 04:32 to 05:30 UTC), the stratiform region forms and the percent of +CG flashes increases.

The temporal evolution of NLDN-detected peak positive and peak negative CG lightning currents from 00:45 to 05:30 UTC are depicted in Fig. 4.18. The average positive and negative peak currents throughout the time period are 17.1 kA and -20.3 kA, respectively. Peak lightning currents remain relatively steady until ~04:15 UTC, after which they increase through the rest of the period. This increase in peak current coincides with the

exit of the convective line and the development of the stratiform region within the radar viewing area. Maximum peak positive (~25.1 kA) and negative (~-22.5 kA) currents occur at the end of the period. These larger stratiform peak current values are also consistent with Petersen et al.'s (1992) observations of higher peak positive CG lightning currents in the stratiform region as compared to the convective line.

The correlation coefficient between the 35-dBZ threshold echo volume aloft trend (Fig. 4.15) and the CG lightning flash trend (Fig. 4.17) is 0.82. The peak in CG lightning occurs while echo volume aloft is rapidly increasing (~01:45 to 2:45 UTC). The peak in CG flashes also lasts longer than the peak in echo volume aloft, but both trends show the same general decrease in activity after 02:45 UTC.

## **4.4 LDAR II Data**

### ***4.4.1 Network's Performance***

The LDAR II network was performing almost optimally during the 12-13 October 2001 event (Fig. 4.19). More than 90% of flashes could be detected out to a 60-km range from the network's central sensor (M. Murphy 2003, personal communication). Total LDAR II sources and flash origins (as determined by the modified NASA algorithm) are analyzed for this study.

### ***4.4.2 VHF Source Trends***

Figure 4.20 depicts the temporal evolution of LDAR II sources that occur within the KFWS radar's viewing region from 00:45 to 05:32 UTC 13 October. The average LDAR II source rate is 13 350.5 sources  $\text{min}^{-1}$ , and at its peak (01:45 UTC), the source rate is 22 196.3 sources  $\text{min}^{-1}$ . The source trend resembles the NLDN-detected CG lightning flash trend,

with a rapid increase from the initial time period to 01:45 UTC, and then a significant decrease after 02:45 UTC. Interestingly, the lightning source rate increased and peaked approximately one hour prior to the increase and peak in echo volume aloft (Fig. 4.15).

An example of a horizontal radar reflectivity image overlaid with LDAR II sources is shown in Fig. 4.21. This image has been rotated 20° so that a vertical cross-sectional line parallel through the convective region can be obtained (Fig. 4.22). Comparing Fig. 4.21 to Fig. 4.14(a), it is evident that LDAR II sources align themselves within moderate reflectivity echoes (35-45 dBZ). More widespread stratiform-type areas (like the small area present at the top of the image behind the convective line) are characterized by a significant decrease in sources as compared to convective precipitation regions.

A vertical cross-section that runs through the leading convective line is shown in Fig. 4.22. This cross-section shows that increased LDAR II sources are located 1) above enhanced ( $> 45$  dBZ) reflectivity convective cores aloft (which is consistent with the presence of strong updrafts), 2) at mid- to high- altitudes (height  $> 5$  km,  $T < -10$  °C), and 3) within regions of moderate reflectivity echoes (35-45 dBZ). Sources that are located above contoured reflectivity echoes ( $\geq 5$  dBZ) are probably still within the convective clouds because cloud tops are generally above measured reflectivity echo tops.

Figure 4.23 identifies the dominant LDAR II source locations occurring within the radar's viewing region with respect to altitude. A high density source region exists between 9 and 12 km (just above  $-40$  °C). A smaller enhanced source maximum exists between 4 and 6 km (from  $0$  °C to  $-20$  °C). Thus, two dominant electrically-active regions exist within this storm system. These two regions correspond to temperature levels that are theoretically favorable for non-inductive charging.

#### ***4.4.3 VHF Flash Origin Trends***

The LDAR II flash origin trend (as determined by the modified NASA algorithm) for the portion of the storm system that evolved within the KFWS radar's viewing region from 00:45 to 05:32 UTC 13 October 2001 is shown in Fig. 4.24. The average flash origin rate for this time period is 1005.1 flashes  $\text{min}^{-1}$ . Similar to the NLDN flash and LDAR II source evolutions, a peak ( $\sim 1,588.6$  flashes  $\text{min}^{-1}$ ) in LDAR II flash origins exists. This peak in flash origins, however, occurs approximately 1 hr later (at 02:45 UTC) than the peak in NLDN flash rate and the peak in LDAR II source rate. The LDAR II flash origin trend follows the echo volume aloft ( $\geq 35$  dBZ) trend more closely than it follows either the NLDN flash rate trend or the LDAR II source rate trend.

Figure 4.25 depicts the dominant LDAR II flash origin altitudes in the portion of the 12-13 October 2001 MCS that passed over the KFWS radar's viewing region from 00:45 to 05:32 UTC 13. Similar to the dominant LDAR II source heights, a small local maximum in flash origins occurs between 5 and 6 km ( $-10$  °C to  $-20$  °C). A second peak in flash origins occurs between 11 and 13 km (just above  $< -50$  °C). Although this second layer is slightly higher than the corresponding peak LDAR II source layer (Fig. 4.23), both the 5-6 km and the 11-13 km electrically-active layers could be associated with the two dominant charge regions theorized in the non-inductive charging mechanism.

The IC:CG ratio trend from 00:45 to 05:32 UTC is depicted in Fig. 4.26. The IC:CG ratio is smallest (12.7) at the beginning of the period when the convective cells are most intense. The ratio slowly increases until the convective cells begin to form a squall line (02:15 UTC), after which the increase becomes more dramatic. At 03:15 UTC, the IC:CG ratio reaches its maximum of 26.9. This IC:CG ratio maximum corresponds to the initial

development of the stratiform region. A rapid decrease in the IC:CG ratio is then observed between 03:45 and 04:15 UTC (from 26.1 to 18.2).

#### **4.5 Summary**

Analysis of the 12-13 October 2001 MCS case study is limited because the convective and stratiform regions only coexisted within the KFWS radar's viewing range for a half hour. During the short time period when they did coexist (04:45-05:15 UTC), there were problems with the KFWS radar data. As a result, only total trends in echo volume aloft, NLDN CG flash rates, and LDAR II source and flash origin rates were examined for this case. Interestingly, both the CG lightning flash and LDAR II source rates peak while the echo volume aloft is rapidly increasing. In this storm system, a strong correlation exists between total CG flash rates and LDAR II sources. A strong correlation also exists between LDAR II flash origins and echo volume aloft  $\geq 35$  dBZ. Since large echo volume aloft indicates the presence of large hydrometeors aloft suspended by strong updrafts (a necessary ingredient for non-inductive charging), it is not surprising that high lightning rates correlate to large echo volume aloft when the convective line is within the analysis area.

Total lightning source and flash rate trends presented in the 12-13 October 2001 MCS case represent convective trends because the convective region is the dominant lightning-producing region, and it is the only region present throughout most of the analysis period. Thus, the two dominant electrically-active charge regions detected by the LDAR II network between 9 and 12 km (just above  $-40$  °C) and between 4 and 6 km ( $\sim 0$  °C to  $-20$  °C) could be the upper positive charge region and main negative charge region theorized to be important in the NIC mechanism. Since negative polarity breakdown in the positive charge region is

noisier than positive polarity breakdown in the negative charge region (in the VHF range), the larger concentration of sources within the 9-12 km layer than within the 4-6 km layer provides further evidence that the upper charge region is positive and the lower charge region is negative in polarity. Thus, a normal dipole of abundant charge is established in the convective region, resulting in a large percentage of –CG lightning flashes and high lightning flash rates, as observed within this MCS.

During the last hour of analysis, the convective line has propagated beyond the analysis region, and the stratiform region now dominates the area. A larger percentage of +CG flashes exists during this time, but since all of the radar data were not recorded (i.e. some data was missing), no comparisons between echo volume aloft and lightning activity within the stratiform region could be performed.

During the beginning of this study's analysis period, a tornado occurred just northwest of Dallas in Decatur, TX. Both CG and LDAR II flash rates associated with this tornadic convective cell peaked ~20-25 min before tornado occurrence. These lightning flash rate characteristics, and previous research relating to this topic, are discussed in Appendix E. Although Appendix E is not related to the key objectives of this research, the occurrence of a tornado within range of the KFWS radar and LDAR II network provides a unique opportunity to explore total lightning characteristics within a tornadic cell and to document the results for future studies. These lightning data were also combined with the other lightning data that occurred within this study's analysis domain to calculate the lightning statistics presented in this chapter.

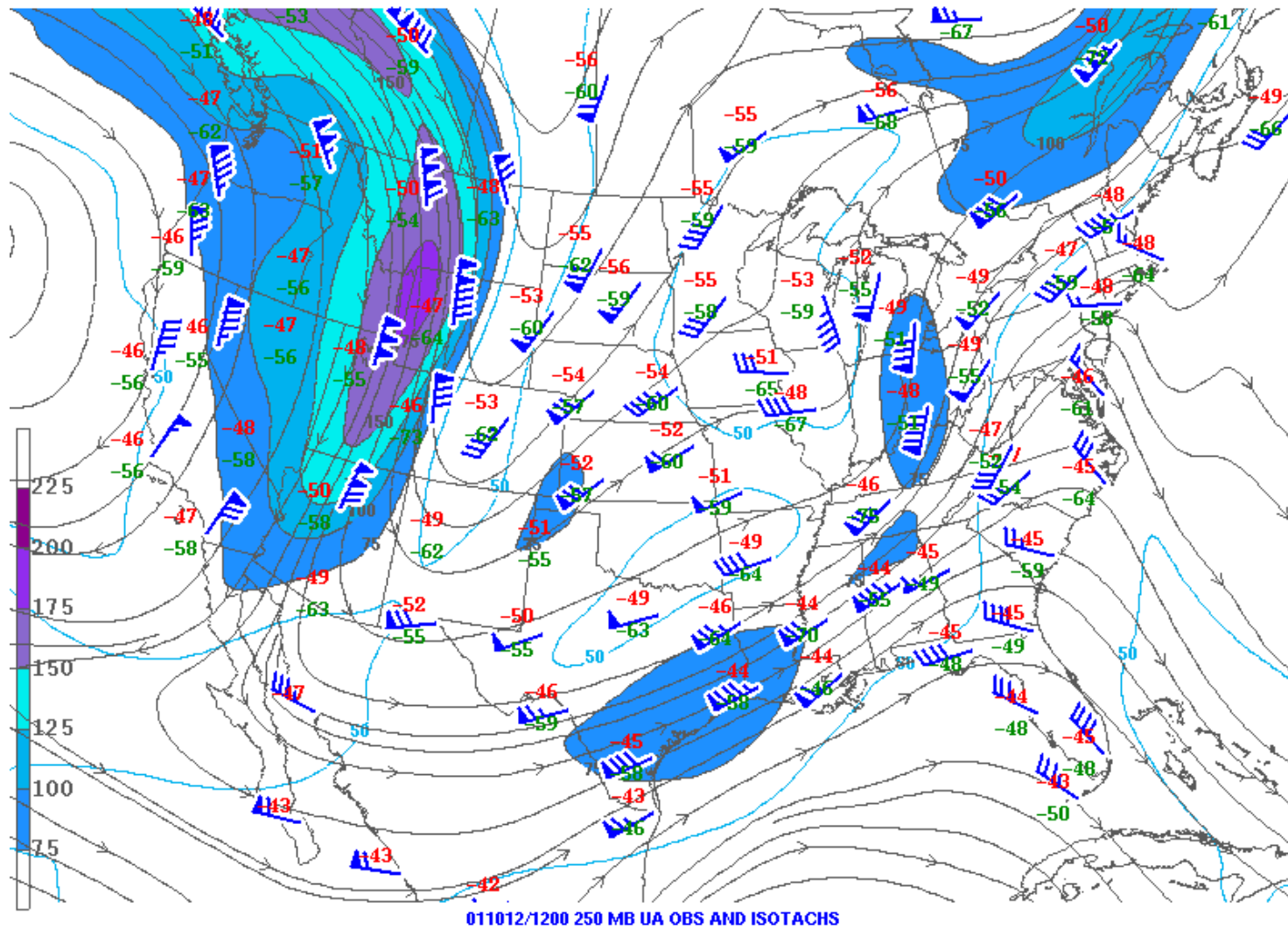


FIG. 4.1. 250-mb analysis for 12 UTC 12 October 2001. Wind speeds  $\geq 75$  kts are shaded according to the contour bar on the left (image courtesy of [www.spc.noaa.gov](http://www.spc.noaa.gov)).

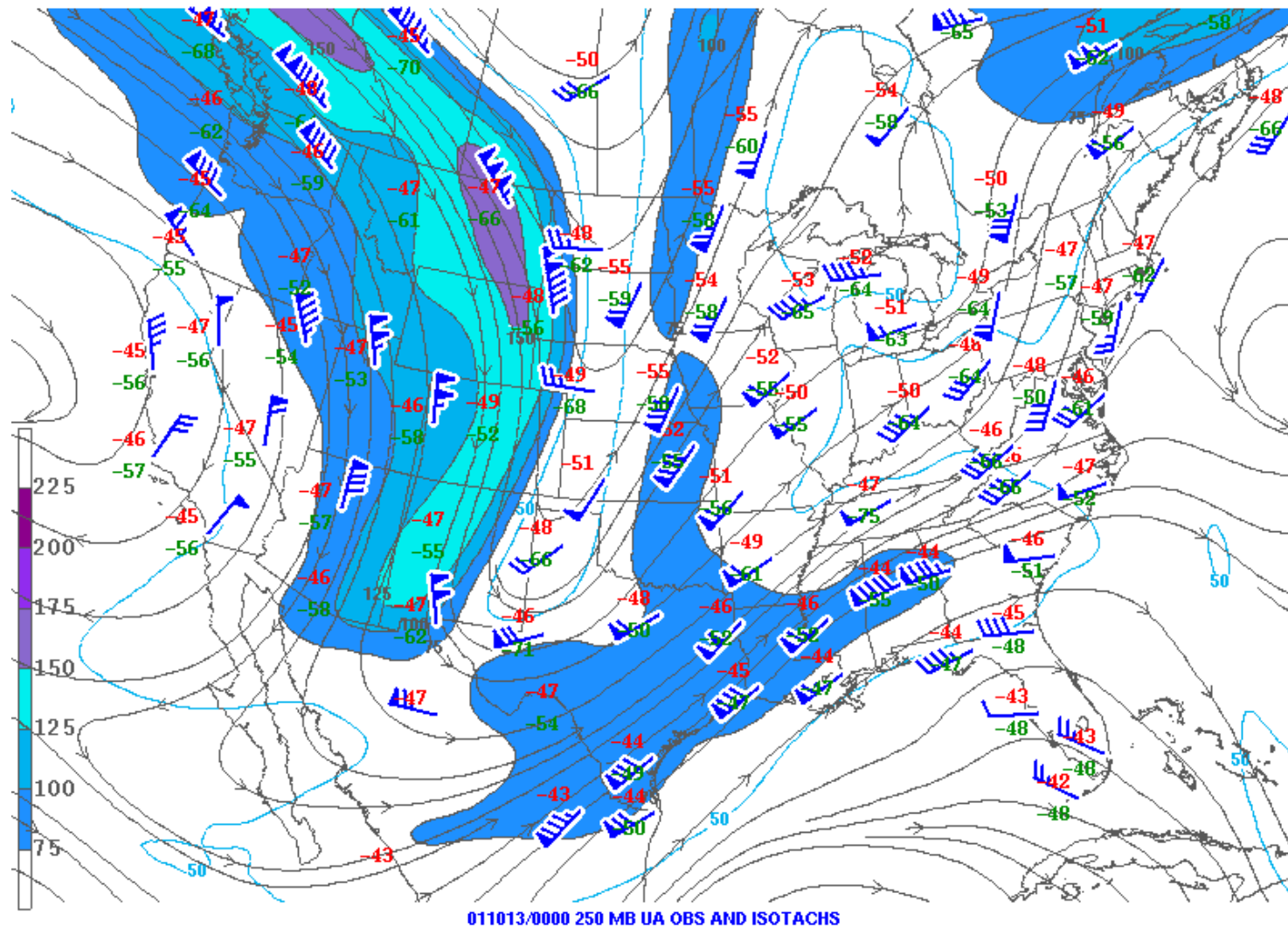


FIG. 4.2. Same as Fig. 4.1, but for 00 UTC 13 October 2001 (image courtesy of [www.spc.noaa.gov](http://www.spc.noaa.gov)).

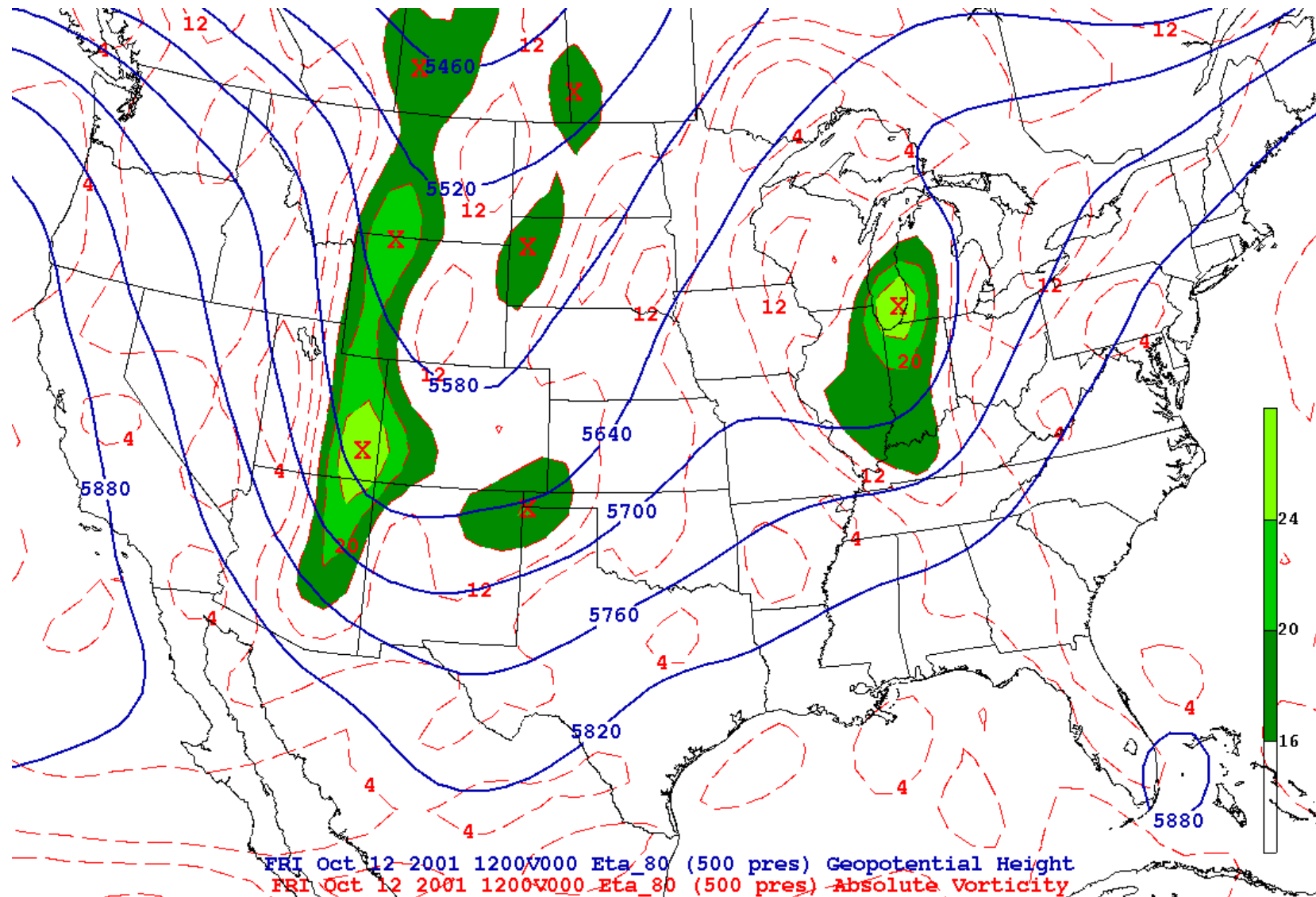


FIG. 4.3. 500-mb analysis for 12 UTC 12 October 2001. Height contours (m) are in solid blue lines, and absolute vorticity contours ( $s^{-1}$ ) are in dashed red lines.

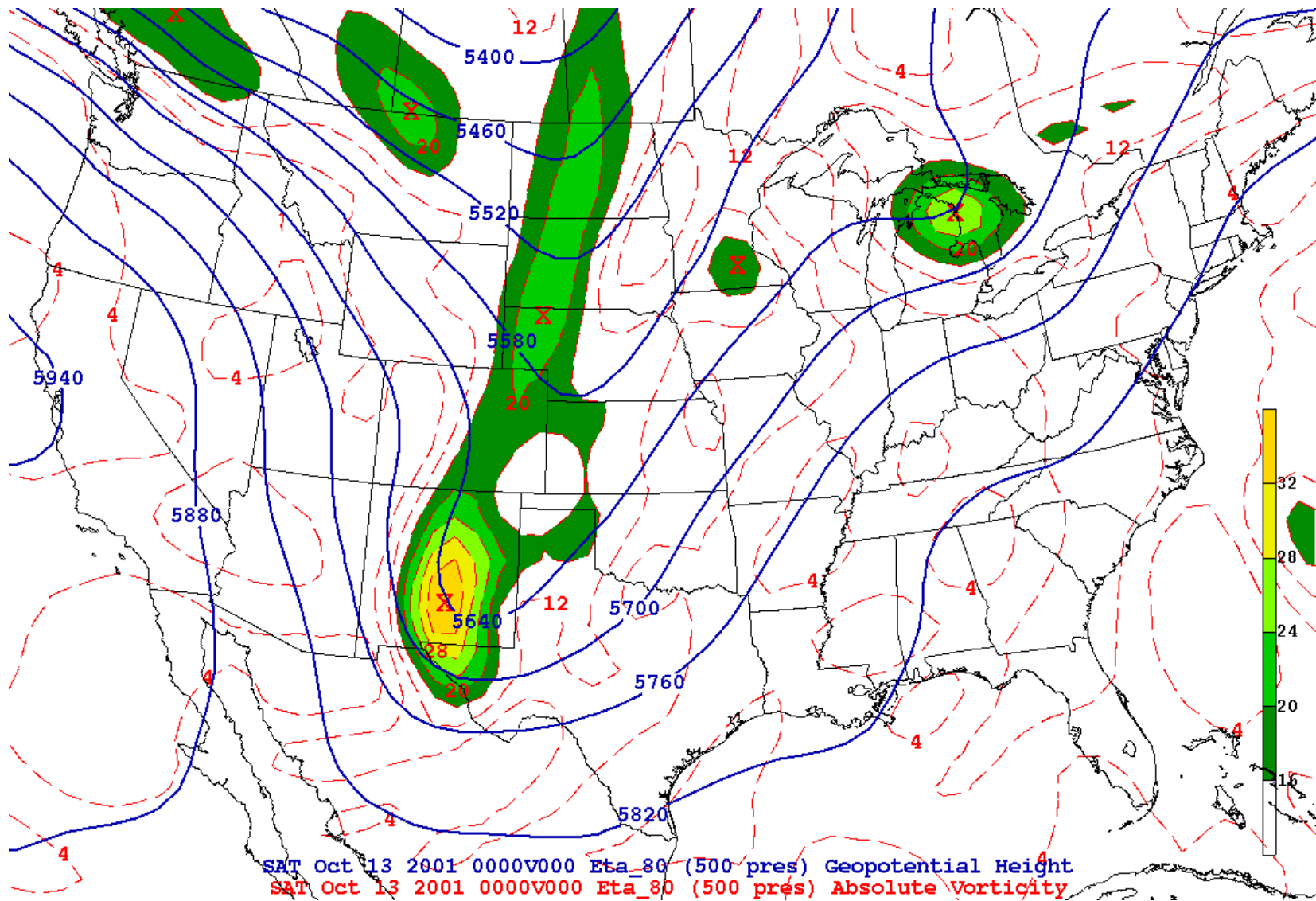


FIG. 4.4. Same as Fig. 4.3, but for 00 UTC 13 October 2001.

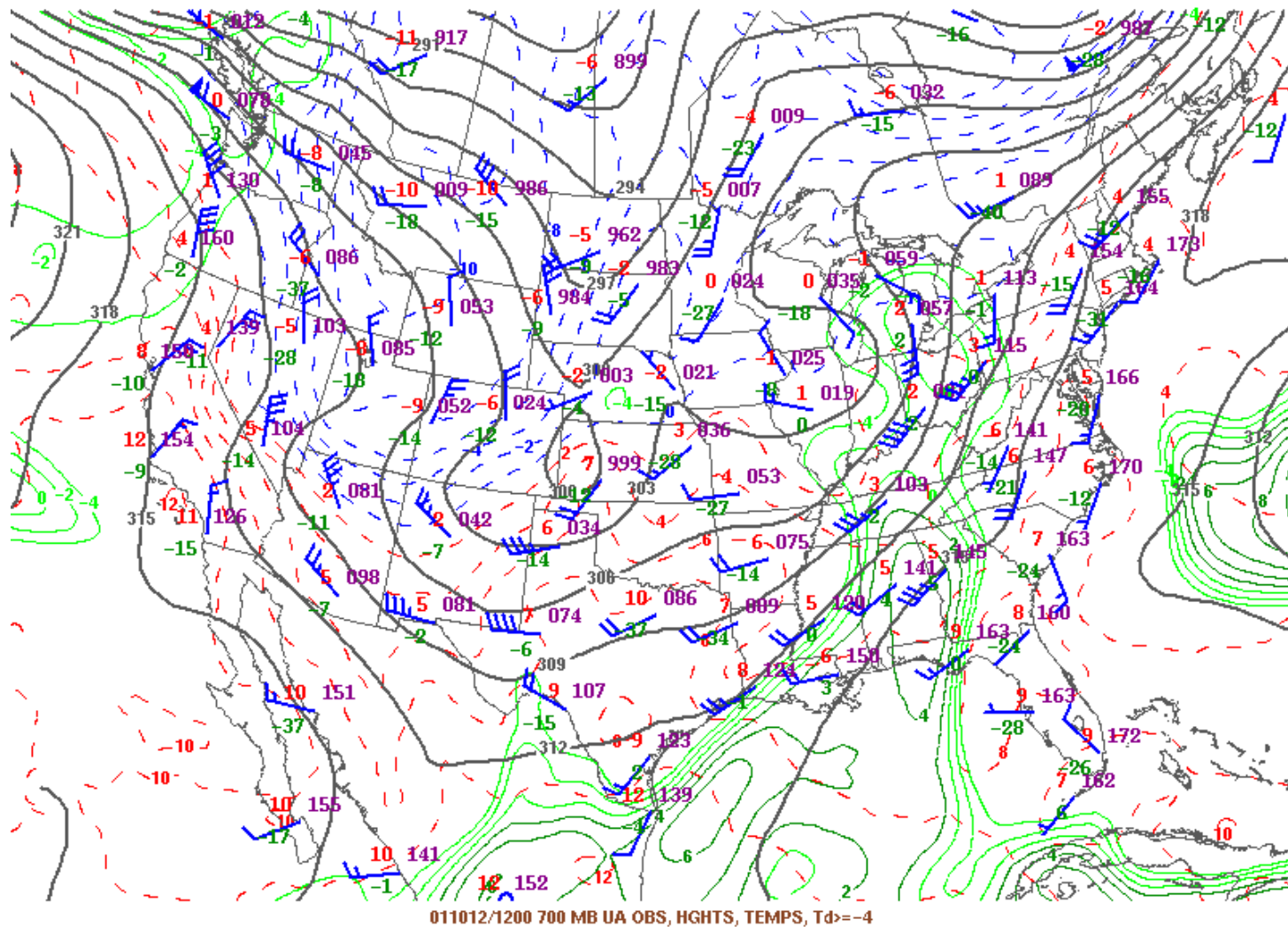


FIG. 4.5. 700-mb analysis for 12 UTC 12 October 2001. Height contours are in solid black lines, isotherms are in dashed red and blue lines, and dew point contours  $\geq -4$  °C are in solid green lines (image courtesy of [www.spc.noaa.gov](http://www.spc.noaa.gov)).

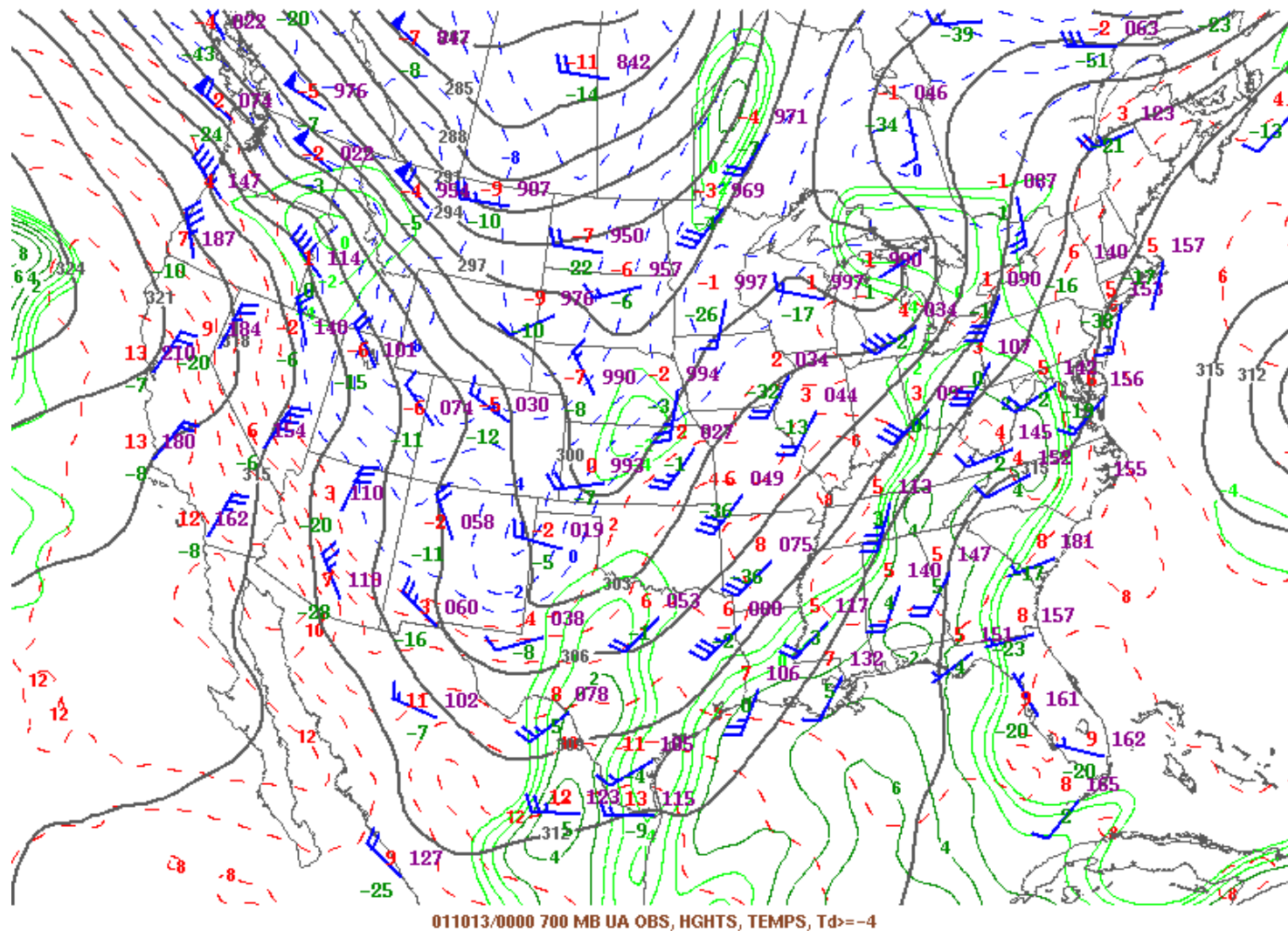


FIG. 4.6. Same as Fig. 4.5, but for 00 UTC 13 October 2001 (image courtesy of [www.spc.noaa.gov](http://www.spc.noaa.gov)).

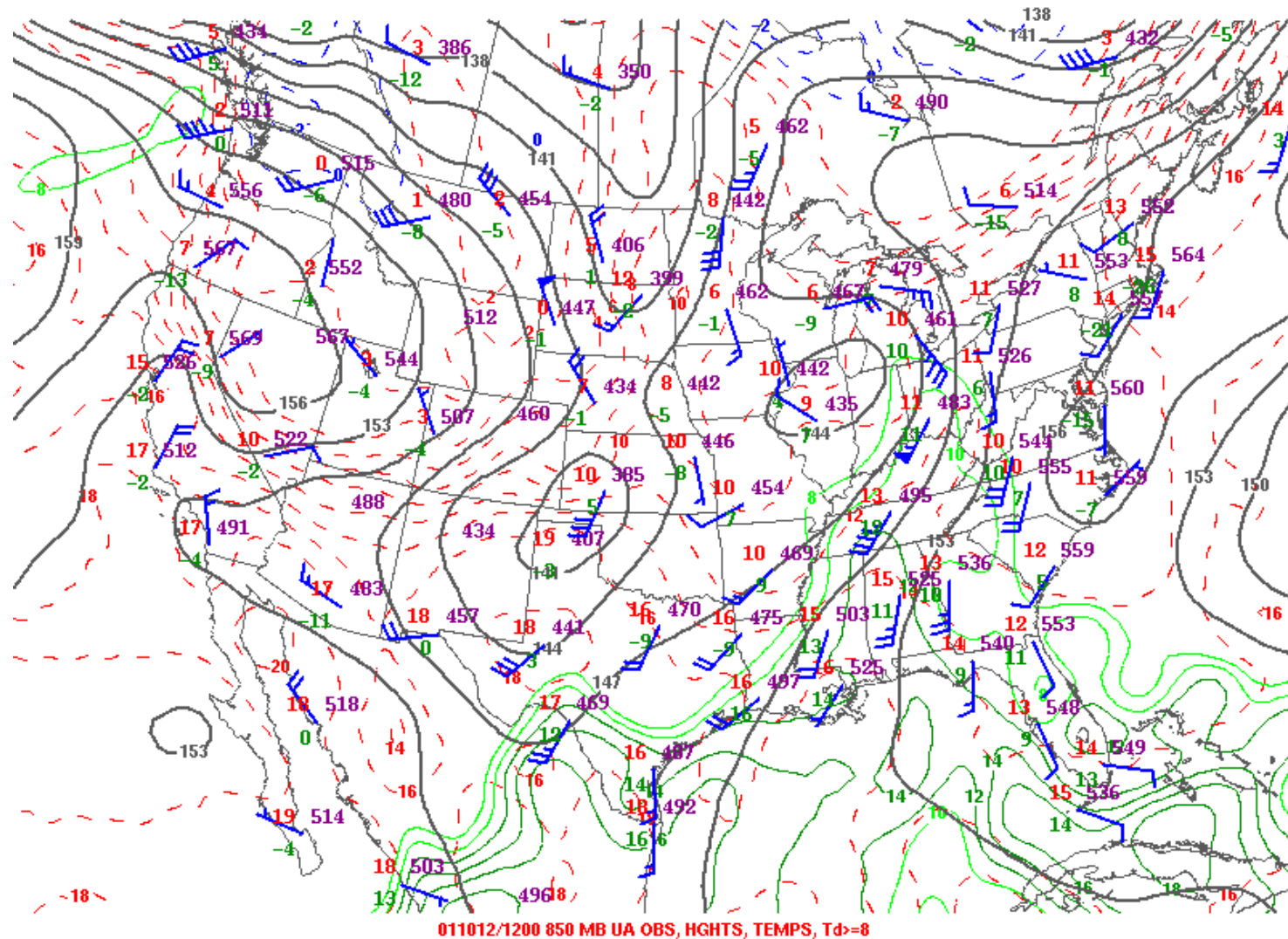


FIG. 4.7. 850-mb analysis for 12 UTC 12 October 2001. Height contours are in solid black lines, isotherms are in dashed red and blue lines, and dew point contours  $\geq 8$  °C are in solid green lines (image courtesy of [www.spc.noaa.gov](http://www.spc.noaa.gov)).

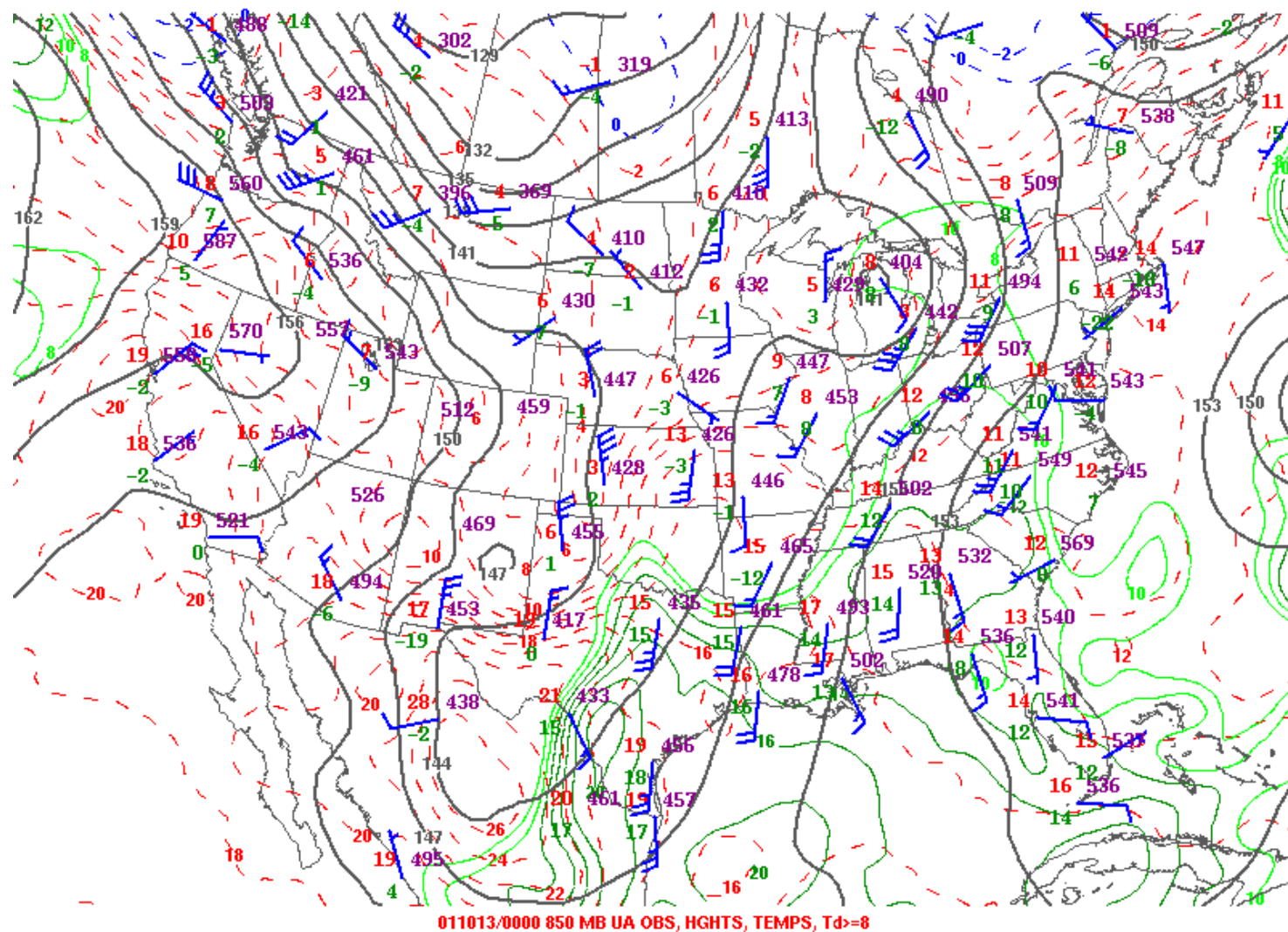


FIG. 4.8. Same as Fig. 4.7, but for 00 UTC 13 October 2001 (image courtesy of [www.spc.noaa.gov](http://www.spc.noaa.gov)).

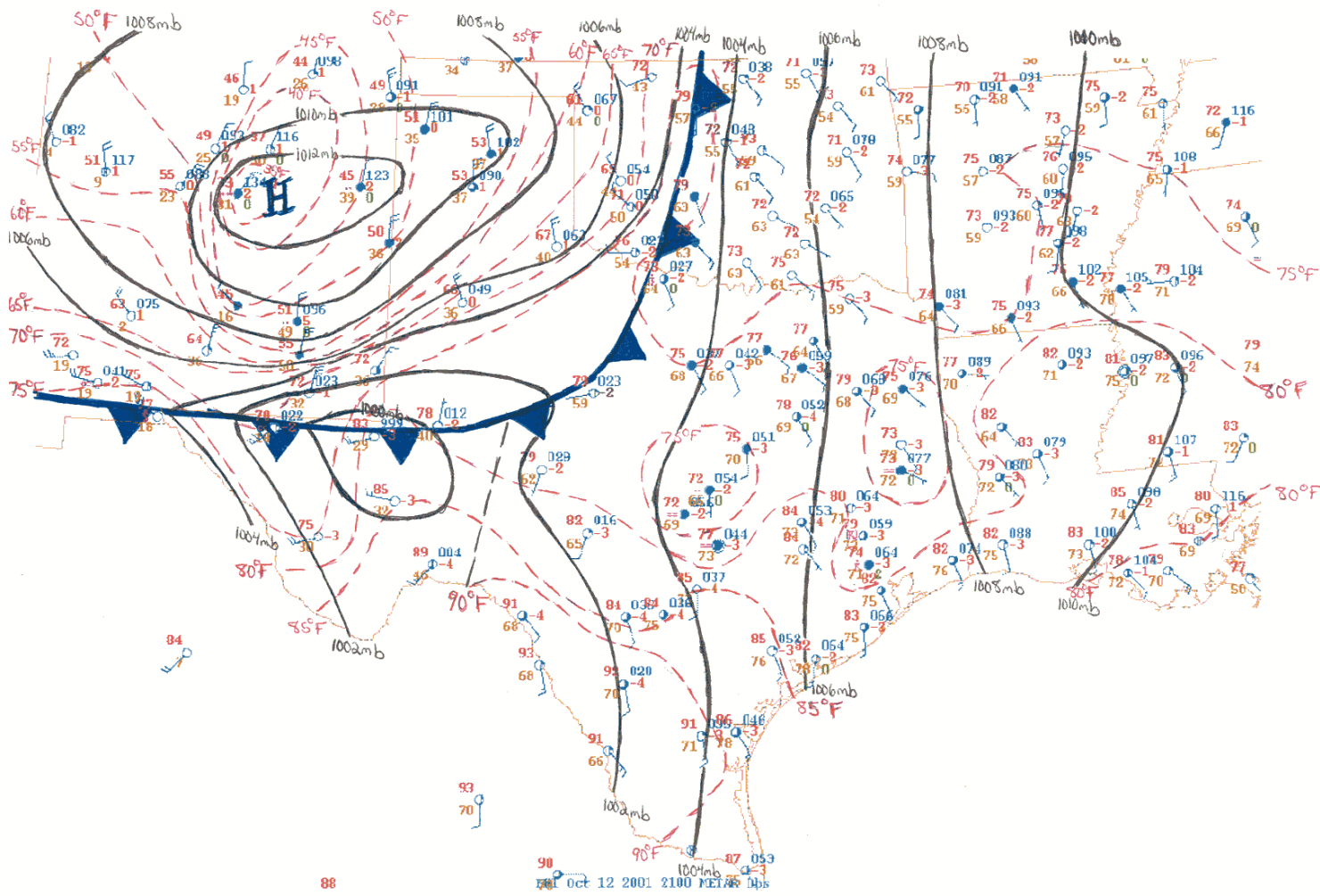


FIG. 4.9. 21 UTC 12 October 2001 surface analysis for Texas and surrounding areas. Isobars (every 2 mb) are in solid black lines, and isotherms (every 5 °F) are in dashed red lines.

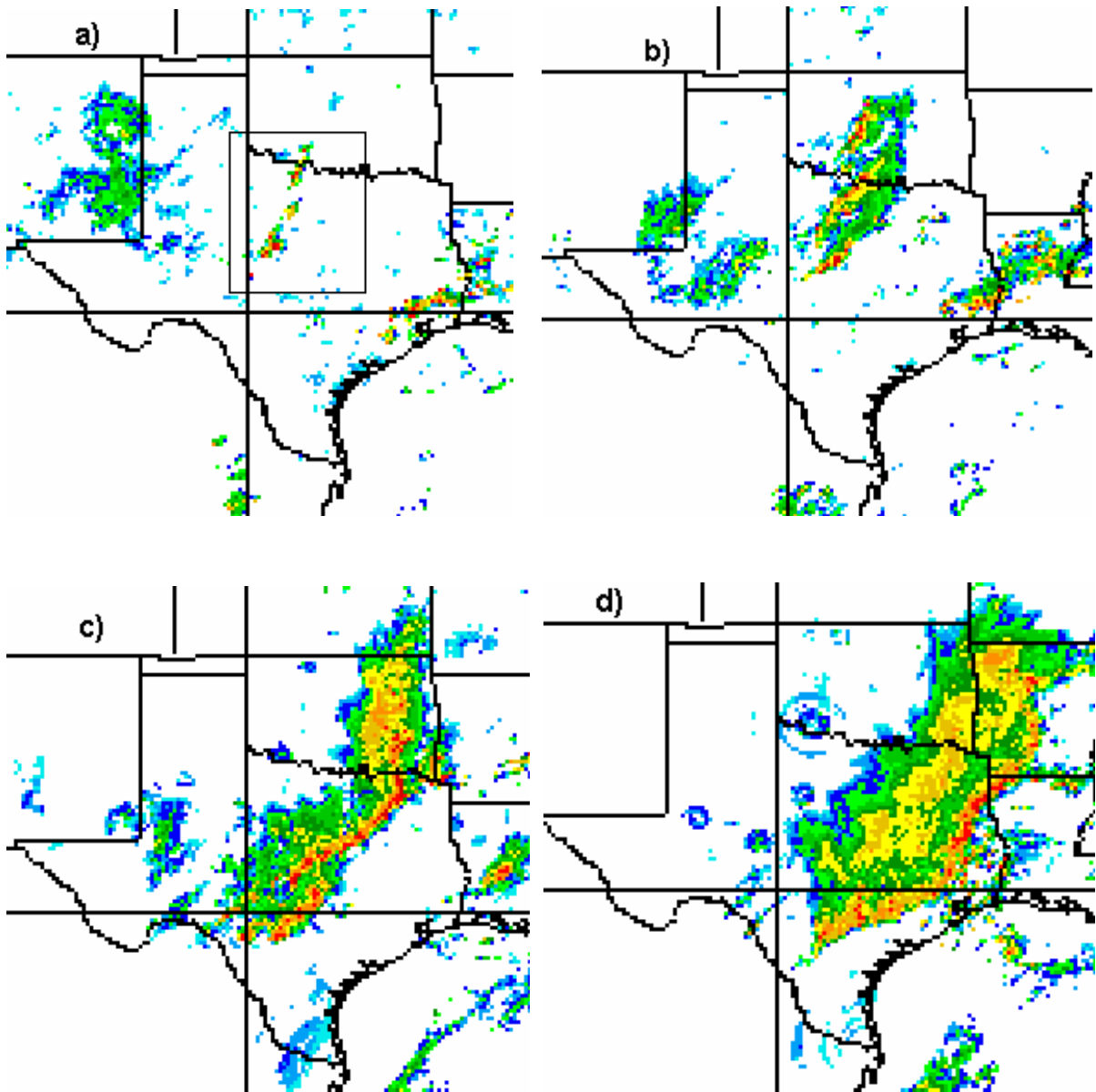


FIG. 4.10. 2-km resolution NEXRAD mosaic reflectivity images from a squall line that evolves into a TS MCS at (a) 21 UTC 12, (b) 00 UTC 13, (c) 4 UTC 13, and (d) 08 UTC 13 October 2001. Image adapted from [www.ncdc.noaa.gov](http://www.ncdc.noaa.gov).

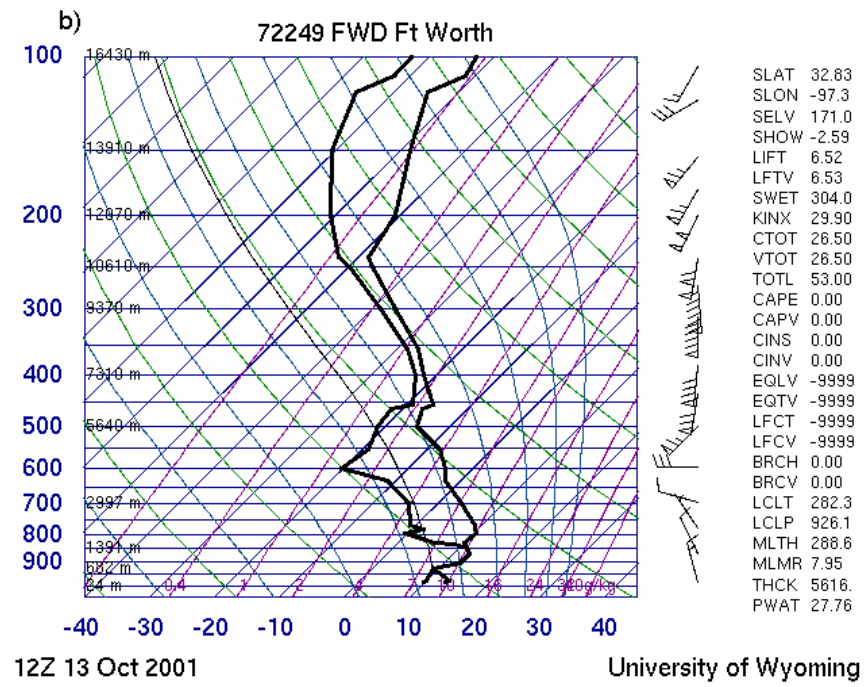
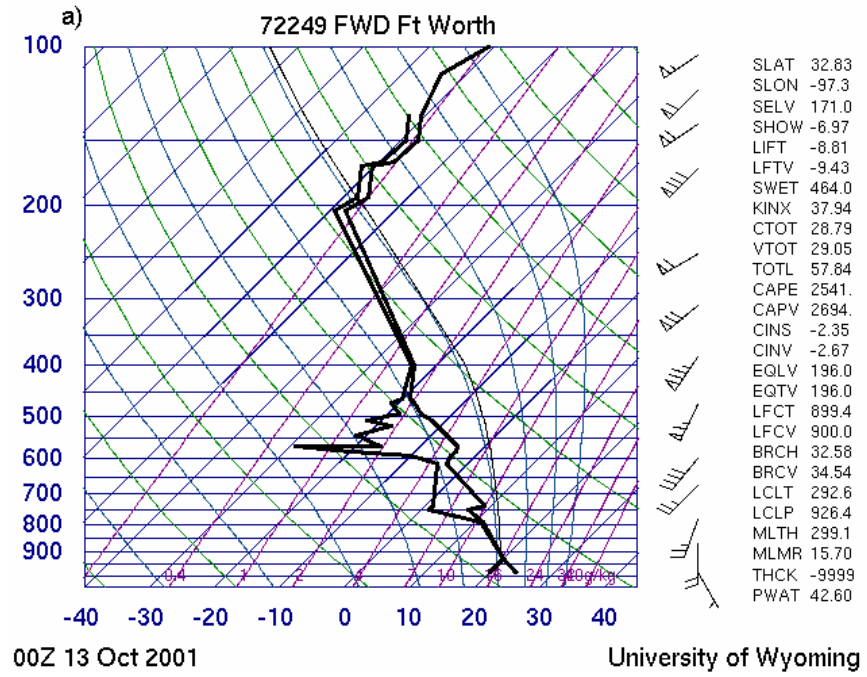


FIG. 4.11. Dallas-Fort Worth, Texas soundings valid for (a) 00 UTC 13, and (b) 12 UTC 13 October 2001. Images courtesy of the University of Washington.

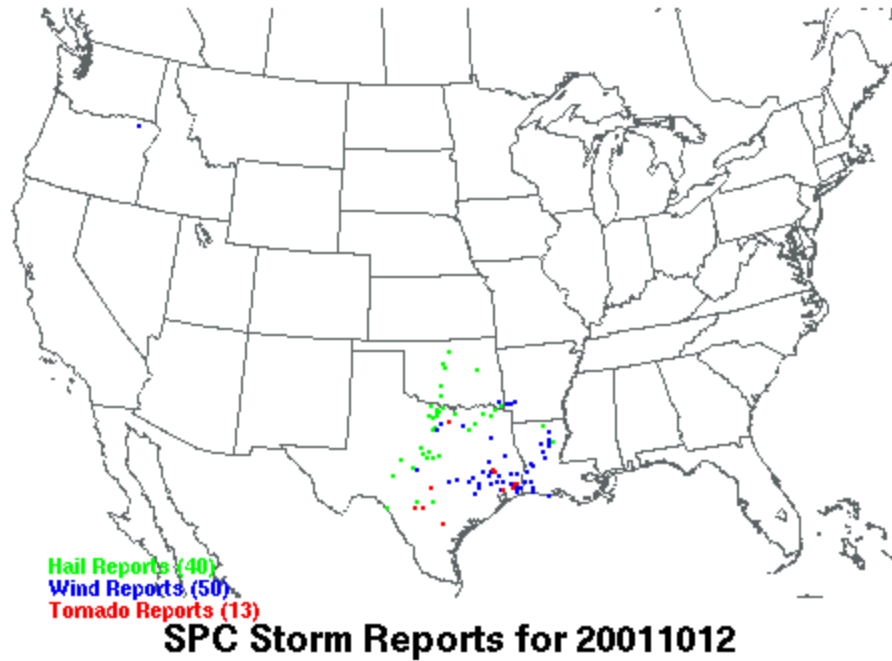


FIG. 4.12. Preliminary severe storm damage reports, including hail ( $\geq 0.75''$ ) (green dots), strong winds ( $\geq 58$  mph) (blue dots), and tornadoes (red dots) from 12 UTC 12 through 12 UTC 13 October 2001 (image courtesy of [www.spc.noaa.gov](http://www.spc.noaa.gov)).

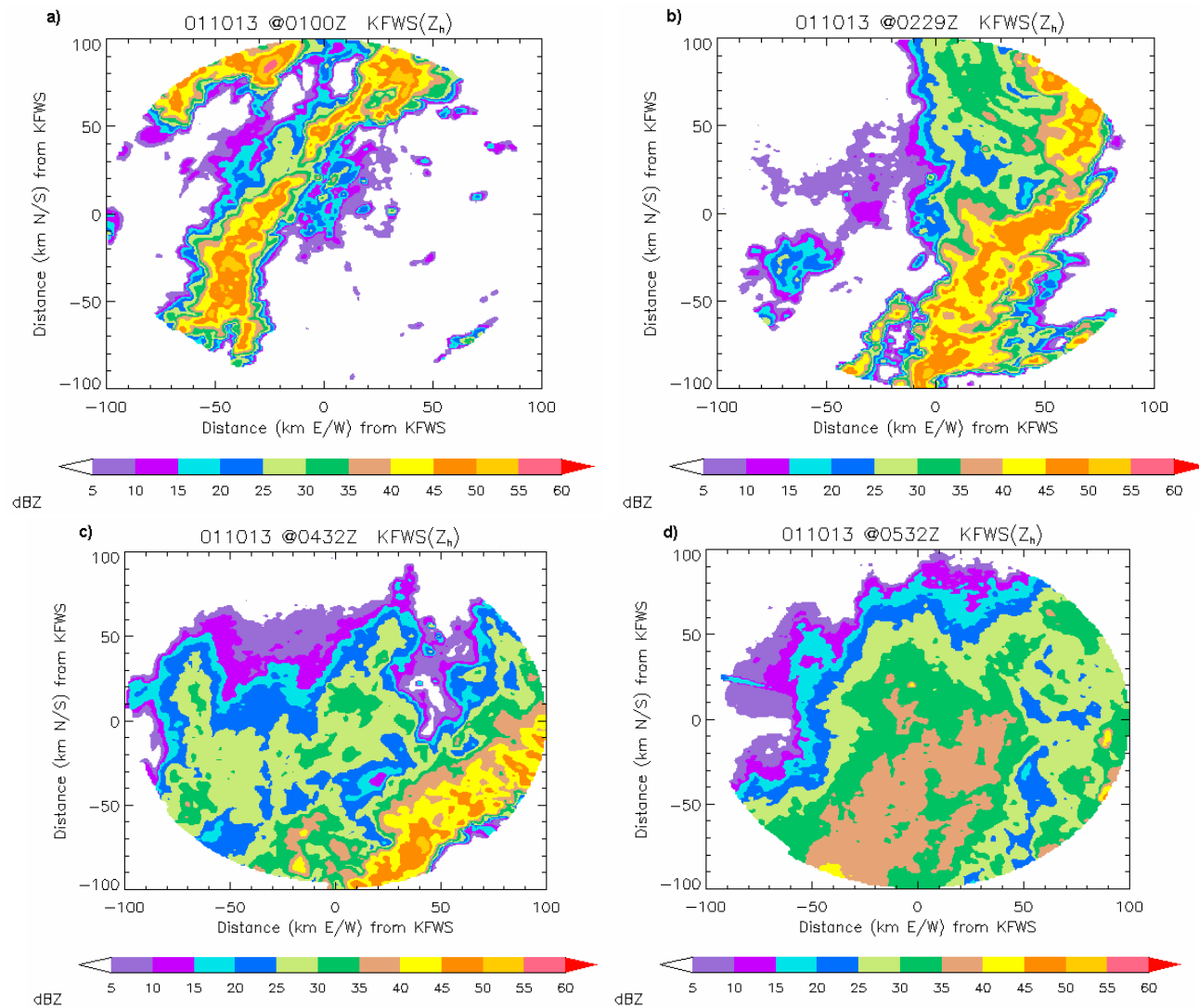


FIG. 4.13. 0.5 km constant altitude radar reflectivity images of the development of the 12-13 October 2001 MCS at (a) 01 UTC, (b) 2:29 UTC, (c) 4:32 UTC, and (d) 5:32 UTC. Radar reflectivity is color-shaded according to the scale, and the KFWS radar is located in the center of the image. The x- and y-axes represent distance (km N/S) and distance (km E/W) from the KFWS radar, respectively.

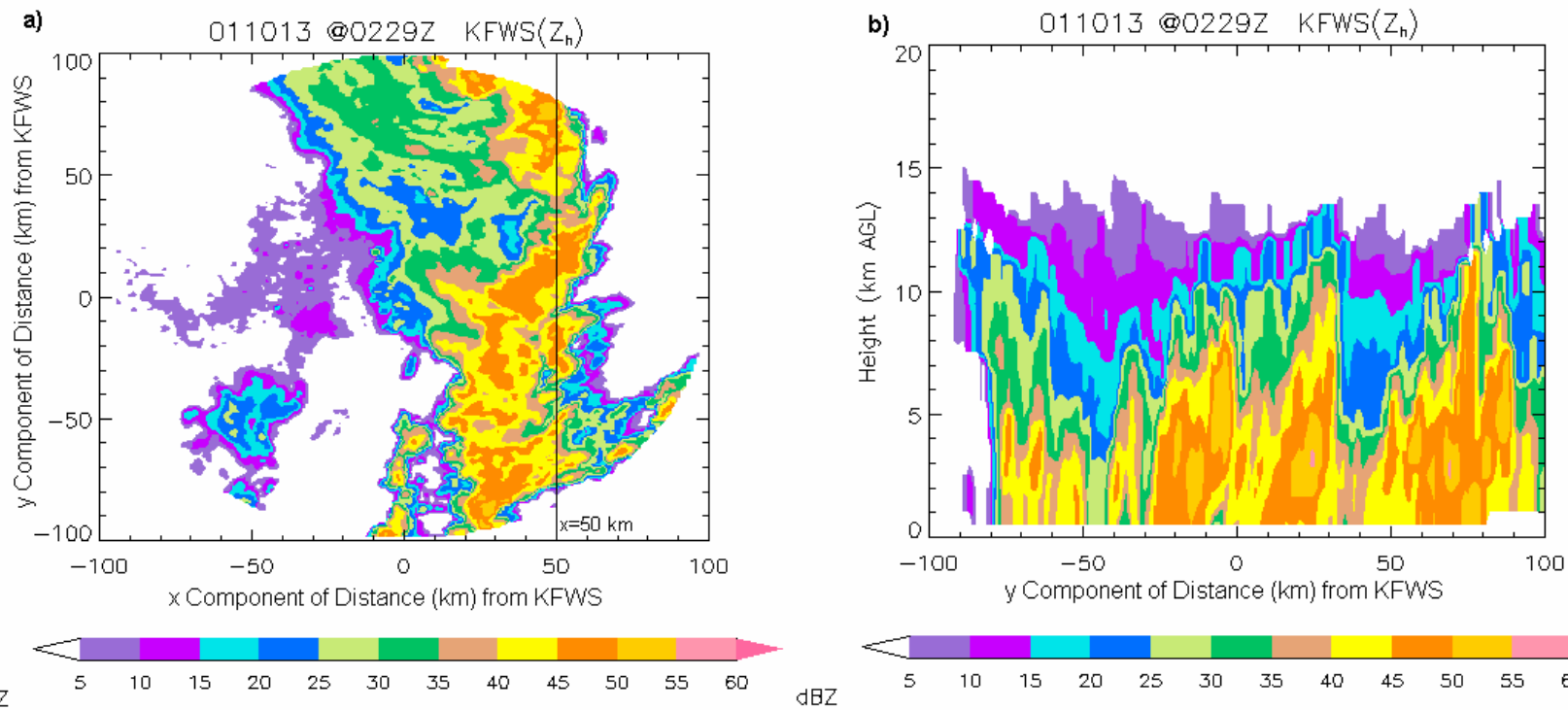


FIG. 4.14. a) A 0.5 km CAPPI image, and b) a vertical cross-section through (a) at  $x = 50$  km at 02:29 UTC 13 October 2001. Radar reflectivity (dBZ) is color-shaded according to the scale. The horizontal image has been rotated counterclockwise  $20^\circ$ .

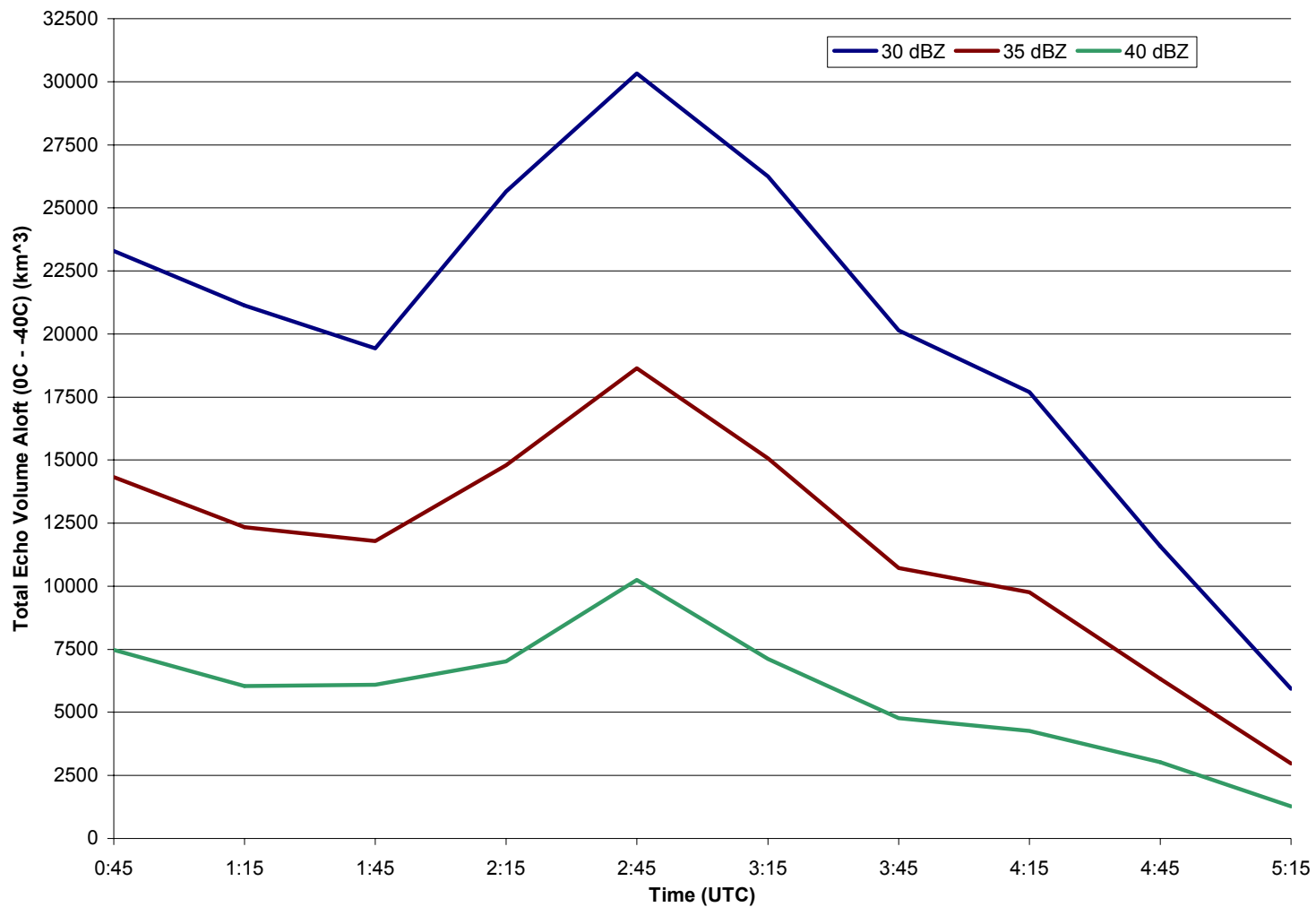


FIG. 4.15. Total echo volume aloft trends  $\geq 30$  dBZ (blue line),  $\geq 35$  dBZ (maroon line), and  $\geq 40$  dBZ (teal line) from 00:45 to 05:32 UTC 13 October 2001, time averaged every 5 min with a 6-point running mean smoother. Total echo volume aloft ( $\text{km}^3$ ) was calculated between the  $0^\circ\text{C}$  to  $-40^\circ\text{C}$  temperature layer. Time is listed along the x-axis, and total echo volume aloft is listed along the y-axis.

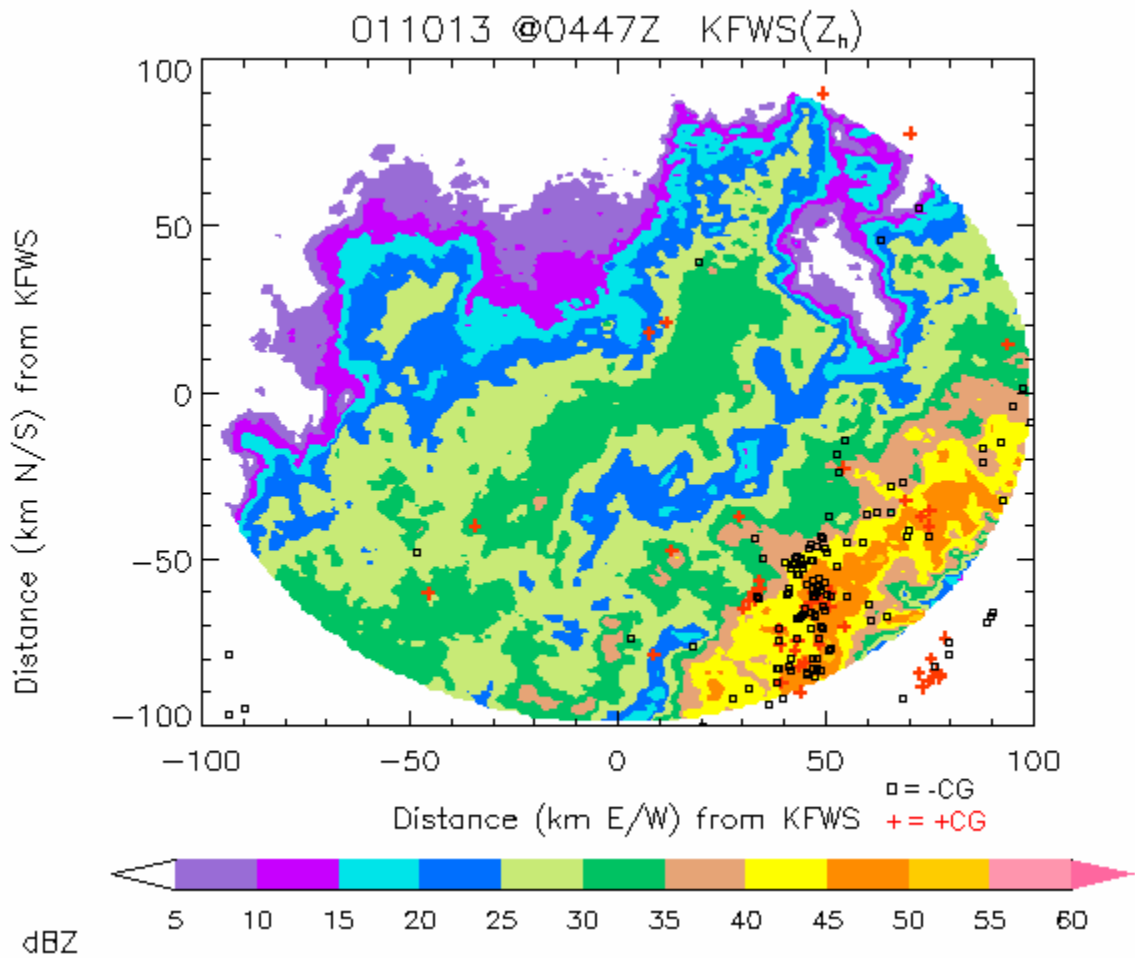


FIG. 4.16. 0.5 km radar reflectivity (dBZ) CAPPI image of the 12-13 October 2001 MCS at 04:47 UTC 13 overlaid with 5 min of NLDN CG lightning flash data (centered on the time of the radar image). -CG lightning flashes are indicated by black squares, and +CG lightning flashes are indicated by red addition signs. Radar reflectivity is color-shaded according to the scale, and the KFWS radar is located in the center of the image. The x- and y-axes represent the distance (km) north/south and east/west of the KFWS radar, respectively.

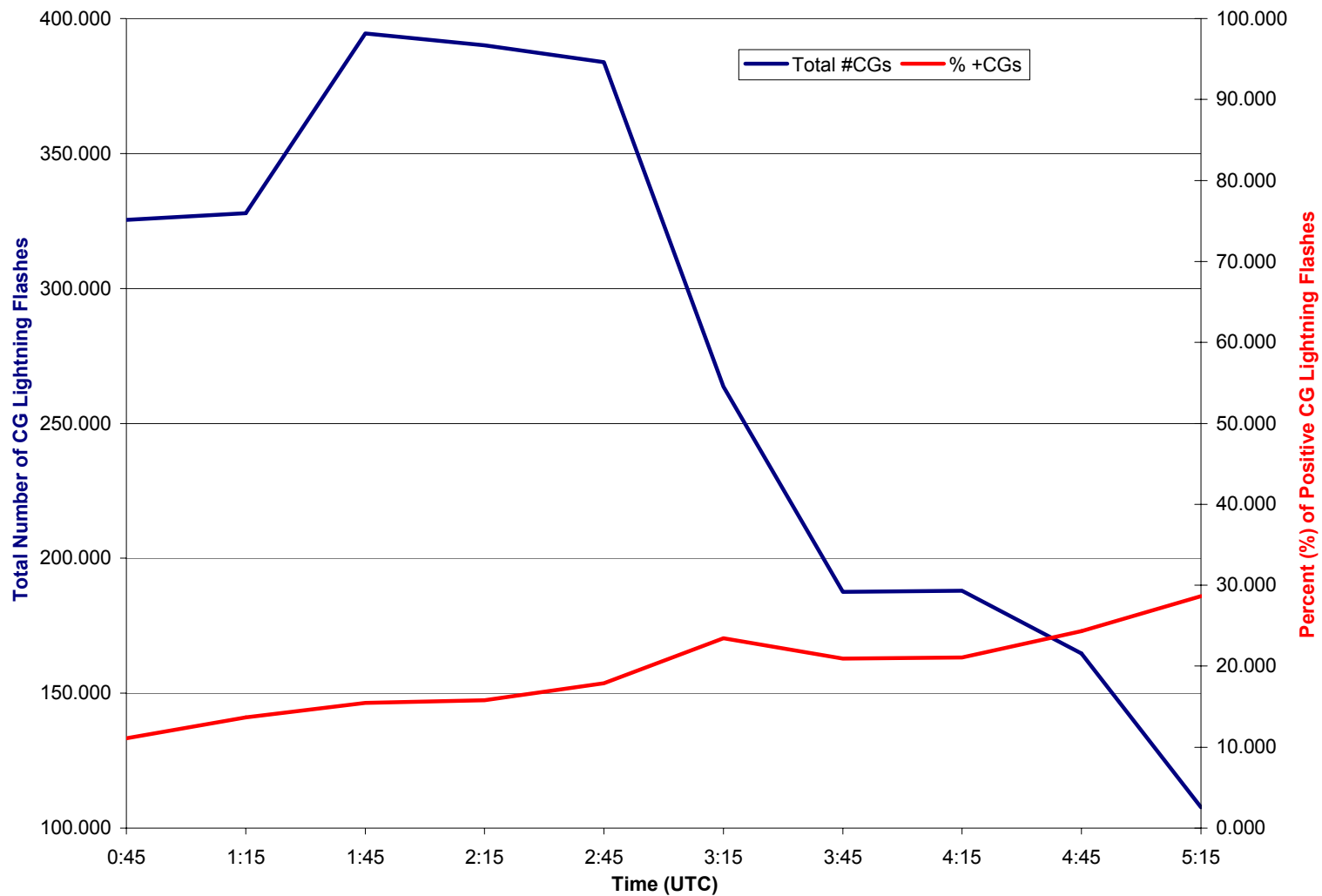


FIG. 4.17. CG lightning flash (blue line) and percent of +CG lightning flash (red line) trends from 00:45 to 05:32 UTC 13 October 2001, time averaged every 5 min with a 6-point running mean smoother. The trend in CG lightning flash (+CG lightning flash percentage) rate are along the primary (secondary) y-axis. The x-axis represents time.

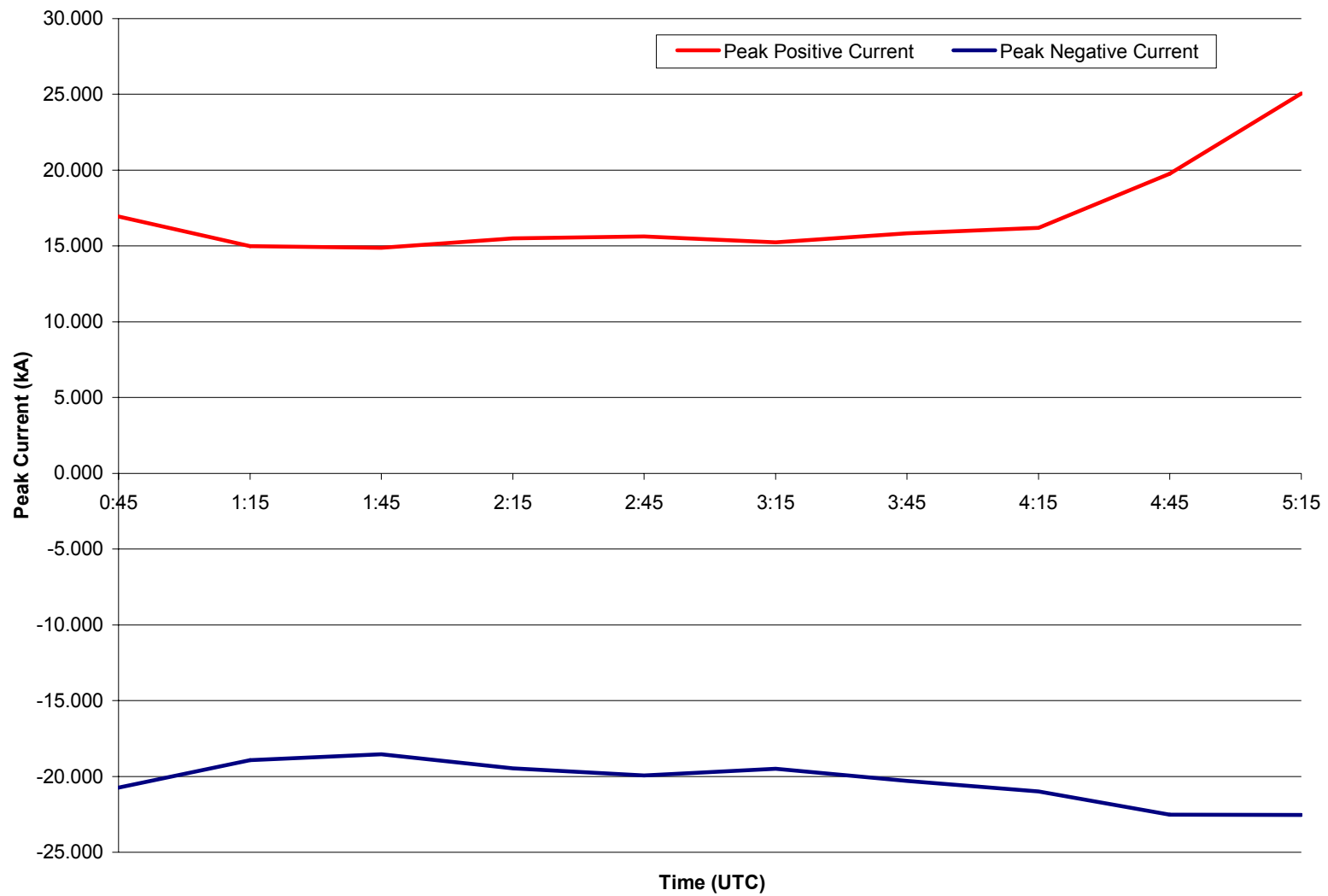


FIG. 4.18. Temporal evolution of the peak positive (red line) and negative (blue line) currents (kA) from 00:45 to 05:32 UTC 13 October 2001, time averaged every 5 min with a 6-point running mean smoother. Time (UTC) is listed along the x-axis, and peak current is listed along the y-axis.

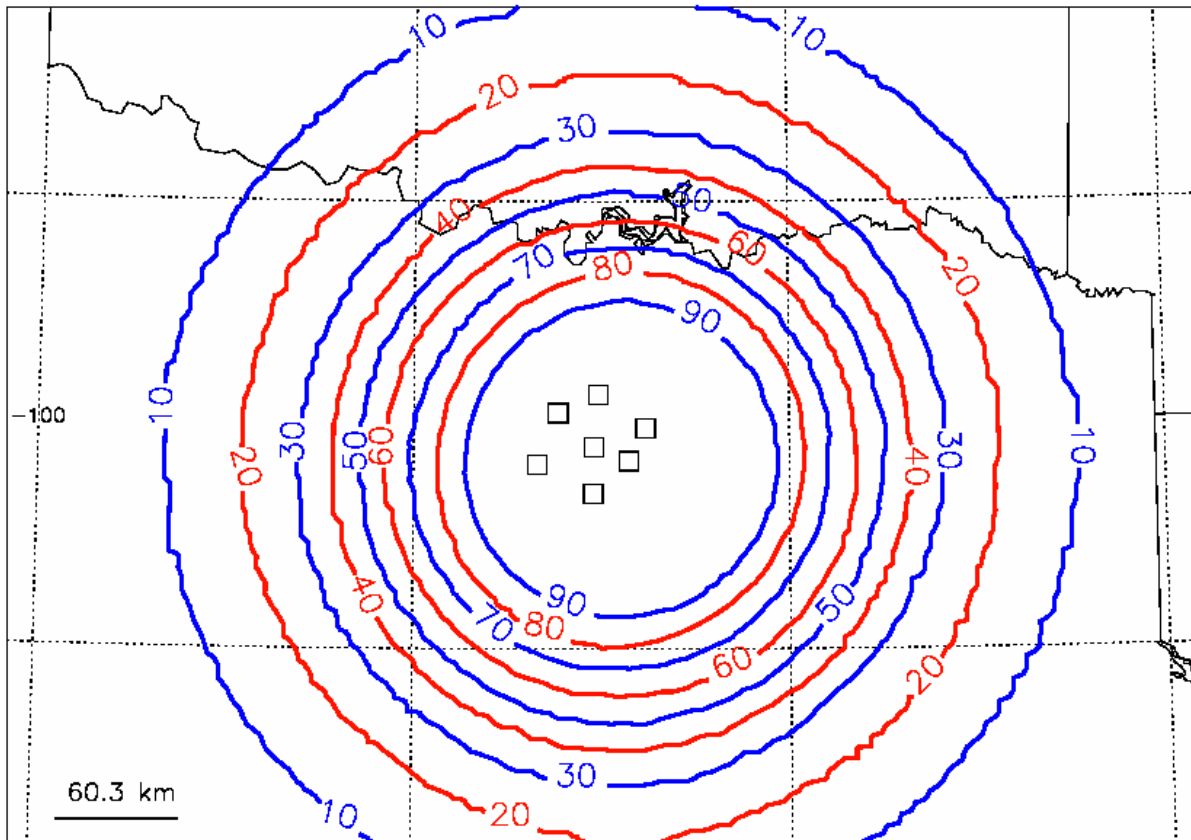


FIG. 4.19. Detection efficiency of the LDAR II network during the 12-13 October 2001 MCS. The seven squares represent the seven LDAR II sensors that were operational during this case study. The circles around the network represent the percent (%) of LDAR II flashes can be detected out to a given range. Within the network's center, > 90% of LDAR II flashes can be detected. (Image adapted from M. Murphy 2003).

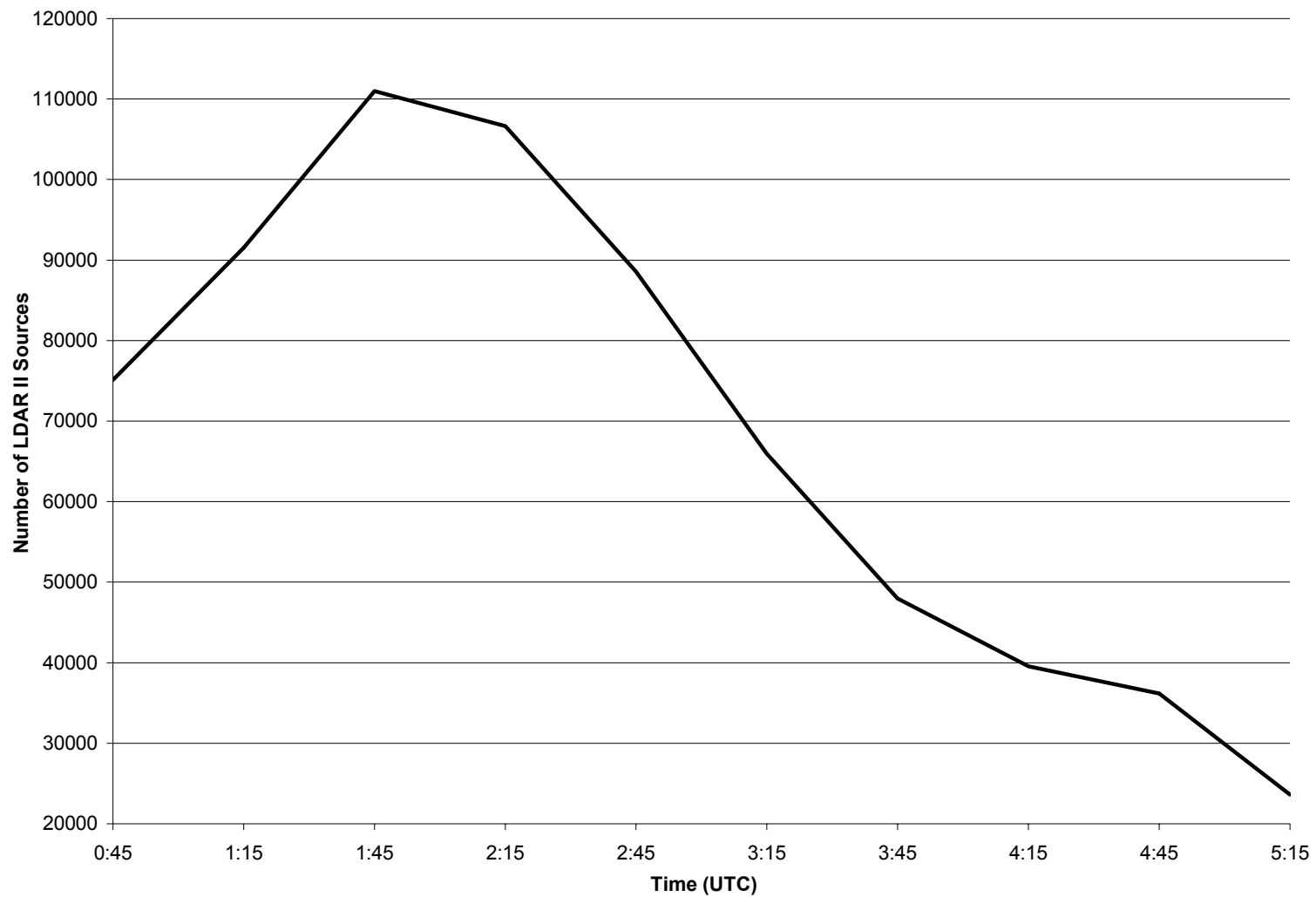


FIG. 4.20. LDAR II source trend from 00:45 to 05:32 UTC 13 October 2001, time averaged every 5 min with a 6-point running mean smoother. Time is listed along the x-axis and the number of LDAR II sources is listed along the y-axis.

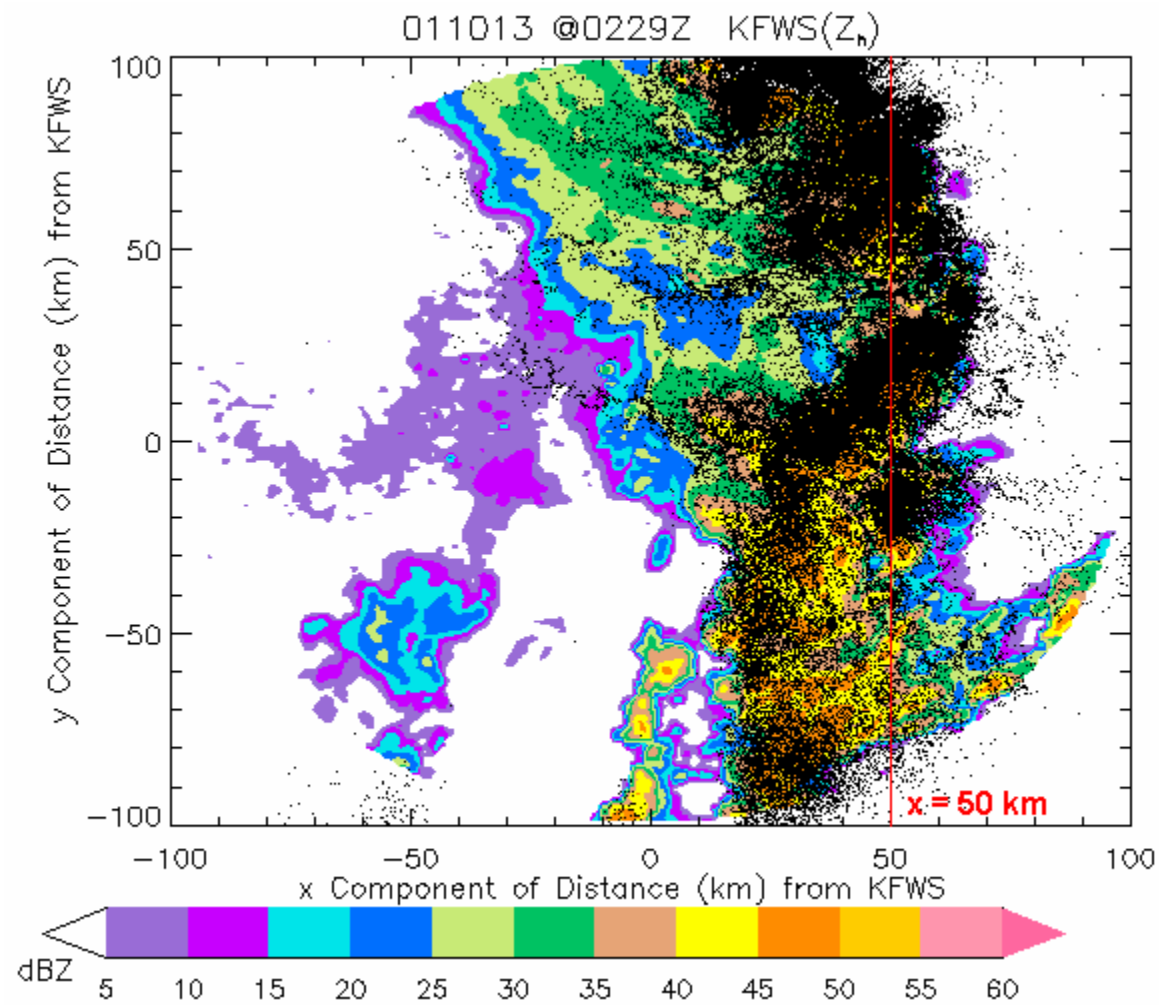


FIG. 4.21. 0.5 km CAPPI image of radar reflectivity (dBZ) with LDAR II sources overlaid (black dots) at 02:29 UTC 13 October 2002. Radar reflectivity is color-shaded according to the scale, and the KFWS radar is located in the center of the image. 5 min of LDAR II sources (at  $x \pm 0.5$  km) occurring at all altitudes centered on the time of the radar image are plotted. The reflectivity and LDAR II data have been rotated counterclockwise by  $20^\circ$  so that the x- and y-axes represent the x and y components of distance (km) from the KFWS radar, respectively. The red vertical line represents the vertical cross-section location in Fig. 4.22.

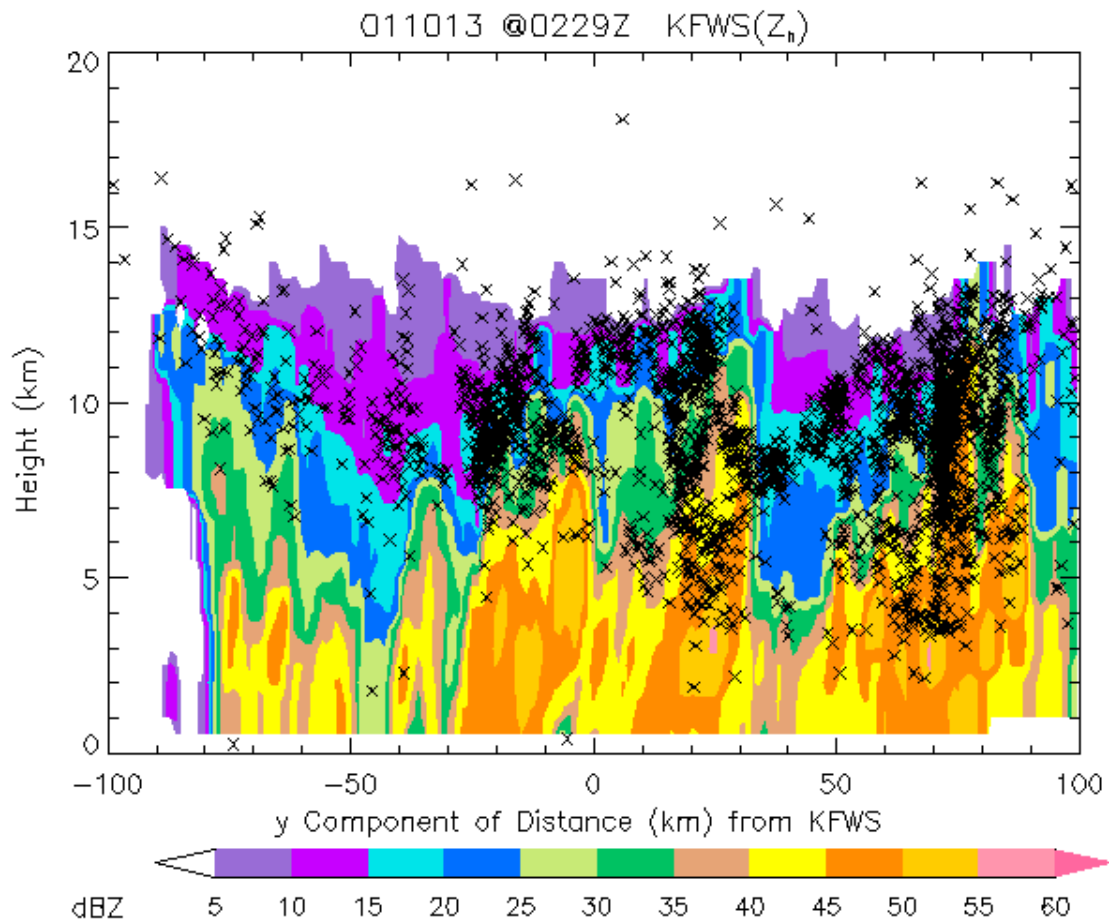


FIG. 4.22. Vertical cross-section of the leading convective line at 02:29 UTC 13 October 2001, taken line parallel through Fig. 4.21 at  $x = 50$  km. Radar reflectivity (dBZ) is color-shaded according to the scale, and LDAR II sources (at  $x \pm 0.5$  km) are overlaid in black "x"s. The y-axis represents height above ground level (km) and the x-axis represents the x component of distance from the KFWS radar. Significant temperature levels ( $0^\circ\text{C}$ ,  $-10^\circ\text{C}$ ,  $-20^\circ\text{C}$ , and  $-40^\circ\text{C}$ ) are listed along the y-axis on the right-hand side of the image.

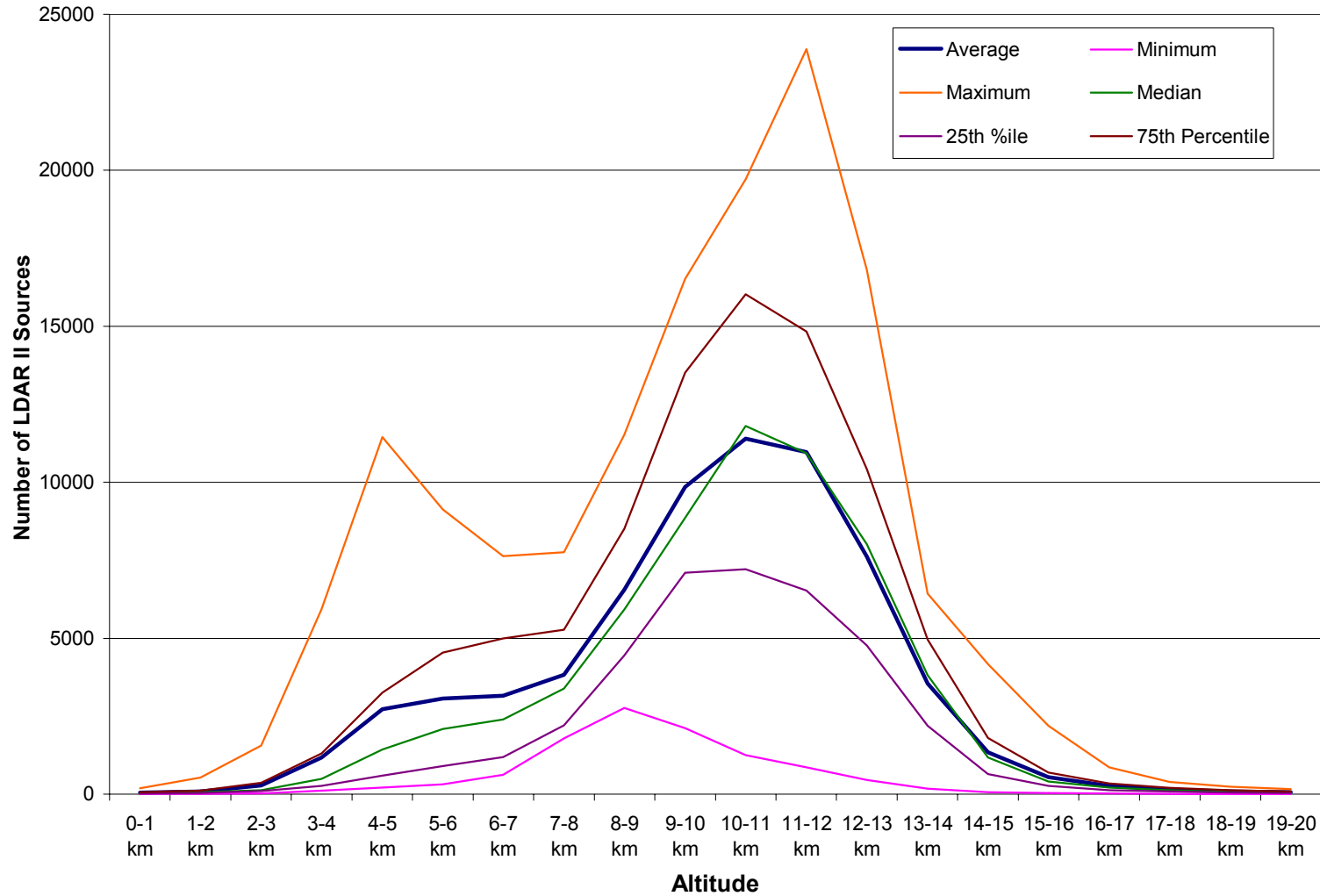


FIG. 4.23. Average (blue line), minimum (pink line), maximum (orange line), median (green line), 25<sup>th</sup> percentile (violet line), and 75<sup>th</sup> percentile (brown line) of LDAR II sources occurring within each 1-km height level from 0 to 20 km from 00:45 to 05:32 UTC 13 October 2001. Altitude (km) is listed along the x-axis, and the number of LDAR II sources is listed along the y-axis.

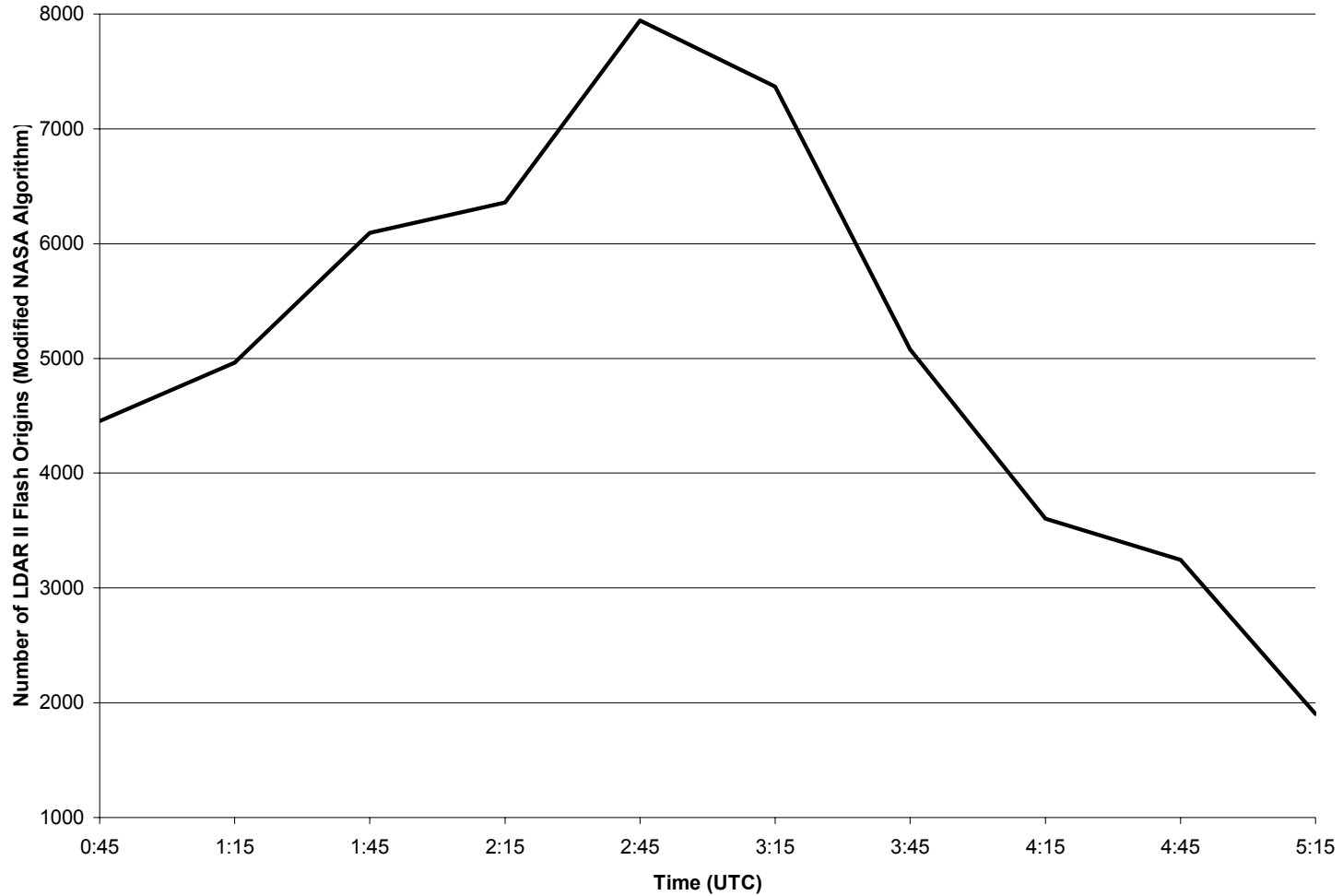


FIG. 4.24. LDAR II flash origin trend (as determined by the modified NASA algorithm) from 00:45 to 05:32 UTC 13 October 2001, time averaged every 5 min with a 6-point running mean smoother. Time is listed along the x-axis and the number of LDAR II flash origins is listed along the y-axis.

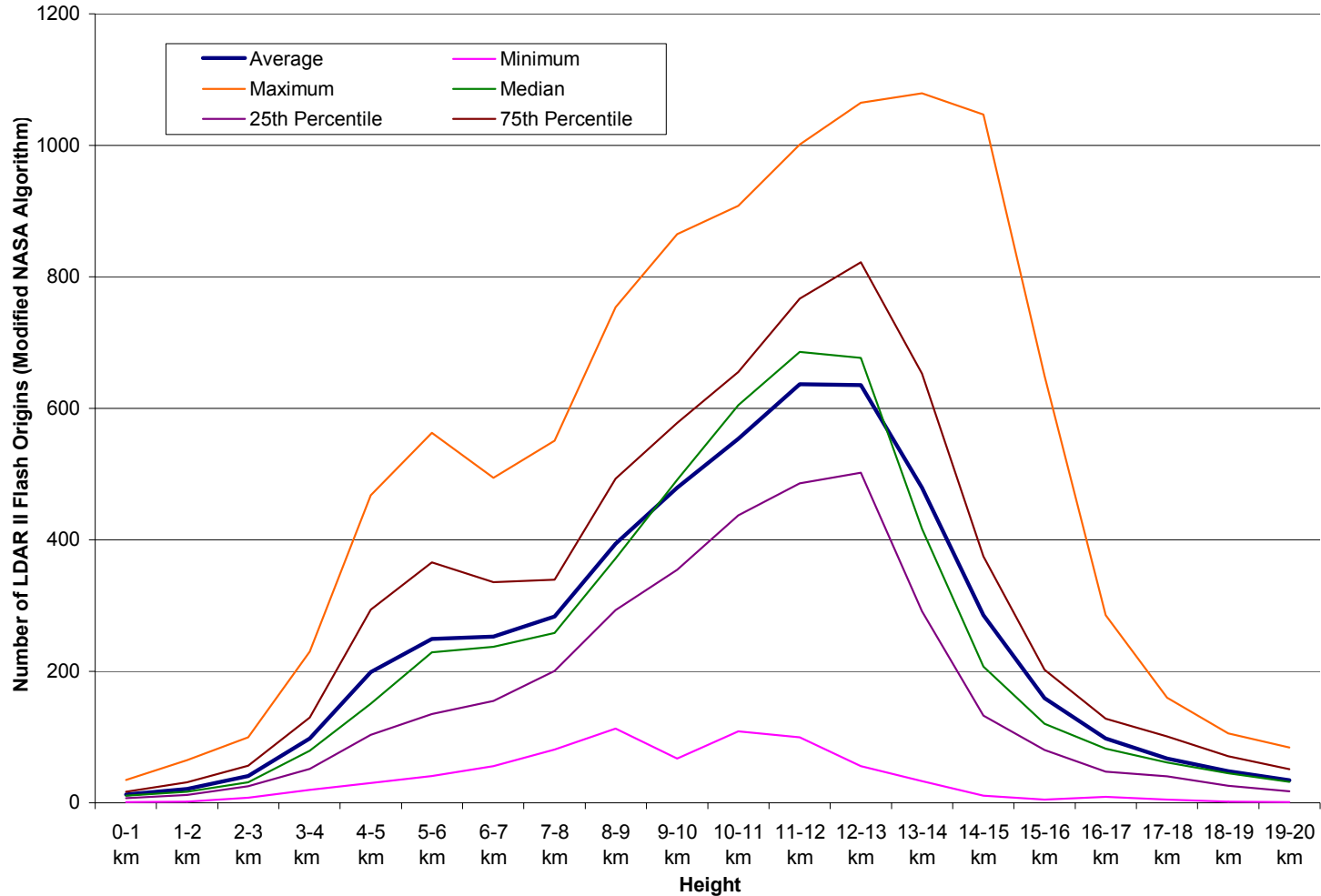


FIG. 4.25. Average (blue line), minimum (pink line), maximum (orange line), median (green line), 25<sup>th</sup> percentile (violet line), and 75<sup>th</sup> percentile (brown line) of LDAR II flash origins occurring within each 1-km height level from 0 to 20 km from 00:45 to 05:32 UTC 13 October 2001. Altitude (km) is listed along the x-axis, and the number of LDAR II flash origins (as determined by the modified NASA algorithm) is listed along the y-axis.

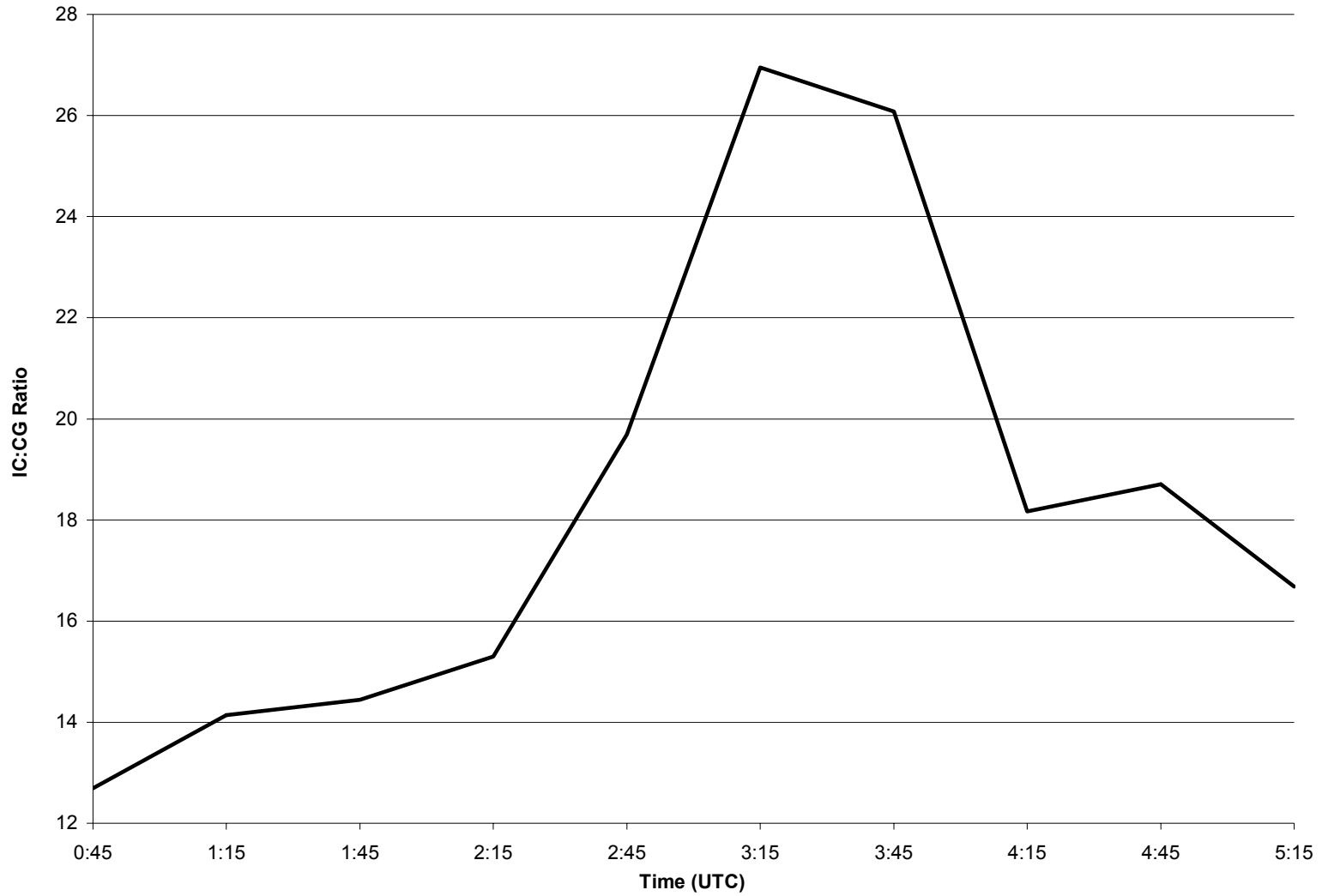


FIG. 4.26. IC:CG ratio trend from 00:45 05:32 UTC 13 October 2001, time averaged every 5 min with a 6-point running mean smoother. Time (UTC) is listed along the x-axis, and the IC:CG ratio is listed along the y-axis.

## **5. CASE STUDY OBSERVATIONS #3: 16 JUNE 2002 MCS**

### **5.1 Background Characteristics**

#### ***5.1.1 Synoptic Overview***

The 16 June 2002 MCS began as a squall line in western Kansas at ~19 UTC 15 June 2002 (Fig. 5.1(a)). The squall line moved south-southeastward towards Oklahoma (Fig. 5.1(b)) as it developed into a mature MCS (Fig. 5.1(c)). As it continued towards the DFW region the convective line began to bow. After passing through the DFW region from 05 to 07 UTC 16 June 2002 (Fig. 5.1(d)), the MCS began to propagate southeastward through Texas and into the Gulf of Mexico. The MCS then dissipated over the Gulf around 16 UTC 16 June 2002. Radar, surface, and upper air data are examined for this case study.

Mandatory pressure level (250-, 500-, 700-, and 850-mb) isobaric analyses of the U.S. at 12 UTC 15 and 00 UTC 16 June 2002 are shown in Figs. 5.2-5.9. At 12 UTC 15 June (Fig. 5.2), western Kansas (the location of initial squall line formation) is within the reentrance region of a 250-mb jet streak. Upper-level winds are northwesterly at 85 kts in western Kansas and northwesterly at 55 kts in DFW. At 00 UTC 16 June (Fig. 5.3), the jet streak is located just to the west of DFW in 250-mb northwesterly winds at 70 kts. These observed high winds result from a strong height gradient over DFW. During the analysis period, an upper-level ridge and an upper-level trough are present to the southwest and northeast of DFW, respectively. Also, the presence of a small trough over Texas and Oklahoma is evident at 00 UTC 16.

The 500-mb analyses at 12 UTC 15 and 00 UTC 16 June 2002 are shown in Figs. 5.4 and 5.5, respectively. The 500-mb ridge to the southwest of DFW and the trough to the

northeast of DFW focus northwesterly winds into Kansas, Oklahoma, and north and central Texas during the analysis period. These winds are as strong as 40 kts in western Kansas and 30 kts at DFW at 12 UTC 15 June. At 00 UTC 16 June, 25 kt northwesterly winds are observed at DFW. The presence of a potent shortwave trough and positive vorticity advection over Texas and Oklahoma is evident, especially at 00 UTC 16.

Both the 12 UTC 15 and 00 UTC 16 June 2002 700-mb analyses (Figs. 5.6 and 5.7, respectively) indicate that abundant moisture is present in Kansas, Oklahoma, and Texas. At 12 UTC 15 June, light (5 kt) west-southwesterly winds are present in western Kansas, and DFW is experiencing northwest winds at 15 kts (Fig. 5.6). By 00 UTC 16 June, winds at DFW shift to the west at 15 kts (Fig. 5.7). At 12 UTC 15 June, 700-mb winds are advecting warm temperatures into both regions. Relatively moist air (as compared to surrounding regions) is already present in western Kansas and DFW. At 00 UTC 16 June, winds within the DFW region continue to advect warm temperatures into the region. Southwesterly winds just to the southwest of DFW are advecting more moisture into DFW.

The 12 UTC 15 and 00 UTC 16 June 2002 850-mb analyses are depicted in Figs. 5.8 and 5.9, respectively. At 12 UTC 15 June, south-southwesterly winds at 25 kts are transporting abundant moisture into the western Kansas region. By 00 UTC 16 June, moisture is also being advected into the DFW region, where winds at this time are southerly at 20 kts. This moisture and warm advection leads to rising motion and cloud and precipitation formation. A shortwave is also present just west of DFW at 00 UTC 16, and veering winds with height can be seen within the region during the analysis period.

Figure 5.10 shows the 12 UTC 15 June 2002 U.S. surface analysis. It is evident that a trough was propagating into the western Kansas region from the north. This trough, along

with instability from daytime heating, low-level moisture, and both speed and directional shear, provide the mechanism for squall line and subsequent MCS development.

DFW 00 UTC 16 June 2002 advecting winds were  $\sim 10$  kts from  $250^\circ$  (Fig. 5.11(a)), and the MCS total system motion was  $\sim 40$  kts from  $310^\circ$  from 05 to 07 UTC. Thus, storm propagation (i.e. total system motion minus advecting winds) was  $\sim 40$  kts from  $330^\circ$ . Storm relative winds at 8 km (i.e. 8 km 00 UTC 16 June sounding winds (Fig. 5.11(a)) minus total system motion) were  $\sim 20$  kts from  $100^\circ$  at DFW. Thus, it appears that this case study should evolve into a TS MCS, and closer inspection of its evolution (Fig. 5.1(c) and (d)) indicates that this storm system did, in fact, develop into a TS MCS. The 0-6 km vertical shear vector from the 00 UTC Dallas-Fort Worth sounding (Fig. 5.11(a)) was  $\sim 30$  kts from  $330^\circ$ . For details on how each of these values was calculated, please see Sec. 3.1.

The DFW 00 UTC 16 June 2002 sounding data (Fig. 5.11(a)) were used to determine altitudes of significant temperature levels for this MCS case study. From this sounding, the  $0^\circ\text{C}$  isotherm corresponds to 4.8 km, the  $-10^\circ\text{C}$  isotherm corresponds to 5.9 km, the  $-20^\circ\text{C}$  isotherm is located at  $\sim 7.6$  km, and the  $-40^\circ\text{C}$  isotherm is located at  $\sim 10.2$  km. These significant temperature levels may have been modified after the 00 UTC DFW sounding by environmental influences or thermodynamic processes within the MCS itself. This study assumes that these changes are insignificant because a  $2\text{-}3^\circ$  temperature change from the leading edge of the convective line to the back edge of the stratiform region (as seen in the 8 April 2002 MCS, Ch. 3) would only result in an altitude change  $< 0.5$  km. In addition, the wet bulb zero height, representing the actual height that liquid (frozen) hydrometeors would freeze (melt), was  $\sim 4.1$  km at 00 UTC 16 June (Fig. 5.11(a)). This wet bulb zero height was  $\sim 0.7$  km lower than the  $0^\circ\text{C}$  isotherm. Since this study's vertical resolution is 0.5 km, using

the 00 UTC 16 0 °C height for calculations involving the MCS convective line may cause slight errors. By 12 UTC 16 June 2002 (Fig. 5.11(b)), at which time the MCS had already propagated through the region, the 0 °C and wet bulb zero heights were ~4.8 km and ~4.3 km, respectively. Since this study's vertical resolution is 0.5 km, and the difference between the 0 °C height at 00 UTC 16 and the wet bulb zero height at 12 UTC 16 is ~0.5 km, using the 00 UTC 16 0 °C height value should not cause significant calculation errors within the stratiform region in this research.

### ***5.1.2 Storm Damage Reports***

The locations and types of storm damage within the U.S. from 12 UTC 15 to 12 UTC 16 June 2002 are shown in Fig. 5.12. By comparing this image to radar images (Fig. 5.1), it is evident that four tornadoes and many reports of hail and damaging winds were associated with this MCS. The four tornadoes listed occurred in Kansas in association with an isolated supercell that likely merged with the MCS at a later time. As the MCS propagated through Oklahoma and Texas, hail reports were more numerous along the western edge of the system. Within the DFW region, only damaging winds were reported from this MCS. These damaging winds are a result of the convective line evolving into a bow echo later in the period (Fig. 5.1(d)).

## **5.2 WSR-88D Radar**

### ***5.2.1 General MCS Characteristics***

The KFWS WSR-88D radar was operating properly in severe weather mode during the 2 hr time period (05-07 UTC) in which the 16 June 2002 MCS propagated through the region (Fig. 5.13(a)-(d)). Radar images show that the leading convective line becomes more

organized and weakens slightly as it propagates into the region (Fig. 5.13(a)-(b)). An outflow boundary associated with the convective bow echo is seen ahead of the leading convective line in Fig. 5.13(a)-(c). This gust front may have caused some of the wind damage that was reported between 05 UTC and ~06:24 UTC (Fig. 5.12). The leading edge of the trailing stratiform region can barely be seen at 05:24 UTC (Fig. 5.13(a)). As it propagates into the region (Fig. 5.13(b)-(c)), small areas of dry air are advected into the outer edges of the stratiform region. This southwest-northeast oriented MCS propagates quickly through the region, and by 06:54 UTC (Fig. 5.13(d)), the convective line has propagated almost entirely out of the radar's viewing range.

Figure 5.14(b) is a vertical cross-section taken at 06:24 UTC through the 40° counterclockwise rotated image shown in Fig. 5.14(a). This vertical cross-section passes through the MCS's stratiform, transition, and convective regions at  $y = 26$  km. A characteristic radar bright band is evident within the stratiform region at ~4.5 km. The transition zone is indicated by weak reflectivity echoes ( $\leq 30$  dBZ) between the stratiform and convective regions. The convective line is characterized by moderate to high reflectivity echoes (~40-55 dBZ) and hence, heavy surface precipitation. Individual cells along the front edge of the convective line appear to tilt eastward with height at ~56° from the horizontal. This forward tilt is a result of the strong northwesterly upper-level winds, which also forms a large ( $> 60$  km) forward anvil in the upper levels of the MCS. At 06:24 UTC, the MCS extends to an altitude of 13 km and a width  $> 200$  km with radar reflectivity echoes  $\geq 5$  dBZ.

### ***5.2.2 Partitioned Echo Volume Aloft***

Temporal trends in convective and stratiform region total echo volume aloft calculated using various reflectivity and temperature layer thresholds are examined for the 16

June 2002 MCS. The two main temperature layers examined include 0 °C to -40 °C and -10 °C to -40 °C, and the various reflectivity echo thresholds include 25-, 30-, 35-, 40-, 45-, 50-, and 55-dBZ.

The temporal trends in convective region echo volume aloft using various thresholds are from 05 to 07 UTC 16 June 2002. Figure 5.15, for example, compares the convective region echo volume aloft trends  $\geq 25$  dBZ,  $\geq 30$  dBZ,  $\geq 35$  dBZ, and  $\geq 40$  dBZ for the 0 °C to -40 °C temperature layer. The correlation coefficient between any two of these four trends is  $> 0.90$ , with the exception of the correlation coefficient between the  $\geq 25$ -dBZ and  $\geq 40$ -dBZ trends ( $\sim 0.85$ ). Echo volume aloft  $\geq 35$  dBZ, in particular, is highly correlated to all other echo thresholds.

The echo volume aloft trend correlation between the two temperature layer thresholds analyzed in this study is also high. Figure 5.16, for example, compares the convective echo volume aloft trend  $\geq 35$  dBZ between the 0 °C to -40 °C and the -10 °C to -40 °C temperature layers. The correlation coefficient between these two lines is 0.93. Since the echo volume aloft trends using different reflectivity and temperature layer thresholds are all similar, and the 35-dBZ echo threshold correlates best with all other reflectivity echo thresholds, the echo volume results using the 35-dBZ threshold for the 0 °C to -40 °C temperature layer will be compared to other reflectivity and lightning trends in this study.

The convective region total echo volume aloft  $\geq 35$  dBZ between 0 °C and -40 °C (Fig. 5.16) depicts the propagation of the convective line into, through, and beyond the analysis volume. From 05 UTC to 06:24 UTC, most of the convective line is within the radar's viewing range (Fig. 5.13), and hence, total convective echo volume aloft is large (Fig. 5.15). The peak echo volume aloft during the analysis period is 10 193.2 km<sup>3</sup> and occurs at

~05:15 UTC. Average echo volume aloft within this time period is 9253.5 km<sup>3</sup>. After ~06:24 UTC, the convective line begins to propagate beyond the viewing range of the KFWS radar, resulting in the observed steady decrease in total convective echo volume aloft through the end of the analysis period (Fig. 5.16).

Embedded within the convective line, there is evidence of convective strength evolution based on the echo volume aloft trend (Fig. 5.16). From this trend, the convective line appears to be strongest from 05:00 to 05:30 UTC. Around 05:45 UTC, a noticeable decrease in echo volume aloft is evident. Afterwards (from ~06 to 06:30 UTC), the convective line strengthens again, although this maximum is not quite as large as the initial convective echo volume aloft peak.

Figure 5.17(a)-(d) shows the low-level reflectivity structure of the convective line before, during, and after the local minimum in convective echo volume aloft (~05:45 UTC). Similar to the echo volume aloft trend, these four images reveal that the convective line is weakening from 05:40 UTC (Fig. 5.17(a)) to 05:44 UTC (Fig. 5.17(b)) to 05:54 UTC (Fig. 5.17(c)), but it restrengthens around 06:09 UTC (Fig. 5.17(d)). Therefore, both the total convective echo volume aloft trend and the low-level reflectivity images are consistent in the way they depict the strength evolution of the MCS.

The various stratiform region total echo volume aloft trends  $\geq 25$  dBZ,  $\geq 30$  dBZ, and  $\geq 35$  dBZ for a layer between 0 °C and -40 °C is shown in Fig. 5.18. These three evolutions appear similar to one another. In fact, the correlation coefficient between any two of these three lines is greater than 0.99. Similarly, stratiform total echo volume aloft trend  $\geq 25$  dBZ,  $\geq 30$  dBZ, and  $\geq 35$  dBZ for a layer between -10 °C and -40 °C is shown in Fig. 5.19. Unlike their 0 °C and -40 °C layer counterparts, these three evolutions differ from one another. The

correlation coefficient between any two of these three lines is less than 0.77. Comparing Fig. 5.18 to Fig. 5.19, the echo volume aloft trends appear to be different, except for the two trends when the radar reflectivity echo constraint is  $\geq 25$  dBZ. These two evolutions have a correlation coefficient of approximately 0.86. The differences in echo volume aloft trends for different thresholds are not surprising because each trend is responding to the concentrations of different size particles, and these concentrations vary in the stratiform region.

The stratiform total echo volume aloft trends  $\geq 25$  dBZ between 0 °C and -40 °C (Fig. 5.18) and between -10 °C and -40 °C (Fig. 5.19) indicate the propagation of the stratiform region into the KFWS radar viewing area. Average total echo volume aloft in the 0 °C to -40 °C layer is 17 686.6 km<sup>3</sup>, which is over 10 times greater than the average echo volume aloft in the -10 °C to -40 °C layer (~1701.7 km<sup>3</sup>). Similarly, peak total echo volume aloft in the 0 °C to -40 °C layer and the -10 °C to -40 °C layer are 31 795.3 km<sup>3</sup> (at 06:45 UTC) and 3195.2 km<sup>3</sup> (at 06:30 UTC), respectively. Comparing these graphs to low-level reflectivity images (Fig. 5.13), it is evident that the steady increase in echo volume aloft throughout the period is due to the propagation of a higher percentage of the stratiform region into the analysis area. Similar to the convective region, the stratiform region's strength changes throughout the period. For example, both the low-level reflectivity images (Fig. 5.17) and the stratiform total echo volume aloft trends (Figs. 5.18-5.19) show some weakening at ~05:45 and 06 UTC. Overall, this MCS is not well suited for Eulerian analysis because it moved so quickly through the analysis region.

### ***5.2.3 Partitioned Rainfall Rates***

Various low-level reflectivity thresholds are compared to one another to determine the sensitivity of rainfall rate to low reflectivity thresholds in the 16 June 2002 MCS. The convective and stratiform region rainfall rate trends using 5-dBZ, 10-dBZ, and 20-dBZ low-level reflectivity echo thresholds are shown in Figs. 5.20-5.21, respectively. Within the convective region, all three reflectivity thresholds show the same general trends. Within the stratiform region, however, the 20-dBZ low-level reflectivity echo threshold differs from the other two echo thresholds. The stratiform region trends in the 20-dBZ threshold correspond to the evolution of the stratiform region itself, whereas the other two thresholds are influenced more by low reflectivity values. This study will analyze the convective and stratiform region rainfall rates using only a 20-dBZ low-level reflectivity echo threshold in order to minimize the effects due to propagation.

The convective rainfall rate trend calculated from convective region reflectivity echoes  $\geq 20$  dBZ is shown in Fig. 5.22. Rainfall rates within the convective region decrease from an initial maximum value of  $22.1 \text{ mm hr}^{-1}$  at 05 UTC to a local minimum value of  $13.1 \text{ mm hr}^{-1}$  at 06 UTC. This decrease is a result of the weakening of the convective line until  $\sim 05:54$  UTC (Fig. 5.17). After  $\sim 06$  UTC, the convective line begins to intensify, and another peak in rainfall rates of  $16.8 \text{ mm hr}^{-1}$  is evident around 06:45 UTC. Afterwards, the convective line begins to propagate out of the KFWS radar viewing range, resulting in a decrease in convective rainfall rates. Average rainfall rates for the convective region during this period (05-07 UTC) are  $16.7 \text{ mm hr}^{-1}$ . Temporal trends in convective rainfall rates tend to lag trends in convective echo volume aloft (Fig. 5.16) by 15-30 min.

Figure 5.22 depicts the stratiform rainfall rate trend from 05 to 07 UTC calculated from stratiform region reflectivity echoes  $\geq 20$  dBZ. The stratiform region rainfall rate increases from an initial minimum value of  $3.4 \text{ mm hr}^{-1}$  as the stratiform region begins to propagate into the analysis region. The rainfall rate continues to increase to a maximum value of  $\sim 5.2 \text{ mm hr}^{-1}$  (over 4 times smaller than the peak convective rainfall rate) by  $\sim 5:45$  UTC, at which time the stratiform region is strengthening. Afterwards, rainfall rates decrease, first slowly (from 05:45 to 06:30 UTC) and then more rapidly (after 06:30 UTC) as the stratiform region continues to evolve. The average rainfall rate for the stratiform region during this period is  $4.5 \text{ mm hr}^{-1}$  (almost 4 times smaller than average convective rainfall rate). Increases (decreases) in stratiform rainfall rate tend to lag increases (decreases) in stratiform total echo volume aloft (Figs. 5.18 and 5.19) by 15 min during the first hour of analysis. During the second hour of analysis, however, stratiform total echo volume aloft increases to a maximum value at  $\sim 6:30$ - $6:45$  UTC while the stratiform rainfall rate decreases.

#### ***5.2.4 Dual-Doppler Analysis***

Reasonable three-dimensional wind results could be obtained via synthetic dual-Doppler analysis of the 16 June 2002 MCS because this MCS remained quasi-steady while both the convective and stratiform regions were well within viewing range. The 05:49 UTC and 06:49 UTC radar volumes were chosen for this analysis. The resulting dual-Doppler baseline for this case study is 72 km because the MCS was propagating at  $\sim 72 \text{ km hr}^{-1}$  and one hour of time passed between the first and second radar volume scans. Horizontal and vertical grid spacing for these two volume scans were set to 2.0 km and 1.0 km, respectively. Also, the horizontal and vertical radii of influence for these two volume scans were set to 6.0 km and 3.0 km, respectively, to fill gaps in the dataset, particularly at upper levels. Leise

filtering (a method of smoothing the data) was also performed during the CEDRIC processing. The differential advection of storm motion in CEDRIC was not performed on any of the synthetic dual-Doppler analyses presented here because fewer errors resulted when this parameter was not used. Also, the minimum beam crossing angle was set to  $30^\circ$  to avoid large errors in the three-dimensional wind field that result from beam crossing angles less than this value. Top-down integration was performed on the continuity equation to calculate the u, v, and w components of the three-dimensional wind field. The three-dimensional vertical motions determined from CEDRIC processing represent a combination of hydrometeor fall velocity and the vertical motion of air.

Composite results from synthetic dual-Doppler analysis of the June 2002 MCS indicate that different vertical and horizontal motions were dominant in different MCS regions. Within the stratiform region, weak upward motion ( $0-0.4 \text{ ms}^{-1}$ ) was present above the freezing level while downward motion ( $0 \text{ ms}^{-1}$  to  $-0.3 \text{ ms}^{-1}$ ) was present below the freezing level (Fig. 5.23). The weak upward motion was generally located along the back of the stratiform region (not shown). Within the convective region, upward motions were stronger than downward motions (Fig. 5.23). Mesoscale front-to-rear flow at mid- to upper-levels behind the convective line was on the order of  $10 \text{ ms}^{-1}$  (further discussed in Section 5.4.2.2).

### **5.3 NLDN CG Lightning Flash Trends**

#### ***5.3.1 Total Trends***

Figure 5.24 shows the trends for the CG lightning flash rate and +CG percent in the portion of the 16 June 2002 MCS that occurred within the KFWS radar's range from 05 to 07

UTC. This MCS averaged 58.1 CG lightning flashes  $\text{min}^{-1}$ , 3.7% of which were positive. The CG lightning flash rate increased from 05 to 05:45 UTC and remained high until ~06:30 UTC. Peak total CG flash rates of ~67.9 flashes  $\text{min}^{-1}$  occurred at 06 UTC and again at 06:30 UTC. The convective region was present within the radar's viewing range during the observed period of high flash rates (Fig. 5.13). When the total CG flash rate increased, the percentage of +CG flashes decreased. As the convective line propagated out of the region (06:30-07 UTC) (Fig. 5.13), the CG flash rate dramatically decreased and the percent of +CGs increased (Fig. 5.24). During the two-hour analysis period, the percent of +CGs increased to a peak value of ~4.6% at 6:15 UTC and then again at 07 UTC. The overall CG flash trend lagged convective echo volume aloft  $\geq 35$  dBZ within the 0 °C to -40 °C and -10 °C to -40 °C temperature layers by 15-30 min (Fig. 5.16).

Figure 5.25 shows the evolution of peak positive and negative currents resulting from CG lightning flashes that occurred within the KFWS radar's range from 05 to 07 UTC 16 June 2002. Average peak positive and negative currents for the time period are 27.9 kA and -13.3 kA, respectively. Positive peak current increases throughout the period, especially when the stratiform region begins to propagate into the analysis region at ~05:45 UTC (Fig. 5.13). A peak positive current of 32.6 kA occurs at 06:30 UTC, which is approximately the same time as stratiform region echo volume aloft  $\geq 25$  dBZ peaks within the -10 °C to -40 °C temperature layer (Fig. 5.19). A peak negative current of -14.8 kA occurs at 05:30 UTC, which is approximately the same time as 1) stratiform region echo volume aloft  $\geq 25$  dBZ peaks within the -10 °C to -40 °C temperature layer (Fig. 5.19), 2) convective region echo volume aloft  $\geq 25$  dBZ peaks within the 0 °C to -40 °C temperature layer (Fig. 5.15), and 3)

convective region echo volume aloft  $\geq 30$  dBZ peaks within the 0 °C to -40 °C temperature layer (Fig. 5.15).

### **5.3.2 Partitioned Trends**

A 0.5-km CAPPI image of the 16 June 2002 MCS is overlaid with NLDN-detected CG lightning flashes at 05:54 UTC (Fig. 5.26). The convective region has a large number of CG lightning flashes, most of which have negative polarity. Relatively few CG flashes occur within the stratiform region. Also, a higher percentage of +CG flashes are produced within the stratiform region than within the leading convective line (Fig. 5.26). CG lightning flashes occur in relatively high reflectivity cores within the convective and stratiform regions, and few flashes exist in the transition zone. In addition, +CGs were associated with the forward anvil of the MCS (not shown).

Figure 5.27 shows the convective, stratiform, and total NLDN-detected CG lightning trends for flashes that occurred in the analysis volume from 05 to 07 UTC. The convective CG flash rate trend is highly correlated to the total CG flash rate trend because the convective region produces ~93% of the total CG flashes in the analysis region within this 2-hr period. The observed decrease in CG lightning activity during the last half hour of the analysis period reflects the propagation of the convective line out of the region. Stratiform region CG lightning flash activity increases throughout the period to an observed peak flash rate at 06:30 UTC, at which time the stratiform region dominates the analysis area (Fig. 5.13).

The convective region total and percent positive CG flash rate trends within the KFWS radar viewing range from 05 to 07 UTC 16 June 2002 are shown in Figs. 5.27 and 5.28, respectively. A peak convective CG flash rate of 62.9 flashes  $\text{min}^{-1}$  occurs at ~06 UTC. The convective region averages 53.6 flashes  $\text{min}^{-1}$  for the 2-hr analysis period, and ~2.0% of

these flashes are positively charged. Throughout the period, the convective region total CG flash rates tend to lag the convective total echo volume aloft  $\geq 25$  dBZ,  $\geq 30$  dBZ, and  $\geq 35$  dBZ within the 0 °C to -40 °C temperature layer by 15-30 min (Figs. 5.15-5.16) and the 0.5-km reflectivity strength by  $\sim 15$  min (Fig. 5.17).

The stratiform region total and percent positive CG flash rate trends are shown in Fig. 5.27 and 5.28, respectively. The stratiform region averages  $\sim 4.5$  CG flashes  $\text{min}^{-1}$  during the analysis period, and 26.5% of these CG flashes are positively charged. A peak stratiform CG flash rate of 8.4 flashes  $\text{min}^{-1}$  occurs at 06:30 UTC, at which time the stratiform region covers a large percentage the analysis area (Fig. 5.13(c)). The stratiform CG flashes lag the stratiform region total echo volume aloft  $\geq 25$  dBZ within the -10 °C to -40 °C temperature layer by 15 min (Fig. 5.18) during the first hour, but these two parameters correlate well during the second hour of analysis. The stratiform rainfall rate trend (Fig. 5.22) and the stratiform CG flash rate trend are similar, but the largest rainfall rate peak corresponds to the second largest CG flash rate peak, and vice versa.

The trends in convective and stratiform region peak positive and negative CG lightning flash currents are shown in Fig. 5.29. The stratiform region has larger peak positive and negative currents than the convective region. Average peak positive and negative currents in the stratiform region are 31.5 kA and -18.0 kA, respectively, whereas the average peak positive and negative currents in the convective region are 22.8 kA and -13.1 kA, respectively. Thus, both average peak positive and negative CG lightning currents are greater in the stratiform region than in the convective line.

## **5.4 LDAR II Data**

### ***5.4.1 Network's Performance***

The LDAR II network was operating optimally during the 05 to 07 UTC 16 June 2002 MCS. The detection efficiency for this case study is shown in Fig. 5.30. Over 90% of lightning flashes were detected from the network's center to a range of ~120 km. Therefore, detection efficiency problems should be minimal.

### ***5.4.2 VHF Source Trends***

#### **5.4.2.1 Total Trends**

Fig. 5.31 shows the total LDAR II source trend from 05 to 07 UTC 16 June 2002 within the analysis volume. VHF source rate activity rapidly increases from 05 UTC to 05:45 UTC. At 05:45, the largest VHF source rate occurs ( $19\,336.7$  sources  $\text{min}^{-1}$ ). Afterwards, the source rate decreases rapidly throughout the rest of the analysis period. The average source rate over the two-hour period is  $10\,444.0$  sources  $\text{min}^{-1}$ . This trend corresponds best with the stratiform region rainfall rate trend, which also shows a peak in activity at ~5:45 UTC (Fig. 5.22). The similarity between these two graphs could be coincidental because both trends are dominated by movement through the network. The convective rainfall rate trend, which has a minimum at ~06 UTC (Fig. 5.22), is inversely related to the LDAR II source trend. Total and convective NLDN-detected CG lightning flash trends are similar to the LDAR II source trend from 05 to 05:45 UTC, but afterwards, the CG flash rates remain relatively large until 06:30 UTC (Fig. 5.27) whereas the LDAR II source rate rapidly decreases after 05:45 UTC.

#### 5.4.2.2 Partitioned Trends

An example of the two-dimensional spatial distribution of LDAR II source locations within the 16 June 2002 MCS is shown in the 06:19 UTC low-level (0.5 km) CAPPI image of reflectivity overlaid with 5 min of source data (centered on the time of the radar image) (Fig. 5.32). Most sources tend to occur in regions of moderate reflectivity echoes (35-45 dBZ), especially within the leading convective line. Sources are also produced along the leading edge of the stratiform region, within the transition zone, and within the forward anvil of the MCS. The six lines drawn through different parts of the MCS in this image represent the locations where various vertical cross-sections have been taken to further analyze dominant LDAR II source locations.

Two vertical cross-section examples through the front and back edges of the leading convective line at 06:19 UTC are shown in Fig. 5.33(a) and (b), respectively. Comparing these two images, it is evident that the cells within the front edge have stronger updrafts, larger reflectivity echoes, and more LDAR II sources than the cells associated with the back edge of the convective line. Therefore, the cells along the front edge are stronger than the cells along the back edge of the convective region. Two enhanced regions of LDAR II sources are found in both images. The upper source region, located near the  $-40\text{ }^{\circ}\text{C}$  level ( $\sim 10.2\text{ km}$  altitude), could be the upper positive charge region, and the lower source region, located in the  $0\text{ }^{\circ}\text{C}$  to  $-20\text{ }^{\circ}\text{C}$  layer ( $\sim 4.8$  to  $7.6\text{ km}$  altitude), could be the main negative and/or lower positive charge region(s) theorized in the non-inductive charging mechanism of electrification. Sources within the lower region tend to occur at higher altitudes above regions of enhanced reflectivity aloft than those sources within convective cells with weaker updrafts. Thus, the average altitude of the lower enhanced source region within the back

edge of the convective line (Fig. 5.33(b)) is ~0.5-1.0 km lower than the altitude of the lower enhanced source region within the front edge of the convective line (Fig. 5.33(a)). Reasons for the high altitude source locations (> 15 km) that appear in both images are beyond the scope of this research.

Two vertical-cross sections through the front and back edges of the stratiform region at 06:19 UTC are shown in Fig. 5.34(a) and (b), respectively. It is evident from these two images that more LDAR II sources are produced within the front edge than the back edge of the stratiform region. A radar bright band can be seen in both images just below the 0 °C temperature level (<4.8 km altitude). An enhanced region of sources is evident in both images in the 0 °C to -10 °C layer (~4.8 to 5.9 km altitude) just above the bright band. Another enhanced region of sources is found around -30 °C (~8.4 km altitude) in both vertical cross-section images. The LDAR II source that was produced at ground level in Fig. 5.34(a) and (b) is most likely associated with a CG lightning flash.

Two line-normal vertical-cross sections through the stratiform region, transition zone, and leading convective line of the June 2002 MCS at 06:19 UTC are shown in Fig. 5.35(a) and (b). The vertical cross-section in Fig. 5.35(b) passes through an enhanced reflectivity “bridge” through the transition zone, whereas the image in Fig. 5.35(a) passes through a low reflectivity region of the transition zone. Within the convective region of both images, one dominant source region exists within the 0 °C to -20 °C layer (~4.8 to 7.6 km altitude), and another dominant source region exists near the -40 °C level (~10.2 km altitude). LDAR II sources near the -40 °C level in both images tend to slope downwards from a peak altitude above the most intense convective cells towards the stratiform region just above the radar bright band. This enhanced source region could be associated with charge advection from

the convective region into the stratiform region. This charge advection may help to electrify the stratiform region. Another enhanced region of sources, disconnected from the downward sloping charge layer, exists within the back edge of the trailing stratiform region at  $\sim -35$  °C to  $-40$  °C ( $\sim 9.0$  to  $10.2$  km altitude) in Fig. 5.35(b). This enhanced source region, located within a weak mesoscale updraft (not shown), could be associated in situ charging within the stratiform region. Thus, in situ charging may also help to electrify the stratiform region.

Even though the LDAR II network was operating optimally during the 16 June 2002 MCS, evidence of the network's limitations due to its line of sight detection can be seen in the two vertical cross-sectional images taken through the convective line (Fig. 5.33(a)-(b)). Lower sources concentrations (or no sources at all) are detected within the lower region of enhanced sources where the y-component of distance from the KFWS radar is  $< -20.0$  km. Low altitude sources that occur at large distances ( $> 80$  km) from the network are less likely to be detected than low altitude sources closer to the network because source detection is based on a line of sight technique.

The convective and stratiform region LDAR II source trends from the portion of the 16 June 2002 MCS that passed through this study's analysis volume from 05 to 07 UTC are shown in Fig. 5.36. The average convective source rate for the period is  $9448.5$  sources  $\text{min}^{-1}$ , almost 9.5 times the average stratiform source rate ( $995.5$  sources  $\text{min}^{-1}$ ). The convective region source rate trend most closely resembles the total LDAR II source trend (Fig. 5.31), and the stratiform region source rate trend most closely resembles the stratiform NLDN-detected CG lightning flash trend (Fig. 5.27). The peak in convective source rate activity ( $18\,836.3$  sources  $\text{min}^{-1}$ ) occurs at 05:45 UTC, whereas the peak in stratiform source rate activity ( $2195.0$ ) sources  $\text{min}^{-1}$  occurs at 06:30 UTC.

Figures 5.37 and 5.38 show the dominant source altitudes within the convective and stratiform regions, respectively. Two dominant source regions exist within the convective region. These two electrically-active regions, at 5-6 km and 9-11 km, correspond approximately to the 0 °C to -15 °C layer and the -40 °C level, respectively. The lower electrically-active region could be associated with the main negative and/or lower positive charge region(s) theorized in the non-inductive charging mechanism. The upper region is most likely associated with the upper positive charge layer of an electrically active thunderstorm. Within the stratiform region, one dominant electrically-active center peaks at 6-7 km (-10 °C to -20 °C). This dominant electrically-active center is associated with the primary source region in Fig. 5.35(a) that slopes downwards and rearwards from ~ -40 °C (~10.2 km altitude) in the convective line to ~0 °C (~ 4.8 km altitude) in the stratiform region just above the radar bright band.

Line-normal composite images of average radar reflectivity and the total LDAR II sources that occurred within the 200 km × 200 km × 20 km KFWS radar volume for various times during the 16 June 2002 MCS are shown in Figs. 5.39-5.45. During the beginning of the analysis period (05:20 UTC), the same two dominant source regions evident in previous figures exist within the convective line at ~5 km (~ 0 °C to -10 °C) and 10 km (~ -40 °C) (Fig. 5.39). Sources produced above intense convective cores are located at higher altitudes than those sources outside of these intense convective cores. The leading edge of the stratiform region is barely visible at this time.

By 06:09 UTC, the stratiform region has entered the analysis region, and the upper enhanced LDAR II source region now slopes downward (at ~6° from the horizontal) from the leading convective line into the stratiform region (Fig. 5.40). This upper source region

appears to split into two smaller regions as it descends towards the radar bright band within the stratiform region. Given that storm relative front-to-rear flow is  $\sim 10 \text{ ms}^{-1}$ , and aggregates behind the convective line have downward motions of  $\sim 1.0 \text{ ms}^{-1}$ , these aggregates would follow the same trajectory from the convective line to the stratiform region as LDAR II sources in this downward-sloping enhanced source region (as seen in Fig. 5.46). Therefore, this observed enhanced source region could result from advection of charged aggregates from the convective line to the stratiform region. Furthermore, this charge region is most likely positive because 1) the convective upper charge region of a normal dipole is an area of upper positive charge, and 2) in the VHF, negative discharge in the positive charge region is noisier than positive discharge in the negative charge region. This main positive charge region is advected into lower altitudes in the stratiform region, establishing an inverted dipole and resulting in a high percentage of +CG flashes.

Five minutes later, at 06:14 UTC, another enhanced region of LDAR II sources has developed at  $\sim 10 \text{ km}$  altitude ( $\sim -40 \text{ }^\circ\text{C}$ ) along the back of the stratiform region (Fig. 5.41). These sources appear to be associated with a weak mesoscale updraft ( $\sim 0\text{-}0.4 \text{ ms}^{-1}$ ) present in the back of the stratiform region above  $0 \text{ }^\circ\text{C}$  ( $> 4.8 \text{ km}$  altitude) (not shown). Either in situ charging or charge advection could have caused the maximum source region and hence, stratiform region electrification.

By 06:19 UTC (Fig. 5.42), the concentration of LDAR II sources within the leading convective line has decreased, although the number of sources within the stratiform region above the bright band has increased. The isolated area of high source concentration along the back half of the stratiform region has decreased in size at this time. At 06:29 UTC, a decrease in convective LDAR II source concentrations, especially within the dominant lower

source region, is evident (Fig. 5.43). The number of sources present above the expanding bright band, which is indicated by radar reflectivity contours, remains relatively high. The other isolated area of sources within the stratiform region has elongated and increased in concentration between 06:19 UTC and 06:29 UTC.

The LDAR II source concentration within the downward sloping source region from the convective line and into the stratiform region becomes more uniform by 06:34 UTC (Fig. 5.44). Corresponding to the dramatic increase in NLDN-detected stratiform CG lightning flashes (Fig. 5.27), two small regions of LDAR II sources have formed above the bright band, and the isolated stratiform charge region from previous images is now located within 10 km of these two charge regions. Within the convective region, the lower enhanced source region is practically nonexistent at this time. This source decrease could explain the significant decrease in convective NLDN-detected CG lightning flashes produced (Fig. 5.27) beginning at this time. The practically nonexistent lower electrically-active source region, however, could be caused by the decreased LDAR II detection efficiency as the convective line propagates further away from the network's center.

By 06:44 UTC, the lower convective LDAR II source region has disappeared, but the upper convective LDAR II source region can still be seen sloping downward from the convective line towards the stratiform region (Fig. 5.45). The isolated stratiform source region has rapidly decreased from 06:34 UTC to 06:44 UTC so that two source regions are no longer evident above the radar bright band (Fig. 5.45). This decrease may be caused by decreased detection efficiency as the MCS propagates away from the LDAR II network.

### **5.4.3 VHF Flash Origin Trends**

#### **5.4.3.1 Total Trends**

The LDAR II flash origin activity trend (as determined from the modified NASA algorithm) for the portion of the 16 June 2002 MCS that passed through the analysis region from 05 to 07 UTC is shown in Fig. 5.47. Flash origin activity increases initially from 2197.1 flashes  $\text{min}^{-1}$  to 4178 flashes  $\text{min}^{-1}$  at 06 UTC. Afterwards, the flash rate decreases rapidly to a minimum value of 1292.3 flashes  $\text{min}^{-1}$  by the end of the analysis period. The average LDAR II flash origin rate during this 2-hr period is 3043.8 flashes  $\text{min}^{-1}$ . LDAR II flash origin trends are similar to the convective and total CG lightning flash rate trends, in which an observed peak in lightning activity is also observed at 06 UTC (Fig. 5.27). These trends oppose the convective rainfall trends (Fig. 5.22), in which decreased rainfall activity is observed beginning at 05 UTC and continuing to a minimum at 06 UTC.

Peaks in IC:CG ratio have been correlated to storm intensity, and strong updrafts have been suggested to enhance IC flash rates but decrease CG flash rates by carrying the lower negative charge center to higher altitudes (MacGorman et al. 1989). Figure 5.48 depicts the IC:CG flash ratio trend for the 16 June 2002 MCS from 05 to 07 UTC. The IC:CG ratio remains large throughout the 2-hr analysis period and peaks between 05:30 and 06:15 UTC, at which time both the convective and stratiform regions are within the analysis volume and LDAR II source rates are largest. The two local maximum IC:CG ratios (60.9 and 60.6) occur at 05:30 UTC and 06:00 UTC, respectively. The average IC:CG ratio during the two-hour analysis period is 49.8.

### 5.4.3.2 Partitioned Trends

LDAR II flash origin locations (as determined by the modified NASA algorithm) for the 16 June 2002 MCS overlaid on low-level radar reflectivity at 06:19 UTC are shown in Fig. 5.49. Flash origins are preferentially located in the same general locations within the MCS as LDAR II sources (Fig. 5.32). The same six vertical cross-sections, now overlaid with LDAR II flash origins instead of sources, are depicted in Figs. 5.50-5.52. LDAR II flash origins appear to be located at similar height levels and show the same general characteristics as LDAR II sources, although the flash density in each image is not as large as the source density, making it difficult to discern these characteristics using LDAR II flash origins.

The convective and stratiform LDAR II flash origin trends (as determined by the modified NASA algorithm) for the portion of the 16 June 2002 MCS that passed through this study's analysis region from 05 to 07 UTC is depicted in Fig. 5.53. The average convective LDAR II flash rate ( $\sim 2542.5$  flashes  $\text{min}^{-1}$ ) is over five times larger than the average stratiform flash rate ( $\sim 501.2$  flashes  $\text{min}^{-1}$ ). The convective flash rate peak of 3730.3 flashes  $\text{min}^{-1}$  occurs at 06 UTC, and the stratiform flash rate peak of 991.2 flashes  $\text{min}^{-1}$  is observed at 6:30 UTC. The convective LDAR II flash origin rate trend closely resembles total LDAR II flash origin trend. These convective flash rates lag both the convective and total LDAR II source rates by  $\sim 15$  min, possibly because of decreased detection efficiency at longer ranges. As the MCS propagates away from the LDAR II network, the decreased source detection efficiency causes the modified NASA algorithm to subset sources into a fictitiously large number of flashes based on its spatial and temporal subsetting technique. The artificial division of one real flash into two or more artificial flashes causes a nonphysical flash rate

peak. The convective CG lightning flash trends are similar to convective LDAR II flash origin trends for the first hour, but unlike the CG flashes, the LDAR II flash origins do not peak again after their 06 UTC peak. In the stratiform region, the LDAR II flash origin trend closely resembles both the CG flash trend and the LDAR II source trend.

Figures 5.54 and 5.55 show the dominant LDAR II flash origin altitudes within the convective and stratiform regions of the 16 June 2002 MCS, respectively. Similar to the convective LDAR II sources, convective LDAR II flash origins are generally located at two distinct height levels, 5-6 km (0 °C to -15 °C) and 9-11 km (-40 °C). The upper electrically-active region may be associated with the upper positive charge region, and the lower electrically-active region may be associated with the main negative and/or lower positive charge region(s) that are important for non-inductive charging. Within the stratiform region, one dominant electrically active region exists at 6-7 km (-10 °C to -20 °C). This dominant electrically-active center is associated with the primary LDAR II flash region evident in Fig. 5.52(a) that slopes downwards and rearwards from approximately -40 °C (~10.2 km altitude) in the convective line into the stratiform region to temperatures as warm as ~0 °C (~ 4.8 km altitude) just above the radar bright band.

The convective and stratiform region IC:CG ratio trends for the portion of the 16 June 2002 MCS that passed through the analysis region from 05 to 07 UTC are shown in Fig. 5.56. It is evident from this graph that the IC lightning percentage is higher in the stratiform region than in the convective region. The average stratiform region IC:CG ratio is 139.7:1 whereas the average convective region ratio is 43.6:1 within this MCS. The convective IC:CG trend closely resembles the total IC:CG trend (Fig. 5.48). If this IC:CG ratio difference between the two regions is physically based (and not a result of detection

efficiency issues), it suggests that a greater percentage of IC flashes are produced within the stratiform region than in the convective line. It may also suggest that dominant charge regions within the stratiform region are located at higher altitudes than charge regions within the convective line, and therefore, more charge is needed to produce a CG flash in the stratiform region.

The IC:CG ratio differences between the two regions could also result from errors in the LDAR II flash algorithm. Since 1) lightning within the stratiform region is probably longer and more branched than lightning within the convective line, and 2) the mean distance from the LDAR II network's center to the stratiform region is larger than the distance from the network to the convective line, the flash algorithm may artificially create more flashes in the stratiform region than in the convective line.

## **5.5 Summary**

The portion of the 16 June 2002 TS MCS that passed through the DFW analysis region from 05 to 07 UTC provided a unique opportunity to examine the three-dimensional electrical and microphysical characteristics of an MCS. Both the KFWS WSR-88D radar and the LDAR II network were working optimally during this case study, minimizing problems associated with detection efficiency.

Temporal trends in echo volume aloft, rainfall rates, NLDN-detected CG flashes, and LDAR II-detected source and flash origin rates within the convective and stratiform regions of the June MCS were analyzed. Within the convective region, the local maxima and minima in echo volume aloft  $\geq 25$  dBZ,  $\geq 30$  dBZ, and  $\geq 35$  dBZ in the 0 °C to -40 °C temperature layer (Figs. 5.15-5.16) precede the analogous maxima and minima in 1)

convective rainfall rates (Fig. 5.22), 2) low-level reflectivity convective strength evolution (Fig. 5.17), and 3) NLDN-detected total and convective CG lightning flashes (Fig. 5.27) by approximately 15-30 min during the entire period. These echo volume aloft trends precede the analogous maxima and minima in convective LDAR II source (Fig. 5.36) and flash (Fig. 5.53) rates by ~15-30 min during the first hour of analysis. However, no secondary peak in LDAR II source and flash rates exists to coincide with the secondary peak in convective echo volume aloft.

The lack of a secondary peak in convective LDAR II source/flash trends may be attributable to detection efficiency. As the convective line propagates away from the LDAR II network, LDAR II source detection efficiency rapidly decreases. During the second hour of analysis, the convective line has propagated far enough away from the LDAR II network that the true number of lightning-related sources cannot be detected. Therefore, a secondary peak in LDAR II source/flash rates goes is not detected at this later time. If the network had a larger detection range, it is likely that a secondary peak in the convective LDAR II source/flash trends would have lagged the secondary peak in the convective echo volume aloft trends.

Even though over 90% of flashes can be detected by the LDAR II network, it is still possible for detection efficiency to affect the source rate and the flash rate algorithm. Flashes determined using the modified NASA algorithm are not the same as the true flashes that a lightning detection network detects. These LDAR II flashes were determined using the modified NASA algorithm, which cannot reproduce the complex nature of a lightning flash and should only be used to determine overall features of a storm.

Within the stratiform region, the trend in echo volume aloft  $\geq 25$  dBZ within the -10 °C to -40 °C temperature layer closely follows three other stratiform region trends: 1) NLDN-detected CG lightning flashes (Fig. 5.27), 2) LDAR II sources (Fig. 5.36), and 3) LDAR II flash origins (Fig. 5.53). The stratiform region rainfall rate trend (Fig. 5.22) does not correspond to other stratiform microphysical and electrical trends, as evidenced by the rainfall rate peaking ~45 min earlier than these other processes. Comparing the two regions, the two local maxima in echo volume aloft within the stratiform region (Fig. 5.19) occur ~15 min after the two local maxima observed within the convective region (Fig. 5.16). Also, the observed peaks in convective CG flashes (Fig. 5.27) and LDAR II flash origins (Fig. 5.53) occur ~30 min before observed peak in stratiform CG flashes (Fig. 5.27) and LDAR II flash origins (Fig. 5.53). Finally, the peak in convective LDAR II sources (Fig. 5.36) occurs ~45 min before an observed peak in stratiform LDAR II sources (Fig. 5.36). Since the strength of the stratiform region depends upon the quantity of hydrometeors advected into the region from the convective line, it is not surprising that peaks in stratiform electrical and microphysical activity lag peaks in convective activity.

Most lightning activity occurs within the convective region of the June MCS. On average, convective CG flash rates are over 11.9 times larger than stratiform CG flash rates. The stratiform region, however, experiences larger peak positive and negative CG currents (Fig. 5.29), a larger percentage of positive CG flashes (Fig. 5.28), and a larger IC:CG (Fig. 5.56) than the convective region (Figs. 5.29, 5.28, and 5.56, respectively). There are ~9.5 times more total LDAR II sources and ~5 times more flash origins in the convective region than in the stratiform region. Within the convective region, dominant source regions exist at 5-6 km (0 °C to -15 °C) and 9-11 km (-40 °C), both of which support the theory of non-

inductive charging. While the convective region is electrically active, these two regions contain similar source concentrations, making it difficult to discern whether the lower altitude source region is the main negative charge layer or a composite of both the main negative layer and the lower positive charge layer. If this lower source region is only associated with negative charge, one would expect source concentrations to be lower since negative polarity breakdown in the positive charge region is inherently noisier in the RF range than positive polarity breakdown in the negative charge region.

A combination of both the in situ and advection mechanisms can explain how the stratiform region acquires enough charge to become electrified and produce lightning. Given that 1) the front-to-rear storm relative flow is  $\sim 10 \text{ ms}^{-1}$ , 2) the fall speed of aggregates is  $\sim 1 \text{ ms}^{-1}$ , and 3) the slant of the downward sloping source region from the convective line to the stratiform region is  $\sim 6^\circ$  from the horizontal (the same slope that an aggregate trajectory would have), charge advection can explain the  $-10^\circ\text{C}$  to  $-20^\circ\text{C}$  electrically-active region above the stratiform region radar bright band.

Dual-Doppler results indicate that a weak mesoscale updraft ( $\sim 0.0\text{-}0.4 \text{ ms}^{-1}$ ) was present above the freezing level in the stratiform region, especially along the back edge of the region. Thus, an in situ process could also be producing the electrically-active charge center within the stratiform region. This charge area is hypothesized to be a positively-charged region, which helps to explain the higher percentage of +CG flashes produced beneath the stratiform region than beneath the convective line. The second isolated region of sources in the back of the trailing stratiform region is associated with a weak mesoscale updraft. This electrically-active region may be associated with an in situ charging mechanism (given that a weak mesoscale updraft is present) and/or advection of small charged ice particles with low

or negligible fall speeds to the region. Nevertheless, these electrically-active layers within the stratiform region have smaller average source concentrations than the source regions present within the convective line. As a result, the stratiform region exhibits less lightning activity than the convective line.

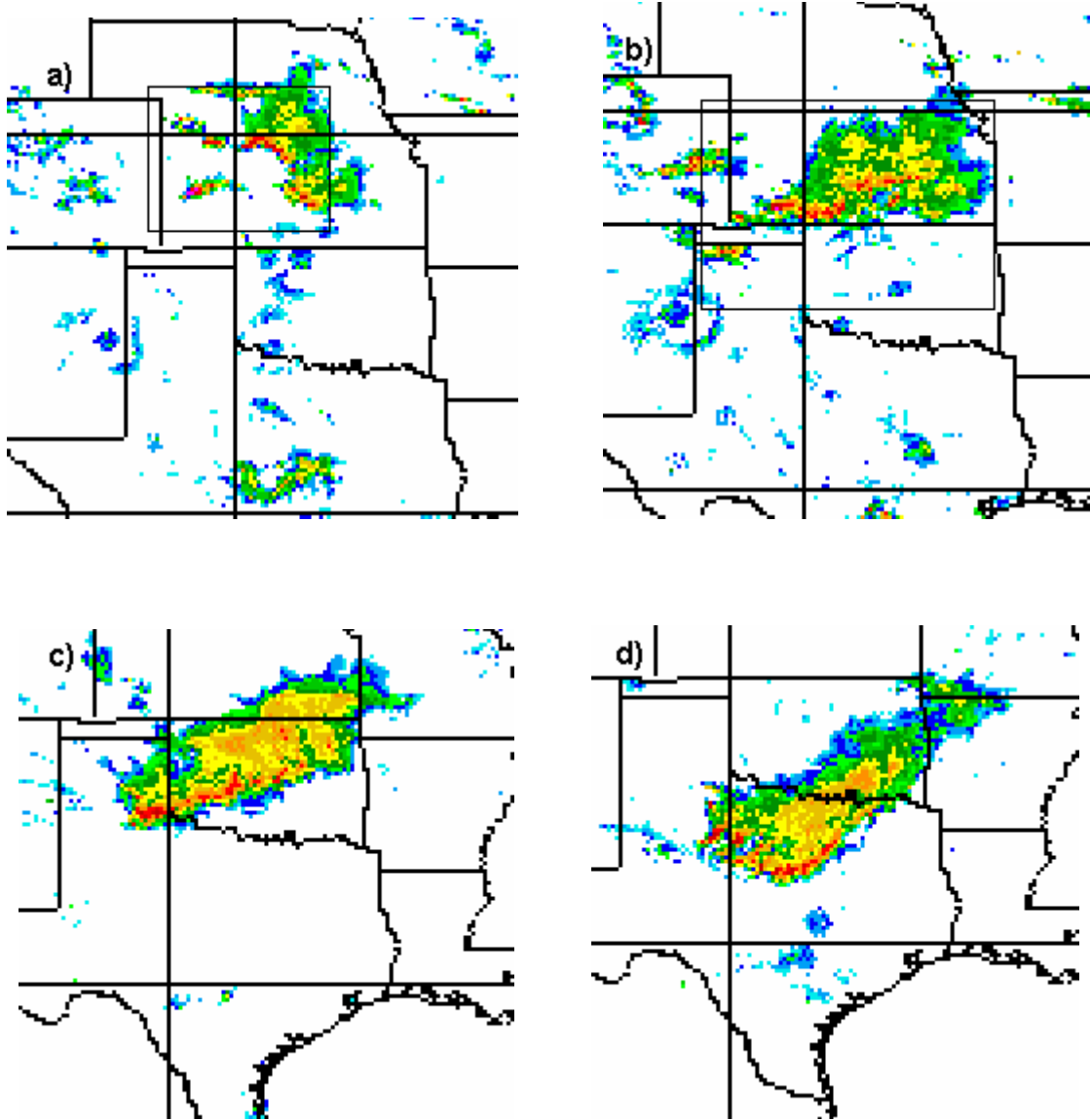


FIG. 5.1. 2-km resolution NEXRAD mosaic reflectivity images from a squall line that evolves into a TS MCS at (a) 19 UTC 15, (b) 22 UTC 15, (c) 02 UTC 16, and (d) 06 UTC 16 June 2002. Image adapted from [www.ncdc.noaa.gov](http://www.ncdc.noaa.gov).

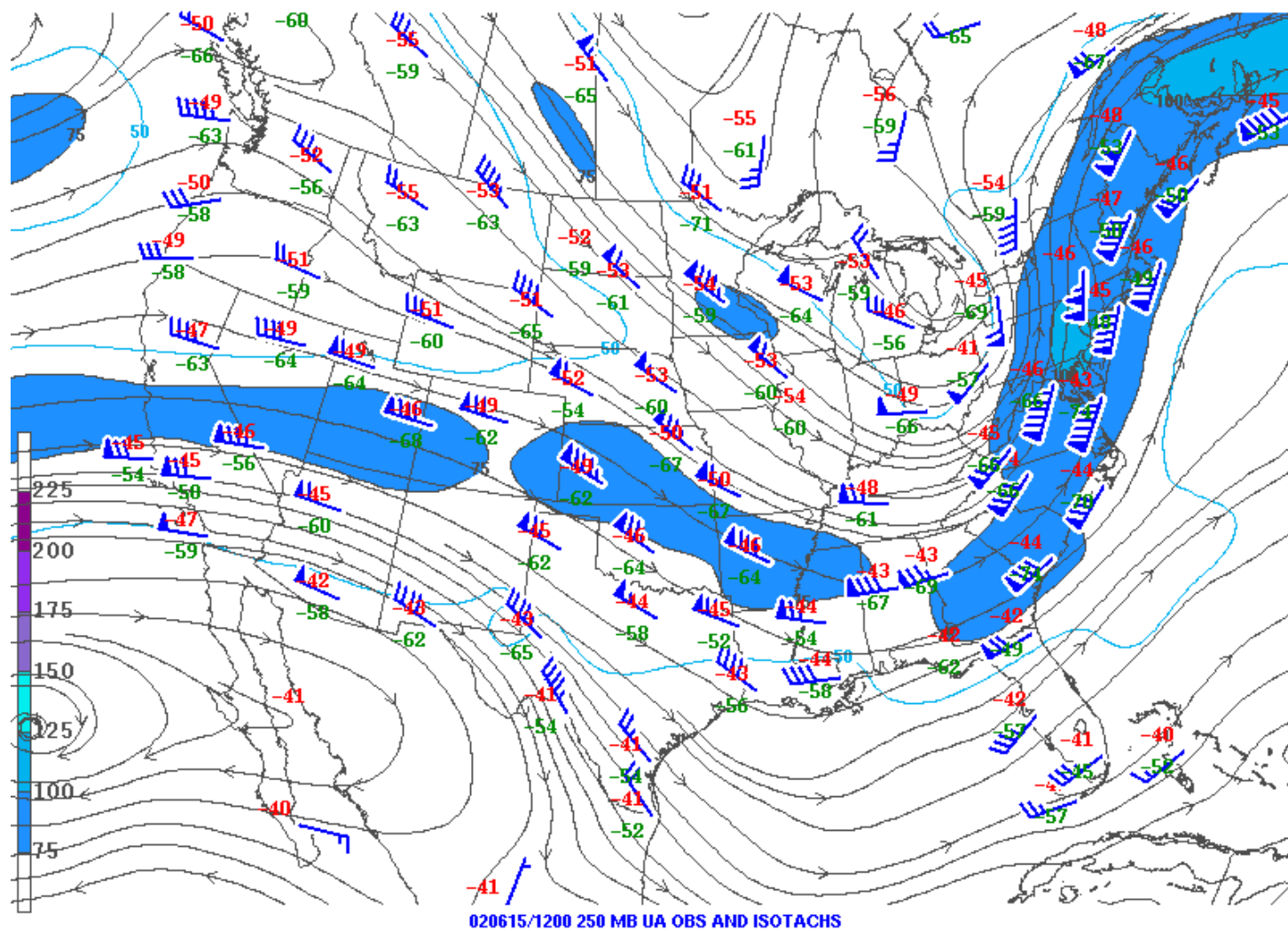


FIG. 5.2. 250-mb analysis for 12 UTC 15 June 2002. Wind speeds  $\geq 75$  kts are shaded according to the contour bar on the left (image courtesy of [www.spc.noaa.gov](http://www.spc.noaa.gov)).

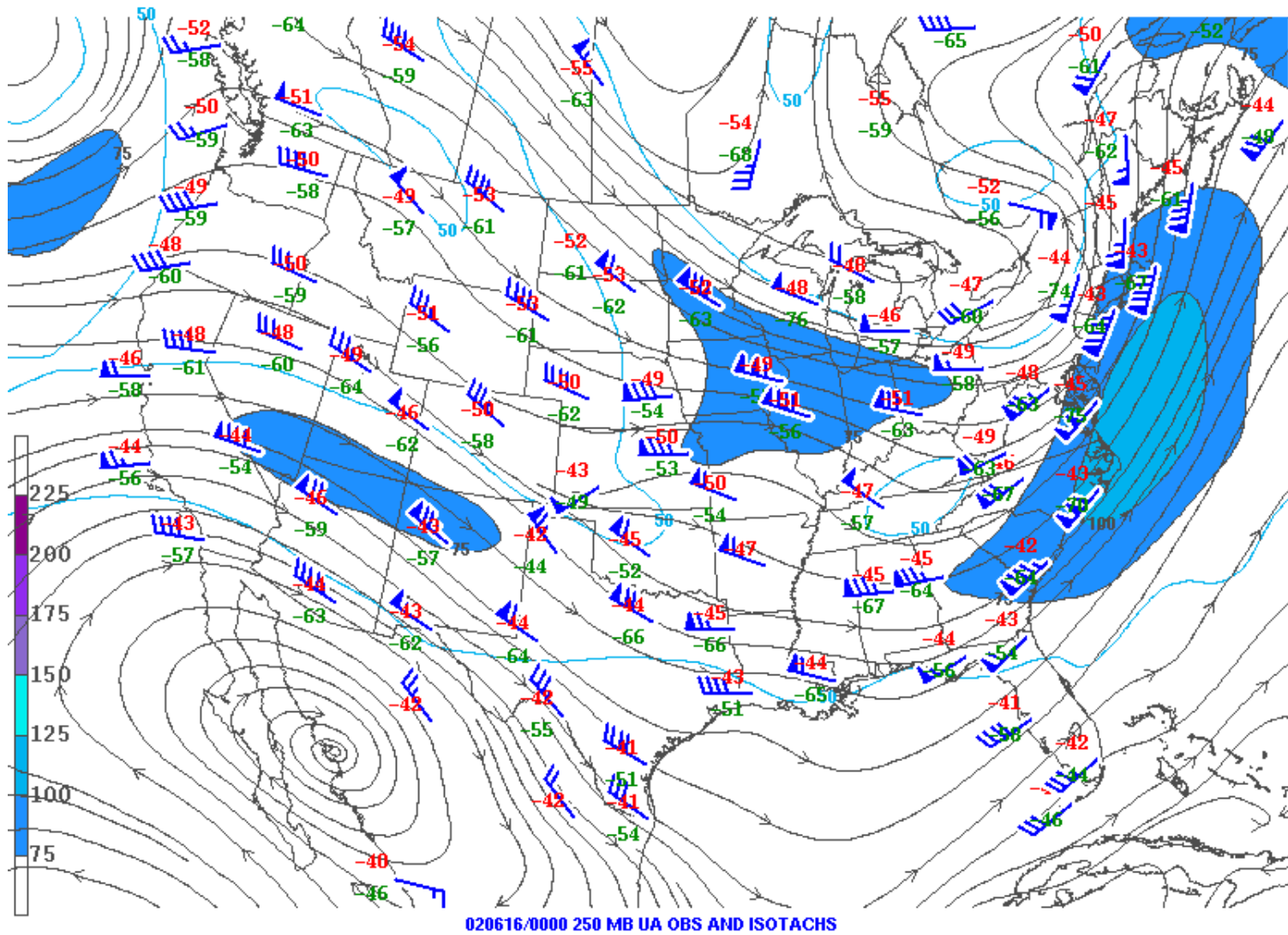


FIG. 5.3. Same as Fig. 5.2, but for 00 UTC 16 June 2002 (image courtesy of [www.spc.noaa.gov](http://www.spc.noaa.gov)).

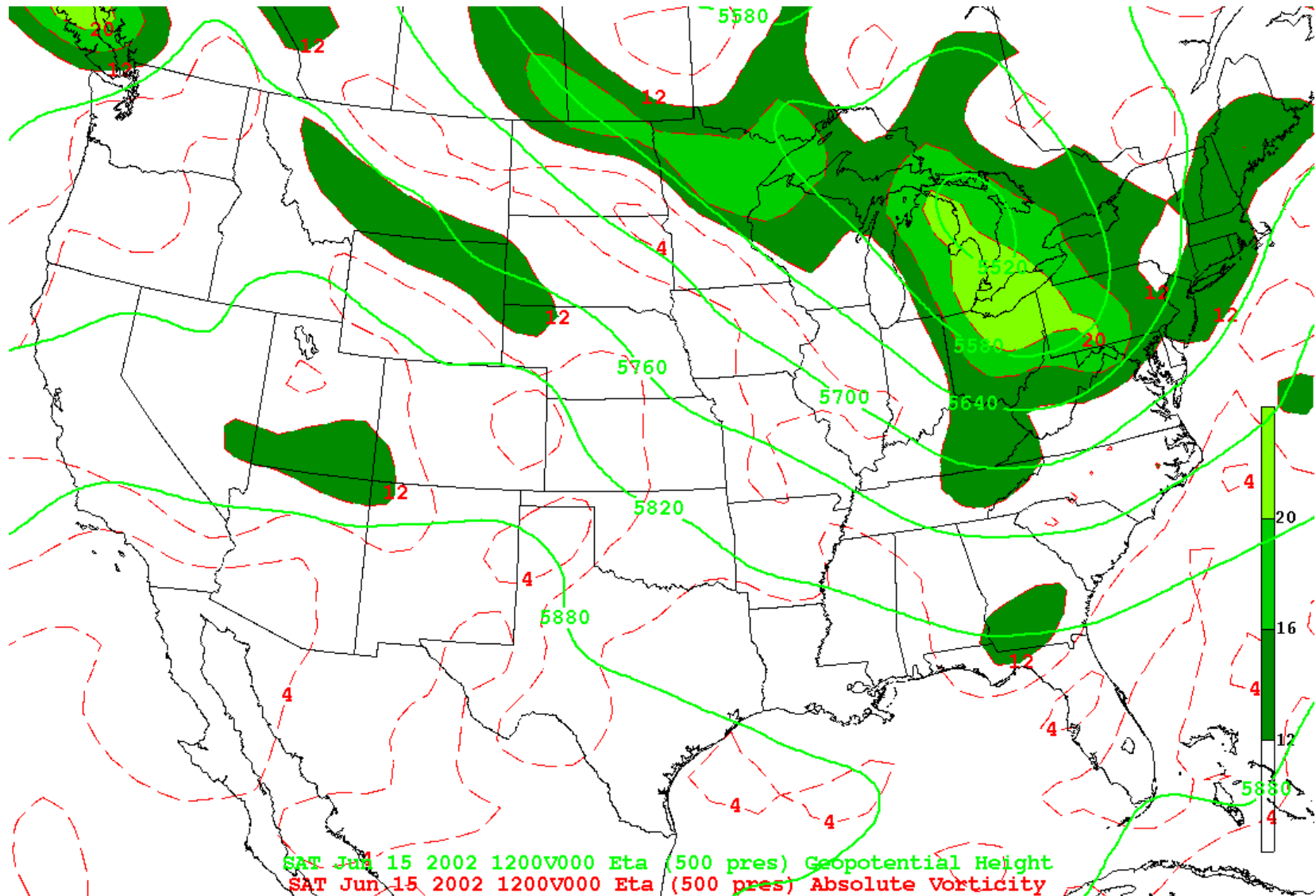


FIG. 5.4. 500-mb analysis for 12 UTC 15 June 2002. Height contours (m) are in solid blue lines, and absolute vorticity contours ( $s^{-1}$ ) are in dashed red lines.

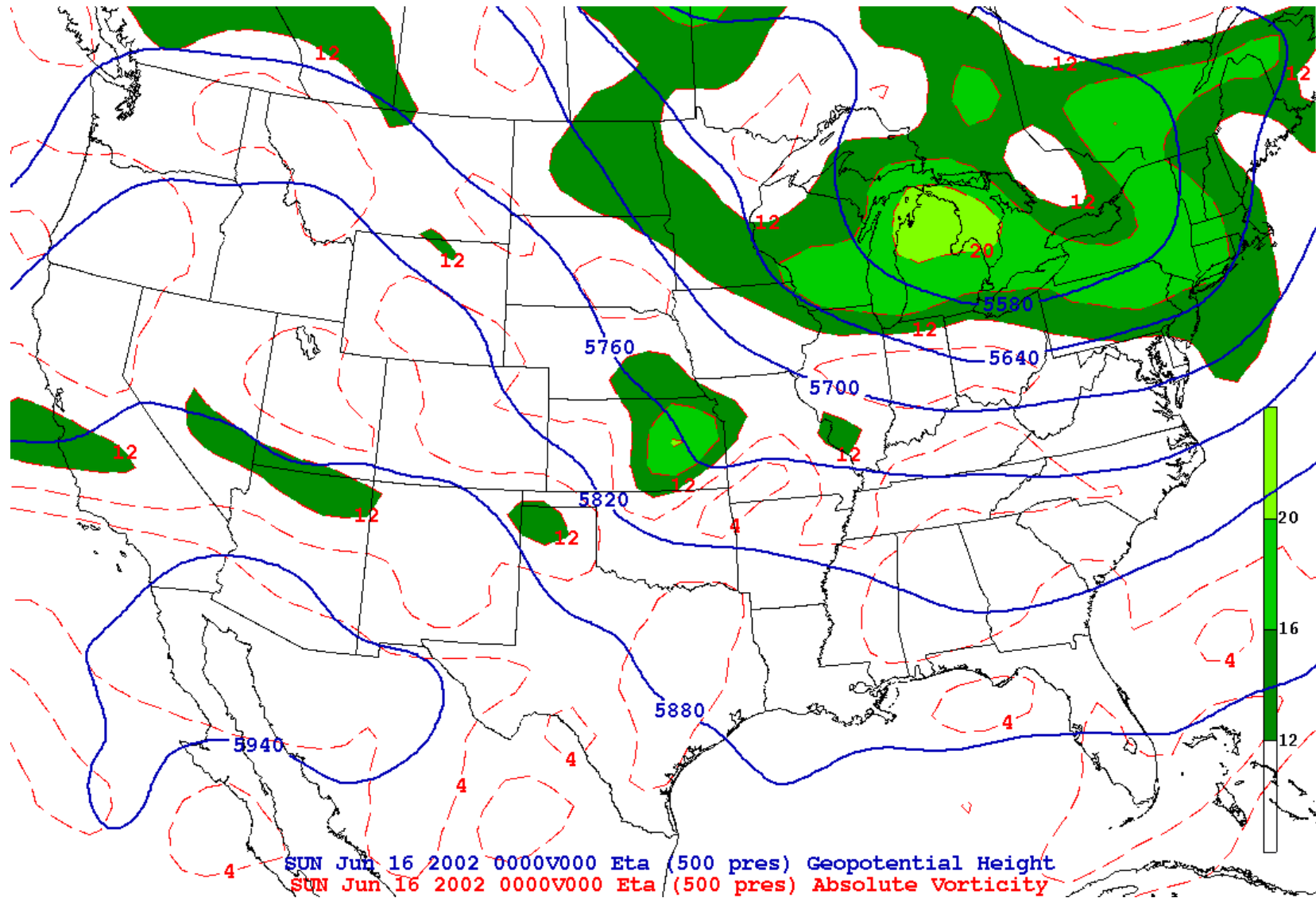


FIG. 5.5. Same as Fig. 5.4, but for 00 UTC 16 June 2002.

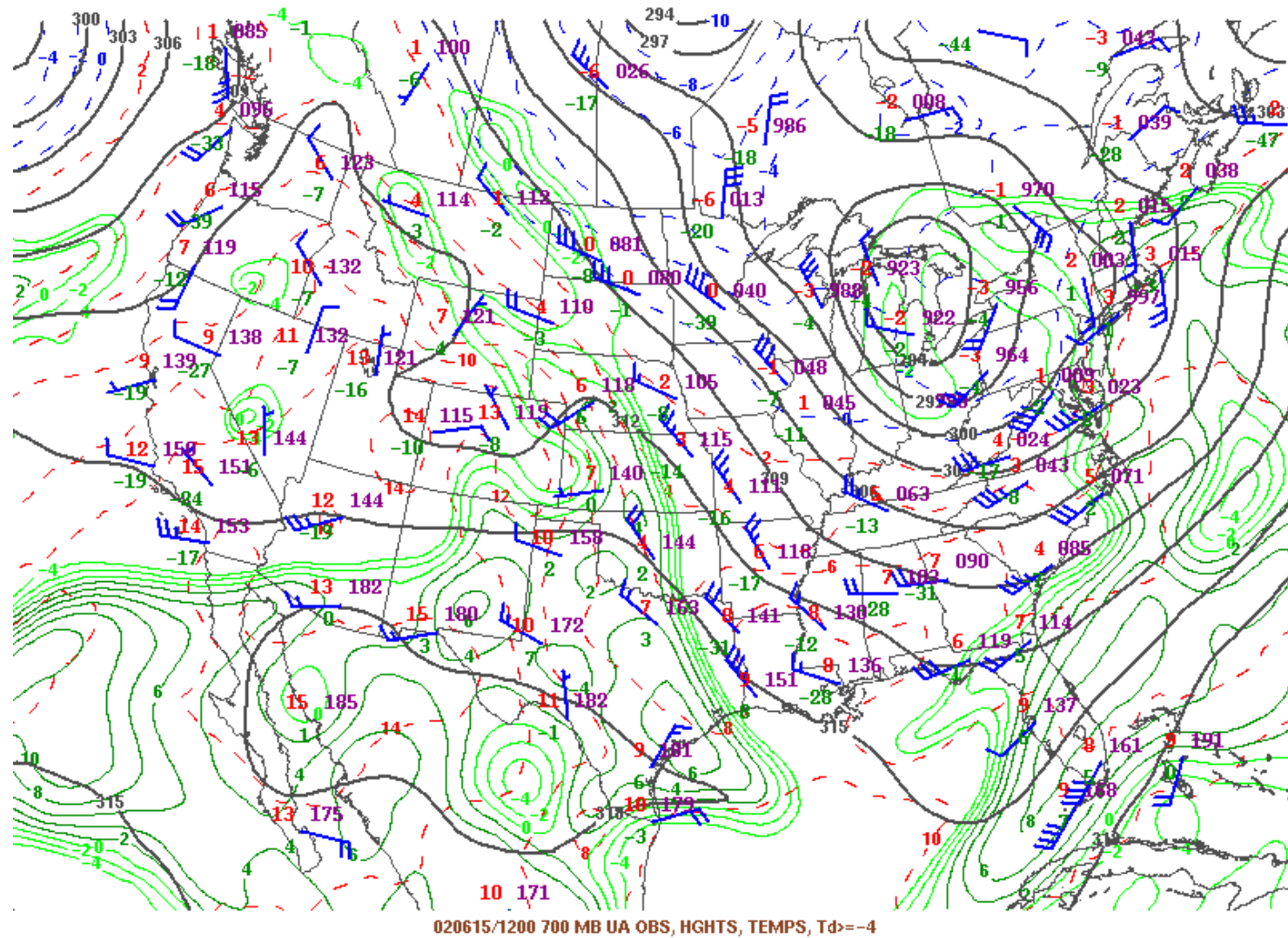


FIG. 5.6. 700-mb analysis for 12 UTC 15 June 2002. Height contours are in solid black lines, isotherms are in dashed red and blue lines, and dew point contours  $\geq -4$  °C are in solid green lines (image courtesy of [www.spc.noaa.gov](http://www.spc.noaa.gov)).

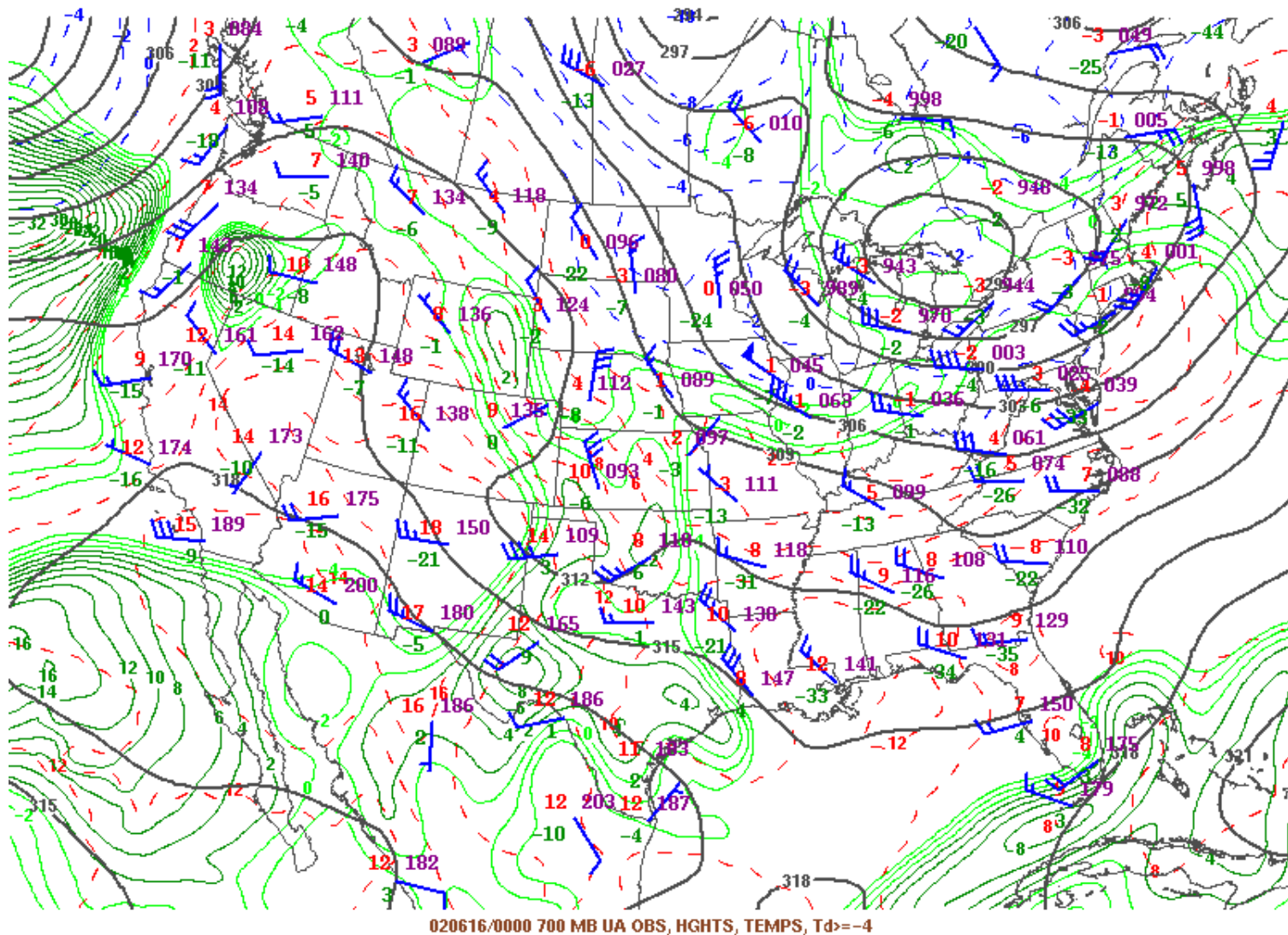


FIG. 5.7. Same as Fig. 5.6, but for 00 UTC 16 June 2002 (image courtesy of [www.spc.noaa.gov](http://www.spc.noaa.gov)).

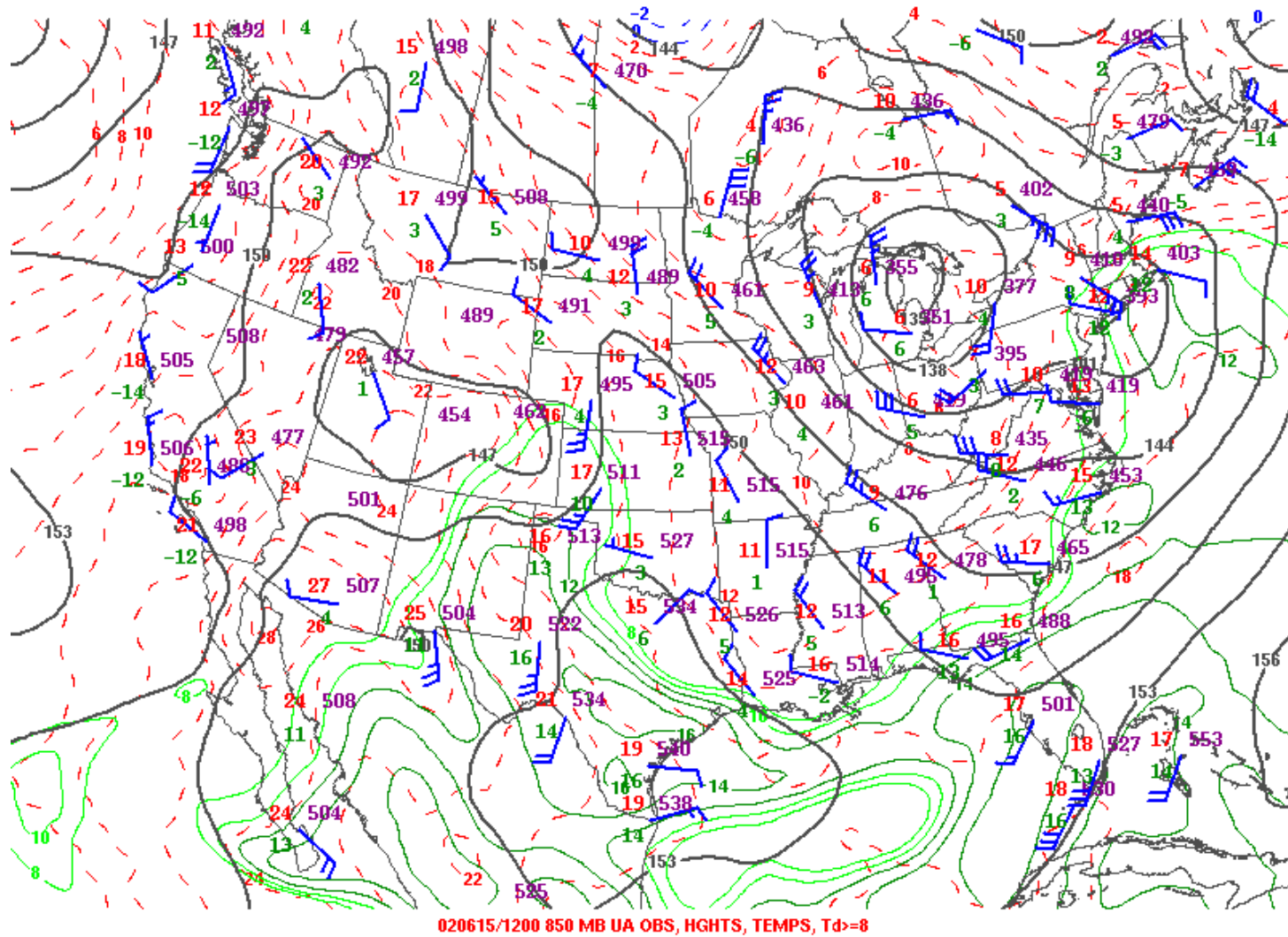


FIG. 5.8. 850-mb analysis for 12 UTC 15 June 2002. Height contours are in solid black lines, isotherms are in dashed red lines, and dew point contours  $\geq 8^\circ\text{C}$  are in solid green lines (image courtesy of [www.spc.noaa.gov](http://www.spc.noaa.gov)).

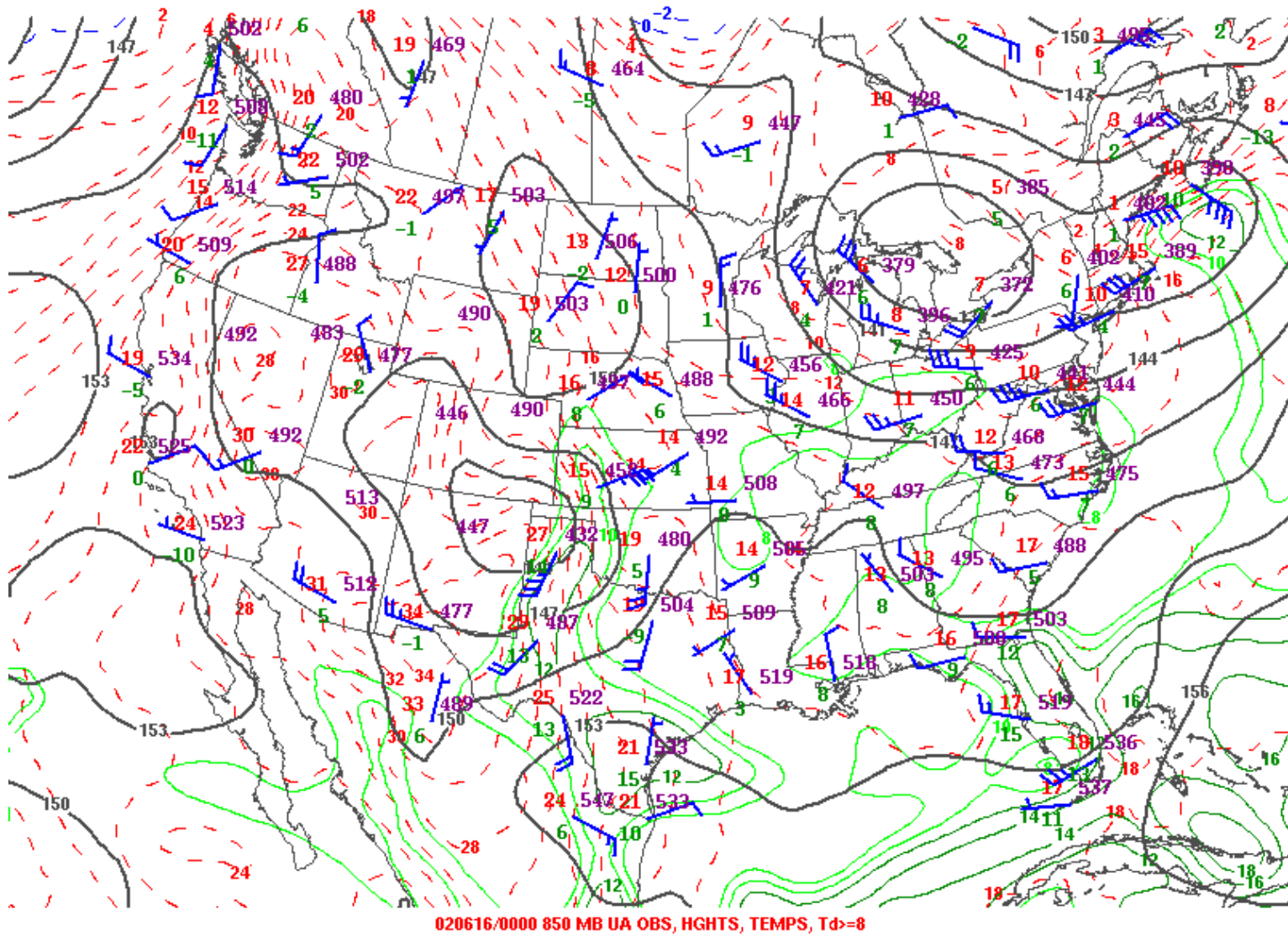
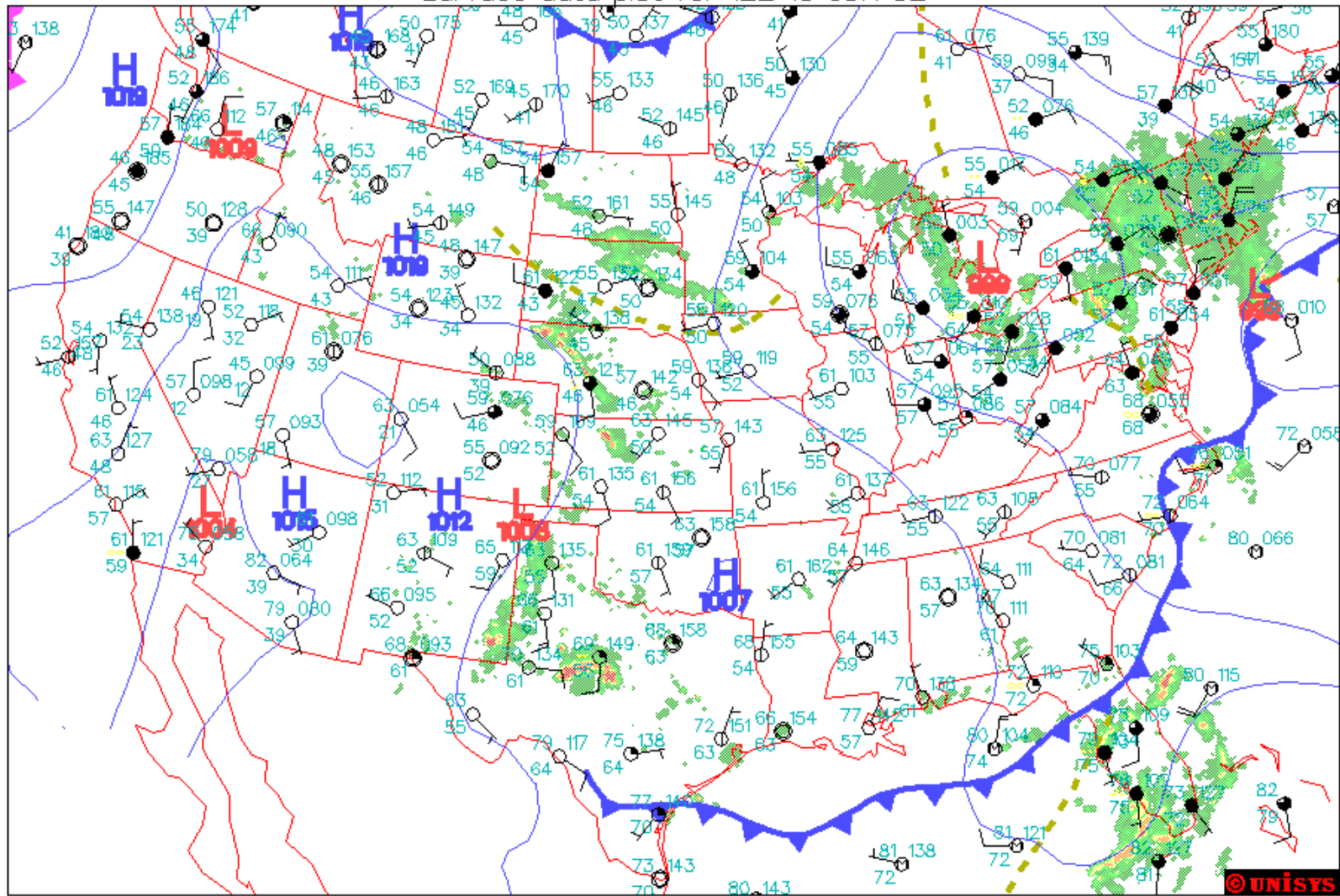


FIG. 5.9. Same as Fig. 5.8, but for 00 UTC 16 June 2002 (image courtesy of [www.spc.noaa.gov](http://www.spc.noaa.gov)).

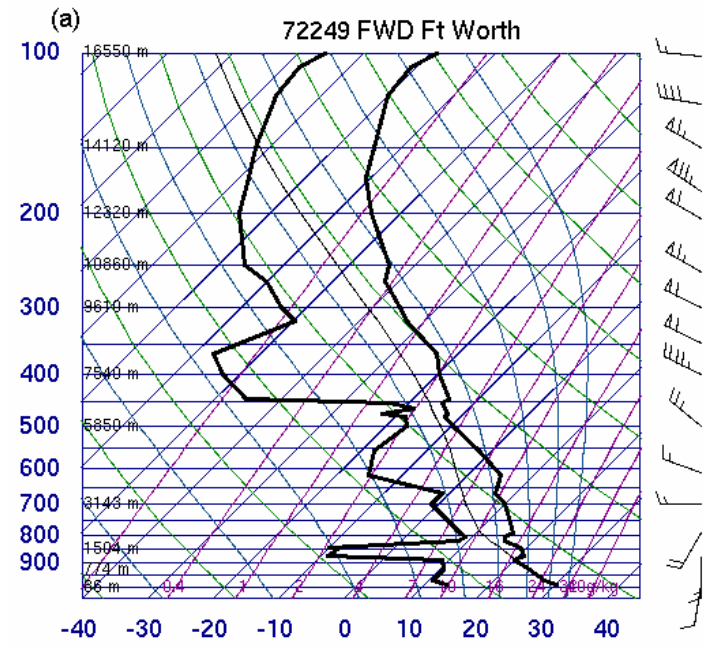
Surface data plot for 12Z 15 JUN 02



Intensities (Dbz): 20 30 40 45 50 55

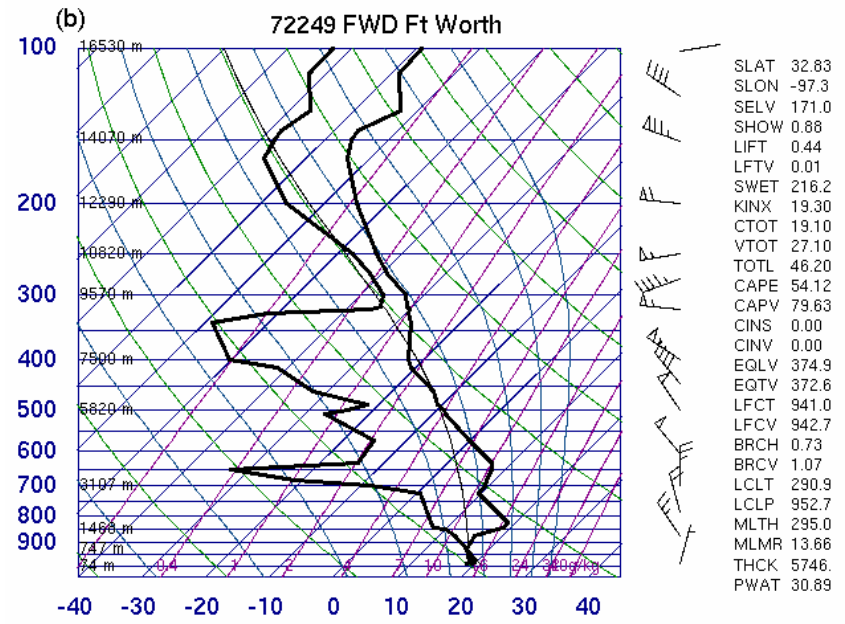
Fronts at 12Z

FIG. 5.10. 12 UTC 15 June 2002 U.S. surface analysis (image courtesy of www.spc.noaa.gov).



00Z 16 Jun 2002

University of Wyoming



12Z 16 Jun 2002

University of Wyoming

FIG. 5.11. Dallas-Fort Worth, Texas soundings valid at a) 00 UTC and b) 12 UTC 16 June 2002. Image courtesy of the University of Wyoming.

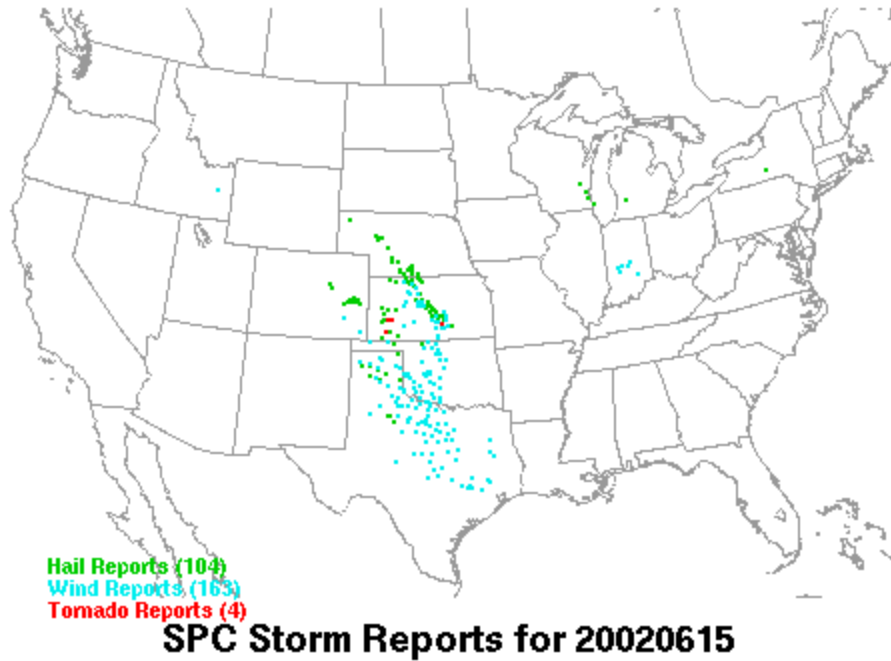


FIG. 5.12. Preliminary severe storm damage reports including hail ( $\geq 0.75''$ ) (green dots), strong winds ( $\geq 58$  mph) (blue dots), and tornadoes (red dots) from 12 UTC 15 through 12 UTC 16 June 2002 (image courtesy of [www.spc.noaa.gov](http://www.spc.noaa.gov)).

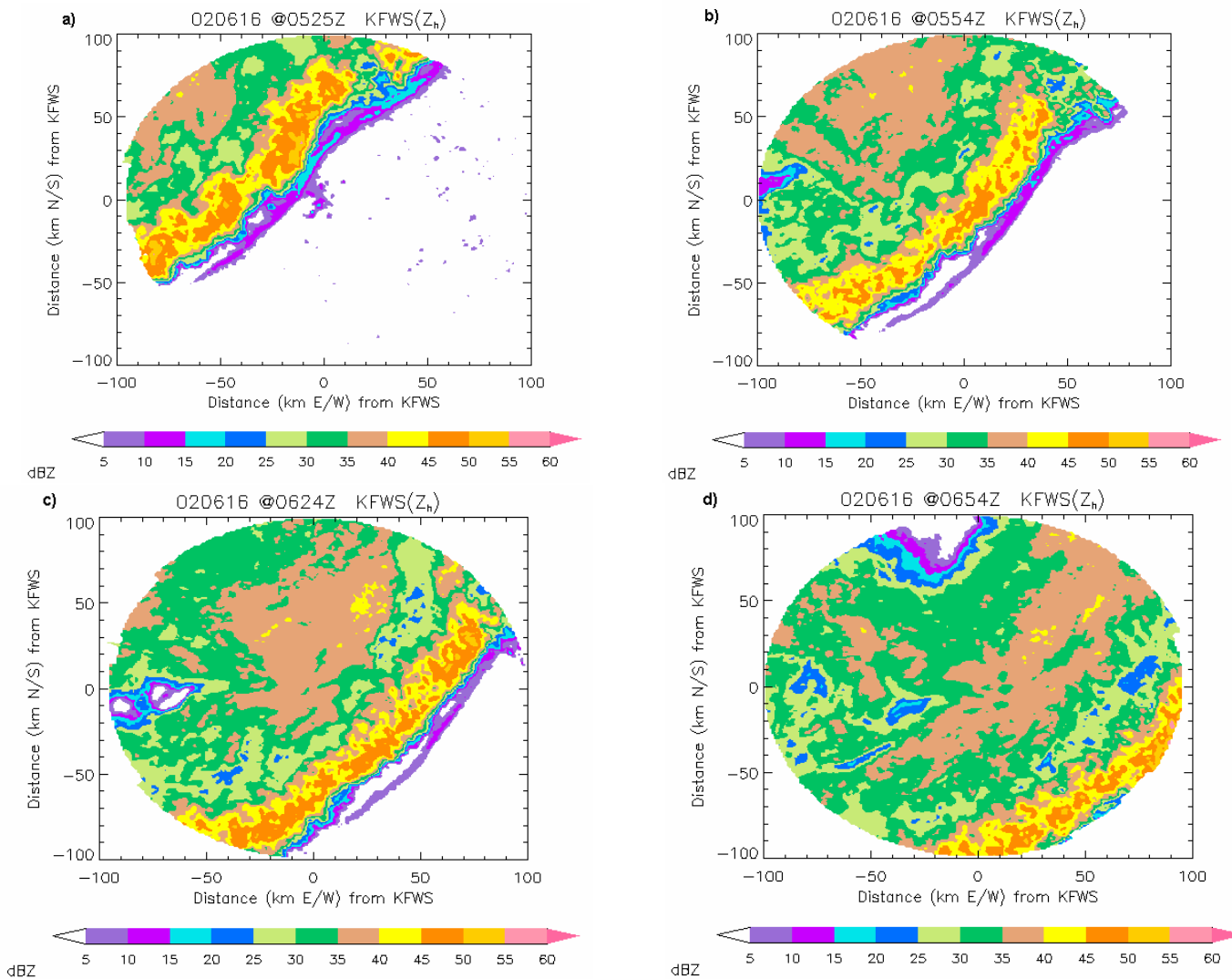


FIG. 5.13. 0.5-km constant altitude radar reflectivity images of the development of the 16 June 2002 MCS at (a) 05:25 UTC, (b) 05:54 UTC, (c) 06:24 UTC, and (d) 06:54 UTC. Radar reflectivity is color-shaded according to the scale, and the KFWS radar is located in the center of the image. The x- and y-axes represent distance (km N/S) and distance (km E/W) from the KFWS radar, respectively.

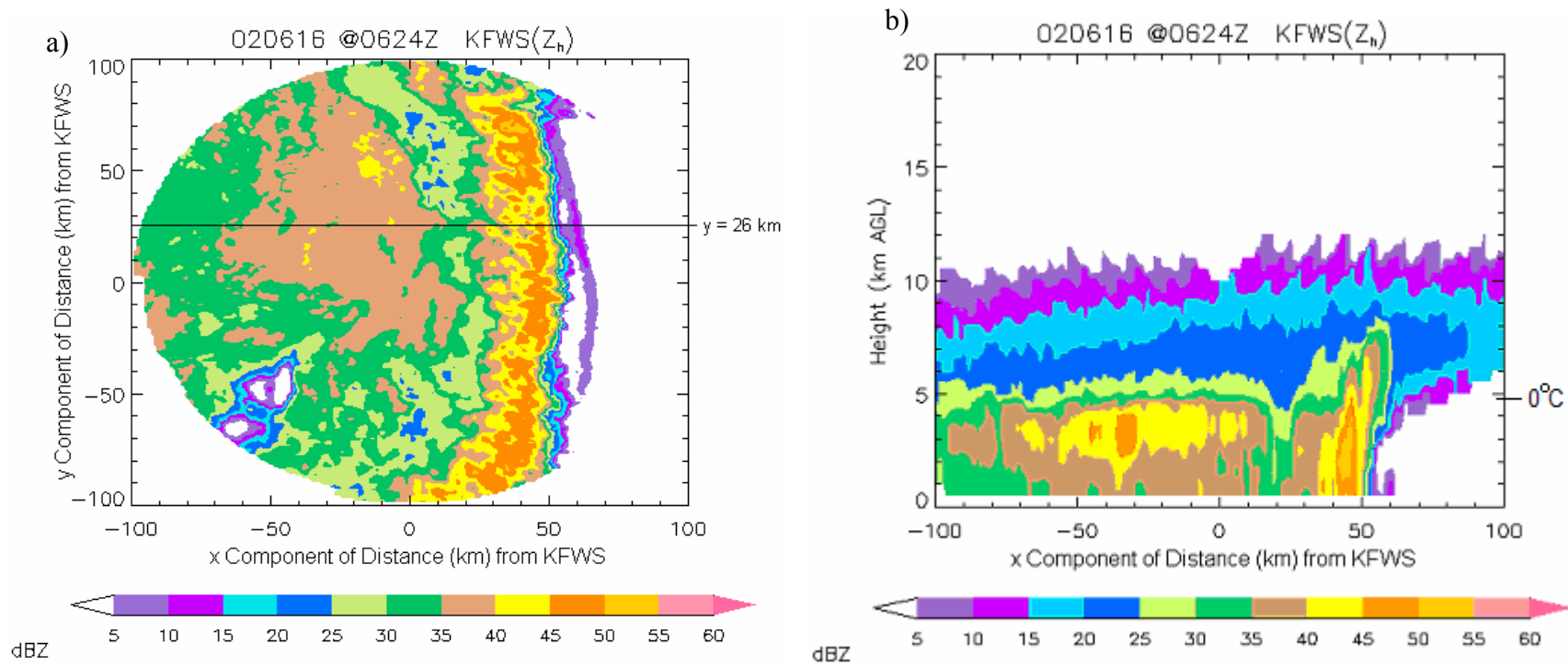


FIG. 5.14. a) A 0.5-km CAPPI image, and b) a line-normal vertical cross-section through (a) at  $y = 26$  km at 06:24 UTC 16 June 2002. Radar reflectivity (dBZ) is color-shaded according to the scale. The horizontal image has been rotated counterclockwise  $40^\circ$ .

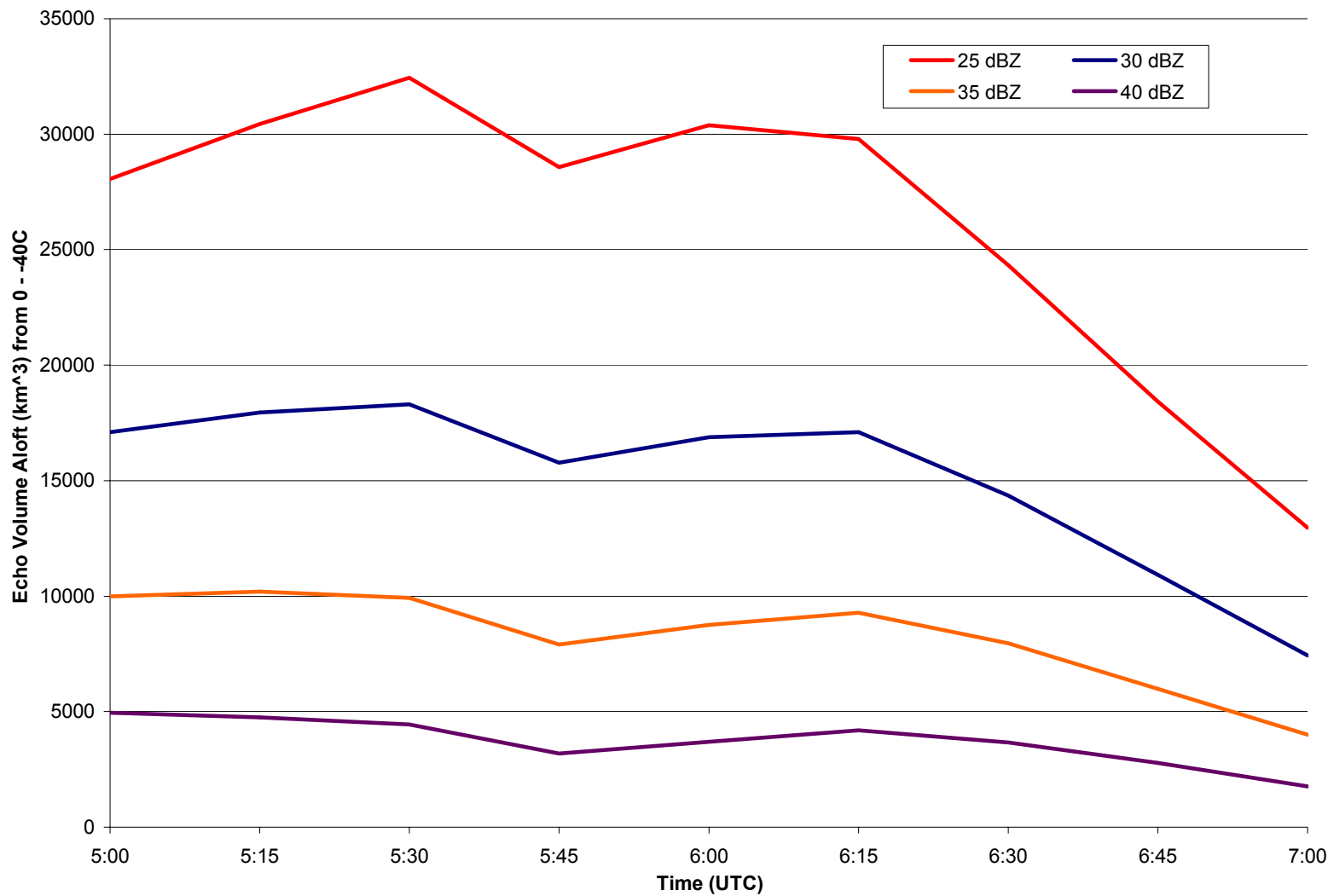


FIG. 5.15. Convective region total echo volume aloft trend ( $\text{km}^3$ )  $\geq 25$  dBZ (red line),  $\geq 30$  dBZ (blue line),  $\geq 35$  dBZ (orange line), and  $\geq 40$  dBZ (violet line) within the  $0^\circ\text{C}$  to  $-40^\circ\text{C}$  temperature layer, time averaged every 15 min. Time is on the x-axis, and total echo volume aloft is on the y-axis.

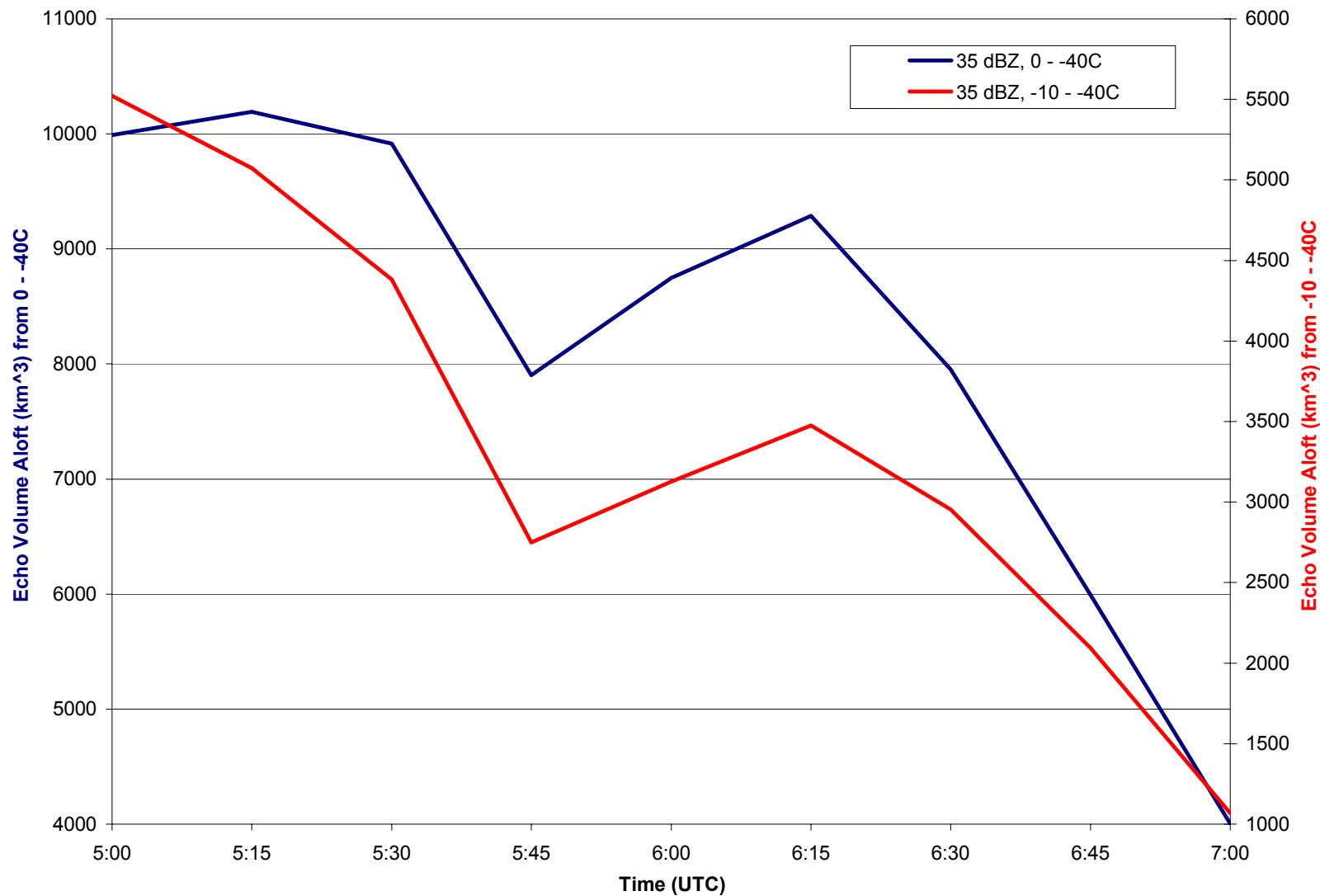


FIG. 5.16. Convective region total echo volume aloft ( $\text{km}^3 \geq 35 \text{ dBZ}$ ) for the 0 to -40 C layer (blue line, values on primary y-axis) and the -10 to -40 C layer (red line, values on secondary y-axis), time averaged every fifteen minutes (x-axis).

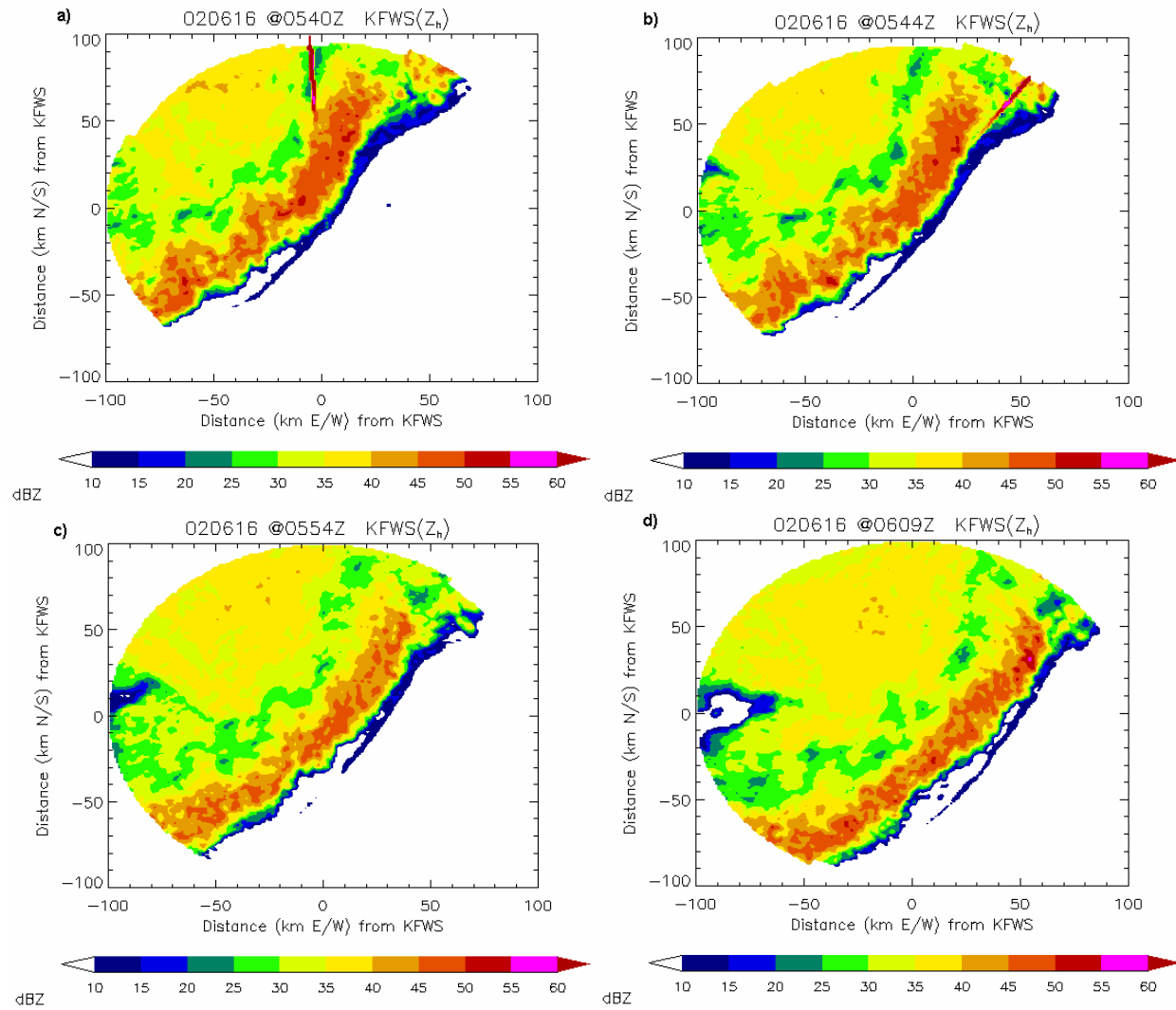


FIG. 5.17. 0.5 km constant altitude radar reflectivity images of the evolution of the 16 June 2002 MCS at (a) 05:40 UTC, (b) 05:44 UTC, (c) 05:54 UTC, and (d) 06:09 UTC. Radar reflectivity is color-shaded according to the scale and the KFWS radar is located in the center of the image. The x- and y-axes represent distance (km N/S) and distance (km E/W) from the KFWS radar, respectively.

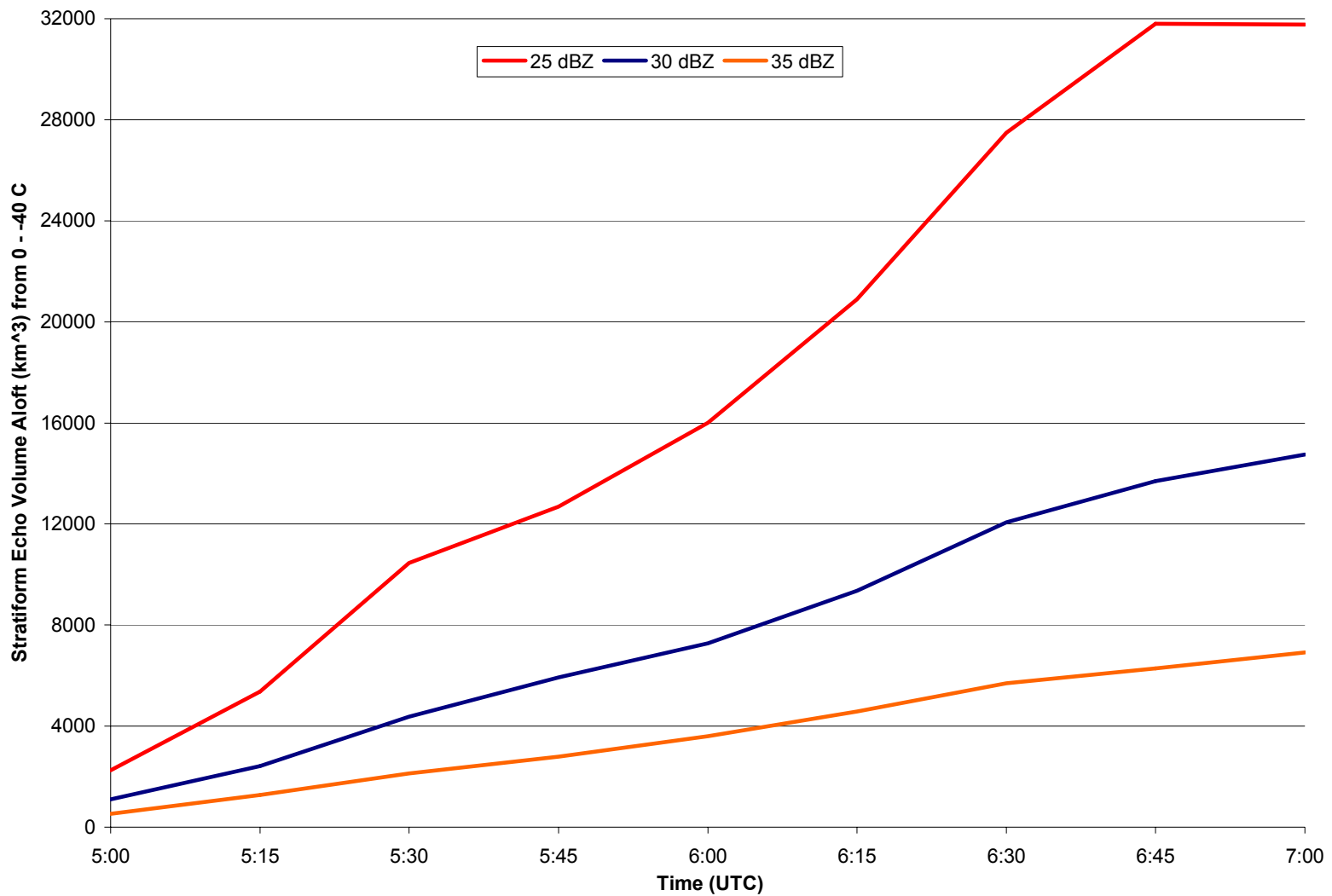


FIG. 5.18. Stratiform region total echo volume aloft trend ( $\text{km}^3$ )  $\geq 25$  dBZ (red line),  $\geq 30$  dBZ (blue line),  $\geq 35$  dBZ (orange line), and  $\geq 40$  dBZ (violet line) and within the  $0^\circ\text{C}$  to  $-40^\circ\text{C}$  temperature layer, time averaged every 5 min with a 3-point running mean smoother. Time is on the x-axis, and total echo volume aloft is on the y-axis.

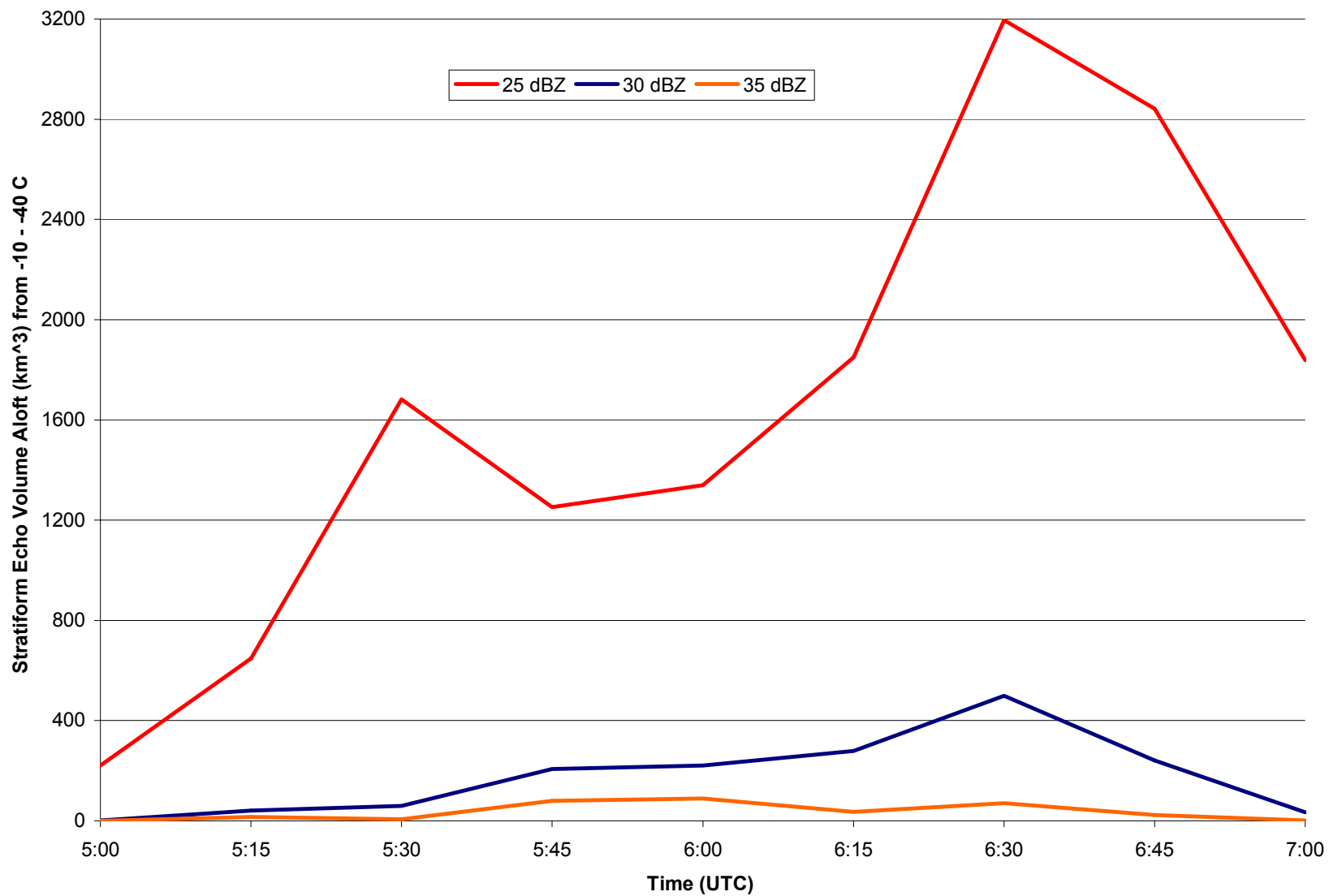


FIG. 5.19. Same as Fig. 5.18, but for echo volume aloft within the -10 °C to -40 °C temperature layer.

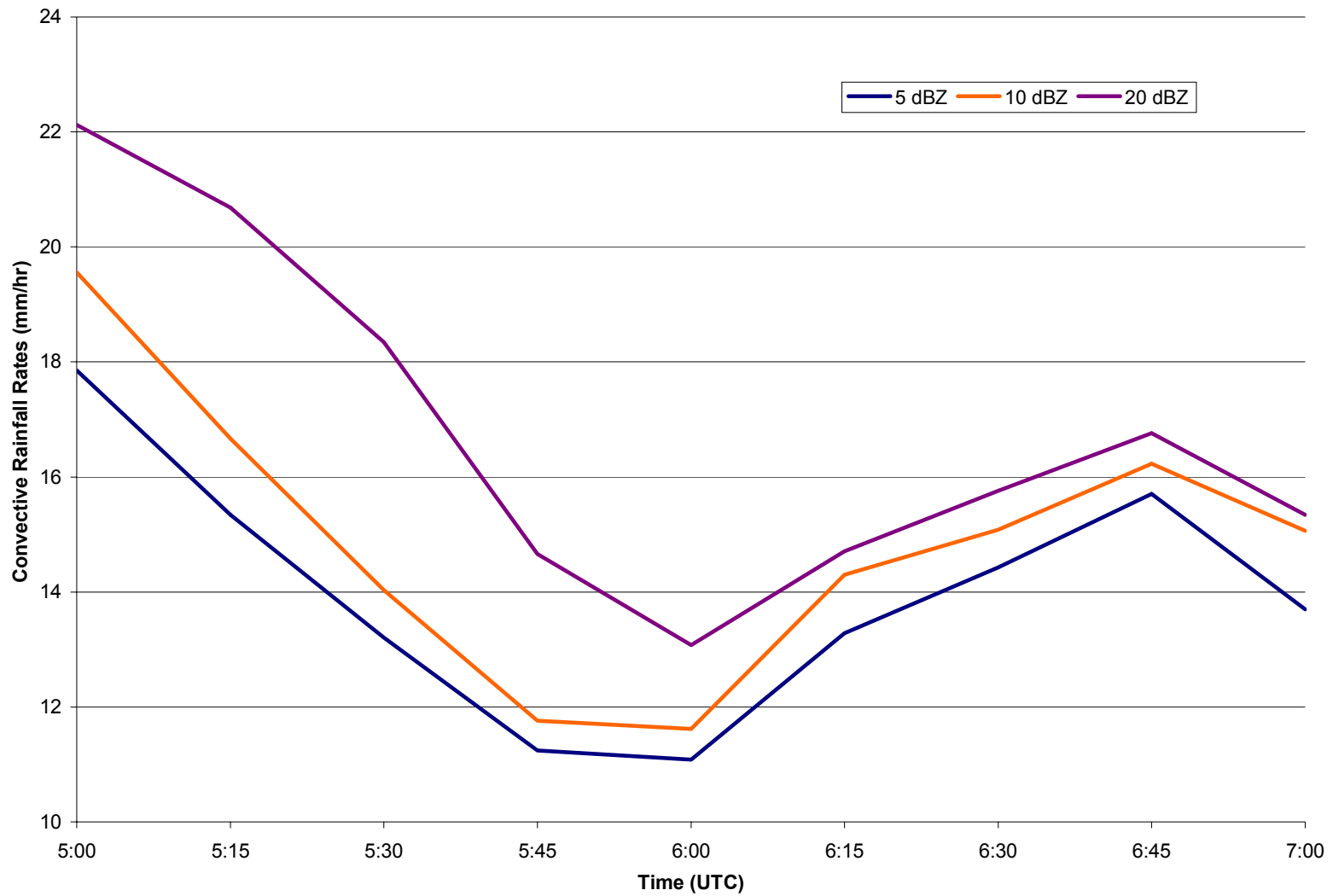


FIG. 5.20. Convective rainfall rate trend determined using a low-level reflectivity threshold of 5 dBZ (blue line), 10 dBZ (orange line), and 20 dBZ (violet line), time averaged every 5 min with a 3-point running mean smoother. Time is located on the x-axis, and convective rainfall rate ( $\text{mm hr}^{-1}$ ) is on the y-axis.

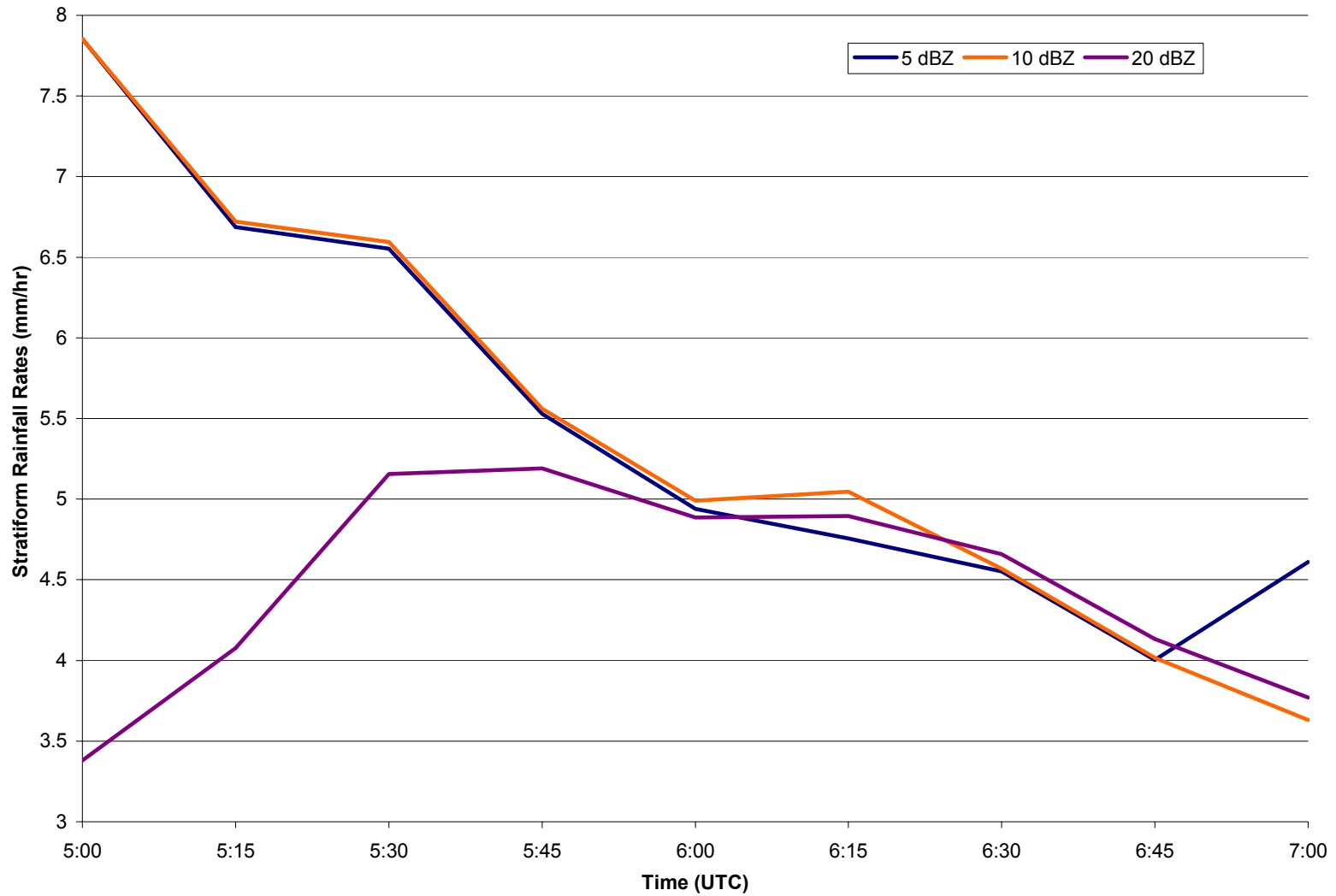


FIG. 5.21. Stratiform rainfall rate trend determined using a low-level reflectivity threshold of 5 dBZ (blue line), 10 dBZ (orange line), and 20 dBZ (violet line), time averaged every 5 min with a 3-point running mean smoother. Time is located on the x-axis, and stratiform rainfall rate ( $\text{mm hr}^{-1}$ ) is on the y-axis.

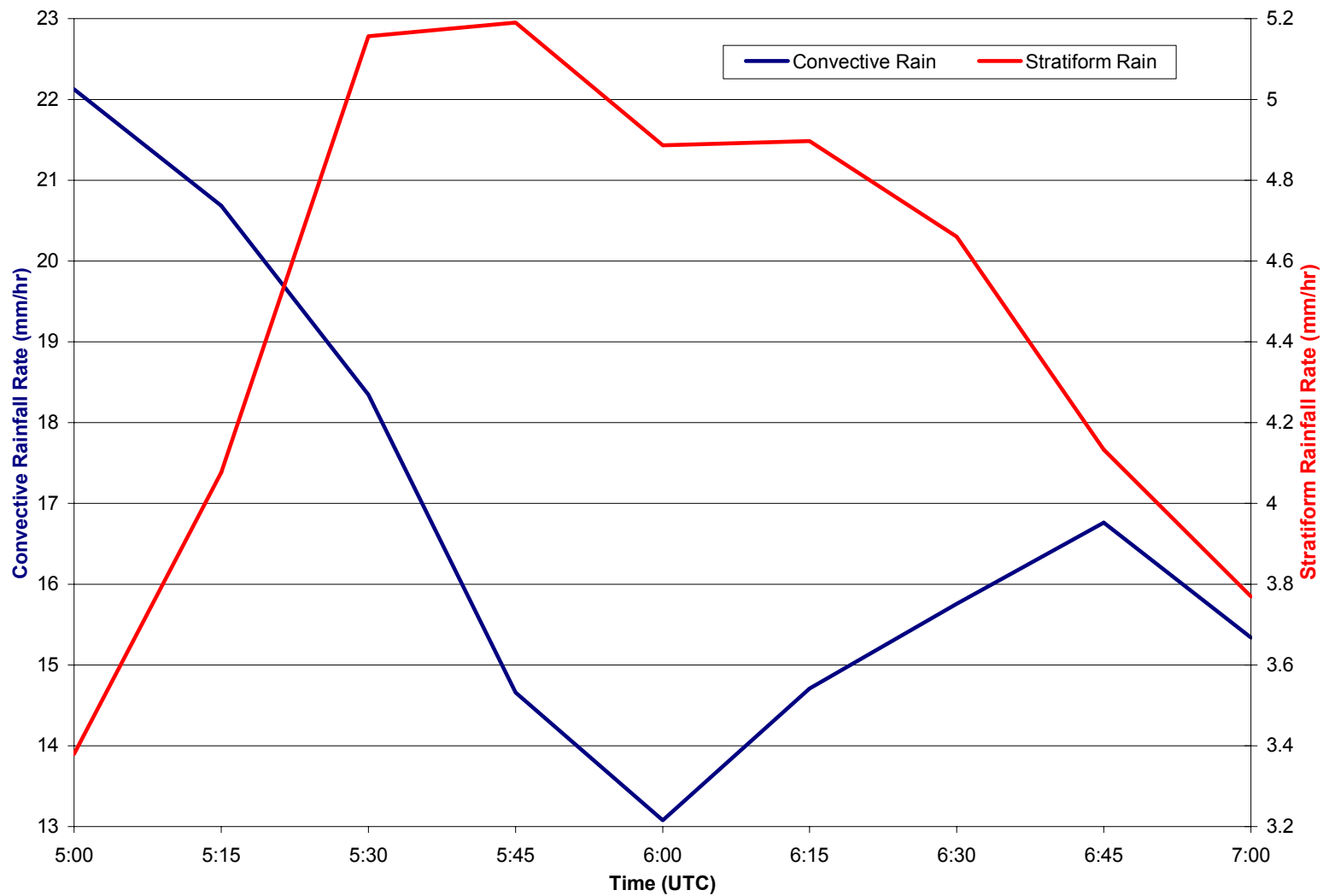


FIG. 5.22. Convective (blue line) and stratiform (red line) region rainfall rate trends from 05:00 to 07:00 UTC 16 June 2002, time averaged every 5 min with a 3-point running mean smoother. Convective and stratiform region rainfall rates correspond to the primary and secondary y-axes, respectively. Time is on the x-axis. Note the different scales of the y-axes.

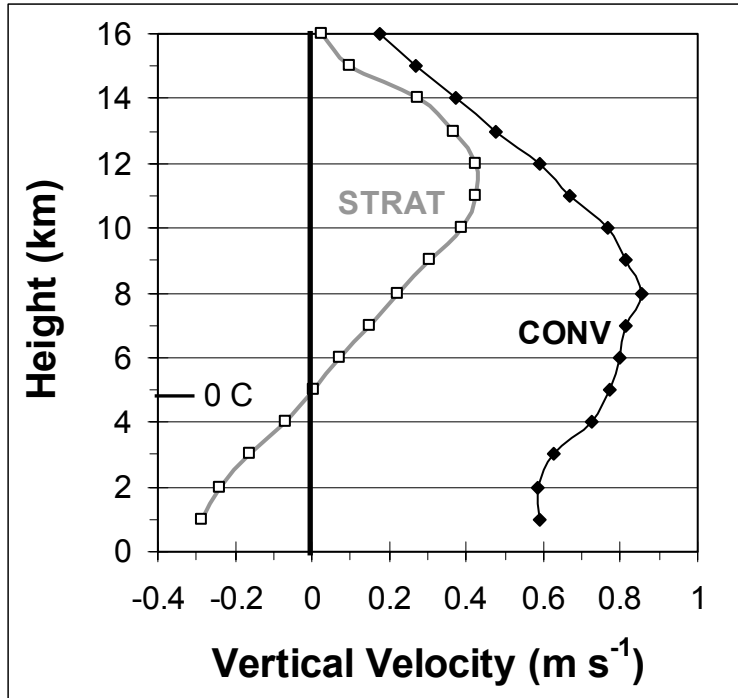


FIG. 5.23. Mean convective region (line with solid diamonds) and stratiform region (line with open squares) vertical velocity ( $\text{m s}^{-1}$ ) from an 80-km long portion of the 16 June 2002 MCS. Convective and stratiform regions were determined using a subjective line partitioning method.

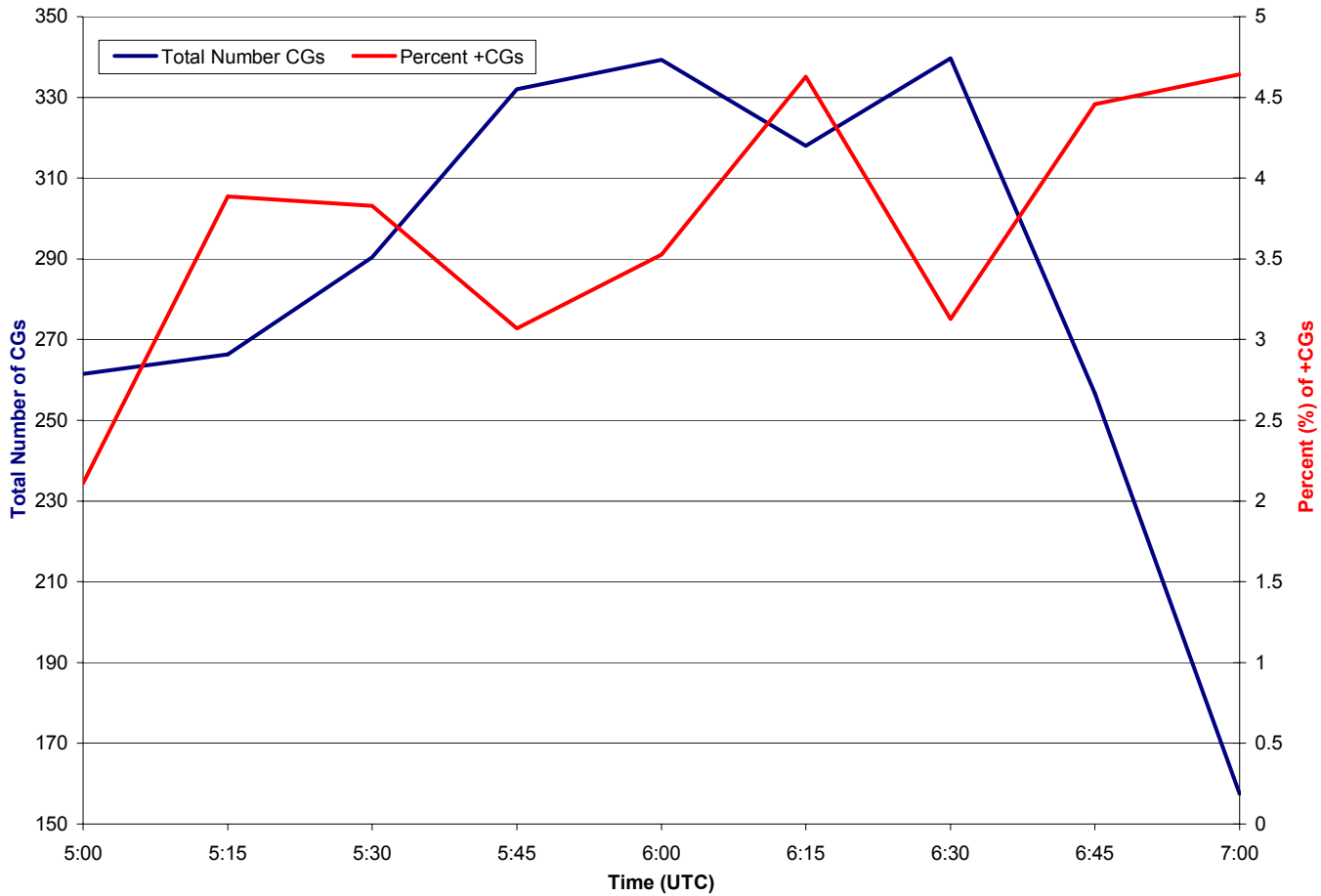


FIG. 5.24. Total NLDN-detected CG flash trend (blue line) and the percent +CG lightning flash trend (red line) from 05:00 to 07:00 UTC 16 June 2002, time average every 5 min with a 3-point running mean smoother. The total number of CG flashes and percent of +CG flashes corresponds to the primary and secondary y-axes, respectively. Time listed along the x-axis.

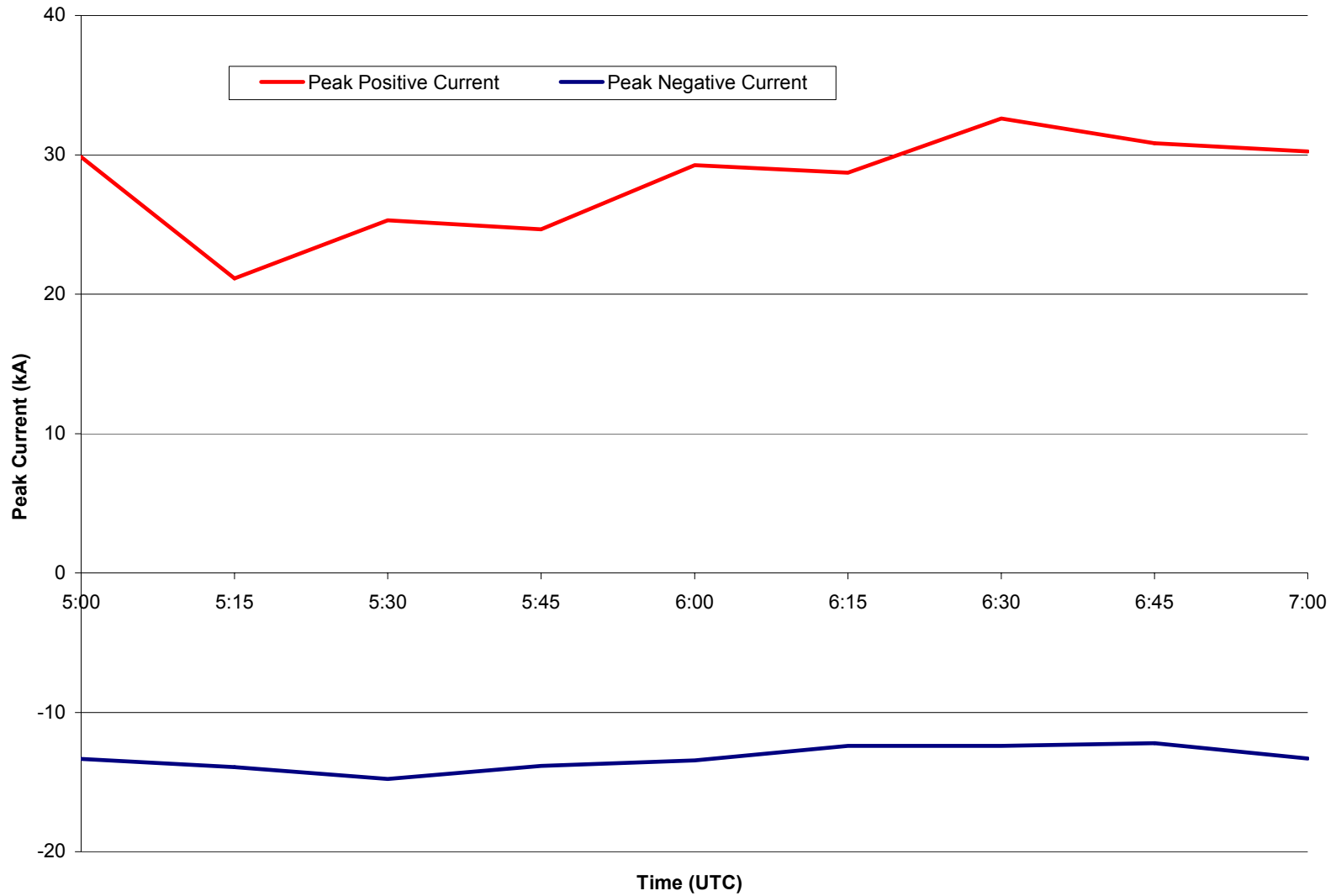


FIG. 5.25. Peak positive (red line) and negative (blue line) CG lightning flash current trends, time averaged every 5 min with a 3-point running mean smoother. Peak current (kA) corresponds to the y-axis, and time is listed on the x-axis.

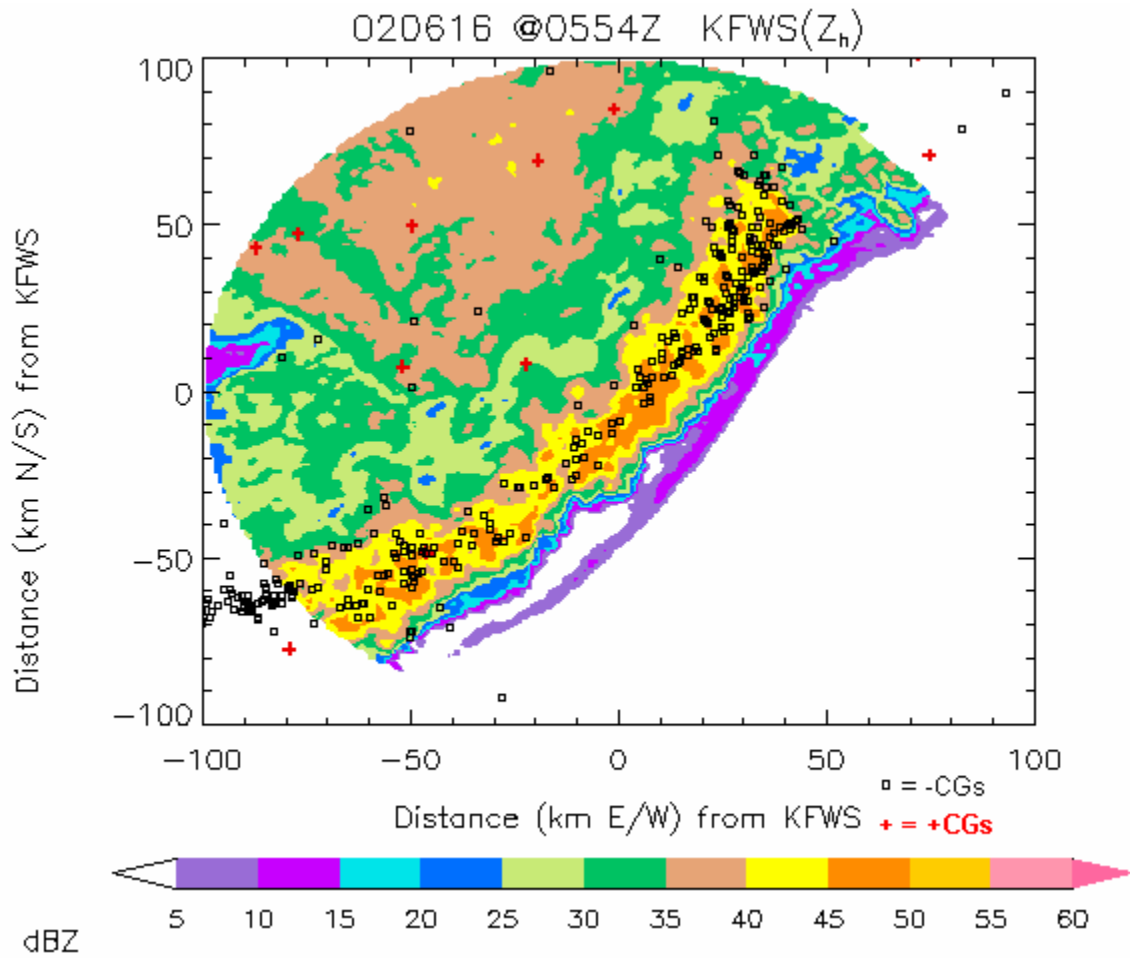


FIG. 5.26. 0.5-km radar reflectivity (dBZ) CAPPI image of the 16 June 2002 MCS at 05:54 UTC overlaid with 5 min of NLDN CG lightning flash data (centered on time of radar image). -CG lightning flashes are indicated on the figure by black squares, and +CG lightning flashes are indicated by red “+” symbols. Radar reflectivity is color-shaded according to the scale, and the KFWS radar is located in the center of the image. The x- and y-axes represent the distance (km) north/south and east/west of the KFWS radar, respectively.

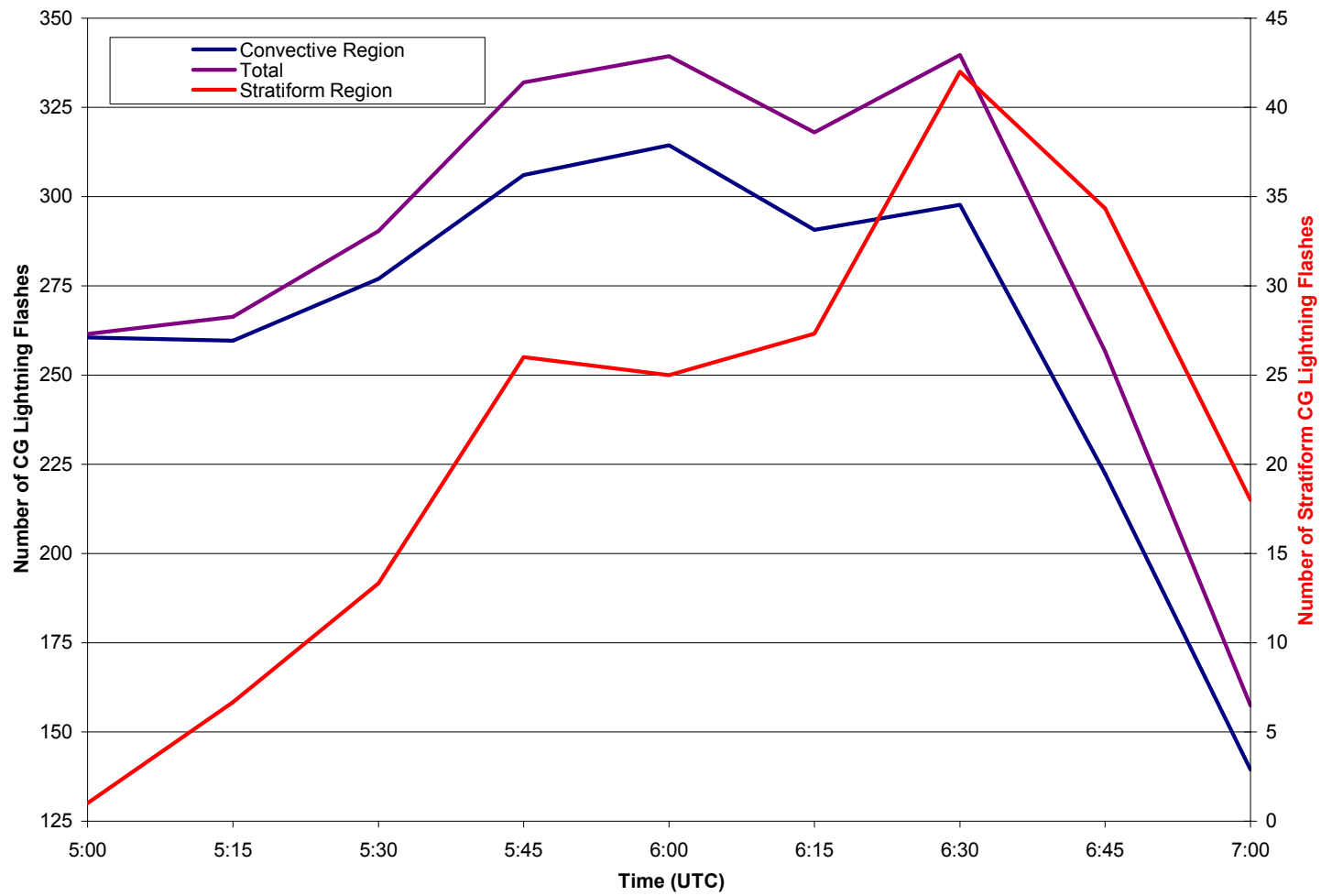


FIG. 5.27. Convective line, stratiform region, and total CG lightning flash trends from 5:00 to 7:00 UTC 16 June 2002, time averaged every 5 min with a 3-point running mean smoother. Time is listed along the x-axis. Note the convective and total number of CG flashes is listed along the primary y-axis and the number of stratiform region CG lightning flashes corresponds to the secondary y-axis.

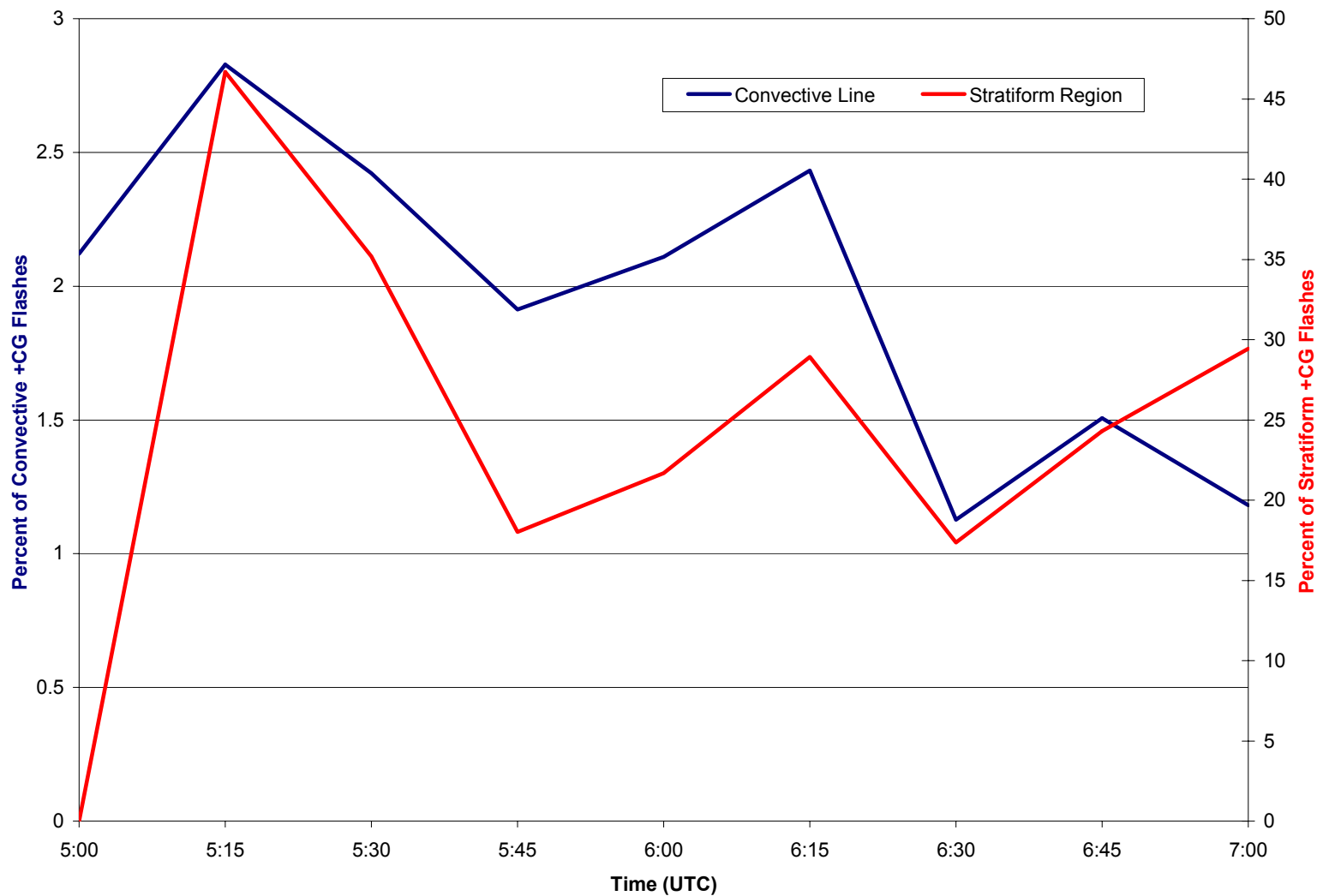


FIG. 5.28. Convective line (blue line) and stratiform region (red line) percent +CG flash trend from 05:00 to 07:00 UTC 16 June 2002, time averaged every 5 min with a 3-point running mean smoother. Time listed along the x-axis. Note the percent of convective +CGs corresponds to the primary y-axis, and the percent of stratiform +CGs corresponds to the secondary y-axis.

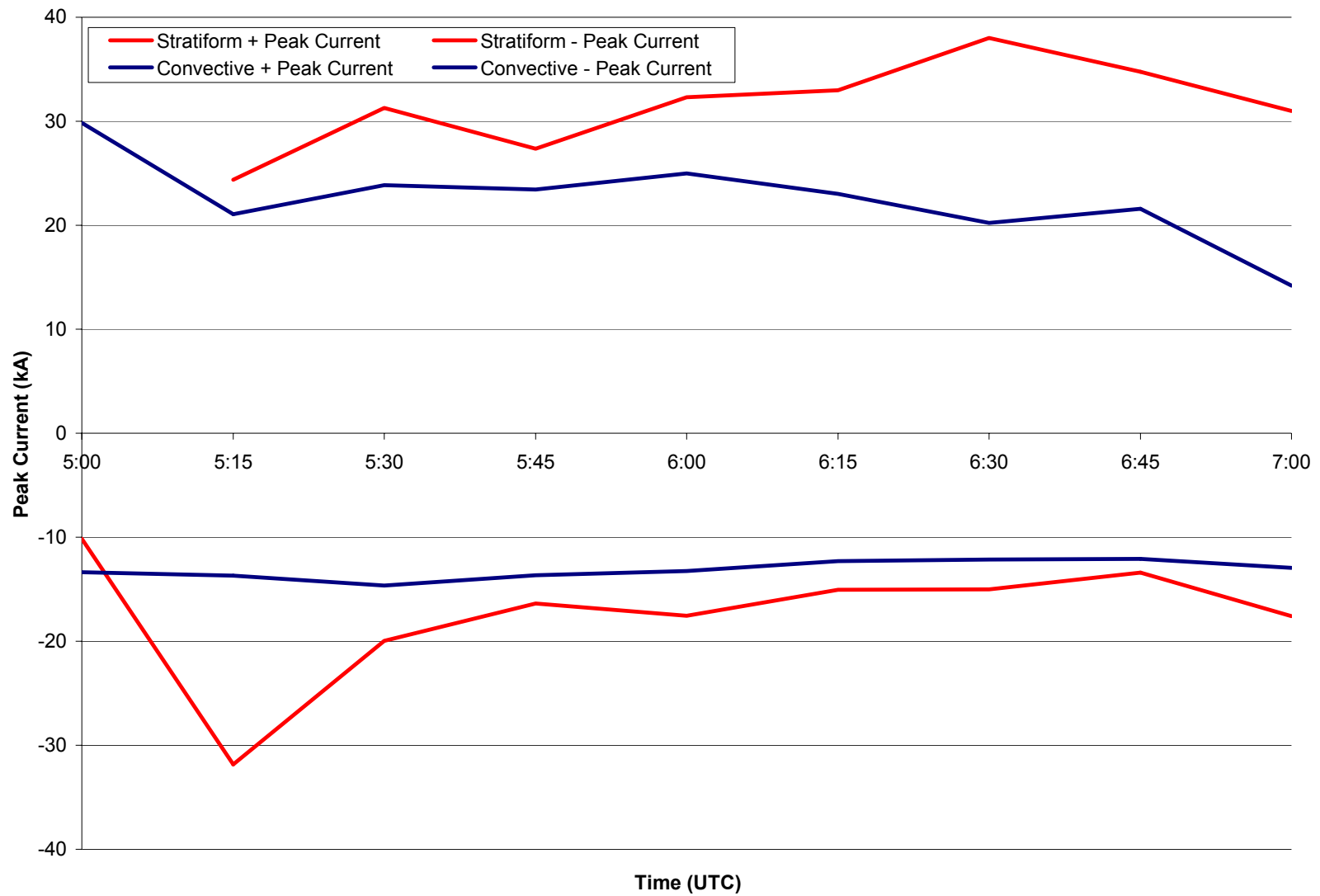


FIG. 5.29. Convective (blue lines) and stratiform (red lines) CG lightning peak positive and negative current trends (kA) from 05:00 to 07:00 UTC 16 June 2002, time averaged every 5 min with a 3-point running mean smoother.

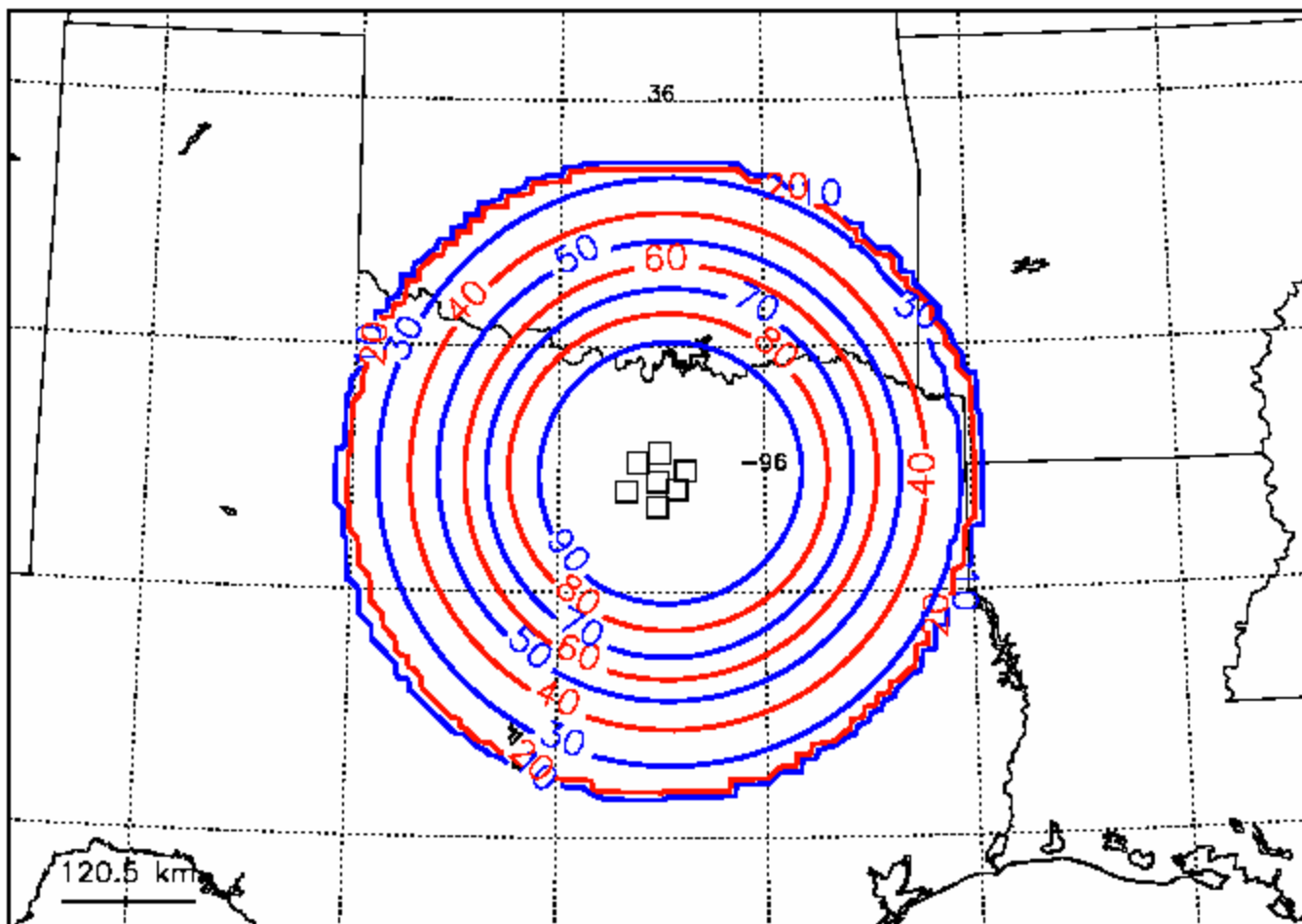


FIG. 5.30. Detection efficiency of the LDAR II network during the 16 June 2002 MCS. The seven squares represent the seven LDAR II sensors used in this case study. The circles around the network represent the percent (%) of LDAR II flashes can be detected out to a given range. (Image adapted from M. Murphy 2003).

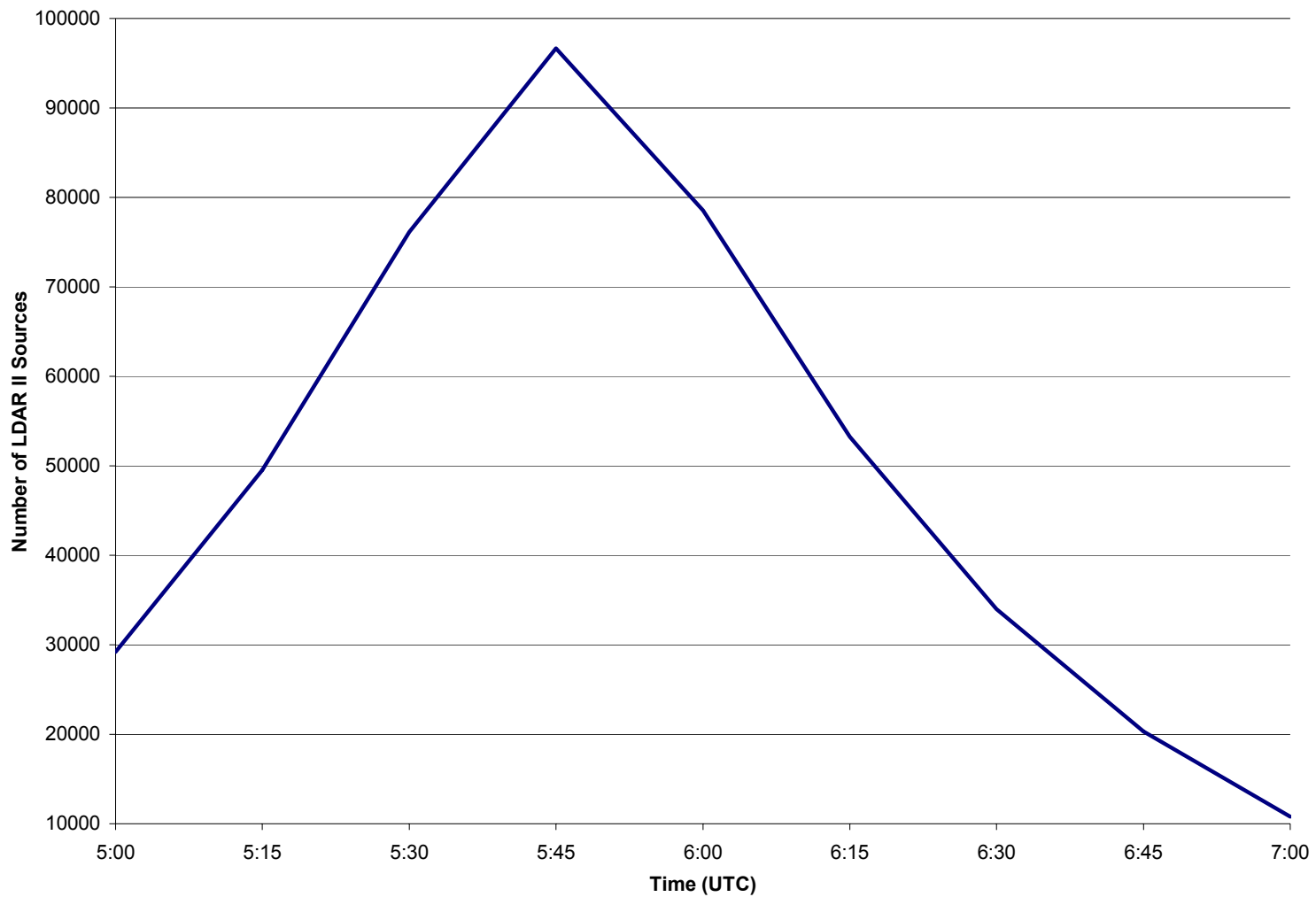


FIG. 5.31. Total LDAR II source trend while the 16 June 2002 MCS was within the KFWS radar viewing range (~05:00-07:00 UTC), time averaged every 5 min with a 3-point running mean smoother. Time listed along the x-axis, and the number of LDAR II sources is listed along the y-axis.

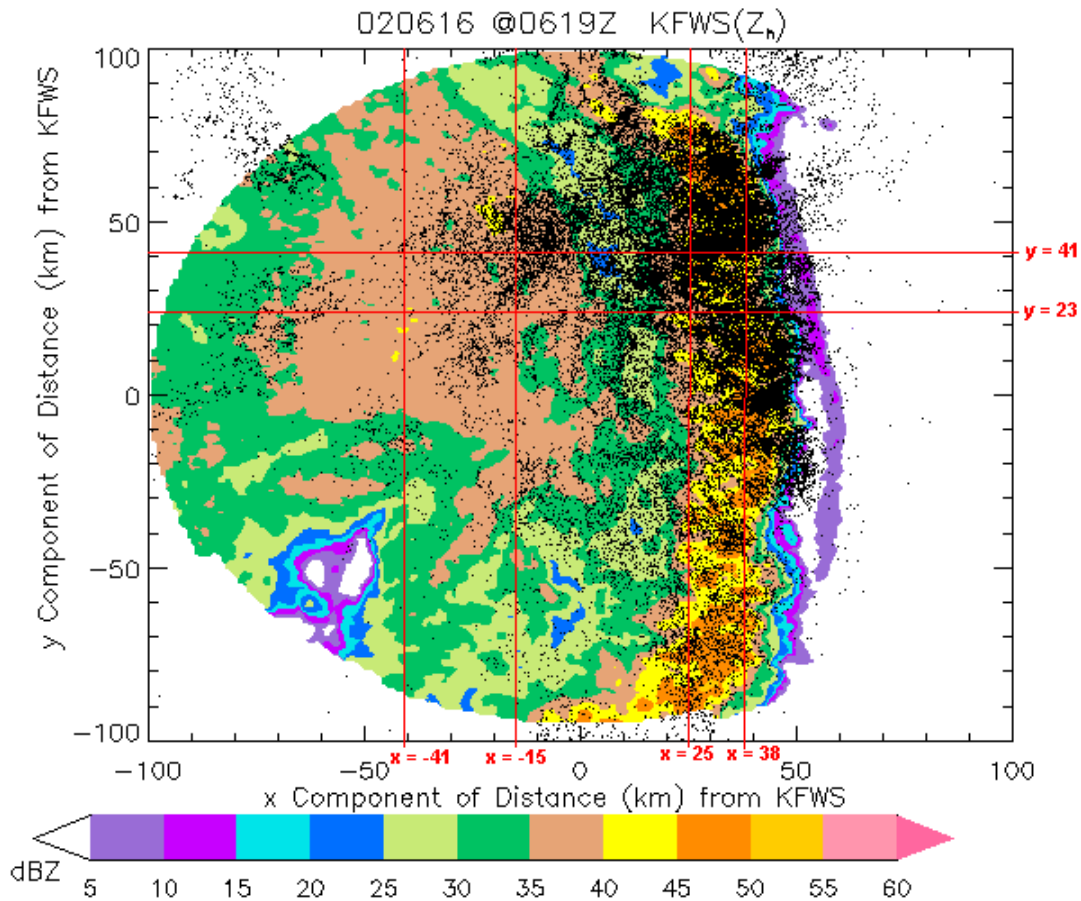


FIG. 5.32. 0.5-km CAPPI image of radar reflectivity (dBZ) with LDAR II sources overlaid (black dots) at 06:19 UTC 16 June 2002. Radar reflectivity is color-shaded according to the scale, and the KFWS radar is located in the center of the image. 5 min of LDAR II sources occurring at all altitudes centered on the time of the radar image are plotted. The reflectivity and LDAR II data have been rotated counterclockwise by  $40^\circ$  so that the x- and y-axes represent the x- and y-components of distance (km) from the KFWS radar, respectively. The four vertical and two horizontal lines represent the line-parallel and line-normal vertical cross-section locations, respectively, in Figs. 5.33-5.35.

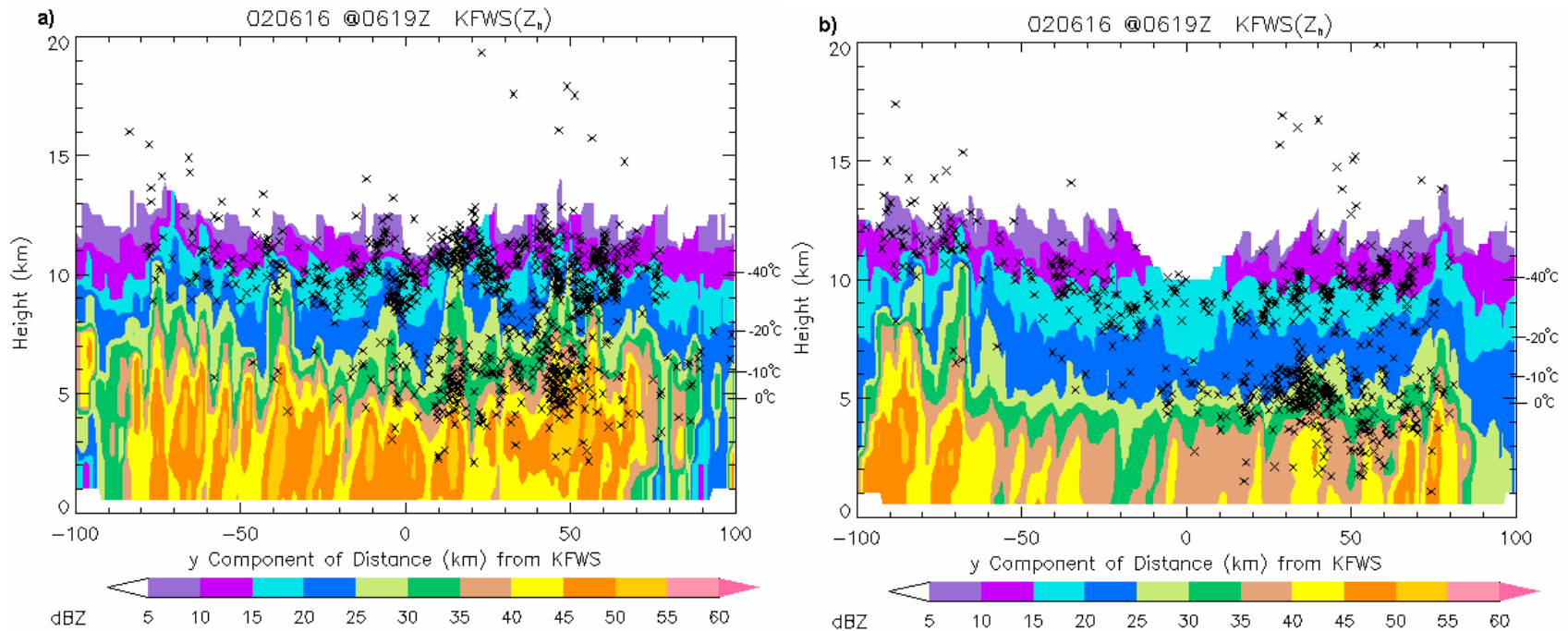


FIG. 5.33. Vertical cross-sections of the convective line at 06:19 UTC 16 June 2002 taken line-parallel through Fig. 5.32 at a)  $x = 38$  km (the leading convective line), and b)  $x = 25$  (the back edge of the convective line). Radar reflectivity (dBZ) is color-shaded according to the scale, and LDAR II sources (at  $x \pm 0.5$  km) are overlaid as black "x"s. The y-axis represents height above ground level (km) and the x-axis represents the x-component of distance from the KFWS radar. Significant temperature levels (0 °C, -10 °C, -20 °C, and -40 °C) are listed along the y-axis on the right-hand side of the image.

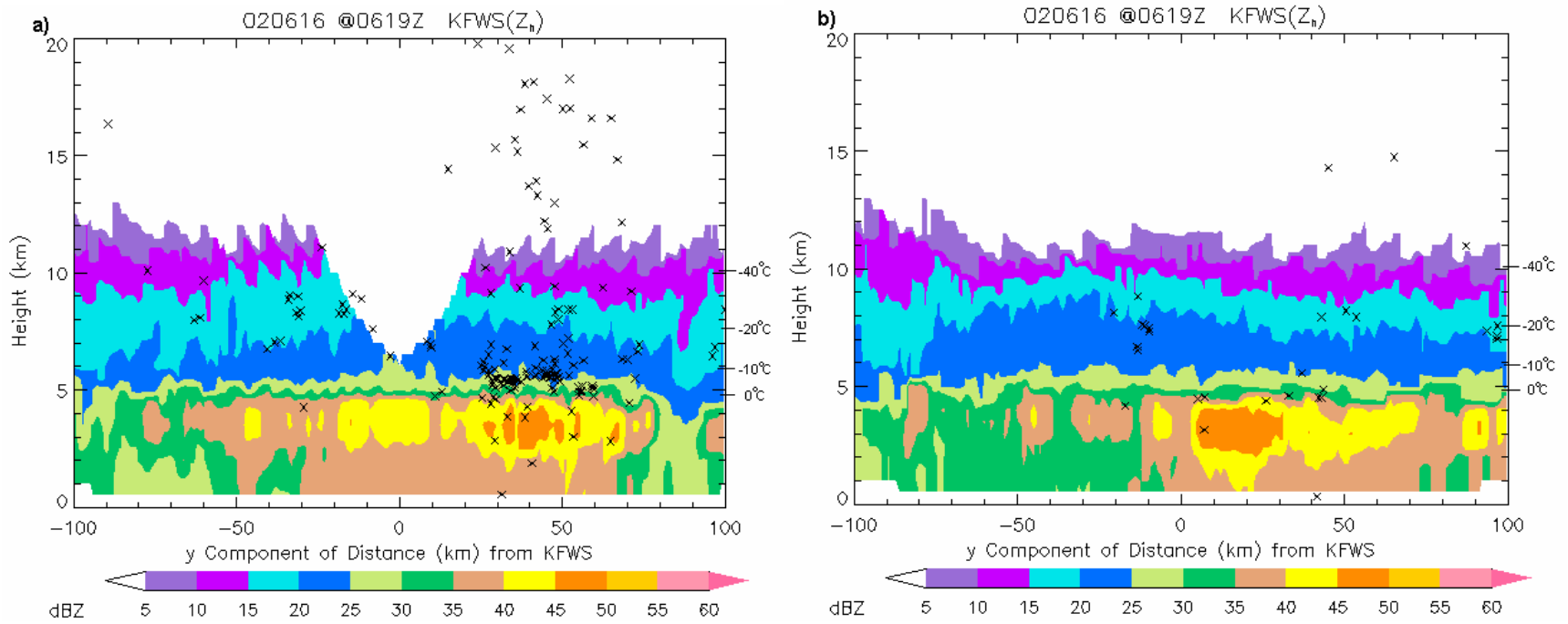


FIG. 5.34. Same as Fig. 5.33, but taken line-parallel through Fig. 5.32 at a) the front edge of the stratiform region at  $x = -15$  km and b) the back edge of the stratiform region at  $x = -41$  km.

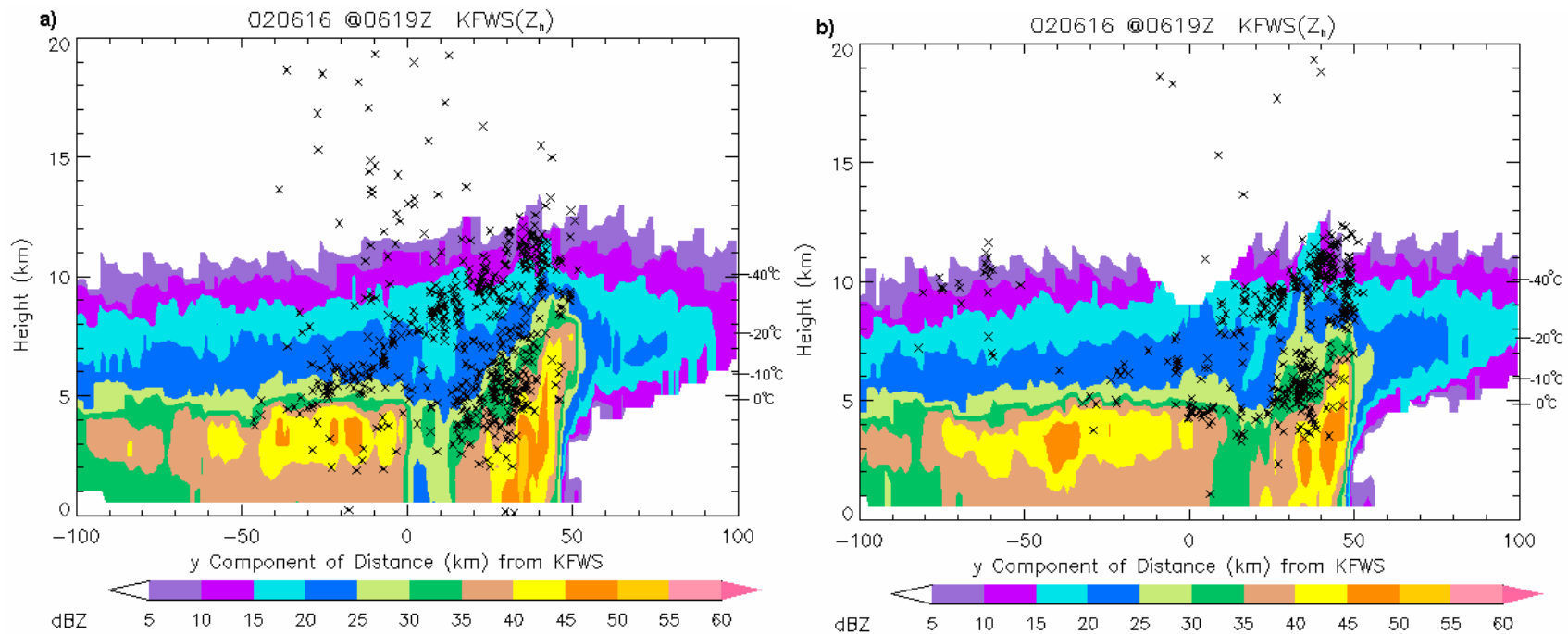


FIG. 5.35. Vertical cross-sections of the 06:19 UTC UTC 16 June 2002 MCS in Fig. 5.32 taken line-perpendicular through a) the stratiform, transition, and convective regions at  $y = 41$  km, and b) the stratiform region, transition zone enhanced reflectivity “bridge”, and convective line at  $y = 23$  km. Radar reflectivity (dBZ) is color-shaded according to the scale, and LDAR II sources (at  $x \pm 0.5$  km) are overlaid as black “x”s. The y-axis represents height above ground level (km) and the x-axis represents the y-component of distance from the KFWS radar. Significant temperature levels (0 °C, -10 °C, -20 °C, and -40 °C) are listed along the y-axis on the right-hand side of the image.

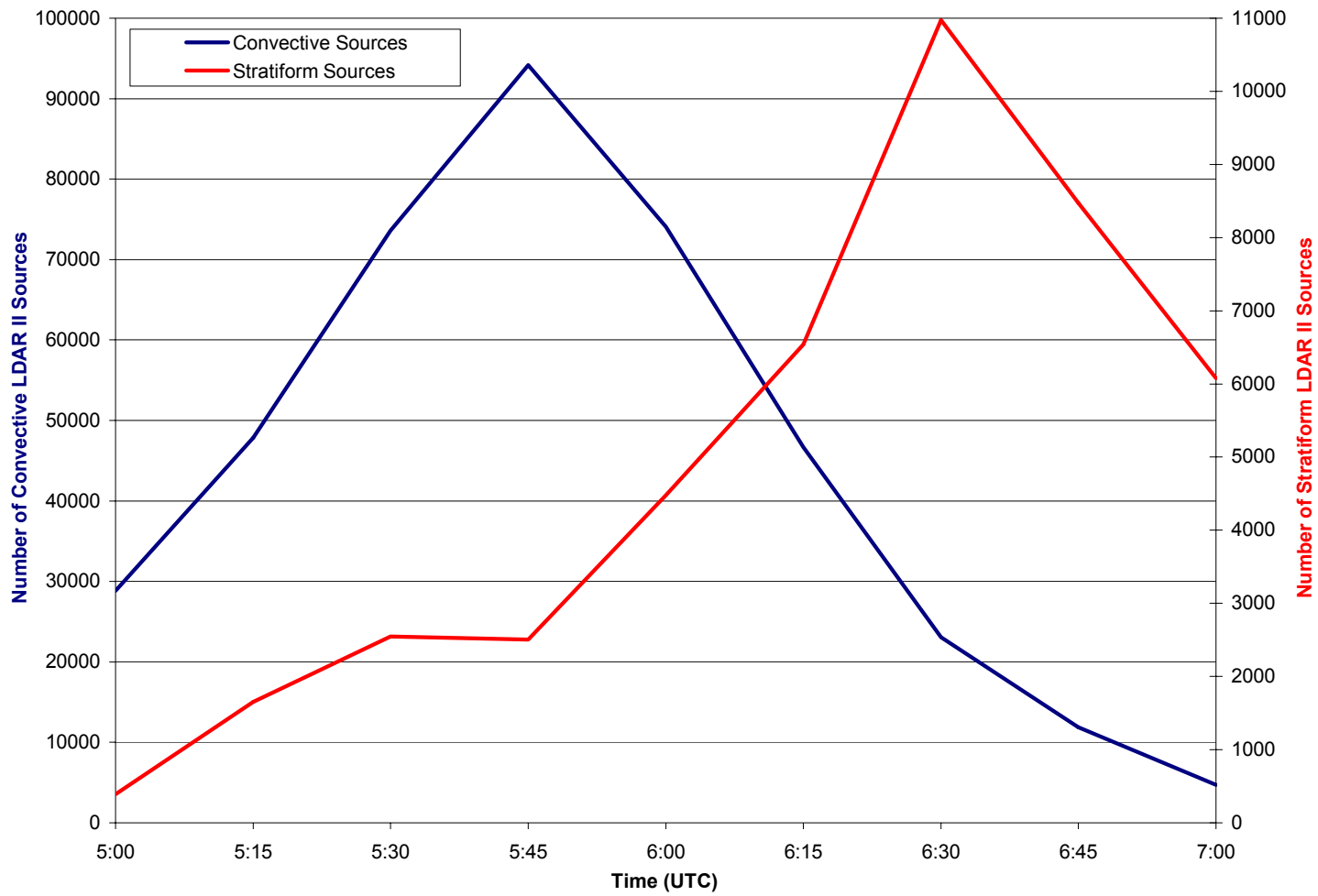


FIG. 5.36. Convective (blue line) and stratiform (red line) region LDAR II source trend from 05:00 to 07:00 UTC 16 June 2002, time averaged every 5 min with a 3-point running mean smoother. Time is listed along the x-axis. Note the number of convective sources corresponds to the primary y-axis, and the number of stratiform sources corresponds to the secondary y-axis.

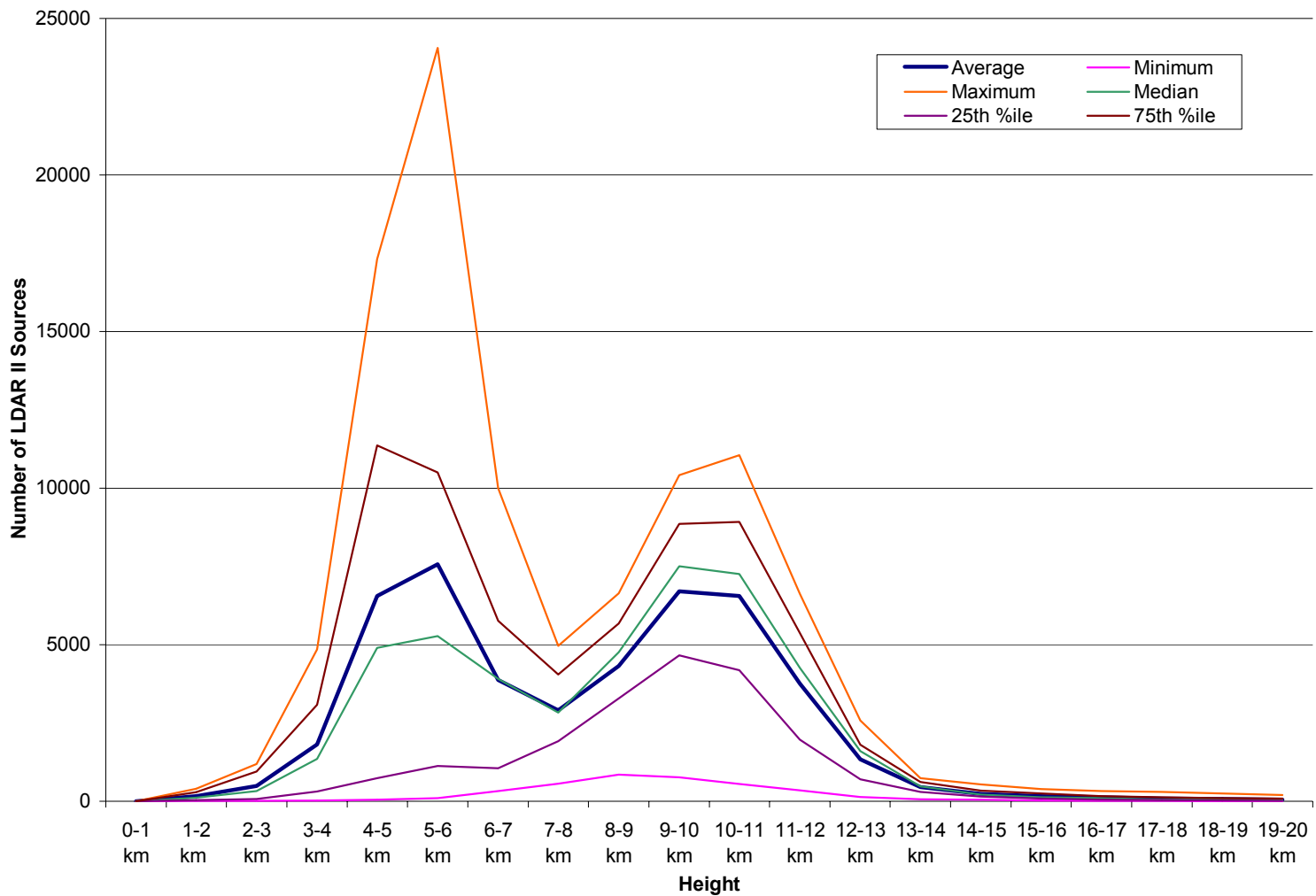


FIG. 5.37. Average (blue line), minimum (pink line), maximum (orange line), median (green line), 25<sup>th</sup> percentile (violet line), and 75<sup>th</sup> percentile (brown line) of sources within the convective region for each 1-km height level from 0 km to 20 km from 05:00 to 07:00 UTC 16 June 2002. Height levels are indicated along the x-axis, and the number of sources per height level is shown along the y-axis.

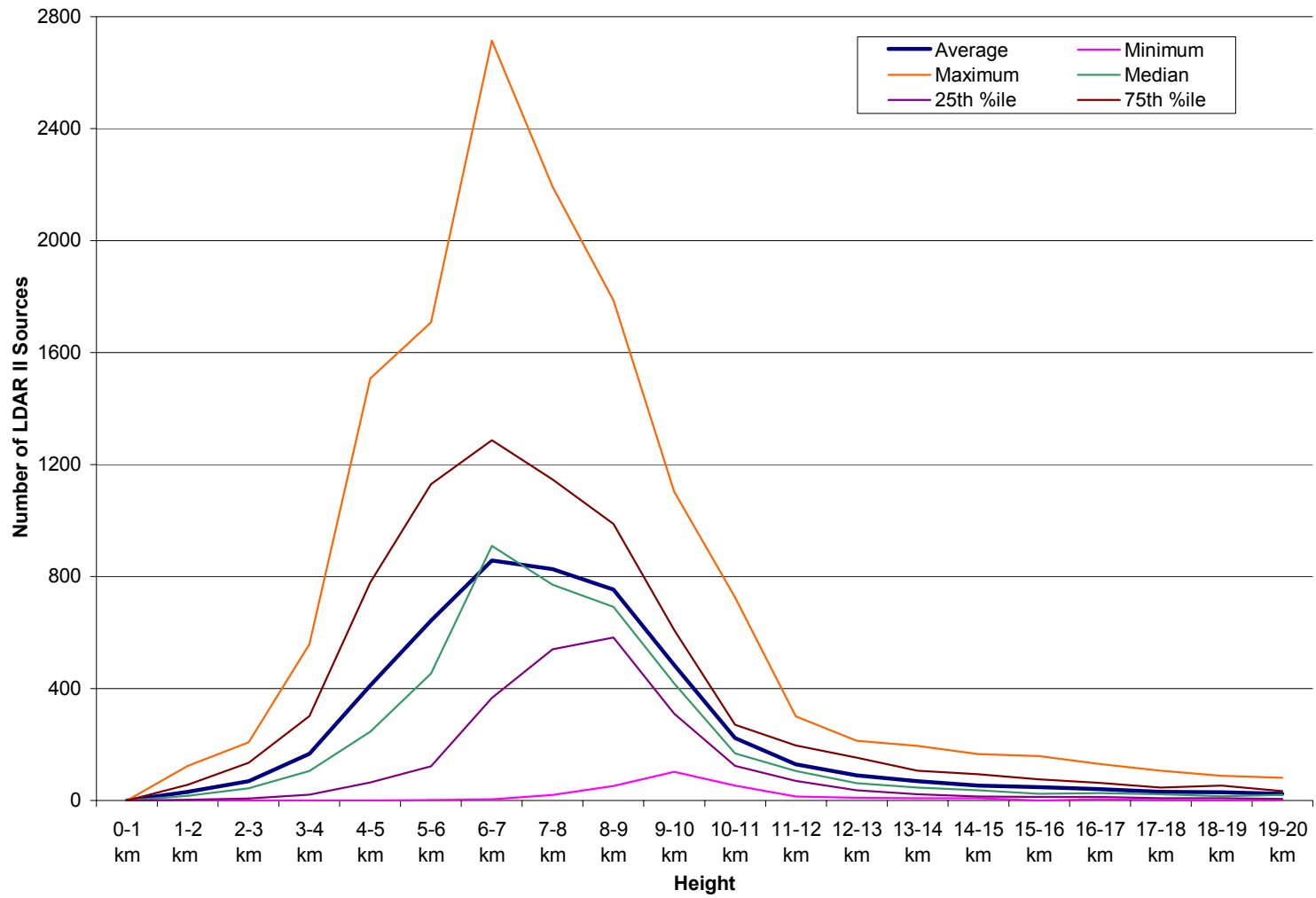


FIG. 5.38. Same as Fig. 5.37, but for the stratiform region.

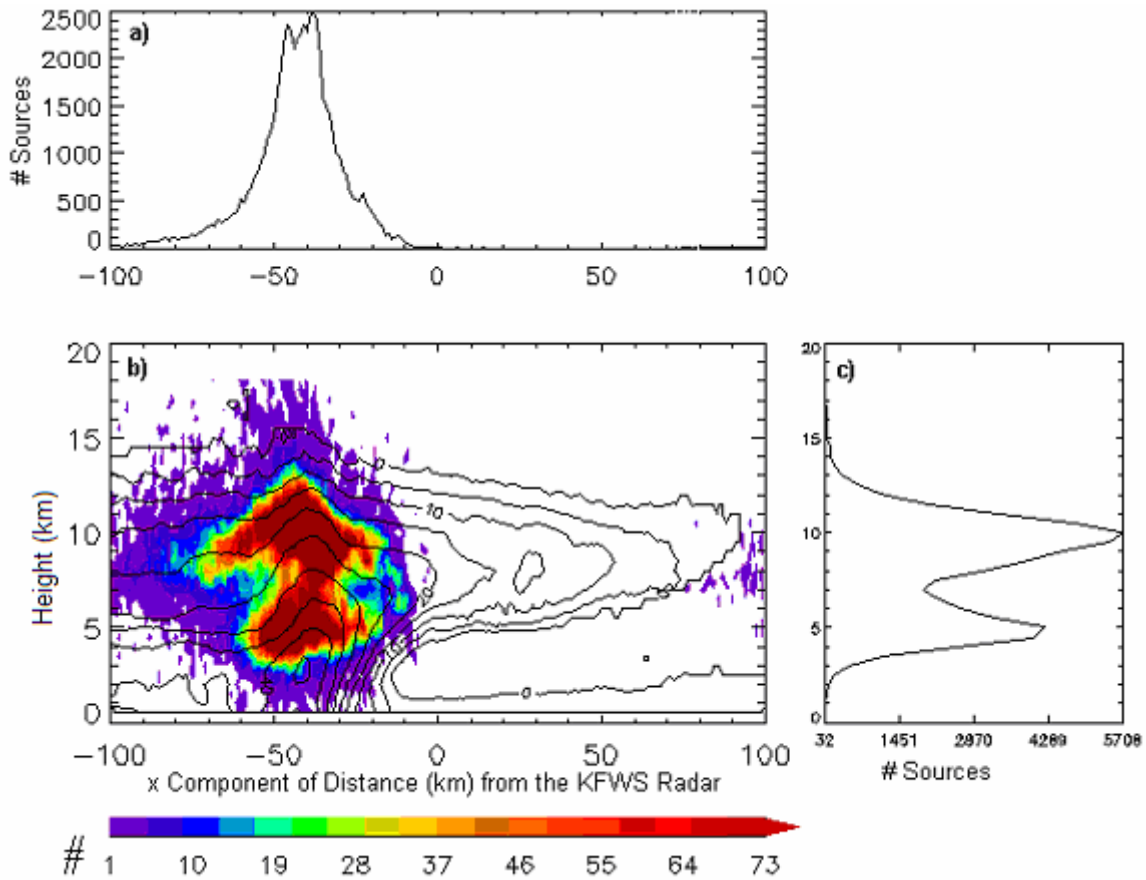


FIG. 5.39. Line-normal composite radar reflectivity and LDAR II source images of the 16 June 2002 MCS at 05:20 UTC, where a) the number of sources versus line-normal horizontal distance is plotted, b) a vertical cross-section (height versus the x-component of distance (km) from the KFWS radar) of average radar reflectivity (dBZ) is line-contoured, and the total number of LDAR II sources is color-shaded according to the scale, and c) the number of sources versus height (km) is plotted. The MCS has been rotated counterclockwise  $40^\circ$  before this image was produced.

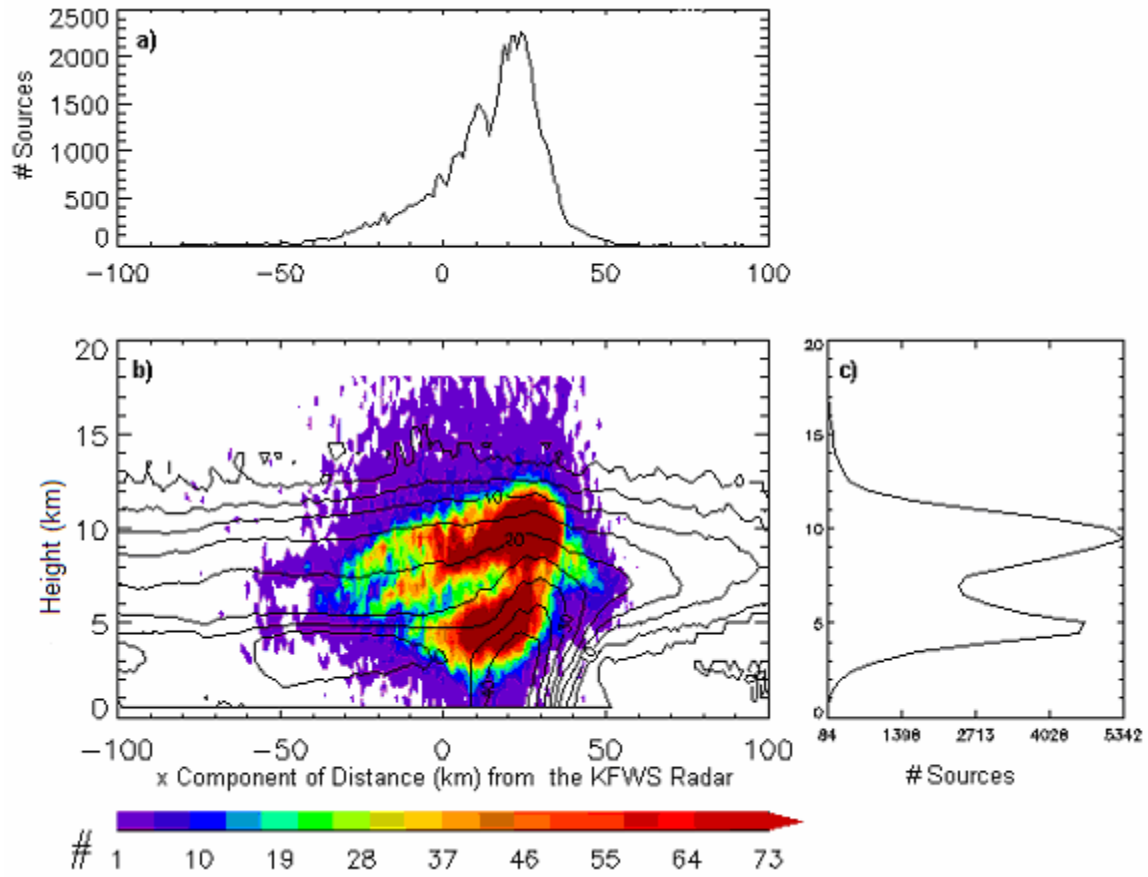


FIG. 5.40. Same as Fig. 5.39, except at 06:09 UTC.

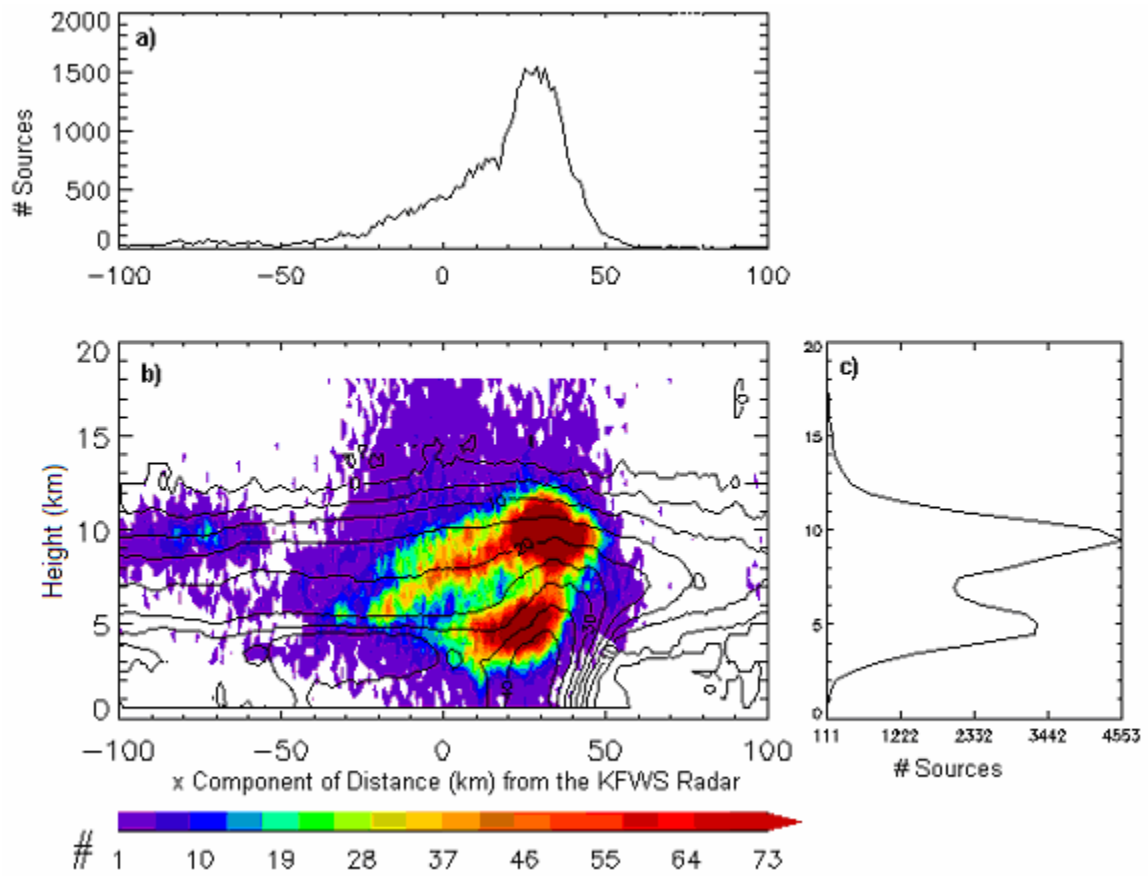


FIG. 5.41. Same as Fig. 5.39, except at 06:14 UTC.

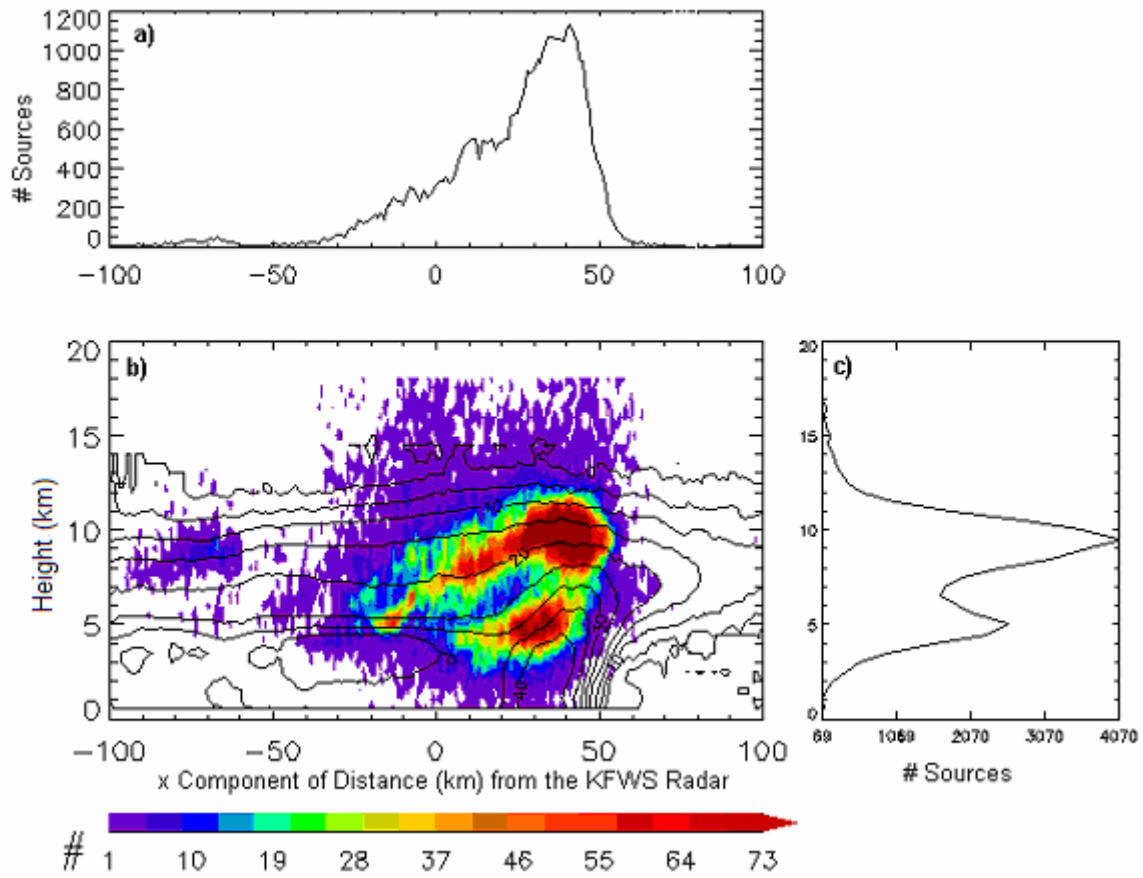


FIG. 5.42. Same as Fig. 5.39, except at 06:19 UTC.

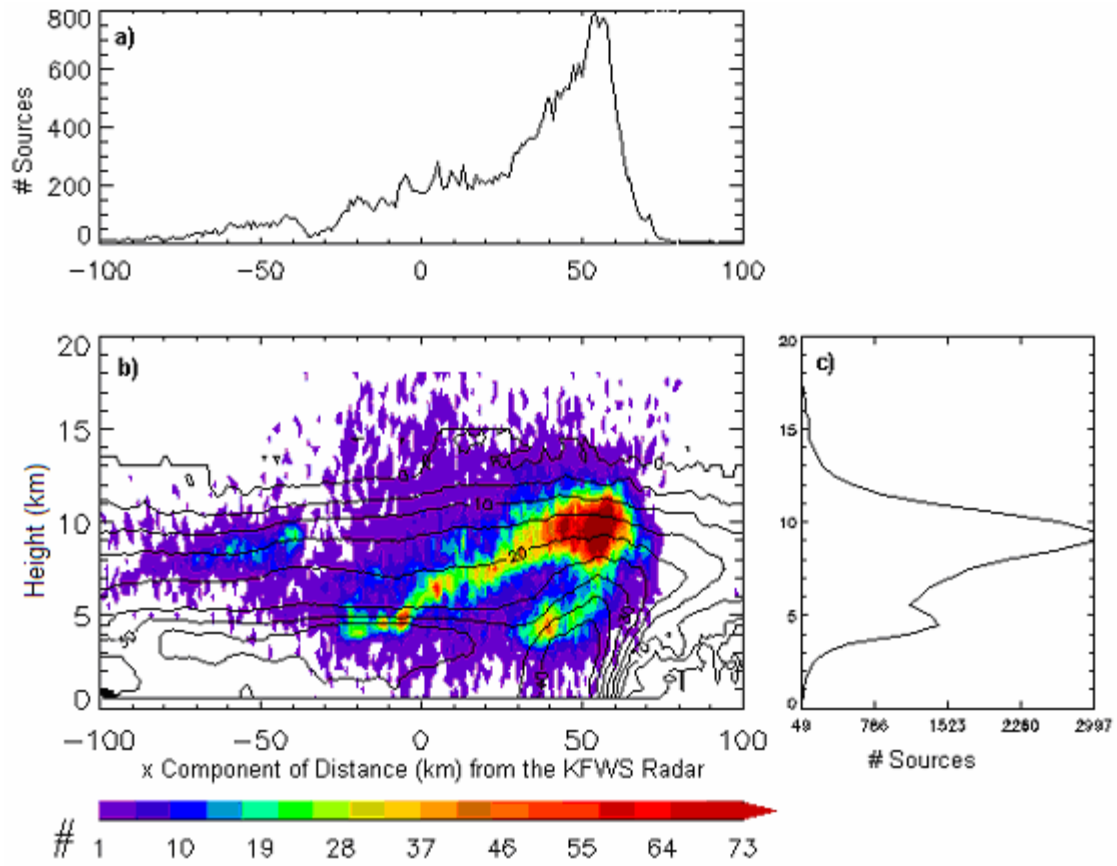


FIG. 5.43. Same as Fig. 5.39, except at 06:29 UTC.

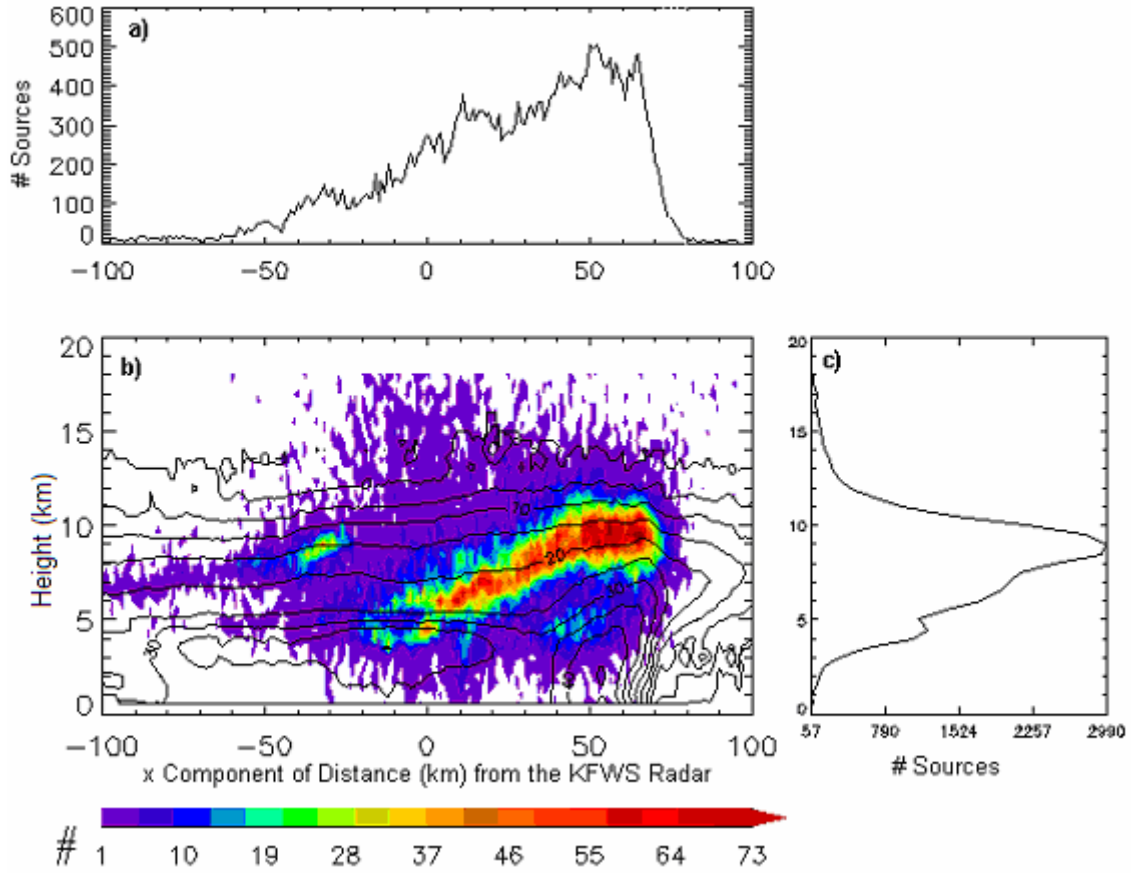


FIG. 5.44. Same as Fig. 5.39, except at 06:34 UTC.

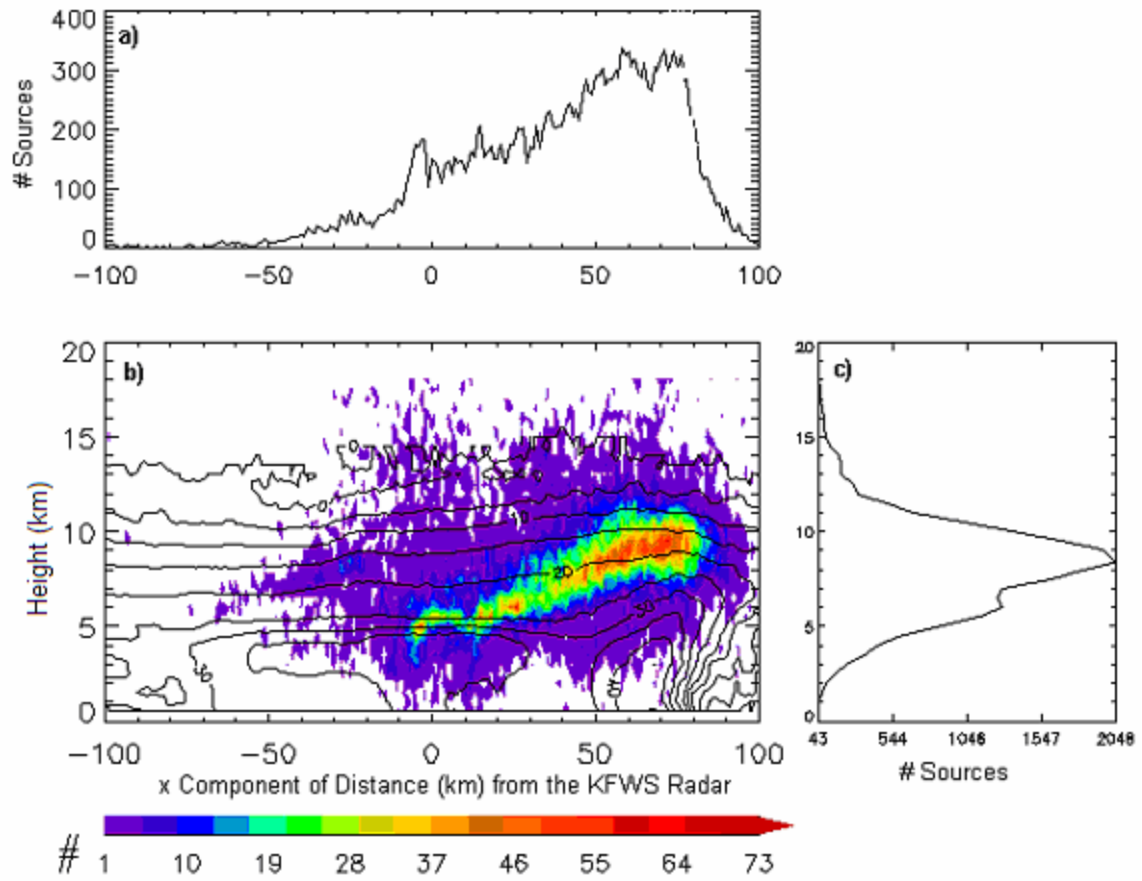


FIG. 5.45. Same as Fig. 5.39, except at 06:44 UTC.

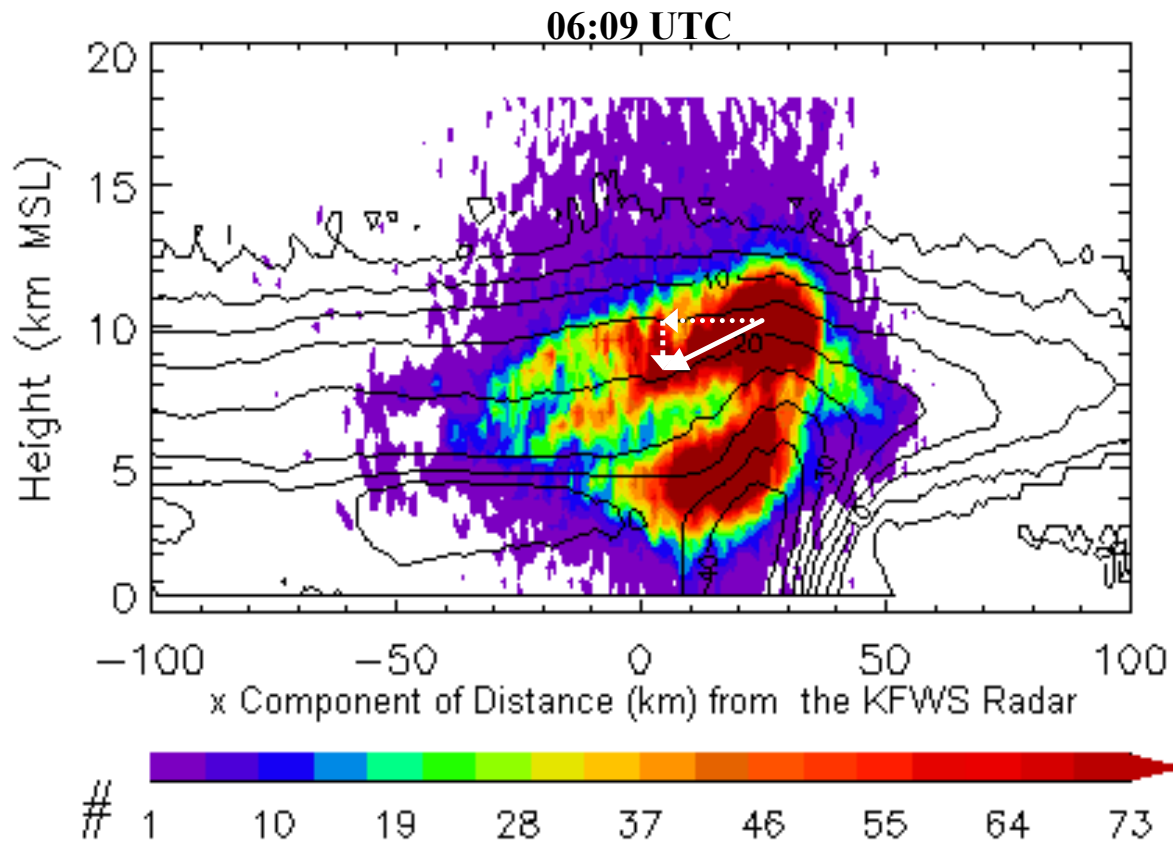


FIG. 5.46. Same as Fig. 5.40(b) but with the  $\sim 10 \text{ ms}^{-1}$  storm-relative front-to-rear flow (horizontal dotted white arrow), the typical hydrometeor fall velocity of  $\sim 1.0 \text{ ms}^{-1}$  (vertical dotted white arrow), and the resulting storm-relative hydrometeor trajectory (slanted solid white arrow) overlaid on the downward and rearward sloping LDAR II source region.

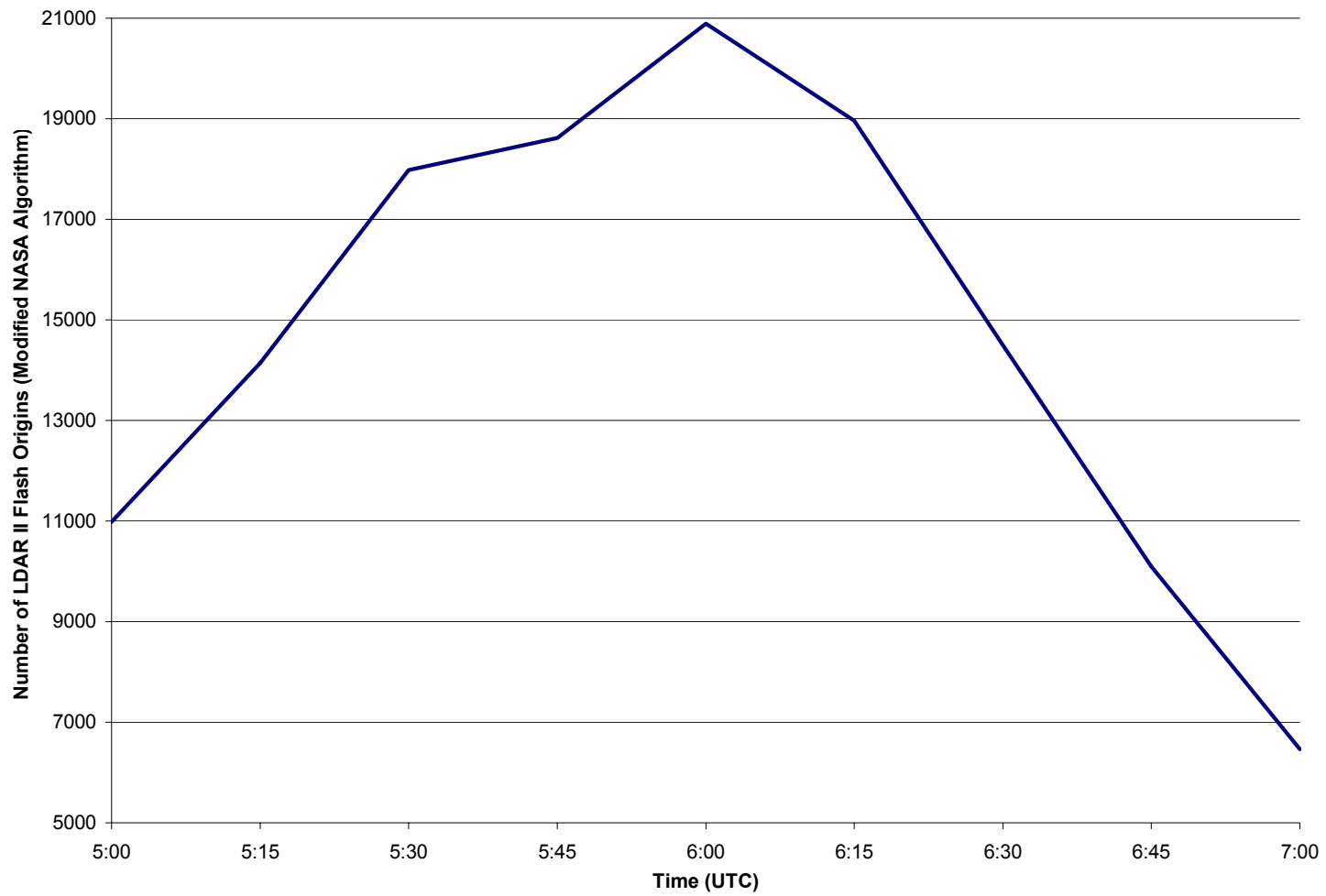


FIG. 5.47. LDAR II flash origin trend for the portion of the 16 June 2002 MCS that was within the KFWS radar viewing range from 05:00 to 07:00 UTC, time averaged every 5 min with a 3-point running mean smoother. Time listed along the x-axis, and the number of LDAR II flash origins are listed along the y-axis. Flash origins were determined using the modified NASA algorithm.

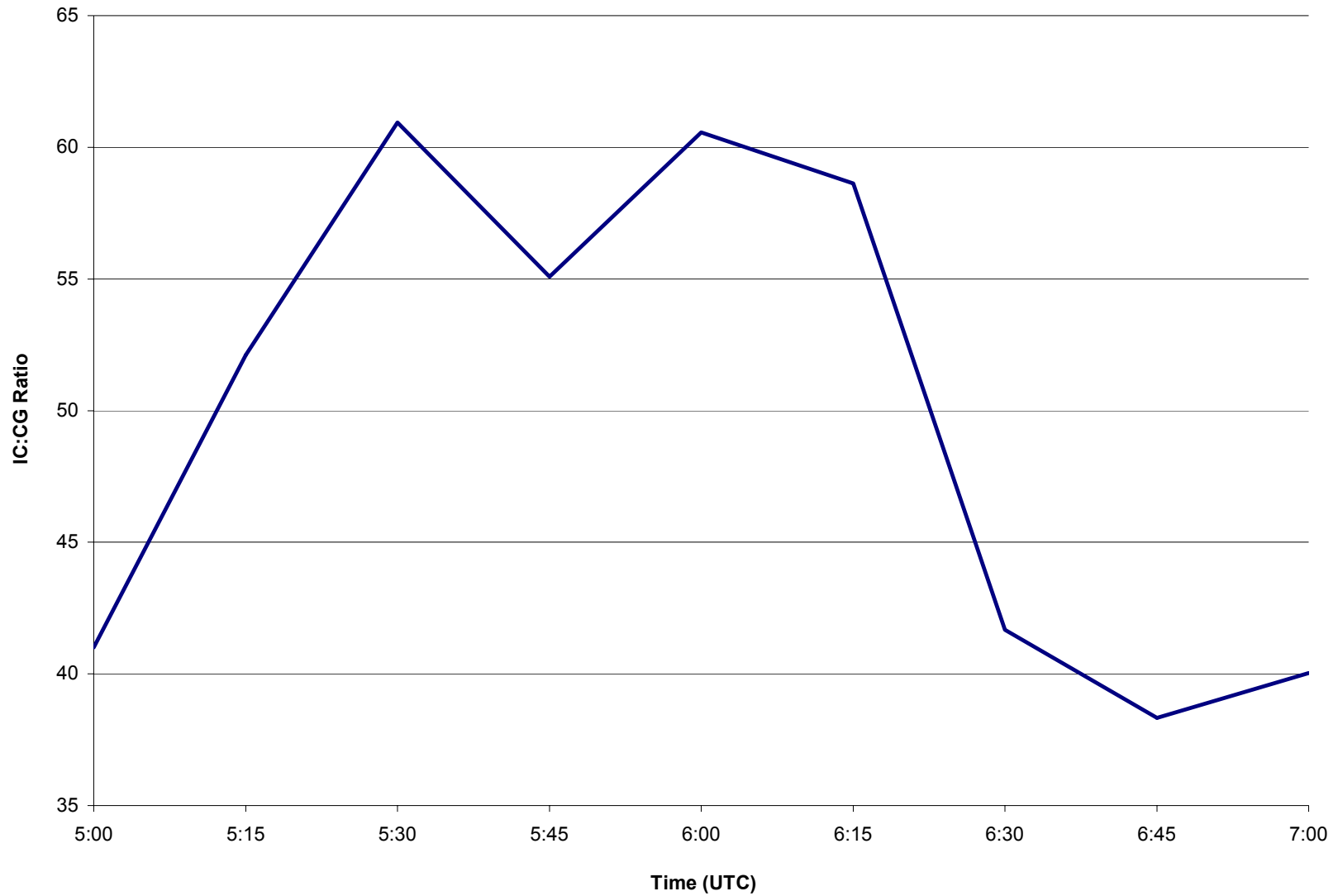


FIG. 5.48. IC:CG ratio trend from 5:00 to 7:00 UTC 16 June 2002, time averaged every 5 min with a 3-point running mean smoother. Time is listed along the x-axis, and the IC:CG ratio is listed along the y-axis.

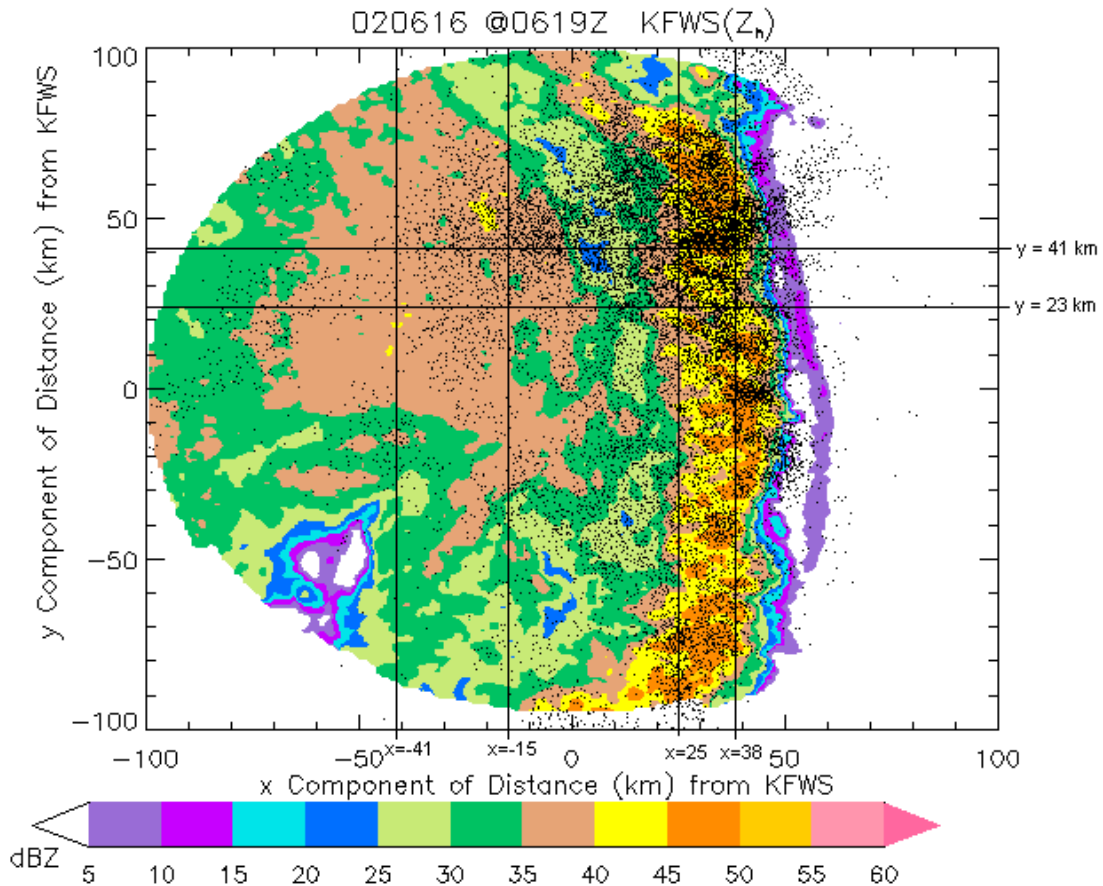


FIG. 5.49. 0.5 km CAPPI image of radar reflectivity (dBZ) with LDAR II flash origins (as determined by the modified NASA algorithm) overlaid (black dots) at 06:19 UTC 16 June 2002. Radar reflectivity is color-shaded according to the scale, and the KFWS radar is located in the center of the image. 5 min of LDAR II flash origins occurring at all altitudes centered on the time of the radar image are plotted. The reflectivity and LDAR II data have been rotated counterclockwise by  $40^\circ$  so that the x- and y-axes represent the x- and y-components of distance (km) from the KFWS radar, respectively. The four vertical and two horizontal lines represent the vertical cross-section locations in Figs. 5.50-5.52.

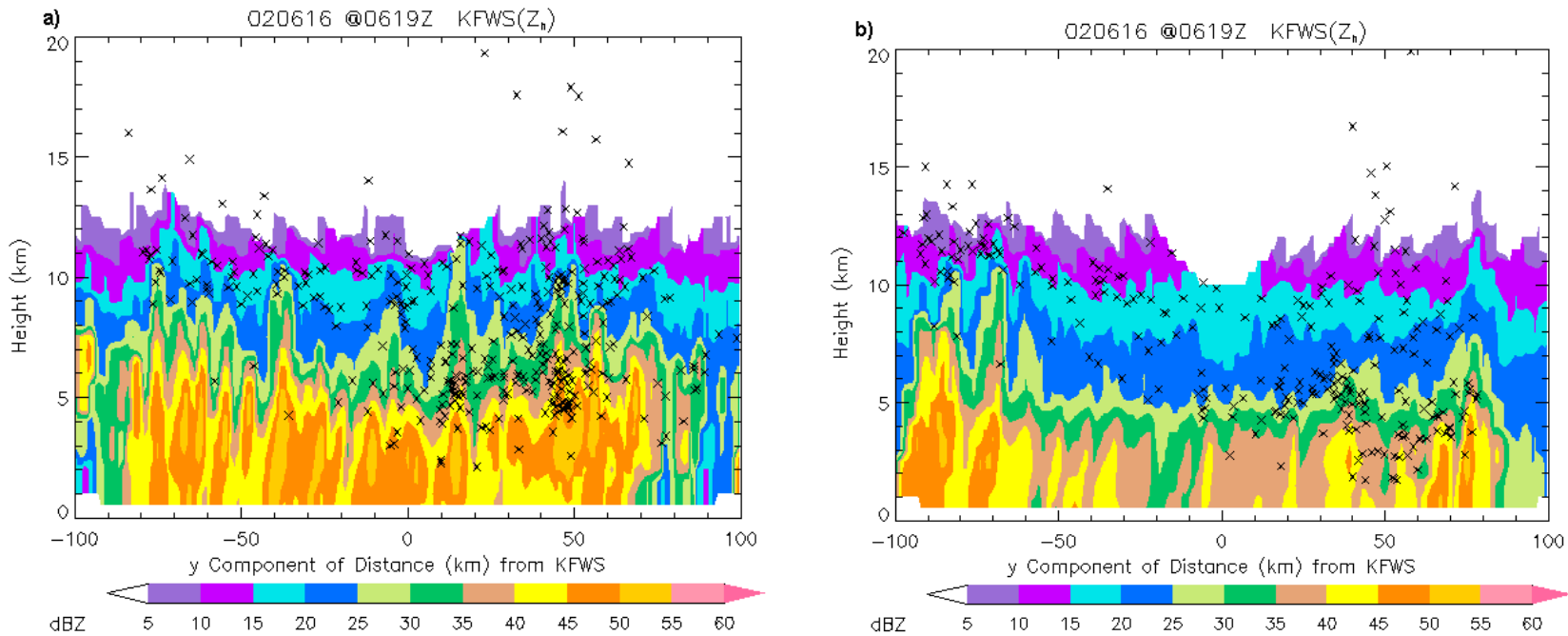


FIG. 5.50. Vertical cross-section of the convective line at 06:19 UTC 16 June 2002 taken line-parallel through Fig. 5.49 at a)  $x = 38$  km (the leading convective line) and b)  $x = 25$  (the back edge of the convective line). Radar reflectivity (dBZ) is color-shaded according to the scale, and LDAR II flash origins (as determined by the modified NASA algorithm) (at  $x \pm 0.5$  km) are overlaid as black "x"s. The y-axis represents height above ground level (km) and the x-axis represents the x-component of distance from the KFWS radar. Significant temperature levels (0 °C, -10 °C, -20 °C, and -40 °C) are listed along the y-axis on the right-hand side of the image.

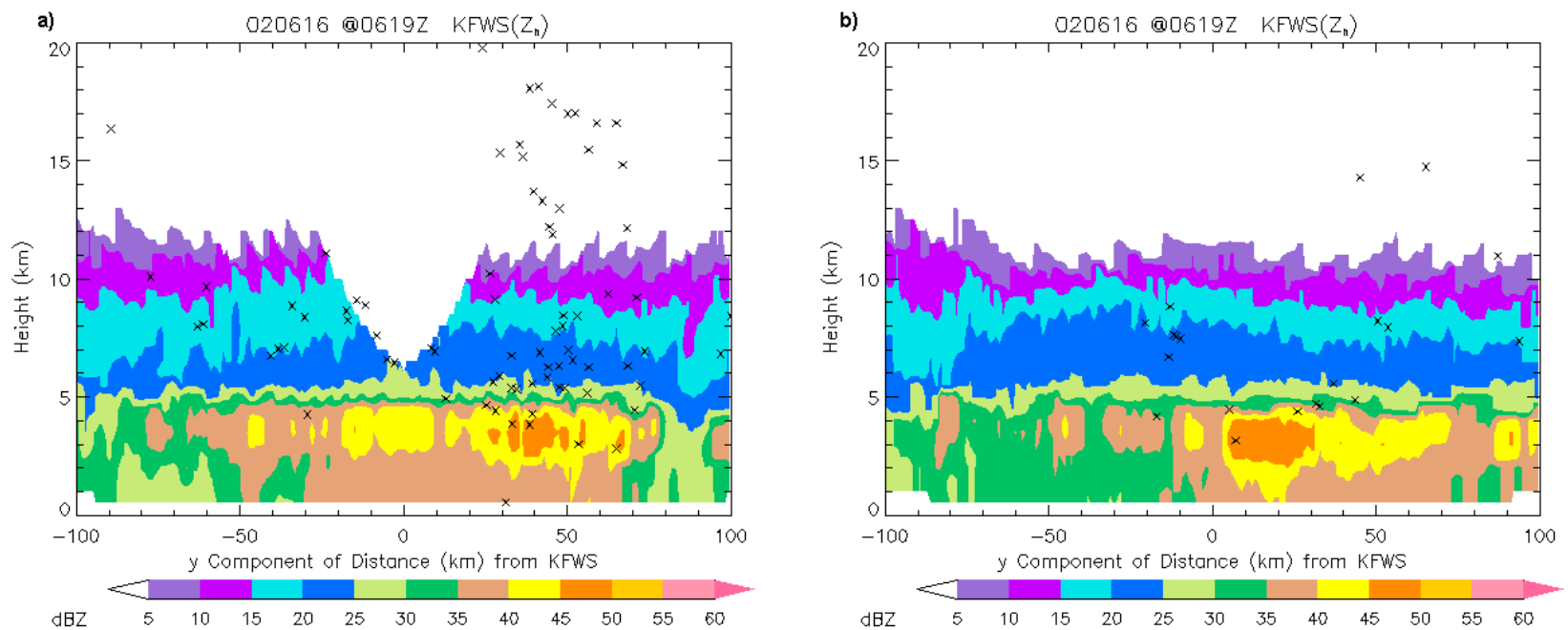


FIG. 5.51. Same as Fig. 5.50, but this vertical cross-section was taken line-parallel through Fig. 5.49 at a) the front edge of the stratiform region at  $x = -15$  km, and b) the back edge of the stratiform region at  $x = -41$  km.

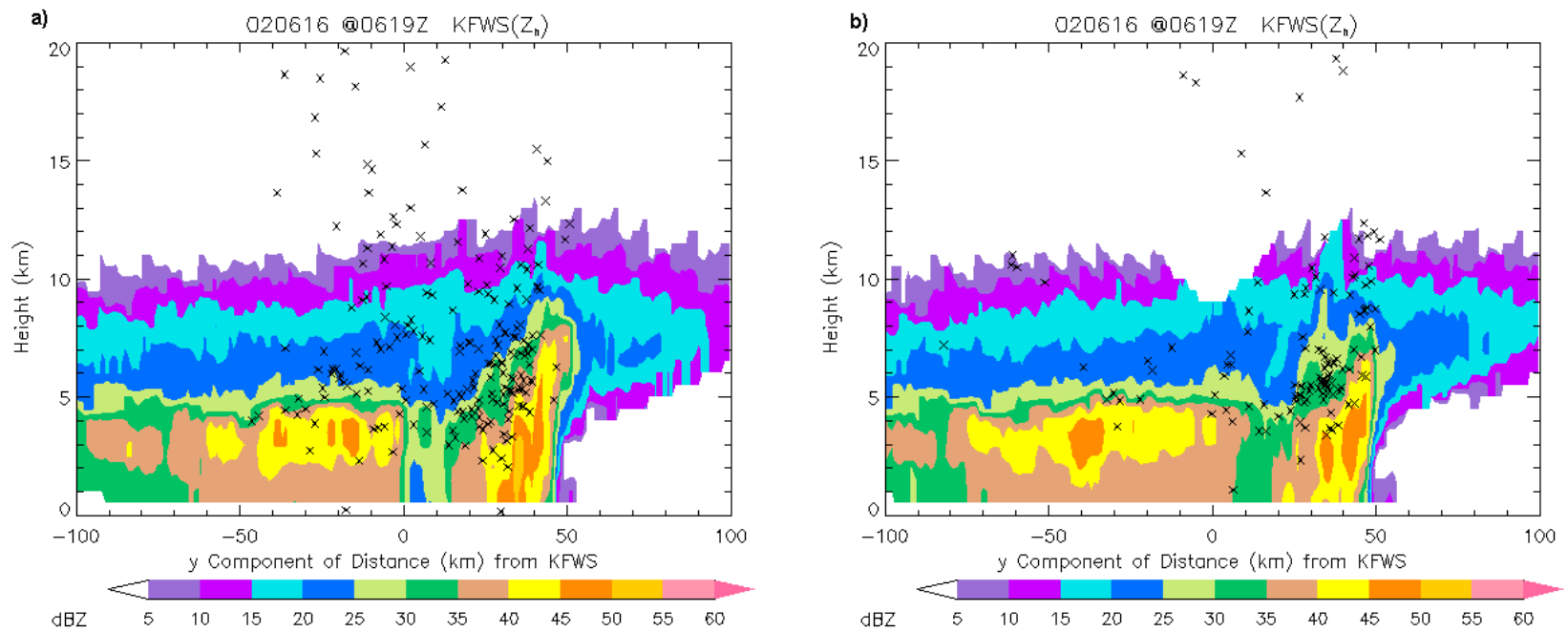


FIG. 5.52. Vertical cross-sections of the 06:19 UTC 16 June 2002 MCS in Fig. 5.49 taken line-perpendicular through a) the stratiform, transition, and convective regions at  $y = 41$  km and b) the stratiform region, transition zone enhanced reflectivity “bridge”, and convective line at  $y = 23$  km. Radar reflectivity (dBZ) is color-shaded according to the scale, and LDAR II flash origins (as determined by the modified NASA algorithm) (at  $x \pm 0.5$  km) are overlaid as black “x”s. The y-axis represents height above ground level (km) and the x-axis represents the y-component of distance from the KFWS radar. Significant temperature levels ( $0^{\circ}\text{C}$ ,  $-10^{\circ}\text{C}$ ,  $-20^{\circ}\text{C}$ , and  $-40^{\circ}\text{C}$ ) are listed along the y-axis on the right-hand side of the image.

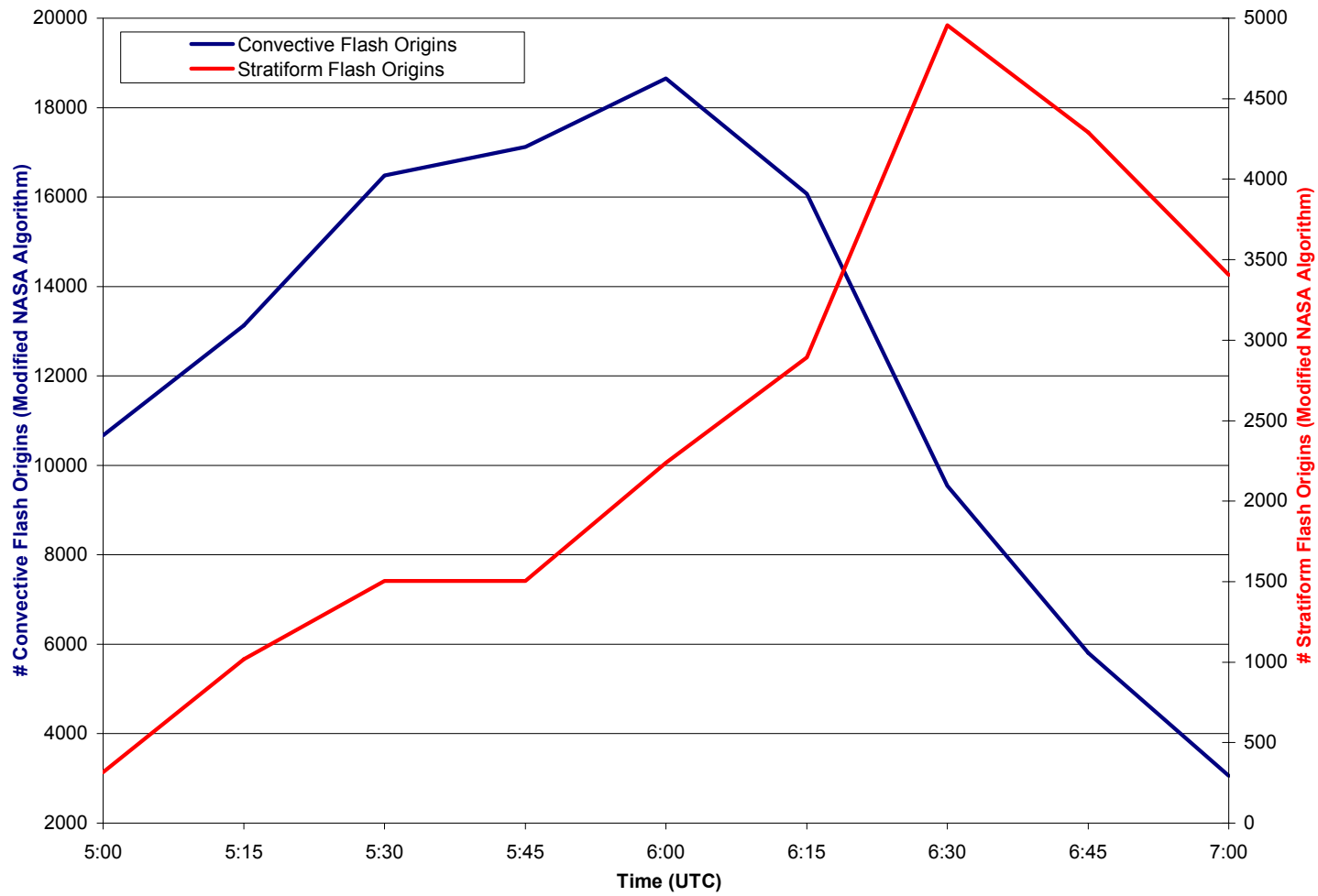


FIG. 5.53. Convective (blue line) and stratiform (red line) LDAR II flash origin trends (as determined by the modified NASA algorithm) from 05:00 to 07:00 UTC 16 June 2002, time averaged every 5 min with a 3-point running mean smoother. Time is listed along the x-axis. The number of convective and stratiform region LDAR II flash origins is listed along the primary and secondary y-axes, respectively.

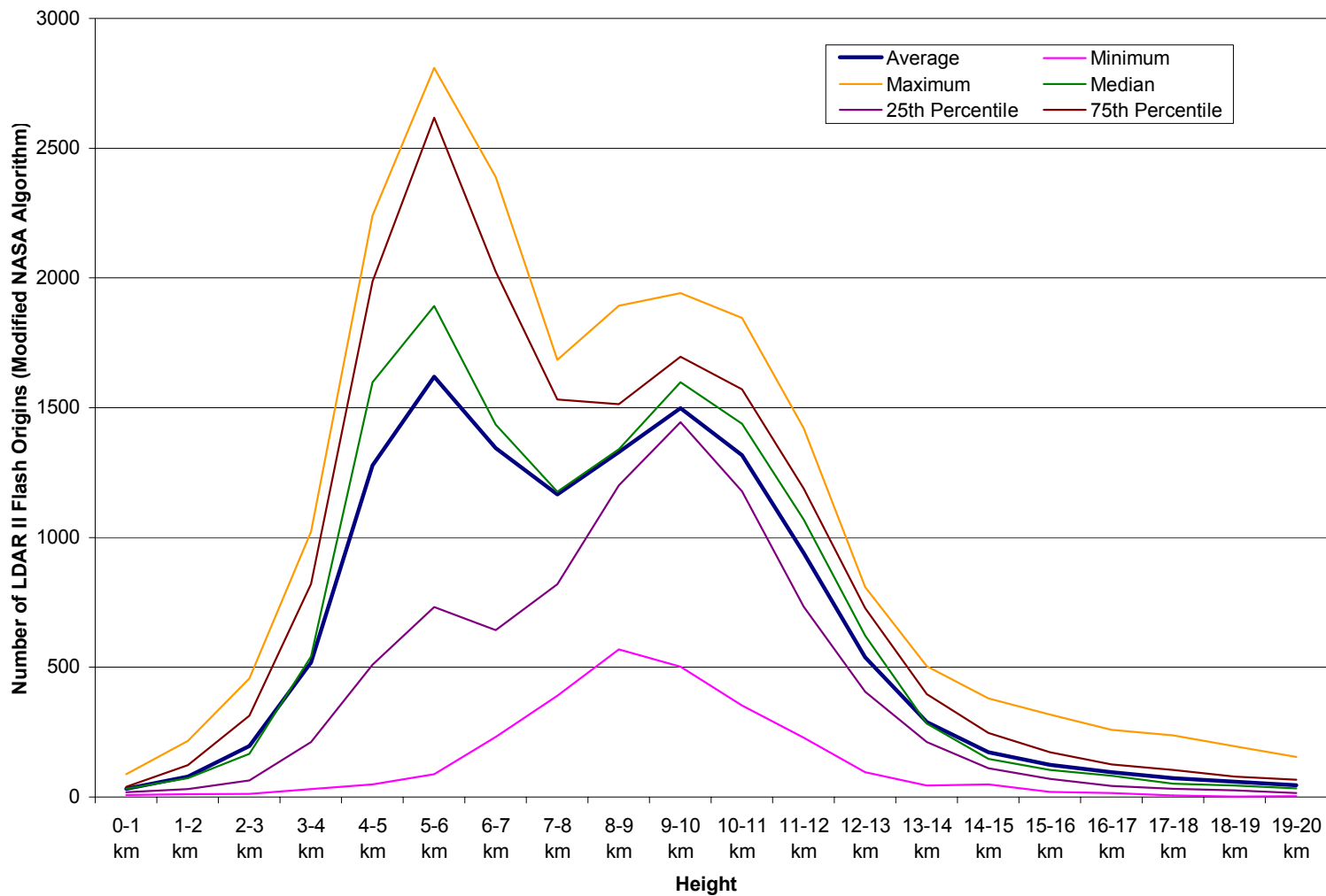


FIG. 5.54. Average (blue line), minimum (pink line), maximum (orange line), median (green line), 25<sup>th</sup> percentile (violet line), and 75<sup>th</sup> percentile (brown line) of LDAR II flash origins within the convective region for each 1-km height level from 0 km to 20 km from 05:00 to 7:00 UTC 16 June 2002. Height levels (km) are listed along the x-axis, and the number of LDAR II flash origins is listed along the y-axis.

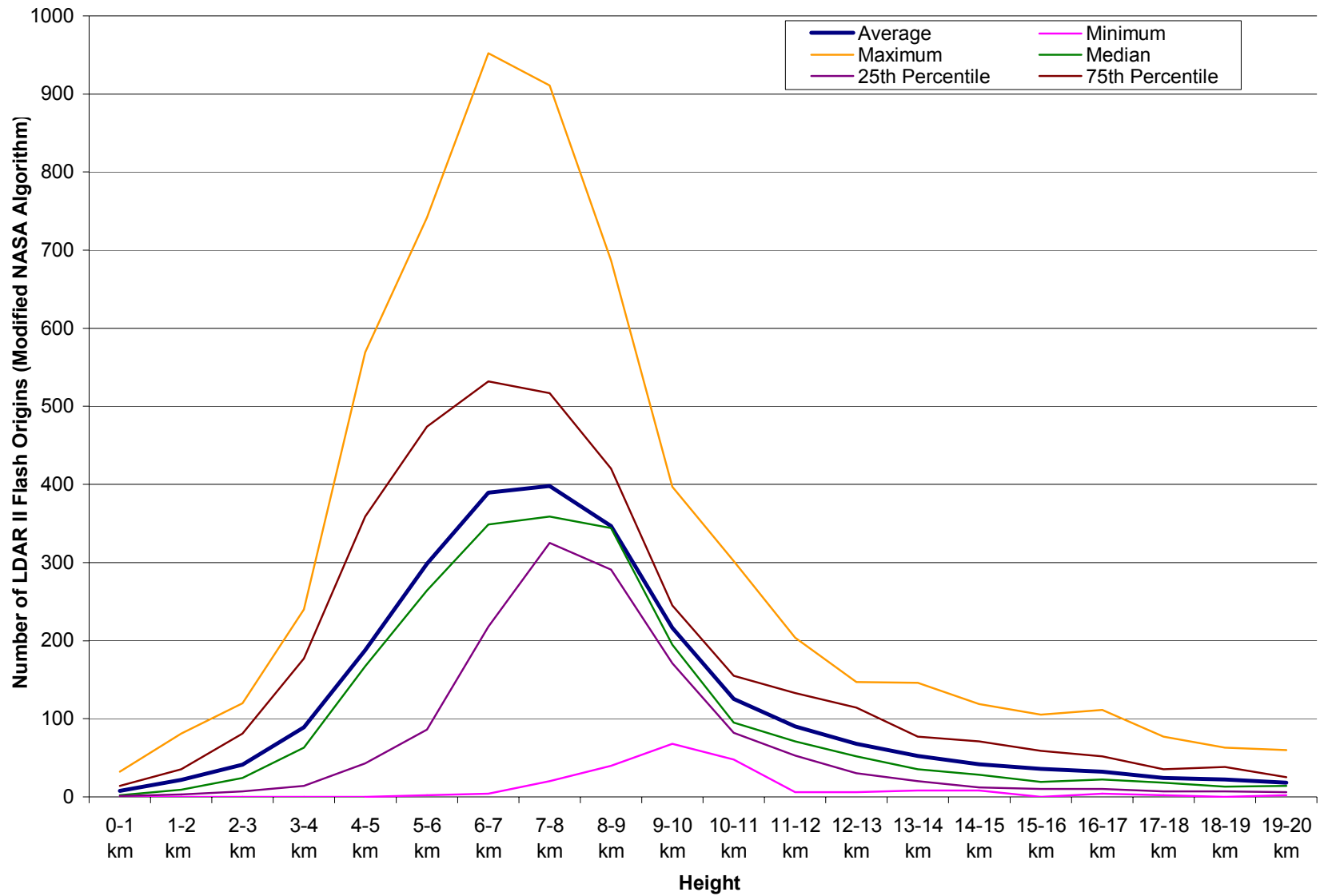


FIG. 5.55. Same as Fig. 5.54, but for the stratiform region.

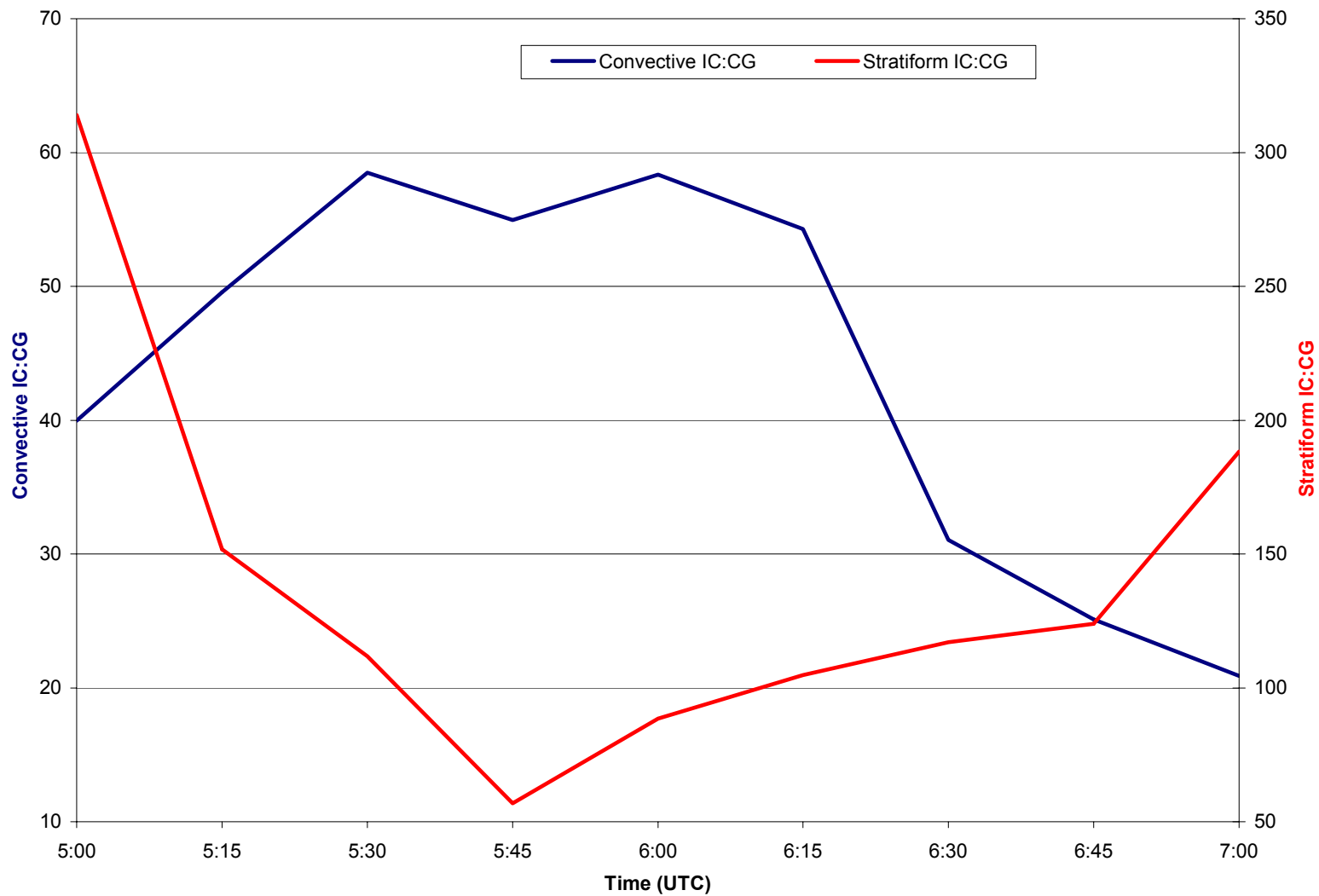


FIG. 5.56. Convective and stratiform IC:CG ratio trends from 05:00 to 07:00 UTC 16 June 2002, time averaged every 5 min with a 3-point running mean smoother. Time is listed along the x-axis, and the convective and stratiform IC:CG ratio is listed along the primary and secondary y-axes, respectively.

## 6. DISCUSSION

Three classic leading convective/trailing stratiform MCSs that passed through the DFW region have been examined in this research. These cases include the 1) 7-8 April 2002, 2) 12-13 October 2001, and 3) 16 June 2002 MCSs. The April MCS was unique in that the stratiform region developed as the convective system propagated through the DFW region. Unfortunately, the LDAR II network was operating with decreased detection efficiency during the April case, because only five of the seven LDAR II sensors were operational. The stratiform region in the October case study did not develop until late in the analysis period, at the approximate time the KFWS radar stopped functioning properly. During the June case study, however, both the radar and lightning networks were working optimally, and the MCS passed over DFW during its mature stage. The microphysical (e.g. large hydrometeor concentration aloft via total echo volume aloft, rainfall rates) and electrical (CG and total lightning) characteristics for each MCS will now be compared.

In all three cases, the trends in total and convective echo volume aloft closely follow the change in strength of the convective line as it propagates through the analysis region. Echo volume increases as the convective line enters the region and decreases when the convective line begins to propagate out of the area. During the time period when the convective line is located within the analysis area, an increase or decrease in echo volume aloft reflects any strengthening or weakening of the convective line.

Total echo volume aloft values for the April and June case studies were similar (the June case had a slightly larger average echo volume aloft than the April case study), but the average October echo volume aloft was significantly larger. According to Houze (1989), an

MCS is most intense during its developing stage when the stratiform region has not yet developed. These intensity stages are consistent with the fact that while over the DFW region, the October MCS was still developing, but the April and June MCSs were already mature. Therefore, the differences in echo volume aloft between the three case studies can be attributed to the different stages of development of each MCS during the analysis period. The large echo volume aloft values observed in all of the MCS cases reflect the ability of strong convective updrafts to suspend large hydrometeors aloft.

Stratiform region echo volume aloft  $\geq 25$  dBZ and  $\geq 30$  dBZ for the April and June case studies were significantly larger in the 0 to  $-40$  °C temperature layer than in the  $-10$  to  $-40$  °C temperature layer, reflecting the contribution of increased aggregation at  $T > -10$  °C and possibly the “smearing” effect of the radar reflectivity bright band during the radar gridding to the total volume of hydrometeor present in the stratiform region. As with the convective region, trends in stratiform region echo volume aloft closely followed the evolution and propagation of the stratiform region. The stratiform region echo volume aloft was much smaller than the convective echo volume aloft, reflecting the lack of large hydrometeors and hence, weaker vertical motions in the stratiform region.

The convective and stratiform rainfall rate trends are similar to the partitioned echo volume aloft trends for the April and June cases. Rainfall rates for the October case were not calculated because this MCS could not be partitioned using the methods discussed in this research. Previous studies have shown that the amount of echo volume aloft is directly correlated to the strength of the updraft (e.g. Carey and Rutledge 1996). As a result of the larger echo volume aloft and hence, stronger vertical motions in the convective line than in the stratiform region, convective rainfall rates averaged 3.4 and 3.7 times larger than

stratiform rainfall rates in the April and June MCSs, respectively. These rainfall rate trends are consistent with previous results including Rutledge and MacGorman (1988) and Molinie et al. (1999) (who also correlated rainfall rates to lightning activity). Similar to the trends in echo volume aloft, the June MCS produced slightly larger average convective and stratiform rainfall rates than the average convective and stratiform rainfall rates produced by the April MCS. Thus, the June MCS was apparently stronger than the April MCS during the analysis period.

Typical of midlatitude MCSs, all three MCS cases are characterized by high CG flash rates (within this study's analysis domain). Consistent with previous studies (e.g. Krehbiel et al. 1979; Rutledge and MacGorman 1988; Reap and MacGorman 1989; Rutledge and Petersen 1994; Toracinta et al. 1996), CG flashes were predominantly associated with high reflectivity cores within the convective and stratiform regions. The June MCS produced the largest average CG lightning flash rate ( $\sim 58.1$  flashes  $\text{min}^{-1}$ ), and the April MCS produced the smallest average CG flash rate ( $\sim 14.5$  flashes  $\text{min}^{-1}$ ) during the analysis period. The higher CG flash rate is consistent with the higher echo volume aloft and rainfall rates in the June MCS as compared to the April MCS. A severe bow echo was also evolving from the convective line of the June case. The presence of this bow echo supports that this case was strong during the analysis period. The relatively small CG flash rate observed in the April MCS is associated with the weakening of the storm system as it propagated through the analysis area (as evidenced by the decrease in echo volume aloft throughout the period), whereas the large CG flash rate in the June MCS reflects its uniform observed strength throughout most of the period (as evidenced by the fairly uniform echo volume aloft trend throughout most of the time period). The average CG flash rate for the October MCS ( $\sim 53.8$

flashes  $\text{min}^{-1}$ ) is slightly smaller than the average CG flash rate in the June MCS. Since average stratiform region CG flash rates are generally much lower than convective CG flash rates, it is possible that the flash rate difference between the October and June cases may be due to the fact that the October analysis period included  $\sim 1$  hr when the stratiform region was the only precipitation region within viewing range, whereas the June analysis period ended while part of the convective region was still within view. It is also possible that the June MCS was, in fact, stronger than the October MCS when the storm system passed over the DFW region.

The April, October, and June MCSs produced 20.1%, 19.7%, and 3.7% +CG flashes, respectively. Results from previous studies (e.g. Rutledge and MacGorman 1988) indicate that the stratiform region produces a greater percentage of +CG flashes than the convective region. Thus, the larger average +CG flash percentages in the April and October cases as compared to the June MCS may result from the relatively short duration of the June MCS stratiform region within the KFWS viewing range. This difference, however, also mirrors the seasonal variation of percent +CG flashes in MCSs, where the lowest +CG flash percentage occurs during the summer months (Orville and Huffines 2001).

Holle et al. (1994) found that 87% of MCS CG flashes occur in the convective region. This percentage is significantly larger than the percentage observed in the April case ( $\sim 68.9\%$ ) but comparable to the June case ( $\sim 93.0\%$ ). In the April MCS, the convective region averaged  $12.3 \text{ flashes min}^{-1}$  (7.5% positive), while in the June MCS, the convective region averaged  $53.6 \text{ flashes min}^{-1}$  (2% positive). These results also agree with previous research (e.g. Holle et al. 1994). The differences in flash rates are a result of the differences

in convective region strength between the two MCSs as indicated by differences in convective rainfall and echo volume aloft.

Flash rate differences can also be a result of the speed at which the convective line propagates out of the analysis area. As long as some portion of the convective line was still within the analysis region, CG flashes associated with this portion of the convective line were included in the statistics. Therefore, the convective CG flash rate decreases as the percentage of the convective line within the analysis region decreases. Once the convective line has completely exited the analysis region, the convective CG flash rate is set to zero. Since the April MCS propagated slowly out of the analysis domain, CG flash rates for only a small percentage of the convective line were used during many of the later time steps to represent the entire convective line. The June MCS, however, propagated more quickly so that most of the convective line CG flash rate statistics represented times in which the line spanned the full length of the analysis region. Therefore, the differences in system motion speeds can account for the lower average April convective CG flash rate as compared to the average June convective CG flash rate. During the times when each MCS was centered within the analysis domain, however, the June MCS clearly showed a higher CG lightning flash rate than the April MCS.

The stratiform region, like previous studies have found (e.g. Rutledge and MacGorman 1988; Rutledge et al. 1990; Hunter et al. 1992; Holle et al. 1994; Toracinta et al. 1996; Shafer et al. 2000), was not an abundant CG lightning-producing region in all three MCS case studies. The stratiform region is inefficient at producing lightning because of its weak vertical motions and low liquid water contents, two important ingredients needed for the NIC mechanism. The stratiform region averaged 2.2 and 4.5 CG flashes  $\text{min}^{-1}$  in the

April and June MCSs, respectively. These values are 5.6 and 11.9 times smaller than convective region flash rates for the April and June MCSs, respectively. The average +CG flash percentage, however, was greater in this region than in the convective region. This +CG flash percentage difference agrees with previous studies (e.g. Rutledge and MacGorman 1988; Rutledge et al. 1990; Hunter et al. 1992; Holle et al. 1994; Toracinta et al. 1996; Shafer et al. 2000). The stratiform region in the April and June MCSs averaged 44.9% and 26.5% +CG lightning flashes, respectively. Also similar to previous studies (e.g. Petersen and Rutledge 1992), the peak positive and negative CG lightning flash currents throughout the analysis time period were larger in the stratiform region than in the convective region in both the April and June case studies. Peak current magnitudes are likely larger in the stratiform region than in the convective line because the charge center responsible for producing +CG flashes is located at a higher altitude (at  $T < -10$  °C) in the stratiform region than the lower positive charge center of the convective line (between 5 °C and -5 °C). Similarly, the negative charge center is located at a higher altitude in the stratiform region (possibly at  $T < -20$  °C) than the main negative charge center in the convective line (between -10 and -25 °C). This increased height would require more charge to pass through the current to the ground and would therefore yield a larger peak current (Orville 1990).

One of the main objectives of this research is to provide further insight into the electrification processes within the stratiform region of a midlatitude MCS. Two main hypotheses have been proposed to explain stratiform midlatitude MCS electrification. These two hypotheses include: 1) the advection mechanism (e.g. Rutledge and MacGorman 1988), and 2) an in situ mechanism (e.g. Engholm et al. 1990; Rutledge et al. 1990). Most studies

suggest that a combination of these two mechanisms explains stratiform electrification (e.g. Rutledge and MacGorman 1988; Rutledge et al. 1990; Schuur and Rutledge 2000b).

Locations of charge centers can provide insight into stratiform electrification. Since 1) the LDAR II network detects VHF radiation emissions produced from the electrical discharge processes (i.e. initial breakdown and ionization) associated with total (IC and CG) lightning, 2) lightning preferentially propagates through space charge (Williams et al. 1985; Coleman et al. 2003), and 3) a presence of net charge can be inferred from lightning channels (Coleman et al. 2003), LDAR II source data can be used to study charge centers associated with lightning.

All three MCSs are characterized by an abundance of LDAR II source and flash activity. Average LDAR II source rates for the April, October, and June MCSs were 2338.3, 13 350.5, and 19 336.7 sources  $\text{min}^{-1}$ , respectively. Average LDAR II flash origin rates (using the modified NASA algorithm) for the April, October, and June MCSs were 103.1, 1005.1, and 3043.8 flashes  $\text{min}^{-1}$ , respectively. April LDAR II source and flash rates are noticeably smaller than the other two MCS cases because of the decreased LDAR II detection efficiency and decreased strength (as shown in low echo volume aloft and rainfall rate magnitudes) during this case study. The average October LDAR II source and flash rates are smaller than the average June source and flash rates because 1) the duration of the stratiform region within the analysis volume was longest for the October case, and 2) the June MCS was stronger than the October MCS, as evidenced by comparisons between total echo volume aloft and rainfall rates in each storm system. It is interesting to note that the average number of sources per flash is 13.3 for the October MCS and 6.4 for the June MCS. It can be speculated that the October MCS is characterized by more sources per flash than the

June MCS because the stratiform region impacts the October LDAR II source and flash rate averages for a longer duration than the June MCS. Hence, the October MCS is characterized by more sources per flash than the June MCS because lightning activity in the stratiform region is characterized by longer-duration flashes than the convective region.

All three MCSs produce more IC than CG lightning flashes throughout each of their analysis periods. Average IC:CG ratios are ~7:1, 18:1, and 50:1 in the April, October, and June MCSs, respectively. Only the June MCS average IC:CG ratio is similar to average midlatitude MCS IC:CG ratio (40:1) reported by Mazur and Rust (1983). The April MCS IC:CG ratio should be disregarded since the LDAR II network was not functioning properly during this case study. Since CG flash rates were only slightly higher in the June case than in the October case, but total flash rates for the June case were over three times greater than the October case, the June IC:CG ratio is almost three times larger than the October IC:CG ratio. The average flash rate for the June case was influenced by the convective line during the entire analysis period, whereas the average October flash rate was influenced by the convective region only until the last hour of analysis, after which only the stratiform region was within viewing range.

The convective region of all three MCSs had abundant LDAR II source and flash activity, similar to the results of Mazur and Rust (1983). The convective region of the June MCS averaged 9448.5 sources  $\text{min}^{-1}$  and 2542.5 flashes  $\text{min}^{-1}$ . The average convective IC:CG ratio for this case study was ~44:1. Since the LDAR II network was not functioning properly during the April case study, and data were not partitioned for the October case study, only trends in partitioned June LDAR II data will be further discussed.

The stratiform region within the June MCS case study is associated with almost 9.5 times fewer LDAR II sources and 5 times fewer LDAR II flash origins than the convective region. The stratiform region of the June MCS averaged 995.5 sources  $\text{min}^{-1}$  and 501.2 flashes  $\text{min}^{-1}$ . The resulting average June IC:CG ratio was 139.7:1. Therefore, the stratiform region produced a larger IC:CG ratio than the convective region according to LDAR II source and flash data. It is possible that since lightning within the stratiform region is likely longer and more branched, more flashes are being split apart into many different flashes in this region as compared to the convective line. Thus, the LDAR II flash algorithm would cause resulting IC:CG ratios to increase, especially in the stratiform region.

In both the April and June MCSs, the maxima and minima in convective echo volume aloft  $\geq 25$  dBZ,  $\geq 30$  dBZ,  $\geq 35$  dBZ, and  $\geq 40$  dBZ within the 0 to  $-40$  °C temperature layer precede the analogous maxima and minima in 1) convective rainfall rates, and 2) NLDN-detected total and convective CG lightning flashes by 15-30 min. In the April MCS, peak convective LDAR II source and flash rates lag convective echo volume aloft peaks by  $\sim 15$  min. In the June MCS, convective LDAR II source and flash rates lag convective echo volume aloft peaks by 15-30 min. These results are similar to the findings of Carey and Rutledge (1996), who found that peak IC lightning lags peak graupel volume aloft by  $\sim 12$  min. Since 1) large echo volume aloft implies the presence of suspended graupel and hail within strong updrafts, 2) results from synthetic dual-Doppler analyses of the June MCS indicate that convective updrafts were on the order of  $\sim 10$   $\text{ms}^{-1}$ , 3) strong updrafts provide liquid water above the freezing level in the convection, 4) ice crystals are also present aloft, and 5) a direct correlation exists between echo volume aloft and lightning activity, these

results 1) support the NIC mechanism of electrification (e.g. Saunders et al. 1991), and 2) explain the abundance of lightning activity in the MCS convective region.

In both the April and June MCSs, stratiform echo volume aloft trends  $\geq 25$  dBZ and  $\geq 30$  dBZ within the -10 to -40 °C temperature layer correlate well with both the stratiform NLDN-detected CG flash rate trend, and the LDAR II flash origin rate trend. In the June MCS, these stratiform echo volume aloft trends also correlate well with stratiform LDAR II-detected source rates, but the correlation is not as strong in the April MCS. The stratiform echo volume aloft trends lag the rainfall rate trend in the April MCS by  $\sim 30$  min, but no correlation between these two quantities exists in the June MCS.

Previous studies have hypothesized that differential sedimentation of aggregates and small ice are important in stratiform region electrification (e.g. Engholm et al. 1990; Rutledge et al. 1990; Schuur and Rutledge 2000a). The magnitude of echo volume aloft is dominated by larger reflectivity echoes. Therefore, larger aggregates within the stratiform region will affect echo volume aloft more than small ice. Since a direct correlation exists between stratiform region echo volume aloft and lightning activity, it is possible that the presence of aggregates is responsible for the electrification of the stratiform region via an in situ NIC mechanism.

Within the convective line of all three MCS cases, LDAR II sources are predominantly found between: 1) 0 and -25 °C, and 2) -35 and -55 °C. These lower and upper electrically-active regions have been associated with the main negative and the upper positive charge centers of a thunderstorm tripole in Shao and Krehbiel (1996). Since previous studies have found a lower positive charge region between  $\sim 5$  and -5 °C and the main negative charge region between  $\sim -10$  and -25 °C in the convective lines of midlatitude

MCSs (Stolzenburg et al. 1998a), it appears that both regions are being detected by the LDAR II network in both the October and the June cases. The LDAR II-detected dominant negative and positive electric charge centers in the convective region are consistent with the NIC mechanism of convective electrification (e.g. Saunders et al. 1991).

Within the stratiform region of both the April and the June MCS cases, one main electrically-active region sloped between  $\sim -10$  and  $-25$  °C and another small horizontally-layered electrically-active region towards the rear of the stratiform region at  $\sim -40$  °C are detected by the LDAR II network. The main charge layer ( $\sim -10$  to  $-25$  °C) is seen in every 5-min composite analysis performed for both cases, and it appears to have been advected into the stratiform region from the upper (positive) charge center within the leading convective line. This convective upper VHF source maximum slopes rearward and downward at an  $\sim 6^\circ$  angle from the horizontal from the convective line into the part of the stratiform region just above the radar reflectivity bright band. Results from dual-Doppler analyses of the June MCS indicate that the front-to-rear flow behind the convective line and above the freezing level was  $\sim 10$   $\text{ms}^{-1}$ . Given that aggregates have typical fall speeds of  $\sim 1.0$   $\text{ms}^{-1}$ , the aggregate trajectory also slopes rearward and downward from the convective line and into the stratiform region by a  $\sim 6^\circ$  angle from the horizontal (Houze et al. 1989). Therefore, it is possible that the stratiform region acquired positive electric charge by the advection mechanism.

Dual-Doppler analyses of the June MCS indicate that a weak mesoscale updraft ( $0.0$ - $0.4$   $\text{ms}^{-1}$ ) was present within the stratiform region above the freezing level and within the back edge of the region. Given the magnitude of this updraft, and the direct correlation between stratiform echo volume aloft and lightning activity, it is possible that an in situ

mechanism via NIC is generating some of the charge apparent in the 5-min composite images of the June MCS LDAR II sources. According to NIC, this updraft could produce a higher altitude negatively-charged center of ice crystals and a lower altitude positively-charged center of aggregates (the electrically-active region depicted in the composite analyses) as a result of rebounding collisions between ice crystals and aggregates followed by differential sedimentation of hydrometeors in the presence of low liquid water content. This process would result in an inverted dipole in the stratiform region. An in situ mechanism of electrification via NIC may also explain the presence of the small LDAR II source maximum along the back edge of the stratiform region because this region is preferentially located within the weak mesoscale updraft.

There are similarities and differences between stratiform region electrification results presented in this study and the results of both balloon-borne electric field sounding studies (e.g. Schuur et al. 1991; Marshall and Rust 1993; Stolzenburg et al. 1994; Stolzenburg et al. 1998a) and aircraft electric field studies (e.g. Mo et al. 2003). Similar to previous studies, a main positive electrically-active charge center slopes downward and rearward from the upper positive charge region in the convective line to the stratiform region. This study, however, shows that this charge region slopes further downward than previous studies have indicated. Thus, this study's observations suggest that a main positively-charged charge center is lower in altitude (between -10 and -25 °C) than the analogous positively-charged center of previous studies (above -25 °C) within the stratiform region. In addition, previous studies (based on balloon soundings launched from multiple isolated locations within an MCS) suggest that the stratiform region charge layers are horizontally-extensive and roughly uniform without having a continuous dataset with which to justify this assumption, whereas this research's

results show a noticeable decrease in source density as distance from the convective line increases. Therefore, this research offers new insight into the charge distribution of the stratiform region of an MCS.

Schuur and Rutledge's (2000b) results from two-dimensional, time-dependent, bulk microphysical numerical model simulations of the MCS stratiform region show that both in situ charging and charge advection are important in the electrification process of the stratiform region. The area of peak snow aggregate mixing ratio in that study's control run at  $t = 3$  hr corresponds to the downward- and rearward-sloping LDAR II source path from the convective region to the stratiform region in this study's April and June MCSs. Schuur and Rutledge (2000b) ran a model simulation with 1) initial aggregate concentrations, 2) the convective region total charge density "type A" profile determined by Marshall and Rust (1993) (i.e. with five charge layers at  $T \leq 0$  °C), 3) Saunders et al. (1991) non-inductive charging (i.e. the charge separation per collision is dependent upon both cloud ice size and collision impact velocity), and 4) charge advection of snow, cloud ice, and cloud water from the convective region to the stratiform region by storm-relative horizontal winds (i.e. the front-to-rear flow). The resulting maximum charge density region from their model run also agrees with the downward- and rearward-sloping LDAR II source path observed in this study's April and June MCS cases.

This study provides supporting evidence that the stratiform region becomes electrified by 1) advection of positive charge from the upper positively-charged center of the convective line to the stratiform region (likely producing the sloped charge region near the convective line) and 2) in situ charging via NIC (likely producing the horizontally-oriented charge layer far behind the convective region). While charged ice particles and aggregates are advected

from the convective line into the stratiform region, it is probable that differential sedimentation of aggregates forms the observed sloped charge layer. The other stratiform charge layer probably forms from an in situ NIC mechanism along the rear of the stratiform region within the mesoscale updraft. These two layers could establish an inverted dipole, which may explain the observed higher percentage of +CG flashes in the stratiform region than in the convective region (where a normal dipole is present).

## 7. CONCLUSIONS AND FUTURE RESEARCH

Midlatitude MCSs are long-lived convective systems that produce severe weather, flooding, and abundant lightning activity. Lightning is the single greatest cause of convective weather-related fatalities in the U.S. Various hypotheses attempt to explain and forecast the onset of electrification and lightning in convection, but questions still exist about these processes, particularly how the stratiform region of a midlatitude MCS becomes electrified. This research presents radar and electrical observations of three MCS case studies that propagated through the DFW region on 7-8 April 2002, 12-13 October 2001, and 16 June 2002. These observations provide supporting evidence that particle-scale differential sedimentation and storm-scale vertical and horizontal advection of mixed-phase hydrometeors (large and small precipitating ice in the presence of supercooled water) drive MCS electrification because hydrometeor collisions during the precipitation process cause a net charge separation.

Abundant lightning activity is produced within the convective line of the three midlatitude MCS cases analyzed in this research. This study and previous studies support the theory that the NIC mechanism explains how the convective line becomes electrified. During electrification, convective updrafts separate charge such that main negative charge region becomes established below the main upper positive charge region, resulting in predominantly negative convective CG flashes. Convective echo volume aloft trends and convective rainfall rates are well correlated to convective electrical activity. Large average convective echo volume aloft and high rainfall rates reveal the production and presence of

numerous precipitation-sized hydrometeors within the convective line, allowing efficient lightning production via NIC.

The stratiform region likely becomes electrified by a combination of in situ charging via NIC and advection of positive charge from the upper convective positively-charged center to low levels in the stratiform region. Since this lower-level main electrically-active charge center in the stratiform region is inferred to be positively-charged (because negative polarity breakdown in the positive charge region is noisier than positive polarity breakdown in the negative charge region in the VHF range), an inverted dipole is established (via NIC). The resulting electrically-active stratiform region produces a greater percentage of positive CG flashes than the convective region. Note, however, that the stratiform region is inefficient at producing lightning activity because it partially relies on charge advection to acquire its charge, and its weak vertical motions prevent much charge from being separated via an in situ mechanism.

Data limitations exist with this research. The June case represents the only one of three cases that occurred when both the KFWS radar and the LDAR II network were operating properly. During the April MCS, the LDAR II network was only functioning with five working sensors; therefore, detection efficiency problems sometimes could not be distinguished from real physical results. Also, source trends could not be compared to the October MCS case because 1) there were problems with the KFWS radar during the last hour of analysis, 2) throughout most of the period, the stratiform region of the October MCS had not yet formed, and 3) the northern third of the convective line within this study's analysis area was propagating with a more southerly component than the southern 2/3 of the convective line. These issues made convective/stratiform line portioning practically

impossible. Therefore, no data were partitioned for the October case study. The June 2002 MCS was best suited for this study because both the KFWS radar and the LDAR II network were functioning properly. April LDAR II source and flash trends were compared to June LDAR II source and flash characteristics. After detailed analyses, it was determined that most electrical characteristics observed in the April MCS represent true physical processes because these same processes were observed in the June MCS.

The results from this research offer various avenues for future research. First, the convective and stratiform echo volume aloft trends, the NDLN-detected CG lightning flashes, and the LDAR II-detected source and flash rates should be reanalyzed by normalizing the microphysical and electrical quantities per convective/stratiform volume present within the analysis viewing area. These analyses would distinguish between MCS propagation and MCS strength evolution. It would also be beneficial to perform more synthetic dual-Doppler analyses with the June MCS case study using different times to determine if the vertical and horizontal motions presented in this research are consistent throughout the period.

Obviously, it would be beneficial to analyze LDAR II sources and radar data from additional MCS cases to determine if other MCSs show similar trends in total lightning activity. Using the modified NASA algorithm, individual LDAR II flashes should be examined to see if any flashes propagate from the convective region to the stratiform region. This analysis would provide more insight into the charging mechanism(s) in MCS stratiform regions. Also, studying the propagation of LDAR II CG flashes and then comparing these flashes to analogous NLDN-detected CG flashes may allow for unambiguous identification

of the sign of charge centers because the polarity of a given NLDN-detected CG flash is known.

The striking similarities among 1) the downward- and rearward-sloping LDAR II source maximum (from the back edge of the convective line to the stratiform region) observed in this research, 2) the model-simulated snow aggregate mixing ratio maximum from Schuur and Rutledge (2000b), 3) the maximum charge density region from Schuur and Rutledge (2000b), and 4) similarly sloped charge structures inferred from in-situ electric charge field studies (e.g. Stolzenberg et al. 1994; Stolzenberg et al. 1998a; Mo et al. 2003) suggest the need for a new MCS electrification field study in the central U.S. (where MCSs are most common) that would pick up where PRE-STORM left off (Gallus and Johnson 1995a) 20 years ago. To understand the dominant physical and electrical processes occurring during stratiform region electrification, more microphysical, kinematic, and electrical data are needed. To gather microphysical data, it would be useful to have polarimetric radar and in-situ aircraft (e.g. UND Citation) that could sample the back edge of the convective line, the transition zone, and the stratiform region so that hydrometeor types, sizes, and fall velocities could be determined within each region. To gather kinematic data, dual-Doppler radars should also be employed so that accurate three-dimensional wind data can be gathered. To gather electrical data, electric field soundings should be taken through the stratiform region, transition zone, and back edge of the convective line, so that the heights and polarity of all charge layers can be determined. It would also be useful to employ an LDAR network (but with more sensors), so that the height and polarity of charge regions determined from the electric field soundings can be compared to the height and polarity of charge regions determined by the LDAR network. Knowing the polarity of the charge centers could either

prove or disprove some of the results presented in this research and in previous studies. Finally, the NLDN network would provide the field campaign with important CG flash data information that might go unreported by the LDAR II network. After gathering all available microphysical, kinematic, and electric data, both observational studies (following a methodology similar to this research) and modeling studies (similar to the simulations performed by Schuur and Rutledge (2000b)) can be performed to further test the main hypothesis presented in this research.

## REFERENCES

- Avila, E. E., and G. M. Caranti, 1994: A laboratory study of static charging by fracture in ice growing by riming. *J. Geophys. Res.*, **99**, 10 611-10 620.
- , ———, N. E. Castellano, and C. P. R. Saunders, 1998: Laboratory studies of the influence of cloud droplet size on charge transfer during crystal-graupel collisions. *J. Geophys. Res.*, **103**, 8985-8996.
- Baker, M. B., J. G. Dash, 1994: Mechanism of charge transfer between colliding ice particles in thunderstorms. *J. Geophys. Res.*, **99**, 10 621-10 626.
- Bateman, M. G., W. D. Rust, B. F. Smull, and T. C. Marshall, 1995: Precipitation charge and size measurements in the stratiform region of two mesoscale convective systems. *J. Geophys. Res.*, **100**, 16 341-16 356.
- Battan, L. J., 1965: Some factors governing precipitation and lightning from convective clouds. *J. Atmos. Sci.*, **22**, 79-84.
- , 1973: *Radar Observation of the Atmosphere*. University of Chicago Press, Chicago, 324 pp.
- Beard, K. V. K., and H. T. Ochs, 1986: Charging mechanisms in clouds and thunderstorms. *The Earth's Electrical Environment, Studies in Geophysics*, National Academy Press, 114-130.
- Biggerstaff, M. I., and R. A. Houze, Jr., 1991: Kinematic and precipitation structure of the 10-11 June 1985 squall line. *Mon. Wea. Rev.*, **119**, 3034-3065.
- Blanchard, D. O., 1990: Mesoscale convective patterns of the southern High Plains. *Bull. Amer. Meteor. Soc.*, **71**, 994-1005.
- Bluestein, H. B., S. D. Hrebenach, C. Chang, and E. A. Brandes, 1994: Synthetic dual-Doppler analysis of mesoscale convective systems. *Mon. Wea. Rev.*, **122**, 2105-2124.
- , and M. H. Jain, 1985: Formation of mesoscale lines of precipitation: Severe squall lines in Oklahoma during the spring. *J. Atmos. Sci.*, **42**, 1711-1732.
- , and D. R. MacGorman, 1998: Evolution of cloud-to-ground lightning characteristics and storm structure in the Spearman, Texas, tornadic supercells of 31 May 1990. *Mon. Wea. Rev.*, **126**, 1451-1467.
- , G. T. Marx, and M. H. Jain, 1987: Formation of mesoscale lines of precipitation: Nonsevere squall lines in Oklahoma during the spring. *Mon. Wea. Rev.*, **115**, 2719-2727.

- Buechler, D. E., and S. J. Goodman, 1990: Echo size and asymmetry: Impact on NEXRAD storm identification. *J. Appl. Meteor.*, **29**, 962-969.
- Carey, L. D., and S. A. Rutledge, 1996: A multiparameter radar case study of the microphysical and kinematic evolution of a lightning producing storm. *Meteor. Atmos. Phys.*, **59**, 33-64.
- , and ———, 1998: Electrical and multiparameter radar observations of a severe hailstorm. *J. Geophys. Res.*, **103**, 13 979-14 000.
- , and ———, 2000: The relationship between precipitation and lightning in tropical island convection: A C-Band polarimetric radar study. *Mon. Wea. Rev.*, **128**, 2687-2710.
- , and ———, 2003: Some characteristics of cloud-to-ground lightning in severe and non-severe thunderstorms over the Central United States from 1989-98. *J. Geophys. Res.*, In press.
- , W. A. Petersen, and S. A. Rutledge, 2003a: Evolution of cloud-to-ground lightning and storm structure in the Spencer, SD, tornadic supercell of 30 May 1998. *Mon. Wea. Rev.*, **131**, 1811-1831.
- , S. A. Rutledge, and W. A. Petersen, 2003b: The relationship between severe storm reports and cloud-to-ground lightning polarity in the contiguous United States from 1989 to 1998. *Mon. Wea. Rev.*, **131**, 1211-1228.
- Chèze, J., and H. Sauvageot, 1997: Area-averaged rainfall and lightning activity. *J. Geophys. Res.*, **102**, 1707-1715.
- Coleman, L. M., T. C. Marshall, M. Stolzenburg, T. Hamlin, P. R. Krehbiel, W. Rison, and R. J. Thomas, 2003: Effects of charge and electrostatic potential on lightning propagation. *J. Geophys. Res.*, **108**, 4298, doi:10.1029/2002JD002718.
- Cressman, G., 1959: An operational analysis system. *Mon. Wea. Rev.*, **87**, 367-374.
- Crum, T. D., R. L. Alberty, and D. W. Burgess, 1993: Recording, archiving, and using WSR-88D data. *Bull. Amer. Meteor. Soc.*, **74**, 645-653.
- Cummins, K. L., M. J. Murphy, E. A. Bardo, W. L. Hiscox, R. B. Pyle, and A. E. Pifer, 1998: A combined TOA/MDF technology upgrade of the U.S. National Lightning Detection Network. *J. Geophys. Res.*, **103**, 9035-9044.
- , ———, and J. V. Tuel, 2000: Lightning detection methods and meteorological applications, *IV International Symposium on Military Meteorology*, Malbork, Poland, 85-100.

- Curran, E. B., R. L. Holle, and R. E. López, 2000: Lightning casualties and damages in the United States from 1959 to 1994. *J. Climate*, **13**, 3448-3464.
- Davies-Jones, R. P., 1979: Dual-Doppler radar coverage area as a function of measurement accuracy and spatial resolution. *J. Appl. Meteor.*, **18**, 1229-1233.
- Demetriades, N. W. S., M. J. Murphy, and K. L. Cummins, 2000: Early results from the Global Atmospheric, Inc. Dallas-Fort Worth Lightning Detection and Ranging (LDAR-II) research network. *VI Symposium on Integrated Observing Systems*, Long Beach, California, Amer. Meteor. Soc.
- Dye, J. E., W. P. Winn, J. J. Jones, and D. W. Breed, 1989: The electrification of New Mexico thunderstorms 1. Relationship between precipitation development and the onset of electrification. *J. Geophys. Res.*, **94**, 8643-8656.
- Engholm, C. D., E. R. Williams, and R. M. Dole, 1990: Meteorological and electrical conditions associated with positive cloud-to-ground lightning. *Mon. Wea. Rev.*, **118**, 470-487.
- Fritsch, J. M., and C. F. Chappell, 1980: Numerical prediction of convectively driven mesoscale pressure systems. Part II: Mesoscale model. *J. Atmos. Sci.*, **37**, 1734-1762.
- , R. J. Kane, and C. R. Chelius, 1986: The contribution of mesoscale convective weather systems to the warm-season precipitation in the United States. *J. Climate Appl. Meteor.*, **25**, 1333-1345.
- Fulton, R., J. Breidenbach, D.-J. Seo, D. Miller, and T. O'Bannon, 1998: The WSR-88D rainfall algorithm. *Wea. Forecasting*, **13**, 377-395.
- Gallus, W. A., Jr., and R. H. Johnson, 1995a: The dynamics of circulations within the trailing stratiform regions of squall lines. Part I: The 10-11 June PRE-STORM system. *J. Atmos. Sci.*, **52**, 2161-2287.
- , ———, 1995b: The dynamics of circulations within the trailing stratiform regions of squall lines. Part II: Influence of the convective line and ambient environment. *J. Atmos. Sci.*, **52**, 2188-2211.
- Gaskell, W., and A. J. Illingworth, 1980: Charge transfer accompanying individual collisions between ice particles and its role in thunderstorm electrification. *Quart. J. Roy. Meteor. Soc.*, **106**, 841-854.
- Glickman, T. S., 2000: *Glossary of Meteorology*, 2<sup>nd</sup> ed. Amer. Meteor. Soc., 855 pp.
- Goodman, S. J., D. E. Buechler, and P. D. Wright, 1988: Lightning and precipitation history of a microburst-producing storm. *Geophys. Res. Lett.*, **15**, 1185-1188.

- , and D. R. MacGorman, 1986: Cloud-to-ground lightning activity in mesoscale convective complexes. *Mon. Wea. Rev.*, **114**, 2320-2328.
- Gremillion, M. S., and R. E. Orville, 1999: Thunderstorm characteristics of cloud-to-ground lightning at the Kennedy Space Center, Florida: A study of lightning initiation signatures as indicated by the WSR-88D. *Wea. Forecasting*, **14**, 640-649.
- Hilgendorf, E. R., and R. H. Johnson, 1998: A study of the evolution of mesoscale convective systems using WSR-88D data. *Wea. Forecasting.*, **13**, 437-452.
- Holle, R. L., A. I. Watson, R. E. López, D. R. MacGorman, and R. Ortiz, 1994: The life cycle of lightning and severe weather in a 3-4 June 1985 PRE-STORM mesoscale convective system. *Mon. Wea. Rev.*, **122**, 1798-1808.
- Hondl, K. D., and M. D. Eilts, 1994: Doppler radar signatures of developing thunderstorms and their potential to indicate the onset of cloud-to-ground lightning. *Mon. Wea. Rev.*, **122**, 1818-1836.
- Houze, R. A., Jr., S. A. Rutledge, M. I. Biggerstaff, and B. F. Smull, 1989: Interpretation of Doppler weather radar displays of midlatitude mesoscale convective systems. *Bull. Amer. Meteor. Soc.*, **70**, 608-619.
- , B. F. Smull, and P. Dodge, 1990: Mesoscale Organization of springtime rainstorms in Oklahoma. *Mon. Wea. Rev.*, **118**, 613-654.
- , 1993: *Cloud Dynamics*. Academic Press, Inc., San Diego, 573 pp.
- Hunter, S. M., T. J. Schuur, T. C. Marshall, and W. D. Rust, 1992: Electric and kinematic structure of the Oklahoma mesoscale convective system of 7 June 1989. *Mon. Wea. Rev.*, **120**, 2226-2239.
- Jayarathne, E. R., C. P. R. Saunders, and J. Hallett, 1983: Laboratory studies of the charging of soft-hail during ice crystal interactions. *Quart. J. Roy. Meteor. Soc.*, **109**, 609-630.
- Johnson, R. H., and P. J. Hamilton, 1988: The relationship of surface pressure features to the precipitation and airflow structure of an intense midlatitude squall line. *Mon. Wea. Rev.*, **116**, 1444-1472.
- Keighton, S. J., H. B. Bluestein, and D. R. MacGorman, 1991: The evolution of a severe mesoscale convective system: Cloud-to-ground lightning location and storm structure. *Mon. Wea. Rev.*, **119**, 1533-1556.
- Klimowski, B. A., and J. D. Marwitz, 1992: The synthetic dual-Doppler analysis technique. *J. Atmos. And Oceanic Technol.*, **9**, 728-745.

- Knupp, K. R., B. Geerts, and S. J. Goodman, 1998: Analysis of a small, vigorous mesoscale convective system in a low-shear environment. Part I: Formation, radar echo structure, and lightning behavior. *Mon. Wea. Rev.*, **126**, 1812-1836.
- Krehbiel, P. R., 1986: The electrical structure of thunderstorms. *The Earth's Electrical Environment, Studies in Geophysics*, National Academy Press, 90-113.
- , M. Brook, and R. A. McCrory, 1979: An analysis of the charge structure of lightning discharges to the ground. *J. Geophys. Res.*, **84**, 2432-2456.
- , R. J. Thomas, W. Rison, T. Hamlin, J. Harlin, and M. Davis, 1999: GPS-based mapping system reveals lightning inside storms. *Eos, Trans. Amer. Geophys. Union*, **81**, 21-25.
- Krider, E. P., 1986: Physics of lightning. *The Earth's Electrical Environment, Studies in Geophysics*, National Academy Press, 30-45.
- Lang, T. J., and S. A. Rutledge, 2002: Relationships between convective storm kinematics, precipitation, and lightning. *Mon. Wea. Rev.*, **130**, 2492-2506.
- , ———, J. E. Dye, M. Venticinque, P. Laroche, and E. Defer, 2000: Anomalously low negative cloud-to-ground lightning flash rates in intense convective storms observed during STERAO-A. *Mon. Wea. Rev.*, **128**, 160-173.
- Laroche, P., A. Bondiou, P. Blanchet, and J. Pigère, 1994: 3D mapping of lightning discharge within storms. *International Aerospace and Ground Conference on Lightning and Static Electricity*, Germany, May 24-25.
- Lennon, C., and L. Maier, 1991: Lightning mapping system. *Proceedings, 1991 International Aerospace and Ground Conf. on Lightning and Static Elec.*, Cocoa Beach, Florida, NASA Conf. Pub. 3106, 89-1 – 89-10.
- LeMone, M. A., 1983: Momentum transport by a line of cumulonimbus. *J. Atmos. Sci.* **40**, 1815-1834.
- Lhermitte, R., and E. Williams, 1985: Thunderstorm electrification: A case study. *J. Geophys. Res.*, **90**, 6071-6078.
- Loehrer, S. M., and R. H. Johnson, 1995: Surface pressure and precipitation life cycle characteristics of PRE-STORM mesoscale convective systems. *Mon. Wea. Rev.*, **123**, 600-621.
- MacGorman, D. R., and C. D. Morgenstern, 1998: Some characteristics of cloud-to-ground lightning in mesoscale convective systems. *J. Geophys. Res.*, **103**, 14 011-14 023.

- , and D. W. Burgess, 1994: Positive cloud-to-ground lightning in tornadic storms and hailstorms. *Mon. Wea. Rev.*, **122**, 1671-1697.
- , and W. D. Rust, 1998: *The Electrical Nature of Storms*, Oxford University Press, New York City, NY, 422 pp.
- , D. W. Burgess, V. Mazur, W. D. Rust, W. L. Taylor, and B. C. Johnson, 1989: Lightning rates relative to tornadic storm evolution on 22 May 1981. *J. Atmos. Sci.*, **46**, 221-250.
- Marshall, T. C., and W. D. Rust, 1993: Two types of vertical electrical structures in stratiform precipitation regions of mesoscale convective systems. *Bull. Amer. Meteor. Soc.*, **74**, 2159-2170.
- , M. Stlozenburg, W. D. Rust, E. R. Williams, and R. Boldi, 2001: Positive charge in the stratiform cloud of a mesoscale convective system. *J. Geophys. Res.*, **106**, 1157-1163.
- Mazur, V., and W. D. Rust, 1983: Lightning propagation and flash density in squall lines as determined with radar. *J. Geophys. Res.*, **88**, 1495-1502.
- Michimoto, K., 1991: A study of radar echoes and their relation to lightning discharge of thunderclouds in the Hokuriko district. Part I: Observation and analysis of thunderclouds in summer and winter. *J. Meteor. Soc. Japan*, **69**, 327-335.
- Miller, L. J., S. M. Fredrick, and W. Anderson, 1993: CEDRIC, *National Center for Atmospheric Research: Mesoscale and Microscale Meteorology Document*, Boulder, CO, 120 pp.
- Mo, Q., A. G. Detwiler, J. Hallett, and R. Black, 2003: Horizontal structure of the electric field in the stratiform region of an Oklahoma mesoscale convective system. *J. Geophys. Res.*, **108**, 4225, doi:10.1029/2001JD001140.
- Molinie, G., S. Soula, and S. Chauzy, 1999: Cloud-to-ground lightning activity and radar observations of storms in the Pyrénées range area. *Quart. J. R. Meteor. Soc.*, **125**, 3103-3122.
- Murphy, M. J., K. L. Cummins, and L. W. Maier, 2000: The analysis and interpretation of three-dimensional lightning flash information. *80th American Meteorological Society Meeting*, Long Beach, CA.
- Nachamkin, J. E., R. L. McAnelly, and W. R. Cotton, 2000: Interactions between a developing mesoscale convective system and its environment. Part I: Observational analysis. *Mon. Wea. Rev.*, **128**, 1205-1224.

- Nielsen, K. E., R. A. Maddox, and S. V. Vasiloff, 1994: The evolution of cloud-to-ground lightning within a portion of the 10-11 June 1985 squall line. *Mon. Wea. Rev.*, **122**, 1809-1817.
- Orville, R. E., 1990: Peak-current variations of lightning return strokes as a function of latitude. *Nature*, **342**, 149-151.
- , R. W. Henderson, and L. F. Bosart, 1988: Bipole patterns revealed by lightning locations in mesoscale storm systems. *Geophys. Res. Lett.*, **15**, 129-132.
- , and G. R. Huffines, 2001: Cloud-to-ground lightning in the United States: NLDN results in the first decade, 1989-98. *Mon. Wea. Rev.*, **129**, 1179-1193.
- Oye, D., and M. Case, 1995: *REORDER: A program for gridding radar data. Installation and use manual for the Unix version*. NCAR Atmospheric Technology Division, Boulder, CO.
- Parker, M. D., and R. H. Johnson, 2000: Organizational modes of midlatitude mesoscale convective systems. *Mon. Wea. Rev.*, **128**, 3413-3436.
- Pereyra, R. G., E. E. Avila, N. E. Castellano, C. P. R. Saunders, 2000: A laboratory study of graupel charging. *J. Geophys. Res.*, **105**, 20 803-20 812.
- Perez, A. H., L. J. Wicker, and R. E. Orville, 1997: Characteristics of cloud-to-ground lightning associated with violent tornadoes. *Wea. Forecasting*, **12**, 428-437.
- Petersen, W. A., and S. A. Rutledge, 1992: Some characteristics of cloud-to-ground lightning in tropical northern Australia. *J. Geophys. Res.*, **97**, 11 553-11 560.
- Ray, P. S., D. R. MacGorman, W. D. Rust, W. L. Taylor, and L. W. Rasmussen, 1987: Lightning location relative to storm structure in a supercell storm and a multicell storm. *J. Geophys. Res.*, **92**, 5713-5724.
- Reap, R. M., and D. R. MacGorman, 1989: Cloud-to-ground lightning: Climatological characteristics and relationships to model fields, radar observations, and severe local storms. *Mon. Wea. Rev.*, **117**, 518-535.
- Rickenbach, T. M., 1990: Precipitation processes and water budget study of the 10-11 June 1985 mesoscale convective system. M.S. thesis, Colorado State University, 180 pp. [Available from Atmos. Sci. Dept., Colorado State University, Ft. Collins, CO, 80523].
- Rison, W., R. J. Thomas, P. R. Krehbiel, T. Hamlin, and J. Harlin, 1999: A GPS-based three-dimensional lightning mapping system: Initial observations in central New Mexico. *Geophys. Res. Lett.*, **26**, 3573-3576.

- Rosenfeld, D. and I. M. Lensky 1998. Satellite-based insights into precipitation formation processes in continental and maritime convective clouds. *Bull. Amer. Meteor. Soc.*, **79**, 2457-2476.
- Rotunno, R., J. B. Klemp, and M. L. Weisman, 1988: A theory for strong, long-lived squall lines. *J. Atmos. Sci.*, **45**, 463-485.
- Rutledge, S. A., and R. A. Houze, Jr., 1987: A diagnostic modeling study of the trailing stratiform region of a midlatitude squall line. *J. Atmos. Sci.*, **44**, 2640-2656.
- , ———, M. I. Biggerstaff, and T. Matejka, 1988: The Oklahoma-Kansas mesoscale convective system of 10-11 June 1985: Precipitation structure and single-Doppler radar analysis. *Mon. Wea. Rev.*, **116**, 1409-1430.
- , C. Lu, and D. R. MacGorman, 1990: Positive cloud-to-ground lightning in mesoscale convective systems. *J. Atmos. Sci.*, **47**, 2085-2100.
- , and D. R. MacGorman, 1988: Cloud-to-ground lightning activity in the 10-11 June 1985 mesoscale convective system observed during the Oklahoma-Kansas PRE-STORM project. *Mon. Wea. Rev.*, **116**, 1393-1408.
- , and W. A. Petersen, 1994: Vertical radar reflectivity structure and cloud-to-ground lightning in the stratiform region of MCSs: Further evidence for in situ charging in the stratiform region. *Mon. Wea. Rev.*, **122**, 1760-1776.
- , E. R. Williams, and W. A. Petersen, 1993: Lightning and electrical structure of mesoscale convective systems. *Atmos. Res.*, **29**, 27-53.
- Saunders, C. P. R., 1993: A review of thunderstorm electrification processes. *J. Appl. Meteor.*, **32**, 642-655.
- , 1994: Thunderstorm electrification laboratory experiments and charging mechanisms. *J. Geophys. Res.*, **99**, 10 773-10 779.
- , W. D. Keith, and R. P. Mitzeva, 1991: The effect of liquid water on thunderstorm charging. *J. Geophys. Res.*, **96**, 11 007-11 017.
- , S. L. Peck, G. G. A. Varela, E. E. Avila, and N. E. Castellano, 2001: A laboratory study of the influence of water vapour and mixing on the charge transfer process during collisions between ice crystals and graupel. *Atmos. Res.*, **58**, 187-203.
- Schuur, T. J., and S. A. Rutledge, 2000a: Electrification of stratiform regions in mesoscale convective systems. Part I: An observational comparison of symmetric and asymmetric MCSs. *J. Atmos. Sci.*, **57**, 1961-1982.

- , and ——, 2000b: Electrification of stratiform regions in mesoscale convective systems. Part II: Two-dimensional numerical model simulations of a symmetric MCS. *J. Atmos. Sci.*, **57**, 1983-2006.
- , B. F. Smull, W. D. Rust, and T. C. Marshall, 1991: Electrical and kinematic structure of the stratiform precipitation region trailing an Oklahoma squall line. *J. Atmos. Sci.*, **48**, 825-842.
- Scott, J. D., and S. A. Rutledge, 1995: Doppler radar observations of an asymmetric mesoscale convective system and associated vortex couplet. *Mon. Wea. Rev.*, **123**, 3437-3457.
- Shafer, M. A., D. R. MacGorman, and F. H. Carr, 2000: Cloud-to-ground lightning throughout the lifetime of a severe storm system in Oklahoma. *Mon. Wea. Rev.*, **128**, 1798-1816.
- Shao, X. M., and P. R. Krehbiel, 1996: The spatial and temporal development of intracloud lightning. *J. Geophys. Res.*, **101**, 26 641-26 668.
- Shepherd, T. R., W. D. Rust, and T. C. Marshall, 1996: Electric fields and charges near 0°C in stratiform clouds. *Mon. Wea. Rev.*, **124**, 919-938.
- Smith, P. L., 1984: Equivalent radar reflectivity factors for snow and ice particles. *J. Clim. Appl. Meteor.*, **23**, 1258-1260.
- Smull, B. F., and R. A. Houze, Jr., 1985: A midlatitude squall line with a trailing region of stratiform rain: Radar and satellite observations. *Mon. Wea. Rev.*, **113**, 117-133.
- Steiner, M., R. A. Houze, Jr., and S. E. Yuter, 1995: Climatological characterization of three-dimensional storm structure from operational radar and rain gauge data. *J. Appl. Meteor.*, **34**, 1978-2007.
- Stolzenburg, M., 1990: Characteristics of the bipolar pattern of lightning locations observed in 1988 thunderstorms. *Bull. Amer. Meteor. Soc.*, **71**, 1331-1338.
- Stolzenburg, M., T. C. Marshall, W. D. Rust, and B. F. Smull, 1994: Horizontal distribution of electrical and meteorological conditions across the stratiform region of a mesoscale convective system. *Mon. Wea. Rev.*, **122**, 1777-1797.
- , W. D. Rust, B. F. Smull, and T. C. Marshall, 1998a: Electrical structure in thunderstorm convective regions, 1. Mesoscale convective systems. *J. Geophys. Res.*, **103**, 14 059-14 078.
- , ——, and T. C. Marshall, 1998b: Electrical structure in thunderstorm convective regions, 2. Isolated storms. *J. Geophys. Res.*, **103**, 14 079-14 096.

- , ——, and ——, 1998c: Electrical structure in thunderstorm convective regions, 3. Synthesis. *J. Geophys. Res.*, **103**, 14 097-14 108.
- Takahashi, T., 1978: Riming electrification as a charge generation mechanism in thunderstorms. *J. Atmos. Sci.*, **35**, 1536-1548.
- Toracinta, E. R., K. I. Mohr, E. J. Zipser, and R. E. Orville, 1996: A comparison of WSR-88D reflectivities, SMM/I brightness temperatures, and lightning for mesoscale convective systems in Texas. Part I: Radar reflectivity and lightning. *J. Appl. Meteor.*, **35**, 902-918.
- Uijlenhoet, R., M. Steiner, and J. A. Smith, 2003: Variability of rainfall drop size distributions in a squall line and implications for radar rainfall estimation. *J. Hydrometeor.*, **4**, 43-61.
- Vincent, B. R., L. D. Carey, D. Schneider, K. Keeter and R. Gonski, 2003: Using WSR-88D reflectivity for the prediction of cloud-to-ground lightning: A Central North Carolina study. *Natl. Wea. Dig.*, In press.
- Wacker, R. S., R. E. Orville, 1999: Changes in measured lightning flash count and return stroke peak current after the 1994 U.S. National Lightning Detection Network upgrade. Part 2: Theory. *J. Geophys. Res.*, **104**, 2159-2162.
- Wallace, J. M., and P. V. Hobbs, 1977: *Atmospheric Science. An Introductory Survey*. Academic Press Inc., San Diego, 467 pp.
- Weisman, M. L., and J. B. Klemp, 1982: The dependence of numerically simulated convective storms on vertical wind shear and buoyancy. *Mon. Wea. Rev.*, **110**, 504-520.
- , ——, and R. Rotunno, 1988: Structure and evolution of numerically simulated squall lines. *J. Atmos. Sci.*, **45**, 1990-2013.
- Wiens, K. C., S. A. Tessendorf, and S. A. Rutledge, 2002: June 29, 2000 STEPS supercell storm: Relationships between kinematics, microphysics, and lightning. *Preprints, 21<sup>st</sup> Conference on Severe Local Storms*, San Antonio, TX, Amer. Meteor. Soc.
- Williams, E. R., 1989: The tripole structure of thunderstorms. *J. Geophys. Res.*, **94**, 13 151-13 167.
- , 2001: The electrification of severe storms. *Severe Convective Storms, Meteor. Monogr.*, No. 50, Amer. Meteor. Soc., 527-561.
- , B. Boldi, A. Matlin, M. Weber, S. Hodanish, D. Sharp, S. Goodman, R. Raghavan, and D. Buechler, 1999: The behavior of total lightning activity in severe Florida thunderstorms. *Atmos. Res.*, **51**, 245-265.

—, C. M. Cooke and K. A. Wright, 1985: Electrical discharge propagation in and around space charge clouds. *J. Geophys. Res.*, **90**, 6059-6070.

Zipser, E. J., and K. R. Lutz, 1994: The vertical profile of radar reflectivity of convective cells: A strong indicator of storm intensity and lightning probability? *Mon. Wea. Rev.*, **122**, 1751-1759.

## **APPENDICES**

## APPENDIX A: THE RADAR BRIGHT BAND

A radar reflectivity bright band is an area of enhanced reflectivity just below the freezing level that exists because of the increase in dielectric and hydrometeor fall velocities as hydrometeors change from snow aggregates into water drops (Battan 1973). As snow aggregates enter the freezing level, they begin to melt into liquid precipitation from the surface inward, increasing the equivalent radar reflectivity factor ( $Z_e$ ) by approximately 6.5 dB due to the factor of 5 increase in dielectric from ice ( $|K_i|^2=0.208$ ) to water ( $|K_w|^2=0.93$ ), since rain scatters more than snow (Battan 1973; Smith 1984). As defined,  $z = \frac{r^2 \bar{P}_r C_R}{|K|^2}$ , and

$$z_e = \frac{r^2 \bar{P}_r C_R}{|K_w|^2}, \text{ where } z \text{ is the radar reflectivity factor, } z_e \text{ is the equivalent radar reflectivity}$$

factor assuming that all targets are liquid water and that Rayleigh scattering is occurring (i.e. the size of the sphere is small relative to the wavelength),  $r$  is range from the radar,  $\bar{P}_r$  is the returned power from scatterers,  $C_R$  is a constant that depends on the radar equipment being used, and  $|K|^2$  is the scatterers' dielectric constant, which differs depending upon the physical properties of the substance. In the case of frozen precipitation (i.e. before melting),

$$\text{combining the two equations above yields } z_e(\text{ice}) = \frac{|K_i|^2}{|K_w|^2} z = \frac{0.208}{0.93} z = 0.244z. \text{ When}$$

targets are all in the form of liquid precipitation (i.e. after melting or partial melting),

$$z_e(\text{rain}) = \frac{|K_w|^2}{|K_w|^2} z = z. \text{ By converting } z_e(\text{mm}^6\text{m}^{-3}) \text{ to } Z_e(\text{dBZ}) \text{ where } Z_e \equiv 10\log_{10}Z_e, \text{ the}$$

result yields  $Z_e(\text{rain})(\text{dBZ}) = Z(\text{ice})(\text{dBZ}) + 6.5 \text{ dB}$  (Houze 1993). Therefore, the solid to

liquid phase change of hydrometeors causes a significant increase in equivalent radar reflectivity in a region just below melting level (Battan 1973; Smith 1984; Houze 1993). Note that *equivalent* reflectivity and not *actual* reflectivity is what is displayed on typical radar images.

The second significant factor that leads to the radar bright band is due to the flux divergence of liquid water drops out of the melting region. As aggregates enter the melting level at relatively slow terminal fall speeds ( $1-3 \text{ ms}^{-1}$ ), they begin to melt as they continue to fall through the region. This melting process changes the hydrometeors' physical characteristics such that when they melt into liquid water drops and exit the region, their terminal fall speeds ( $\sim 5-10 \text{ ms}^{-1}$ ) significantly increase. Since the mean concentration of liquid water drops leaving the melting region is much greater than the mean concentration of snow aggregates entering the region, there is a decrease in  $Z_e$  below this bright band region (Battan 1973; Houze 1993).

## APPENDIX B: THE BULK RICHARDSON NUMBER

Bulk Richardson number measures the ratio of convective available potential energy (CAPE) to kinetic energy from the 500-m to 6-km vertical shear vector, where 500-m horizontal winds represent storm-relative inflow and 6-km horizontal winds represent mean background flow. The Bulk Richardson number is defined as

$$R_i = \frac{CAPE}{\frac{1}{2}[(\bar{U}_6 - \bar{U}_{0.5})^2 + (\bar{V}_6 - \bar{V}_{0.5})^2]} \quad [1.4]$$

where the variables in the denominator represent the mean pressure-weighted velocity from 0.5-6.0 km, and CAPE is a measure of the thermodynamic potential instability (i.e. the total buoyant energy available). CAPE can be defined as

$$CAPE = \int_{z_1}^{z_2} g \left( \frac{\theta_c - \theta_{env}}{\theta_{env}} \right) dz \quad [1.5]$$

where  $g$  is gravity,  $\theta_c$  is the potential temperature of an air parcel lifted from a given level or layer near the surface (e.g. the surface, lowest 50 mb, lowest 100 m) up to the level of free convection (LFC) ( $z_1$ ),  $\theta_{env}$  is the potential temperature of the unsaturated environment, and  $z_2$  is the equilibrium level (EL), which is the level of no potential temperature excess (i.e. where the parcel's temperature equals the environmental temperature) (Weisman and Klemp 1982; Bluestein and Jain 1985). By varying the magnitude of buoyancy and vertical shear in various severe storm environmental conditions using a three-dimensional numerical cloud model, Weisman and Klemp (1982) found that low values of  $R_i$  (~15-35) favor supercellular development, whereas high  $R_i$  values (>40) favor multicellular storm development.

## APPENDIX C: THE DUAL-DOPPLER METHOD

Using two Doppler radars, the three-dimensional wind field at each given height level can be determined. Figure C.1 represents the location of two radars in relation to a given precipitation volume they are sampling. If radar #1 is located at  $(x_1, y_1, z_1)$ , radar #2 is located at  $(x_2, y_2, z_2)$ , and a given hydrometeor is located at  $(x, y, z)$ , then  $u(x, y, z)$ ,  $v(x, y, z)$ , and  $W(x, y, z)$  can be determined, assuming the earth's curvature is negligible over the distance between the radars and the precipitation volume and, for simplicity, the terrain differences are negligible as well (i.e. at the ground,  $z = 0$ ). Vertical velocity ( $W$ ) is defined as the hydrometeor's terminal fall velocity ( $V_t$ ) plus the vertical motion of air ( $w$ ). Thus, the velocity of the hydrometeor at  $(x, y, z)$  is  $(u, v, w+V_t)$ , where  $V_t$  is defined by the following relationship:

$$V_t = -A \left( 10.0^{0.1(\text{dBZ})B} \right) \times \left( \frac{\rho_0}{\rho_z} \right)^C \quad [\text{C.1}]$$

where  $A$ ,  $B$ , and  $C$  are constants, dBZ is the radar reflectivity in dBZ units, and  $\rho_0$  is the density of air (Miller and Fredrick 1993).

To begin, relate radial velocity to the wind components by starting with the three-dimensional equation for the distance between the hydrometeor and each radar.

$$R_1^2 = (x - x_1)^2 + (y - y_1)^2 + (z - z_1)^2 \quad [\text{C.2}]$$

$$R_2^2 = (x - x_2)^2 + (y - y_2)^2 + (z - z_2)^2 \quad [\text{C.3}]$$

Take the temporal derivative  $\left( \frac{d}{dt} \right)$  of equations [C.2] and [C.3] to determine the horizontal wind components of motion.

$$2R_1 \frac{dR_1}{dt} = 2(x - x_1) \frac{dx}{dt} + 2(y - y_1) \frac{dy}{dt} + 2(z - z_1) \frac{dz}{dt} \quad [\text{C.4}]$$

$$2R_2 \frac{dR_2}{dt} = 2(x - x_2) \frac{dx}{dt} + 2(y - y_2) \frac{dy}{dt} + 2(z - z_2) \frac{dz}{dt} \quad [\text{C.5}]$$

Manipulating equations [C.4] and [C.5], and recalling that  $u = \frac{dx}{dt}$ ,  $v = \frac{dy}{dt}$ , and

$W = w + V_t = \frac{dz}{dt}$ , yields:

$$V_1 = u \left( \frac{x - x_1}{R_1} \right) + v \left( \frac{y - y_1}{R_1} \right) + (w + V_t) \left( \frac{z - z_1}{R_1} \right) \quad [\text{C.6}]$$

$$V_2 = u \left( \frac{x - x_2}{R_2} \right) + v \left( \frac{y - y_2}{R_2} \right) + (w + V_t) \left( \frac{z - z_2}{R_2} \right) \quad [\text{C.7}]$$

Equations [C.6] and [C.7] could be written in terms of the radar's elevation ( $\alpha$ ) and azimuth ( $\beta$ ) angles using the following geometric relations:

$$\left( \frac{x - x_m}{R_m} \right) = \cos \alpha_m \sin \beta_m, \quad \left( \frac{y - y_m}{R_m} \right) = \cos \alpha_m \cos \beta_m, \quad \text{and} \quad \left( \frac{z - z_m}{R_m} \right) = \sin \alpha_m.$$

Thus, there are two equations but three unknown variables ( $u$ ,  $v$ , and  $w$ ). Later, the continuity equation will be used as the third equation to close the system. Since all other variables are known, for simplicity,

$$\text{let } A_m = \left( \frac{x - x_m}{R_m} \right), \quad B_m = \left( \frac{y - y_m}{R_m} \right), \quad C_m = \left( \frac{z - z_m}{R_m} \right), \quad \text{and} \quad D_m = V_m.$$

Thus, equation [C.6] becomes:

$$uA_1 + vB_1 + (w + V_t)C_1 = D_1 \quad [\text{C.8}]$$

and similarly, equation [C.7] becomes:

$$uA_2 + vB_2 + (w + V_t)C_2 = D_2 \quad [\text{C.9}]$$

Taking  $B_2$  [C.8] -  $B_1$  [C.9] and rearranging, the u wind component becomes:

$$u = \frac{D_1 B_2 - D_2 B_1}{A_1 B_2 - A_2 B_1} + (w + V_t) \frac{C_2 B_1 - C_1 B_2}{A_1 B_2 - A_2 B_1}$$

[C.10]

Similarly, taking  $A_2$  [C.8] -  $A_1$  [C.9] and rearranging, the v wind component becomes:

$$v = \frac{D_2 A_1 - D_1 A_2}{A_1 B_2 - A_2 B_1} + (w + V_t) \frac{A_2 C_1 - A_1 C_2}{A_1 B_2 - A_2 B_1} \quad [C.11]$$

According to the dual-Doppler method, use equations [C.10] and [C.11] to calculate the horizontal wind field at every height level by assuming  $w = 0$ . It is reasonable to assume  $w = 0$  since a Doppler radar only scans at low elevation angles (0.5-19.5°) and thus radial velocity is largely affected by horizontal motions and not vertical motions. The influence that vertical velocity has on the horizontal wind field is defined by  $w \sin \alpha$ . Therefore, at low elevation angles, the effect of vertical motion is approximately zero. At a Doppler radar's maximum elevation angle, radial velocity is only affected by 0.33w.

Once initial values are determined for the horizontal wind field, the continuity equation is integrated to determine w. From the anelastic continuity equation,

$$\frac{\partial \rho}{\partial t} + \nabla \cdot (\rho \vec{u}) = 0 \quad [C.12]$$

Rearranging,

$$\frac{\partial \rho}{\partial t} + \frac{\partial(\rho u)}{\partial x} + \frac{\partial(\rho v)}{\partial y} + \frac{\partial(\rho w)}{\partial z} = 0 \quad [C.13]$$

$$\frac{\partial \rho}{\partial t} + \rho \frac{\partial u}{\partial x} + u \frac{\partial \rho}{\partial x} + \rho \frac{\partial v}{\partial y} + v \frac{\partial \rho}{\partial y} + \rho \frac{\partial w}{\partial z} + w \frac{\partial \rho}{\partial z} = 0 \quad [C.14]$$

Assume  $\rho = \rho(z)$ . Thus,

$$\rho \frac{\partial u}{\partial x} + \rho \frac{\partial v}{\partial y} + \rho \frac{\partial w}{\partial z} + w \frac{\partial \rho}{\partial z} = 0 \quad [\text{C.15}]$$

$$\frac{w}{\rho} \frac{\partial \rho}{\partial z} + \frac{\partial w}{\partial z} = - \left( \frac{\partial u}{\partial x} + \frac{\partial v}{\partial y} \right) \quad [\text{C.16}]$$

$$w \frac{\partial \rho}{\partial z} + \rho \frac{\partial w}{\partial z} = - \rho \left( \frac{\partial u}{\partial x} + \frac{\partial v}{\partial y} \right) \quad [\text{C.17}]$$

$$\frac{\partial(\rho w)}{\partial z} = - \rho \left( \frac{\partial u}{\partial x} + \frac{\partial v}{\partial y} \right) \quad [\text{C.18}]$$

Integrate equation [C.18] from the current level,  $c$ , to the upper level,  $p$ .

$$\int_c^p \frac{\partial(\rho w)}{\partial z} dz = - \int_c^p \rho \left( \frac{\partial u}{\partial x} + \frac{\partial v}{\partial y} \right) dz \quad [\text{C.19}]$$

$$(\rho w)_c = (\rho w)_p + \left[ \rho \left( \frac{\partial u}{\partial x} + \frac{\partial v}{\partial y} \right) \right]_{p-c} \Delta z \quad [\text{C.20}]$$

Therefore, an initial estimate for  $w_c$  at every height level can be calculated by rearranging equation [C.20] and remembering that  $w = 0$  initially.

$$w_c = \frac{\left[ \rho \left( \frac{\partial u}{\partial x} + \frac{\partial v}{\partial y} \right) \right]_{p-c} \Delta z}{\rho_c} \quad [\text{C.21}]$$

Once  $w_c$  is calculated at every height level, this value can be inserted into equations [C.10] and [C.11] to determine a new horizontal wind at every height level. If the values for the new horizontal wind differ from the initial values by more than a certain threshold (0.005 in this study), then the continuity equation is integrated again using these new horizontal wind values and a new  $w_c$  is calculated for every height level. This iterative method is used until the new and older horizontal wind values for each level differ by less than the predetermined

threshold values. When this process is finished, the latest three-dimensional winds calculated for each height level represent the three-dimensional wind field (Miller and Fredrick 1993).

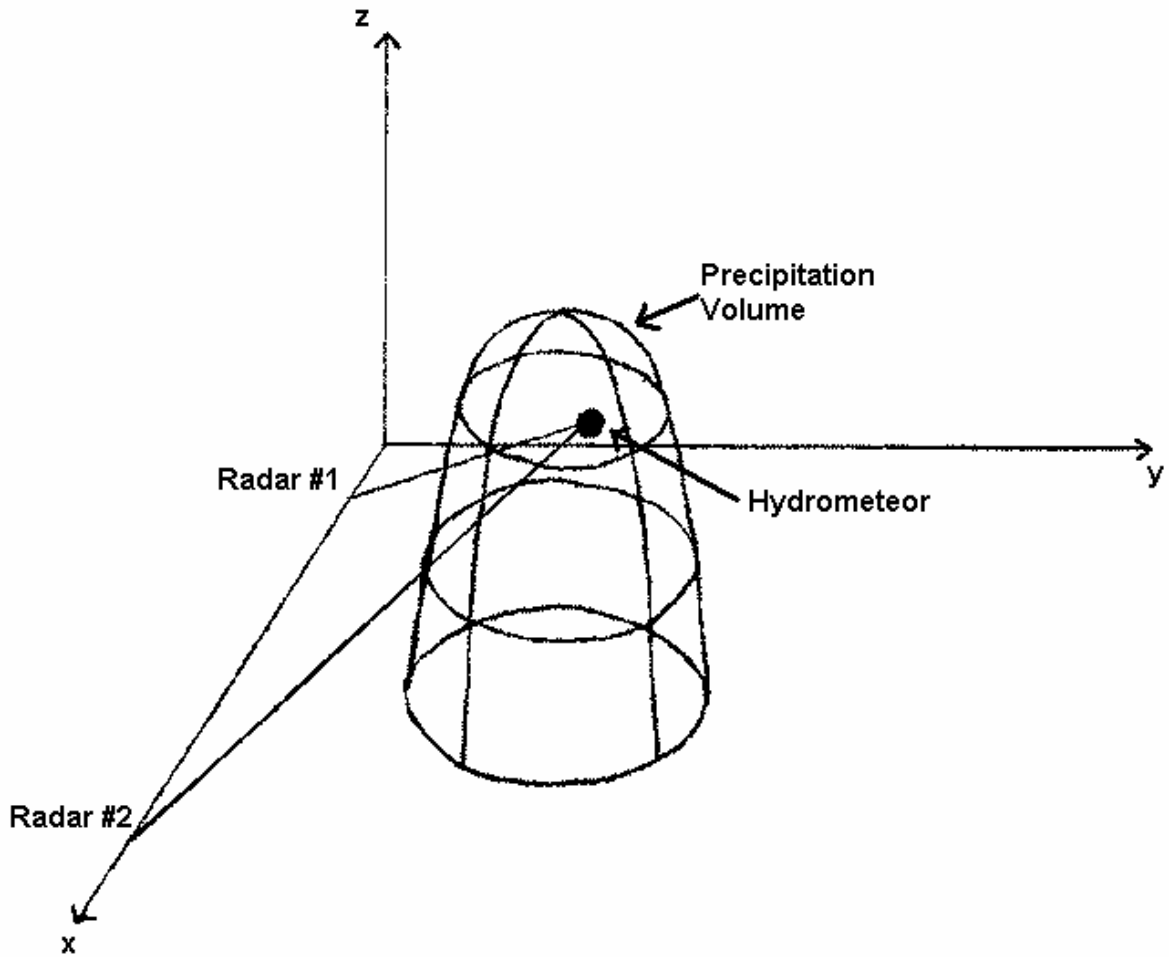


FIG. C.1. Diagram of two Doppler radars at different locations sampling a hydrometeor within a precipitation volume.

## APPENDIX D: LDAR II FLASH ALGORITHMS

LDAR II flash algorithms provide a way to examine 3-dimensional lightning characteristics, including their origin and propagation. VHF source emissions are grouped into flashes using various temporal and spatial constraints based on the lightning discharge propagation speeds (which average from approximately  $10^2$  to  $10^4$  km s<sup>-1</sup>) (Laroche et al. 1994; MacGorman and Rust 1998). Seven various algorithms were created based on the methods of previous studies, and their results were analyzed in this study.

Previous studies have also used various flash algorithms to study total (both IC and CG) lightning in various types of storms (severe and non-severe). Williams et al. (1999) created flashes from LDAR-I sources with an algorithm that classifies sources as part of the same flash if they occur within 0.3 sec and 5.0 km of one another and if subsequent sources occur within 5.0 sec of the flash origin. This study found that a large number of one source flashes existed in the dataset, and a possible problem with decomposing one large flash into multiple smaller flashes exists. Wiens et al. (2002) created flashes from LMA sources using a similar algorithm that classifies sources as part of the same flash if they occur within 0.15 sec and 3.0 km of one another, with the additional constraint that flashes must be composed of at least 10 sources. This additional constraint was added to eliminate low source number flashes.

National Aeronautics and Space Administration (NASA) has created a hierarchical algorithm for LDAR-I source data that first groups sources into branches and then groups branches into flashes according to spatial and time constraints. To be considered part of the same branch, two sources must occur within 0.03 sec of each other and within a specified

spatial region that varies as a function of distance away from the LDAR-I network center. Between 0.0 km and 40.0 km from the network center, VHF source emissions must be within 2.0 km of one another to be part of the same “flash.” Further away, the criteria is determined by the linear relationship  $y = 0.05x$ , where  $y$  is the maximum allowed distance between sources and  $x$  is the distance from the network center (Murphy et al. 2000). A modified NASA algorithm, based on the original NASA algorithm, was created by Vaisala to accelerate computer processing time. This modified algorithm is similar to the original in that it groups sources into branches and then branches into a flash, but unlike the original algorithm, it cannot account for the repeated branching effect of a lightning flash (i.e. it can only handle the initial branching effect) (M. Murphy 2003, personal communication).

This study used the following six algorithms that differ in space, time, and duration constraints, respectively: 1) 3.0-km, 0.15-sec, and 2.0-sec, 2) 3.0-km, 0.15-sec, and 4.0-sec, 3) 3.0-km, 0.30-sec, and 2.0-sec, 4) 5.0-km, 0.15-sec, and 2.0-sec, 5) 5.0-km, 0.30-sec, and 2.0-sec, and 6) 5.0-km, 0.30-sec, and 4.0-sec, as well as the modified NASA algorithm. While comparing these seven algorithms for three given 5 min increments from the April 2002 MCS (Fig. D.1), the two algorithms with a duration constraint of 4.0 sec were discarded since they were identical to the equivalent algorithms with a 2.0 sec duration. The largest difference in the number of flashes occurred between the modified NASA algorithm and the 3.0-km, 0.15-sec, 2.0-sec algorithm (Fig. D.1). A comparison among the remaining five various algorithms for the October 2001 MCS shows similar results (Fig. D.2). On average, the 3.0-km, 0.15-sec, 2.0-sec algorithm has a flash rate 2.54 times greater than the modified NASA algorithm for the October MCS (Table D.1) and 3.432 times greater than the modified NASA algorithm for the April MCS (Table D.2). The mean ratio of the 3.0-km, 0.15-sec,

2.0-sec algorithm to the 3.0-km, 0.30-sec, 2.0-sec algorithm, as well as the 5.0-km, 0.15-sec, 2.0-sec algorithm to the 5.0-km, 0.30-sec, 2.0-sec algorithm, is close to one for both MCS cases (Table D.1 and Table D.2), suggesting that the temporal increase in subsetting the LDAR II sources does *not* significantly decrease the resulting number of flashes. In contrast, the mean ratio of the 3.0-km, 0.15-sec, 2.0-sec algorithm to the 5.0-km, 0.15-sec, 2.0-sec algorithm, as well as the 3.0-km, 0.30-sec, 2.0-sec algorithm to the 5.0-km, 0.30-sec, 2.0-sec algorithm, is approximately 1.7 – 1.9 for both MCS cases (Table D.1 and Table D.2), suggesting that the spatial increase in subsetting the LDAR II sources *does* significantly decrease the resulting number of flashes. For more comparisons between the algorithms, please see Table D.1 for the October MCS and Table D.2 for the April MCS.

The various algorithms were also compared by overlaying algorithm-derived LDAR II flash origins at all heights on 0.5-km level radar reflectivity images of each MCS at 1:19 UTC 8 April 2002 (Fig. D.3-D.6) and at 4:47 UTC 13 October 2001 (Fig. D.7-D.10). These images indicate that a larger decrease in the number of flashes occurs when the algorithm's spatial constraint is increased from 3.0 km to 5.0 km (Figs. D.3 and D.5 for April and Figs. D.7 and D.9 for October MCS), than when the algorithm's temporal constraint is increased from 0.15 sec to 0.30 sec (April: Figs. D.3 and D.4 and October: Figs. D.7 and D.8). The decrease in flashes from Fig. D.3 to Fig. D.4 (Fig. D.7 to Fig. D.8), from Fig. D.3 to Fig. D.5 (Fig. D.7 to Fig. D.9), and from Fig. D.3 to Fig. D.6 (Fig. D.7 to Fig. D.10) for the April (October) MCS occurs in all regions (stratiform, convective and transition). Of particular interest, though, is the relatively few number of resulting flash origins located in the MCS transition zone when the modified NASA algorithm is used (Fig. D.6 and Fig. D.10 as

compared to the other three algorithms in Figs. D.3-D.5 (for April) and Figs. D.7-D.9 (for October).

Next, the temporal distribution of the number of LDAR II flash origins at all altitudes was analyzed using the five remaining algorithms for both the October 2001 MCS (Fig. D.11) and the April 2002 MCS (Fig. D.12) as they passed over the LDAR II network. It is evident from these figures that all algorithms show the same general trends (with respect to the given MCS case) in the number of LDAR II flash origins throughout time. By graphing the flash origin trends through time in 2.0-km height increments for the October MCS and April MCS (not shown), it is evident that there is less agreement between the different algorithms at low levels due to the decreased detection efficiency of the LDAR II network. At mid- to upper- levels, however, the correlation between the algorithms is excellent. For example, the correlation coefficient between the modified NASA algorithm and the 3.0-km, 0.15-sec, 2.0-sec algorithm for the October MCS at the 0 – 2 km level is 0.80, but at mid-levels (4 – 6 km) it is 0.97, and overall (0 – 20 km) it is 0.98 (for more information, see Table D.3). The correlation coefficient between the modified NASA algorithm and the 3.0-km, 0.15-sec, 2.0-sec algorithm for the April MCS at the 0 – 2 km level is only 0.52, but at mid-levels (4 – 6 km) it increases to 0.92, and overall (0 – 20 km) it is 0.92 (for more information, please see Table D.4).

Among the seven algorithms, the modified NASA algorithm seemed to handle overall lightning characteristics the best. In addition to being the only algorithm that accounts for the branching nature of lightning (a fact known before the above sensitivity experiments were performed), these experiments showed that the modified NASA algorithm was the only one that depicted a decrease in flash origin concentration in the transition zone. Since the

transition zone is characterized by low lightning flash rates (Mazur and Rust 1983), one would expect a relatively few number of LDAR II flash origins in this region. Therefore, the modified NASA algorithm was used for the remainder of this study.

Table D.1. Statistical comparisons between each LDAR II flash algorithm for 04:00-05:00 UTC 13 October 2001 at all height levels.

<b>Ratios of the number of flashes using the 1st algorithm to the number of flashes using the 2nd algorithm listed 4:00-5:30 UTC 13 October 2001</b>											
<b>1st Algorithm:2nd Algorithm</b>											
<b>3km, 150ms/ M. NASA Alg.</b>	<b>0-2</b>	<b>2-4</b>	<b>4-6</b>	<b>6-8</b>	<b>8-10</b>	<b>10-12</b>	<b>12-14</b>	<b>14-16</b>	<b>16-18</b>	<b>18-20</b>	<b>0-20</b>
	<b>(km)</b>	<b>(km)</b>	<b>(km)</b>	<b>(km)</b>	<b>(km)</b>	<b>(km)</b>	<b>(km)</b>	<b>(km)</b>	<b>(km)</b>	<b>(km)</b>	<b>(km)</b>
<b>Mean</b>	2.258	2.558	2.768	2.755	2.532	2.534	2.540	2.466	1.974	1.540	2.540
<b>Minimum</b>	1.800	2.030	2.433	2.361	2.153	2.010	1.919	1.717	1.306	1.167	2.064
<b>Maximum</b>	3.000	3.105	3.104	2.916	2.794	2.800	2.967	2.911	2.335	1.776	2.737
<b>Median</b>	2.273	2.567	2.753	2.773	2.583	2.588	2.522	2.459	1.899	1.528	2.544
<b>25th Percentile</b>	2.053	2.402	2.670	2.656	2.451	2.348	2.457	2.223	1.808	1.415	2.463
<b>75th Percentile</b>	2.389	2.641	2.924	2.831	2.659	2.665	2.725	2.696	2.044	1.624	2.616
<b>3km, 300ms/ M. NASA Alg.</b>											
<b>Mean</b>	2.244	2.474	2.633	2.605	2.351	2.285	2.290	2.328	1.943	1.532	2.345
<b>Minimum</b>	1.775	1.909	2.359	2.255	2.054	1.900	1.833	1.697	1.306	1.167	1.971
<b>Maximum</b>	3.000	3.070	2.969	2.725	2.656	2.480	2.741	2.766	2.311	1.746	2.512
<b>Median</b>	2.273	2.495	2.617	2.619	2.411	2.321	2.317	2.356	1.849	1.519	2.349
<b>25th Percentile</b>	2.045	2.318	2.562	2.527	2.266	2.149	2.194	2.157	1.792	1.415	2.293
<b>75th Percentile</b>	2.372	2.545	2.759	2.690	2.466	2.374	2.464	2.511	2.009	1.616	2.406
<b>5km, 150ms/ M. NASA Alg.</b>											
<b>Mean</b>	2.024	2.025	1.950	1.689	1.463	1.466	1.561	1.680	1.658	1.478	1.576
<b>Minimum</b>	1.625	1.652	1.621	1.327	1.226	1.177	1.225	1.230	1.125	1.167	1.262
<b>Maximum</b>	2.821	2.488	2.088	1.900	1.569	1.609	1.675	1.931	1.930	1.701	1.694
<b>Median</b>	2.000	1.984	1.955	1.704	1.480	1.475	1.560	1.627	1.628	1.469	1.569
<b>25th Percentile</b>	1.861	1.924	1.863	1.583	1.433	1.384	1.506	1.574	1.565	1.363	1.521
<b>75th Percentile</b>	2.162	2.117	2.051	1.790	1.517	1.544	1.629	1.809	1.667	1.558	1.629
<b>5km, 300ms/ M. NASA Alg.</b>											
<b>Mean</b>	1.972	1.901	1.762	1.523	1.291	1.234	1.298	1.460	1.558	1.413	1.372
<b>Minimum</b>	1.600	1.500	1.458	1.197	1.121	1.052	1.122	1.095	1.125	1.080	1.151
<b>Maximum</b>	2.714	2.360	1.953	1.893	1.393	1.320	1.445	1.737	1.822	1.657	1.429
<b>Median</b>	1.976	1.873	1.735	1.529	1.308	1.235	1.306	1.527	1.545	1.426	1.389

<b>25th Percentile</b>	1.799	1.800	1.705	1.427	1.266	1.185	1.254	1.414	1.494	1.351	1.340
<b>75th Percentile</b>	2.129	2.017	1.811	1.593	1.328	1.280	1.362	1.601	1.611	1.523	1.417

**3km, 150ms/**

**3km, 300ms**

<b>Mean</b>	1.006	1.034	1.051	1.058	1.077	1.109	1.109	1.059	1.016	1.005	1.083
<b>Minimum</b>	1.000	1.011	1.028	1.032	1.048	1.058	1.047	1.012	1.000	1.000	1.047
<b>Maximum</b>	1.032	1.063	1.068	1.074	1.106	1.135	1.140	1.095	1.031	1.017	1.100
<b>Median</b>	1.000	1.031	1.054	1.060	1.079	1.109	1.105	1.046	1.017	1.000	1.088
<b>25th Percentile</b>	1.000	1.024	1.046	1.047	1.068	1.090	1.078	1.031	1.002	1.000	1.067
<b>75th Percentile</b>	1.012	1.047	1.056	1.064	1.085	1.122	1.123	1.061	1.022	1.009	1.092

**3km, 150ms/**

**5km, 150ms**

<b>Mean</b>	1.116	1.263	1.420	1.631	1.731	1.729	1.627	1.468	1.191	1.042	1.612
<b>Minimum</b>	1.063	1.216	1.341	1.517	1.638	1.583	1.438	1.247	1.094	1.000	1.541
<b>Maximum</b>	1.217	1.365	1.564	1.791	1.853	1.838	1.829	1.635	1.285	1.090	1.672
<b>Median</b>	1.119	1.255	1.408	1.627	1.744	1.754	1.642	1.468	1.160	1.036	1.626
<b>25th Percentile</b>	1.089	1.225	1.398	1.569	1.673	1.691	1.592	1.392	1.146	1.018	1.584
<b>75th Percentile</b>	1.136	1.293	1.450	1.761	1.792	1.766	1.707	1.510	1.216	1.053	1.648

**3km, 150ms/**

**5km, 300ms**

<b>Mean</b>	1.145	1.346	1.571	1.809	1.961	2.053	1.957	1.689	1.268	1.090	1.852
<b>Minimum</b>	1.065	1.146	1.284	1.518	1.709	1.881	1.710	1.377	1.116	1.000	1.770
<b>Maximum</b>	1.237	1.437	1.713	1.998	2.159	2.167	2.173	2.229	1.640	1.410	1.935
<b>Median</b>	1.137	1.354	1.586	1.814	1.986	2.070	1.959	1.634	1.213	1.056	1.849
<b>25th Percentile</b>	1.118	1.312	1.558	1.776	1.916	1.999	1.884	1.489	1.173	1.020	1.829
<b>75th Percentile</b>	1.172	1.389	1.612	1.933	2.029	2.103	2.040	1.729	1.279	1.080	1.885

**3km, 300ms/**

**5km, 150ms**

<b>Mean</b>	1.109	1.222	1.350	1.542	1.607	1.559	1.467	1.386	1.172	1.037	1.488
<b>Minimum</b>	1.043	1.156	1.270	1.423	1.517	1.440	1.305	1.202	1.081	1.000	1.407
<b>Maximum</b>	1.200	1.340	1.496	1.725	1.725	1.658	1.689	1.553	1.256	1.090	1.562
<b>Median</b>	1.107	1.215	1.337	1.530	1.630	1.572	1.503	1.380	1.160	1.030	1.502
<b>25th Percentile</b>	1.083	1.183	1.323	1.465	1.551	1.533	1.431	1.344	1.132	1.015	1.467
<b>75th Percentile</b>	1.131	1.252	1.395	1.675	1.674	1.596	1.557	1.437	1.193	1.052	1.536

3km, 300ms/

5km, 300ms

<b>Mean</b>	1.138	1.301	1.494	1.710	1.821	1.851	1.764	1.595	1.247	1.085	1.710
<b>Minimum</b>	1.043	1.118	1.219	1.435	1.583	1.728	1.584	1.328	1.103	1.000	1.652
<b>Maximum</b>	1.220	1.411	1.638	1.915	2.002	1.955	1.945	2.036	1.603	1.402	1.777
<b>Median</b>	1.136	1.300	1.512	1.713	1.842	1.865	1.788	1.565	1.207	1.054	1.720
<b>25th Percentile</b>	1.113	1.271	1.481	1.659	1.772	1.811	1.697	1.443	1.173	1.018	1.687
<b>75th Percentile</b>	1.167	1.348	1.528	1.863	1.890	1.884	1.847	1.626	1.269	1.071	1.735

5km, 150ms/

5km, 300ms

<b>Mean</b>	1.026	1.065	1.106	1.109	1.133	1.188	1.203	1.151	1.065	1.046	1.149
<b>Minimum</b>	1.000	0.910	0.919	0.981	1.043	1.119	1.092	1.051	1.000	0.981	1.097
<b>Maximum</b>	1.057	1.114	1.142	1.144	1.167	1.231	1.306	1.463	1.276	1.361	1.185
<b>Median</b>	1.032	1.071	1.122	1.116	1.139	1.192	1.195	1.094	1.048	1.015	1.148
<b>25th Percentile</b>	1.015	1.054	1.095	1.106	1.123	1.159	1.164	1.078	1.031	1.000	1.130
<b>75th Percentile</b>	1.034	1.092	1.133	1.126	1.147	1.205	1.209	1.145	1.054	1.027	1.155

Table D.2. Same as Table D.1 but for 01:00-02:00 UTC 8 April 2002.

**Ratios of the number of flashes using the 1st algorithm to  
the number of flashes using the 2nd algorithm listed  
1:00-2:00 UTC 8 April 2002**

1st Algorithm:2nd Algorithm

3km, 150ms/

M. NASA Alg.

	0-2	2-4	4-6	6-8	8-10	10-12	12-14	14-16	16-18	18-20	0-20
	(km)										
<b>Mean</b>	5.065	3.983	3.860	3.739	3.434	3.217	3.108	2.751	1.997	1.731	3.432
<b>Minimum</b>	2.556	2.633	3.075	3.032	2.652	1.988	1.633	1.778	1.281	1.077	2.607
<b>Maximum</b>	8.333	5.569	4.636	4.896	4.364	4.327	4.069	3.739	3.053	2.600	4.244
<b>Median</b>	5.500	3.672	3.684	3.495	3.325	3.239	3.446	2.500	1.829	1.786	3.312
<b>25th Percentile</b>	4.000	3.500	3.502	3.389	3.188	2.804	2.705	2.161	1.462	1.375	3.016
<b>75th Percentile</b>	5.750	4.377	4.356	3.958	3.944	3.830	3.727	3.000	2.241	2.000	3.848

3km, 300ms/

M. NASA Alg.

<b>Mean</b>	4.922	3.734	3.530	3.475	3.250	3.030	2.978	2.679	1.971	1.704	3.223
<b>Minimum</b>	2.444	2.600	2.849	2.847	2.495	1.958	1.596	1.750	1.273	1.000	2.501
<b>Maximum</b>	8.167	5.157	4.185	4.484	4.056	4.030	3.758	3.623	3.053	2.600	3.896
<b>Median</b>	5.500	3.475	3.457	3.294	3.187	2.978	3.365	2.438	1.829	1.733	3.123
<b>25th Percentile</b>	3.800	3.297	3.151	3.197	3.061	2.693	2.641	2.161	1.462	1.375	2.867
<b>75th Percentile</b>	5.750	4.073	3.945	3.669	3.730	3.590	3.610	2.900	2.207	2.000	3.605

**5km, 150ms/****M. NASA Alg.**

<b>Mean</b>	3.195	2.293	2.130	1.944	1.818	1.705	1.803	1.856	1.596	1.505	1.886
<b>Minimum</b>	1.833	1.898	1.765	1.542	1.488	1.179	1.229	1.306	1.182	1.077	1.493
<b>Maximum</b>	5.167	3.059	2.497	2.548	2.235	2.200	2.267	2.280	2.368	2.000	2.225
<b>Median</b>	3.250	2.208	2.020	1.782	1.823	1.700	1.797	1.863	1.512	1.500	1.787
<b>25th Percentile</b>	2.800	2.066	1.849	1.751	1.742	1.451	1.610	1.613	1.269	1.375	1.716
<b>75th Percentile</b>	3.750	2.375	2.319	2.096	1.993	2.024	2.078	2.176	1.793	1.750	2.103

**5km, 300ms/****M. NASA Alg.**

<b>Mean</b>	3.000	2.023	1.803	1.728	1.674	1.560	1.677	1.771	1.537	1.457	1.703
<b>Minimum</b>	1.833	1.610	1.561	1.442	1.361	1.155	1.174	1.278	1.091	1.000	1.389
<b>Maximum</b>	5.000	2.824	2.078	2.190	2.006	2.006	2.095	2.179	2.316	2.000	1.973
<b>Median</b>	2.800	1.938	1.721	1.633	1.683	1.543	1.662	1.750	1.488	1.444	1.638
<b>25th Percentile</b>	2.500	1.795	1.616	1.596	1.601	1.360	1.519	1.613	1.269	1.375	1.577
<b>75th Percentile</b>	3.500	2.127	1.930	1.793	1.819	1.809	1.922	1.973	1.684	1.600	1.861

**3km, 150ms/****3km, 300ms**

<b>Mean</b>	1.029	1.067	1.093	1.076	1.057	1.062	1.044	1.027	1.013	1.016	1.065
<b>Minimum</b>	1.000	1.013	1.065	1.050	1.036	1.015	1.010	1.000	1.000	1.000	1.042
<b>Maximum</b>	1.111	1.085	1.116	1.118	1.076	1.097	1.088	1.056	1.051	1.077	1.090
<b>Median</b>	1.000	1.071	1.092	1.074	1.057	1.054	1.024	1.024	1.000	1.000	1.060
<b>25th Percentile</b>	1.000	1.056	1.076	1.060	1.043	1.041	1.022	1.009	1.000	1.000	1.052
<b>75th Percentile</b>	1.032	1.080	1.105	1.082	1.064	1.069	1.039	1.031	1.025	1.010	1.071

**3km, 150ms/****5km, 150ms**

<b>Mean</b>	1.585	1.738	1.812	1.923	1.889	1.887	1.724	1.482	1.251	1.150	1.819
<b>Minimum</b>	1.143	1.317	1.713	1.789	1.782	1.687	1.328	1.183	1.051	1.000	1.746
<b>Maximum</b>	1.909	1.983	2.087	2.084	2.016	2.047	2.010	2.048	1.456	1.444	1.908
<b>Median</b>	1.571	1.763	1.812	1.922	1.892	1.905	1.759	1.362	1.210	1.136	1.814
<b>25th Percentile</b>	1.379	1.664	1.740	1.884	1.829	1.791	1.648	1.279	1.121	1.071	1.782
<b>75th Percentile</b>	1.800	1.814	1.873	1.961	1.937	1.960	1.795	1.534	1.289	1.167	1.839

**3km, 150ms/****5km, 300ms**

<b>Mean</b>	1.688	1.969	2.141	2.164	2.052	2.061	1.853	1.554	1.299	1.188	2.016
<b>Minimum</b>	1.143	1.491	1.919	1.986	1.900	1.722	1.391	1.246	1.051	1.000	1.877

<b>Maximum</b>	2.105	2.343	2.359	2.436	2.209	2.219	2.228	2.168	1.523	1.625	2.151
<b>Median</b>	1.665	1.991	2.173	2.142	2.037	2.088	1.912	1.396	1.230	1.139	2.027
<b>25th Percentile</b>	1.571	1.839	2.032	2.123	1.976	1.968	1.702	1.340	1.156	1.111	1.928
<b>75th Percentile</b>	1.909	2.074	2.225	2.223	2.131	2.157	1.942	1.632	1.383	1.167	2.057

**3km, 300ms/  
5km, 150ms**

<b>Mean</b>	1.541	1.629	1.657	1.787	1.787	1.777	1.652	1.444	1.235	1.132	1.709
<b>Minimum</b>	1.143	1.300	1.565	1.680	1.676	1.610	1.299	1.150	1.051	0.929	1.671
<b>Maximum</b>	1.909	1.829	1.942	1.955	1.886	1.966	1.951	1.984	1.456	1.444	1.751
<b>Median</b>	1.571	1.658	1.624	1.803	1.790	1.790	1.661	1.340	1.200	1.136	1.706
<b>25th Percentile</b>	1.368	1.540	1.605	1.750	1.766	1.739	1.632	1.279	1.121	1.040	1.694
<b>75th Percentile</b>	1.667	1.686	1.701	1.860	1.814	1.859	1.738	1.453	1.289	1.167	1.716

**3km, 300ms/  
5km, 300ms**

<b>Mean</b>	1.641	1.846	1.958	2.012	1.942	1.941	1.775	1.513	1.282	1.170	1.893
<b>Minimum</b>	1.143	1.472	1.779	1.866	1.806	1.696	1.359	1.211	1.051	1.000	1.800
<b>Maximum</b>	2.053	2.162	2.196	2.178	2.067	2.083	2.163	2.101	1.523	1.625	1.974
<b>Median</b>	1.633	1.835	1.947	2.031	1.923	1.972	1.786	1.370	1.230	1.139	1.897
<b>25th Percentile</b>	1.571	1.702	1.858	1.961	1.894	1.882	1.686	1.306	1.156	1.083	1.832
<b>75th Percentile</b>	1.800	1.958	2.051	2.055	2.016	2.004	1.896	1.582	1.362	1.167	1.925

**5km, 150ms/  
5km, 300ms**

<b>Mean</b>	1.065	1.133	1.182	1.125	1.086	1.092	1.075	1.048	1.038	1.033	1.108
<b>Minimum</b>	1.000	1.083	1.107	1.069	1.046	1.021	1.022	0.988	1.000	1.000	1.065
<b>Maximum</b>	1.300	1.182	1.243	1.204	1.114	1.121	1.124	1.103	1.106	1.125	1.137
<b>Median</b>	1.033	1.133	1.174	1.111	1.093	1.095	1.081	1.044	1.031	1.000	1.101
<b>25th Percentile</b>	1.000	1.105	1.140	1.091	1.076	1.067	1.048	1.021	1.016	1.000	1.089
<b>75th Percentile</b>	1.080	1.167	1.199	1.154	1.100	1.109	1.082	1.064	1.046	1.077	1.125

Table D.3. Correlation coefficients between each algorithm at various 2.0-km height increments for 04:00 – 05:30 UTC 13 October 2001.

Alg. Begin Compared		Correlation Coefficients (from 4:00-5:30 UTC 13 October 2001)										
		0-2 Km	2-4 Km	4-6 km	6-8 km	8- 10 km	10- 12 km	12- 14 km	14- 16 km	16- 18 km	18- 20 km	0- 20 km
M. NASA	3km,0.15s	0.80	0.89	0.97	0.97	0.93	0.95	0.97	0.97	0.96	0.97	0.98
M. NASA	3km,0.3s	0.79	0.89	0.97	0.97	0.93	0.95	0.97	0.98	0.96	0.97	0.98
M. NASA	5km,0.15s	0.80	0.88	0.98	0.97	0.96	0.96	0.99	0.98	0.96	0.97	0.98
M. NASA	5km,0.3s	0.81	0.88	0.98	0.94	0.96	0.97	0.99	0.94	0.93	0.90	0.99

<b>3km,0.15s</b>	<b>3km,0.3s</b>	1.00	1.00	1.00	1.00	1.00	1.00	1.00	1.00	1.00	1.00	1.00
<b>3km,0.15s</b>	<b>5km,0.15s</b>	0.99	0.99	0.99	0.99	0.98	0.98	0.99	0.99	1.00	1.00	0.99
<b>3km,0.15s</b>	<b>5km,0.3s</b>	0.99	0.97	0.97	0.97	0.96	0.98	0.98	0.97	0.97	0.97	0.99
<b>3km,0.3s</b>	<b>5km,0.15s</b>	0.99	0.99	0.99	0.99	0.98	0.98	0.99	0.99	1.00	1.00	0.99
<b>3km,0.3s</b>	<b>5km,0.3s</b>	0.99	0.97	0.97	0.97	0.96	0.99	0.98	0.97	0.97	0.97	1.00
<b>5km,0.15s</b>	<b>5km,0.3s</b>	1.00	0.98	0.98	0.98	0.99	1.00	1.00	0.98	0.98	0.96	1.00

Table D.4. Same as Table D.3 but for 01:00 – 02:00 UTC 8 April 2002.

Alg. Being Compared		Correlation Coefficients (from 1:00-2:00 UTC 8 April 2002)										
		0-2 Km	2-4 km	4-6 km	6-8 km	8- 10 km	10- 12 km	12- 14 km	14- 16 km	16- 18 km	18- 20 km	0- 20 km
<b>M. NASA</b>	<b>3km,0.15s</b>	0.52	0.79	0.92	0.73	0.66	0.80	0.79	0.94	0.81	0.88	0.92
<b>M. NASA</b>	<b>3km,0.3s</b>	0.52	0.80	0.92	0.76	0.68	0.81	0.79	0.94	0.82	0.88	0.92
<b>M. NASA</b>	<b>5km,0.15s</b>	0.60	0.84	0.95	0.80	0.76	0.87	0.88	0.95	0.85	0.91	0.94
<b>M. NASA</b>	<b>5km,0.3</b>	0.55	0.81	0.96	0.83	0.77	0.88	0.90	0.95	0.86	0.91	0.94
<b>3km,0.15s</b>	<b>3km,0.3s</b>	1.00	1.00	1.00	1.00	1.00	1.00	1.00	1.00	1.00	1.00	1.00
<b>3km,0.15s</b>	<b>5km,0.15s</b>	0.93	0.98	0.99	0.99	0.98	0.99	0.98	0.96	0.99	0.99	1.00
<b>3km,0.15s</b>	<b>5km,0.3s</b>	0.93	0.96	0.98	0.97	0.97	0.99	0.98	0.97	0.98	0.97	1.00
<b>3km,0.3s</b>	<b>5km,0.15s</b>	0.93	0.98	0.99	0.99	0.99	0.99	0.98	0.96	0.99	0.99	1.00
<b>3km,0.3s</b>	<b>5km,0.3s</b>	0.93	0.96	0.99	0.98	0.98	0.99	0.97	0.96	0.98	0.98	1.00
<b>5km,0.15s</b>	<b>5km,0.3s</b>	0.98	0.99	1.00	0.99	0.99	1.00	1.00	1.00	1.00	1.00	1.00

### Comparison of Different LDAR II Flash Algorithms 8 April 2002

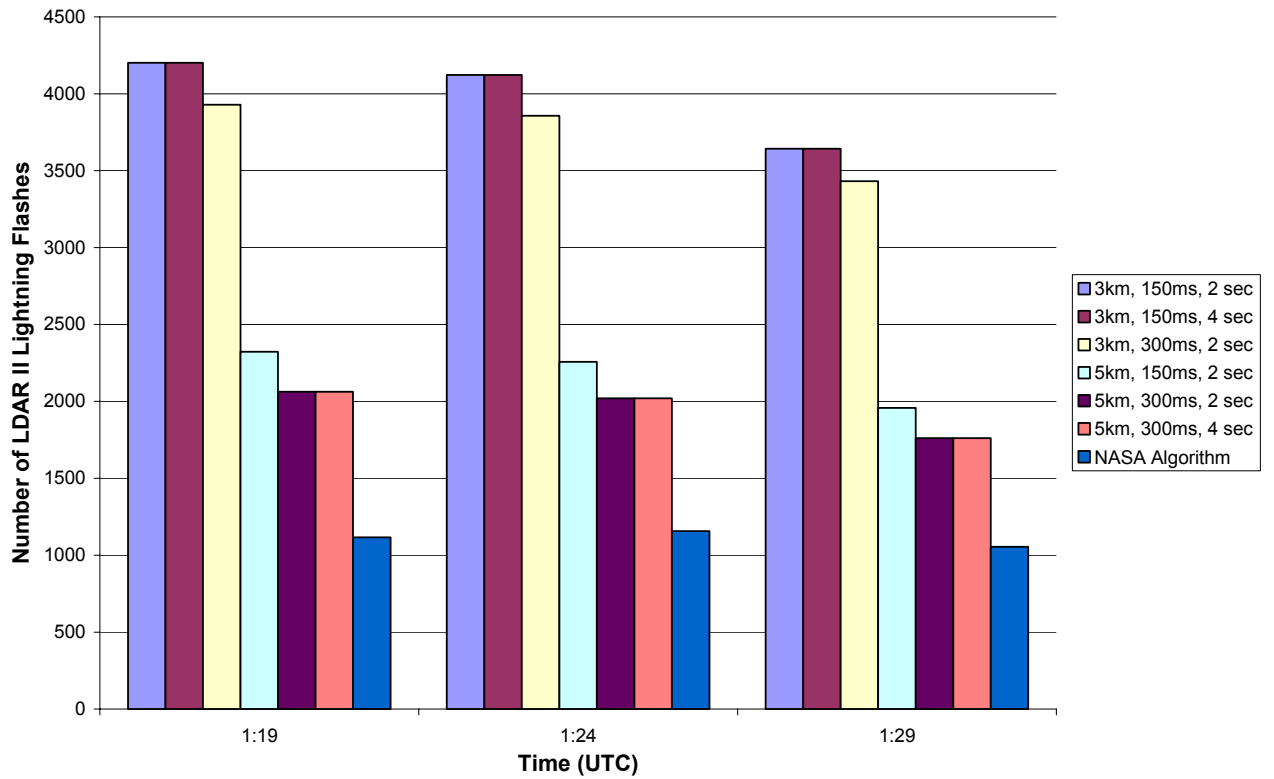


FIG. D.1. Comparison of seven different algorithms used to group LDAR II sources into flashes for the 8 April 2002 MCS. Notice there is no difference in the number of resulting flashes between the 3.0-km, 0.15-sec, 2.0-sec algorithm and the 3.0-km, 0.15-sec, 4.0-sec algorithm or between the 5.0-km, 0.30-sec, 2.0-sec algorithm and the 5.0-km, 0.30-sec, 4.0-sec algorithm. The largest difference (by a factor of approximately 4) occurs between the modified NASA algorithm and the 3.0-km, 0.15-sec, 2.0-sec algorithm.

### Comparison of Various LDAR-II Flash Algorithms 13 October 2001

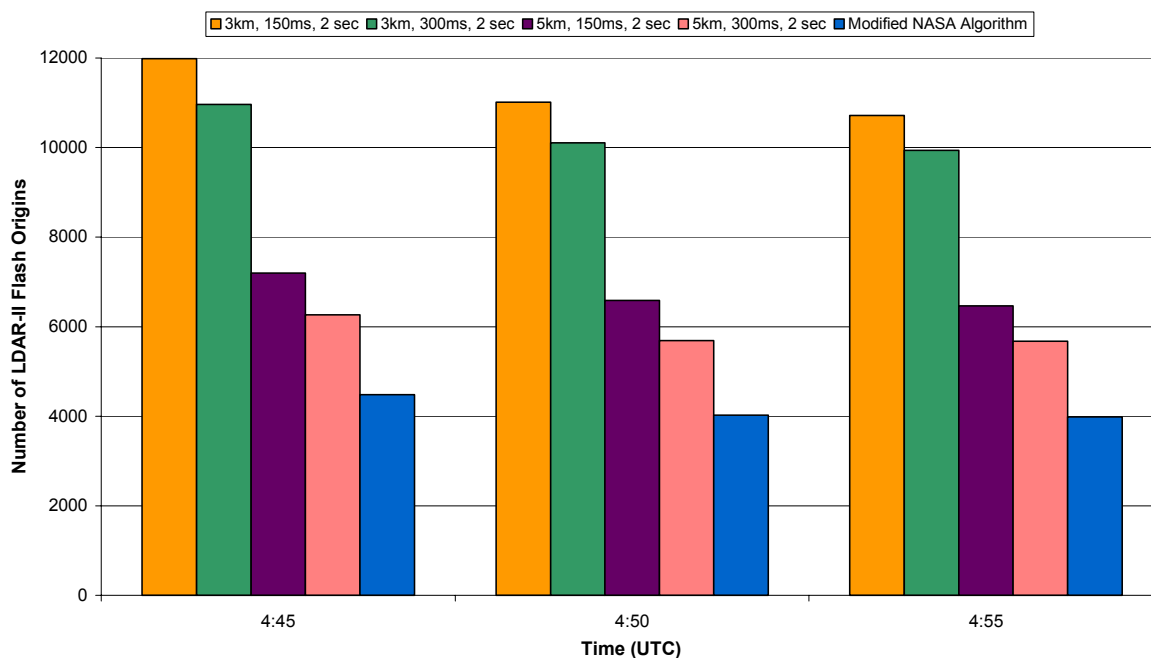


FIG. D.2. Comparison of five various LDAR II flash algorithms including the 3.0-km, 0.15-sec; 3.0-km, 0.30-sec; 5.0-km, 0.15-sec; 5.0-km, 0.30-sec; and modified NASA algorithms for the 13 October 2001 MCS. The largest difference between algorithms occurs between the 3.0-km, 0.15-sec algorithm and the modified NASA algorithm.

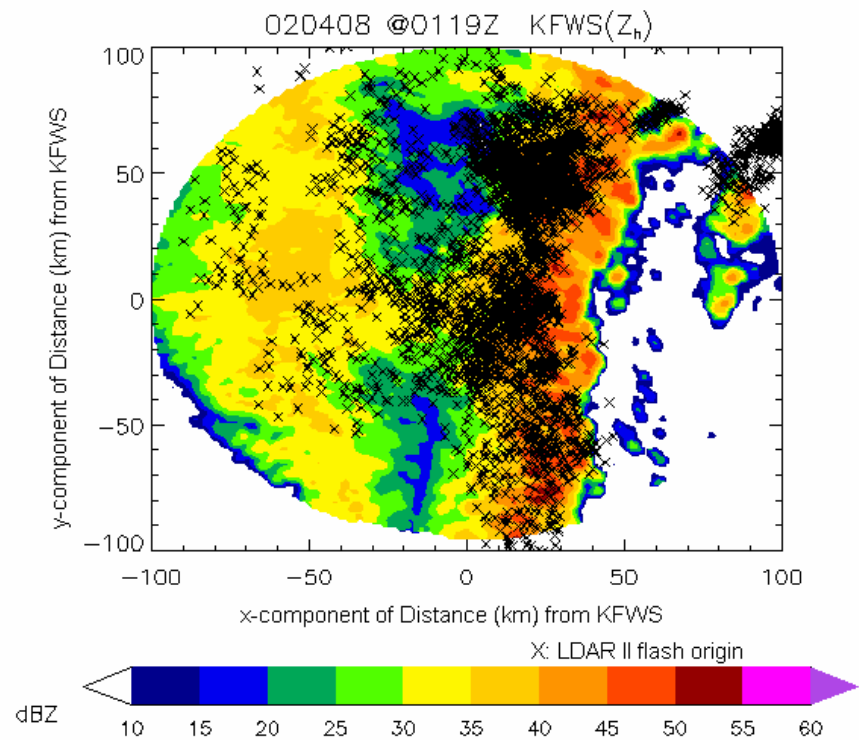


FIG. D.3. LDAR II flash origins at all heights created by the 3.0-km, 0.15-sec, 2.0-sec algorithm overlaid on the 0.5-km radar reflectivity height level of the Dallas/Fort Worth, TX area (KFWS) ( $200 \times 200$  km area) for 1:19 UTC 8 April 2002 MCS. The KFWS radar is located in the center of this image.

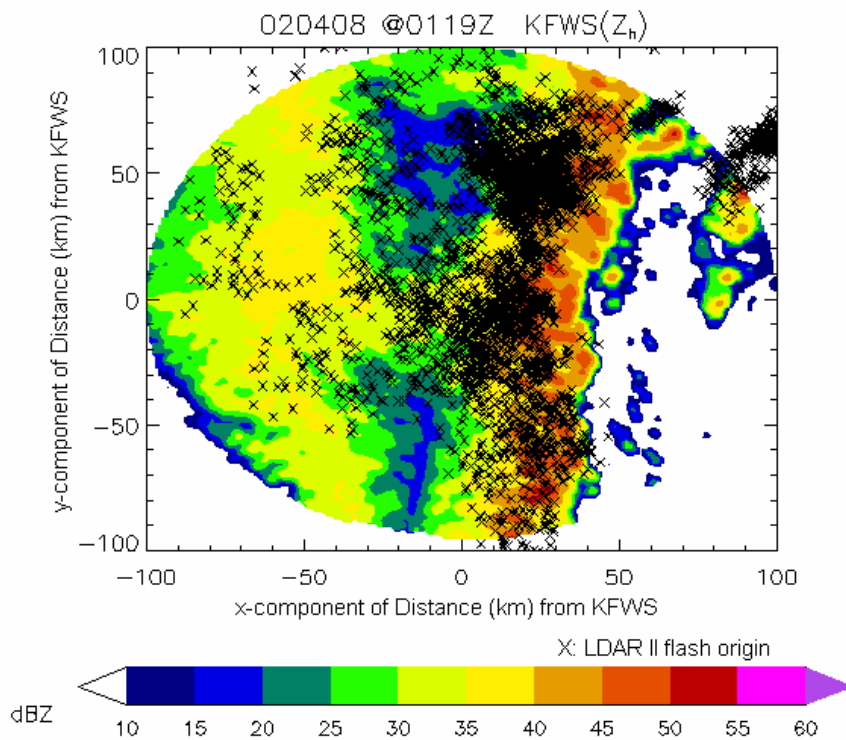


FIG. D.4. Same as Fig. D.3 but for the 3.0-km, 0.30-sec, 2.0-sec algorithm.

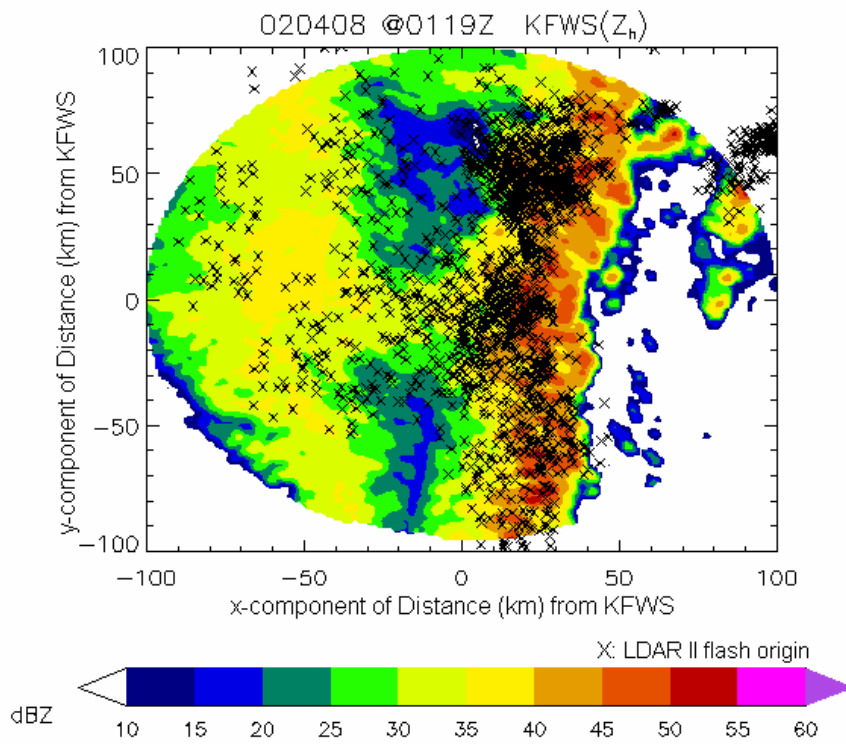


FIG. D.5. Same as Fig. D.3 but for the 5.0-km, 0.15-sec, 2.0-sec algorithm.

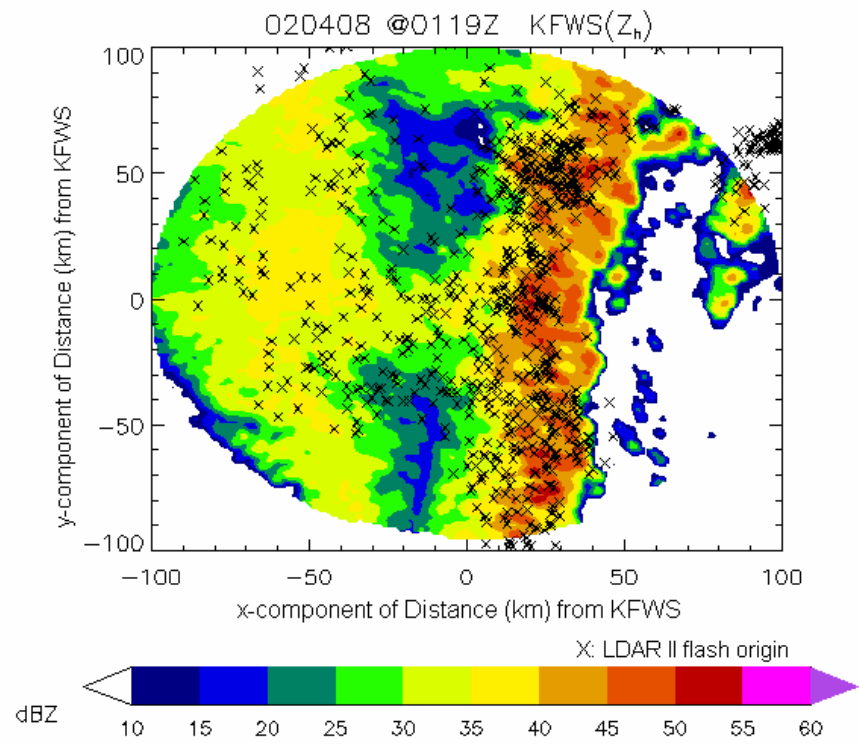


FIG. D.6. Same as Fig. D.3 but for the modified NASA algorithm.

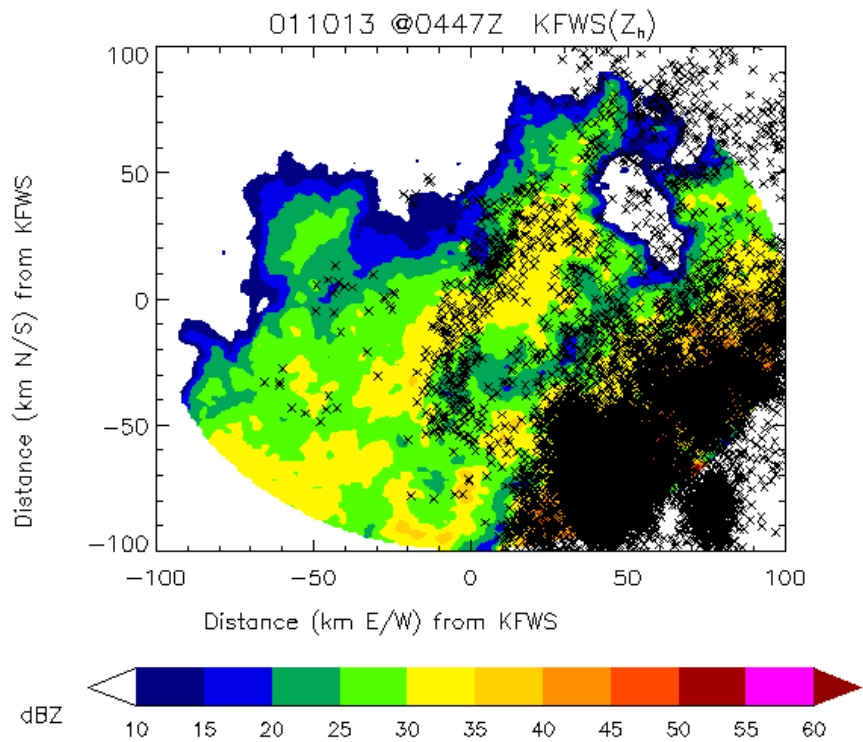


FIG. D.7. LDAR II flash origins at all heights created by the 3.0-km, 0.15-sec, 2.0-sec algorithm overlaid on the 0.5-km radar reflectivity height level of the Dallas/Fort Worth, TX area (KFWS) ( $200 \times 200$  km area) for 4:47 UTC 13 October 2001 MCS. The KFWS radar is located in the center of this image.

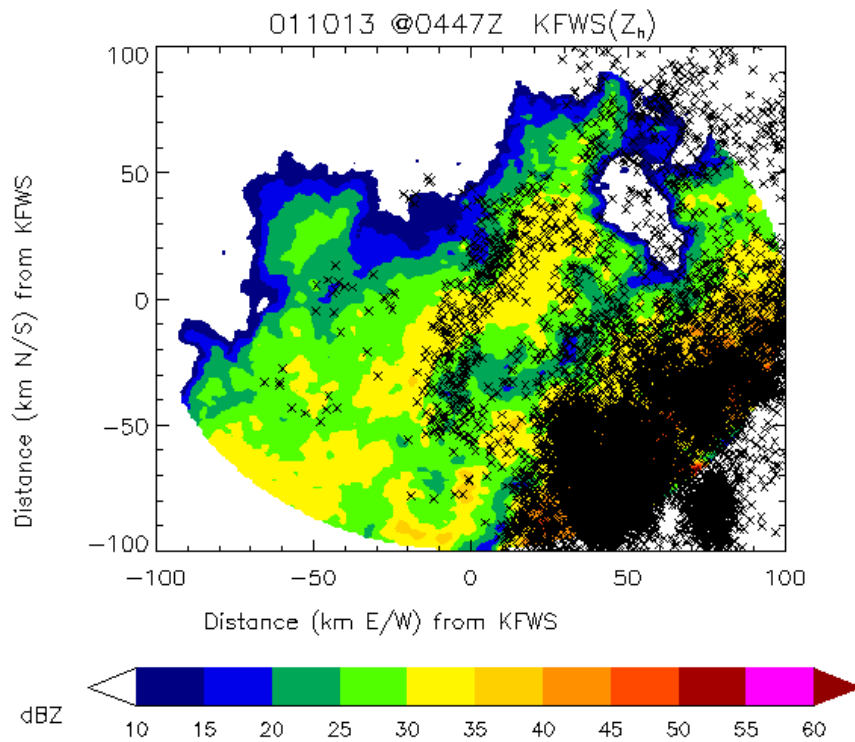


FIG. D.8. Same as Fig. D.7 but for the 3.0-km, 0.30-sec, 2.0-sec algorithm.

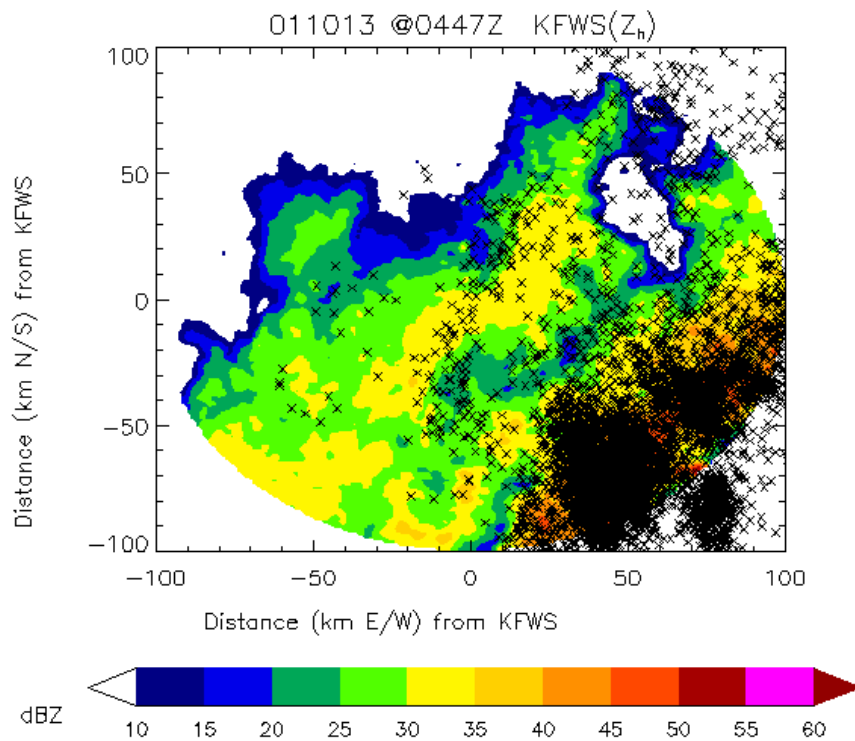


FIG. D.9. Same as Fig. D.7 but for the 5.0-km, 0.15-sec, 2.0-sec algorithm.

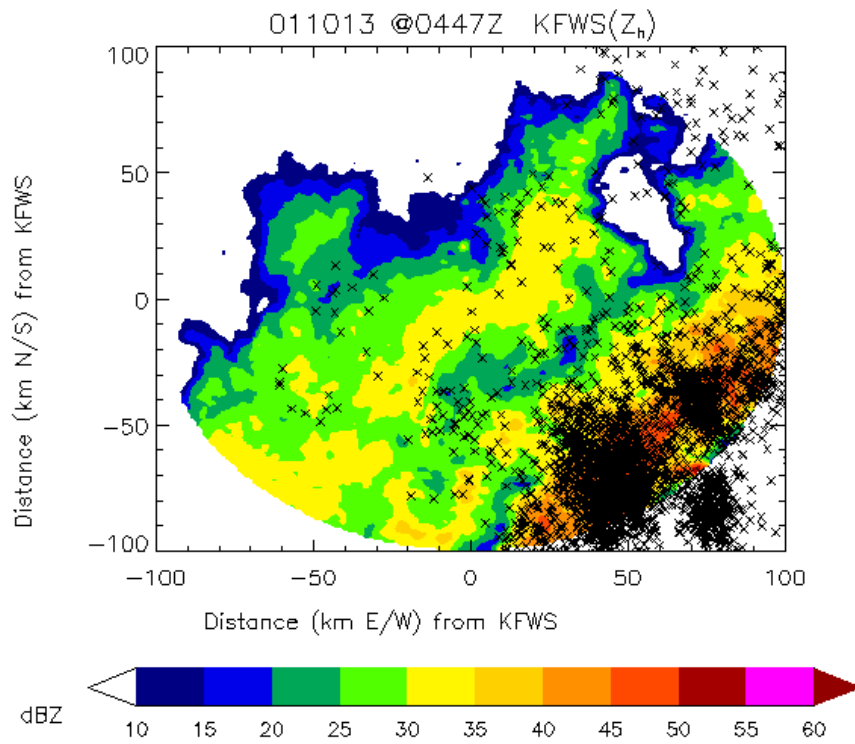


FIG. D.10. Same as Fig. D.7 but for the modified NASA algorithm.

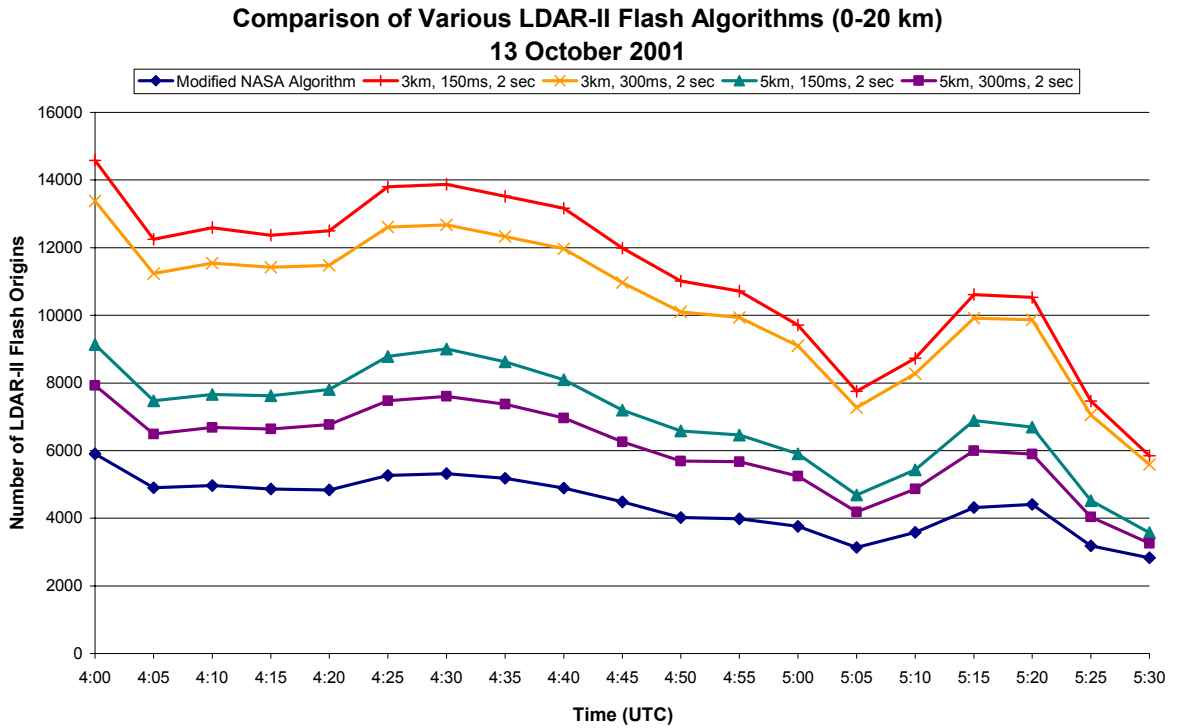


FIG. D.11. Comparison of the temporal variation of various LDAR II flash algorithms (including the 3.0-km, 0.15-sec; 3.0-km, 0.30-sec; 5.0-km, 0.15-sec; 5.0-km, 0.30-sec; and the modified NASA algorithms) at all heights (0 – 20 km) when the 12 – 13 October 2001 MCS was centered within the LDAR II network.

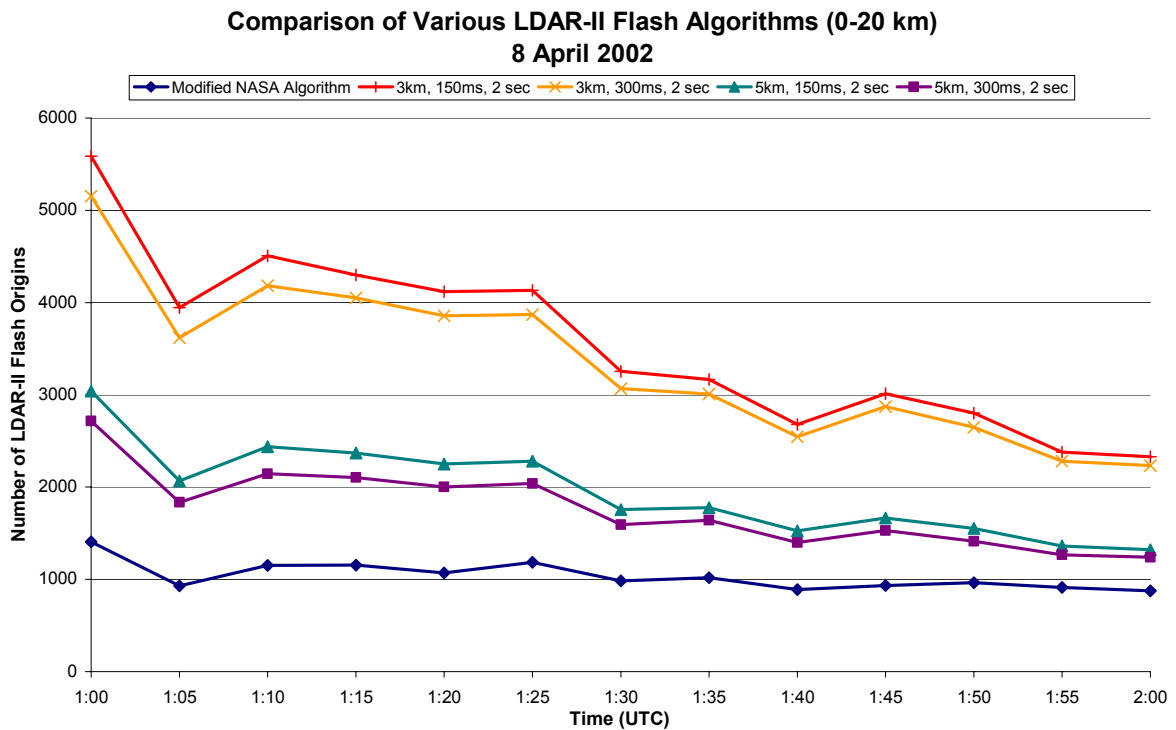


FIG. D.12. Same as Fig. D.11 but for 8 April 2002.

## APPENDIX E: THE TORNADIC CELL

Previous studies have shown noticeable trends in CG lightning flashes associated with severe convective cells. Significant peaks in both total lightning activity and +CG flash rates have been documented to occur prior to tornadogenesis. During tornadogenesis, CG flash rate activity has been found to either be at a local minimum (Keighton et al. 1991; Seimon 1993; Bluestein and MacGorman 1998) or approaching a local minimum (MacGorman et al. 1995; Bluestein and MacGorman 1998). For example, Bluestein and MacGorman (1998) analyzed four tornadic supercell storms in the Texas panhandle region and found that the majority of tornadoes began at or near the time of minimum CG flash rates. +CG flash rates in one of the four storms in Bluestein and MacGorman's (1998) study peaked (at  $\sim 7.4$  flashes  $\text{min}^{-1}$ ) before tornadogenesis. For 10 min while the tornado was on the ground, a rapid decrease in CG lightning activity ( $\sim 0$  flashes  $\text{min}^{-1}$ ) was noted. Seimon (1993), in a study of the F5 Plainfield, Illinois tornado on 28 August 1990, determined that a peak in flash rates ( $\sim 17$  flashes  $\text{min}^{-1}$ ) dominated by +CG flashes (91-100%), followed by a rapid decrease in flash rates, preceded tornadogenesis. During the 20-min period when the tornado was on the ground, flash rates were at a minimum ( $\sim 1-2$  flashes  $\text{min}^{-1}$ ) and dominant CG polarity switched to negative. Various studies have shown that these trends are not universal (e.g. MacGorman and Burgess 1994; Perez et al. 1997; Bluestein and MacGorman 1998; Carey et al. 2003a). MacGorman and Burgess (1994), for example, found that 34 of the 42 tornadoes studied were produced when CG flash rates were either at a minimum or less than  $0.5$  flashes  $\text{min}^{-1}$ . In addition, Carey et al. (2003a) found that the percent of +CG

flashes and +CG flash rates within the supercell storm rapidly increased during the time period when the F4 Spencer tornado was on the ground.

Peaks in intracloud flash rates before severe weather have also been observed in previous studies (e.g. Carey and Rutledge 1998; Williams et al. 1999; Demetriades et al. 2000). Carey et al. (1998) noted a direct correlation between the initial formation of hail aloft and a rapid increase in the IC:CG ratio in a severe hailstorm. Williams et al. (1999) found a rapid increase in IC flash rate (varying in magnitude from 20 to 160 flashes  $\text{min}^{-1}$ ) 1-15 min before the occurrence of severe weather. Demetriades et al. (2000) noted a peak in LDAR II flash rates (as determined by the modified NASA algorithm) ~5-15 min before a severe weather event.

Based on previous results, the convective cell that produced the Decatur, Texas tornado at ~01 UTC in this case study is analyzed to determine if a noticeable peak in CG and total flash rate activity occurs prior to tornadogenesis. NLDN and LDAR II data will be used to analyze CG and total flash rates, respectively.

To determine the trends in CG and IC lightning flash rates associated with the Decatur, Texas tornadic cell, each low-level (0.5 km altitude) radar reflectivity image of the severe cell that produced the tornado from 23:40 UTC 12 October through 01:10 UTC 13 October were first overlaid with 5 min of NLDN-detected CG lightning flashes (beginning with the time of each radar image). The number of +CG and -CG lightning flashes associated with the convective cell were manually counted in each image. This process was repeated for LDAR II flash origins (determined using the 5.0-km, 0.3-sec algorithm). The resulting CG and LDAR II flash data were then entered into Excel and graphed.

Results indicate a noticeable increase in NLDN-detected CG lightning activity ~20-25 min prior to tornadogenesis (Fig. E.1). Total CG flash rate increases from ~4.8 flashes  $\text{min}^{-1}$  to ~18.8 flashes  $\text{min}^{-1}$  (the maximum flash rate observed) in 20 min (Fig. E.1). The flash rate then decreases from its maximum value to 4.6 flashes  $\text{min}^{-1}$  (at 01 UTC, the time of tornado occurrence) in 20-25 min, and then the flash rate continues to decrease to a local minimum value of 1.8 flashes  $\text{min}^{-1}$  at approximately 01:07:30 UTC. CG flash rates are dominated by negative polarity, with an average of 13.2% +CGs produced throughout the period. At the time of peak CG flash rates, the percent of +CGs actually decreases to 7.44%. Trends show an overall slight decrease in positive CG percentage throughout the time period, but this decrease is not significant.

Figure E.2 compares the NLDN-detected CG flash rate trend to the trend in LDAR II flash origin rates. A peak in LDAR II flash rates also occurs ~20-25 min prior to tornadogenesis. An increase in total LDAR II flash rates from ~404.8 flashes  $\text{min}^{-1}$  to ~902.6 flashes  $\text{min}^{-1}$  (the peak flash rate observed) occurs over a 20 min period. Flash rates then begin to significantly decrease for 20-25 min to 371.2 flashes  $\text{min}^{-1}$  at the time of tornadogenesis. These flash rates continue to decrease to a local minimum of 203.6 flashes  $\text{min}^{-1}$  at 1:07:30 UTC.

Although not all tornadic convective cells experience a peak in lightning activity prior to tornadogenesis, the cell associated with the Decatur, Texas tornado did experience a peak in both NLDN-detected CG lightning activity (dominated by negative polarity) and LDAR II flash origin activity 20-25 min prior to tornadogenesis. The flash rates in this study represent relative values. The flash algorithm used to partition LDAR II source data, for example, produces the largest flash rates among the five algorithms tested in this research (for more

information, please see Appendix D). In fact, flash rates for this algorithm outnumbered the modified NASA algorithm (the algorithm that produced the lowest flash rates) by a factor of five. Since all algorithms tested in this study showed the same general temporal trends (Appendix D), the same characteristic peak in LDAR II flash origin activity prior to tornadogenesis would result from using any one of the other algorithms to group sources into flashes. Although this appendix is not related to the key objectives of this research, the occurrence of a tornado within range of the KFWS radar and LDAR II network provides a unique opportunity to explore total lightning characteristics within a tornadic cell and document the results for future studies.

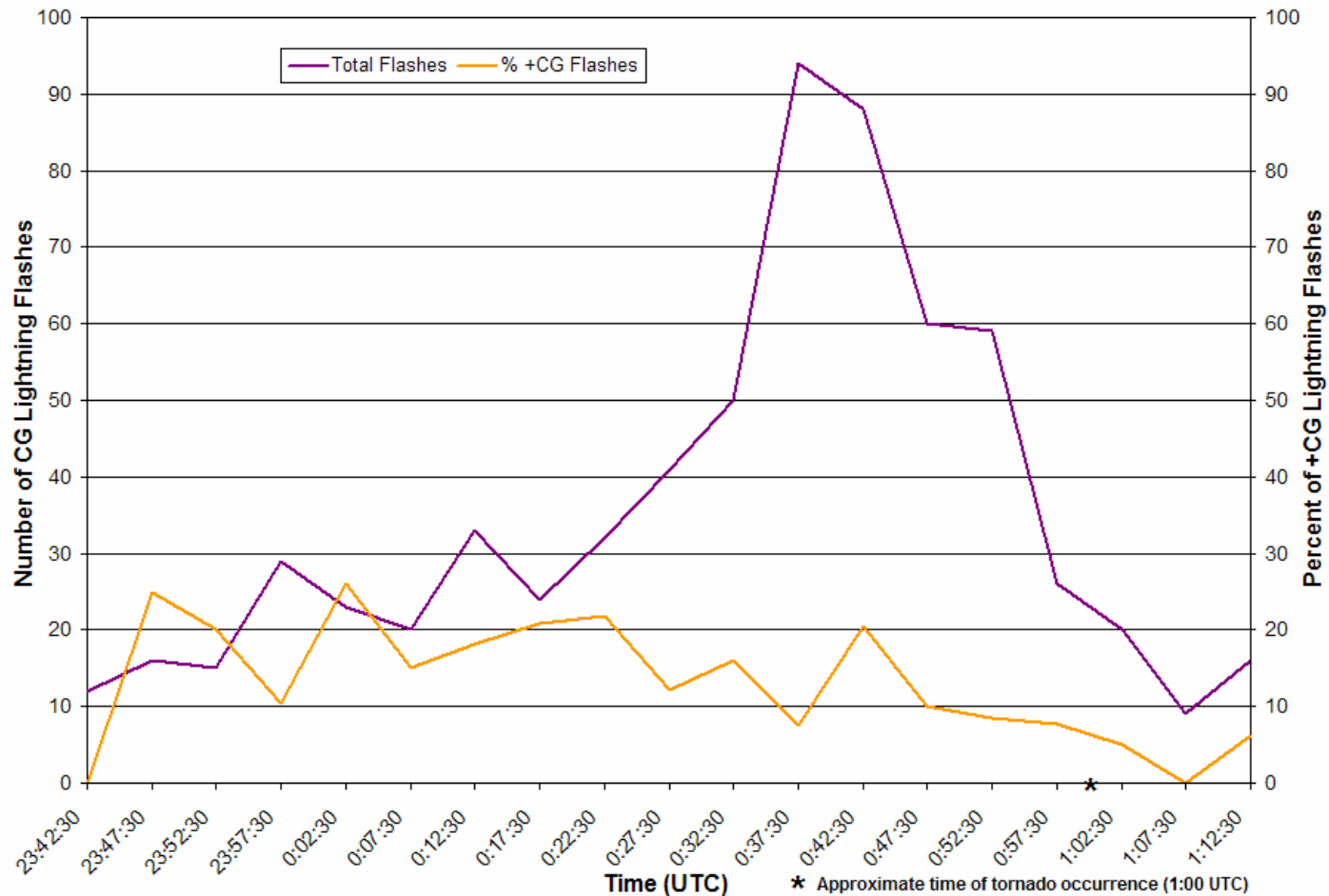


FIG. E.1. CG lightning flash trend (violet line) and the percent of +CGs (orange line) for the Decatur, Texas tornadic cell from 23:40 UTC 12 to 1:15 UTC 13 October 2001. Time (along the x-axis) is the midpoint of the 5 min increments of NLDN data analyzed for each reflectivity image. The primary y-axis represents the number of CG lightning flashes occurring per 5 min, and the secondary y-axis is the percent of +CGs produced during a given 5-min interval. The Decatur, TX tornado was produced at approximately 01 UTC (as marked with an asterisk).

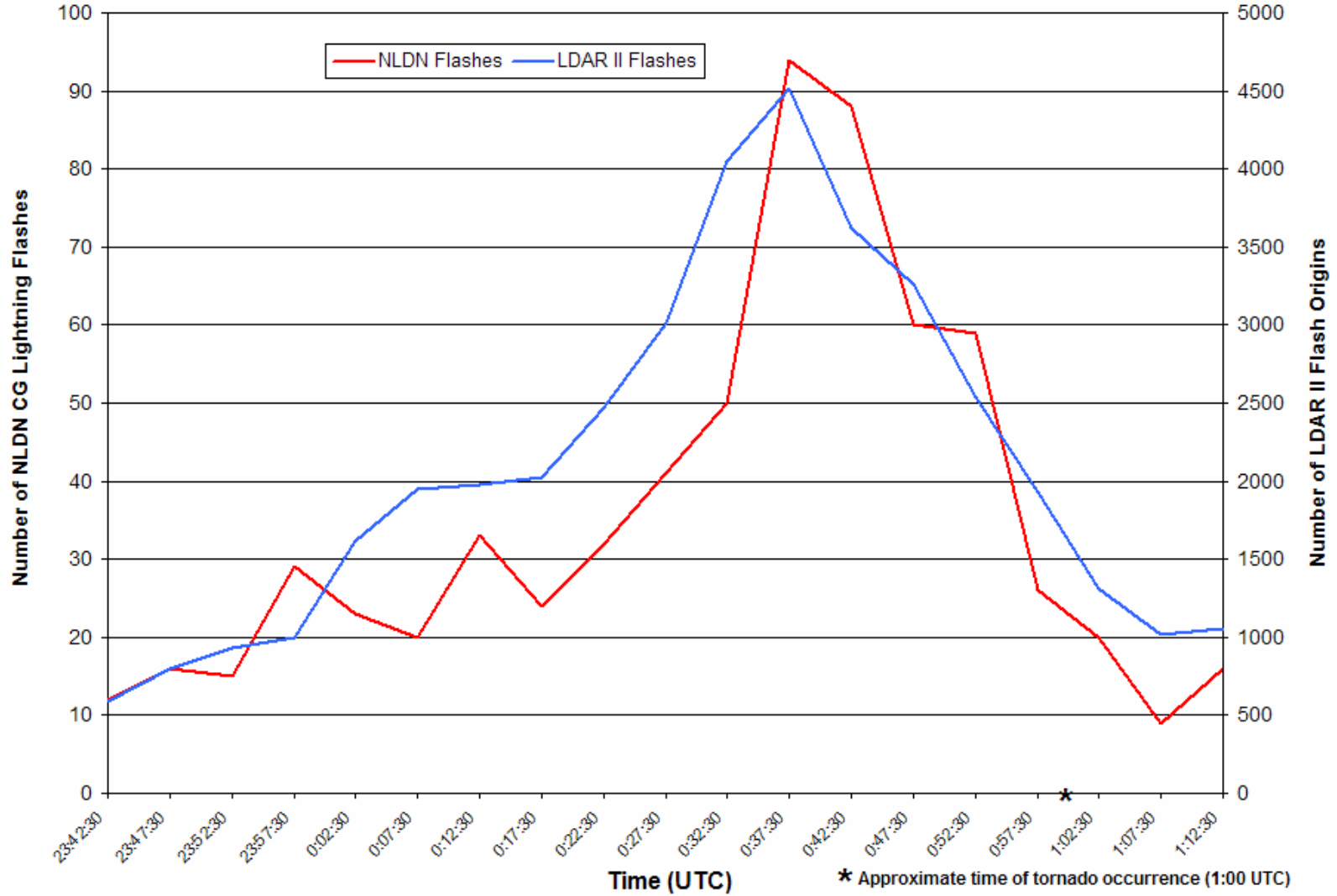


FIG. E.2. Same as Fig. E.1, except the secondary y-axis represents the number of LDAR II flash origins (blue line) produced during a given 5-min time interval, and the number of CG flashes is plotted in red.